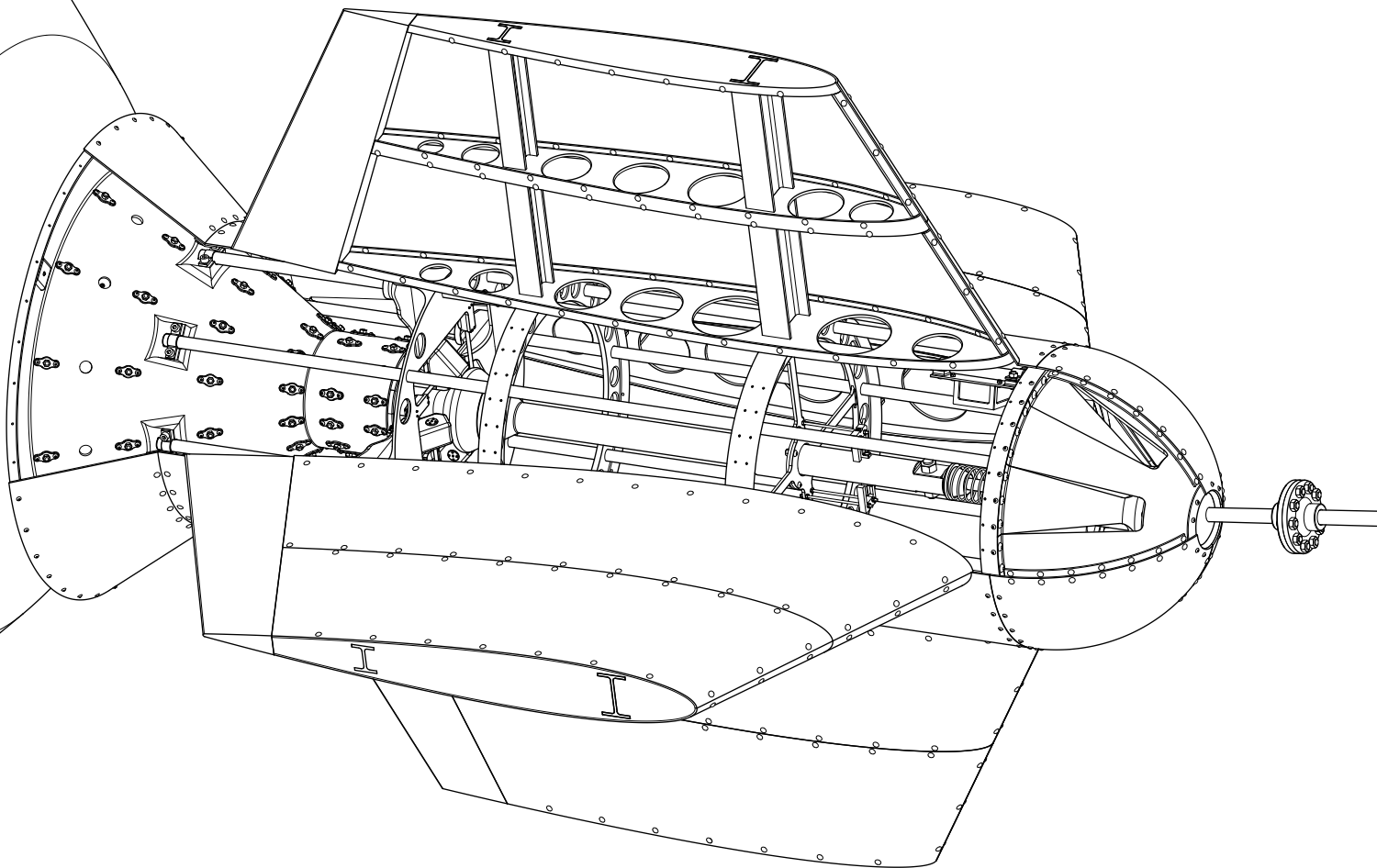


ICARUS

In-Air Capturing Apparatus for Recovering
Unpropelled Stages

MSc Thesis Aerospace Engineering
Briek Luyten



ICARUS

In-Air Capturing Apparatus for Recovering Unpropelled Stages

by

Briek Luyten

to obtain the degree of Master of Science
at the Delft University of Technology,
to be defended publicly on Tuesday September 10, 2024.

Course code: AE5822 (new programme)
Project duration: November 27, 2023 – August 12, 2024
Thesis committee: Dr. A. Menicucci, TU Delft, committee chair
Ir. B. T. C. Zandbergen, TU Delft, supervisor
Ir. S. Singh, DLR, supervisor
Dr. P. P. Sundaramoorthy, TU Delft, external examiner

This thesis is confidential and cannot be made public until April 1, 2025.

Cover: Cutaway Drawing of an Aerodynamically Controlled Capturing
Device Attached to the Nose of a Reusable Launch Vehicle.

An electronic version of this thesis is available at <http://repository.tudelft.nl/>.



Preface

It goes without saying that this work would not have been possible without the support, assistance, and presence of a host of people. In particular, I would like to thank my supervisors at DLR and TU Delft, who provided me with all the freedom and independence I could wish for, while sharing their insights at key moments. By extension, I'm grateful to everyone who found time amidst their own busy schedules to provide much-appreciated feedback and advice concerning all aspects of this thesis - be it its general direction, illustration style, or preface length.

Furthermore, I'm indebted to those who helped make Bremen a second home from home. In particular, my fellow students at DLR, who were always down for a chat when languor troubled our vision, and progress was slow. These rejuvenating exchanges never failed to reinvigorate Monday mornings and Friday afternoons. In general, I'm deeply appreciative for everyone at SART for creating a pleasant and welcoming work environment, and for their suspension of disbelief regarding the importance and value of this work.

Finally, and foremostly, to those manning the parapets of Ithaca while I was away: thank you for keeping my Lighthouse ablaze, and being my reason to come back home.

"What is that feeling when you're driving away from people and they recede on the plain till you see their specks dispersing? - it's the too-huge world vaulting us, and it's good-by. But we lean forward to the next crazy venture beneath the skies." - J. Kerouac

*Briek Luyten
Sint-Martens-Latem, August 2024*

Contents

Preface	iii
Contents	viii
List of Figures	xii
List of Tables	xiv
Nomenclature	xv
Abstract	xix
1 Introduction	1
2 Background	5
2.1 In-Air Capturing	5
2.1.1 Mission Scenario	5
2.1.2 Reference Vehicles	6
2.1.3 Dynamic Simulink Tool	7
2.2 Aerodynamically Controlled Capturing Device	8
2.2.1 Aerodynamic Shell Definition	8
2.2.2 Previous Electromechanical Design	10
3 Towing System	13
3.1 Requirements	13
3.2 Towing Model	14
3.2.1 Requirements	14
3.2.2 Aerodynamically Controlled Capturing Device	16
3.2.3 Tether	17
3.2.4 Reusable Launch Vehicle	19
3.2.5 Towing Aircraft	19
3.2.6 Wake	22
3.2.7 Assumptions	22
3.2.8 Outputs	24
3.2.9 Verification	26
3.3 ACCD Design Space	28
3.3.1 Mass	28
3.3.2 Centre of Gravity	28
3.3.3 Pitch Control Deflection	29
3.3.4 Tether Properties	30
3.4 Extreme Towing Loads	30
3.4.1 Sensitivity Analysis	30
3.4.2 Extreme Operating Points	32
3.5 Conclusion	33
4 Relative Navigation	35
4.1 Requirements and Risks	35
4.2 Sensor System	36
4.2.1 Background	37
4.2.2 Proposed Solution	38
4.3 VisNav Model	39
4.3.1 Requirements	39
4.3.2 Sensor Configuration	40

4.3.3	Beacon Configuration	41
4.3.4	Visibility Conditions	43
4.3.5	Sensor Image Projection	45
4.3.6	Assumptions	47
4.3.7	Outputs	48
4.3.8	Verification	49
4.4	VisNav Configuration Comparison	51
4.4.1	Rim-Mounted Beacons	52
4.4.2	Cone-Mounted Beacons	53
4.4.3	Final Configuration	54
4.5	Conclusion	55
5	Avionics and Power System	57
5.1	Requirements and Risks	57
5.2	Operational Modes	58
5.2.1	Homing Mode	58
5.2.2	Towing Mode	58
5.2.3	Release Mode	60
5.3	Avionics	60
5.3.1	On-Board Computer	61
5.3.2	Navigation Sensors	61
5.3.3	Communication Module	62
5.3.4	Control Actuators	62
5.3.5	Locking Actuators	63
5.3.6	Docking Sensors	66
5.4	Power System	68
5.5	Mounting System	68
5.6	Conclusion	69
6	Mechanical Design	71
6.1	Requirements and Risks	71
6.1.1	Structural Requirements	72
6.1.2	Docking Requirements	73
6.1.3	Release Requirements	74
6.1.4	Risks	75
6.2	Background	75
6.2.1	Docking Phases	75
6.2.2	Docking Systems	76
6.3	Tether Attachment	76
6.3.1	Functional Trade-Off	76
6.3.2	Design	78
6.3.3	Analysis	78
6.4	Structural Frame	79
6.4.1	Load-Bearing Frame	79
6.4.2	Wing Structure	81
6.4.3	Analysis	82
6.5	Shock-Absorbing Assembly	84
6.5.1	Industrial Shock Absorber	84
6.5.2	Design	85
6.5.3	Analysis	87
6.6	Docking Mechanism	88
6.6.1	RLV Boom	89
6.6.2	Locking Mechanism	90
6.6.3	Guiding Cone	93
6.7	Release System	94
6.8	Conclusion	95

7	Design Overview and Reflection	97
7.1	Vehicle Properties	97
7.1.1	Breakdown Analysis	97
7.1.2	Towing Behaviour	99
7.1.3	Sensitivity Analysis	100
7.2	VisNav Performance	102
7.3	Requirement Compliance	104
7.4	Conclusion	104
8	Conclusion	107
9	Recommendations	109
9.1	Complementary Analyses	109
9.2	Prototyping	110
9.3	Aerodynamic Redesign	110
	References	111
A	Requirements and Risks	125
A.1	Design Requirements	125
A.1.1	System	126
A.1.2	Structural	126
A.1.3	Docking	127
A.1.4	Release	127
A.1.5	Towing	127
A.1.6	Power	127
A.1.7	Avionics	128
A.1.8	Detection	128
A.1.9	Categorization of Subsystem Requirements	128
A.2	Model Requirements	129
A.2.1	Towing Model	129
A.2.2	VisNav Model	130
A.3	Risks	130
A.3.1	Detection	130
A.3.2	Approach	131
A.3.3	Docking	131
A.3.4	Towing	131
A.3.5	Release	132
A.3.6	Risk Map	132
B	Launch Vehicle Reusability	135
C	Bills of Materials	139
D	Atmospheric Model	145
E	Aerodynamic Data	147
F	Rigid Tether Model	151
G	Reference Frames	153
H	TA Thrust Model	155
I	Tether Design Space	157
I.1	Tether Length	157
I.2	Tether Diameter	157
J	Relative Navigation Paper	159
K	Signal Blocking Solution	181
L	Reference Approach Trajectory	185

M Commercial Components	189
M.1 On-Board Computer	189
M.2 GNSS Module	190
M.3 Communication Module	191
M.4 Actuators	191
M.5 Docking Sensors	192
M.6 Industrial Shock Absorber	192
M.7 Linear Bearing	193
N Nominal Docking Sequence	195
O Technical Drawings	199

List of Figures

All figures in this work are created by, and property of the author. Where inspiration or data was taken from other work, appropriate sources are provided in the caption of the figure.

1.1	Schematic of the In-Air Capturing (IAC) Procedure for Recovering Reusable Launch Vehicles (RLVs) with a Towing Aircraft (TA)	1
1.2	Schematic Depiction of the Aerodynamically Controlled Capturing Device (ACCD), in Final Approach with the RLV	2
1.3	Flow Diagram of the Overall Thesis Structure, in Relation to High-Level System Requirements and Design Metrics	4
2.1	Overview of a Typical IAC Mission Scenario	6
2.2	Schematic of the Airbus A340-600 Reference TA	6
2.3	Schematic of the RLVC4-III-B Three-Stage-to-Orbit (3STO) Launch Vehicle	7
2.4	Trajectories and Attitudes of the TA and RLV During a Reference Formation Flight	8
2.5	Schematic Definition of the ACCD's Aerodynamic Shell	9
2.6	Definition of the ACCD's NACA0012 Wing Root and Wing Tip Profiles	9
2.7	Comparison of Three-Degrees-of-Freedom (3DoF) Control for Two Cruciform ACCD Configurations	10
2.8	Schematic Cross-Section of Heide's ACCD Design, with a Definition of Major Functional Subassemblies	11
3.1	Illustration of the Towing System during Formation Flight and Tow-Back	13
3.2	Flowchart of the Towing Model, and Integration into the Overall Systems Engineering Approach	15
3.3	Free-Body Diagram of the ACCD, as Towed by the TA	16
3.4	Flowchart for Iteratively Solving the ACCD's Angle of Attack (AoA)	17
3.5	Definition of the Catenary Tether Model	18
3.6	Definition of Non-Accelerating and Excess-Thrust Towing Conditions	19
3.7	Free-Body Diagram of the TA	20
3.8	Free-Body Diagram of the Towing System under Excess-Thrust Conditions	21
3.9	Definition of the Wake Stay-Out Zone Compared to CFD (Computational Fluid Dynamics)-Characterized Airflow Velocity Data	22
3.10	Example of a Towing Position Plot During Formation Flight	24
3.11	Example of an ACCD Free-Body Diagram During Formation Flight	25
3.12	Example of a Towing Position Plot During Tow-Back	25
3.13	Example of an RLV-ACCD Free-Body Diagram During Tow-Back	26
3.14	Definition of Positive Pitch Deflection	26
3.15	Comparison of Simulink and Steady-State Towing Model Outputs	27
3.16	Convergence of the Simulink Transient Solution to its Steady-State Conditions and the Towing Model Results	27
3.17	Sensitivity of the ACCD's Towing Position to its Total Mass	28
3.18	Sensitivity of the ACCD's Towing Position to the Location of its CoG	29
3.19	Sensitivity of the ACCD's Towing Position to its Pitch Control Deflection	29
3.20	Characterization of the Relevant ACCD Design Space	30
3.21	Sensitivity of Towing Loads to the RLV's Inertial Properties	31
3.22	Definition of the Zone of Operations for RLV Towing	31
3.23	Sensitivity of Excess-Thrust Towing Loads to Environmental Parameters	32
4.1	Schematic Comparison of Sensor Solutions for Relative Navigation	37
4.2	Schematic Working Principle of an Electro-Optical Grid Reference System	38

4.3	Flowchart of the VisNav Model, and Integration into the Overall Systems Engineering Approach	40
4.4	Definition of the VisNav Model Reference System and Variables	41
4.5	Comparison of Two Main VisNav Beacon Mounting Configurations	41
4.6	Schematic Depiction of the Directional Emittance Pattern of a Lambertian Emitter	43
4.7	Normalized Directional Signal Intensity and Range for a Lambertian Beacon Model	43
4.8	Schematic Depiction of Visibility Condition c_{i1} , Concerning the Sensor's Field of View (FoV)	44
4.9	Schematic Depiction of Visibility Condition c_{i2} , Concerning Signal Blocking	45
4.10	Projection of a Three-Dimensional (3D) Point \vec{P}_0 onto the Sensor Plane	46
4.11	Comparison of Imagery Behaviour Before and After Normalization	46
4.12	Examples of Two-Dimensional (2D) VisNav Position Studies	48
4.13	Schematic Overview of the Integration of the VisNav Model into a Relative Navigation Simulator	49
4.14	Visualization of a Beacon Mounting Configuration for Model Verification	50
4.15	Example of Visual Verification of the Signal Blocking Detection Algorithm	50
4.16	Example of a Sensor PoV Image for VisNav Model Verification	51
4.17	Comparison of Approach Corridors at $Z = 0 m$, for a Low and High Sensor Mounting Angle μ , with Beacon Configuration 1	52
4.18	Comparison of Approach Corridors at $Z = 0 m$, for a Low and High Sensor Mounting Angle μ , with Beacon Configuration 2	53
4.19	Comparison of Approach Corridors at $X = 50 m$, for a Small and Large Number of Beacons N Mounted in Configuration 2	53
4.20	Comparison of Approach Corridors at $Z = 0 m$, for a Small and Large Beacon Mounting Diameter d_i , with Beacon Configuration 2	54
4.21	Aft View of the Proposed Representative Beacon Configuration	55
5.1	Geographic Overview of the RLV Tow-Back Trajectory	59
5.2	Sensitivity of the Tow-Back Duration to Flight Altitude and Mach Number	59
5.3	Schematic Cross-Section of the ACCD's Electronic Design, with Major Subsystems Highlighted	60
5.4	3D View of a Preliminary VisNav Beacon Design	62
5.5	Schematic Cross-Section of Control Surface Actuation	63
5.6	Comparison of Two Main Locking Actuation Configurations, with Corresponding Limiting Load Scenarios	64
5.7	Minimal Duration of a 100 mm Stroke Deployment as a Function of Peak Actuator Velocity and Acceleration	65
5.8	Schematic Depiction of a Tripartite Docking Sensor Solution	66
5.9	Schematic Depiction of Boom Thickness Measurement Using Four Acoustic Distance Measuring Sensors	66
5.10	Schematic Depiction of Plunger Sensors Activation	67
5.11	3D Views of the Avionics Mounting Structures	69
6.1	Schematic Cross-Section of the ACCD's Mechanical Design, with Major Subsystems Highlighted	72
6.2	Schematic Overview of the Main Docking Phases	75
6.3	Comparison of Androgynous and Probe-Drogue Docking Systems	76
6.4	Schematic Representation of the Tether Attachment	77
6.5	Comparative Analysis of Equivalent von-Mises Stress in Tether Attachments with Different Internal Radii R_i	77
6.6	Cross-Section of the Tether Attachment Design, at a Peak Deflection of 27.2°	78
6.7	Equivalent von-Mises Stress in the Tether Attachment under an Extreme Towing Load	79
6.8	Maximum Bending and Shear Stress Inside the Load-Bearing Frame as a Function of its Inner Radius	80
6.9	3D View of the Load-Bearing Frame Design, Using Twelve Bars and Three Hoops	81
6.10	Schematic Depiction of a Wing Structure Using a Combination of Ribs and Spars	82
6.11	3D View of the Wing Structure Design	82

6.12	Equivalent von-Mises Stress in the Load-Bearing Frame under an Extreme Towing Load	83
6.13	Equivalent von-Mises Stress in the Wing Structure under an Extreme Aerodynamic Load	84
6.14	3D View of the Shock Absorber Housing Design, and Interface with the Tether Attachment	85
6.15	Cross-Section of the Shock-Absorbing Plunger Design	86
6.16	Minimal Diameter and Mass for Solid and Hollow Shock-Absorbing Plungers, with and without Added Support	86
6.17	Cross-Section of the Shock-Absorbing Assembly Design and its Constituent Components	87
6.18	Equivalent von-Mises Stress in the Shock Absorber Housing under an Extreme Impact Load	88
6.19	Equivalent von-Mises Stress in the Shock Absorber Plunger under an Extreme Impact Load	88
6.20	Schematic Comparison of Different Boom-Locking Solutions	89
6.21	Comparative Analysis of Equivalent von-Mises Stress in RLV Booms with an Additive and Subtractive Design	89
6.22	Side View of the Angled Boom Design	90
6.23	Equivalent von-Mises Stress in the RLV Boom under an Extreme Towing Load	90
6.24	Schematic Depiction of the Locking Mechanism Design and Deployment	91
6.25	3D View of the Locking Mechanism Design with Extended Actuators	92
6.26	Equivalent von-Mises Stress in the Locking Mechanism under an Extreme Towing Load	92
6.27	Cross-Section of the Guiding Cone Design	93
6.28	3D View of the Release System Design	94
6.29	Cross-Section of the Final ACCD Design	95
7.1	Operational Range of the Final ACCD Design During Formation Flight	99
7.2	Steady-State Attitude and Local Tether Angle as a Function of the ACCD's Pitch Control Deflection	100
7.3	Comparison of Subassembly Masses for Three Design Iterations	100
7.4	Comparison of CoG Contributions for Three Design Iterations	101
7.5	Comparison of Three Design Iterations' Safety Factors (SFs) Relative to the Stress Requirement	102
7.6	Comparison of Three Design Iterations' Peak Deformations Relative to the Deformation Requirement	102
7.7	Approach Corridor of the Final VisNav Configuration	103
7.8	Close-Up of the Final VisNav Configuration's Approach Corridor	103
9.1	Example of an Alternative Control Method Used in Automated Aerial Refuelling (AAR)	110
A.1	Categorization of (Sub)system Requirements According to their Feasibility	129
A.2	Pre-Mitigated Risk Map	133
B.1	Schematic Overview of Vertical-Takeoff/Vertical-Landing (VTVL) and Vertical-Takeoff/Horizontal-Landing (VTHL) RLV Recovery Techniques	135
B.2	Two Examples of Wildly Different RLV Recovery Techniques: VTHL FB and VTVL Splash-down	136
B.3	Comparison of the Estimated Inert Mass Ratio and Total First Stage Propellant Mass for Different RLV Recovery Techniques	137
B.4	Comparison of Estimated Recovery Costs for Different RLV Recovery Techniques	137
D.1	Temperature and Pressure Profile as a Function of Mean Sea Level (MSL) Altitude, as Computed with the 1976 US Standard Atmosphere Model	146
D.2	Airflow Velocity as a Function of Mach Number and MSL Altitude, as Computed with the 1976 US Standard Atmosphere Model	146
E.1	ACCD Lift and Drag Coefficients as a Function of AoA and Control Deflection	148
E.2	RLV Lift and Drag Coefficients as a Function of AoA and Control Deflection	148
E.3	ACCD and RLV Pitching Moment Coefficients as a Function of AoA and Control Deflection	149

E.4	TA Lift and Drag Coefficients as a Function of AoA and Control Deflection, for a Diving Configuration	149
E.5	TA Lift and Drag Coefficients as a Function of AoA and Control Deflection, for a Clean Configuration	150
E.6	TA Pitching Moment Coefficients as a Function of AoA and Control Deflection	150
F.1	Free-Body Diagram of a Rigid Link Tether Model	151
F.2	Comparison of Towing Positions Computed with Rigid Link and Catenary Tether Models	152
G.1	Definition of Principal Reference Frames	153
H.1	Combined Peak Thrust of the A340-600 TA, as a Function of Flight Altitude and Airflow Velocity	155
I.1	Sensitivity of the ACCD's Towing Position to the Tether Length	157
I.2	Sensitivity of the ACCD's Towing Position to the Tether Diameter	158
L.1	Relative Position of IAC Vehicles During the Reference RLV Approach, in the ACCD Body Reference Frame	185
L.2	Relative Pitch Attitude of the RLV During its Reference Approach, in the ACCD Body Reference Frame	187
L.3	Visibility of VisNav Beacons During the Reference RLV Approach	187
L.4	Frames from a VisNav Sensor PoV Animation During the Reference RLV Approach	187
M.1	Schematic of the Pixhawk 6X Pro OBC, Interfaced with a Standard Baseboard	189
M.2	Schematic of the DroneCAN H-RTK F9P Rover GNSS Module	190
M.3	Schematic of the Microhard P840 RF Communication Module	191
M.4	Schematic of the ECI-63.20-K4-B00 Control Actuator	191
M.5	Schematic of the LM1247-100-11 Linear Locking Actuator	191
M.6	Schematic of the U300.D50-DPMJ.72N Ultrasonic Distance Measuring Sensor	192
M.7	Schematic of the Omron E3Z-G62 Grooved Photoelectric Sensor	192
M.8	Comparison of Deceleration Profiles of a Number of Typical Energy-Absorbing Solutions	193
M.9	Schematic of the ACE MC6140/MC64150 Industrial Shock Absorber, in an Uncompressed State	193
M.10	Schematic of the Ewellix LBBR 50-2LS/HV6 Linear Ball Bearing	193
N.1	Step 1 of a Nominal Docking Sequence: First Contact Between the RLV Boom and the ACCD's Guiding Cone	195
N.2	Step 2 of a Nominal Docking Sequence: as the RLV Boom Enters the Cylindrical Section of the Guiding Cone, Four Boom Sensors Monitor its Position	196
N.3	Step 3 of a Nominal Docking Sequence: the RLV Boom Interfaces with the Plunger, and the Shock Absorber Starts Compressing and Absorbing Energy	196
N.4	Step 4 of a Nominal Docking Sequence: the Plunger Sensors are Triggered, and the Locking Actuators Engage	197
N.5	Step 5 of a Nominal Docking Sequence: with the Locking Mechanism Engaged, and the Compressive Force of the Shock Absorber, the Entire Assembly is in a Stable, Docked State	197

List of Tables

2.1	Main Characteristics of the Reference TA and RLV	7
2.2	Overview of Parameters Characterizing the IAC Formation Flight	8
3.1	Reference Model Inputs for Generating Exemplary Towing Model Outputs During Formation Flight	24
3.2	Reference Model Inputs for Generating Exemplary Towing Model Outputs During Tow-Back	25
3.3	Reference Model Inputs for Simulink Verification	26
3.4	Definition of the Extreme RLV Tow-Back Operating Points	33
3.5	Axial and Radial Towing Forces Corresponding to the Extreme RLV Tow-Back Operating Points	33
3.6	Compliance of the Towing Model to its Model Requirements	34
4.1	Comparison of Computer Vision and Electro-Optical Grid Reference Systems for Use in IAC Relative Navigation	38
4.2	Reference Model Inputs for Generating Exemplary VisNav Model Outputs	49
4.3	Overview of Beacon Visibility as a Function of Beacon Number i	51
4.4	Reference Model Inputs for VisNav Configuration Comparisons	52
4.5	Characteristics of the Proposed Representative VisNav Beacon and Sensor Configuration	54
4.6	Compliance of the VisNav Model to its Model Requirements	55
5.1	Characteristics and Features of the Pixhawk 6X Pro On-Board Computer (OBC)	61
5.2	Characteristics of the DroneCAN H-RTK F9P Rover GNSS (Global Navigation Satellite System) Module	61
5.3	Characteristics of the Microhard P840 Radio-Frequency (RF) Communication Module	62
5.4	Characteristics of the ECI-63.20-K4-B00 Control Actuator	63
5.5	Characteristics of the LM1247-100-11 Linear Locking Actuator	65
5.6	Characteristics of the U300.D50-DPMJ.72N Ultrasonic Distance Measuring Sensor	66
5.7	Characteristics of the Omron E3Z-G62 Grooved Photoelectric Sensor	67
5.8	SWaP Footprint of Electronic Subsystems, with Cumulative Power and Energy Requirements	68
5.9	Energy, Mass and Volume Estimate of a Lithium-Ion Battery System	68
6.1	Characteristics of the MC64100 and MC64150 Industrial Shock Absorbers	85
7.1	Comparison of Design Loads used by Heide et al. and by this Work (ICARUS)	97
7.2	Comparative Mass, Stress, and Deformation Breakdown for Three ACCD Design Iterations	98
7.3	Model Inputs for the Towing Analysis of the Final ACCD Design	99
7.4	Characteristics of the Final VisNav Configuration	103
7.5	Compliance of the Subsystem Design Requirements	104
A.1	Definition of the Criticality Keyword in Design Requirement Identifiers	125
A.2	Definition of the (Sub)system Keyword in Design Requirement Identifiers	126
A.3	Definition of the Operational Phase Keyword in Risk Identifiers	130
A.4	Definition of Degrees of Likelihood for Risk Mapping	132
A.5	Definition of Degrees of Severity for Risk Mapping	132
C.1	Mass Breakdown of the ACCD's Release System	139
C.2	Bill of Materials (BoM) for ACCD Design Iteration 0	140
C.3	BoM for ACCD Design Iteration 1	140
C.4	BoM for the Final ACCD Design Iteration	141

D.1	Data Points for the 1976 US Standard Atmospheric Model	145
E.1	Reference Geometry for the Aerodynamic Coefficients of IAC Vehicles	147
L.1	Relative Position and Attitude Data for the Reference RLV Approach, in the ACCD Body Reference Frame	186
M.1	Features of the Pixhawk 6X Pro OBC	190
M.2	Features of the DroneCAN H-RTK F9P Rover GNSS Module	190
M.3	Characteristics of the Microhard P840 RF Communication Module	191

Nomenclature

Abbreviations

Abbreviation	Definition
3STO	Three-Stage-to-Orbit
AAR	Automated Aerial Refuelling
ABS	Acrylonitrile Butadiene Styrene
ACCD	Aerodynamically Controlled Capturing Device
AoA	Angle of Attack
BoM	Bill of Materials
CAD	Computer-Aided Design
CCD	Charge-Coupled Device
CFD	Computational Fluid Dynamics
CoG	Centre of Gravity
COTS	Commercial-off-the-Shelf
DC	Direct Current
DLR	German Aerospace Centre (Deutsches Zentrum für Luft- und Raumfahrt)
DRL	Downrange Landing
ELV	Expendable Launch Vehicle
EMF	Electromotive Force
ENTRAIN	European Next Reusable Ariane
FALCon	Formation Flight for In-Air Launcher First Stage Capturing Demonstration
FB	Fly-Back
FEM	Finite Element Method
FoV	Field of View
FPA	Flight Path Angle
GNC	Guidance, Navigation and Control
GNSS	Global Navigation Satellite System
GPU	Graphical Processing Unit
GTO	Geostationary Transfer Orbit
HiSST	High-Speed Vehicle Science and Technology Conference
IAC	In-Air Capturing
ICARUS	In-Air Capturing Apparatus for Recovering Unpropelled Stages
IMU	Inertial Measurement Unit
INS	Inertial Navigation System
I/O	Input-Output
IR	Infrared
L/D	Lift-to-Drag Ratio
LED	Light-Emitting Diode
LFBB	Liquid Fly-Back Booster
LH2	Liquid Hydrogen
LiDAR	Light Detection and Ranging
LoS	Line of Sight
LOX	Liquid Oxygen
LVLH	Local-Vertical, Local-Horizontal (Reference Frame)
MAR	Mid-Air Recovery
MIT	Massachusetts Institute of Technology
MRP	Moment Reference Point
MSL	Mean Sea Level

Abbreviation	Definition
nD	n -Dimensional
nDoF	n Degrees of Freedom
OBC	On-Board Computer
PMMA	Polymethyl Methacrylate
PoV	Point of View
PSD	Position-Sensitive Device
RAM	Random-Access Memory
RF	Radio-Frequency
RLV	Reusable Launch Vehicle
RTLS	Return-to-Launch-Site
SART	DLR's Department of Space Launcher Systems Analysis (Systemanalyse Raumtransport)
SF	Safety Factor
SLME	SpaceLiner Main Engine
SRAM	Static RAM
SRB	Solid Rocket Booster
STS	Space Transportation System
SWaP	Size, Weight and Power
TA	Towing Aircraft
TPS	Thermal Protection System
TRL	Technology Readiness Level
UAV	Unmanned Aerial Vehicle
UHMWPE	Ultra-High-Molecular-Weight Polyethylene
VKI	von Karman Institute for Fluid Dynamics
VTHL	Vertical-Takeoff/Horizontal-Landing
VTVL	Vertical-Takeoff/Vertical-Landing

Symbols

Symbol	Definition	Unit
a	Catenary Parameter	[m]
A	Area	[m^2]
c	Beacon Visibility Condition	[-]
C_A	Axial Aerodynamic Coefficient	[-]
C_D	Drag Coefficient	[-]
C_L	Lift Coefficient	[-]
C_M	Pitching Moment Coefficient	[-]
C_N	Normal Aerodynamic Coefficient	[-]
d	Diameter	[m]
d_f	Flight Distance	[m]
D	Drag	[N]
e	Distance Between Vehicle Nose and CoG	[m]
E	Modulus of Elasticity	[Pa]
f	Distance Between Vehicle CoG and MRP	[m]
F	Force	[N]
\vec{f}	Vector Function	[-]
FoV	Field of View Half Angle	[$^\circ$]
h	Cone Surface Parametric Variable	[-]
H	Altitude	[m]
$[I]$	Inertia Tensor	[-]
I_c	Second Moment of Area	[m^4]
k	Gain	[-]

Symbol	Definition	Unit
K_e	Back-EMF Constant	$[Vs/m]$
l	Length	$[m]$
lat	Latitude	$[^\circ]$
lon	Longitude	$[^\circ]$
L	Lift	$[N]$
m	Mass	$[kg]$
M	Moment	$[Nm]$
Ma	Mach Number	$[-]$
\vec{n}	Normal/Pointing Vector	$[-]$
N	Number of Beacons	$[-]$
$\mathcal{N}(\mu, \sigma)$	Normal Distribution with Expected Value μ and Standard Deviation σ	$[-]$
p	Pressure	$[Pa]$
\vec{p}	Direction Vector	$[-]$
P	Power	$[W]$
\vec{P}	Position Vector	$[-]$
Q	First Moment of Area	$[m^3]$
r	Beacon Range	$[m]$
R	Radius	$[m]$
s	LoS Parametric Variable	$[-]$
S	Actuator Stroke	$[m]$
\dot{S}_m	Peak Actuator Velocity	$[m/s]$
\ddot{S}_m	Peak Actuator Acceleration	$[m/s^2]$
t	Time	$[s]$
T	Temperature	$[K]$
u	Deformation	$[m]$
U	Voltage	$[V]$
v_i	Beacon Visibility	$[-]$
V	Velocity	$[m/s]$
w	Width/Thickness	$[m]$
W	Weight	$[N]$
x	X-Coordinate	$[m]$
\ddot{x}	X-Component of Acceleration	$[m/s^2]$
y	Y-Coordinate	$[m]$
\ddot{y}	Y-Component of Acceleration	$[m/s^2]$
z	Z-Coordinate	$[m]$
α	Angle of Attack	$[^\circ]$
β	Beacon Clock Angle	$[^\circ]$
γ	Flight Path Angle	$[^\circ]$
δ	Pitch Control Surface Deflection	$[^\circ]$
Δ	Difference	$[-]$
ΔK	Collision Energy	$[J]$
ϵ	Threshold	$[-]$
ζ	Atmospheric Temperature Lapse Rate	$[K/m]$
θ	Tether Angle	$[^\circ]$
θ_o	Joint Opening Angle	$[^\circ]$
θ_f	Joint Freedom Angle	$[^\circ]$
Θ	Angle of Emittance	$[^\circ]$
ι	Beacon Intensity	$[W/m^2]$
λ	Docking Cone Half Angle	$[^\circ]$
μ	Sensor Mounting Angle	$[^\circ]$
ξ	Beam Effective Length Factor	$[-]$
ρ	Density	$[kg/m^3]$
σ	Stress	$[Pa]$

Symbol	Definition	Unit
τ	Shear Stress	[Pa]
ϕ	Pitch Angle	[°]
ψ	Cone Surface Parametric Variable	[-]
Ω	Angular Velocity	[rad/s]

Constants

Symbol and Value	Definition
$g = 9.81 \text{ m/s}^2$	Earth's Gravitational Acceleration at Sea Level
$R_{air} = 287.052 \text{ J/kgK}$	Specific Gas Constant of Air
$R_{\oplus} = 6371 \text{ km}$	Average Radius of the Earth
$\kappa_{air} = 1.4$	Isentropic Expansion Coefficient of Air

Abstract

With the advent of Reusable Launch Vehicles (RLVs) on the European launch market, the German Aerospace Centre (DLR)'s In-Air Capturing (IAC) recovery technique promises a competitive reduction in launch costs. Central to this IAC procedure is the Aerodynamically Controlled Capturing Device (ACCD), which is deployed from a Towing Aircraft (TA) by means of a tether. It intercepts a returning RLV, and provides a structural interface between the TA and RLV during tow-back. Once in the vicinity of a landing site, the ACCD releases the towing connection, and the RLV lands autonomously. Whereas the aerodynamic shell of the ACCD has been defined and studied in the past, an in-depth exploration of its electromechanical design space has not been performed previously. This work proposes a systems engineering approach to fill the corresponding design gap, based on the definition of key requirements and risks characterizing the ACCD's functionalities, and its operational environment.

First, the behaviour of the ACCD as part of a larger towing system is analysed. For this, a two-dimensional (2D), quasi-steady-state Towing Model is developed, enabling a swift exploration of the ACCD's design space, as well as a preliminary estimation of extreme tow-back loads. This Towing Model shows that the ACCD's towing position relative to the TA is highly sensitive to the ACCD's Centre of Gravity (CoG); in order to stay clear of the TA's disturbing wake zone, a maximum allowable CoG position of 1 m behind the vehicle's nose is defined. Additionally, a significant pitch control authority is demonstrated, indicating substantial manoeuvrability. Finally, a study of extreme tow-back conditions results in the definition of a 300 kN axial towing design load - representing a 72% increase compared to previous estimates.

Next, the ACCD's relative navigation system is studied, used to estimate the position and attitude of the RLV. A comparison between state-of-the-art systems is made, and the so-called *VisNav* solution is proposed - with a sensor attached to the RLV, and active beacons mounted on the ACCD. In order to identify a representative configuration for this system, a geometric VisNav Model is developed, analysing the visibility of beacons from the sensor's Point of View (PoV). Based on comparative studies performed with this model, a design with three asymmetric rings of twelve beacons is proposed. Combined with Global Navigation Satellite System (GNSS) and Inertial Navigation System (INS) data, this configuration enables relative position and attitude estimation with an accuracy of 20 cm and 1°.

A representative electromechanical design for the ACCD is then proposed, based on results from the foregoing design space exploration. On the one hand, the selection of Commercial-off-the-Shelf (COTS) avionics is covered, as well as a preliminary dimensioning of the vehicle's power system. Here, the ACCD's actuators are identified to be the main drivers of its electronic design in terms of Size, Weight and Power (SWaP) footprint. Additionally, the feasibility of a battery-powered design is demonstrated. On the other hand, a Computer-Aided Design (CAD) study of mechanical subassemblies is performed, which are further analysed in terms of extreme operational loads. Most noticeably, a separation of the docking and release systems is proposed, as combining both into a single mechanism is deemed infeasible, due to the continuous presence of significant towing loads. Based on the presented design, a Bill of Materials (BoM) for the ACCD is established, yielding a total functional mass of 159.14 kg. Because of the substantial impact of the vehicle's wings and docking system on its overall CoG, an additional 16.3 kg trim mass is required to reach the desired CoG position. Compared to previous studies, the final estimate for the ACCD's total mass has increased by 33%.

Concluding the study, compliance with the vast majority of the postulated design requirements is demonstrated, while a number of future improvements and complementary studies are identified. These include an aerodynamic redesign and shortening of the ACCD's shell, to eliminate the need for a trim mass. Additionally, prototyping of this unique vehicle is highly recommended, in order to further study its behaviour, and validate the theoretical design proposed in this work.

1

Introduction

With over half a century of space heritage under Humanity's belt, launch vehicles are still the primary cost driver for endeavours outside the Earth's atmosphere [1], [2]. Hence, a reduction in launch costs is essential to increasing access to space. While programs such as the Space Transportation System (STS) and Buran tried to achieve this using Reusable Launch Vehicles (RLVs), they ultimately faced a host of economic, administrative, and technical challenges [3]–[6]. More recently, systems such as SpaceX's Falcon 9 have demonstrated the cost-reducing promise of RLVs, with each successful launch and recovery further strengthening their technological and economic feasibility [7].

In the context of these past and present efforts, the German Aerospace Centre (Deutsches Zentrum für Luft- und Raumfahrt, DLR) has proposed the In-Air Capturing (IAC) method of recovering RLVs [8]. This approach, illustrated in Figure 1.1, uses a repurposed commercial airliner to act as a Towing Aircraft (TA), and capture an unpowered, returning RLV in mid-air. After a successful capture, the TA then tows the RLV back to the vicinity of a landing site, where it is released and lands autonomously. Compared to other methods of recovering RLVs, the IAC approach promises a competitive reduction in launch costs [9].

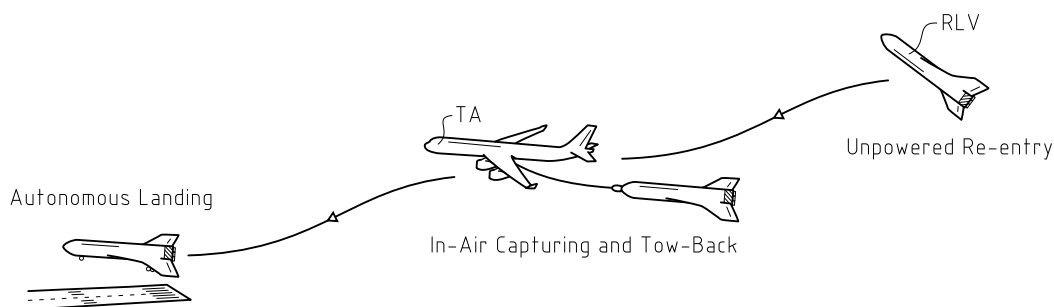


Figure 1.1: Schematic of the In-Air Capturing (IAC) Procedure for Recovering Reusable Launch Vehicles (RLVs) with a Towing Aircraft (TA)

To capture the RLV, the IAC method uses an Aerodynamically Controlled Capturing Device (ACCD), depicted in Figure 1.2. This ACCD is connected to the TA by means of a tether, and uses its control surfaces to intercept the RLV. After docking with the nose of the RLV, it forms the critical tow-back interface between the RLV and TA - which is ultimately disengaged to allow for the former's autonomous landing.

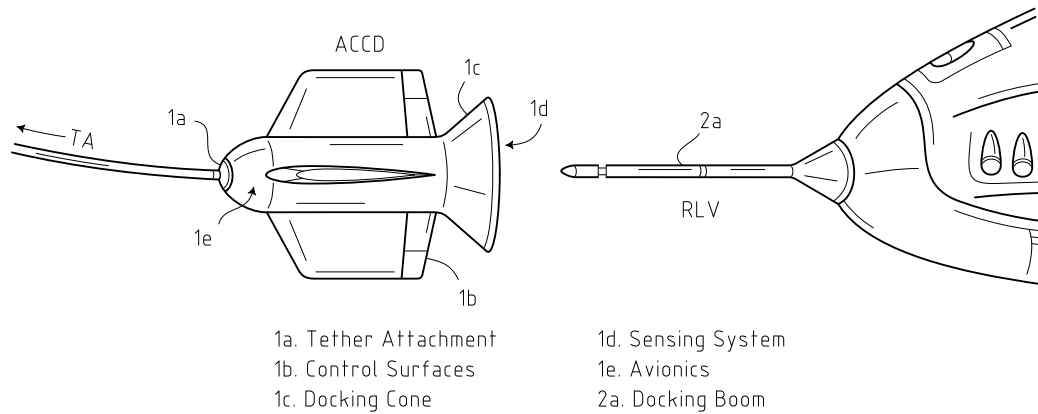


Figure 1.2: Schematic Depiction of the Aerodynamically Controlled Capturing Device (ACCD), in Final Approach with the RLV.

Although the operational regime of the ACCD shares significant resemblances with that of devices used in Automated Aerial Refuelling (AAR), as well as with general Unmanned Aerial Vehicles (UAV), the required structural towing interface makes the ACCD an essentially unique vehicle. Its design space is a largely uncharted territory, which only a limited number of previous studies have explored [10]–[12]. Such designs were based on multiple simplifying assumptions, including a severe underestimation of design loads. Furthermore, vital mechanical subsystems were not defined, while the ACCD’s full-scale electronic design was not studied. Hence, this work (ICARUS) aims to fill the existing design gap, by answering the following research question:

What is a suitable electromechanical design space for an Aerodynamically Controlled Capturing Device used for In-Air Capturing of Reusable Launch Vehicles?

In essence, the goal of this thesis is twofold: on the one hand, exploring the ACCD’s design space by understanding how its electromechanical properties affect its behaviour, while on the other hand generating a representative preliminary design. The keyword *representative* indicates that the design should be adequate in terms of formulated requirements, but does not represent an ‘optimal’ one. Instead, its main value lies in the corresponding design and requirements space exploration, while serving as a reference point for future studies.

From a high-level system perspective, seven main requirements drive the ACCD’s electromechanical design. They are listed below, with a definition of their identifiers included in Appendix A, and further rationale provided in subsequent chapters. Aside from these system requirements, the relevant design space is further limited by two important boundary conditions. On the one hand, the internal mechanism of the ACCD’s control surfaces is not included into the design space. On the other hand, the ACCD’s pre-defined aerodynamic shell is considered as a fixed boundary condition [12], [13].

- KY-SYS.NF-01:** The ACCD shall be deployed from an Airbus A340-600 TA, connected by means of a tether [14].
- CR-SYS.NF-02:** During every stage of operations, the ACCD shall remain within safe structural limits [10].
- KY-SYS.NF-03:** The ACCD shall be able to remain operational during a period of at least 2h 35m.
- CR-SYS.F-11:** The ACCD shall enable relative position and attitude estimation between itself and a representative 80-ton RLV, in a robust and reliable manner [15].
- CR-SYS.F-12:** The ACCD shall be able to manoeuvre relative to the TA, in order to intercept the RLV [14].
- CR-SYS.F-13:** The ACCD shall be able to dock with the RLV, and ensure a solid interface between the two systems, in a reliable manner. The ACCD shall remain latched onto the RLV during the complete tow-back phase [10].

CR-SYS.F-15: It shall be possible to disengage the connection between the TA and the RLV at any point in the mission [16].

As a further concretization of the main research question, six design metrics are proposed, based on the high-level system requirements formulated above. These metrics are outputs of the design effort documented throughout this work, and are listed below. They will be tackled throughout subsequent chapters, with the aforelisted high-level requirements serving as a starting point for deriving subsystem requirements.

- METR-01:** Preliminary definition of essential subsystem requirements.
- METR-02:** Definition of an inertial design space for the ACCD, taking into account effects on the vehicle's towing behaviour.
- METR-03:** Definition of a representative sensor solution for relative position and attitude estimation.
- METR-04:** Selection of representative Commercial-off-the-Shelf (COTS) avionics, and preliminary definition of a corresponding power system.
- METR-05:** Computer-Aided Design (CAD) model of a preliminary ACCD design, in accordance with its requirements.
- METR-06:** Bill of Materials (BoM) for the proposed ACCD design, with a corresponding mass breakdown analysis and Centre of Gravity (CoG) estimate.

First, a general overview of the relevant state-of-the-art is provided in chapter 2, presenting the most recent mechanical and aerodynamic design of the ACCD (**CR-SYS.F-12**), while defining reference RLV and TA vehicles. Next, chapter 3 studies the ACCD as part of a larger towing system (**KY-SYS.NF-01**), exploring its corresponding design space, and obtaining a more accurate estimation of towing loads compared to previous studies. Chapter 4 then proposes a specific sensor solution for performing relative position and attitude estimation between the RLV and ACCD (**CR-SYS.F-11**), analysing its corresponding performance.

Next, the ACCD's overarching electronic design is presented in chapter 5, establishing Size, Weight and Power (SWaP) estimates for essential avionics subsystems, as well as for the vehicle's power system (**KY-SYS.NF-03**). Chapter 6 then generates a preliminary (structural) mechanical ACCD design (**CR-SYS.NF-02**, **CR-SYS.F-13**, and **CR-SYS.F-15**), including a major innovation in terms of the vehicle's docking system: whereas previous studies assumed the ACCD to be disconnected from the RLV using a single docking/release mechanism, a case will be made for decoupling the docking and release functionalities into two separate mechanisms - resulting in a design where the attachment between the ACCD and the tether is disconnected, with the former remaining attached to the RLV during its landing.

Closing the design loop, chapter 7 presents the complete electromechanical design of the ACCD, and verifies its feasibility in light of the formulated design requirements. Finally, chapter 8 combines major conclusions accumulated throughout previous chapters, while chapter 9 lists a number of recommendations for future analysis and design efforts. The overall structure of the thesis is further illustrated in Figure 1.3, which indicates the flow of results and conclusions between different chapters, as well as relevant high-level requirements and design metrics. Metric **METR-01** is not highlighted, as it is related to the thesis as a whole, with subsystem requirements being formulated in chapters 3 through 6.

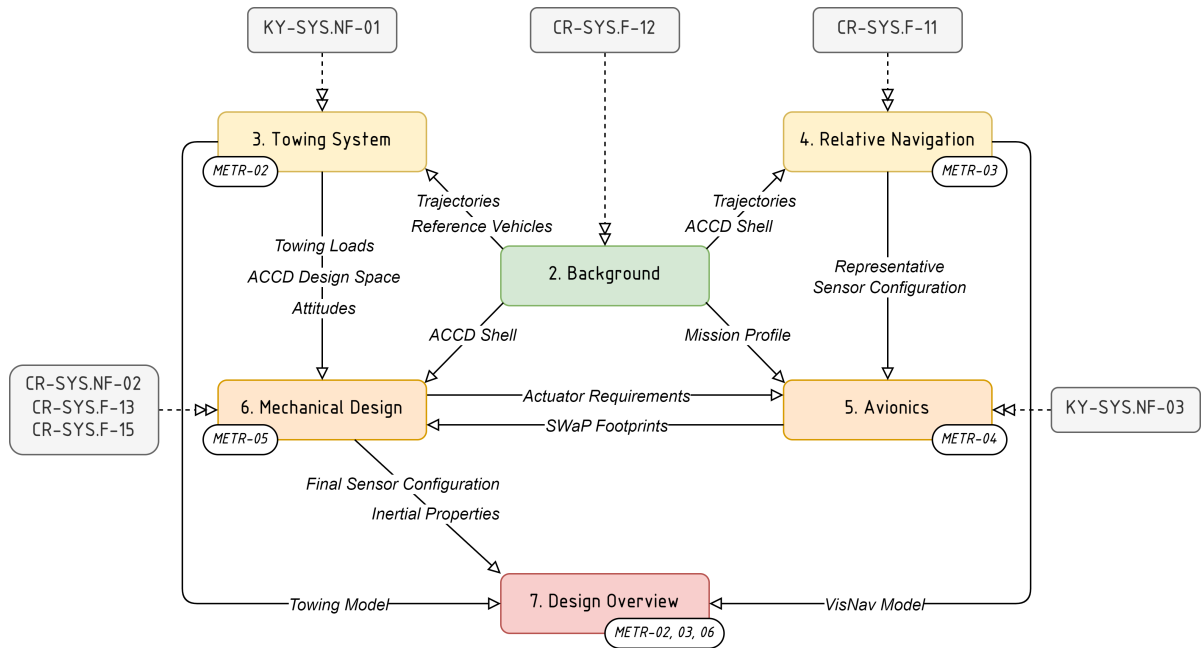


Figure 1.3: Flow Diagram of the Overall Thesis Structure, in Relation to High-Level System Requirements and Design Metrics.

2

Background

Before starting the design exploration, and generating a preliminary ACCD design, an overview of the current state-of-the-art is required as a reference point. Throughout this chapter, relevant background information is presented concerning the project at hand, with a particular focus on work performed at DLR's Department of Space Launcher Systems Analysis (Systemanalyse Raumtransport, SART). First, in section 2.1, a brief overview is given of the overarching IAC recovery technique, defining its main characteristics and vehicles. Then, section 2.2 zooms in on the ACCD itself, discussing the research framework in which ICARUS is grounded.

2.1. In-Air Capturing

After having envisioned and patented the IAC recovery technique in the early 2000s [8], various studies at DLR have looked into aspects such as trajectories [17], [18], vehicle control [14], [19], and cost-effectiveness [20], [21]. A cursory overview of the latter can be found in Appendix B, which discusses the benefits of IAC in the broader context of launch vehicle reusability. In the following sections, aspects of the IAC procedure relevant for the ACCD's design are briefly discussed. First, subsection 2.1.1 gives a general overview of a typical IAC mission and its constituent phases - highlighting where the ACCD comes into play. Next, subsection 2.1.2 defines reference TA and RLV configurations, which are vital for the analysis of the towing system in chapter 3. Finally, subsection 2.1.3 discusses an essential tool developed at SART, capable of simulating the dynamic behaviour of IAC vehicles. Additionally, characteristics of the formation flight between the RLV and TA are presented, analysed using said tool.

2.1.1. Mission Scenario

The IAC recovery procedure can be characterized by a sequence of distinct operational phases - visualized in Figure 2.1, and listed below [22]. Keeping this general mission profile in mind throughout subsequent chapters is crucial in understanding vital system requirements, risks, and design choices.

1. The first stage of a launch vehicle uses all of its propellant, and separates from the upper stages - which continue to orbit. Throughout this work, the separated first stage is referred to as the RLV.
2. The RLV descends back towards the Earth, using lift- and drag-generating surfaces (i.e. wings) to perform the majority of its deceleration [23]. Eventually, it settles into a stable gliding descent at a Flight Path Angle (FPA) of around -9° [18].
3. The TA, which has been loitering in the vicinity of the RLV's expected re-entry location, moves in to intercept it. In order to match the RLV's aerodynamic properties, the TA transitions into a *diving* configuration by deploying gears and spoilers [24]. As a result, the TA enters a similar trajectory as the RLV, with an FPA of around -6.5° [18].
4. Meanwhile, the ACCD is released from the TA, similar to how a tanker aircraft deploys a refuelling drogue. During the formation flight, the ACCD uses its control surfaces to execute fine course corrections, and captures the RLV by locking onto a boom that extends from its nose.

5. The TA then performs a pull-up manoeuvre, regains a stable, horizontal flight, and tows the RLV towards a landing site.
6. When in the vicinity of the landing site, the ACCD releases the connection between the TA and the RLV, and the latter performs an autonomous landing - similar to vehicles such as the X-37B [25] and Buran spacecraft [5].

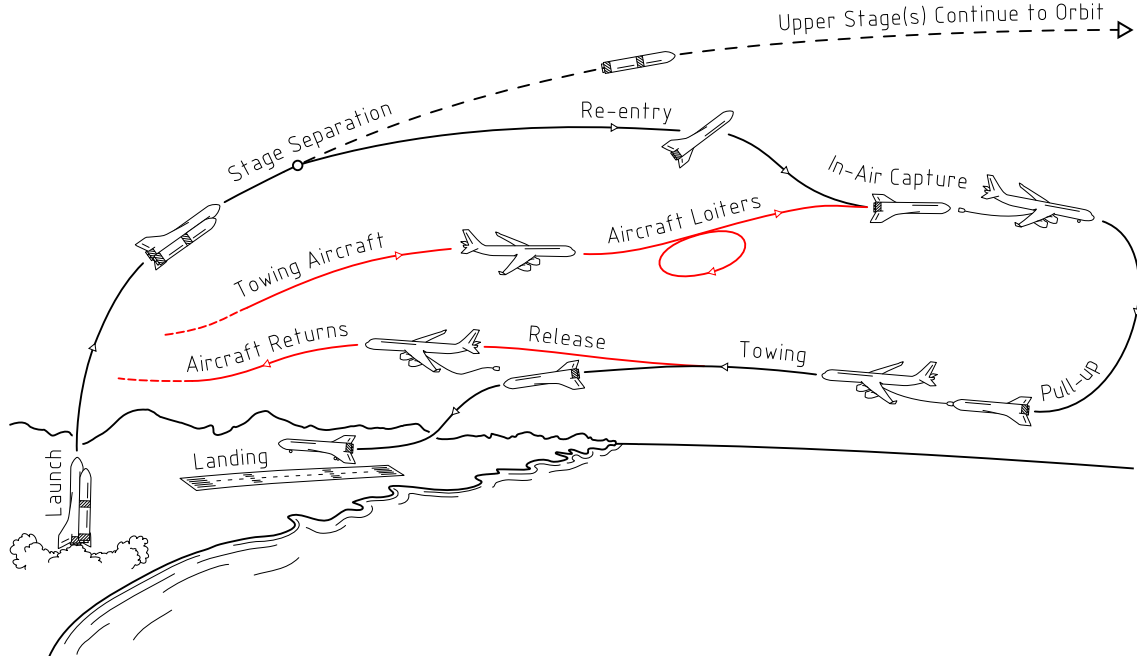


Figure 2.1: Overview of a Typical IAC Mission Scenario. The TA (red) either takes off and lands on a separate runway (*not depicted*), or operates on the same one as used by the RLV.

2.1.2. Reference Vehicles

Throughout this work, reference configurations for the RLV and TA are used, which were defined during Project FALCon (*Formation Flight for In-Air Launcher First Stage Capturing Demonstration*). For the TA, the A340-600 has been proposed as a reference airliner [26], requiring only minimal structural modifications. Before its release, the ACCD can potentially be stored inside the TA's central landing gear bay [18], [27]. A schematic of the reference TA is shown in Figure 2.2.

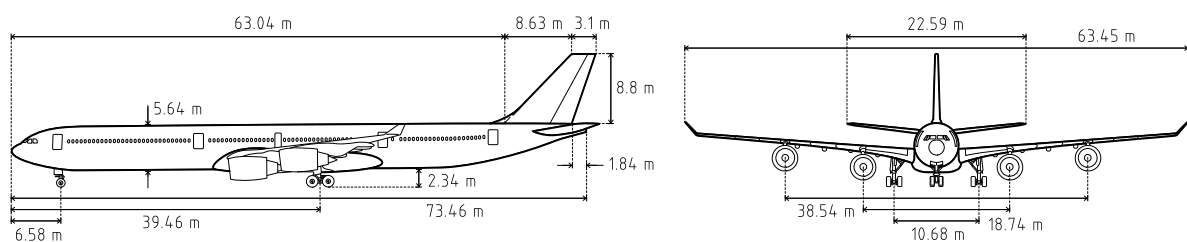


Figure 2.2: Schematic of the Airbus A340-600 Reference TA [27].

As indicated in subsection 2.1.1, measures need to be taken in order to match the TA's aerodynamic properties with that of the RLV during formation flight. Because of this, two configurations have been defined for the TA. In the first one - the so-called *clean* configuration - the TA's landing gear is fully retracted, and spoilers are nominally undeployed. This configuration is maintained during the majority of IAC phases, including tow-back. The second, *diving* configuration aims to achieve the aforementioned drag-increase during formation flight. This is done by deploying the vehicle's front and main landing gear, while setting all spoilers to 20° [18]. Additional side-slip manoeuvres, or applying reverse thrust could potentially further generate drag [18], [24].

When it comes to the RLV on the other hand, conceptual studies at SART have defined a large number of candidate vehicles and configurations [28]–[30], from which the RLVC4-III-B vehicle has been chosen as a reference case. The H370 first stage of this Three-Stage-to-Orbit (3STO) launcher serves as the RLV throughout this work, and features a variable swept wing design [31]. The stage is powered by four SpaceLiner Main Engines (SLMEs) with a staged combustion architecture, running on liquid hydrogen (LH2) and liquid oxygen (LOX) [32]. Figure 2.3 shows a schematic of the overall 3STO launcher, while the main characteristics of the reference RLV and TA are listed in Table 2.1.

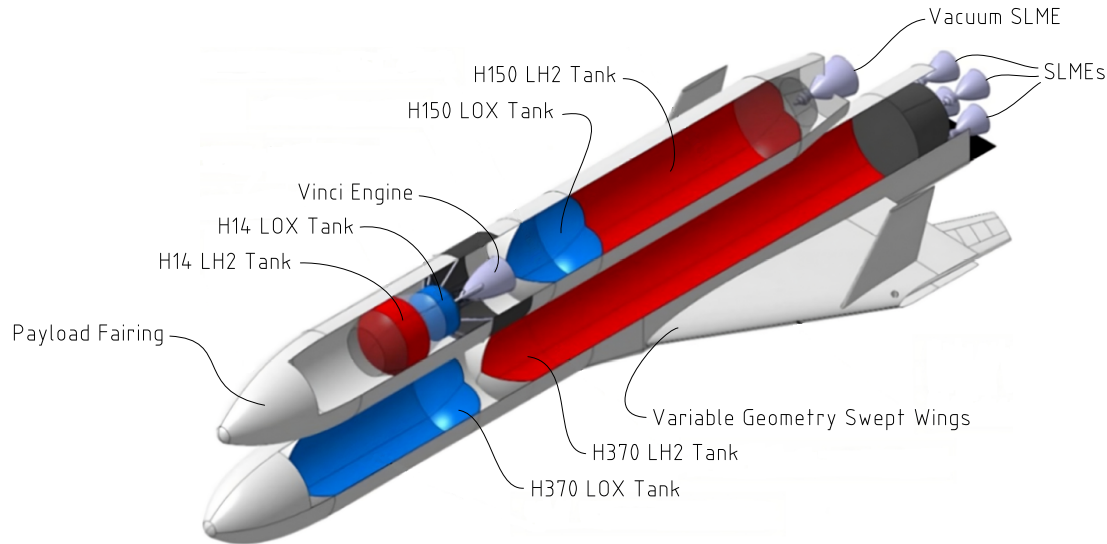


Figure 2.3: Schematic of the RLVC4-III-B Three-Stage-to-Orbit (3STO) Launch Vehicle [33].

Property	TA	RLV
Nominal Mass [Mg]	280 [18]	80 [31]
Length [m]	74.77 [27]	59.5 [30]
Centre of Gravity [m]	38 [34]	39.013 [35]
Pitch Deflection Range [$^{\circ}$]	-15-30 [36]	± 20 [19]

Table 2.1: Main Characteristics of the Reference TA and RLV. The listed nominal mass refers to the vehicle mass during IAC; for the RLV, this corresponds to its dry mass. The Centre of Gravity (CoG) distance is measured from the nose of the vehicle.

Finally, the tether used to tow the ACCD has also been studied in the past, including preliminary dimensioning and dynamic simulations [37]. An Ultra-High-Molecular-Weight-Polyethylene (UHMWPE) tether was proposed for its high-strength and lightweight properties, with a diameter of 24 mm [37], and a length in the range of 150-300 m - although longer lengths could be desirable [38].

2.1.3. Dynamic Simulink Tool

In order to analyse dynamic aspects of the IAC procedure, an intricate Simulink model has been developed at SART, capturing the Six-Degrees-of-Freedom (6DoF) dynamic behaviour of the TA, RLV, and ACCD [38]. This model serves as an important benchmark when analysing the behaviour of the towing system in chapter 3, where it is used as a reference point for a simplified, two-dimensional (2D) steady-state model. An illustration of the functionalities of the Simulink model is shown in Figure 2.4, which is used as a reference at various stages throughout this work [18]. Here, it can be seen that the RLV approaches the TA from above, as it has a more negative FPA - which will be important when studying the relative navigation system in chapter 4.

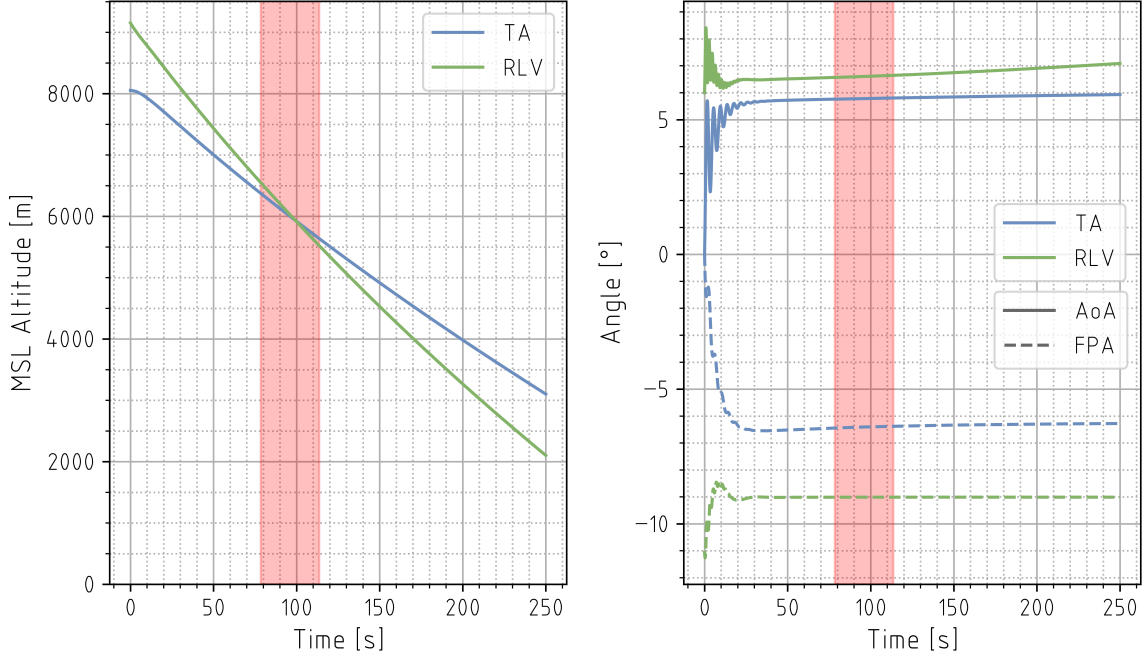


Figure 2.4: Trajectories and Attitudes of the TA and RLV During a Reference Formation Flight [18].

In the figure above, the red area indicates the period of formation flight between the TA and the RLV, as defined by Table 2.2. In the context of this work, this definition is mainly relevant as a reference point for environmental parameters used in chapter 3, while also indicating the window of opportunity that is available for a successful RLV capture (i.e. 60-180 s).

Parameter	Range
Altitude Range [m]	3000-8000 [18]
Air Speed [-]	< Mach 0.55 [39]
Relative Distance [m]	150-350 [18]
Relative Velocity [m/s]	< 3.5 [18]
Duration [s]	60-180 [40], [41]

Table 2.2: Overview of Parameters Characterizing the IAC Formation Flight. The listed relative distance and velocity are measured between the TA and RLV; between the RLV and ACCD, a relative velocity up to 5 m/s is expected [42].

2.2. Aerodynamically Controlled Capturing Device

With background on the overall IAC procedure provided, the following sections will present the current state-of-the-art of the ACCD itself. First, subsection 2.2.1 defines the aerodynamic shell of the ACCD, which is used as a fixed boundary condition in this work. Next, subsection 2.2.2 presents the most recent (electro)mechanical design of the ACCD's internal structure, highlighting its main shortcomings and differences compared to the design effort documented in this work.

2.2.1. Aerodynamic Shell Definition

While some minor iterations have taken effect over the years, the ACCD's general aerodynamic shell has remained virtually unchanged since its initial definition in 2003 [13]. Shown in Figure 2.5, it consists of a central cylindrical assembly, equipped with a conical docking cone and a cruciform set of symmetric NACA0012 aerofoils [43] - further visualized in Figure 2.6 [24], [43]. All four wings carry control surfaces that can deflect up to 15° in both directions, and which can be used in unison to aerodynamically control the ACCD (**CR-SYS.F-12**) [12].

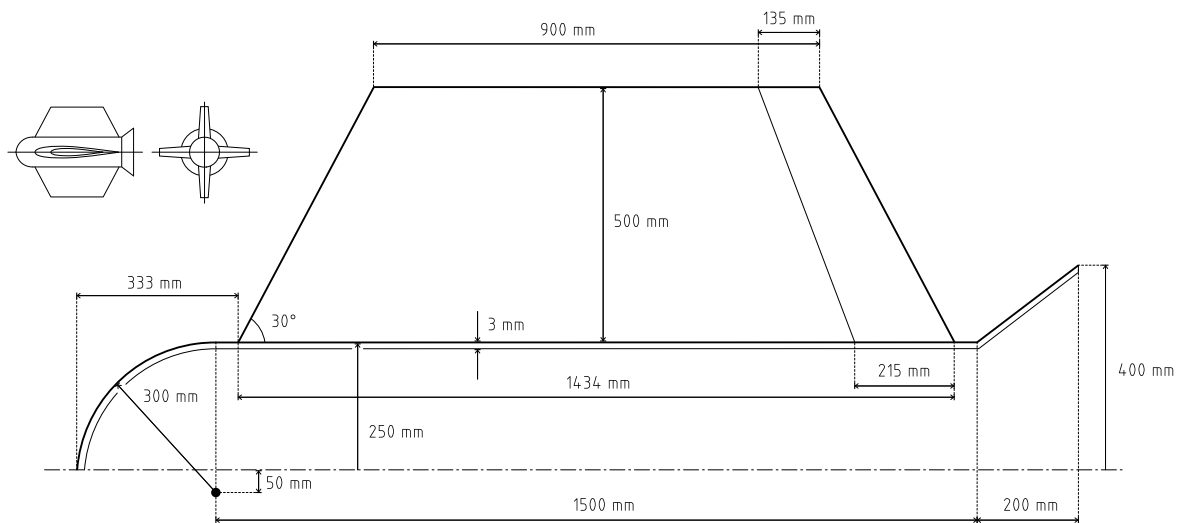


Figure 2.5: Schematic Definition of the ACCD's Aerodynamic Shell [12]. Because of its axial symmetry, only one quarter of the vehicle is shown.

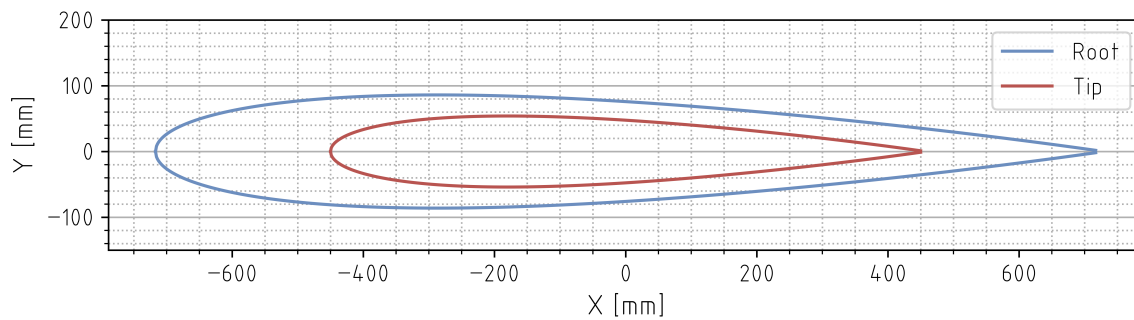


Figure 2.6: Definition of the ACCD's NACA0012 Wing Root and Wing Tip Profiles [44].

As illustrated in Figure 2.7, the cruciform fin assembly can either be configured in a '+'-shape (*Configuration A*), or in an 'x'-shape (*Configuration B*), with both configurations requiring different control commands [45]. Additionally, manoeuvrability and stability characteristics of both configurations differ somewhat, with *Configuration B* generally being more stable, yet less manoeuvrable [46]. Nevertheless, their electromechanical design does not differ significantly, and no distinction between both configurations is made throughout this work - with *Configuration A* being used as a reference.

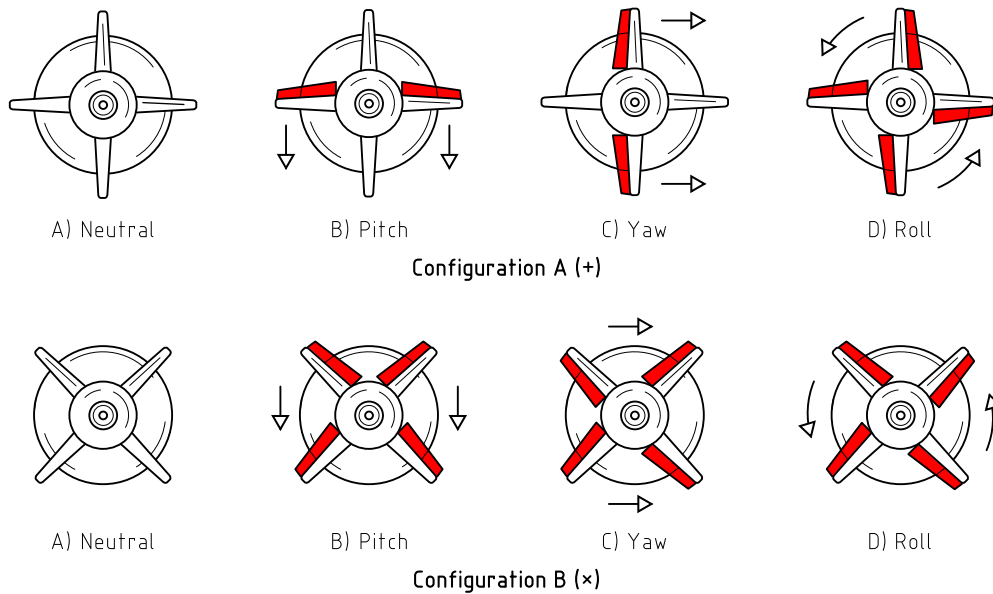


Figure 2.7: Comparison of Three-Degrees-of-Freedom (3DoF) Control for Two Cruciform ACCD Configurations. The diagrams show a front view of the ACCD, and indicate the resulting displacement relative to the TA.

2.2.2. Previous Electromechanical Design

Design of the ACCD's electromechanical interior started with a 2005 study by Heide [10], complemented by a 2006 analysis by Atanassov [11]. Although Stappert performed additional estimations of the ACCD's overall inertial properties in 2021 [12], further design iterations have not been performed since. As such, the studies by Heide and Atanassov serve as the reference point for the electromechanical design proposed in this work, and will be discussed in this section.

Heide's study starts by identifying two major load scenarios for the ACCD. On the one hand, the vehicle has to absorb the energy associated with the docking sequence between the ACCD and RLV. On the other hand, it needs to accommodate towing forces generated by the RLV during tow-back. Assuming that the RLV's lift counteracts its weight, and using a Lift-to-Drag (L/D)-ratio of 4.5, an initial estimation of 175 kN was obtained for the towing design load. However, a more detailed analysis of the tow-back regime in chapter 3 will show that this value is a severe underestimation of extreme tow-back loads. Furthermore, additional load scenarios will be defined in chapter 6, which further characterize the ACCD's operational environment.

After defining and analysing the aforementioned load scenarios, Heide used simplified conceptual analyses, in combination with the aerodynamic shell defined in subsection 2.2.1, to arrive at a final vehicle design, shown schematically in Figure 2.8. In this design, the following five distinct functional subassemblies can be identified:

- A fixed **Structural Housing**, which handles the main towing loads.
- An industrial **Shock Absorber** assembly, which absorbs the energy associated with the RLV capture.
- An **Axially Moving Sled** is free to translate inside the ACCD housing, transferring the capture impact onto the shock absorber.
- A spherical joint acts as the **Locking Mechanism**, interfacing with a boom mounted at the nose of the RLV. An elastic ring around the outside of the joint generates a restoring torque, so that it always returns to its neutral position (*as depicted*).
- A diverging **Guiding Cone** helps steer the RLV's boom into the locking receptacle. Springs are used to accommodate initial impact shocks.

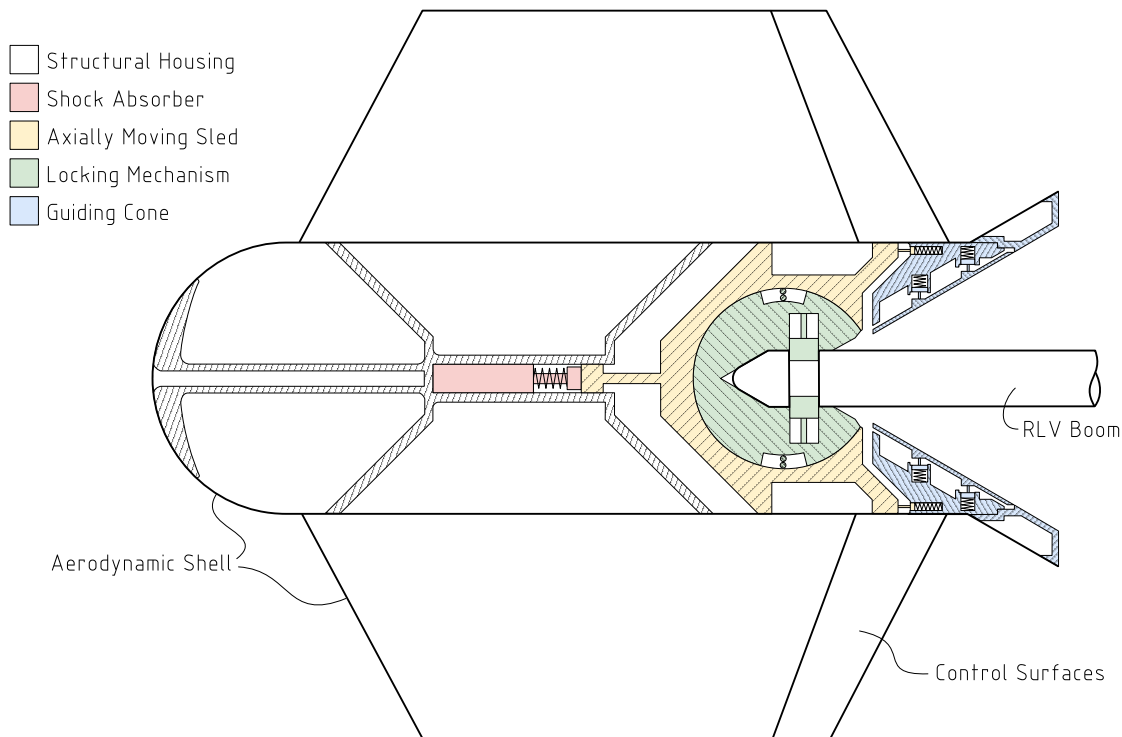


Figure 2.8: Schematic Cross-Section of Heide's ACCD Design, with a Definition of Major Functional Subassemblies [10].

Overall, Heide obtained a structural mass of 143.58 kg, excluding the electronics, wings, and aerodynamic shell [10]. Shortly thereafter, Atanassov analysed and iterated upon Heide's design, significantly reducing its structural mass down to 79.7 kg [11]. More recently, a 2021 study by Stappert looked at an updated mass estimate, addressing a number of the systems that had previously been omitted - actuators, wings, and general avionics. Furthermore, he proposed the addition of a trim mass, in order to move the overall CoG towards the vehicle's nose [12]. A detailed mass breakdown of the resulting ACCD design, combining estimates from Heide, Atanassov and Stappert, is included in Appendix C.

Although this iteration of the ACCD's design forms a valuable reference point, a number of vital aspects have not yet been included - listed below. As an example, the proposed locking assembly could prove technically challenging from an electronic point of view - both in terms of the required actuator SWaP footprint, as well as their power and data connections. Subsequent chapters hope to resolve such issues, by analysing a truly *electromechanical* vehicle design - where electronic and structural considerations are intricately linked.

- Underestimation of towing loads
- Tether attachment missing
- Manufacturability or ease of (dis)assembly not assessed; no fasteners included
- Very preliminary estimation of wing mass; no internal structure defined
- No dimensioning of locking or control actuators
- Very preliminary mass estimates of avionics and electronics; no COTS solutions selected
- Power system not analysed; no power/energy estimates for any subsystem
- Electronic subsystems not included into mechanical design

3

Towing System

A vital aspect of the ACCD's operational environment is the fact that it is connected to the TA via a tether (**KY-SYS.NF-01**). Because of this connection, the vehicle does not act as an independent entity; instead, it is a part of a larger towing system. As shown in Figure 3.1, this towing system consists of the TA, tether, and ACCD, while also including the coupled RLV during tow-back. Together, they form a highly complex multi-body system, where properties such as the ACCD's mass and CoG affect both the dynamic and static behaviour of the whole. Conversely, characteristics of the TA and RLV influence the operational environment of the ACCD, imposing certain attitudes and towing loads on the vehicle.

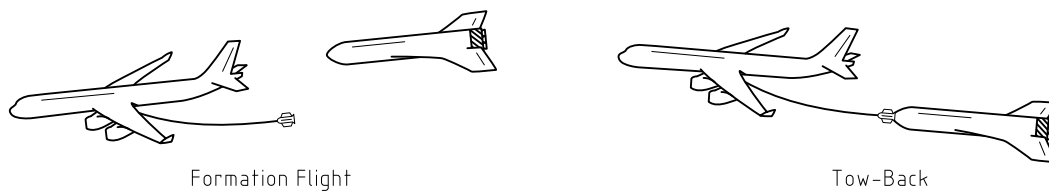


Figure 3.1: Illustration of the Towing System during Formation Flight and Tow-Back. Note that the RLV is not considered a part of the towing system during formation flight.

In order to arrive at sensible and representative design requirements for the ACCD, a solid understanding of the behaviour of the towing system is vital. By doing so, a first delineation of the ACCD's design space can be obtained. Additionally, modelling the towing system is also key in estimating the expected loads on the ACCD - which is vital for the structural mechanical design discussed in chapter 6.

Before actually modelling the towing system, section 3.1 first provides systems engineering foundations concerning the ACCD's towing behaviour. Section 3.2 then presents the development of a Towing Model, from the definition of model requirements until the verification of its outputs. With this model, the ACCD's design space is then explored in section 3.3, while extreme towing loads are estimated in section 3.4. Finally, section 3.5 gathers the main conclusions and takeaways from this chapter, and indicates their importance for subsequent chapters.

3.1. Requirements

Before covering the behaviour of the entire towing system, it serves well to first focus on the ACCD itself. Starting from system requirement **KY-SYS.NF-01**, the following list of subsystem requirements is generated, specifying the behaviour of the ACCD as part of the total towing system. Details concerning the requirements are provided in Appendix A.

CR-TOW.NF-01/10: The ACCD shall be aerodynamically stable when in a passive towed configuration.

- KY-TOW.NF-01/11:** The ACCD's equilibrium state shall have a steady-state pitch angle within a range of $\pm 5^\circ$, independent of its pitch control deflection.
- KY-TOW.NF-01/12:** The ACCD shall stay outside a cone with a half angle of 7.5° , extending from the TA's tail, and aligned with the TA's flight path.
- KY-TOW.F-12/01:** The ACCD shall be capable of a ± 30 m lateral translation in the Y/Z-direction, relative to its trimmed equilibrium position.
- KY-TOW.F-12/02:** The ACCD shall be able to traverse a lateral distance of 30 m in the Y/Z direction within 20 s.

First of all, aerodynamic stability (**CR-TOW.NF-01/10**) is a vital prerequisite for the ACCD to be able to intercept and dock with the RLV (**CR-SYS.F-12** and **CR-SYS.F-13**). This stability should be achieved without any active control, in order for the system to be robust, and independent of the implementation of the control system. Furthermore, the pitch attitude of the ACCD needs to remain within certain bounds (**KY-TOW.NF-01/11**), so that its docking cone is properly aligned with the RLV during docking. This is highly linked with the allowable docking misalignments (**KY-DCK.F-13/02**), in conjunction with typical RLV attitudes during formation flight.

Next, studies performed during Project FALCon identified the TA's wake as a major source of disturbances for the ACCD's stability and controllability [41]. Hence, the ACCD should avoid this wake area (**KY-TOW.NF-01/12**) - of which a simplified model is presented in subsection 3.2.6. Finally, a preliminary definition of the ACCD's manoeuvrability is provided, both in terms of range (**KY-TOW.F-12/01**) and responsiveness (**KY-TOW.F-12/02**). When trimming the control surfaces, it is particularly vital that enough control surplus is maintained, so that the control surfaces do not saturate when manoeuvring.

3.2. Towing Model

With the aforementioned requirements in mind, the main goal of this chapter can now be tackled: modelling the behaviour of the towing system. Although the SART Simulink model discussed in chapter 2 offers such capabilities, its highly complex nature is reflected in terms of computational effort and time. This is not ideal, as the design space exploration and estimation of extreme loads require rapid iterations, and the simulation of a large number of data points. As such, a new model is needed.

In subsection 3.2.1, model requirements are generated, which serve as the foundation for developing the new Towing Model. Sections 3.2.2 through 3.2.5 then present the core of the Towing Model, covering the implementation of the ACCD, tether, RLV, and TA respectively. Additionally, a simplified representation of the TA's wake is defined in subsection 3.2.6. With the model's core thus documented, subsection 3.2.7 then lists its main assumptions. Finally, subsection 3.2.8 presents the model's core outputs, and subsection 3.2.9 covers verification efforts.

3.2.1. Requirements

With the objectives of rapid iterations and model simplicity in mind, nine model requirements are generated, shown below.

- TWM.NF-01:** The Towing Model shall analyse 2D steady-state conditions of the towing system. This 2D plane is defined as the TA's plane of symmetry, which is assumed to be coincident with the planes of symmetry of all other vehicles.
- TWM.F-02:** The Towing Model shall analyse the relative position and attitude of the ACCD/RLV with respect to the TA. The model shall furthermore be able to visualize this towing configuration graphically, including a representation of the TA's wake.
- TWM.F-03:** The Towing Model shall analyse the towing loads on the ACCD. In order to determine extreme scenarios, the model shall take into account potential excess thrust (i.e. more thrust than is required to maintain steady-state conditions) provided by the TA.

- TWM.F-04:** The Towing Model shall investigate the effect of the ACCD’s mass, CoG, and pitch control deflection on the towing position (**TWM.F-02**), in order to characterize the design space and operational environment of the ACCD.
- TWM.NF-05:** The Towing Model shall use high-fidelity Computational Fluid Dynamics (CFD) data for estimating aerodynamic forces on all vehicles.
- TWM.NF-06:** As inputs, the Towing Model shall use the TA’s altitude, air speed, and FPA, while differentiating between a *clean* and *diving* TA configuration.
- TWM.NF-07:** The Towing Model’s steady-state solution shall not deviate more than $\pm 5\%$ from the equilibrium solution found with SART’s Simulink model. The equilibrium solution of said model is reached when the relative derivatives of the towing position are below 2%; i.e. $\partial y / \partial t < 0.02 \cdot y$.
- TWM.F-08:** For the purposes of model verification, the Towing Model shall be able to visualize the forces on the ACCD/RLV.
- TWM.NF-09:** The Towing Model shall be able to analyse towing conditions (**TWM.NF-01** through **TWM.F-03**) in less than 1% of the computation time needed by SART’s Simulink model, using similar inputs, and the same workstation.

By confining the model to a 2D plane (**TWM.NF-01**) the total number of degrees of freedom is halved compared to the Simulink model. Additionally, removal of the time-dimension by focusing on steady-state conditions allows for a (partial) decoupling of the different vehicles in the towing system. Combining both of these aspects leads to significantly simplified computations (**TWM.NF-09**).

Looking at the model’s core outputs, a visualization of the vehicles’ relative position (**TWM.F-02**) provides general insight into the behaviour of the towing system, and aids in the design space exploration (**TWM.F-04**). Furthermore, in order to obtain a sensible towing design load, it is important to consider extreme operational scenarios, including ones where the TA is accelerating (**TWM.F-03**). Finally, relevant aerodynamic (**TWM.NF-05**) and environmental (**TWM.NF-06**) inputs are defined, while two model verification techniques are proposed (**TWM.NF-07** and **TWM.F-08**).

Combining all requirements, a 2D, (quasi) steady-state, reduced-complexity Python-model is proposed, with a general flow of variables shown in Figure 3.2. Here, the essential outputs are the ACCD’s position and towing forces. The flow diagram also shows the relevance of the Towing Model within the overarching ACCD design, with inputs and outputs directly linked to other chapters in this work.

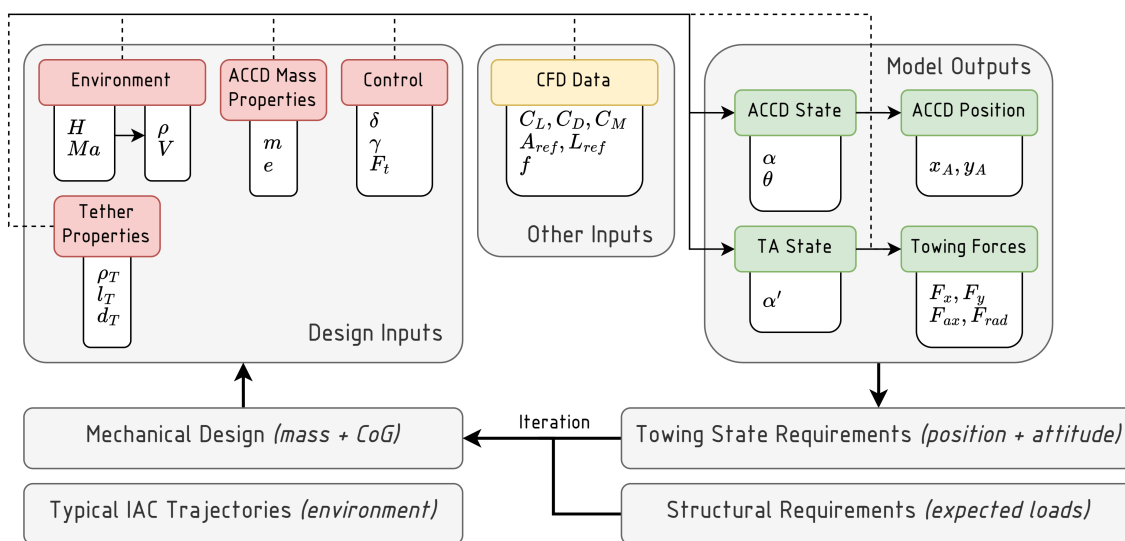


Figure 3.2: Flowchart of the Towing Model, and Integration into the Overall Systems Engineering Approach. Definitions of the various parameters and symbols are provided in subsections 3.2.2 through 3.2.6.

With a general architecture for the Towing Model presented, the following sections can now discuss the actual implementation of different components of the towing system. As a baseline, a non-accelerating system is used, where static force and moment equilibria dictate the relative position of the different vehicles.

3.2.2. Aerodynamically Controlled Capturing Device

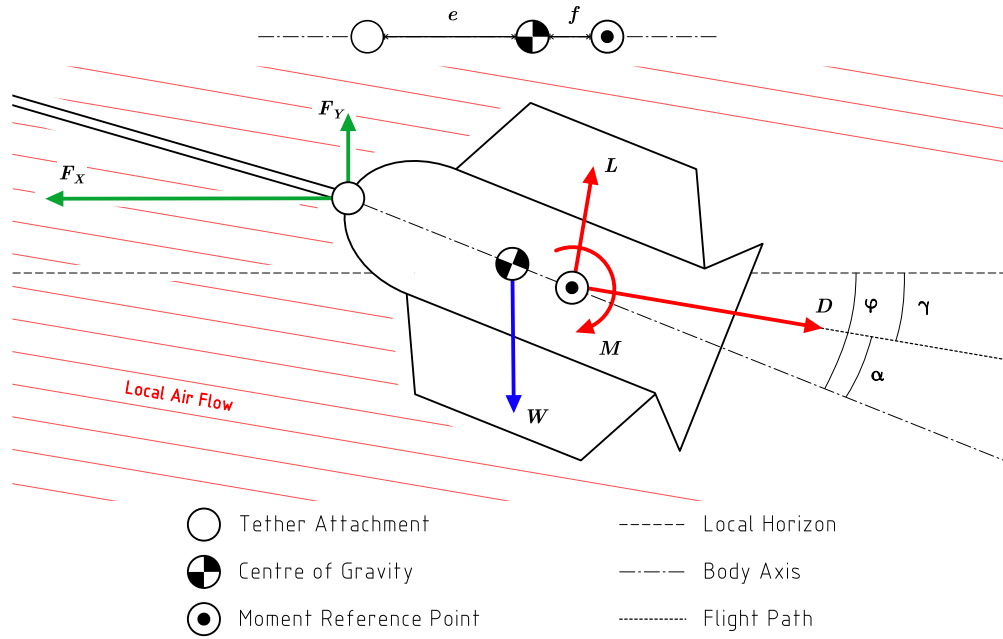


Figure 3.3: Free-Body Diagram of the ACCD, as Towed by the TA. Note that the size of the displayed forces is not to scale.

Looking first at a free-body diagram of the ACCD, shown in Figure 3.3, a number of different forces and torques can be identified. The weight W of the ACCD acts at the vehicle's CoG, while aerodynamic effects - lift L , drag D , and pitching moment M - act on the Moment Reference Point (MRP), and are expressed in the aerodynamic frame. Finally, a towing force acts on the vehicle's tether attachment, and is divided into a horizontal component F_x and a vertical component F_y - with positive magnitudes as shown in Figure 3.3. Given the axisymmetry of the ACCD, the CoG, MRP, and tether attachment all coincide with the vehicle's body axis. The positions of the CoG and MRP along the body axis are then fully characterized by the dimensions e and f respectively - for which Figure 3.3 shows the positive sign convention.

Assuming a negligible contribution of wind to the airflow, the aerodynamic frame coincides with the flight path of the vehicle - which is fully characterized by the FPA γ in this 2D setup. Combining this angle with the ACCD's Angle of Attack (AoA) α , the overall pitch angle ϕ of the vehicle can be found with Equation 3.1 [47]. Once more, the configuration depicted in Figure 3.3 shows the positive sign convention for these angles.

$$\phi = \gamma + \alpha \quad (3.1)$$

Under steady-state conditions (**TWM.NF-01**), this free-body diagram allows three equilibrium equations to be established. They define the horizontal, vertical, and moment equilibrium, and are shown in Equations 3.2, 3.3, and 3.4 respectively. The moment equilibrium is established around the tether attachment, in order to simplify subsequent computations.

$$F_x = L \cdot \sin \gamma + D \cdot \cos \gamma \quad (3.2)$$

$$F_y + L \cdot \cos \gamma = W + D \cdot \sin \gamma \quad (3.3)$$

$$M + W \cdot e \cdot \cos \phi = (L \cdot \cos \alpha + D \cdot \sin \alpha) \cdot (e + f) \quad (3.4)$$

Assuming a known ACCD mass m , its weight follows as $W = m \cdot g$, where $g = 9.81 \text{ m/s}^2$ is the Earth's gravitational acceleration at sea-level [48]. Similarly, geometric parameters e and f are known for a given ACCD configuration. Furthermore, under steady-state conditions, all vehicles in the towing system have the same FPA γ - which is a model input (**TWM.NF-06**). Finally, the aerodynamic forces can be broken down into Equations 3.5 through 3.7 [49].

$$L = 1/2 \cdot \rho \cdot V^2 \cdot A_{ref} \cdot C_L(\alpha, \delta) \quad (3.5)$$

$$D = 1/2 \cdot \rho \cdot V^2 \cdot A_{ref} \cdot C_D(\alpha, \delta) \quad (3.6)$$

$$M = 1/2 \cdot \rho \cdot V^2 \cdot A_{ref} \cdot l_{ref} \cdot C_M(\alpha, \delta) \quad (3.7)$$

In these equations, the dynamic pressure $1/2 \cdot \rho \cdot V^2$ is considered an environmental boundary condition, as it is governed by the local air density ρ and flow velocity V . Both are determined as a function of flight altitude H and Mach number Ma , which in turn are model inputs (**TWM.NF-06**). For this conversion, the 1976 US Standard Atmosphere Model is used - included in Appendix D. Next, A_{ref} and l_{ref} are the reference surface area and length corresponding to the aerodynamic coefficients C_L , C_D , and C_M . These three coefficients are dependent on the vehicle's AoA α , as well as its pitch control deflection δ [41] - which is a model input (**TWM.F-04**). The corresponding aerodynamic functions $C_L(\alpha, \delta)$, $C_D(\alpha, \delta)$, and $C_M(\alpha, \delta)$ have previously been analysed within the context of Project FALCon [43], [50], and are also model inputs (**TWM.NF-05**). Further details concerning these aerodynamic functions can be found in Appendix E.

Combining all of the above considerations, the ACCD's AoA α is the only unknown in Equation 3.4. Because of the piece-wise interpolated nature of the aerodynamic data, in combination with the geometric functions in Equation 3.4, it is not possible to generate a closed-form solution for the AoA. Instead, an iterative approach is necessary, which can be achieved using a number of different numerical schemes. For this model, the dynamically inspired technique shown in Figure 3.4 is used, where the AoA is varied until the net torque M_{net} on the ACCD equals zero.

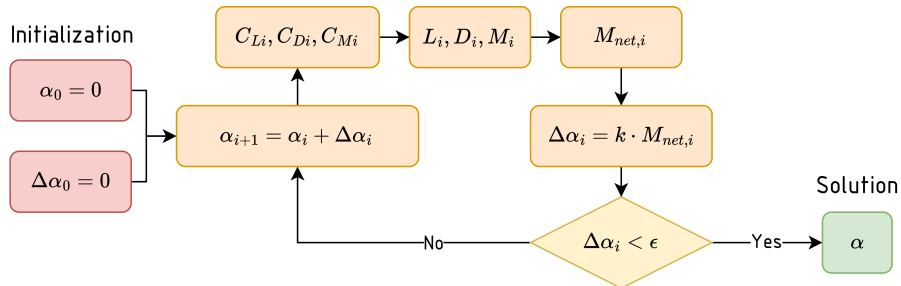


Figure 3.4: Flowchart for Iteratively Solving the ACCD's Angle of Attack (AoA). This uses a dynamically inspired approach, where the iteration increment $\Delta\alpha$ is proportional to the net torque acting on the ACCD - characterized by a gain k . The iterations cease as soon as this increment drops below a given threshold ϵ - typically chosen as a few arcseconds.

Once the ACCD's AoA has thus been found, Equations 3.2 and 3.3 can be solved for the final two unknowns - F_X and F_Y . With this, the equilibrium attitude of the ACCD has been obtained, as well as the force acting at the tether-ACCD interface (**TWM.F-02** and **TWM.F-03**). However, additional steps are required to obtain information about the relative position between the ACCD and TA. In order to achieve this, a tether model is implemented.

3.2.3. Tether

When it comes to modelling the tether's steady-state behaviour, a number of different possibilities arise, ranging from a simple rigid link model to a highly complex multibody system approach [37]. In order to minimize the complexity of this part of the Towing Model (**TWM.NF-09**), while still offering sufficient modelling accuracy (**TWM.NF-07**), a catenary tether model was chosen. An alternative, rigid link model is presented in Appendix F, where a comparison between both options is also provided.

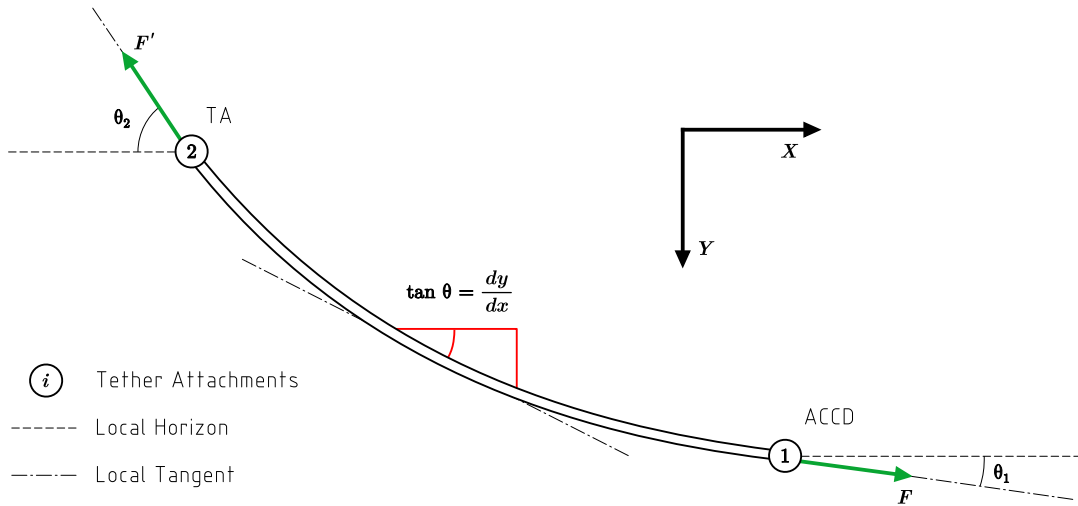


Figure 3.5: Definition of the Catenary Tether Model. The catenary frame is not drawn to scale, while tether force components are combined into a single vector.

For the catenary model, illustrated in Figure 3.5, the tether is assumed to have a uniform density and cross-section, while being perfectly flexible. Furthermore, aerodynamic forces on the tether are neglected, so that it is only subject to its own weight. Under such conditions, the shape of the tether forms a catenary curve, which can be described with Equation 3.8 [51]. In this equation, a is a parameter characterizing the shape of the catenary; with a downwards-facing Y-axis, its value is negative. The function describes the tether in a local catenary reference frame, where the coordinates of the ACCD's and TA's attachments are denoted as (x_1, y_1) and (x_2, y_2) respectively.

$$y = f(x) = a \cdot \cosh\left(\frac{x}{a}\right) \quad (3.8)$$

At the ACCD's tether attachment, the forces F_X and F_Y calculated in subsection 3.2.2 act. At the TA's attachment, similar forces F'_X and F'_Y are present, which are given by $F'_X = F_X$ and $F'_Y = F_Y + W_T$. Here, W_T is the weight of the tether, which can be calculated using its length l_T , density ρ_T , and cross-sectional diameter d_T . Assuming the towing forces to be aligned with the tether at both attachments, the corresponding tether angles θ_1 and θ_2 follow from Equation 3.9. This assumption is true for an idealized tether, which is infinitely thin and flexible - in which case the tension force is aligned with the tether throughout its entire length [52].

$$\begin{cases} \theta_1 = \arctan(F_Y/F_X) \\ \theta_2 = \arctan((F_Y + W_T)/F_X) \end{cases} \quad (3.9)$$

At the same time, the local angle of the catenary function can be found by computing the derivative of Equation 3.8 in both tether attachments - (x_1, y_1) and (x_2, y_2) . With this derivative, the local angle can then be found using the given that $\tan \theta = dy/dx$. Solving the resulting equation with the known values for θ_1 and θ_2 yields expressions for the parameters x_1 and x_2 as a function of a , as shown in Equation 3.10.

$$\begin{cases} x_1 = a \cdot \operatorname{arsinh}(\tan \theta_1) \\ x_2 = a \cdot \operatorname{arsinh}(\tan \theta_2) \end{cases} \quad (3.10)$$

The unknown value for a can then be determined by equating the total arc length between both attachments to the known tether length l_T . Applying the general expression for the arc length of a curve to the catenary function yields Equation 3.11, which can be solved for a - as shown in Equation 3.12.

$$\begin{aligned} l_T &= \int_{x_1}^{x_2} \sqrt{1 + \left(\frac{dy}{dx}\right)^2} dx \\ &= a \cdot \sinh\left(\frac{x_1}{a}\right) - a \cdot \sinh\left(\frac{x_2}{a}\right) \end{aligned} \quad (3.11)$$

$$a = \frac{l_T}{\tan \theta_1 - \tan \theta_2} \quad (3.12)$$

With values for a , x_1 and x_2 known, the corresponding Y-coordinates of the tether attachments can then be found using the catenary curve expression, as shown in Equation 3.13. This uses the fact that $\cosh(\operatorname{arsinh} x) = \sqrt{1+x^2}$, and $1 + \tan^2 x = \sec^2 x$.

$$\begin{cases} y_1 = a \cdot \cosh(\operatorname{arsinh}(\tan \theta_1)) = a \cdot \sqrt{1 + \tan^2 \theta_1} = a \cdot \sec \theta_1 \\ y_2 = a \cdot \cosh(\operatorname{arsinh}(\tan \theta_2)) = a \cdot \sqrt{1 + \tan^2 \theta_2} = a \cdot \sec \theta_2 \end{cases} \quad (3.13)$$

As a concluding step, the tether coordinates (x_1, y_1) and (x_2, y_2) - expressed in the catenary frame - are transformed into a global Local-Vertical, Local-Horizontal (LVLH) reference frame. This frame, which is further defined in Appendix G, has its origin in the TA's tether attachment, a positive X-axis pointing backwards along the local horizon, and a positive Y-axis pointing nadir. Transforming points (x_1, y_1) and (x_2, y_2) into this global frame, they become (x_A, y_A) and $(0, 0)$. The former is the ACCD's relative towing position, given by Equation 3.14.

$$\begin{cases} x_A = a \cdot \operatorname{arsinh}(\tan \theta_1) - a \cdot \operatorname{arsinh}(\tan \theta_2) \\ y_A = a \cdot \sec \theta_1 - a \cdot \sec \theta_2 \end{cases} \quad (3.14)$$

3.2.4. Reusable Launch Vehicle

Combining the results from subsections 3.2.2 and 3.2.3, the steady-state towing position of the ACCD with respect to the TA can be determined (**TWM.F-02**). As such, the effect of different ACCD configurations can be investigated during the IAC formation flight (**TWM.F-04**). During the subsequent tow-back phase, where the RLV is also a part of the towing system, different conditions arise. In essence however, the entire computational methodology presented in the previous two sections remains valid. For the inertial properties (mass and CoG), contributions from the ACCD and RLV are combined, while the aerodynamic effect of the ACCD is neglected [24], and CFD data for the RLV is used. Any resulting modelling inaccuracies are compensated for by overestimating the extreme towing conditions in section 3.4.

3.2.5. Towing Aircraft

Finally, a model of the TA wraps up the core of the Towing Model. It is mainly important for an estimation of extreme towing loads, which are largely governed by the thrust supplied by the TA (**TWM.F-03**). In particular, in case of excess-thrust conditions, the TA imparts an acceleration onto the towing system, in turn resulting in increased towing forces. Under such conditions however, the different vehicles are no longer decoupled, and the previous free-body analyses no longer hold. Finding the true steady-state equilibrium becomes a highly iterative process, requiring a significantly increased computational effort (**TWM.NF-09**). Hence, a different approach is chosen, illustrated in Figure 3.6. First, a non-accelerating system is considered, and the TA's thrust and attitude are determined. Then, a different thrust level is applied as a step function at $t = 0$, and the resulting force equilibrium is analysed at the same instant. In the following two subsections, both of these scenarios are modelled.

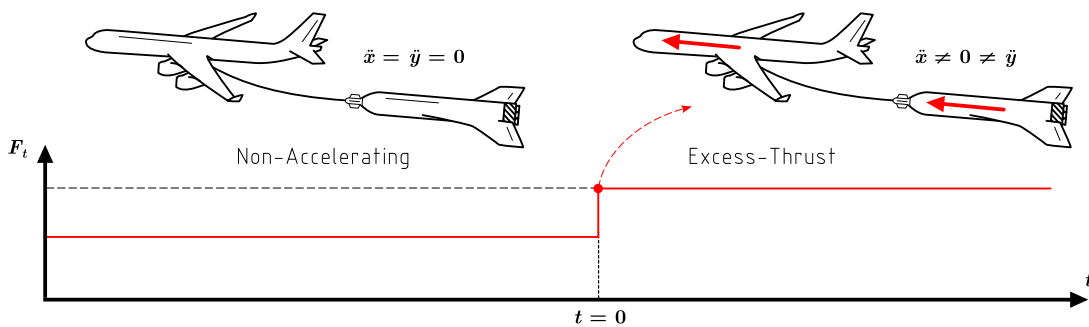


Figure 3.6: Definition of Non-Accelerating and Excess-Thrust Towing Conditions. Note that the excess-thrust scenario is defined at the exact time that the TA applies additional thrust.

Non-Accelerating Steady-State

The main goal of the non-accelerating analysis is to obtain the TA's attitude, which determines the thrust direction in the subsequent excess-thrust study. Looking at the free-body diagram of the TA in Figure 3.7, the main difference with respect to the ACCD/RLV is the additional application of engine thrust F_t . Tether forces F'_X and F'_Y are those determined in subsection 3.2.3, while other forces are calculated as in subsection 3.2.2. In general, parameters F_t , α' , and δ' are unknown, and can be found by solving the forces and moment equilibria.

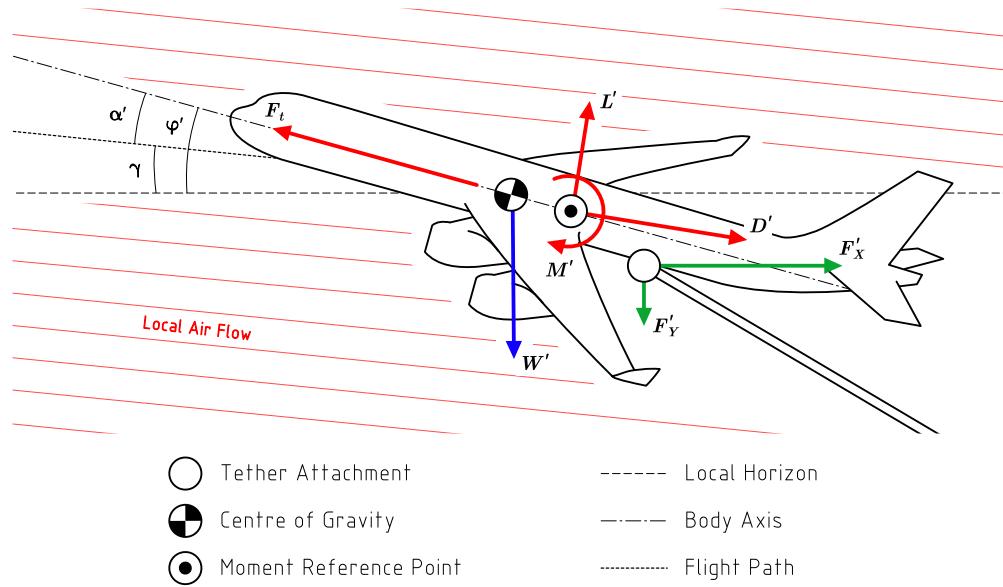


Figure 3.7: Free-Body Diagram of the TA. Note that the size of the displayed forces is not to scale, while the exact location of their acting points is not defined.

However, establishing the moment equilibrium requires knowledge about where the different forces act. This is not trivial, as it introduces a number of unknown parameters, such as the exact CoG, or the location of the tether attachment. To circumvent this, the two force equilibria are decoupled from the moment equilibrium, by neglecting the effect of the pitch control deflection δ' on the TA's lift and drag - which can be observed in the aerodynamic data included in Appendix E. Aerodynamic force functions are simplified accordingly as $C'_L(\alpha', \delta') \approx C'_L(\alpha', \delta' = 0) = C'_L(\alpha')$ - removing the δ' -dependency of the TA's force equilibria.

Establishing such a force equilibrium along the TA's body axis then yields Equation 3.15, which is solved in an iterative manner for α' - using the approach shown in Figure 3.4. A similar perpendicular force equilibrium is used to obtain an expression for the required steady-state engine thrust F_t - shown in Equation 3.16. This thrust can be compared to the propulsion model discussed in the next subsection, indicating the feasibility of the analysed steady-state configuration.

$$L' \cdot \cos \alpha' + D' \cdot \sin \alpha' + F'_X \cdot \sin(\alpha' + \gamma) = (W' + F'_Y) \cdot \cos(\alpha' + \gamma) \quad (3.15)$$

$$F_t = D' \cdot \cos \alpha' + F'_X \cdot \cos(\alpha' + \gamma) + (W' + F'_Y) \cdot \sin(\alpha' + \gamma) - L' \cdot \sin \alpha' \quad (3.16)$$

With this, only the control surface deflection δ' is left unknown. Theoretically, it can be found using a moment equilibrium, and would yield additional information concerning the feasibility of the considered steady-state conditions. However, it is not vital to any of the postulated model requirements, while requiring a significant additional analysis effort. As such, this aspect is not included in the Towing Model.

Excess-Thrust

Once the non-accelerating steady-state attitude of the TA has been found, the more demanding excess-thrust scenario can be modelled. In order to apply realistic thrust levels, a rudimentary propulsion model

is implemented, which simulates the performance of the TA's four turbofan engines as a function of altitude and airspeed. Data for this model has been obtained during previous analyses at DLR [19], and is documented in Appendix H.

Under excess-thrust conditions, the overall acceleration of the combined towing system can be determined by analysing the free-body diagram shown in Figure 3.8. Using Newton's second law, the X- and Y-components of the acceleration are computed with Equation 3.17 and Equation 3.18 respectively. Here, it is assumed that all other external forces remain exactly the same as before the change in thrust levels - which is true at $t = 0$, when the vehicles' attitudes have not yet changed. In these, and subsequent equations, m_T denotes the tether mass.

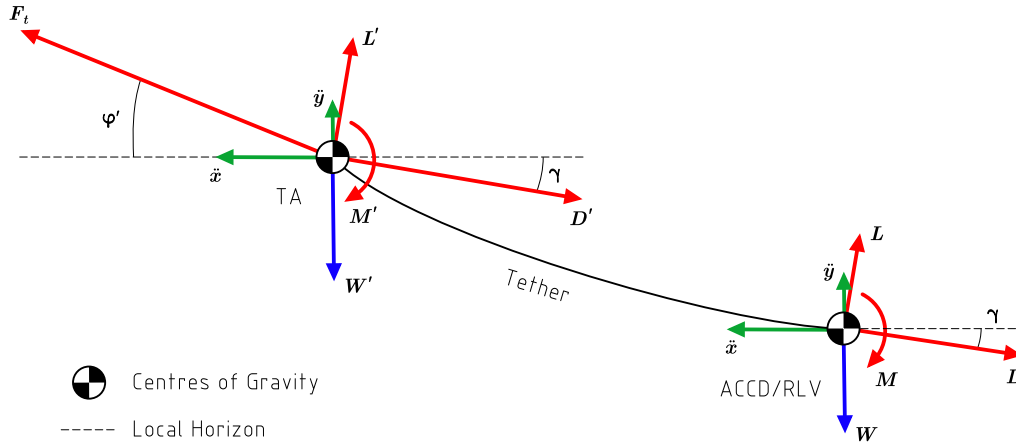


Figure 3.8: Free-Body Diagram of the Towing System under Excess-Thrust Conditions. All vehicles are represented as point masses for clarity's sake, while the size of the displayed forces is not to scale.

$$\ddot{x} = \frac{-F_t \cdot \cos(\alpha' + \gamma) + (L + L') \cdot \sin \gamma + (D + D') \cdot \cos \gamma}{m + m' + m_T} \quad (3.17)$$

$$\ddot{y} = \frac{F_t \cdot \sin(\alpha' + \gamma) + (L + L') \cdot \cos \gamma - (D + D') \cdot \sin \gamma}{m + m' + m_T} - g \quad (3.18)$$

For ease of analysis, it is assumed that all vehicles in the towing system experience the same acceleration. This is the case if all CoGs are aligned with the thrust force, and the tether behaves as a rigid link. During tow-back (i.e. the main use-case for this part of the Towing Model), this is indeed generally the case, as illustrated in section 3.4. Under this assumption, the excess-thrust towing forces at the ACCD's tether attachment can be found with a modified version of the free-body diagram shown in Figure 3.3 - now with two additional d'Alembert forces $-m \cdot \ddot{x}$ and $-m \cdot \ddot{y}$ acting on the vehicle's CoG. The new tether forces F_{X2} and F_{Y2} then follow from horizontal and vertical force equilibria, shown in Equation 3.19. Note that for the tow-back phase, m represents the mass of the RLV.

$$\begin{cases} F_{X2} = -m \cdot \ddot{x} + L \cdot \sin \gamma + D \cdot \cos \gamma \\ F_{Y2} = m \cdot \ddot{y} + L \cdot \cos \gamma - W - D \cdot \sin \gamma \end{cases} \quad (3.19)$$

With the above equations, worst-case scenarios in terms of towing loads can be analysed (**TWM.F-03**), which are the direct drivers for the ACCD's structural design requirements. One final practicality, which is important when applying representative forces to the ACCD in subsequent analyses, concerns the conversion of the towing forces from the global reference frame into the ACCD body frame. This is achieved using Equation 3.20, where a positive axial force F_{ax} corresponds to a tensile load.

$$\begin{cases} F_{ax} = F_X \cdot \cos \phi + F_Y \cdot \sin \phi \\ F_{rad} = -F_X \cdot \sin \phi + F_Y \cdot \cos \phi \end{cases} \quad (3.20)$$

3.2.6. Wake

A final important aspect of the towing system concerns a model of the TA's wake. During Project FAL-Con, CFD analyses [24], [43] and subsequent simulations [14], [41] have demonstrated the disturbing influence of this turbulent region behind the TA. As a consequence, the ACCD is required to stay clear of the TA's wake at all times (**KY-TOW.NF-01/12**). In order to graphically verify this, a simplified representation of the wake is added to the model (**TWM.F-02**). For this, a stay-out zone is defined, centred around the TA's flight path, with an initial width of 9.5 m, and subtending a half angle of 7.5° . Instead of modelling the AoA-dependence of the wake visible in Figure 3.9, such a constant, diverging stay-out zone conservatively covers flight regimes up to $\alpha' = \pm 10^\circ$, offering a safety margin to compensate for potential modelling inaccuracies. Since only the lower edge of the stay-out zone is relevant for the ACCD, its upper edge is defined symmetrically because of simplicity's sake.

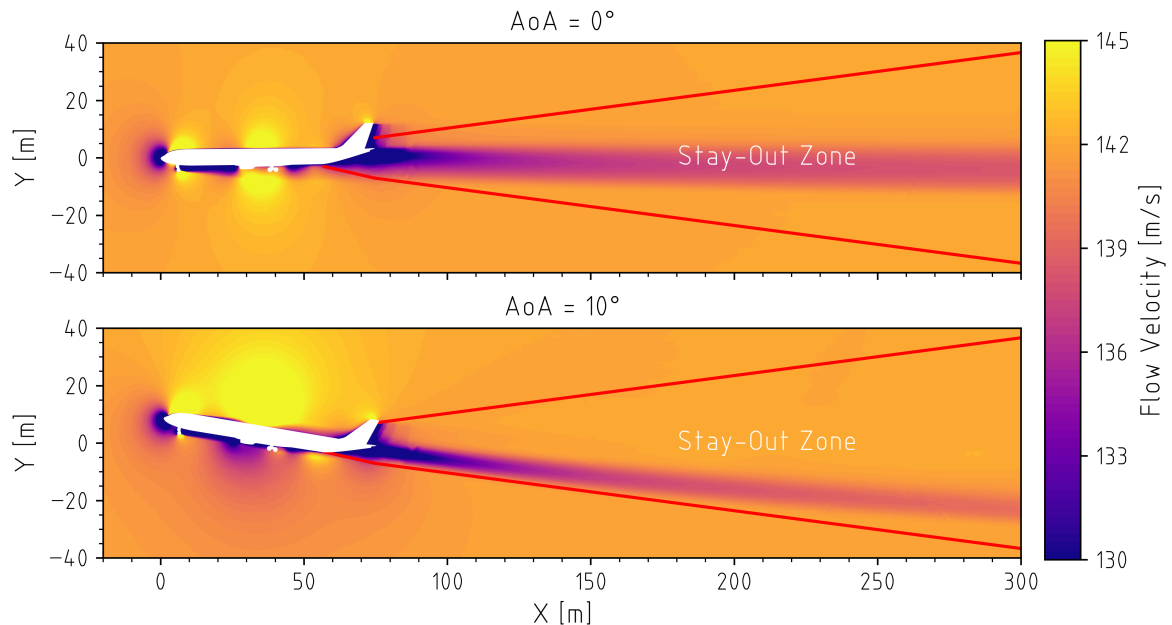


Figure 3.9: Definition of the Wake Stay-Out Zone Compared to CFD (Computational Fluid Dynamics)-Characterized Airflow Velocity Data [43]. The CFD data is a contour plot of the absolute airflow velocity in the TA's plane of symmetry. Note that the displayed range of 130-145 m/s merely serves demonstrative purposes, and does not reflect the full velocity range.

3.2.7. Assumptions

With this, the entire core of the Towing Model has been established and presented. Throughout the previous sections, a number of assumptions have been made, either to simplify resulting calculations, or to prevent the addition of unneeded complexities. These assumptions are re-iterated below, each with a unique **TMA-XX** identifier:

TMA-01 The roll and yaw angles, as well as sideslip translation between all vehicles is negligible.

*This is a crucial assumption related to model requirement **TWM.NF-01**, concerning the 2D nature of the Towing Model. All of the three phenomena are limited during typical IAC procedures [14], and do not have a significant influence on the ACCD's design space.*

TMA-02 The altitude, velocity, and flight path of the towing system are assumed to be constant.

*This corresponds to requirement **TWM.NF-06**. The constant velocity and FPA reflect the majority of formation flight and tow-back, while changes in altitude would only affect the dynamic pressure on a large timescale.*

TMA-03 The tether attachment and CoG of the ACCD and RLV are aligned with the body axis of these vehicles.

For the ACCD, this assumption matches very closely with the mechanical design presented in chapter 6. For the RLV, any radial misalignments are relatively minor compared to the axial length of the vehicle.

- TMA-04** The ACCD is flown in the '+'-configuration, as defined in subsection 2.2.1.
This assumption corresponds to the CFD data used for computing aerodynamic forces on the ACCD. When flying in the 'x'-configuration, the ACCD's manoeuvrability should be slightly decreased [46]; however, essential conclusions from this chapter still hold.
- TMA-05** The effect of air speed on aerodynamic coefficients is neglected.
This assumption again concerns the aerodynamic data that is used by the model, which hold for a Mach number of 0.45.
- TMA-06** The contribution of wind to local airflow is neglected.
Although additional wind could increase the dynamic pressure on all vehicles, this effect is compensated for by overestimating the extreme flight conditions in section 3.4.
- TMA-07** The altitude-dependence of air pressure and temperature is assumed to match the 1976 US Standard Atmosphere Model.
Minor deviations from this model are compensated for by overestimating the extreme flight conditions in section 3.4.
- TMA-08** The tether is assumed to be perfectly flexible and infinitely thin, with a uniform density and cross-section.
In reality, the tether has a diameter of 24 mm, which is negligible compared to the total length of around 250 m [37]. Furthermore, the UHMWPE material provides ample flexibility to the tether [53].
- TMA-09** Aerodynamic forces on the tether are neglected.
This assumption is verified in subsection 3.2.9, where the catenary tether is compared to the fully dynamic Simulink model, which includes aerodynamic forces [37].
- TMA-10** Aerodynamic on the ACCD are negligible compared to those acting on the RLV.
This assumption can be verified with the CFD data included in Appendix E, or by comparing Figures 3.11 and 3.13.
- TMA-11** The effect of the TA's pitch control deflection on its lift and drag is neglected.
Since the TA model is aimed at an estimation of extreme towing loads, and since these extremes occur during tow-back, this assumption mainly concerns the TA's clean configuration. As shown in Figure E.5, the relative insensitivity of the TA's aerodynamic force coefficients to its control deflections is especially pronounced for this configuration.
- TMA-12** The TA applies excess thrust as a step function, aligned with the vehicle's body axis.
This instantaneous nature of the excess-thrust application results in an overestimation of resulting towing forces, which partly compensates other model assumptions. In reality, the TA's thrust angle is minor [27].
- TMA-13** All elements of the towing system experience the same acceleration.
In reality, different accelerations result in a new towing position. However, during tow-back (which poses the largest towing loads), the RLV adjusts its control deflections to match the TA's behaviour, causing the overall towing position to stay relatively constant.
- TMA-14** The influence of the TA's wake does not extend more than 7.5° below its flight path.
As illustrated in Figure 3.9, this is a valid assumption for AoAs up to 10°, with local velocity differences outside this region not exceeding 2 m/s.

Next to these assumptions, another major simplifying factor in the Towing Model stems from the analysis of steady-state conditions (**TWM.NF-01**). Except for the modelling of excess-thrust scenarios, dynamic effects are largely neglected. When it comes to the ACCD design space exploration, the essential objective concerns the observation of general trends, rather than exact values. As such, inaccuracies introduced by the aforesaid simplifying assumptions are not impactful, and do not directly influence the ACCD's design. For the modelling of extreme towing loads on the other hand, where numerical values are essential, an overestimation of extreme flight conditions in section 3.4, as well as the application of a 1.5 Safety Factor (SF) in chapter 6 provide design margin.

3.2.8. Outputs

With the fundamental groundworks, as well as assumptions and limitations of the Towing Model established, a number of major model outputs can now be presented. As defined in subsection 3.2.1, these outputs serve as insight-accelerators, as well as requirement generators and verification tools. The following two subsections cover the most important model outputs, corresponding with the formation flight and tow-back scenarios as defined in Figure 3.1.

Formation Flight

During formation flight, only the ACCD is being towed, while the RLV flies in formation with the towing system. This part of flight is mainly relevant for the ACCD design space exploration (**TWM.F-04**). Given a specific set of inputs (e.g. Table 3.1), position plots such as Figure 3.10 can be generated (**TWM.F-02**). It shows the steady-state towing position of the ACCD relative to the TA, expressed in the global LVLH reference frame (i.e. relative to the TA's tether attachment). For the same setup, a free-body diagram such as Figure 3.11 can also be obtained, visualizing the relevant forces acting on the ACCD (**TWM.F-08**). Here, a LVLH reference frame is again used, but now attached to the ACCD's CoG.

ACCD Properties		Tether Properties	
m	178.4 kg	l_T	250 m
e	0.9 m	d_T	24 mm
f	-0.3 m	ρ_T	755 kg/m ³
δ	6°	Environmental Parameters	
TA Properties		H	6000 m
m'	280 Mg	Ma	0.55
δ'	0°	γ	-6.5°

Table 3.1: Reference Model Inputs for Generating Exemplary Towing Model Outputs During Formation Flight. For the TA, a *diving* configuration is used.

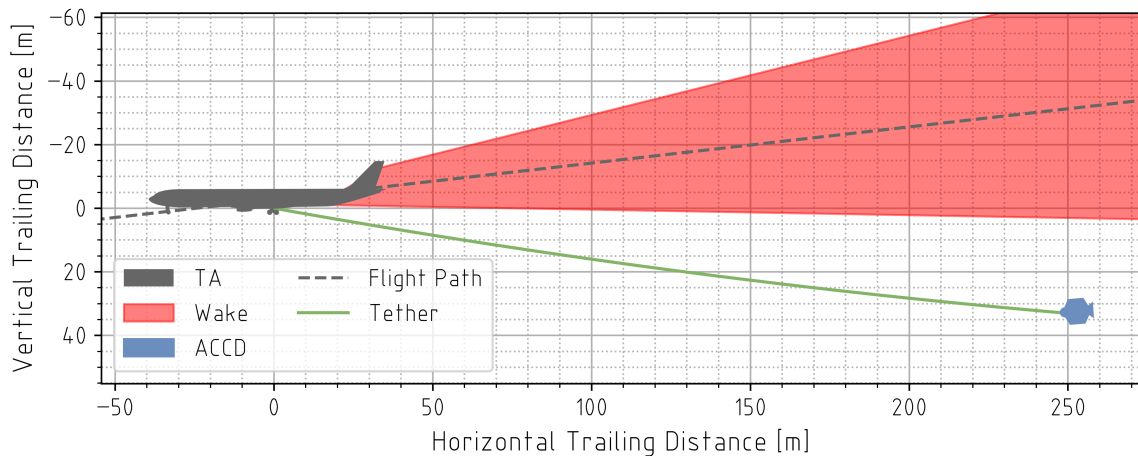


Figure 3.10: Example of a Towing Position Plot During Formation Flight. As is the case for all position plots depicting the formation flight phase, the ACCD is enlarged with a scale factor 5, to improve the figure's clarity.

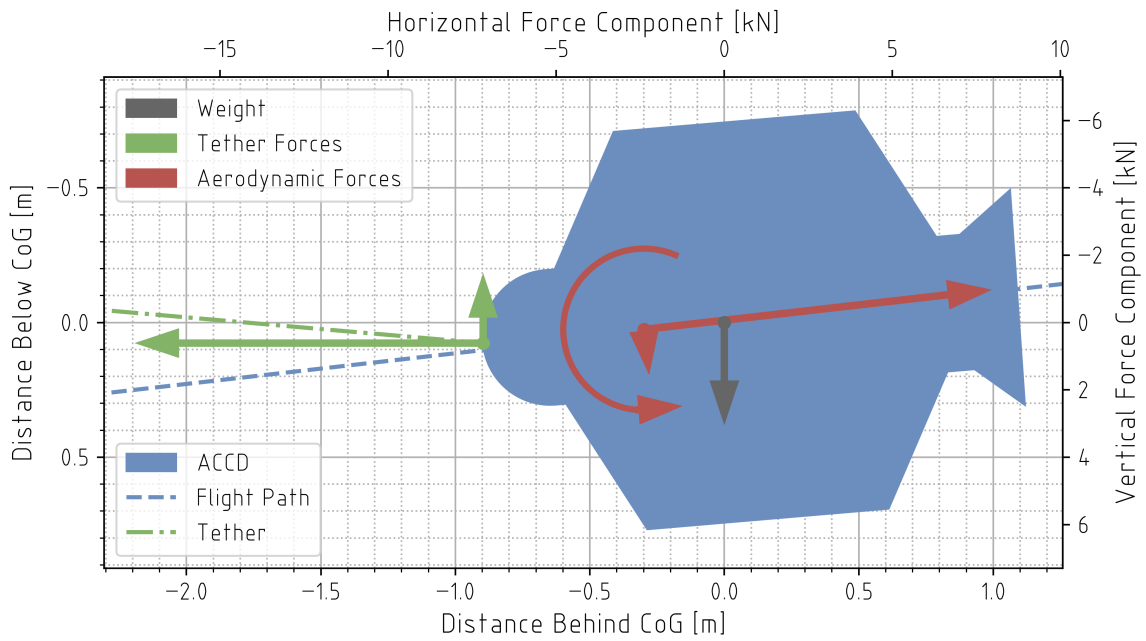


Figure 3.11: Example of an ACCD Free-Body Diagram During Formation Flight.

Tow-Back

The tow-back phase of IAC, where the RLV has been connected to the ACCD, is particularly relevant for the definition of extreme towing loads (TWM.F-03). In a similar manner as for the formation flight, position plots such as Figure 3.12 can be generated. Corresponding changes to the model inputs from Table 3.1 are listed in Table 3.2. Again, free-body diagrams such as Figure 3.13 can also be generated (TWM.F-08).

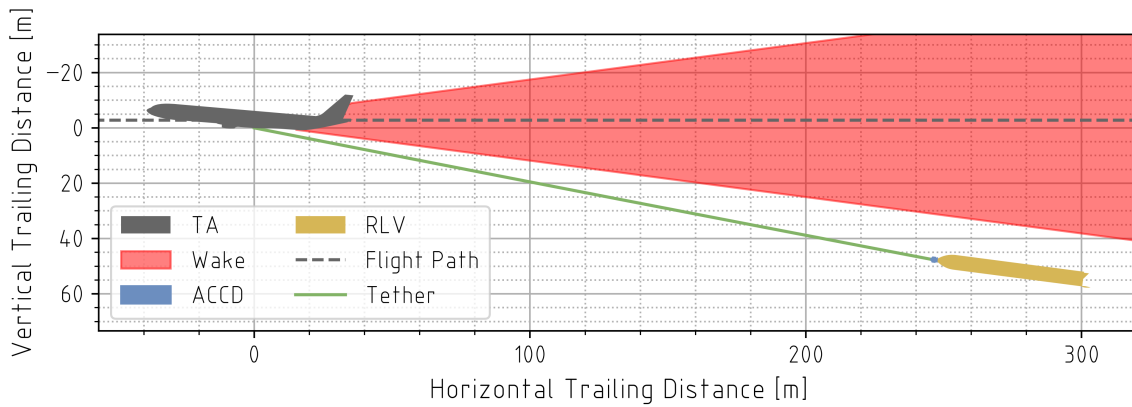


Figure 3.12: Example of a Towing Position Plot During Tow-Back.

RLV Properties	
m	80.178 Mg
e	41.013 m
f	0 m
δ	11°
Environmental Parameters	
γ	0°

Table 3.2: Reference Model Inputs for Generating Exemplary Towing Model Outputs During Tow-Back. For the TA, a clean configuration is used.

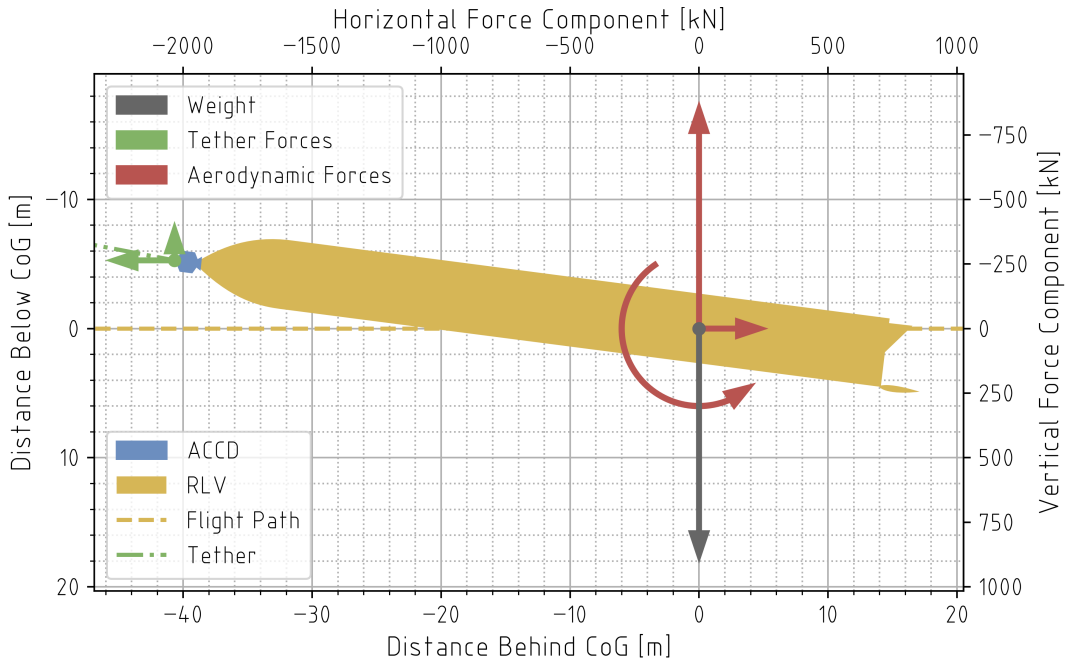


Figure 3.13: Example of an RLV-ACCD Free-Body Diagram During Tow-Back.

3.2.9. Verification

Model verification is performed in a number of different ways. For one, free-body diagrams such as Figures 3.11 and 3.13 allow for a visual verification of the modelled forces and torques. For example, in Figure 3.11, the ACCD has a near-zero AoA ($\alpha = 1.6^\circ$) and a pitch deflection $\delta = 6^\circ$. Using a positive deflection as defined in Figure 3.14, this results in negative, downwards-facing lift - as can be observed in Figure 3.11. Additionally, the Towing Model performs internal sanity checks, which verify in a more rigorous manner if force and moment equilibria are satisfied.



Figure 3.14: Definition of Positive Pitch Deflection.

Furthermore, the steady-state towing conditions can also be compared with results generated using SART's 6DoF transient Simulink simulator discussed in chapter 2. An example of such a comparison is shown in Figure 3.15, with corresponding model inputs listed in Tables 3.1 and 3.3. For the Simulink model, an average of 44 s was needed to reach the steady-state at $t = 32$ s. Using the Python Towing Model, analysis of equivalent conditions takes a mere 49 ms. Both of these values are averaged between five separate computational runs.

ACCD Properties	
m	164.5 kg
e	0 m
f	0 m
δ	0°
Environmental Parameters	
γ	0°

Table 3.3: Reference Model Inputs for Simulink Verification.

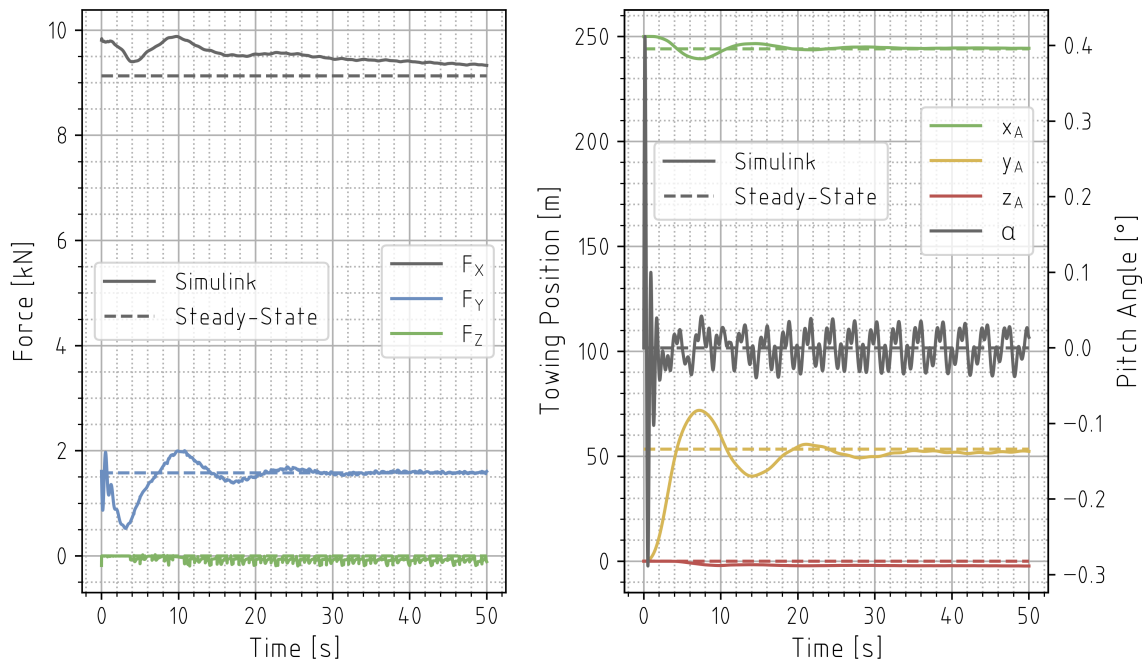


Figure 3.15: Comparison of Simulink (Solid Lines) and Steady-State (Dashed Lines) Towing Model Outputs. Since the steady-state model does not include a Z-dimension, the steady-state values for F_z and z_A are set to zero.

Despite the significantly more complex nature of the Simulink model, Figure 3.15 clearly shows that its results converge towards the solution found with the steady-state model. This is further illustrated by Figure 3.16, which visualizes the convergence of the Simulink solution to a steady-state condition - which is reached at $t = 32\text{ s}$ (**TWM.NF-07**). Additionally, it also shows the convergence of the Simulink solution to the steady-state results computed with the Towing Model (**TWM.NF-07**). The relatively slow convergence of F_x can be attributed to the dynamic behaviour of the TA, which has a non-zero acceleration in the Simulink model - resulting in additional inertial towing forces. For the dimensioning of towing loads, such phenomena are captured with the excess-thrust TA model discussed in subsection 3.2.5. Furthermore, the attitude oscillations, as well as Z-component of positions and forces in the Simulink data, are caused by numerical artefacts - for example when interpolating CFD data.

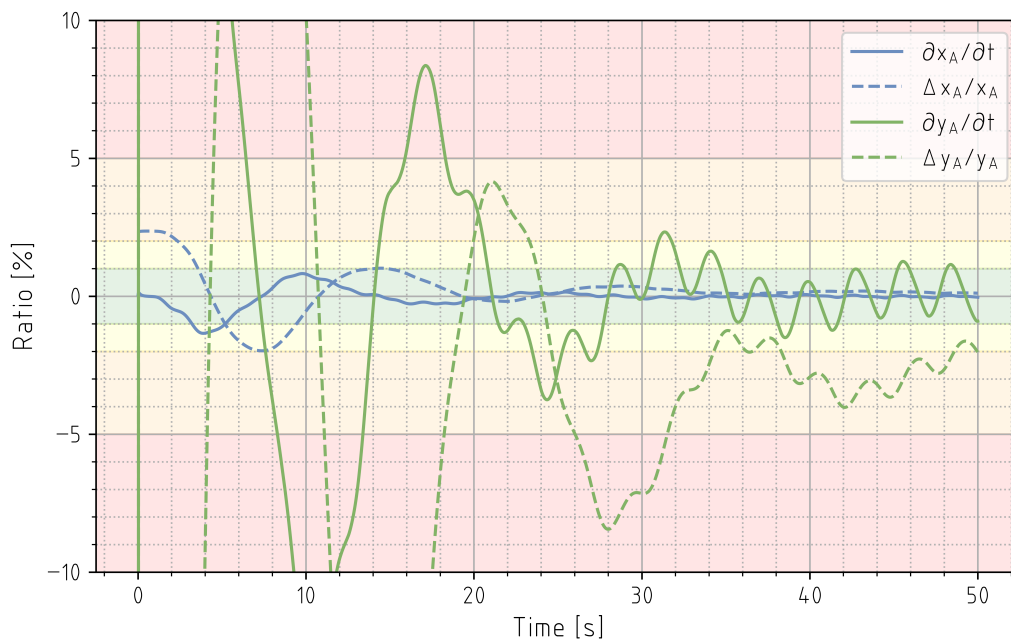


Figure 3.16: Convergence of the Simulink Transient Solution to its Steady-State Conditions (Solid) and the Towing Model Results (Dashed).

With the entire Towing Model presented and verified, it can now be used in subsequent sections to fulfil two major model requirements. On the one hand, sensitivity analyses during formation flight allow a design space exploration (**TWM.F-04**). On the other hand, an extreme load analysis can be performed using the model's tow-back configuration (**TWM.F-03**).

3.3. ACCD Design Space

Throughout the following subsections, the ACCD's design space is explored - particularly focused on configurations that do not interfere with the TA or its wake. Because forces during formation flight are only of secondary importance, their behaviour is not studied. The main variable parameters are the ACCD's mass and CoG, analysed in subsections 3.3.1 and 3.3.2 respectively, as well as its pitch control deflection, studied in subsection 3.3.3. Finally, subsection 3.3.4 briefly discusses the tether design space, with further details provided in Appendix I.

3.3.1. Mass

Figure 3.17 illustrates the effect of the ACCD's mass on its towing position, exhibiting only a minor sensitivity. This is a crucial finding, as it shows that the steady-state conditions of the towing system do not impose any practical restrictions on the allowable ACCD mass. Interesting to note further is the fact that the observed relation between the ACCD mass and towing position depends on the location of the vehicle's CoG, with a forwards-located CoG (e.g. $e = 0.3 m$) resulting in an inversion of the observed relation (i.e. heavier ACCDs hanging lower). For CoG positions $e \approx 0.6 m$ (i.e. coinciding with the MRP), the towing position is almost fully insensitive to the ACCD mass.

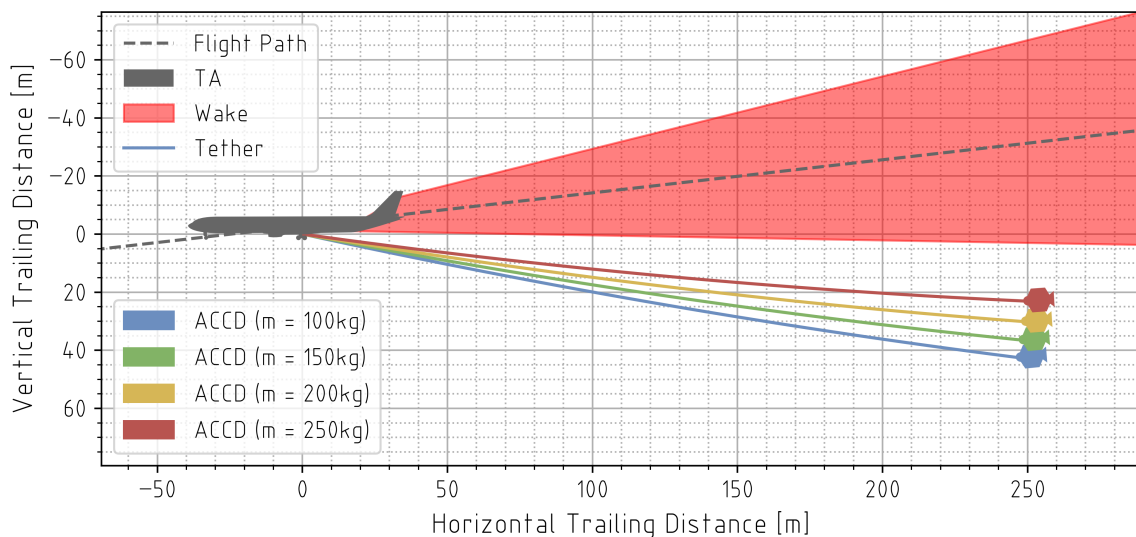


Figure 3.17: Sensitivity of the ACCD's Towing Position to its Total Mass. Constant model inputs are listed in Table 3.1.

3.3.2. Centre of Gravity

When it comes to the location of the ACCD's CoG, Figure 3.18 shows a significantly more pronounced effect on the steady-state towing position, with aft-located CoGs resulting in a higher towing position - potentially interfering with the TA's wake. On the other hand, the position of the ACCD's CoG also has an influence on the aerodynamic stability of the vehicle [12]. Because of this, Stappert previously advocated the addition of a trim mass, which moves the CoG forwards [12]. Based on the sensitivity analysis shown below, as well as a first iteration of the mechanical design, a target CoG position at the vehicle's midway point ($e = 1 m$) is proposed.

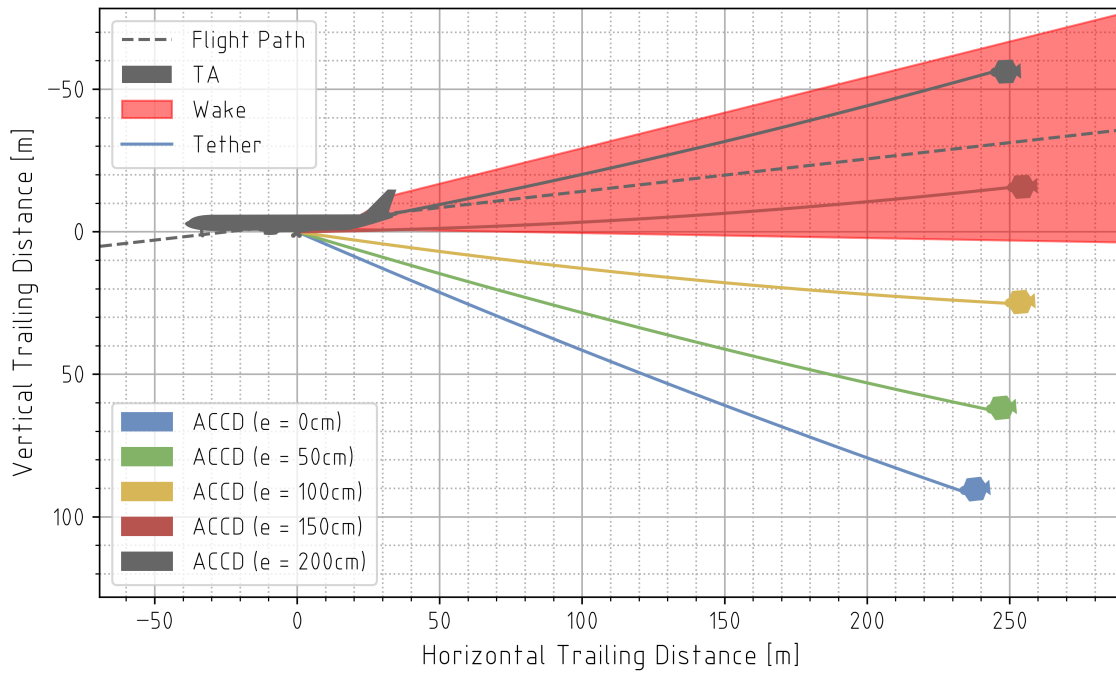


Figure 3.18: Sensitivity of the ACCD's Towing Position to the Location of its CoG. Constant model inputs are listed in Table 3.1. Note that the extrema of $e = 0\text{ m}$ $e = 2\text{ m}$ represent the (physically unrealistic) edge cases of the ACCD's aerodynamic shell.

3.3.3. Pitch Control Deflection

Next, pitch control deflections can be varied to study the ACCD's manoeuvrability, and identify its reachable area. Results from such an analysis are presented in Figure 3.19, which clearly shows a very large sensitivity to the pitch control input. This shows that the ACCD has ample aerodynamic control capabilities, and can effectively reach any desired towing position. By trimming the control surfaces, the ACCD can compensate for a lot of adverse effects caused by parameters such as vehicle mass and CoG. Even in an extreme case where the CoG is located 1.8 m behind the nose of the ACCD, a deflection of 10° can still bring the ACCD down below the TA's wake.

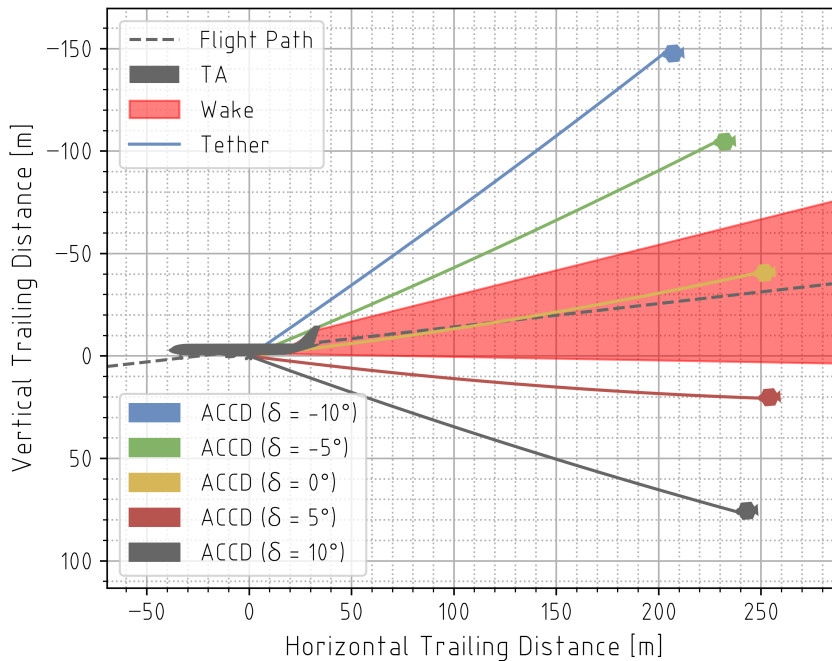


Figure 3.19: Sensitivity of the ACCD's Towing Position to its Pitch Control Deflection. Constant model inputs are listed in Table 3.1. The $\pm 10^\circ$ extrema represent the limits of the available CFD data.

3.3.4. Tether Properties

Although the tether is no direct part of the ACCD design space (**TWM.F-04**), analysing its effect on the towing system can offer additional insight and verification value for the model. Further details concerning this analysis can be found in Appendix I, with the main conclusions being that an increased diameter and length help keep the ACCD away from the TA's wake to a certain degree.

Finally, combining results from the three previous sections, the overall design space of the ACCD can be characterized with Figure 3.20. For a given pitch deflection, this figure defines the available ACCD inertial design space in terms of vehicle mass and CoG. Configurations *below* a specific curve are able to stay clear of the TA's wake (under that specific control deflection). Looking at the target CoG position of 1 m, this design map show that expected ACCD masses (100-200 kg) result in an upper towing position corresponding to a pitch deflection between 2.5° and 5°.

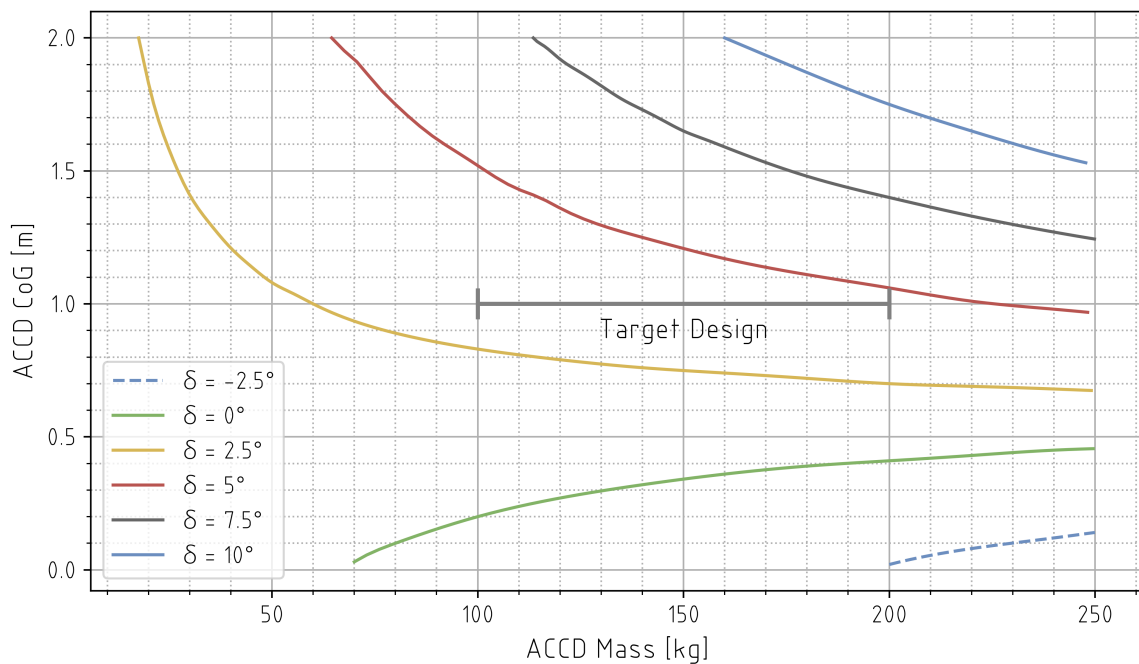


Figure 3.20: Characterization of the Relevant ACCD Design Space. Constant model inputs are listed in Table 3.1.

3.4. Extreme Towing Loads

With an initial exploration of the ACCD design space performed in the previous section, the second major use case of the Towing Model can now be considered: an analysis of extreme towing loads (**TWM.F-03**). In order to identify such extreme loads, subsection 3.4.1 first performs a number of sensitivity analyses on the tow-back phase of IAC, from which extreme operating conditions are identified. These are then analysed in more detail in subsection 3.4.2, and a design towing load is derived for use in later chapters.

3.4.1. Sensitivity Analysis

During tow-back, a number of input parameters affect the magnitude of towing loads - listed below. The FPA is not considered as a variable parameter, since it should be fixed at zero during tow-back. Additionally, the TA is always flying in a *clean* configuration during this part of IAC. The variability of the RLV's mass and CoG is related to uncertainty regarding the final design of this vehicle, as well as the potential presence of residual propellant. For the cruising altitude and velocity of the TA, similar uncertainty concerning the exact flight profile exists.

- **RLV mass** affects the vertical weight force.

- **RLV CoG** influences the moment equilibrium.
- **Altitude** influences the air density, changing the dynamic pressure and aerodynamic forces. Additionally, it also affects the performance of the TA's engines.
- **Velocity** similarly affects both the dynamic pressure and the TA's engine performance.

To investigate the effect of the inertial parameters (mass and CoG), a sensitivity study is performed under a *ceteris paribus* assumption and non-accelerating conditions. Results from the study are illustrated in Figure 3.21, which shows a double-faceted relation between RLV mass and towing forces. On the one hand, axial forces increase with increasing weight; on the other hand, radial loads are higher when the RLV is lighter. In order to properly study all relevant scenarios, both mass extremes need to be investigated. For the CoG, the observed relation is more straightforward, with the magnitude of axial and radial loads decreasing for aft-located CoGs.

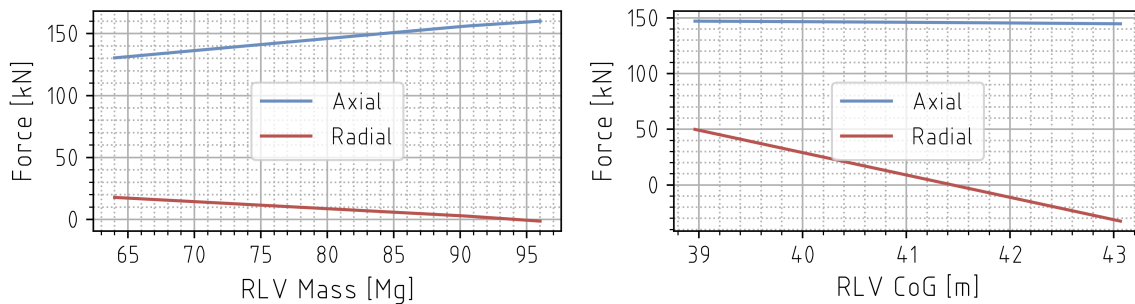


Figure 3.21: Sensitivity of Towing Loads to the RLV's Inertial Properties. Constant model inputs are listed in Table 3.2.

In theory, the pitch control deflections of the RLV can also affect the towing loads. However, because the towing system is very sensitive to this control input, not all available deflections result in realistic towing scenarios. Because of this, a zone of operations is defined, shown in Figure 3.22. The upper limit of this zone is determined by the pitch angle of the TA, as higher positions would cause the tether to interfere with the TA's body. The lower limit is fixed at 10° below the local horizon. For a given configuration (RLV properties and environmental parameters), both extreme towing positions are then characterized by corresponding control deflections δ . This way, the parameter δ is transformed into a *dependent*, rather than an *independent* variable. An additional module inside the Towing Model iteratively finds the control deflection that corresponds to these upper and lower towing limits.

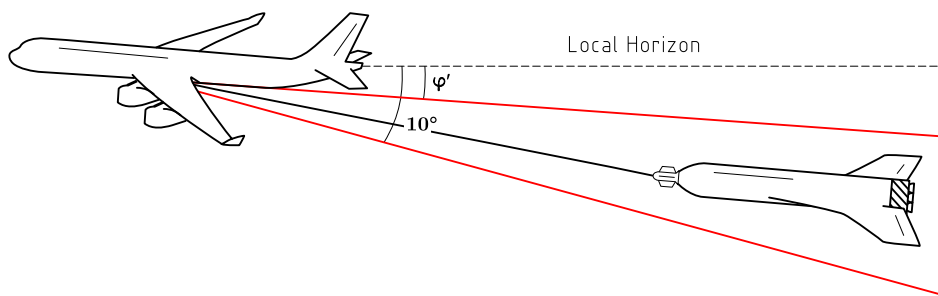


Figure 3.22: Definition of the Zone of Operations for RLV Towing.

Finally, when it comes to the environmental parameters (altitude and velocity), a more in-depth analysis is required. This is because they affect the TA's engine performance, with peak thrust being inversely related to air speed - as illustrated in Appendix H. In other words, although increased cruising speeds result in higher aerodynamic forces, the aircraft's available thrust is also reduced. Results from a 2D sensitivity study are presented in Figure 3.23, which shows the excess-thrust axial loads corresponding to the lower towing limit defined above. Unattainable scenarios in terms of TA thrust are identified, while unrealistic scenarios in terms of TA attitude are also marked. For the latter, a limit of a 5° AoA is considered, which leaves an RLV towing zone spanning 5° .

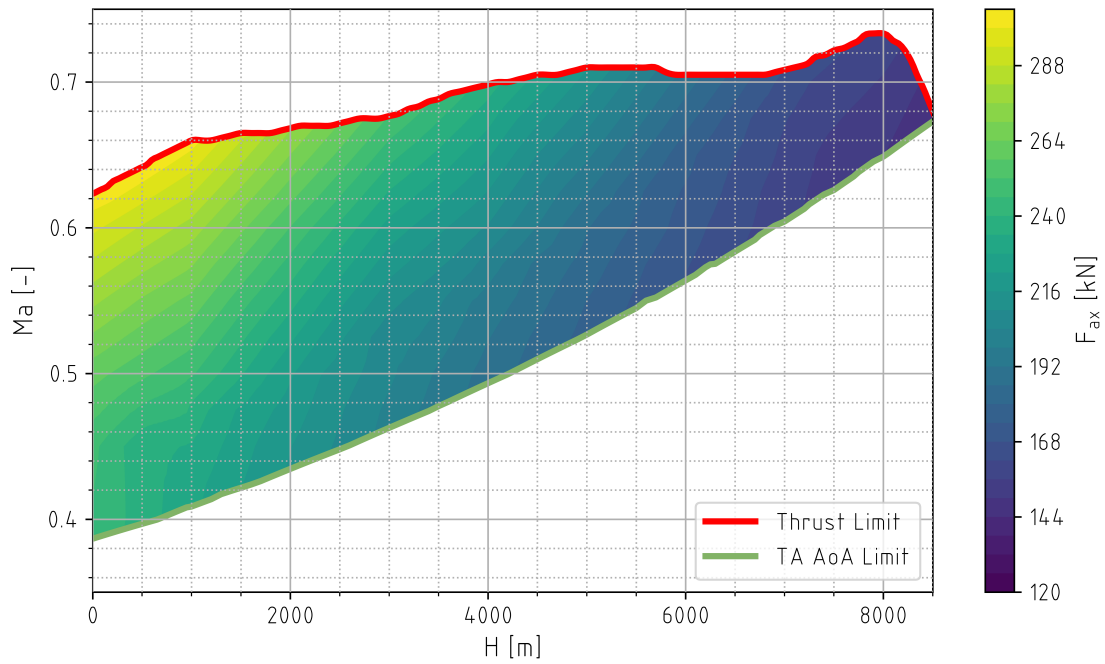


Figure 3.23: Sensitivity of Excess-Thrust Towing Loads to Environmental Parameters. Constant model inputs are listed in Table 3.2.

As can be seen in Figure 3.23, the increase in dynamic pressure at high velocities outweighs the reduction in TA thrust. This is consistent with the underlying equations, as the dynamic pressure is related to the square of the velocity, while the thrust relations shown in Appendix H are only proportional to $1/V$. Based on these observations, as well as a typical RLV release altitude of 1000 m, the extreme environmental scenario characterized by Equation 3.21 is defined. These conditions are a deliberate overestimation of the true extreme operating conditions of the towing system, meant to compensate for the Towing Model assumptions listed in subsection 3.2.7. In particular, the overestimated environmental conditions serve as a safety margin to account for additional dynamic loads, which are not included in the model.

$$\begin{cases} Ma = 0.65 \\ H = 1000 \text{ m} \end{cases} \quad (3.21)$$

3.4.2. Extreme Operating Points

Combining the extreme environmental scenario with the observations concerning the RLV's inertial properties and towing position, four extreme operating points are defined - listed in Table 3.4. These correspond to forward- and aft-located CoGs, as well as upper and lower towing positions. For the CoG, a 5% deviation relative to the nominal value is considered, while the extreme RLV mass is taken as 105% of the nominal mass. To differentiate between the four points, they are given the identifiers *FU*, *FL*, *AU*, and *AL* - where the first letter refers to the CoG position (*Forward* or *Aft*), and the second indicates the towing position (*Upper* or *Lower*).

		CoG Position	
		Forward (F)	Aft (A)
Towing Position	Upper (U)	$m = 84 Mg$ $e = 39.062 m$ $H = 1000 m$ $Ma = 0.65$ $\delta = 2.76^\circ$	$m = 84 Mg$ $e = 42.963 m$ $H = 1000 m$ $Ma = 0.65$ $\delta = 6.77^\circ$
	Lower (L)	$m = 84 Mg$ $e = 39.062 m$ $H = 1000 m$ $Ma = 0.65$ $\delta = 4.83^\circ$	$m = 84 Mg$ $e = 42.963 m$ $H = 1000 m$ $Ma = 0.65$ $\delta = 8.90^\circ$

Table 3.4: Definition of the Extreme RLV Tow-Back Operating Points. The control deflections δ listed above are automatically computed by the towing simulator, corresponding to the desired towing position. At each point, peak excess thrust is applied.

Analysing each of the extreme scenarios individually, corresponding loads listed in Table 3.5 are obtained. From these results, it can be seen that operating point *AL* presents the highest axial load, while the radial force peaks at point *FL*. In general, an aft-located CoG results in higher axial loads, while the lower towing limit shows the highest radial loads. Finally, at the upper towing limit, radial loads are negative, indicating a downwards force (from the ACCD's perspective). Because of this sign switch, it can be inferred that there exists a towing position where radial loads are fully eliminated. Based on the presented extreme load analysis, an axial towing load of 300 kN is proposed. The margin of this load stems from the overestimated environmental conditions, while an additional 1.5 SF is further applied in chapter 6. In this initial iteration of the ACCD design, the radial towing force is not considered; however, results below indicate a representative design load in the order of 15-30 kN.

		CoG Position	
		Forward (F)	Aft (A)
Towing Position	Upper (U)	$F_{ax} = 292.24 kN$ $F_{rad} = -11.90 kN$	$F_{ax} = 296.81 kN$ $F_{rad} = -15.53 kN$
	Lower (L)	$F_{ax} = 295.66 kN$ $F_{rad} = 29.78 kN$	$F_{ax} = 303.56 kN$ $F_{rad} = 27.19 kN$

Table 3.5: Axial and Radial Towing Forces Corresponding to the Extreme RLV Tow-Back Operating Points

3.5. Conclusion

In this chapter, the concept of the IAC towing system was presented, and the importance of its behaviour highlighted. Based on a set of requirements, a 2D, steady-state Towing Model was developed and verified. Compliance of these model requirements is summarized in Table 3.6, while future studies of physical towing systems are required for model validation. Using the Towing Model, an analysis of the formation flight - where only the ACCD is attached to the TA - provides an opportunity for exploring the ACCD's design space. Based on this exploration, a target CoG located 1 m behind the ACCD's nose is proposed, while its mass shows a negligible influence, and sensitivity to control deflections demonstrates the vehicle's ample manoeuvrability. Furthermore, a study of the tow-back phase - where the RLV is also part of the towing system - enables an estimation of extreme operating conditions and corresponding towing loads. From this, an axial design load of 300 kN is proposed. Both main results (design load and target CoG) will be used as crucial reference points for the mechanical design in chapter 6.

Requirement	Compliance
TWM.NF-01	Fully compliant; model simulates 2D steady-state behaviour of the towing system.
TWM.F-02	Fully compliant; position plots presented in subsection 3.2.8.
TWM.F-03	Fully compliant; extreme load analysis performed in section 3.4, including TA excess-thrust scenarios.
TWM.F-04	Fully compliant; effect of ACCD mass, CoG, and control deflection analysed in section 3.3.
TWM.NF-05	Fully compliant; vehicle CFD data integrated into model.
TWM.NF-06	Fully compliant; all required parameters are model inputs.
TWM.NF-07	Largely compliant; towing position is within required accuracy range, but Simulink towing forces do not reach a steady-state condition.
TWM.F-08	Fully compliant; exemplary force plots presented in subsection 3.2.8.
TWM.NF-09	Fully compliant; typical model solution only takes 0.11 % of the time required for Simulink model to arrive at a (quasi) steady-state.

Table 3.6: Compliance of the Towing Model to its Model Requirements

4

Relative Navigation

After having obtained a solid understanding of the ACCD's towing behaviour, another major aspect of the vehicle can now be investigated, concerning its relative navigation system - which it uses to perform relative attitude and position estimation of the RLV (**CR-SYS.F-11**). This is a vital function of the ACCD, as it enables the successful manoeuvring, and eventual docking between both vehicles. Decisions regarding the implementation of the relative navigation system have significant implications on the electronic and mechanical design of the ACCD. In particular, the sensor system that is used to achieve this position and attitude estimation needs to be investigated.

First, a list of relevant requirements and risks is established in section 4.1, defining the functionalities and constraints of the sensor system. Section 4.2 presents a number of typical sensor solutions found in literature, from which a particularly promising option - called VisNav - is selected. This solution is then further analysed in section 4.3, where a model is described that enables simulation and characterization of the sensor's performance. In section 4.4, said model is used to analyse the VisNav system, and to derive a final representative configuration for its integration into the ACCD. Finally, section 4.5 reiterates the main conclusions from this chapter.

4.1. Requirements and Risks

The overall relative navigation system, or detection system, should satisfy four major requirements, listed below. These follow from high-level system requirement **CR-SYS.F-11**, and further specify the scope of the relative position and attitude estimation. Further details are provided in Appendix A.

KY-DTC.F-11/01: The detection system shall be able to measure the relative position between the RLV and ACCD with a minimal accuracy of 20 cm, while measuring its relative attitude with a minimal accuracy of 1°.

KY-DTC.F-11/02: The detection system shall be able to start its measurements defined in **KY-DTC.F-11/01** within a range of at least 400 m, and within an angle of view of at least 90°.

KY-DTC.NF-11/03: The detection system shall have a minimal measurement frequency of 50 Hz, in order to enable responsive vehicle control.

CR-DTC.F-11/04: The detection system shall be able to fulfil **KY-DTC.F-11/01** until **KY-DTC.NF-11/03** under any lighting or weather condition, including at night, or in fog/clouds.

First of all, the required accuracy of the system (**KY-DTC.F-11/01**) is directly related to the misalignments allowed by the docking mechanism - defined in chapter 6. Dynamically, the vehicles' attitude is of greater importance than their position, because parameters such as the AoA significantly affect aerodynamic forces. Because of this, the required sensing accuracy is tighter in rotational than in translational dimensions. Inaccuracies in the latter can also be more easily accommodated thanks to the

ACCD's relatively large docking cone.

Next, the required operational range (**KY-DTC.F-11/02**) and refresh rate (**KY-DTC.NF-11/03**) of the system are estimated based on initial analyses [15]. Although these values are mostly tentative, the key takeaway is that the system's area of operations - defined by its range and Field of View (FoV) - should be as large as possible, so that there is enough time for manoeuvring both vehicles. This is especially crucial given the relatively short formation flight between the TA and RLV [40]. Furthermore, relative sensing measurements should be collected at a high enough frequency, as short reaction times are vital in the final docking approach between both vehicles.

Finally, **CR-DTC.F-11/04** can be seen as the keystone requirement for this system. It is derived from the fact that RLV capture and recovery should be possible in all expected environmental scenarios [15]. Especially when launching from Kourou, French Guyana [18], the RLV capture is likely to happen under cloudy conditions [54], at night, or during twilight. To prevent a severe reduction of the permitted operational regime of the IAC procedure, the ACCD's detection system thus has to be able to operate under all these conditions.

Apart from the aforelisted requirements, six different risks related to the detection system can be identified - listed below. Within the scope of this work, no requirements are formulated concerning these (and other) risks; nevertheless, they are kept in mind when analysing and designing different aspects of the ACCD. Further details concerning system risks are provided in Appendix A.

- DTC-01:** The RLV and ACCD never get within range of the detection system, or do not stay there long enough to ensure relative navigation.
- DTC-02:** The RLV and ACCD never enter within the FoV of the detection system, or do not stay in it long enough to ensure relative navigation. This can be either due to the RLV's position, attitude, or sensor mounting configuration.
- DTC-03:** After successful initial detection, sensor connection is (temporarily) lost, due to range or FoV issues, or caused by an external obstruction (e.g. cloud) passing through the Line of Sight (LoS).
- DTC-04:** The detection system loses power.
- DTC-05:** Communication is lost between the ACCD and the TA/RLV.
- APR-04:** The relative navigation measurements are too coarse/noisy for proper alignment between the ACCD and RLV.

The first two risks (**DTC-01** and **DTC-02**) are directly related to the system's required operational range (**KY-DTC.F-11/02**), further emphasizing the need for aerodynamically stable vehicles, which do not oscillate significantly (**CR-TOW.NF-01/10**). Additionally, the risk of a connection loss (**DTC-03**) is vital, as these are very likely to occur, and the relative navigation system should be robust enough to handle them [15]. Next, risks **DTC-04** and **DTC-05** primarily have implications for the ACCD's electronic design, discussed in chapter 5 - with the latter being important because most relative navigation systems rely on mutual communication between the ACCD and RLV. The final risk (**APR-04**) is related to the approach between both vehicles, and further emphasizes the need for accurate measurements (**KY-DTC.F-11/01**).

4.2. Sensor System

In general, the effectiveness and performance of the relative navigation system is highly dependent on the chosen sensor system. As such, a proper overview and comparison of available options is paramount to determine an adequate solution for the investigated IAC application. To this end, a brief literature overview of available and relevant sensor solutions is presented in subsection 4.2.1 - particularly inspired by AAR applications, where similar systems have been investigated. Using the requirements postulated in section 4.1, a trade-off between the most promising technologies is then made in subsection 4.2.2, and a sensor solution is proposed.

4.2.1. Background

In general, each sensor offers a solution to the universal trade-off between accuracy and range. As such, systems found in AAR typically employ two or more different types of sensors, in an effort to combine fine accuracy with a large range [55]. The aim is to create a complementary set of sensors, where data diversity increases robustness against degradation of one of more sources (**DTC-03**) [56]. A similar approach was followed for subscale flight demonstrations performed during Project FALCon [57].

For initial, coarse measurements, GNSS (Global Navigation Satellite System) solutions are often used [55], [57], [58]. Such systems come with a number of advantages, including maturity [59], worldwide coverage [60], and minimal processing [61]. However, GNSS sensors have limited accuracy and bandwidth [62], which are insufficient for the final, close-proximity approach between the RLV and ACCD. Furthermore, the TA is at risk of blocking the sensor's satellite connection [63]. Finally, different potential sources of error exist, including satellite drop-out [60], integer ambiguity [64], and ionospheric scintillation [56]. In order to mitigate these issues, GNSS data is typically complemented by an Inertial Navigation System (INS). This use rate- and acceleration-measuring devices (e.g. three-ring laser gyroscopes [65]) in combination with an integration scheme, in order to estimate vehicle attitude, velocity, and position [46], [63].

Nevertheless, the resulting measurements are typically still not accurate enough for the final phases of approach and docking [58]. Hence, a third type of sensor is typically used in AAR, which can generally be classified as 'electromagnetic detection systems'. Within this sensor class, two major technological branches can be discerned, illustrated in Figure 4.1, and discussed in the following two subsections: computer vision, and electro-optical grid reference systems. Other solutions, such as ultrasonic sensors [65], time-of-flight sensors [66] or radar [58] are not suited to meet the IAC requirements - either because of insufficient range and environmental robustness [61], or because of excessive SWaP footprints [67]. Finally, LiDAR (Light Detection and Ranging) systems have also been considered for similar applications [55], [57]. Although more robust to the effects of clouds, ambient light, and motion-blur [68], they suffer from attenuation due to atmospheric water vapour [58], while having a significant SWaP footprint, and a limited FoV [69].

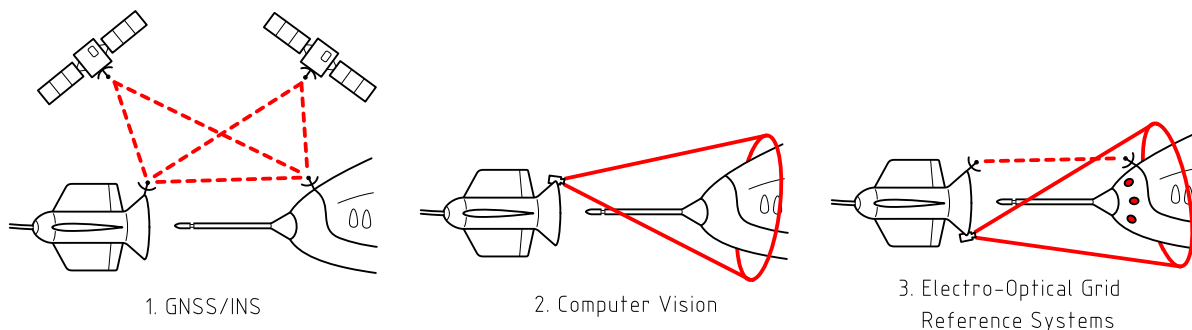


Figure 4.1: Schematic Comparison of Sensor Solutions for Relative Navigation. Note that the depicted configurations merely serve illustrative purposes.

Computer Vision

Computer vision systems typically use one [70] or two [71] generic, grayscale [72] or colour-sensitive [59] cameras. They rely on feature extraction, point matching, and pose estimation steps to extract relevant data [73]–[76]. In most applications, the target body is left unaltered, while some solutions apply active markers to the target to increase the system's robustness [77]. Generally, computer vision is a rapidly advancing field, but comes at the cost of significant computational power - typically requiring dedicated Graphical Processing Units (GPUs) [78]. Additionally, the inherent reliance on visible-wavelength data creates a crucial sensitivity to environmental parameters, with most systems not being robust to low-light or low-visibility conditions [67].

Electro-Optical Grid Reference Systems

On the other hand, electro-optical grid reference systems rely on a number of active beacons - such as Light-Emitting Diodes (LEDs) or laser diodes - that are detected by a Charge-Coupled Device (CCD), (quadrant) photodiode, or Position-Sensitive Device (PSD) [58], [62] - as illustrated schematically in Figure 4.2. Specific systems include the so-called VisNav technology - developed at the Texas A&M University [79] - and a similar solution studied at the University of Pisa, Italy [80]. They typically have a limited SWaP footprint thanks to their elementary detectors, which require less post-processing than computer vision [62]. Additionally, robustness against environmental and lighting conditions can be introduced by operating within the infrared (IR) spectrum [64]. A practical downside is the required addition of active beacons to the target, which can pose problems for AAR applications [67]. However, in the case of IAC, it forms less of an issue.

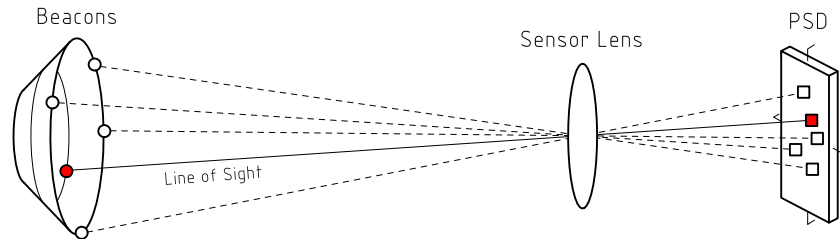


Figure 4.2: Schematic Working Principle of an Electro-Optical Grid Reference System [15].

4.2.2. Proposed Solution

Comparing computer vision and electro-optical grid reference systems, a trade-off is presented in Table 4.1 in terms of relevant subsystem requirements (**KY-DTC.F-11/01** through **CR-DTC.F-11/04**). Based on this comparison, electro-optical grid reference systems appear more tailored to the IAC application, especially concerning robustness against environmental conditions (**CR-DTC.F-11/04**). Furthermore, the need for a dedicated GPU in the case of computer vision is undesirable, as it would increase the required mass and power budgets for the ACCD.

Requirement	Computer Vision	Electro-Optical Grid Reference Systems
KY-DTC.F-11/01	Up to 2-10 cm [63], [81]	Up to 2 mm, 0.01° [62]
KY-DTC.F-11/02	Sensor-dependent	Sensor- and beacon-dependent
KY-DTC.NF-11/03	Up to 60 Hz [67]	Up to 100 Hz [62]
CR-DTC.F-11/04	Reduced performance in case of light interference, low light, or low visibility (clouds/fog) [67]	Robust to virtually all conditions [62]
Limitations	Requires a Graphical Processing Unit (GPU) [78]	Requires active beacons and communication [67], [79]
Benefits	Entirely passive [67]	Minimal Size, Weight and Power (SWaP) and processing [62]

Table 4.1: Comparison of Computer Vision and Electro-Optical Grid Reference Systems for Use in IAC Relative Navigation.

In conclusion, IAC poses demanding requirements on the relative navigation system, particularly in terms of environmental robustness, performance, and SWaP footprint. Based on the major technological trends identified in the previous subsection, a tripartite set of sensors is proposed for the IAC application: a combined GNSS/INS system for coarse position and attitude estimation, complemented by a fine-scale electro-optical grid reference system for precise relative navigation during final approach. For the latter, VisNav is chosen as a representative reference technology. In the field of AAR, similar systems have already been studied, fusing computer vision data with GNSS-based measurements [82], potentially further supported by INS data [83]. Additionally, studies have already looked into fusing VisNav with GNSS and INS systems [15], [84] - with further details provided in Appendix J.

4.3. VisNav Model

Having proposed a specific sensor solution, a significant design space still needs to be explored. Although both GNSS and INS systems have been extensively researched in the past [61], [85], their exact implementation only has limited implications for the overall ACCD design. In contrast, the VisNav technology has not yet been studied in depth for this type of application, while its sensor and beacons have more direct consequences for the ACCD. This is because they can potentially interfere with the ACCD's docking mechanism, while their mechanical mounting configuration can have a large influence on the system's performance [86].

In order to explore the available design space, and assess the effects that different VisNav configurations have, a comprehensive model is needed. In subsection 4.3.1, a set of requirements is generated that define this model in terms of its functionalities and constraints, while an overview of the overall Input/Output (I/O) flow is also presented. Next, subsections 4.3.2 and 4.3.3 describe the sensor and beacon configurations analysed by the model, while subsections 4.3.4 and 4.3.5 dive into its mathematical depths - respectively covering the analysis of beacon visibility and sensor image projection. Wrapping up, subsection 4.3.6 reiterates all model assumptions, and subsection 4.3.7 presents its main outputs. Finally, in subsection 4.3.8, model verification efforts are discussed.

4.3.1. Requirements

In the context of the ACCD's design, and overarching relative navigation research at SART, six VisNav Model requirements have been defined. They are listed below, and capture all major functionalities of the VisNav Model, while specifying the way in which they should be implemented.

- VNM.F-01:** The VisNav Model shall analyse the visibility of a three-dimensional (3D) VisNav beacon configuration, from the Point of View (PoV) of a VisNav sensor.
- VNM.NF-02:** The VisNav Model shall consider beacons mounted along the docking cone of the ACCD, either mounted inside the cone's surface, or along its aft rim. The sensor shall be mounted on the nose of the RLV.
- VNM.NF-03:** In order to allow for integration into an overarching relative navigation simulator, the VisNav Model shall include the following I/O-flow: given a certain beacon configuration and RLV position and attitude, the model shall output the visibility of each individual beacon. Relevant vectors shall be expressed in the ACCD body frame of reference.
- VNM.F-04:** The VisNav Model shall provide a means of comparing different beacon and sensor configurations, by determining corresponding approach corridors. These approach corridors are defined as the region in 3D space where the sensor detects enough beacons to perform relative position and attitude estimation.
- VNM.F-05:** Using the I/O-flow described in **VNM.NF-03**, the VisNav Model shall be able to analyse time-dependent beacon visibility, given a specific RLV trajectory.
- VNM.F-06:** To provide model insight and verification, the VisNav Model shall be able to produce sensor PoV imagery, where the visibility of individual beacons is visualized.

Within the confines of this work, the ultimate aim of the VisNav Model is to enable the definition of a representative beacon and sensor configuration, used as a baseline in subsequent chapters. To this end, the model should generate approach corridors (**VNM.F-04**), which offer a comparative measure for a configuration's performance. A definition, as well as an example of such an approach corridor is given in subsection 4.3.7. Essentially, they measure how many beacons are visible from a given point in space, which is a vital metric for the VisNav's performance [76]. Hence, the visibility of each individual beacon should be modelled (**VNM.F-01**). The specific configurations that are to be analysed (**VNM.NF-02**) are further defined in subsections 4.3.2 and 4.3.3.

Looking at the bigger picture of IAC Guidance, Navigation and Control (GNC) research at SART, the current VisNav Model needs to be integratable into an overarching relative navigation simulator

(VNM.NF-03). The required I/O interface allows beacon visibility to be analysed as a function of time, corresponding to a given RLV approach trajectory (**VNM.F-05**). Finally, the VisNav Model should also be able to generate images from the sensor's PoV (**VNM.F-06**), which are mainly used for model verification - as discussed in subsection 4.3.8.

Based on these requirements, the general flow of the VisNav Model is summarized in Figure 4.3. It considers a particular beacon and sensor configuration, together with the relative position and attitude of the ACCD and RLV. Using the sensor's and beacons' geometry, the total number of visible beacons is computed - which is the most essential output of the VisNav Model. The following subsections present the mathematical way in which this is achieved.

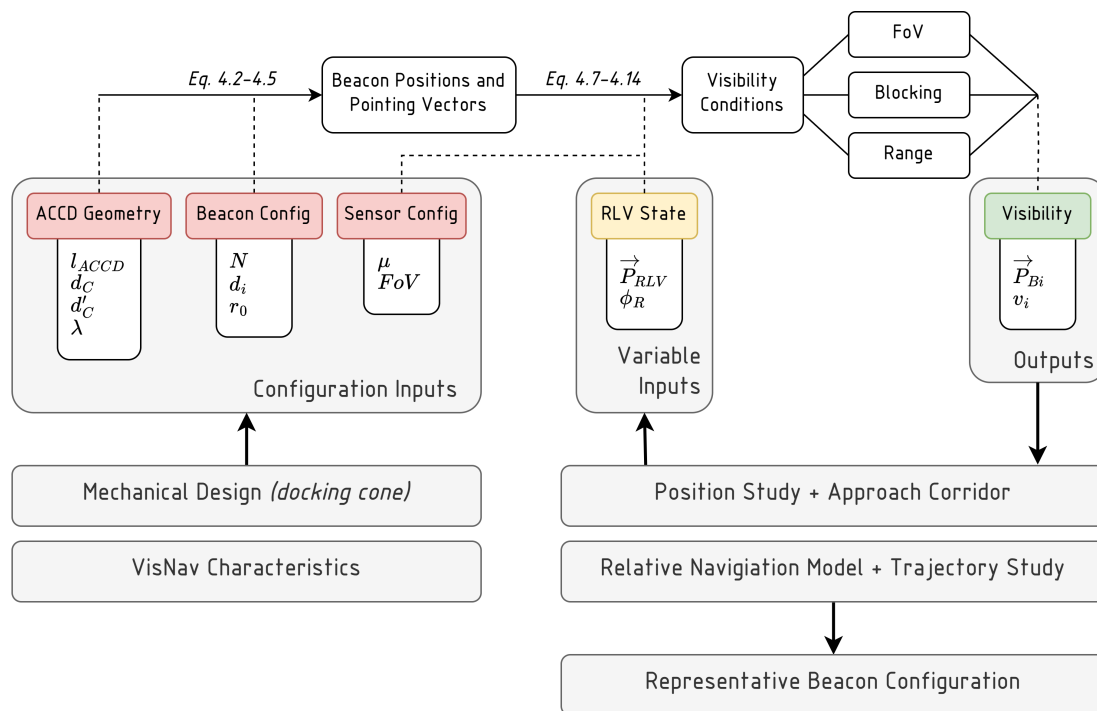


Figure 4.3: Flowchart of the VisNav Model, and Integration into the Overall Systems Engineering Approach. Definitions of the various parameters are provided in subsections 4.3.2 through 4.3.4.

4.3.2. Sensor Configuration

As defined in the previous subsection, the VisNav Model assumes the sensor to be mounted on the RLV, with beacons being attached to the ACCD (**VNM.NF-02**). This corresponds to typical AAR applications, where beacons are mounted to the refuelling drogue, with a sensor located on the refuelling aircraft [87]. Mechanically, this means that only a single element (the sensor) needs to be integrated into the RLV's Thermal Protection System (TPS), as opposed to multiple dispersed beacons. Furthermore, the conical shape of the ACCD's docking cone can be leveraged to point beacons in different directions, increasing the overall range and FoV of the system. Finally, placing the sensor on the ACCD would disturb its axisymmetry, resulting in more stringent roll control requirements in order for the sensor to always be pointing towards the RLV.

Mathematically, the sensor configuration is simplified by assuming that the RLV's plane of symmetry is parallel to that of the ACCD. This corresponds to an ideal, nominal approach, where roll and yaw angles between both vehicles are minimized [14]. Furthermore, the RLV's geometry is abstracted to a single point, located at the nose of the actual vehicle. The VisNav sensor is mounted at this same location, and its pointing vector coincides with the RLV's plane of symmetry. Overall, a definition of the VisNav Model reference system can be seen in Figure 4.4.

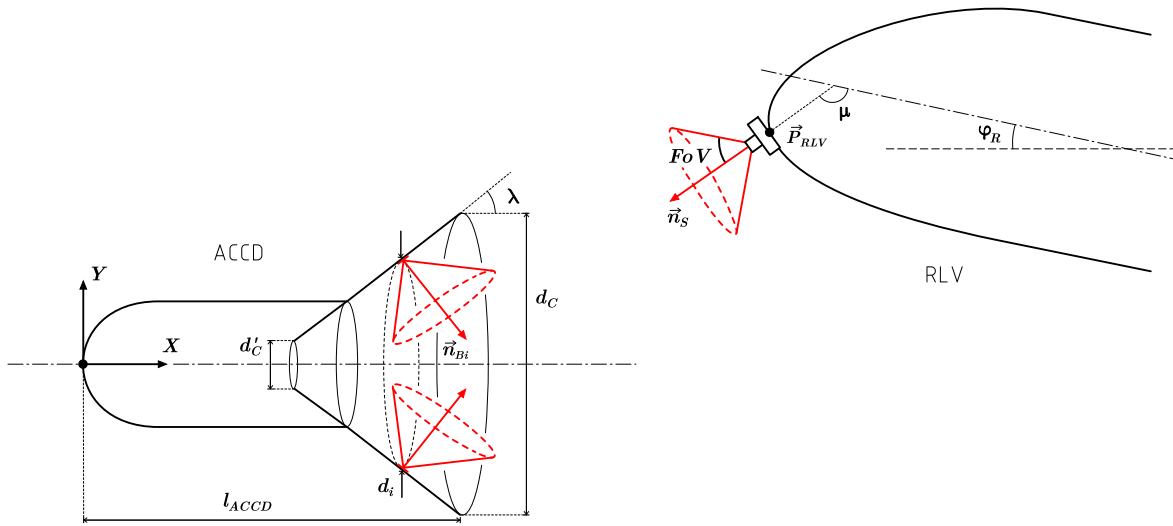


Figure 4.4: Definition of the VisNav Model Reference System and Variables. As in subsequent figures, the ACCD's docking cone has been enlarged for clarity's sake, while the RLV is not drawn to scale.

Under such conditions, the sensor mounting configuration can be fully characterized by a single angle μ , measured relative to the RLV's roll axis. The corresponding pointing vector \vec{n}_S can then be calculated with Equation 4.1, where ϕ_R is the RLV's pitch angle relative to the ACCD. Since the RLV is modelled as a single point, the corresponding sensor position \vec{P}_S trivially follows as $\vec{P}_S = \vec{P}_{RLV}$, which is a model input (**VNM.NF-03**).

$$\vec{n}_S = \begin{bmatrix} \cos(\phi_R + \mu) \\ -\sin(\phi_R + \mu) \\ 0 \end{bmatrix} \quad (4.1)$$

4.3.3. Beacon Configuration

For the beacons, less simplifications are made, because the model should be capable of properly assessing the impact of different beacon configurations (**VNM.F-04**). Hence, increased modelling accuracy is required. Given the pre-defined shape of the ACCD's outer shell, two main beacon configurations are analysed. These are shown schematically in Figure 4.5, and are characterized by the surface on which they are mounted. In the first case, beacons are located along the aft rim of the ACCD, pointing directly backwards. In the second one, the beacons are mounted *inside* the ACCD's docking cone, pointing partly inwards. In both of these configurations, beacons are assumed to be mounted equidistantly along a circle with diameter d_i .

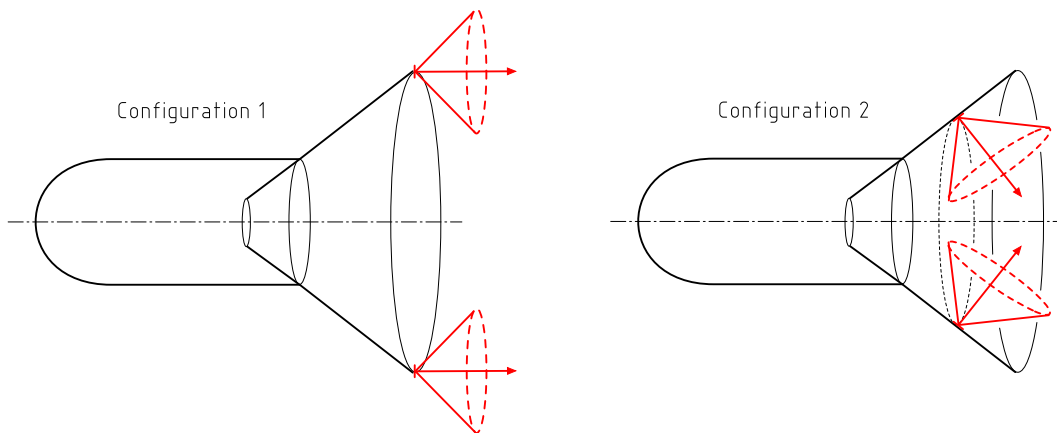


Figure 4.5: Comparison of Two Main VisNav Beacon Mounting Configurations.

Looking first at *Configuration 1*, N beacons mounted along the ACCD's aft rim have position vectors \vec{P}_{Bi} as defined by Equation 4.2 - where l_{ACCD} is the total length of the ACCD. The parameter β_i in this equation is dubbed the beacon's 'clock angle'. Corresponding pointing vectors follow trivially as $\vec{n}_{Bi} = [1 \ 0 \ 0]$.

$$\vec{P}_{Bi} = \begin{bmatrix} l_{ACCD} \\ d_i/2 \cdot \sin \beta_i \\ d_i/2 \cdot \cos \beta_i \end{bmatrix} \quad \text{where } \beta_i = i \cdot \frac{2\pi}{N}, \quad i = 1 \dots N \quad (4.2)$$

For *Configuration 2*, beacon positions and pointing vectors depend on the geometry of the docking cone. Using its inner diameter d'_C , outer diameter d_C , and half angle λ , Equation 4.3 provides a mathematical expression for this conical surface, as a function of parametric variables h and ψ . Beacon positions are then calculated by evaluating this expression in $h = d_i/(2 \cdot \sin \lambda)$ and $\psi = \beta_i$.

$$\vec{f}_C(h, \psi) = \begin{bmatrix} h \cdot \cos \lambda + l_{ACCD} - d_C/(2 \cdot \tan \lambda) \\ h \cdot \sin \lambda \cdot \sin \psi \\ h \cdot \sin \lambda \cdot \cos \psi \end{bmatrix} \quad \text{where } \begin{cases} h \in [d'_C, d_C]/(2 \cdot \sin \lambda) \\ \psi \in [0, 2\pi] \end{cases} \quad (4.3)$$

As the beacons are assumed to be mounted perpendicular to the cone's surface, their pointing vectors are defined by the surface normal, as calculated in Equation 4.4. For practical purposes, this expression is further normalized, yielding beacon pointing vectors \vec{n}_{Bi} as shown in Equation 4.5. Here again, the vector corresponding to a particular beacon can be found by substituting $\psi = \beta_i$. Note that the resulting expression is consistent, as it is independent of parametric variable h - all beacons with the same clock angle β_i have identical pointing vectors, regardless of their position along the cone.

$$\begin{aligned} \frac{\partial \vec{f}_C}{\partial \psi} \times \frac{\partial \vec{f}_C}{\partial h} &= \begin{bmatrix} 0 \\ h \cdot \sin \lambda \cdot \cos \psi \\ -h \cdot \sin \lambda \cdot \sin \psi \end{bmatrix} \times \begin{bmatrix} \cos \lambda \\ \sin \lambda \cdot \sin \psi \\ \sin \lambda \cdot \cos \psi \end{bmatrix} \\ &= \begin{bmatrix} h \cdot \sin^2 \lambda \\ -h \cdot \sin \lambda \cdot \cos \lambda \cdot \sin \psi \\ -h \cdot \sin \lambda \cdot \cos \lambda \cdot \cos \psi \end{bmatrix} \end{aligned} \quad (4.4)$$

$$\vec{n}_{Bi} = \begin{bmatrix} \sin \lambda \\ -\cos \lambda \cdot \sin \psi \\ -\cos \lambda \cdot \cos \psi \end{bmatrix} \quad (4.5)$$

Finally, all beacons are modelled as Lambertian surface emitters, as illustrated in Figure 4.6. This is approximately true for LEDs [88], which are typically used in VisNav applications [67]. The directional intensity $\iota(\Theta)$ of such a Lambertian emitter is characterized by Equation 4.6, where Θ is the angle of emittance under consideration, and ι_0 is the beacon's peak intensity [89].

$$\iota(\Theta) = \iota_0 \cdot \cos \Theta \quad (4.6)$$

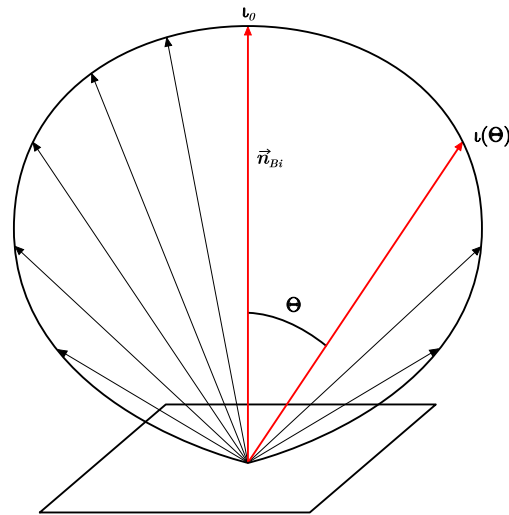


Figure 4.6: Schematic Depiction of the Directional Emittance Pattern of a Lambertian Emitter.

In the context of the VisNav Model, implementing such an emittance pattern is mainly relevant to accurately represent each beacon's range - which is a deciding factor for its visibility. Here, range is defined as the distance at which the beacon signal drops below a certain detectable threshold. Since signal strength diminishes according to the square of the travelled distance [89], it follows that intensity should quadruple in order for the range to double. Hence, signal range is related to the square root of its intensity, so that the directional range $r(\Theta)$ can be modelled with Equation 4.7 - where r_0 is the beacon's peak range. A comparison of the resulting directional intensity and range is shown in Figure 4.7.

$$r(\Theta) = r_0 \cdot \sqrt{\cos \Theta} \quad (4.7)$$

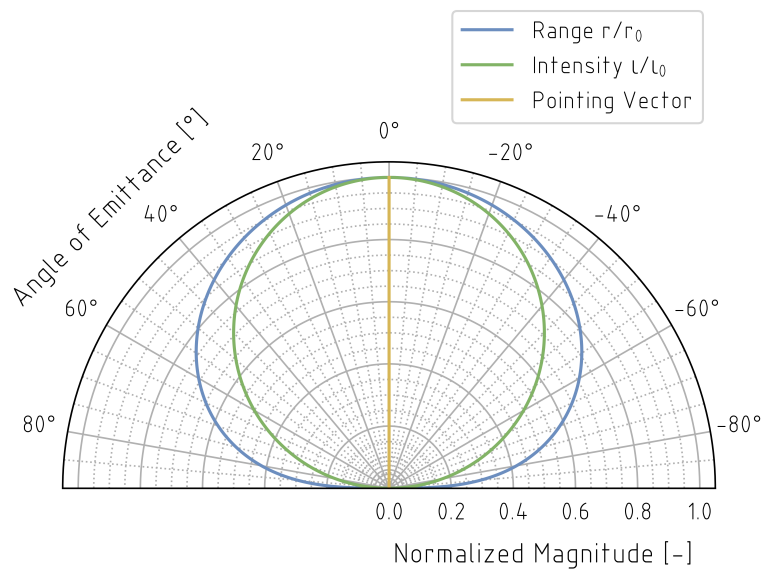


Figure 4.7: Normalized Directional Signal Intensity and Range for a Lambertian Beacon Model.

4.3.4. Visibility Conditions

With the complete geometric setup defined, each beacon's visibility can now be assessed. In essence, visibility v_i is dependent on three main conditions, c_{i1} , c_{i2} , and c_{i3} , which all need to be fulfilled - as expressed in Equation 4.8. They respectively concern the sensor's FoV, signal blocking, and signal range, and are discussed in the following three subsections.

$$v_i \Leftrightarrow c_{i1} \wedge c_{i2} \wedge c_{i3} \quad (4.8)$$

Sensor Field of View

The first visibility condition requires that a given beacon is within the sensor's FoV, while its signal is emitted towards said sensor. The latter part of this condition is fully captured in the Lambertian emittance model, while its former part can be analysed by defining a sensor FoV half angle FoV , as well as an LoS vector \vec{p}_{BiS} between the sensor and each beacon - calculated with Equation 4.9.

$$\vec{p}_{BiS} = \frac{\vec{P}_S - \vec{P}_{Bi}}{\|\vec{P}_S - \vec{P}_{Bi}\|} \quad (4.9)$$

The condition c_{i1} is then fulfilled when the LoS vector is within the bounds of the sensor's conical FoV, as illustrated in Figure 4.8. Mathematically, this can be expressed with Equation 4.10, which determines the angle between the LoS and sensor pointing vectors, and compares it to their maximum allowable value - the FoV half angle.

$$c_{i1} \Leftrightarrow \arccos(\vec{p}_{BiS} \cdot \vec{n}_s) \leq FoV \quad (4.10)$$

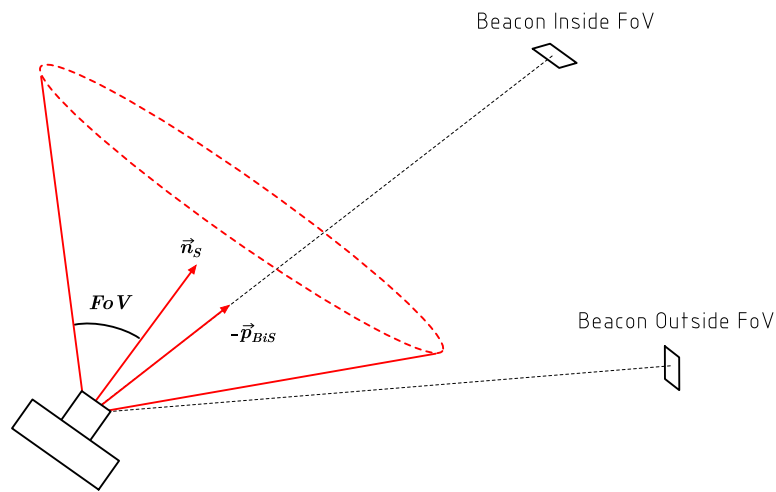


Figure 4.8: Schematic Depiction of Visibility Condition c_{i1} , Concerning the Sensor's Field of View (FoV).

Signal Blocking

As a second visibility condition c_{i2} , the LoS vector should not be obstructed by any physical obstacle. In practice, only the ACCD's docking cone forms a potential source of obstruction for the configurations defined in Figures 4.4 and 4.5. In order to identify such obstructions, the intersection point(s) between the LoS vector and cone surface are computed. This is done by solving Equation 4.11 for unknown parameters h , ψ , and s - where the right-hand side represents the LoS as a function of parametric variable s .

$$\vec{f}_C(h, \psi) = \vec{P}_{Bi} + \vec{p}_{BiS} \cdot s \quad (4.11)$$

This equation - for which a closed-form solution is included in Appendix K - will yield either one, two, or infinite solutions. They can further be filtered by demanding that $s > 0$, which corresponds to the part of the LoS between the beacon and sensor. Finally, only intersection points located on the *physical* docking cone are relevant - as opposed to those being a part of the *virtual* continuation of said cone, as illustrated in Figure 4.9. This is analysed by verifying whether the h -parameter of the intersection point is within a specific range, corresponding to the physical limits of the cone¹. Summarizing, the second visibility condition can be written as Equation 4.12.

¹Although the physical docking cone only starts at $h \geq d'_C (2 \cdot \sin \lambda)$, intersection points with a h -value smaller than this still result in signal blockage by the rest of the ACCD's structure.

$$\neg c_{i2} \Leftrightarrow \exists (h, \psi, s) : \begin{cases} \vec{f}_C(h, \psi) = \vec{P}_{Bi} + \vec{p}_{BiS} \cdot s \\ s > 0 \\ h \in [0, d_C / (2 \cdot \sin \lambda)] \end{cases} \quad (4.12)$$

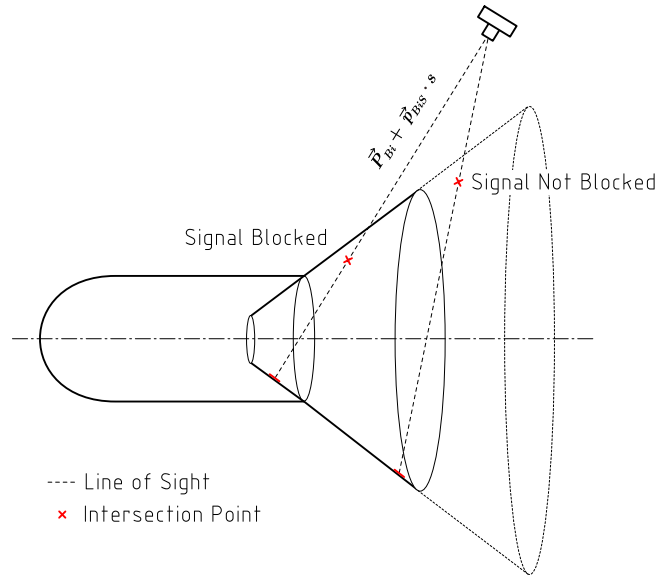


Figure 4.9: Schematic Depiction of Visibility Condition c_{i2} , Concerning Signal Blocking.

Range

Finally, the last visibility condition c_{i3} demands that the beacon should be within range of the sensor, so that its signal is strong enough to be detected. For this, the Lambertian model described in subsection 4.3.3 is used, which is a function of the angle of emittance Θ between the sensor and beacon - calculated with Equation 4.13. Verifying c_{i3} is then done by comparing this range with the distance between the beacon and sensor, as shown in Equation 4.14.

$$\Theta = \arccos(\vec{p}_{BiS} \cdot \vec{n}_{Bi}) \quad (4.13)$$

$$c_{i3} \Leftrightarrow \|\vec{P}_S - \vec{P}_{Bi}\| \leq r(\Theta) \quad (4.14)$$

4.3.5. Sensor Image Projection

As a final feature of the VisNav Model, sensor PoV imagery is generated (**VNM.F-06**) - in other words, the setup is shown through the 'eyes' of the sensor. In order to generate such PoV images, the 3D model space needs to be projected onto the sensor plane. The orientation of this plane is defined by the sensor pointing vector, while its borders are directly related to the sensor FoV. Image projection is achieved using a two-step approach: first, a geometric projection of each point onto the sensor plane; then, a normalization of the projected points based on their distance to the sensor, in order to account for perspective effects.

Mathematically, the first step can be characterized with Equations 4.15 through 4.17 [90], as shown schematically in Figure 4.10. Here, a physical point \vec{P}_0 - expressed as a vector in the ACCD's frame of reference - is projected onto the sensor plane, yielding \vec{P}_1 . The corresponding vector \vec{P}_2 from the sensor position to this point is then computed with Equation 4.16. However, the resulting vector is still expressed in body frame components, whereas it should be denoted in a 2D sensor frame. Therefore, a new 3D frame is defined, with a Z-axis coinciding with the sensor pointing vector $\vec{n}_S = [n_{SX} \ n_{SY} \ n_{SZ}]$. Transforming \vec{P}_2 into this sensor frame using Equation 4.17 yields \vec{P}_{2s} , which has no Z-component. With this algorithm, each point in the setup is reduced to an equivalent 2D vector in the sensor frame.

$$\vec{P}_1 = \vec{P}_0 - \left((\vec{P}_0 - \vec{P}_S) \cdot \vec{n}_S \right) \vec{n}_S \quad (4.15)$$

$$\vec{P}_2 = \vec{P}_1 - \vec{P}_S \quad (4.16)$$

$$\vec{P}_{2s} = \begin{bmatrix} 1 & 0 & 0 \\ 0 & \cos \psi_S & -\sin \psi_S \\ 0 & \sin \psi_S & \cos \psi_S \end{bmatrix} \cdot \begin{bmatrix} \cos \phi_S & -\sin \phi_S & 0 \\ \sin \phi_S & \cos \phi_S & 0 \\ 0 & 0 & 1 \end{bmatrix} \cdot \vec{P}_2 \quad (4.17)$$

where $\begin{cases} \psi_S = \arccos n_{SZ} \\ \phi_S = \arctan (n_{SX}/n_{SY}) \end{cases}$

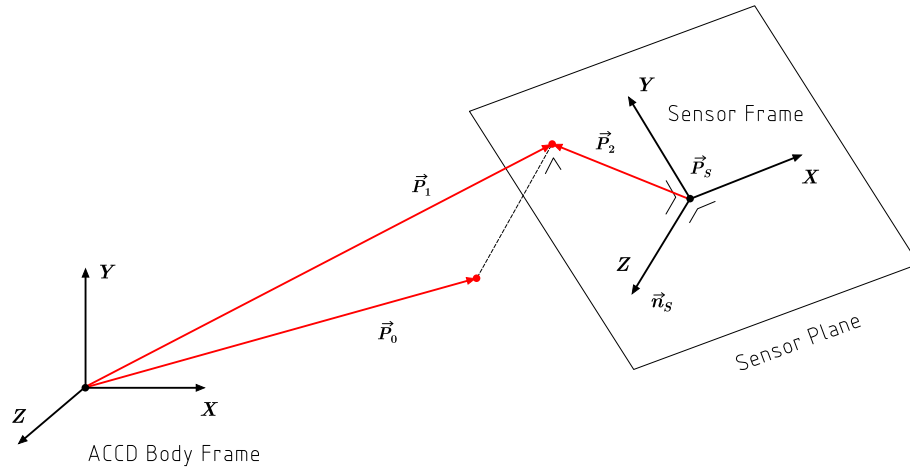


Figure 4.10: Projection of a Three-Dimensional (3D) Point \vec{P}_0 onto the Sensor Plane.

Next, perspective explicitly needs to be taken into account, because the orthogonal projection in Equation 4.15 treats points irrespective of their distance to the sensor. In order to remedy this, Equation 4.18 adds a normalization step, which accounts for the shortening of projected images at increased distances. This is further illustrated in Figure 4.11, which compares imagery behaviour before and after normalization.

$$\vec{P}_3 = \frac{\vec{P}_{2s}}{\left((\vec{P}_0 - \vec{P}_S) \cdot \vec{n}_S \right)} \quad (4.18)$$

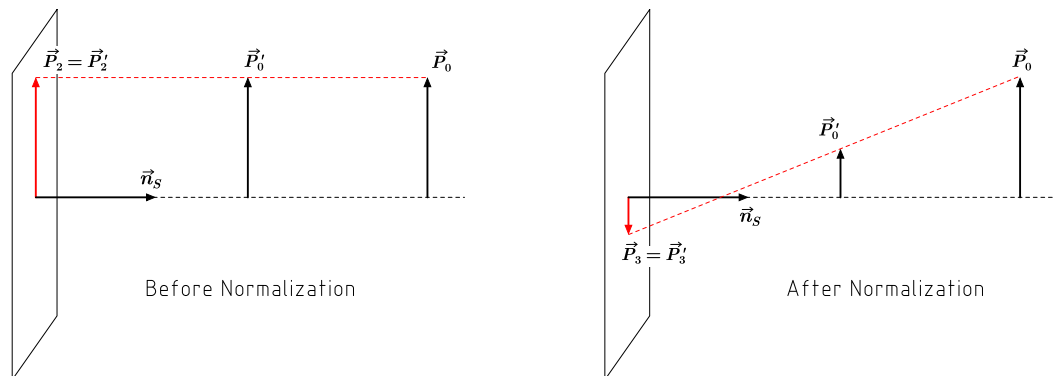


Figure 4.11: Comparison of Imagery Behaviour Before and After Normalization. Note how Equation 4.18 omits the additional -1 scale factor that can be observed in this figure, and which causes the sensor imagery to be flipped.

Finally, the boundaries of the sensor's FoV are applied at the end, by only displaying points that satisfy visibility condition c_{i1} . Combining the aforementioned steps, a complete sensor PoV image is

generated, including perspective and FoV effects. Furthermore, visibility conditions c_{i2} and c_{i3} are graphically visualized - as demonstrated in subsection 4.3.8. Such PoV imagery can either cover a single setup, or a sequence of different ACCD-RLV positions. In the latter case, an approach animation is obtained, such as the one included in Appendix L.

4.3.6. Assumptions

Throughout the foregoing sections, a number of implicit and explicit assumptions have been made in establishing the VisNav Model. An overview of these assumptions - numbered **VMA-01** to **VMA-08** - is given below, with additional details concerning rationale and resulting model limitations.

VMA-01 Beacons are mounted on the inner surface of the ACCD's docking cone, or along its aft rim - in both cases flush with the vehicle's surface. Furthermore, they are equally distributed along concentric circles, centred around the ACCD's roll axis.

This limits the number of beacon configurations that can be analysed. Although these configurations represent the most important ones, additional design space could be explored - for example by considering beacons that are not mounted perpendicular to the vehicle's surface.

VMA-02 Beacons are Lambertian surface emitters, with a directional range varying according to the square root of the cosine of the emittance angle.

This is only approximately true for LEDs, and can affect the long-distance behaviour of the system - near the beacon's range limit.

VMA-03 Local atmospheric effects on visibility and range are neglected.

Although this affects time-varying performance of the system in trajectory studies, it has no effect on the generation of a representative beacon configuration.

VMA-04 The sensor is mounted at the tip of the RLV's nose, with its pointing vector in the vehicle's plane of symmetry.

This again limits the total design space that can be explored. However, the exact position of the sensor has no major implications for the ACCD's design, nor for the VisNav's performance - as long as its FoV is not obstructed by the RLV's body.

VMA-05 The sensor has an axisymmetric FoV.

This is an approximation of real VisNav sensors, which have a rectangular FoV. However, resulting inaccuracies only arise near the edges of the FoV, and do not significantly affect the results of the VisNav Model.

VMA-06 The inner surface of the ACCD's docking cone is perfectly conical.

In reality, minor deviations from this conical surface have a negligible effect on the model outputs.

VMA-07 The sensor's FoV can only be obstructed by the ACCD's docking cone.

Given the design of the IAC vehicles, this is true as long as the VisNav sensor is mounted in such a way that no part of the RLV is within its FoV.

VMA-08 Relative to the ACCD, the RLV's yaw and roll angles are zero.

This represents an ideal approach scenario between the RLV and ACCD [14]. In reality, some yaw and roll oscillations may occur, with minor effects to the VisNav's performance.

Summarizing, the model assumptions either limit the overall design space that can be explored (**VMA-01**, **VMA-04**, and **VMA-06**), or describe an idealized scenario in terms of VisNav performance and approach trajectory (**VMA-02**, **VMA-03**, **VMA-05**, **VMA-07**, and **VMA-08**). The former mainly affect the obtained representative VisNav configuration (**VNM.F-04**), which may not represent the 'optimal'

one. However, such an optimization is not yet required within the context of this work's electromechanical design. The latter then have an impact on the simulated time-dependent performance of the VisNav system (**VNM.F-05**), which is reduced due to additional disturbances and non-idealities. However, there are again no essential implications for the ACCD's electromechanical design, so that no margins are needed within this work.

4.3.7. Outputs

With these assumptions recapitulated and kept in mind, the major outputs of the VisNav Model can now be presented. In general, there are three main types of output: approach corridors (**VNM.F-04**), trajectory studies (**VNM.F-05**), and sensor PoV imagery (**VNM.F-06**). They will be briefly discussed in the following three subsections.

Approach Corridor

In order to define an approach corridor, a relative position study between the RLV and ACCD is performed. For this, the RLV's position is varied in a grid-wise manner, while the total number of visible beacons is assessed at each of the analysed positions. By doing so, plots such as Figure 4.12 can be generated, providing essential insight into the effectiveness of a given configuration. Because VisNav requires a minimum of four visible beacons to perform relative navigation [64], the corresponding approach corridor is defined as the region in space where this condition is met. For practical applications, a larger number of beacons is desirable for the system's redundancy and robustness, and this definition can be extended to contain higher numbers of beacons. Analysing the size and orientation of such approach corridors, different configurations can then be compared (**VNM.F-04**) - as discussed in section 4.4. Finally, similar position studies and approach corridors can also be analysed in 3D scenarios.

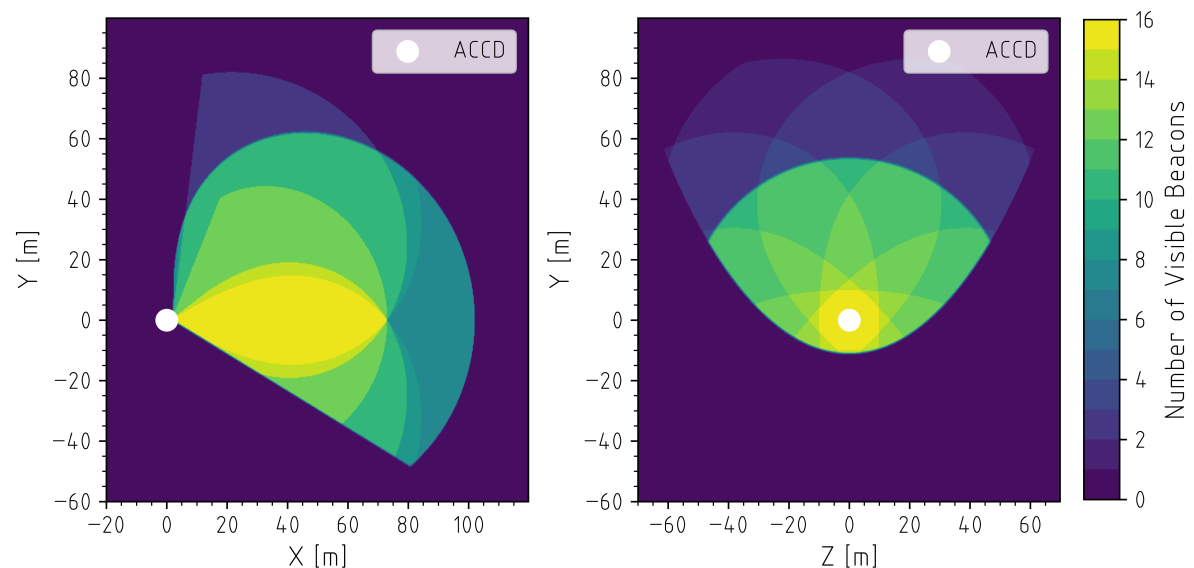


Figure 4.12: Examples of Two-Dimensional (2D) VisNav Position Studies. The left and right images respectively show a side ($Z = 0\text{ m}$) and front ($X = 20\text{ m}$) view of the approach corridor. Model inputs are listed in Table 4.2.

Trajectory Study

Next, specific approach trajectories between the RLV and ACCD can be analysed (**VNM.F-05**). For this, both the RLV's position and attitude are varied according to a pre-defined approach path, and the number of visible beacons is monitored as a function of time. An example of such a trajectory study is included in Appendix L. Additionally, this functionality can be leveraged to integrate the VisNav Model into an overarching relative navigation simulator (**VNM.NF-03**), as illustrated in Figure 4.13. Consequently, the general performance of the relative position and attitude estimation is simulated, fusing VisNav data with measurements from GNSS and INS systems. Further details are provided in

Appendix J, which includes a copy of a paper presented at the 2024 High-Speed Vehicle Science and Technology Conference (HiSST) in Busan, South Korea.

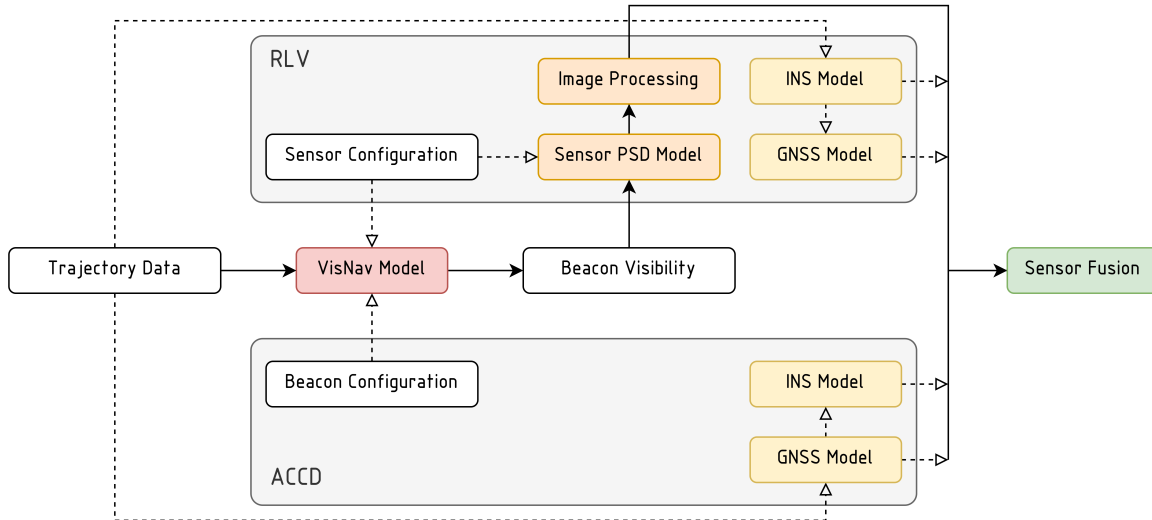


Figure 4.13: Schematic Overview of the Integration of the VisNav Model into a Relative Navigation Simulator [15].

Sensor PoV Imagery

Finally, the VisNav Model can generate imagery from the sensor’s PoV (**VNM.F-06**) - either a single still image, or an animation corresponding to a specific RLV trajectory. An example of the latter is included in Appendix L, while the former is discussed in subsection 4.3.8 - where it is used for model verification.

Parameter	Value	
ϕ_R	-1.57°	
d_C	$0.7\ m$	
d'_C	$0.2\ m$	
λ	30°	
μ	150°	
FoV	60°	
Beacon Configuration	1	2
N	8	8
d_i	$770\ mm$	$630\ mm$
r_0	$100\ m$	$100\ m$

Table 4.2: Reference Model Inputs for Generating Exemplary VisNav Model Outputs. This setup uses two separate beacon rings.

4.3.8. Verification

Given the unique nature of the VisNav Model, verification methods are limited - especially in terms of quantitative comparisons to similar models or data. Hence, the bulk of model verification is performed in a qualitative, ad-hoc manner, of which three examples are presented in this section. They are further complemented by internal sanity checks, which alert the user when an off-nominal situation has occurred. These provide continuous verification, by being performed whenever the model is used. As an example, the position study shown in Figure 4.12 analyses a grid of nearly 500,000 RLV positions. Combined with eight cone-mounted beacons, a total of almost four million intersection solutions were computed, each passing their internal sanity checks.

First of all, verification of the beacon configuration modelling discussed in subsection 4.3.3, is performed by generated 3D plots such as Figure 4.14. These are compared to the expected physical

dimensions of the docking cone and beacon rings, while the orthonormality of pointing vectors with respect to the local docking cone's surface is assessed.

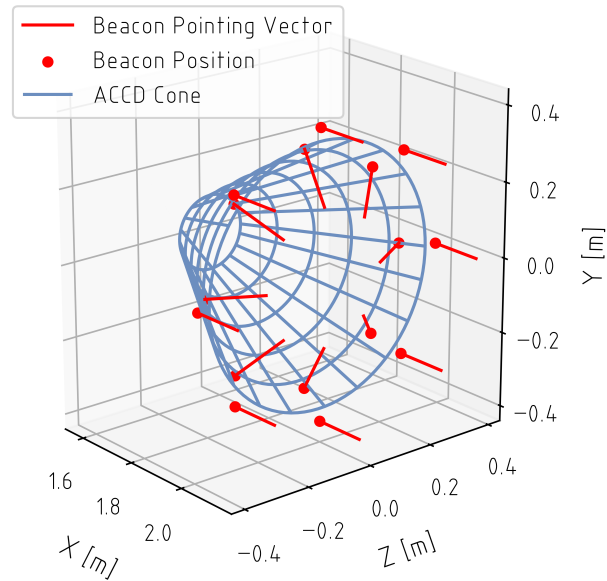


Figure 4.14: Visualization of a Beacon Mounting Configuration for Model Verification. Model inputs are listed in Table 4.2.

Moving on to beacon visibility modelling, condition c_{i2} (signal blocking) is the most vital to verify, because it has the highest complexity - as evinced by the size of its closed-form solution included in Appendix K. Verification is again performed graphically, using plots such as Figure 4.15 - visualizing the computed intersection points relative to the docking cone and LoS. In the figure below, three beacons are blocked by the docking cone, which is confirmed by the fact that the corresponding intersection points are located on the physical ACCD cone.

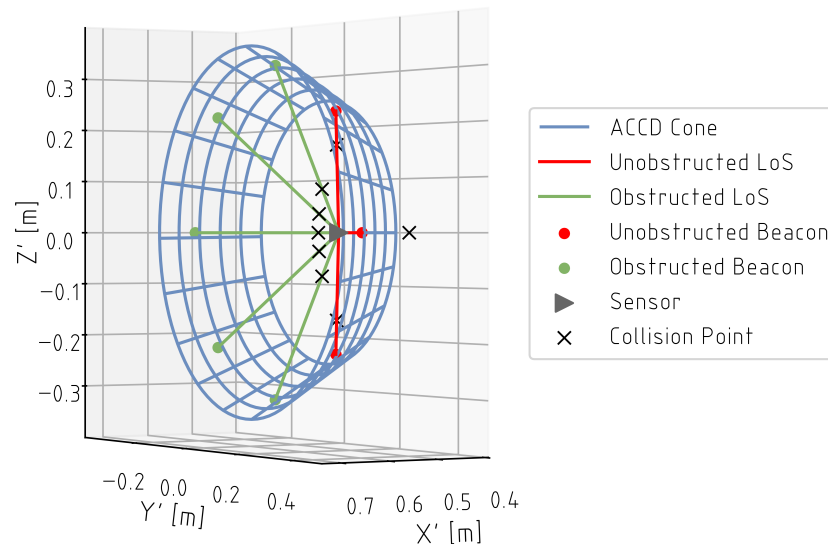


Figure 4.15: Example of Visual Verification of the Signal Blocking Detection Algorithm. Model inputs are listed in Table 4.2, with an RLV located at $X = 2.1\text{ m}$, $Y = 0.5\text{ m}$, and $Z = 0\text{ m}$. The coordinate system $X'Y'Z'$ corresponds to the local docking cone frame described in Appendix K. For the central blocked beacon, the relevant intersection point coincides with the beacon itself.

Finally, model verification is also performed by comparing sensor PoV images to the beacons' visibility values. An example is shown in Figure 4.16, with corresponding visibility conditions listed in Table 4.3. Here, beacons 1 and 9 respectively correspond to the upper cone- and rim-mounted ones,

with subsequent beacons numbered in an anticlockwise fashion. Beacons 1 and 2 are blocked by the ACCD's cone ($c_{i2} = 0$), while beacons 6 to 8, and 14 to 16 are outside the sensor's FoV ($c_{i1} = 0$) - as reflected in both the visibility conditions and PoV image. Additionally, because beacons 1 and 2 are pointing away from the sensor, their range in the LoS direction is zero ($c_{i3} = 0$). All other beacons point (partly) towards the sensor, and are thus within range.

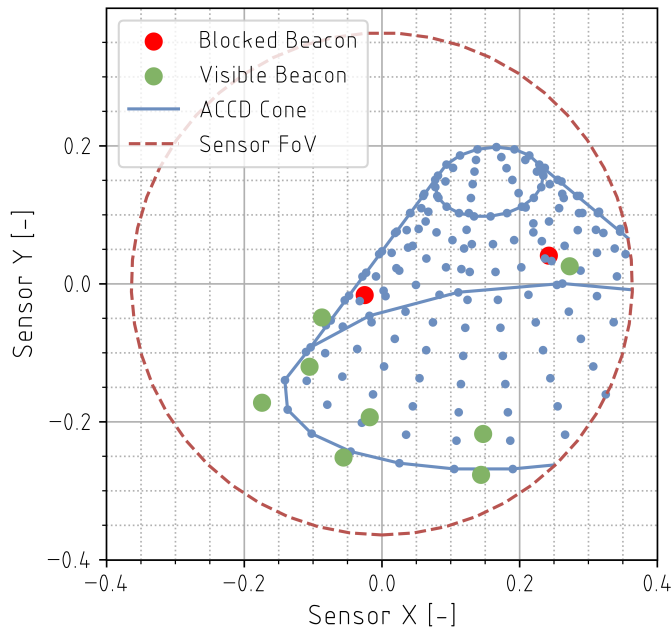


Figure 4.16: Example of a Sensor PoV Image for VisNav Model Verification. Beacon configuration inputs are defined in Table 4.2, while the sensor properties are $FoV = 20^\circ$ and $\mu = 120^\circ$, and the RLV is located at $X = 2.4\text{ m}$, $Y = 1\text{ m}$, and $Z = 0.2\text{ m}$.

i	Cone-Mounted Beacon Ring								Rim-Mounted Beacon Ring							
	1	2	3	4	5	6	7	8	9	10	11	12	13	14	15	16
c_{i1}	1	1	1	1	1	0	0	0	1	1	1	1	1	0	0	0
c_{i2}	0	0	1	1	1	1	1	0	1	1	1	1	1	1	1	1
c_{i3}	0	0	1	1	1	1	1	1	1	1	1	1	1	1	1	1
v_i	0	0	1	1	1	0	0	0	1	1	1	1	1	0	0	0

Table 4.3: Overview of Beacon Visibility as a Function of Beacon Number i . The values listed in this table correspond to the PoV image shown in Figure 4.16, and the model inputs specified there.

4.4. VisNav Configuration Comparison

With the overall VisNav Model established and verified, it can now be used to generate a representative beacon and sensor configuration (**VNM.F-04**). In order to limit the overall complexity of the analysis, and in light of the model's limitation discussed in subsection 4.3.6, a globally 'optimal' configuration is not targeted, and a full design space exploration not executed. Instead, the two beacon configurations defined in Figure 4.5 are studied separately in subsections 4.4.1 and 4.4.2. Observing how relevant parameters affect corresponding approach corridors, a representative configuration is then proposed in subsection 4.4.3. On the one hand, the size of the approach corridor should be maximized (**KY-DTC.F-11/02**). On the other hand, its orientation is also vital, because the RLV performs a steeper descent than the TA, approaching the ACCD from above [18].

4.4.1. Rim-Mounted Beacons

Starting with rim-mounted beacons, their configuration is defined by three parameters. The first one, mounting diameter d_i , has only minimal design freedom because of the limited size of the ACCD's aft rim. Furthermore, the total number of beacons N has a trivial influence on the approach corridor, as it does not affect its size or orientation. Finally, the range r_0 has a similarly predictable effect, scaling the size of the approach corridor, without affecting its shape or orientation. Consequently, the sensor mounting angle μ is the only design parameter that needs to be analysed.

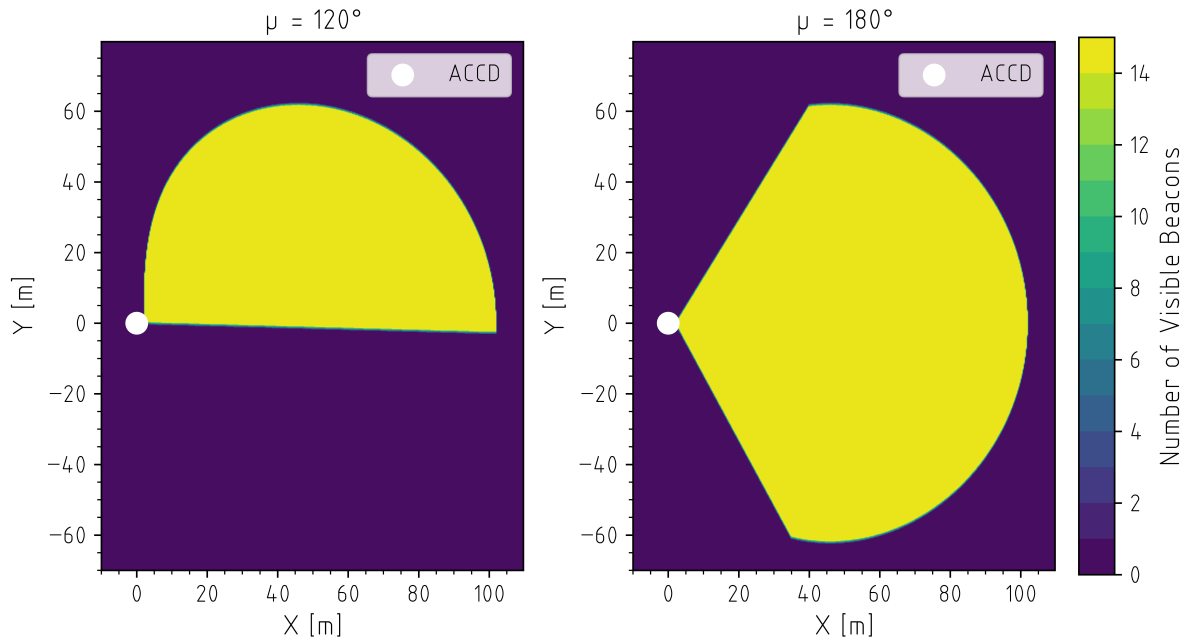


Figure 4.17: Comparison of Approach Corridors at $Z = 0\text{ m}$, for a Low and High Sensor Mounting Angle μ , with Beacon Configuration 1. Constant model inputs are listed in Table 4.4.

A comparison of a downwards-facing ($\mu = 120^\circ$) and forwards-facing ($\mu = 180^\circ$) sensor is provided in Figure 4.17, showing a side view of the resulting approach corridors. Although decreasing the mounting angle successfully rotates the approach corridor upwards, such a re-orientation is inherently limited by the Lambertian nature of the beacons: at high emittance angles, their range is limited, causing the approach corridor to be cut off at a short distance from the ACCD. This highlights an important limitation of rim-mounted beacons, as they are unable to cover large distances in the Y- and Z- directions. Because of this, beacons mounted according to Configuration 2 are of vital importance.

Parameter	Value	
ϕ_R	-1.57°	
d_C	0.7 m	
d'_C	0.2 m	
λ	30°	
μ	150°	
FoV	60°	
Beacon Configuration	1	2
N	15	15
d_i	735 mm	665 mm
r_0	100 m	100 m

Table 4.4: Reference Model Inputs for VisNav Configuration Comparisons. Contrary to Table 4.2, each setup now only uses a single beacon ring, mounted either according to Configuration 1, or according to Configuration 2.

4.4.2. Cone-Mounted Beacons

Moving on to cone-mounted beacons, the same parameters act as variable model inputs. Again, beacon range r_0 is not analysed, and is kept at a reference value of 100 m. Looking at the effect of the sensor mounting angle, Figure 4.18 indicates similar behaviour as previously observed. However, thanks to the inwards-pointing beacons, a significantly larger range is achieved in the Y- and Z-directions. Where $\mu = 120^\circ$ in *Configuration 1* could only reach distances below 50 m at $X < 20$ m, the same sensor setup can achieve a range of nearly 100 m in this direction using *Configuration 2*.

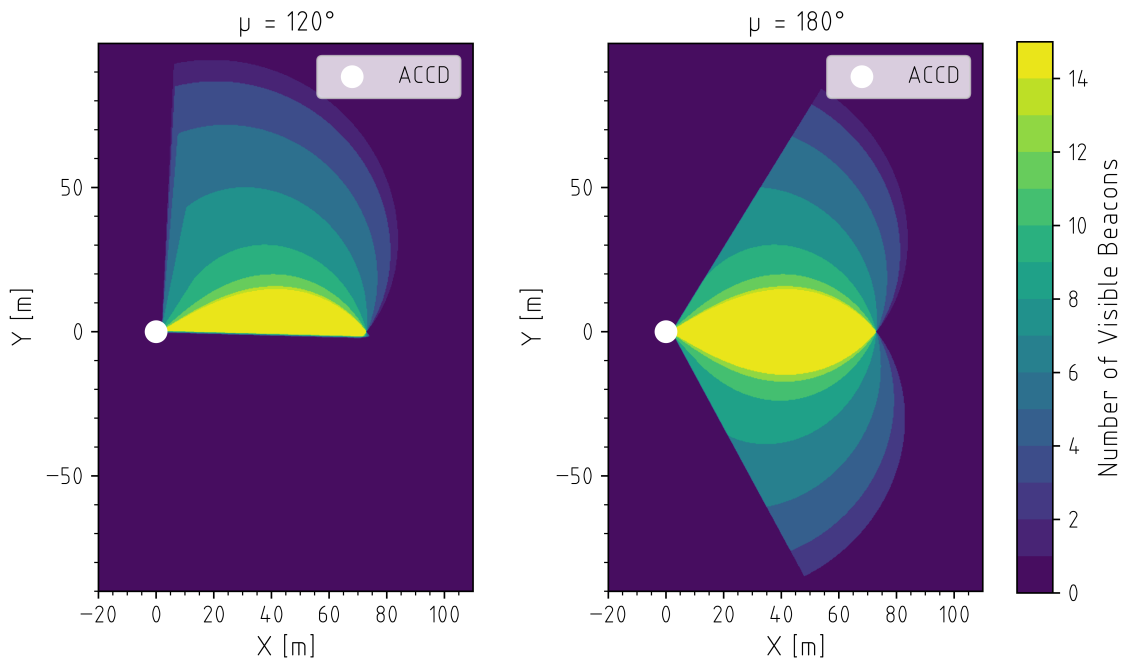


Figure 4.18: Comparison of Approach Corridors at $Z = 0$ m, for a Low and High Sensor Mounting Angle μ , with Beacon *Configuration 2*. Constant model inputs are listed in Table 4.4.

Contrary to the rim-mounted case, the total number of beacons N has a pronounced effect for *Configuration 2*. This is demonstrated in Figure 4.19, which depicts front views of approach corridors corresponding to $N = 5$ and $N = 25$. Adding more beacons increases the number of visible beacons inside the approach corridor, while also slightly expanding the outer limits of this corridor - especially in the YZ-plane. However, increasing N yields diminishing returns, as the approach corridor does not grow indefinitely.

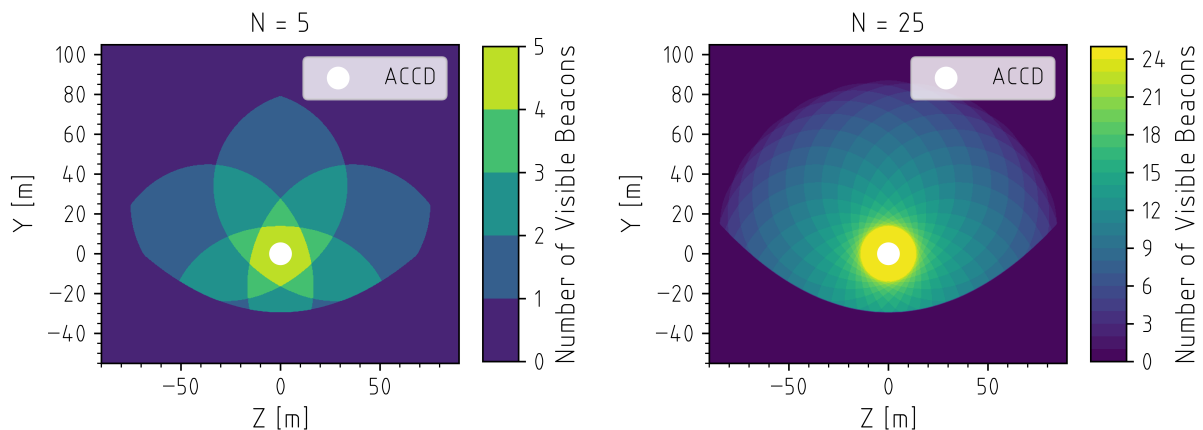


Figure 4.19: Comparison of Approach Corridors at $X = 50$ m, for a Small and Large Number of Beacons N Mounted in *Configuration 2*. Constant model inputs are listed in Table 4.4.

Finally, the mounting diameter d_i has more design freedom than in *Configuration 1*, as beacons can be placed deeper inside the ACCD's docking cone. A comparison of an aft-mounted beacon ring ($d_i = 650 \text{ mm}$) and a forward-mounted one ($d_i = 400 \text{ mm}$) is shown in Figure 4.20, which depicts a side view of the resulting approach corridors. Placing the beacons deeper inside the docking cone is almost exclusively detrimental to the approach corridor, as they suffer more from signal blockage. This can clearly be observed for the $d_i = 400 \text{ mm}$ case, where the upper edge of the corridor is a continuation of the ACCD's docking cone.

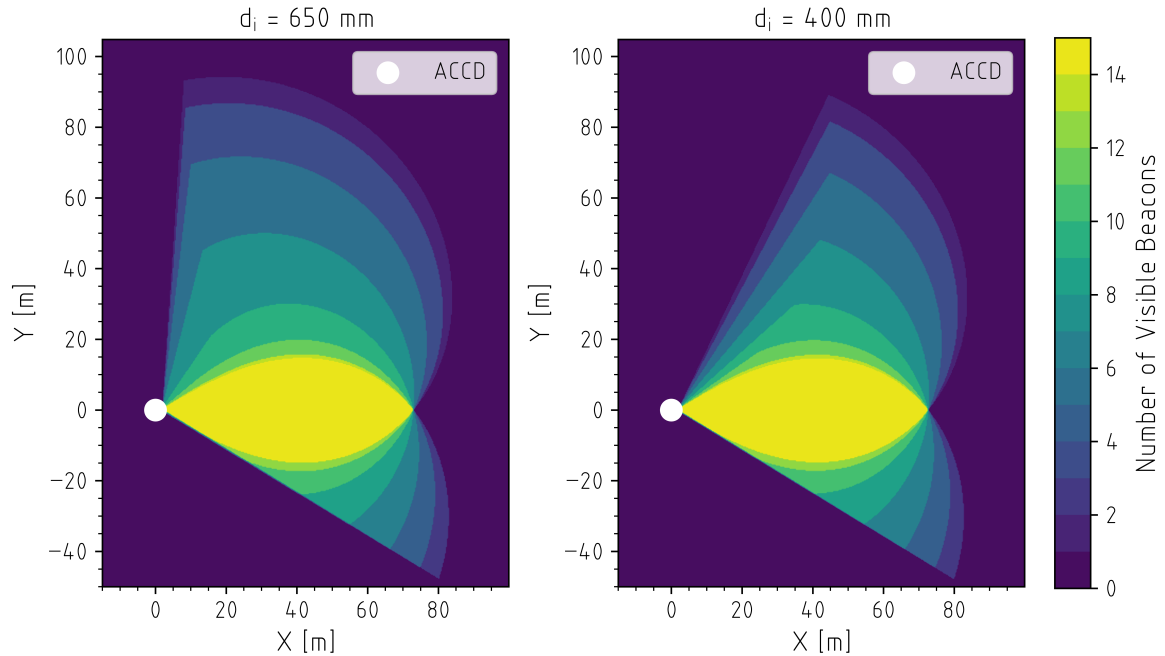


Figure 4.20: Comparison of Approach Corridors at $Z = 0 \text{ m}$, for a Small and Large Beacon Mounting Diameter d_i , with Beacon *Configuration 2*. Model inputs are listed in Table 4.4.

4.4.3. Final Configuration

Based on the foregoing comparative analyses, the representative VisNav configuration defined by Table 4.5 and shown schematically in Figure 4.21, is proposed. Combining rim- and cone-mounted beacons, the former's axial range is complemented by the latter's upwards and sideways coverage. By using a total of twelve beacons, visibility of at least four is ensured throughout the majority of the system's range. Further increasing the number of beacons has a negligible effect on the approach corridor, while potentially hampering the accuracy and speed of the relative navigation system [15]. Although observations based on Figure 4.20 indicate that larger mounting diameters are beneficial for cone-mounted beacons, initial studies have shown that an asymmetric, three-ringed design yields significantly better solution convergence during final approach [15]. Hence, the proposed beacon configuration includes two separate cone-mounted rings, at $d_i = 455 \text{ mm}$ and $d_i = 665 \text{ mm}$.

Parameter	Value		
d_C	0.7 m		
d'_C	0.2 m		
λ	30°		
μ	150°		
FoV	60°		
Beacon Configuration	1	2	2
N	5	4	3
d_i	735 mm	665 mm	455 mm
r_0	100 m	100 m	100 m

Table 4.5: Characteristics of the Proposed Representative VisNav Beacon and Sensor Configuration. This setup uses three rings of beacons: one mounted along the aft rim (*Configuration 1*), and two along the docking cone's inner surface (*Configuration 2*.)

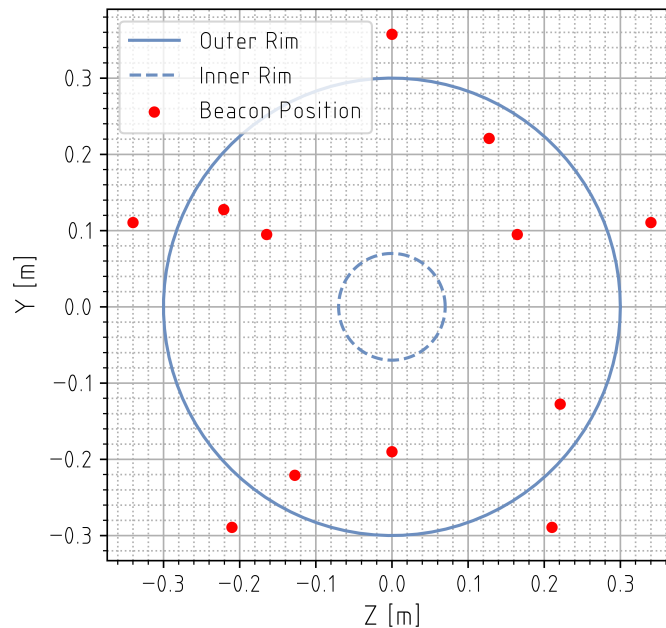


Figure 4.21: Aft View of the Proposed Representative Beacon Configuration. The depicted inner and outer rim concern the edges of the docking cone's surface. Model inputs corresponding to this figure are listed in Table 4.5.

For the sensor mounting angle, an intermediate value of $\mu = 150^\circ$ is proposed. This rotates the approach corridor slightly upwards, while still maintaining sufficient coverage around the ACCD's roll axis. Additionally, a 60° FoV is used as a representative value for sensors in VisNav systems [86]. Finally, the reference 100 m beacon range from previous analyses is adopted here as well, with a more representative estimate obtained in chapter 5.

4.5. Conclusion

In conclusion, this chapter proposes the use of a VisNav electro-optical reference system to enable relative navigation between the ACCD and the RLV, in conjunction with GNSS and INS systems. This decision is based on a number of different requirements and risks, as well as an extensive analysis of available sensor options. Especially in terms of environmental disturbances, VisNav promises better robustness than similar systems.

To analyse the performance of such a VisNav solution, and to explore the available design space, a model was developed. This model uses geometric relations to assess the visibility of different beacons, as seen from the sensor's PoV. It is based on a number of model requirements, for which compliance is listed in Table 4.6. Although multiple verification steps have been performed, future validation efforts are recommended. These could include the development of a physical test setup, with which the visibility of beacons can empirically be assessed.

Requirement	Compliance
VNM.F-01	Fully compliant; model analyses the visibility of 3D beacon configurations.
VNM.NF-02	Fully compliant; both types of beacon configurations are included.
VNM.NF-03	Fully compliant; integration into a relative navigation model is demonstrated in Appendix J.
VNM.F-04	Fully compliant; comparative analysis is presented in section 4.4.
VNM.F-05	Fully compliant; exemplary trajectory study is shown in Figure L.3.
VNM.F-06	Fully compliant; verification using PoV imagery is demonstrated in subsection 4.3.8.

Table 4.6: Compliance of the VisNav Model to its Model Requirements

Exploiting the model's capabilities, a comparative analysis between beacon and sensor configurations was performed, and a representative one was proposed. This configuration is used as a starting point for subsequent studies, including simulations of the relative navigation system (Appendix J), dimensioning of the ACCD's power system (chapter 5), as well as mechanical design of its docking cone (chapter 6).

5

Avionics and Power System

Given the *electromechanical* nature of the ACCD, a SWaP estimate of its avionics and power system is essential. With a relative navigation solution decided upon in chapter 4, other electronic subsystems are studied in this chapter. To this end, relevant requirements and risks are formulated in section 5.1, while three operational modes for the ACCD's power system are defined in section 5.2. Section 5.3 then analyses major electronic subsystems, which are combined in section 5.4 to generate power and energy requirements for the battery system. Finally, a mechanical mounting structure for essential avionics is proposed in section 5.5, and relevant conclusions are recapitulated in section 5.6.

5.1. Requirements and Risks

The principal high-level requirement concerning the ACCD's power system is **KY-SYS.NF-03**, which defines a minimal operational duration of 2h 35m. Breaking this further down, three subsystem-level power requirements are formulated. They are listed below, and are further detailed in Appendix A. With an in-depth rationale for these requirements provided in section 5.2, they essentially define three separate operational modes for the ACCD. These correspond with different phases in the IAC procedure, and require specific subsystems to be active during a given period.

KY-PWS.NF-03/01: The ACCD shall be able to remain in *Homing* mode for a period of at least 10 minutes. *Homing* mode entails a fully active vehicle state, with all electronic subsystems powered on.

KY-PWS.NF-03/02: The ACCD shall be able to remain in *Towing* mode for a period of at least 2 hours and 15 minutes. *Towing* mode concerns a semi-passive vehicle state, with only the subsystems required for communications (**CR-AVN.F-01/20**) and towing powered on.

KY-PWS.NF-03/03: The ACCD shall be able to remain in *Release* mode for a period of at least 10 minutes. *Release* mode includes the activation of all subsystems required to ensure a safe nominal release of the RLV (**CR-RLS.F-15/01**).

Additional requirements regarding the ACCD's avionics are also defined, and shown below. They are based on subscale flight tests during Project FALCon, which concluded that communication and telemetry logging systems should be integrated into the ACCD, because wirelessly transmitting data to the TA is unfeasible without the use of intermediate amplifiers [91]. Furthermore, the need for communication with the RLV (**TN-AVN.F-01/21**) is strengthened by the VisNav system proposed in chapter 4, as it requires an active feedback loop between its sensor and beacons [67].

CR-AVN.F-01/20: The ACCD shall be able to wirelessly communicate with the TA.

TN-AVN.F-01/21: The ACCD shall be able to wirelessly communicate with the RLV.

KY-AVN.F-01/22: The ACCD shall have a telemetry logging functionality.

Finally, a number of risks concerning the ACCD's electronics have been identified, and are included in Appendix A. In general, they mostly cover the possibility of losing power to a vital subsystem of the ACCD. When not mitigated properly, such a scenario can result in the loss of the RLV, and potentially the TA. Hence, sufficient redundancy in this aspect of the ACCD's design is essential, both for the power and sensor systems. Subsequent sections aim to achieve such redundancy by overestimating energy and power requirements, while also including multiple individual sensor units.

5.2. Operational Modes

Based on the overall IAC mission scenario presented in chapter 2, three main operational modes can be defined for the ACCD's power system. These have specific durations, and impose different requirements in terms of active electronic subsystems. In a chronological order, they are the following:

- **Homing Mode** covers the period between ACCD deployment and successful RLV capture.
- **Towing Mode** coincides with the tow-back flight, during which the ACCD is attached to the RLV.
- **Release Mode** starts *just before* RLV release, and ends when the RLV has touched down.

By defining three separate modes, a more accurate estimation of the ACCD's overall power and energy requirements is obtained. In subsections 5.2.1 through 5.2.3, all three modes are analysed in more detail, estimating their respective duration, and defining the required active subsystems.

5.2.1. Homing Mode

The first operational mode starts as soon as the ACCD is deployed, and covers interception (*homing*) and docking manoeuvres. It includes active use of the vehicle's control surfaces and relative navigation system, as well as communication with the TA and the RLV. Furthermore, the ACCD's docking sensors and actuators are required to respectively detect and execute a docking attempt.

The duration of the *Homing* mode is directly related to the diving formation flight between the TA and the RLV. Based on the reference trajectory presented in chapter 2, the TA's diving flight is expected to take no longer than five minutes [18], of which 60-90 s are spent in formation flight with the RLV [40]. Including an additional margin of five minutes to allow for subsystem checks prior to the dive [38], the overall duration of the *Homing* mode is estimated at ten minutes (KY-PWS.NF-03/01).

5.2.2. Towing Mode

The *Towing* mode covers the entire tow-back phase of IAC, where the RLV is connected to the ACCD. During this phase, neither active control nor relative navigation of the ACCD is needed, so corresponding subsystems can be powered off - or put in a standby mode. Other systems, such as the communication module and docking sensors, are required to actively monitor the ACCD's state, while its docking actuators should ensure a constant connection with the RLV.

To get an estimate for the duration of the *Towing* mode, the tow-back flight regime is analysed. For this, an RLV capture location above the Atlantic Ocean is used, at 4° 59' 10" N and 46° 5' 6" W - based on a typical launch from Kourou, French Guyana [18]. Assuming that the RLV's landing site is close to its launch site [92], an RLV release location of 5° 10' 8" N and 52° 41' 2" W is used [93]. Denoting the capture and release coordinates as (lat_1, lon_1) and (lat_2, lon_2) respectively, the total tow-back flight distance d_f can be estimated with the Haversine formula, shown in Equation 5.1 [94] - where $R_{\oplus} = 6371 \text{ km}$ is the average radius of the Earth [95]. For this, the tow-back is assumed to occur at a constant altitude H , and along an orthodrome of the Earth. The corresponding tow-back trajectory is illustrated in Figure 5.1.

$$d_f = 2 \cdot (R_{\oplus} + H) \cdot \arcsin \sqrt{\sin^2 \left(\frac{lat_2 - lat_1}{2} \right) + \cos lat_2 \cdot \cos lat_1 \cdot \sin^2 \left(\frac{lon_2 - lon_1}{2} \right)} \quad (5.1)$$

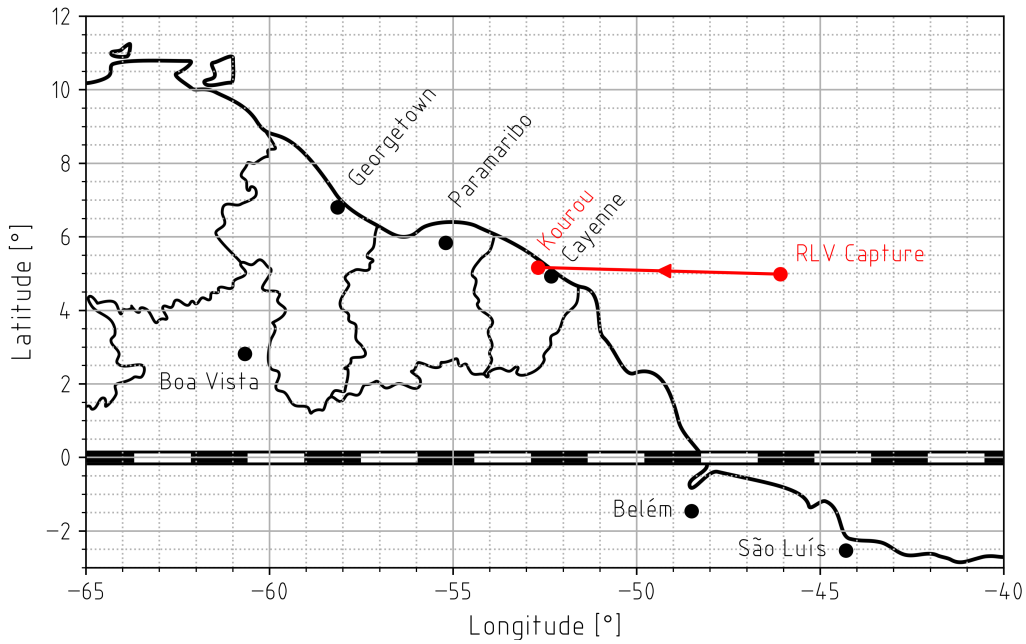


Figure 5.1: Geographic Overview of the RLV Tow-Back Trajectory.

Assuming a tow-back altitude of 10 km, the resulting flight distance then totals 732.32 km. Although this altitude is a preliminary estimate, Equation 5.1 is relatively insensitive to the value of H : between altitudes of 0 and 20 km, flight distances only differ 2.29 km, or less than 0.5%. Further assuming a constant ground speed of Mach 0.4, the corresponding flight time is estimated at 1h 42m - using the atmospheric model discussed in Appendix D. Adding an additional 30% margin, the total *Towing* mode is expected to last no longer than 2h 15m (KY-PWS.NF-03/02). Figure 5.2 further illustrates the sensitivity of this analysis, indicating that the postulated flight duration is a safe estimate for all velocities above Mach 0.31. In comparison, the environmental sensitivity analysis in subsection 3.4.1 shows that tow-back velocities below Mach 0.4 result in undesirable TA attitudes.

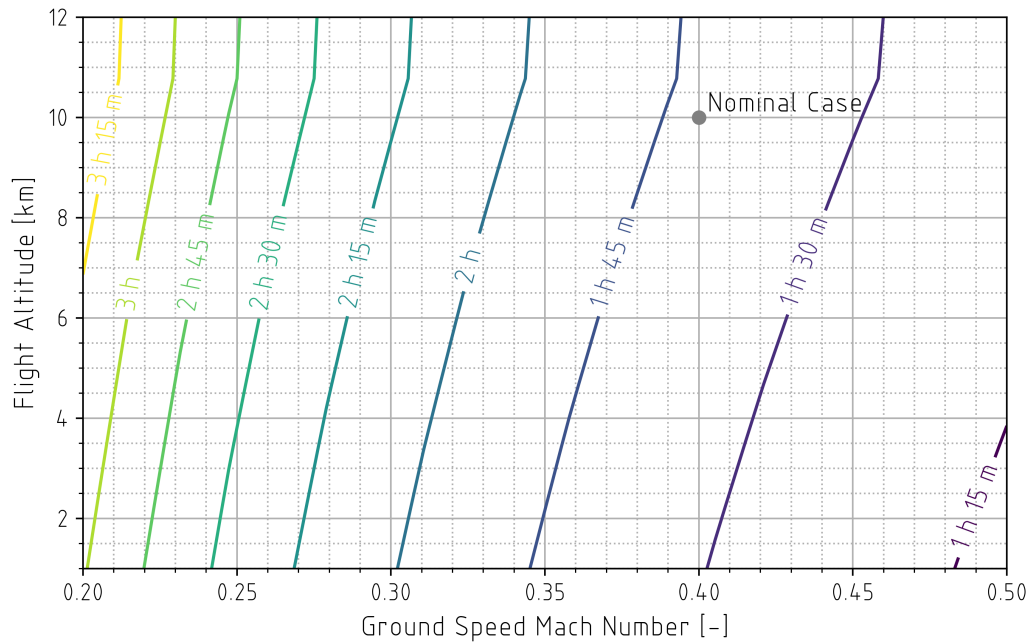


Figure 5.2: Sensitivity of the Tow-Back Duration to Flight Altitude and Mach Number. Both capture and release locations are kept fixed for this analysis.

5.2.3. Release Mode

Finally, The ACCD's *Release* mode covers the period between the RLV release and its touchdown. As will be discussed in chapter 6, the proposed release mechanism disconnects the TA's tether from the ACCD, which remains attached to the RLV during landing. In essence, the electronic regime of the ACCD is very similar compared to the *Towing* mode, potentially with the additional use of its control actuators - depending on the behaviour of the coupled ACCD-RLV system.

Because the nominal release should only take a few seconds (**KY-RLS.F-15/02**) [10], the majority of *Release* mode consists of the autonomous RLV landing. Although IAC landing manoeuvres and trajectories have not yet been studied, a preliminary release altitude is set at 1000 m. Given this relatively low altitude and the unpowered state of the RLV, touchdown has to occur within a few minutes after release. As a safe estimate, a total of ten minutes is used for the duration of the *Release* mode (**KY-PWS.NF-03/03**).

5.3. Avionics

With three operational modes defined, the major electronic subsystems inside the ACCD can now be analysed. Based on the requirements and risks formulated in section 5.1, as well as subscale test flights performed under Project FALCon [16], [72], a number of essential electronic subsystems can be identified. These are shown schematically in Figure 5.3, and are listed below.

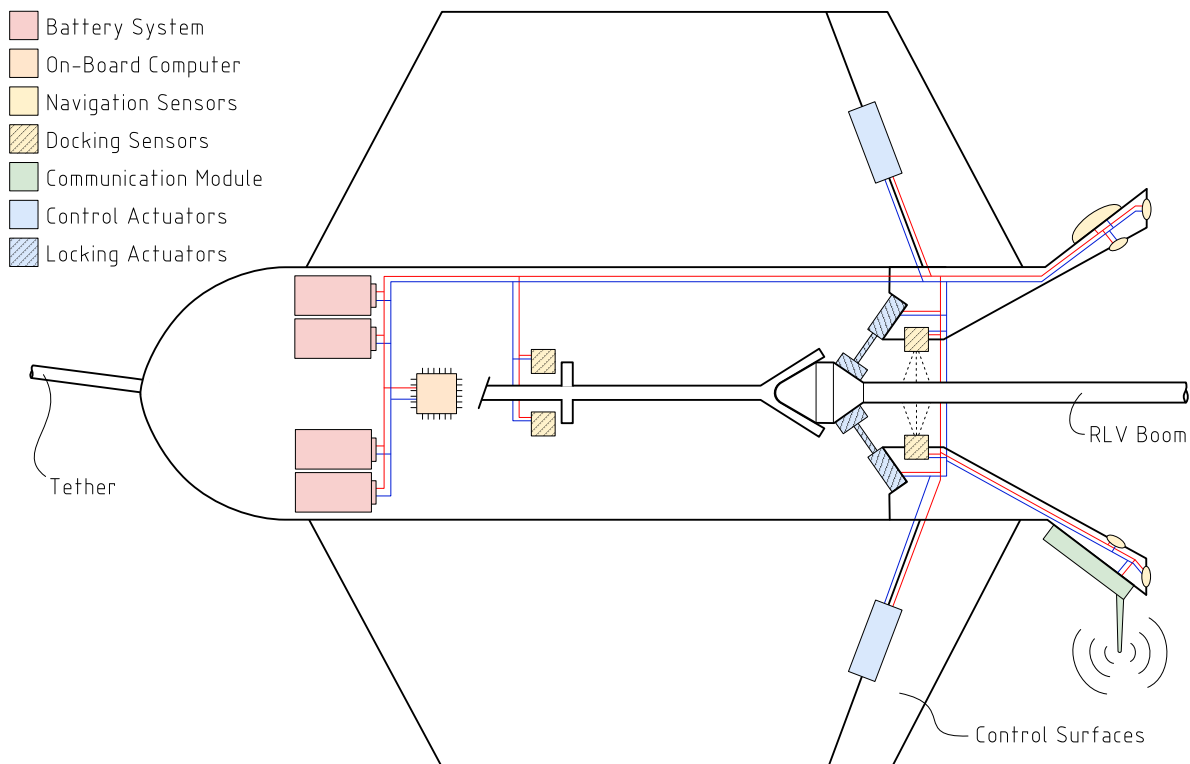


Figure 5.3: Schematic Cross-Section of the ACCD's Electronic Design, with Major Subsystems Highlighted. Red lines indicate a power connection between components, while blue lines indicate data connections.

- The **On-Board Computer (OBC)** serves as the central core of the ACCD's avionics, receiving data from various sensors, and relaying tasks to actuators and other systems.
- **Navigation Sensors** enable the relative navigation discussed in chapter 4, using GNSS, INS, and VisNav.
- The **Communication Module** provides Radio-Frequency (RF) communication between the ACCD on the one hand, and the TA/RLV on the other (**CR-AVN.F-01/20** and **TN-AVN.F-01/21**).

- **Control Actuators** steer the ACCD's control surfaces, enabling it to manoeuvre (**CR-SYS.F-12**).
- **Locking Actuators** engage or disengage the locking mechanism presented in chapter 6, ensuring the mechanical interface between the ACCD and RLV (**CR-SYS.F-13**).
- **Docking Sensors** monitor the state of the locking mechanism, triggering its deployment when necessary, while supplying the OBC with a confirmation of (un)successful docking.
- The **Battery System** powers all of the above electronic subsystems.

In the following subsections, the avionics subsystems (i.e. everything except the battery system), are analysed, starting with the OBC and navigation sensors in subsections 5.3.1 and 5.3.2. Next, subsection 5.3.3 discusses the communication module, while subsections 5.3.4 and 5.3.5 respectively study the control and locking actuators. Finally, a set of docking sensors is proposed in subsection 5.3.6.

5.3.1. On-Board Computer

To prevent an in-depth bandwidth and performance analysis of the OBC, Project FALCon's subscale demonstrator-ACCD is used as a reference point. For this vehicle, the Pixhawk architecture was selected [45], offering autopilot support, built-in sensors, telemetry logging (**KY-AVN.F-01/22**), and a communication interface [96]. To account for the increased complexity of the full-scale ACCD, the most advanced COTS option is proposed: the Pixhawk 6X Pro. Its main relevant features are listed in Table 5.1, with further details provided in Appendix M. Although additional studies are required to investigate the environmental compatibility and performance of this system, the OBC's nominal power input can be (over)estimated using the electronic footprint of the 6X Pro, yielding 18 W.

Sensors	
Inertial Measurement Units (IMUs)	3
Barometers	2
Magnetometer	1
Electronic Footprint	
Peak Voltage	6 V
Peak Current	3 A
Mechanical Footprint	
Dimensions	52 x 102 x 36 mm
Mass	112.5 g

Table 5.1: Characteristics and Features of the Pixhawk 6X Pro On-Board Computer (OBC) [96].

5.3.2. Navigation Sensors

As argued in chapter 4, the ACCD's relative navigation is enabled using INS, GNSS, and VisNav systems. For INS data, the OBC's built-in Inertial Measurement Units (IMUs) can be used, while a separate high-precision module is proposed for collecting GNSS measurements. As a representative system, the DroneCAN H-RTK F9P Rover is proposed, which accuracy of 0.01 m at 8 Hz [97] should be sufficient for the ACCD's application [15]. Essential characteristics are listed in Table 5.2, with additional data included in Appendix M. The nominal power consumption is estimated at 1.5 W.

Electronic Footprint	
Nominal Voltage	4.75-5.25 V
Nominal Current	250 mA
Mechanical Footprint	
Dimensions	80 x 80 x 20 mm
Mass	123 g

Table 5.2: Characteristics of the DroneCAN H-RTK F9P Rover GNSS (Global Navigation Satellite System) Module [97].

For the VisNav system, a 2010 study states that 1.2 W beacons have a range of up to 3600 m [86] - which is more than sufficient for the current application (**KY-DTC.F-11/02**). Based on this, their nominal power consumption is estimated at 1.5 W per beacon. Because no mechanical descriptions of VisNav beacons are available, a custom preliminary design is used as a reference, shown in Figure 5.4. With an injection-moulded ABS (Acrylonitrile Butadiene Styrene) case, and a transparent PMMA (Polymethyl Methacrylate) cover, the beacon's mass is estimated at 50 g.

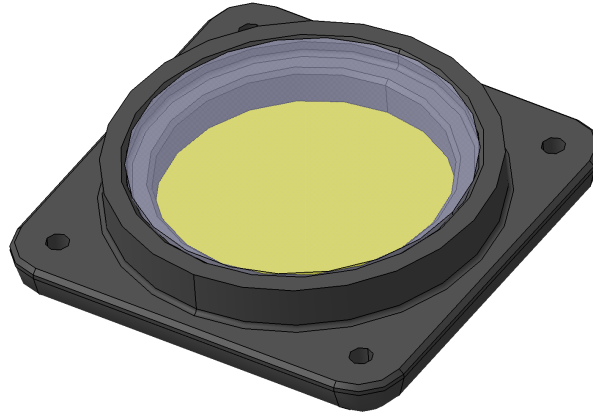


Figure 5.4: 3D View of a Preliminary VisNav Beacon Design.

5.3.3. Communication Module

In terms of the communication module, a typical COTS UAV solution is again used as a reference point: the Microhard P840, operating in the 840-845 MHz band [98]. Its 100 km range is certainly sufficient for IAC applications, while additional bandwidth analyses are required to assess the adequacy of its 345 kbps link rate [98]. Including a margin to account for the antenna itself, the total mass of the communication module is estimated at 100 g, while a nominal power consumption of 6.6 W is derived from characteristics listed in Table 5.3. Further details are provided in Appendix M.

Electronic Footprint	
Nominal Voltage	3.3 V
Peak Current	2 A
Mechanical Footprint	
Dimensions	74 x 37 x 12 mm
Mass	69 g

Table 5.3: Characteristics of the Microhard P840 Radio-Frequency (RF) Communication Module [99].

5.3.4. Control Actuators

For the ACCD's actuators, electrical, pneumatic, and hydraulic solutions can be envisioned [100]. However, these last two types would require an additional pneumatic/hydraulic system inside the ACCD, which would be detrimental to its mass, while potentially interfering with its volumetric constraints. Hence, electrical actuators are proposed for this application.

Dimensioning of the control actuators is performed using the setup illustrated in Figure 5.5. A control surface of length l_c and area A_c , deflected over an angle δ , experiences an aerodynamic force F_c as a result of the dynamic pressure $1/2 \cdot \rho \cdot V^2$. Assuming a constant pressure distribution, the corresponding torque M_c around the control surface hinge is then estimated with Equation 5.2.

$$M_c = F_c \cdot \frac{l_c}{2} = \frac{1}{4} \cdot \rho \cdot V^2 \cdot A_c \cdot \sin \delta \cdot l_c \quad (5.2)$$

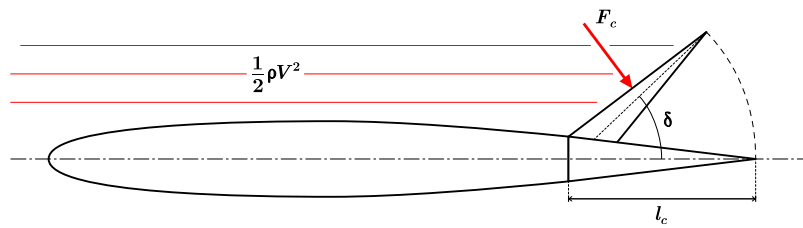


Figure 5.5: Schematic Cross-Section of Control Surface Actuation.

As depicted in Figure 5.5, Equation 5.2 assumes local airflow to be aligned with the wing itself. As this is not the case for typical ACCD conditions, additional AoA-effects need to be accounted for. This is done by significantly overestimating the control deflection δ - which also offers a safety margin for other modelling inaccuracies. As the ACCD's control surfaces are limited to a deflection of $\pm 15^\circ$ [24], a value of $\delta = 30^\circ$ offers ample safety margin in this analysis. Additionally, extreme environmental conditions are considered, using $V = 200 \text{ m/s}$ and a density equivalent to an altitude of 100 m. Given the control surface's trapezoidal geometry, its average length of 0.175 m is used for l_c , while the total surface area is estimated as $A_c = 0.0875 \text{ m}^2$. The resulting control torque then equals 92.9 Nm.

In order to arrive at an estimation for the actuator's power, its angular velocity Ω_c is needed - which depends on the control surface's internal mechanism, as well as the ACCD's overall control responsiveness. Since these are not yet defined, a rough estimate of 15 rpm is used - equivalent to covering the full control range in one third of a second. As a reference point, the F16's stabilators have a rate limit of $60^\circ/\text{s}$ [101] - or 67% of the proposed ACCD control surface speed. The corresponding actuator output power is then calculated with $P_c = M_c \cdot \Omega_c = 145.9 \text{ W}$.

Because of the high torque and low speed requirements, an additional gearbox is needed to convert typical high-speed/low-torque outputs from DC (Direct Current) motors. As an example, the ECI-63.20-K4-B00 geared brushless DC motor from ebm-papst GmbH is proposed, which has a nominal power output of 178 W, and a typical torque of 0.425 Nm [102]. This solution is chosen because of its simplicity and low-voltage input (24V), while the brushless interior increases efficiency and longevity [103]. Motor characteristics are listed in Table 5.4 and Appendix M, yielding an estimated power input of 204 W.

Nominal Operating Point	
Output Speed	4000 rpm
Output Torque	0.425 Nm
Electronic Footprint	
Nominal Voltage	24 V
Nominal Current	8.5 A
Mechanical Footprint	
Dimensions	63 x 63 x 265 mm
Mass	0.85 kg

Table 5.4: Characteristics of the ECI-63.20-K4-B00 Control Actuator [102].

For the gearbox on the other hand, a solution such as the J53-400 can be used. With a 400:1 conversion ratio and 85% efficiency [104], this results in a power input of 151.3 W applied to the control surfaces. Using the J53's mass of 170 g, and applying a margin to account for additional components in the control surface mechanism, the total gearbox assembly mass is estimated at 500 g.

5.3.5. Locking Actuators

Before dimensioning the locking actuators, a fundamental analysis of the ACCD's locking mechanism is required. The main purpose of this mechanism is to dock with the RLV, and ensure a structural interface between both vehicles (**CR-SYS.F-13**). Additionally, an ideal locking mechanism would also offer a release functionality, so that the RLV can be disconnected from the TA when required (**CR-**

SYS.F-15). However, initial analyses show that combining the locking and release functions into a single mechanism results in unfeasible design requirements for the corresponding actuators. This is illustrated in Figure 5.6, which shows two major configurations for such a mechanism.

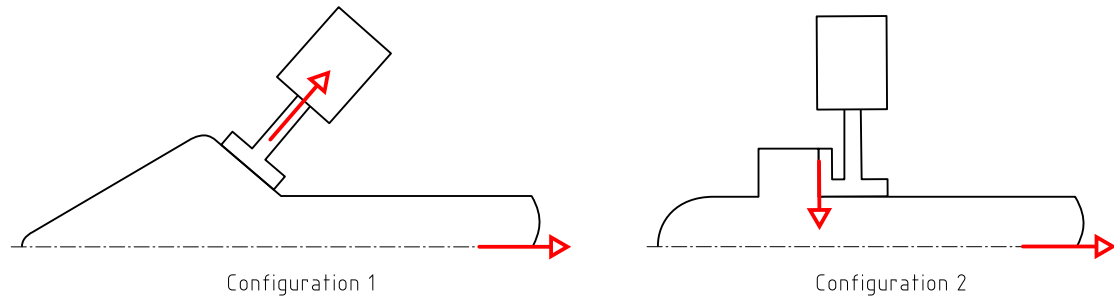


Figure 5.6: Comparison of Two Main Locking Mechanism Configurations, with Corresponding Limiting Load Scenarios.

In the first configuration, towing loads are transferred onto the locking actuators, which need to deliver a force in the order of 10-50 kN to maintain the ACCD-RLV interface throughout the entire tow-back. In the second one, towing loads induce significant frictional forces between the actuators and the RLV boom, which need to be overcome at the time of release. Even with lubricated aluminium surfaces [105], these forces are in the order of 10-20 kN. In both cases, actuators that are sufficiently powerful to supply the required forces, are either unacceptably massive or slow [106]. Additionally, the continuous application of locking forces in *Configuration 1* results in a significant increase in energy requirements, given the long duration of the *Towing* mode.

One solution could be to increase the design's complexity, in order to off-load the actuators and decrease frictional forces. However, this requires additional actuators and intricate mechanisms, which increase the overall system mass, and have a risk of jamming [66]. Another solution, proposed in this work, consists of decoupling the locking and release functionalities, and dedicating a separate mechanism to each. By doing so, *Configuration 2* can be used for the locking mechanism, since the actuators are no longer required to disengage. Instead, detachment between the RLV and TA is handled by a second system, which doubles as an emergency release mechanism (**CR-RLS.F-15/03**). This separate release system will be further discussed in chapter 6.

With the above solution in mind, a preliminary analysis of the locking actuators can now be made. Based on the design of the locking mechanism - presented in chapter 6 - linear actuators are required, which can complete a stroke of 100 mm in less than 0.5 s. This is an important metric, because actuators are typically limited in terms of peak deployment velocity and acceleration. Figure 5.7 further analyses this concept, by plotting the minimal duration t_d of a 100 mm stroke S deployment, as a function of peak acceleration \ddot{S}_m and velocity \dot{S}_m - as calculated with Equation 5.3.

$$t_d = \begin{cases} \sqrt{2 \cdot S / \ddot{S}_m} & \text{if } 1/2 \cdot V^2 / \ddot{S}_m \geq S \\ \dot{S}_m / \ddot{S}_m + (S - 1/2 \cdot \dot{S}_m^2 / \ddot{S}_m) / \dot{S}_m & \text{else} \end{cases} \quad (5.3)$$

Using Figure 5.7, the deployment requirement can be translated into two equivalent metrics. On the one hand, the maximum deployment velocity needs to be at least 230 mm/s, while the peak acceleration on the other hand should be higher than 1.1 m/s². Assuming a total accelerating mass of 500 g (based on the mechanical design presented in subsection 6.6.2) the minimal acceleration can further be converted into a required deployment force of 0.55 N. Finally, given the geometric constraints of the ACCD's interior, the undeployed length of the actuator needs to be smaller than 200 mm.

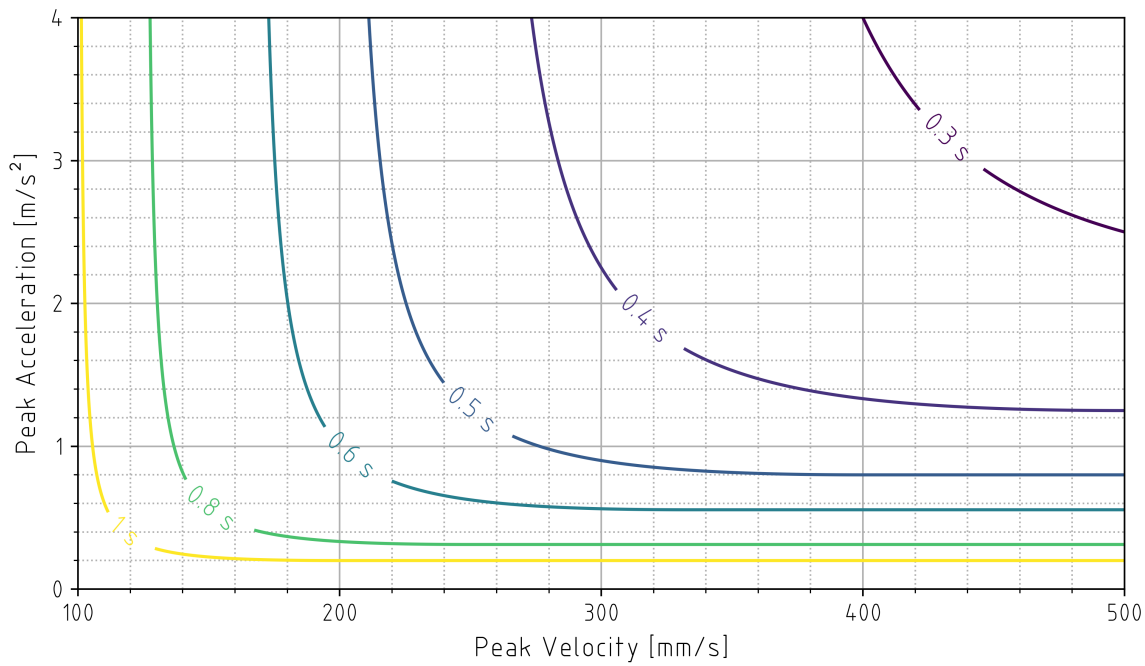


Figure 5.7: Minimal Duration of a 100 mm Stroke Deployment as a Function of Peak Actuator Velocity and Acceleration.

Combining all of the aforementioned requirements, the pool of available COTS solutions is drastically reduced - particularly due to the high deployment velocity, large stroke, and limited undepleted length. Nevertheless, the Faulhaber LM1247-100-11 linear DC actuator - shown in Appendix M - was found to meet all criteria. Based on its characteristics listed in Table 5.5, and using a total stroke of 82 mm (derived from the final mechanical design), its resulting *unloaded* deployment time equals 43.74 ms. However, when accounting for the actuator's peak force, and using an accelerating mass of 325 g (again based on the final mechanical design), this value increases to 71.25 ms - still well below the required 0.5 s.

Deployment Characteristics	
Maximum Stroke	100 mm
Maximum Velocity	3000 mm/s
Maximum Acceleration	91.4 m/s ²
Maximum Force	10.5 N
Electronic Footprint	
Back-EMF Constant	5.25 V/s/m
Peak Current	1.64 A
Mechanical Footprint	
Dimensions	13 x 19 x 172 mm
Mass	78 g

Table 5.5: Characteristics of the LM1247-100-11 Linear Locking Actuator [107].

With the back-EMF (Electromotive Force) constant K_e listed in Table 5.5, the peak input voltage U to the actuator can further be estimated using Equation 5.4 [108]. This assumes an unloaded actuator, and neglects additional mechanical losses. With a maximum velocity $\dot{S}_m = 3000 \text{ mm/s}$, the corresponding peak voltage is then $U = 15.75 \text{ V}$. Combining this value with the peak current of 1.64 A, the nominal actuator power is overestimated as 25.83 W. In reality, the actuators will only supply this power during a few seconds, rather than for the entire duration of the operational modes. Hence, the proposed overestimation offers margin to compensate for the simplified peak voltage calculation.

$$U = K_e \cdot \dot{S}_m \quad (5.4)$$

5.3.6. Docking Sensors

As a final cornerstone to the ACCD's avionics, a set of docking sensors is required. With the need for sufficient fault-tolerance and redundancy in mind, a tripartite sensor solution is proposed, shown schematically in Figure 5.8. These three types of sensors are discussed in the following subsections.

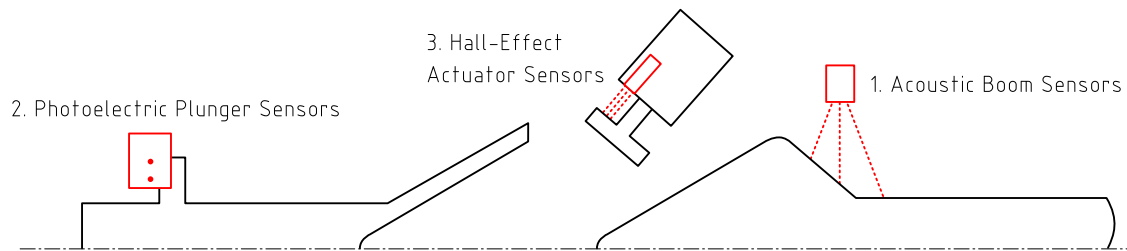


Figure 5.8: Schematic Depiction of a Tripartite Docking Sensor Solution. The plunger sensors' optical signal is sent perpendicular to the figure.

Acoustic Boom Sensors

First of all, acoustic distance measuring sensors monitor when the RLV boom has entered into the ACCD's locking mechanism. As illustrated in Figure 5.9, their distance measurements can be combined with knowledge about the boom's geometry to estimate its axial position. To account for radial misalignments, three sensors are required; a fourth one is added to offer redundancy to the system. In case of acoustic interference between the different sensors, a rapidly cascading operating scheme can be used, where only a single sensor is active at any point in time.

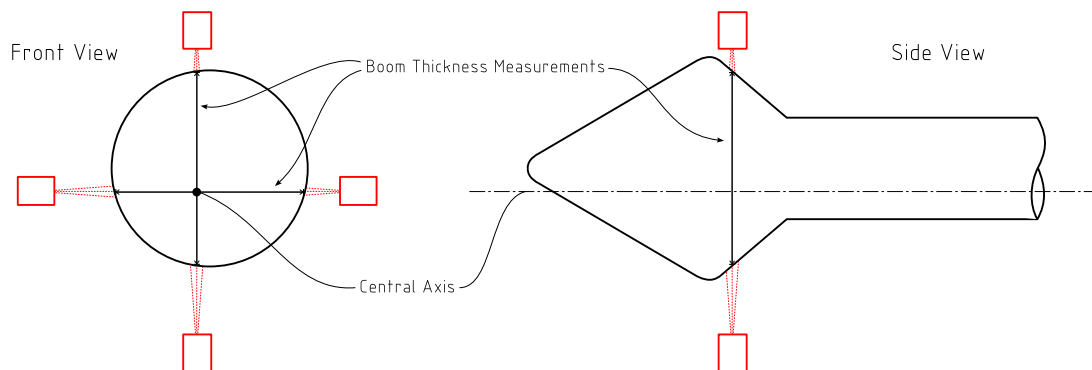


Figure 5.9: Schematic Depiction of Boom Thickness Measurement Using Four Acoustic Distance Measuring Sensors.

The particular solution proposed for this task is the Baumer U300.D50-DPMJ.72N ultrasonic sensor shown in Appendix M - chosen based on its compact size, limited blind zone, fine resolution, and high responsiveness [109]. General characteristics are listed in Table 5.6, from which a nominal power estimate of 1.05 W is derived.

Sensor Characteristics		
Range		15-500 mm
Resolution		< 0.3 mm
Response Time		< 40 ms
Electronic Footprint		
Nominal Voltage		12-30 V
Nominal Current		35 mA
Mechanical Footprint		
Dimensions		13 x 39 x 23 mm
Mass		21 g

Table 5.6: Characteristics of the U300.D50-DPMJ.72N Ultrasonic Distance Measuring Sensor [109].

Photoelectric Plunger Sensors

A second set of sensors relies on a more binary detection method, by being triggered when a plunger is compressed past a certain threshold - as shown in Figure 5.10. As will be discussed in chapter 6, this plunger interfaces with the RLV boom, and its axial position indicates when the locking mechanism should be activated. Small protrusions are added to the plunger, which acts as the triggering mechanism when passing the sensor. Here again, a double set of sensors is proposed, for the purpose of redundancy and fault-tolerance. Additional details regarding a nominal docking sequence are provided in Appendix N.

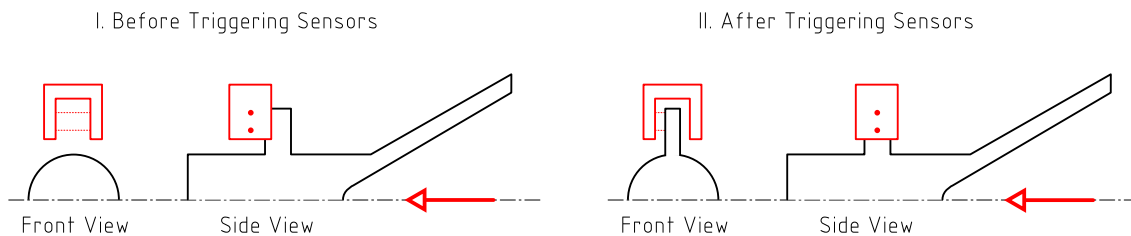


Figure 5.10: Schematic Depiction of Plunger Sensors Activation.

As a representative COTS solution, the Omron E3Z-G62 grooved photoelectric sensor is proposed, with main characteristics listed in Table 5.7, and further details provided in Appendix M [110]. As the response time of this sensor is only 1 ms, it allows for a very rapid triggering of the locking mechanism, so that the required deployment time of 0.5 s is not jeopardized. Furthermore, modifying the axial position of the sensors enables adjustability of the trigger pulse timing. Based on the electrical footprint of the E3Z-G62, a nominal power consumption of 0.96 W is used for these sensors.

Sensor Characteristics	
Resolution	1.5 mm
Response Time	1 ms
Electronic Footprint	
Nominal Voltage	12-24 V
Nominal Current	40 mA
Mechanical Footprint	
Dimensions	40 x 50 x 11 mm
Mass	30 g

Table 5.7: Characteristics of the Omron E3Z-G62 Grooved Photoelectric Sensor [110]. The listed resolution refers to the minimal object size needed to ensure proper triggering of the sensor.

Hall-Effect Actuator Sensors

The third set of sensors are built into the LM1247-100-11 linear locking actuators proposed in subsection 5.3.5. These are analogue Hall sensors, relaying information about the extension state of each actuator. In conjunction with data from the infrasonic sensors, they provide a confirmation of successful capture, or notice of an unsuccessful one.

Combining the three aforementioned types of docking sensors creates data diversity, increasing the system's robustness and minimizing false positives. For example, only using the plunger sensors would entail a risk of triggering the locking mechanism without the RLV boom being inserted into the ACCD. By introducing measurements from the infrasonic sensors into the data pool, the likelihood of such scenarios is drastically reduced. This is further illustrated in Appendix N, where an overview is provided of a nominal docking sequence - indicating how the different measurements are combined to monitor and control the docking and locking actions.

5.4. Power System

With all major avionics subsystems analysed, their SWaP footprints can be combined to generate an estimation of the required battery system. This is done in Table 5.8, where cumulative power requirements for each of the three operational modes are defined. Because of uncertainty concerning the nominal power usage of some subsystems during certain operational modes, a distinction is made between *active* and *possibly active* subsystems - marked with a '+' and '-' respectively. Correspondingly, lower and upper limits are used to define resulting power and energy requirements - the latter of which are based on the duration of the operational modes estimated in section 5.2.

Subsystem	Properties			Operational Phases		
	Volume [mm^3]	Mass [kg]	Power [W]	Homing	Towing	Release
1x OBC	102 x 52 x 36	0.113	18.0	+	+	+
1x RF Module	74 x 37 x 12	0.069	6.6	+	+	+
1x GNSS Module	80 x 80 x 20	0.123	1.5	+	+	+
12x VisNav Beacons	45 x 45 x 11	0.600	18.0	+		
4x Control Actuators	63 x 63 x 265	3.400	816.0	+		-
4x Locking Actuators	13 x 19 x 172	0.312	103.3	+	-	-
4x Infrasonic Sensors	13 x 39 x 23	0.084	4.2	+	+	+
2x Photoelectric Sensors	40 x 50 x 11	0.060	1.9	+	+	+
Battery						
Lower Power Requirement [W]				969.5	32.2	32.2
Upper Power Requirement [W]				969.5	135.5	951.5
Nominal Duration [min]				10	135	10
Lower Energy Requirement [kJ]				581.7	261.0	19.3
Upper Energy Requirement [kJ]				581.7	1097.9	570.9

Table 5.8: SWaP Footprint of Electronic Subsystems, with Cumulative Power and Energy Requirements. Power and mass values concern the total subsystem, while reported volumes are unit volumes.

Combining the three operational modes in Table 5.9, total battery energy requirements are obtained - ranging between 239.5 and 625.1 Wh. The substantial range of this energy estimate is mainly related to the *Towing* mode, because the power usage needed to maintain the locking actuators in an extended position is uncertain, and requires further analysis. This energy range can then be converted into equivalent battery masses and volumes, assuming a lithium-ion architecture with a gravimetric energy density of 175 Wh/kg [111], and a volumetric energy density of 450 Wh/l [112].

	Energy [kJ]	Energy [Wh]	Mass [kg]	Volume [mm^3]
Lower Limit	862.0	239.5	1.37	81 x 81 x 81
Upper Limit	2250.5	625.1	3.57	112 x 112 x 112

Table 5.9: Energy, Mass and Volume Estimate of a Lithium-Ion Battery System.

Based on the above estimates, a 700 Wh battery system is proposed - equivalent to a 1.12 SF relative to the calculated upper energy limits. With the purpose of modularity and fault-tolerance, the battery system is further divided into four 175 Wh modules, each with an estimated weight of 1 kg, and a volume of 100 x 70 x 60 mm. This volume includes a 1.1 safety margin compared to the specific volumetric energy of 450 Wh/l, to account for additional peripheral equipment. Furthermore, as lithium-ion batteries can achieve specific powers well above 250 W/kg [113], the proposed system should have no problem supplying the required peak power of 969.5 W during *Homing* mode.

5.5. Mounting System

With the essential core of the ACCD's electronic design presented, the only aspect left to analyse concerns their mechanical interface to the rest of the vehicle. For that purpose, a polyvalent and multifunctional mounting platform is proposed, attached to the ACCD's structural frame using eight M8

Class 8.8 bolts - which are more than sufficient to support the loaded platform's mass of up to 2.1 kg. The axial position of these platforms can easily be modified to manipulate the location of the vehicle's CoG.

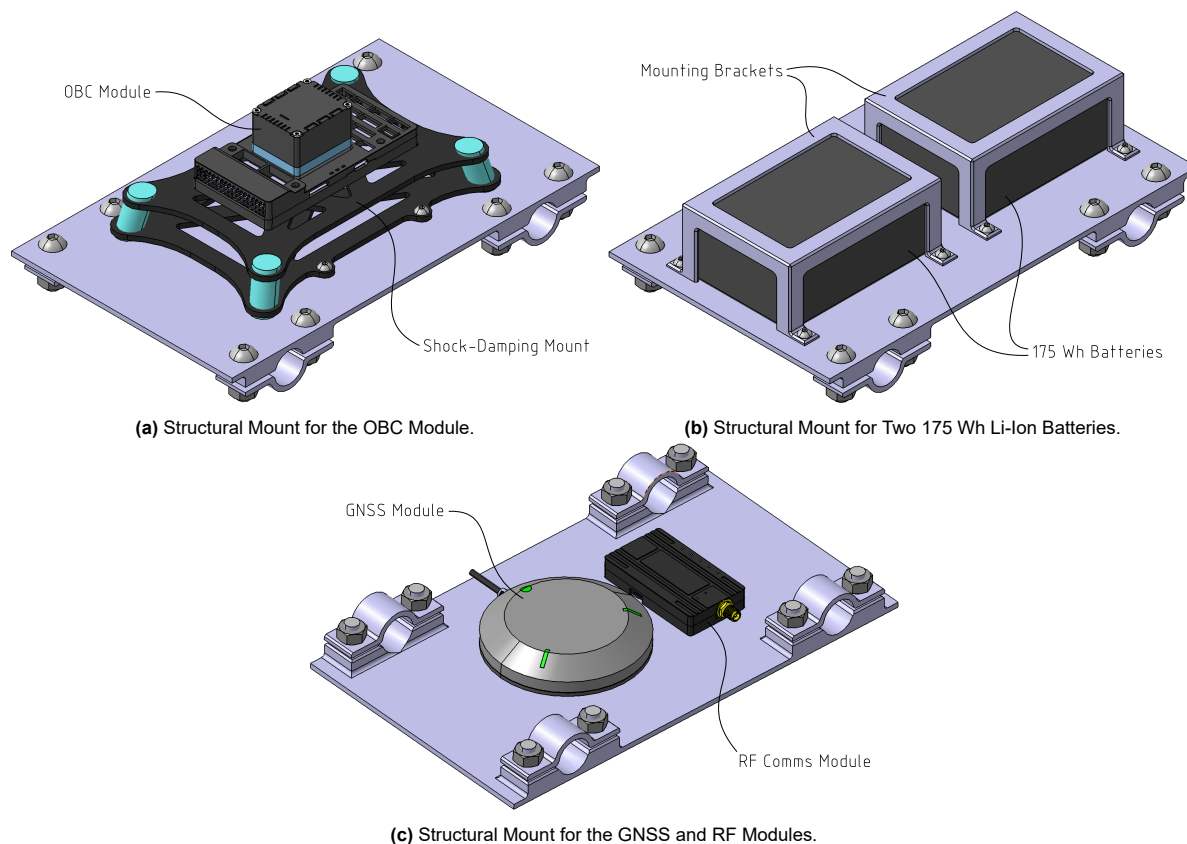


Figure 5.11: 3D Views of the Avionics Mounting Structures.

Figure 5.11 shows three platform variations that are included in the final design, each with different avionics attachment points. The first one (Figure 5.11a) accommodates the OBC, which is attached via an intermediate mounting system designed to dampen out vibrations and enable proper IMU read-outs [114]. A second platform (Figure 5.11c) houses the GNSS and communication modules, which require sufficient hemispherical coverage [97], [99]. As such, their platform is located at the ACCD's aft, with both modules pointing outwards. Finally, a third platform type carries two 175 Wh batteries. Two such platforms are included in the final design, with extra ones easily being added (or removed).

Other avionics components, such as the locking actuators, docking sensors, and VisNav beacons, are attached directly to the ACCD's structural elements - respectively the locking frame, plunger support assembly, and docking cone. Because the interior of the control surfaces is not defined within the scope of this work, the precise attachment of the control actuators is left unspecified. However, ample space is available inside the wings and control surfaces to accommodate the actuators and gearbox proposed in subsection 5.3.4.

5.6. Conclusion

In this chapter, a preliminary design for the ACCD's avionics and power system has been presented. Based on a set of relevant requirements and risks, three distinct operational modes were defined, and an estimation of their duration was obtained. Apart from the battery system, six main avionics sub-systems were identified and subsequently analysed. Using representative COTS components as a reference point, estimates for their SWaP footprints were obtained - which was especially crucial in the case of the control and locking actuators. For other elements, such as the docking sensors, limited

SWaP footprints allow for improved redundancy and robustness, by combining multiple individual components. For systems such as the OBC and RF module, further studies are required to assess their suitability in terms of available bandwidth and processing power. Additionally, environmental compatibility with the ACCD's operating conditions should be verified for all proposed COTS components.

A core finding of this chapter is that the continuous presence of significant towing forces imposes demanding requirements on the locking actuators. Combined with their required high deployment speed, and the ACCD's limited mass and size budgets, a universal locking/release mechanism was found to be unfeasible. Instead, two separate mechanisms are dedicated to both functions.

Combining power estimates of the different subsystems with duration estimates for each operational mode, a conservative energy requirement for the battery system was then derived in Tables 5.8 and 5.9. Using a lithium-ion technology, the battery's volume and mass were subsequently estimated, from which the feasibility of a battery-powered vehicle architecture was verified. Finally, a mechanical mounting structure for specific avionics components was proposed, integrated into the mechanical design presented in the following chapter.

6

Mechanical Design

At the very core of the ACCD is its mechanical design. Not only does it enable major functionalities such as interfacing with the RLV and providing a secure towing connection, but it also serves as the platform for the electronic design described in chapter 5. Throughout this chapter, the internal structure of the ACCD will take shape, using important insights and conclusions from previous chapters.

First, in section 6.1, the systems engineering foundations for the mechanical design are laid, identifying relevant requirements and risks. Next, section 6.2 presents a short state-of-the-art overview of general docking systems - as this is the core functionality of the ACCD's internal mechanism. Sections 6.3 through 6.7 then document the mechanical design itself, covering all relevant subsystems identified in section 6.1: the tether attachment, structural frame, shock-absorbing assembly, docking mechanism, and release system. For each of these subsystems, the design effort typically starts with a first-principles approach, using a high level of abstraction. Based on this, a detailed final design is then presented and analysed in terms of relevant loads. Finally, section 6.8 combines this chapter's main conclusions, presenting the final mechanical ACCD assembly.

6.1. Requirements and Risks

When it comes to the ACCD's mechanical design, its essential goal is to provide RLV docking (**CR-SYS.F-13**) and release (**CR-SYS.F-15**) functionalities, while remaining within safe structural limits (**CR-SYS.NF-02**). Furthermore, the addition of a tether attachment is also vital, as it enables the ACCD to be towed by the TA (**KY-SYS.NF-01**). Based on these high-level requirements, a number of functional subsystems can be identified. They are listed below, and are depicted schematically in Figure 6.1.

- The **Tether Attachment** has a dual function: on the one hand, it provides the vehicle with sufficient kinematic freedom relative to the tether, so that it can manoeuvre with respect to the TA. On the other hand, it is part of the main load-bearing path inside the ACCD, and should safely transfer towing forces to the tether.
- The **Structural Frame** forms the core of the ACCD, acting as its principal load-bearing path. It also includes the wing support structure, which ensures that aerodynamic loads on the four wings are adequately transferred onto the main structure.
- The goal of the **Shock-Absorbing Assembly** is to absorb virtually all energy that is released upon docking between the ACCD and the RLV.
- The **Docking Mechanism** has two main purposes: on the one hand, its diverging entrance acts as a guiding cone, reducing misalignments with the RLV boom upon first contact. On the other hand, its locking mechanism establishes a rigid towing connection between the ACCD and RLV, and forms the interface between both vehicles.

- The **Release System** offers nominal and emergency release functionalities, by disconnecting the ACCD from the tether. As described in chapter 5, such a separate solution is proposed in favour of a universal docking/release mechanism.

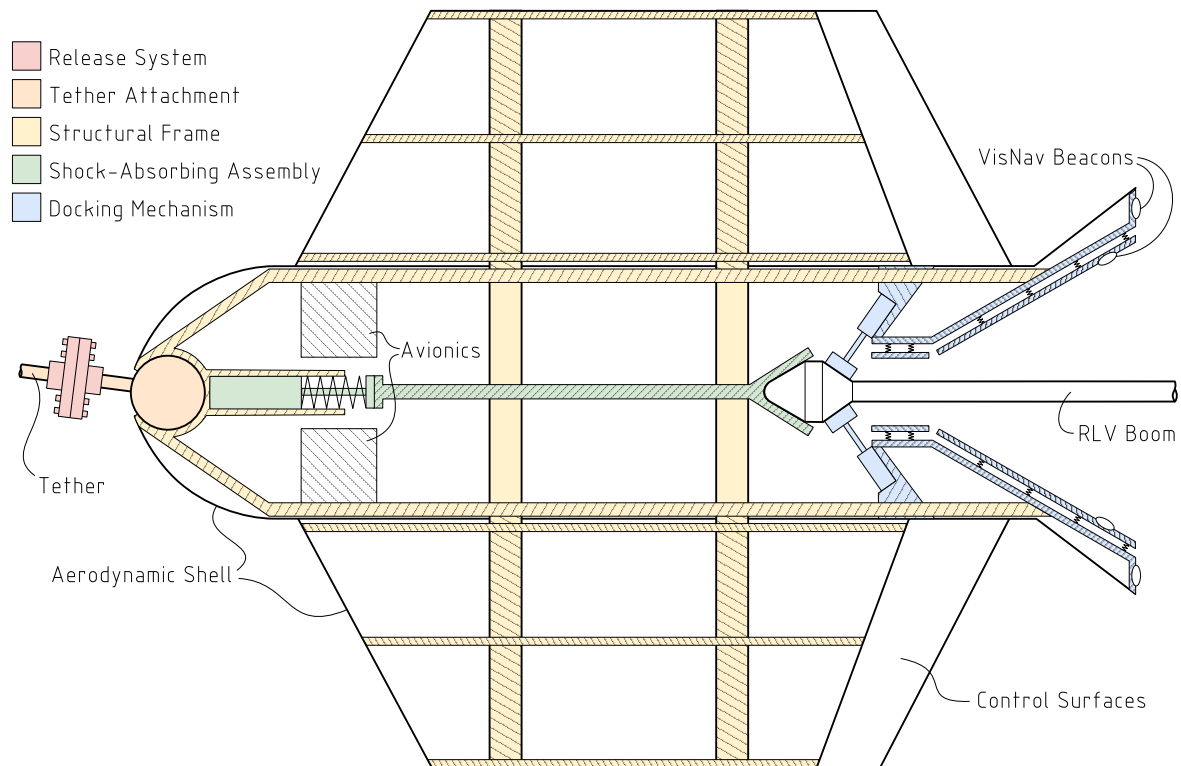


Figure 6.1: Schematic Cross-Section of the ACCD's Mechanical Design, with Major Subsystems Highlighted. The interior mechanism of the aerodynamic control surfaces is not defined in this work.

Based on this functional breakdown, and the high-level requirements listed above, a set of subsystem requirements can be generated. These are presented and discussed in subsections 6.1.1 until 6.1.3, respectively covering the ACCD's overarching structure, docking, and release functionalities. Additionally, a number of relevant risks are highlighted in subsection 6.1.4.

6.1.1. Structural Requirements

Treating the ACCD's structure as a whole, the following requirements can be generated in terms of overall size, inertia, loads, and stresses. Further details regarding these - and subsequent - requirements are listed in Appendix A.

- TN-STR.NF-01/01:** The ACCD shall have an outer shell as defined in subsection 2.2.1, with a total length of 2 m, and a diameter of 1.5 m (including wings).
- TN-STR.NF-01/02:** The ACCD's design shall strive to maximize axisymmetry. As a quantifiable indication, the yaw and pitching moments of inertia shall not differ more than 1%.
- KY-STR.NF-01/03:** The connection between the ACCD and tether shall provide three Degrees of angular kinematic Freedom (3DoF), within a cone of 25° half angle.
- CR-STR.NF-02/01:** The ACCD shall be able to accommodate axial and radial shocks associated with the capture and release procedures between the ACCD and RLV.
- CR-STR.NF-02/02:** The ACCD shall be able to accommodate an axial compressive load of 50 kN, in order to withstand the docking impact with the RLV.

- CR-STR.NF-02/03:** The ACCD shall accommodate an axial tensile load of 300 kN, in order to withstand extreme tow-back regimes.
- KY-STR.NF-02/04:** The structural design of the ACCD's wings shall be able to withstand a load of 15 kN per wing, applied perpendicularly and uniformly to its upper surface.
- KY-STR.NF-02/05:** All Von Mises stresses shall remain below 66% of the yield strength of their respective materials.
- KY-STR.NF-02/06:** All deformations inside kinematically critical components shall remain below 1 mm, as to not hinder the functioning of internal mechanisms. Other parts of the ACCD shall not deform more than 5 mm.

First of all, a volumetric boundary condition for the ACCD's mechanical design is defined (**TN-STR.NF-01/01**), based on the definition of the aerodynamic shell presented in chapter 2. Furthermore, general axisymmetry around the ACCD's roll axis is desirable (**TN-STR.NF-01/02**), as it offers several advantages. On the one hand, it eliminates the need for strict roll orientation requirements between the ACCD and RLV. By relaxing this degree of freedom, less stringent control algorithms are required, and likelihood of a successful capture is increased. Additionally, it allows for flexibility in the operational configuration of the ACCD, as described in chapter 2: whether the device is deployed in an 'x'- or '+'-configuration has no essential impact on the mechanical design. The tentatively required 1% metric then serves as a quantifiable measure to verify such axisymmetry. Although not forming conclusive evidence for the vehicle's axisymmetry, the relative difference between its yaw and pitching moments of inertia provides an initial indication.

Next, kinematic rotational freedom inside the tether attachment (**KY-STR.NF-01/03**) is essential to allow for sufficient manoeuvrability, and to prevent reaction torques. The conical half angle of 25° is based on expected maximum values of tether angles θ_1 and pitch angles ϕ estimated with chapter 3's Towing Model. The quantification of this parameter is further elaborated upon in section 6.3.

Analysing essential vehicle loads, these can be divided into four main categories: shocks related to (dis)connection events (**CR-STR.NF-02/01**), impact loads during docking (**CR-STR.NF-02/02**), axial loads during tow-back (**CR-STR.NF-02/03**), and aerodynamic loads on the vehicle's wings (**KY-STR.NF-02/04**). In this work, shock loads are not quantified; rather, the general principle of shock-attenuating structures is kept in mind while designing the ACCD. Impact loads depend heavily on the design of the shock-absorbing assembly, with rationale for the 50 kN design load provided in section 6.5. The extreme towing design load of 300 kN on the other hand has been derived in chapter 3. Similarly, a quantification of the 15 kN aerodynamic load is provided in section 6.4.

Finally, a 1.5 SF is used for structural analyses (**KY-STR.NF-02/05**) - which is a typical value for the design of aerodynamic vehicles [115]. It provides an additional margin compared to the 1.18 SF used in Heide's and Atanassov's design [11], to account for the static nature of the load analyses. The material's yield strength rather than its ultimate strength is used as an upper limit, since plastic deformation could hinder the kinematic functioning of internal mechanisms, while also potentially jeopardizing the reusability of the ACCD. Similarly, the kinematics of internal mechanisms require elastic deformations in crucial assemblies to remain limited (**KY-STR.NF-02/06**). For other components, increased deformations can be tolerated.

6.1.2. Docking Requirements

Since the docking mechanism represents the main functional subsystem inside the ACCD's mechanical interior (**CR-SYS.F-13**), it requires some additional attention in terms of tailored subsystem requirements - as listed below.

- KY-DCK.F-13/01:** Successful docking shall be possible for relative axial velocities between the ACCD and RLV within a range of 2-5 m/s, and relative radial velocities below 1 m/s.

KY-DCK.F-13/02: Successful docking shall be possible in case of an angular yaw/pitch misalignment between the ACCD and RLV of up to 10°, and lateral misalignments of up to 25 cm.

TN-DCK.F-13/03: Successful docking shall be independent of the relative roll alignment between the ACCD and RLV.

CR-DCK.NF-13/04: The docking mechanism shall be reusable.

CR-DCK.F-13/05: The ACCD shall reliably detect when successful docking has been achieved.

CR-DCK.F-13/06: The docking mechanism shall ensure a fully inelastic collision between the ACCD and RLV, while safely absorbing the associated impact energy.

The first three requirements (**KY-DCK.F-13/01**, **KY-DCK.F-13/02**, and **TN-DCK.F-13/03**) jointly define the operational environment of the docking mechanism. In order to obtain a robust system and increase the likelihood of a successful RLV capture, multiple degrees of uncertainty should be accommodated. In terms of relative impact velocities, the 2-5 m/s range stems from previous SART studies [10], [40], [42], with the lower limit being relevant in case the locking mechanism relies on external activation energy. On the other hand, the 1 m/s radial velocity is a tentative estimate, corresponding to a radial velocity component of roughly 20%. Finally, the allowable misalignments (**KY-DCK.F-13/02**) can also be traced back to past SART studies [10], [116], and are governed by the design of the ACCD's aerodynamic shell. The roll misalignment on the other hand should have no effect on the docking mechanism - which follows directly from the ACCD's axisymmetry requirement (**TN-STR.NF-01/02**).

Although studies such as in-depth life cycle analyses are not included in the scope of this work, general reusability of the ACCD's essential core is required (**CR-DCK.NF-13/04**) to limit the overall cost of IAC. Additionally, monitoring of the docking procedure is important (**CR-DCK.F-13/05**), for a number of purposes. As described in chapter 5 and Appendix N, it governs the (de)activation of avionics subsystems, while also triggering the transition between different operational modes. Alternatively, detection of a non-successful capture either prompts a second capture attempt, or an abort.

Finally, the last requirement (**CR-DCK.F-13/06**) stems from a past SART study [116], and essentially demands that the ACCD and RLV have no residual relative velocity after docking. It is directly related to the shock-absorbing assembly inside the ACCD, which ensures the inelastic nature of this collision.

6.1.3. Release Requirements

Similar to the docking mechanism, the importance of the ACCD's release system (**CR-SYS.F-15**) prompts the definition of additional subsystem requirements - shown below.

CR-RLS.F-15/01: The ACCD shall have a nominal release mode, where the RLV is decoupled from the towing system when in close proximity to a landing site.

KY-RLS.F-15/02: The nominal release defined in **CR-RLS.F-15/01** shall take no longer than 5 s.

CR-RLS.F-15/03: The ACCD shall have an emergency release mode, allowing the disconnection of the RLV from the TA at any point during flight.

KY-RLS.F-15/04: The emergency release defined in **CR-RLS.F-15/03** shall take no longer than 1.5 s.

In essence, two release scenarios are defined: a nominal one, and an emergency one. On the one hand, nominal release (**CR-RLS.F-15/01**) follows directly from the IAC mission scenario presented in chapter 2. It should have a limited duration in order to increase the system's responsivity - with a 5 s criterion (**KY-RLS.F-15/02**) adopted from Heide's 2005 study [10]. On the other hand, an emergency release mode (**CR-RLS.F-15/03**) is crucial to minimize the risk of damaging or losing the TA - especially when it is manned [16]. Because emergency release could be triggered in various adverse conditions, it should happen significantly faster than nominal release. Hence, a 1.5 s criterion (**KY-RLS.F-15/04**) is proposed.

6.1.4. Risks

Considering the entire mechanical design of the ACCD, various risks have been identified, listed in Appendix A. Without covering the details of each risk individually, a number of general trends can be observed. For one, risks regarding excessive or off-nominal loads on the ACCD (e.g. **TOW-01**) are (partially) mitigated by the introduction of the 1.5 SF (**KY-STR.NF-02/05**). Additionally, main mechanical risks are related to the vehicle's docking and release functionalities. Especially for the former, this emphasizes its crucial role inside the ACCD, and the special care that its design requires. For the latter, identified risks further advocate the requirement for an emergency release mode. Finally, both types of risks are mitigated as much as possible during the mechanical design presented in subsequent sections, by aiming towards a simple, fast, and robust design implementation.

6.2. Background

Given the key role of the ACCD's docking mechanism - as demonstrated in previous sections - a brief literature overview of state-of-the-art docking solutions can provide valuable insights for subsequent design efforts. In general, such docking systems have applications in land vehicles [117], boats [118], and UAVs [119]–[121]. In particular however, the docking of spacecraft offers a wealth of solutions to a design problem that is (relatively) similar to the one at hand. As such, relevant observations found within this research discipline are presented in subsections 6.2.1 and 6.2.2 - respectively covering a theoretical abstraction of the docking problem, and practical solutions to said problem.

6.2.1. Docking Phases

Based on work by Lion et al. [66], a general docking procedure can be divided into a number of distinct phases, visualized in Figure 6.2, and listed below.

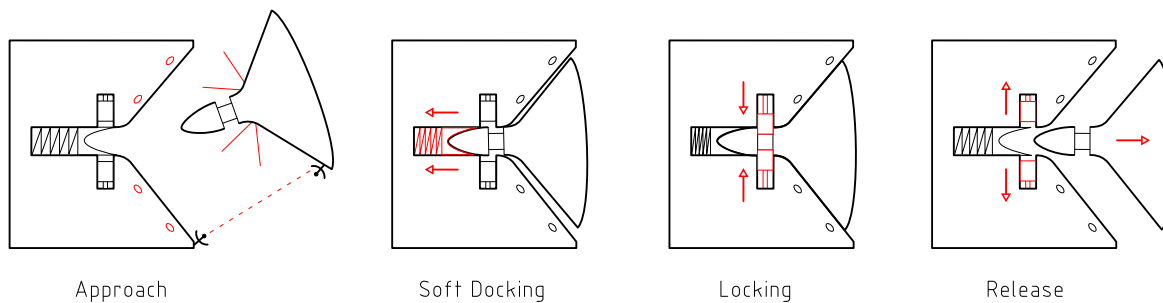


Figure 6.2: Schematic Overview of the Main Docking Phases.

- During **Approach**, sensors (cf. chapter 4) and actuators are used to manoeuvre both vehicles towards each other. For IAC, this corresponds to the formation flight phase.
- **Soft Docking** starts with the initial contact between both vehicles. Misalignments are accommodated and minimized, while both systems are guided into close contact. The main goal of this phase is to achieve a temporary holding force, so that a more permanent connection can be secured.
- **Hard Docking/Locking** covers the establishment of a rigid connection between both vehicles, using a locking mechanism. Rigidity of the connection is typically maintained by means of a preloading force (e.g. springs) [122], [123].
- Finally, both vehicles are separated again during **Undocking/Release**. In space applications, this is typically facilitated by an impelling agent [122]; under atmospheric conditions, other forces (e.g. drag) can be exploited [124]. For the ACCD, release is handled by a separate system.

There are three key take-aways from this theoretical abstraction. First of all, initial misalignments (**KY-DCK.F-13/02**) need to be accommodated and reduced. Secondly, the duration of the soft-docking phase is directly related to the deployment of the locking mechanism. This has driven the actuator

speed requirements in chapter 5, since they need to be deployed before the end of the soft-docking phase (i.e. shock-absorbing stroke). Finally, a compressive force - which pushes both vehicles together after mating - is vital in ensuring a rigid docking interface.

6.2.2. Docking Systems

Looking then at practical implementations of docking systems, existing solutions can generally be divided into two main categories: *androgynous* [125] and *probe-drogue* systems [126], [127]. Examples of both mechanism types are shown in Figure 6.3. Although androgynous systems offer flexibility and universality, they also typically come with an added level of complexity [128], [129]. Additionally, most conventional androgynous docking systems require alignment in the roll-axis [130], conflicting with requirement **TN-DCK.F-13/03**. On the other hand, the distinct ‘male’ and ‘female’ parts of a probe-drogue system show significant resemblances to AAR applications, and boast improved simplicity and robustness [131], [132]. Hence, such a system is proposed for the current ACCD design - in line with Heide’s study [10], and subscale flight tests [45].

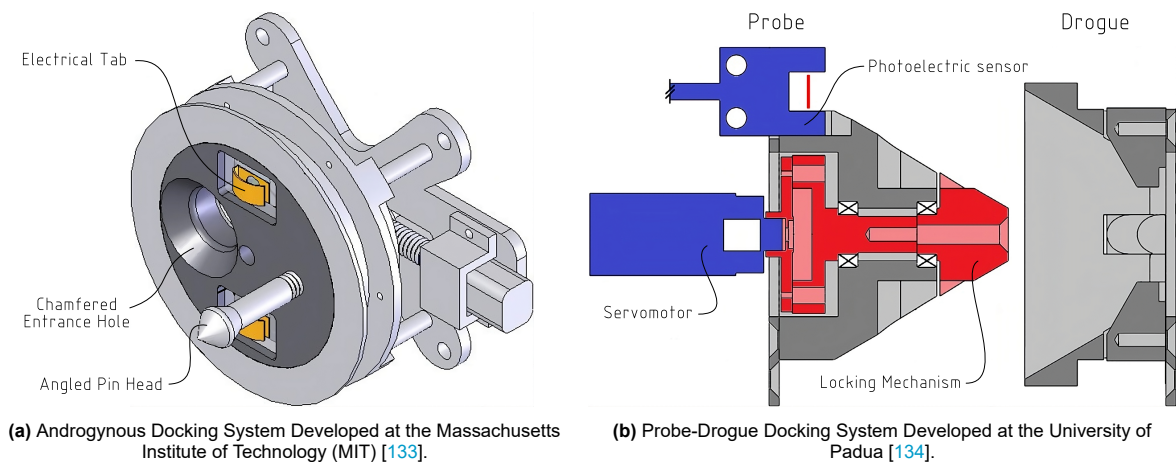


Figure 6.3: Comparison of Androgynous (left) and Probe-Drogue (right) Docking Systems.

Combining these state-of-the-art considerations with the systems engineering background provided in section 6.1, subsequent sections can now look into the design of the ACCD’s mechanical subsystems - starting with the tether attachment in section 6.3.

6.3. Tether Attachment

The tether attachment forms the interface between the tether and the ACCD, and has two major functions: transferring towing loads, while providing kinematic freedom (**KY-STR.NF-01/03**). As will be discussed in subsection 6.3.1, both functions are essentially polar opposites, between which a sensible trade-off needs to be performed. Subsection 6.3.2 then presents the resulting mechanical design, which is analysed in subsection 6.3.3.

6.3.1. Functional Trade-Off

Given its required rotational 3DoF, the tether attachment is essentially a ball joint, with a socket housed inside the ACCD structure. This configuration is favoured over an alternative system, where the joint socket is attached to the tether, because of manufacturability and assembly concerns. As visualized in Figure 6.4, the geometry of the ball joint can be characterized with three parameters: the joint’s internal and external radii R_i and R_o , as well as its opening angle θ_o .

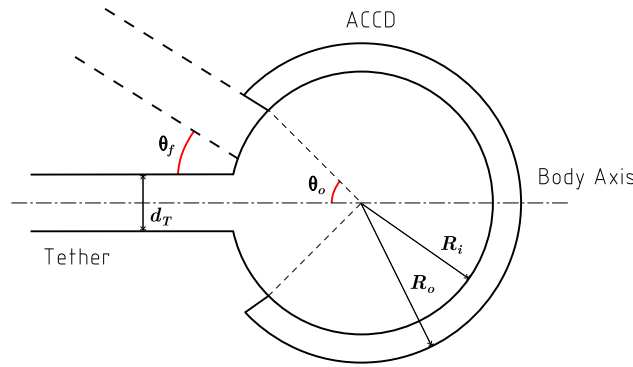


Figure 6.4: Schematic Representation of the Tether Attachment.

As can be seen in the above figure, the mechanical opening angle θ_o does not correspond directly to the joint's yaw and pitch freedom - characterized by the freedom angle θ_f . This is due to the non-zero thickness d_T of the tether, which slightly reduces the available rotational freedom inside the joint. Mathematically, Equation 6.1 can be used to determine the minimum opening angle θ_o required to achieve a desired freedom angle θ_f .

$$\theta_f = \theta_o - \arcsin\left(\frac{d_T}{2 \cdot R_i}\right) \tag{6.1}$$

Given the operational environment of the ACCD, a 25° freedom angle is required (**KY-STR.NF-01/03**). This value is based on typical angles between the tether and the ACCD's body axis, and is verified in chapter 7. For the tether diameter, the previously proposed value of $d_T = 24\text{ mm}$ is used [37]. Finally, the inner radius R_i offers design freedom, determining the total contact surface area and stresses inside the joint. A stress analysis of the corresponding design space is shown in Figure 6.5 - where the socket wall thickness is kept fixed at 5 mm (i.e. $R_o = R_i + 5\text{ mm}$).

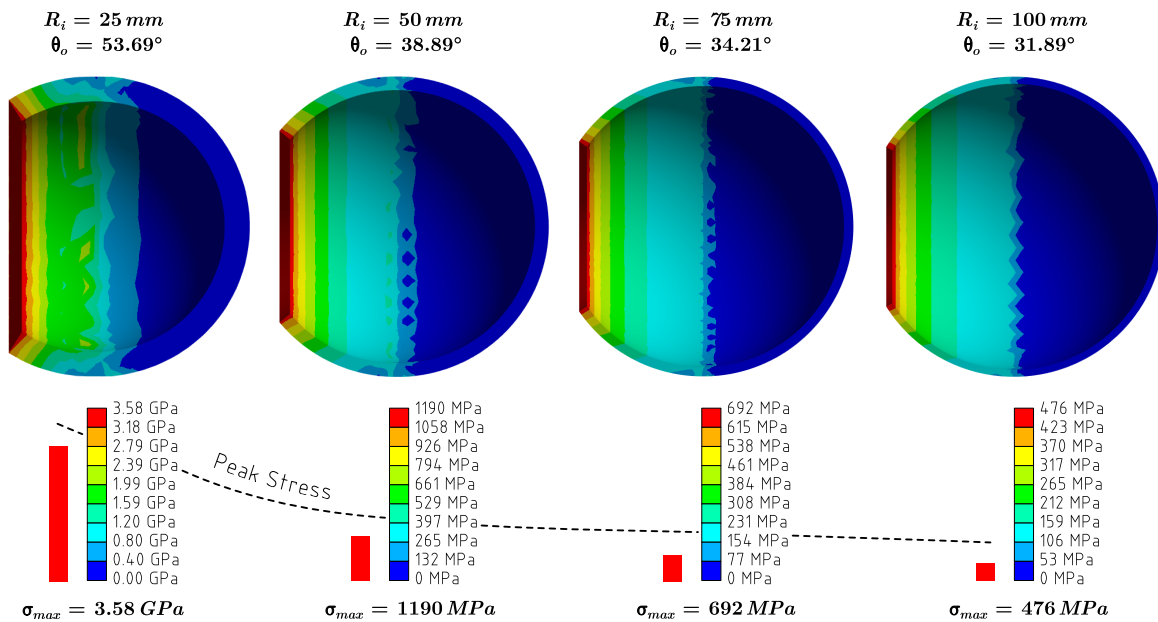


Figure 6.5: Comparative Analysis of Equivalent von-Mises Stress in Tether Attachments with Different Internal Radii R_i . A fixed support is applied to the socket's outer ring, while an axial load of 400 kN is exerted on the tether (not depicted).

As expected, the above comparison shows that increasing R_i reduces towing stresses - albeit with diminishing returns. On the other hand, enlarging the inner radius results in a mass increase - especially for the joint ball, which volume increases according to R_i^3 . Additionally, the size of the tether attachment is physically limited by the available volume inside the ACCD, so that values of $R_i > 250\text{ mm}$ are not feasible.

6.3.2. Design

Based on the foregoing exploratory analysis, an inner radius $R_i = 75\text{ mm}$ and opening angle $\theta_o = 35^\circ$ are proposed. The resulting design, shown in Figure 6.6, has a sufficient freedom angle $\theta_f = 27.2^\circ$ (**KY-STR.NF-01/03**). Compared to the schematic design shown in Figure 6.4, the majority of the joint's aft half is removed to reduce mass and volume. This part of the joint only experiences minimal forces, and is not loaded during towing (cf. Figure 6.5). A small portion of the aft-facing socket half is preserved, so that the joint ball cannot translate axially, and the joint's kinematic freedom is not hampered. Technical drawings of the relevant components are included in Appendix O.

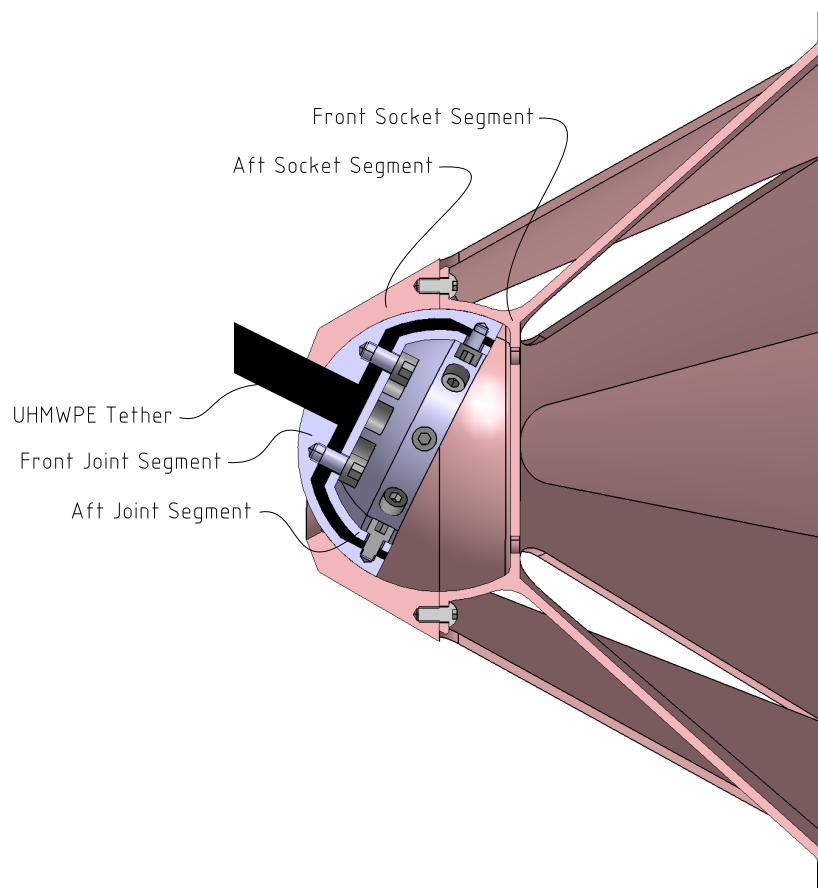


Figure 6.6: Cross-Section of the Tether Attachment Design, at a Peak Deflection of 27.2° .

To facilitate (dis)assembly, and allow manufacturing using standard casting and milling operations, the socket consists of two halves - made from Al2024-T6 aluminium. They are connected with 12 M8x16mm Class 12.9 metric bolts, and attach to the overall structural towing frame discussed in section 6.4 with 36 M8x22mm Class 12.9 metric bolts. Furthermore, 8 tapped M4 holes provide attachment points for the ACCD's aerodynamic nose cone, while 6 M8 clearance holes form the interface to the shock-absorbing assembly presented in section 6.5. The joint ball also consists of two Al2024-T6 parts, attached to the end of the UHMWPE tether using 8 M10x18mm Class 12.9 and 8 M8x12mm Class 12.9 metric bolts. Assuming a density of 2700 kg/m^3 for Al2024-T6 [135], the tether attachment's static frame has a mass of 5.331 kg - excluding fasteners. An in-depth mass breakdown of all subsystems is provided in Appendix C.

6.3.3. Analysis

To verify the suitability of the proposed design, a Finite Element Method (FEM) analysis is performed using the 300 kN axial towing load derived in chapter 3. For this - and all subsequent analyses - the *Static Structural* module in Ansys Mechanical Workbench is used. The design load is applied

to the tether, with rigid supports added at the structural interfaces with the main towing frame. The contact surface between the joint ball and socket is modelled using a static friction coefficient of 0.3 - corresponding to a lubricated aluminium-aluminium interface [105]. To limit the complexity of the analysis, bolt interfaces are modelled as perfectly bonded connections, while the tether and aft part of the joint ball are omitted - due to the non-uniform behaviour of the UHMWPE material [53]. As visible in Figure 6.7, the peak von-Mises stress equals 222 MPa, equivalent to a 1.55 SF - using a tensile yield strength of 345 MPa for the Al2024-T6 material [136]. The peak deformation is 0.551 mm, which is well below the required 1 mm (KY-STR.NF-02/06).

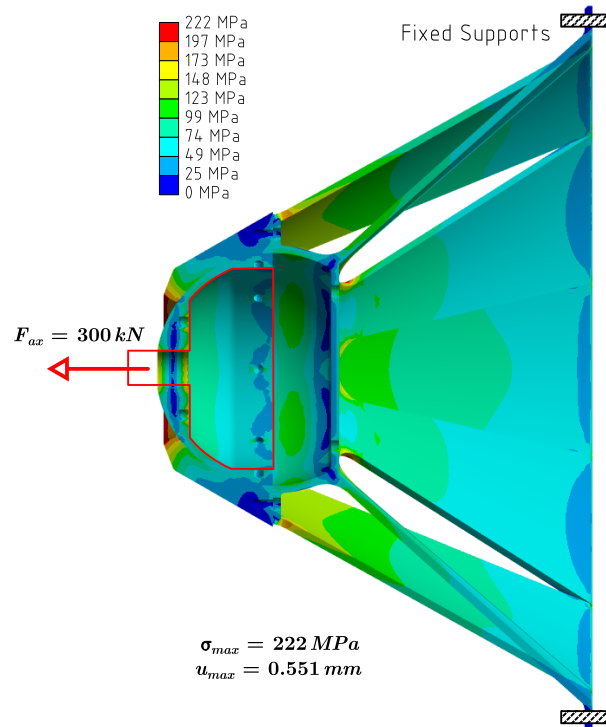


Figure 6.7: Equivalent von-Mises Stress in the Tether Attachment under an Extreme Towing Load. The tether and aft part of the joint ball are not depicted in this figure.

6.4. Structural Frame

As the ACCD's mechanical backbone, the structural frame provides rigidity to the entire vehicle, and bears the majority of applied loads. Broadly speaking, forces on the structural frame can be divided into two main categories: those induced by towing loads, and those related to aerodynamic effects. Correspondingly, the structural frame is split into two functional subassemblies: the load-bearing frame, and the wing structure. Their designs are presented in subsections 6.4.1 and 6.4.2 respectively, and analysed in 6.4.3.

6.4.1. Load-Bearing Frame

With the locking mechanism situated towards the ACCD's aft, and the tether attachment located at its nose (cf. Figure 6.1), a significant structural gap exists between both. It is bridged by the load-bearing frame, which acts as the primary load path for towing forces through the ACCD. In light of the ACCD's axisymmetry requirement (TN-STR.NF-01/02), this frame should have a cylindrical cross-section. The available design space is then characterized by an inner radius R_{in} and an outer radius R_{out} - with the frame's length being determined by the distance between the tether attachment and locking mechanism.

As a starting point for the design of the load-bearing frame, a simplified scenario is studied, combining an axial force F_{ax} , radial force F_{rad} , and bending moment M_b . Torsional moments are not

considered, as they are virtually eliminated by the roll-freedom of the tether attachment. The peak values of corresponding normal stresses σ_{ax} and σ_b , as well as shear stresses τ can be calculated with Equations 6.2 through 6.4 [137]. Here, Q and I_c are the cross-section's first and second moments of area respectively, while A and w_e represent its area and effective width.

$$\sigma_{ax} = \frac{F_{ax}}{A} = \frac{F_{ax}}{\pi \cdot (R_{out}^2 - R_{in}^2)} \quad (6.2)$$

$$|\sigma_b| = \frac{M_b \cdot R_{out}}{I_c} = \frac{4 \cdot M_b \cdot R_{out}}{\pi \cdot (R_{out}^4 - R_{in}^4)} \quad (6.3)$$

$$\tau = \frac{F_{rad} \cdot Q}{I_c \cdot w_e} = \frac{4 \cdot F_{rad} \cdot (R_{out}^2 + R_{out} \cdot R_{in} + R_{in}^2)}{3 \cdot \pi \cdot (R_{out}^4 - R_{in}^4)} \quad (6.4)$$

Using Equation 6.2, the 2D design space can first be reduced to a one-dimensional one, by combining the 300 kN axial design load (**CR-STR.NF-02/03**) with a 1.5 SF (**KY-STR.NF-02/05**). Additionally, a 345 MPa yield strength is assumed, reflecting the properties of Al2024-T6 [136]. Together, they dictate the minimally required cross-sectional area A of the frame, in turn linking the values of R_{in} and R_{out} . Using the internal radius as the independent parameter, the resulting design space then boils down to the following question:

Given a fixed mass and axial stress, what is the pareto-optimal cross-section of the load-bearing frame in order to minimize bending and shear stress. Should the structural mass be concentrated around the central axis ($R_{in} = 0$), or should it be spread out away from this axis ($R_{in} \rightarrow \infty$)?

To study this question, Figure 6.8 plots the bending and shear stress inside the frame as functions of its internal radius R_{in} . This uses $F_{rad} = 20 \text{ kN}$ and $M_b = 40 \text{ kNm}$, where the former is based on chapter 3's towing analysis, while the latter combines this radial force with a 2 m moment arm (i.e. the longest possible moment arm inside the ACCD). Given the geometry of the ACCD's aerodynamic shell, only values $R_{in} < 250 \text{ mm}$ are considered. The corresponding outer radius R_{out} is computed using the aforementioned minimal cross-sectional area.

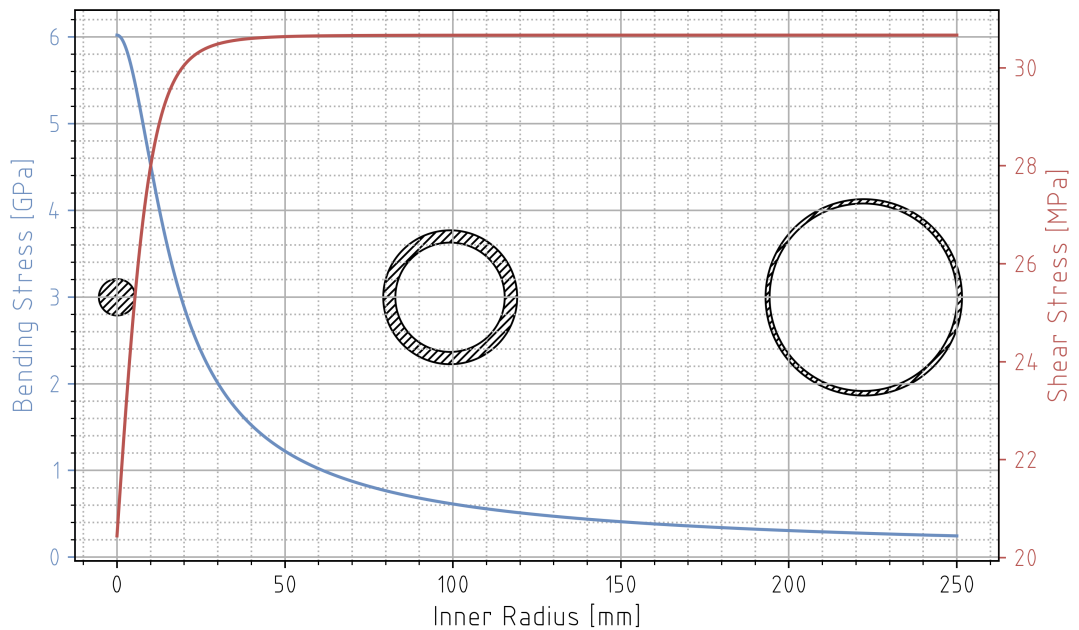


Figure 6.8: Maximum Bending and Shear Stress Inside the Load-Bearing Frame as a Function of its Inner Radius. Note the different axis scale for both stresses.

This figure clearly shows the mirrored effect of R_{in} on both stresses, with a solid beam ($R_{in} = 0$) experiencing low shear stress, but increased bending stress. However, it also reveals that peak shear stresses always remain significantly smaller than bending stresses. In fact, in order for both stresses

to reach similar orders of magnitude, the bending moment would have to drop to 200 Nm - which corresponds to a moment arm of 0.01 m. Hence, shear stresses in the load-bearing frame are neglected, and a large value for R_{in} is proposed to increase the frame's bending strength. Such a cylindrical structure also doubles as an attachment point for the ACCD's aerodynamic shell, which can be mounted directly onto this frame when $R_{in} \approx 250$ mm.

However, a perfectly axisymmetric cylinder would entail practical difficulties, by sealing off the ACCD's interior. Additionally, given a minimal cross-sectional area of 1304 mm², a design with $R_{in} = 250$ mm would equate to a wall thickness of 0.83 mm - which is undesirable in terms of manufacturability and strength against localized loads [135]. Instead, the proposed design - shown in Figure 6.9 - uses an assembly of parallel bars spread around the ACCD's outer rim, and interconnected with hoops. The bars provide the axial load-bearing capacity of the frame, while the hoops add bending stiffness and offer attachment points for the aerodynamic shell.

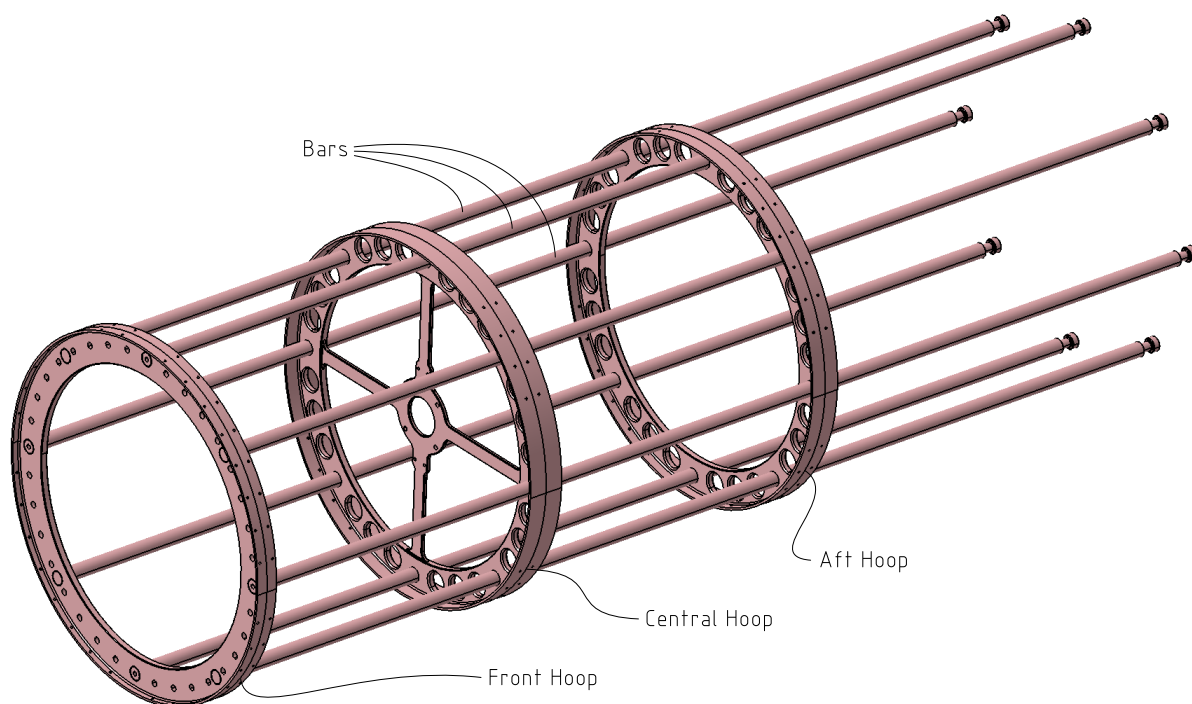


Figure 6.9: 3D View of the Load-Bearing Frame Design, Using Twelve Bars and Three Hoops. The left side of the image corresponds with the ACCD's nose.

Appendix O includes technical drawings for the bar and hoop designs, which are welded together to increase the strength of the assembly. At the frame's front-facing side, it is connected to the tether attachment using the M8 bolts discussed in section 6.3. At its aft, the docking mechanism presented in section 6.6 attaches by means of welded and bolted interfaces. Additionally, the central hoop provides mounting points for the plunger sensors described in chapter 5, while also supporting the shock-absorbing assembly presented in section 6.5. Finally, each hoop includes between 32 and 64 tapped M4 holes, serving as mounting points for the cylindrical shell of the ACCD. A detailed BoM is included in Appendix C, yielding a total subassembly mass of 15.696 kg.

6.4.2. Wing Structure

The other main subassembly of the ACCD's core frame is its wing structure. Although the design of these wings is not central to the current study, a representative outline of their internal structure is needed to get an initial estimate of their mass. Because of its simplicity and proven design heritage, a rib-spar assembly is used, illustrated in Figure 6.10 [138].

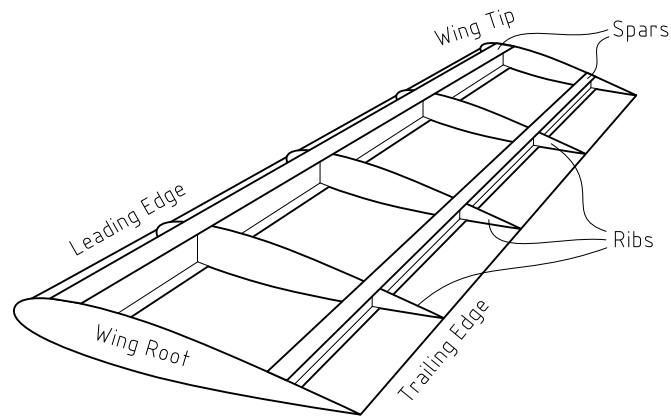


Figure 6.10: Schematic Depiction of a Wing Structure Using a Combination of Ribs and Spars.

Based on such a design methodology, the wing structure shown in Figure 6.11 is proposed, using a welded assembly of three ribs and two spars. The ribs' flanges act as attachment points for the wings' aerodynamic shell, while also increasing bending strength. Given the significant moment arm of the spars relative to the ACCD's core, I-profiles are used [138]. These have a constant cross-section, in order to improve the spars' simplicity and manufacturability. Because of the wing's significant taper, a trade-off had to be made between maximizing the spars' height, and minimizing the length of unsupported rib segments. Additionally, the double-spar design provides improved support for the ribs, while also increasing the assembly's torsional stiffness, and adding structural redundancy [139]. Spars and ribs are constructed out of Al2024-T6, while a less performant Al6061-T3 alloy is proposed for the wing skin. This skin is split into four segments, connected to each other and to the wing frame with 88 4mm x 10mm button head rivets. Technical drawings and a BoM can be found in Appendices O and C respectively - yielding a structural mass of 14.453 kg per wing (excluding the control surface).

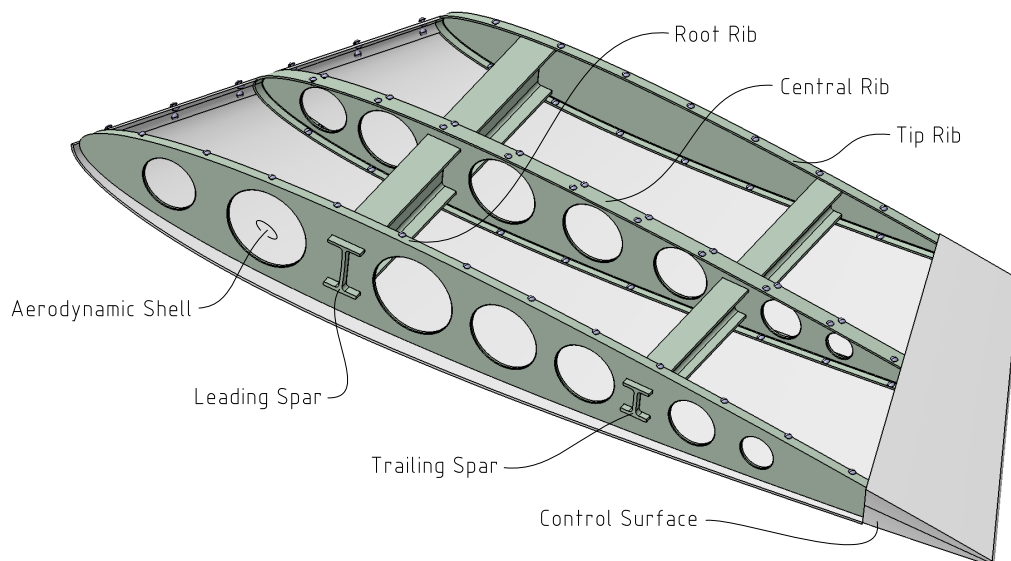


Figure 6.11: 3D View of the Wing Structure Design. The apparent divergence of the spars is an optical illusion caused by the isometric perspective, while the control surface is implemented as a volumetric black box.

6.4.3. Analysis

To verify the required towing strength of the load-bearing frame, an FEM analysis is performed using the 300 kN axial design load (**CR-STR.NF-02/03**) - which is applied to the front hoop. Welds between the hoops and bars are modelled as perfectly bonded interfaces, with a rigid support added at the position of the locking mechanism. As can be seen in Figure 6.12, resulting von-Mises stresses remain below 228 MPa, yielding a sufficient 1.51 SF (**KY-STR.NF-02/05**). Furthermore, the peak deformation

of 1.904 mm is significantly below the required 5 mm limit for kinematically non-critical components (**KY-STR.NF-02/06**) - especially given that deformations are almost exclusively in the axial direction.

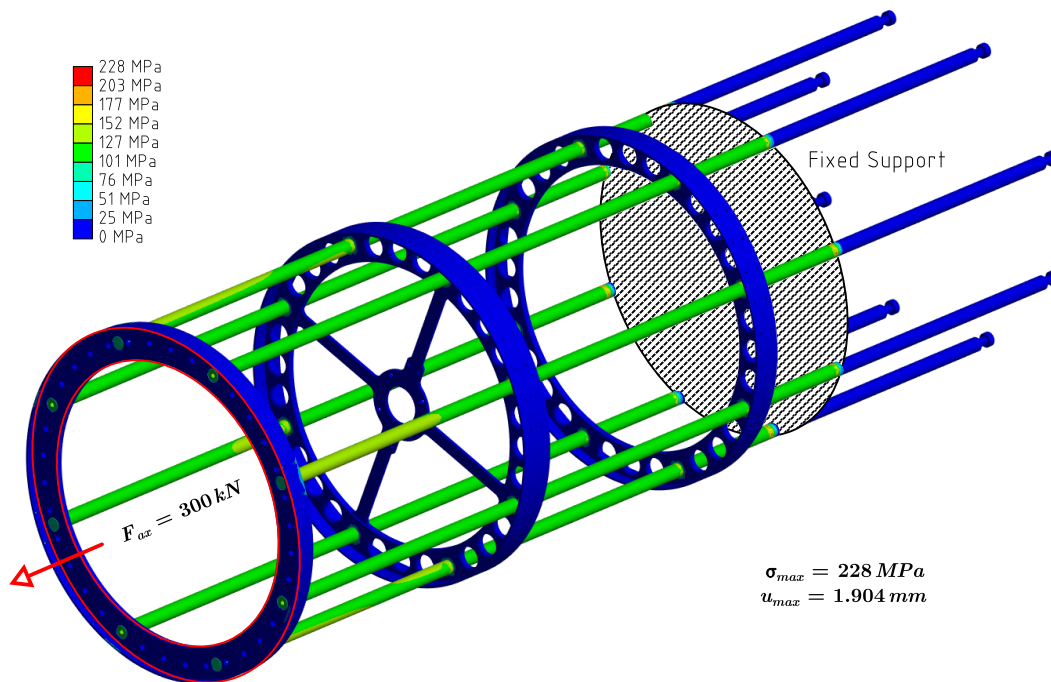


Figure 6.12: Equivalent von-Mises Stress in the Load-Bearing Frame under an Extreme Towing Load.

Before moving on to the analysis of the wing structure, an aerodynamic design load needs to be obtained (**KY-STR.NF-02/04**). To reduce complexity, and because detailed CFD data for a single wing are not available, a simplified estimate is used. Instead of a locally varying pressure distribution, a uniformly distributed load is applied to the entire wing surface. The value of this load is based on a 90° AoA in a 200 m/s airflow, at an altitude of 100 m. This is a significant overestimation of the wing's extreme aerodynamic conditions, in order to compensate for the aforementioned simplifying assumptions. Combining the corresponding dynamic pressure with the projected wing surface of 0.5835 m², the resulting force equals 14.12 kN. Rounding this up, an aerodynamic design load $F_{ae} = 15 \text{ kN}$ is obtained.

Applying this load to the upper surface of the wing, and rigidly supporting the spars' roots, a FEM analysis is performed - shown in Figure 6.13. All interfaces between components are modelled as bonded connections, while the control surface is omitted from the analysis. Inside the Al2024-T6 structure, von-Mises stresses remain below 219 MPa - equivalent to a 1.57 SF. Stresses in the Al6061-T3 wing skin do not exceed 93 MPa, which is also sufficiently safe compared to the 280 MPa yield limit (**KY-STR.NF-02/05**) [136]. Additionally, the maximum deformation is 3.810 mm, which is safely below the required 5 mm (**KY-STR.NF-02/06**). Since the control surface is excluded from this analysis, a more detailed study is required to determine whether these deformations create potential issues for kinematically critical mechanisms inside the control surface.

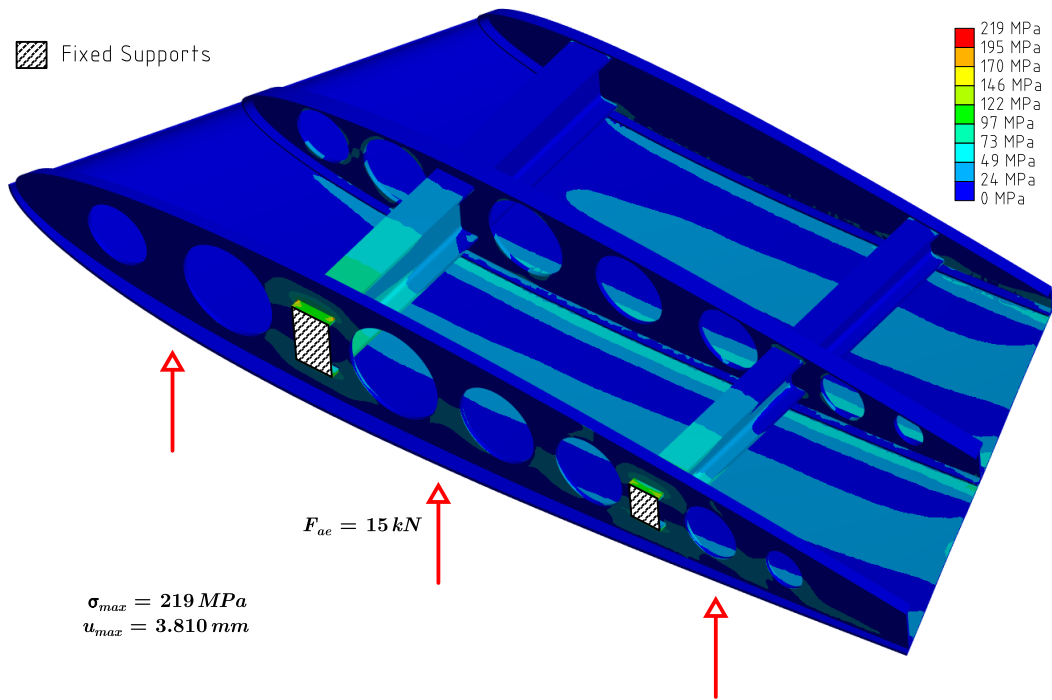


Figure 6.13: Equivalent von-Mises Stress in the Wing Structure under an Extreme Aerodynamic Load. The upper part of the wing's aerodynamic shell is hidden for display purposes.

6.5. Shock-Absorbing Assembly

The main purpose of the shock-absorbing assembly is to ensure the inelasticity of the docking impact (**CR-DCK.F-13/06**), by absorbing the kinetic energy difference ΔK between the RLV and ACCD. As shown in Equation 6.5, ΔK can be written as a function of the ACCD's and RLV's masses m and m_{RLV} , as well as velocities V and V_{RLV} (*before* docking). V^* is the velocity of the combined ACCD-RLV system *after* docking. Given the significantly higher inertia of the RLV, and using an RLV-fixed reference frame, this can further be reduced to a function of the ACCD mass and its velocity relative to the RLV [10].

$$\begin{aligned} \Delta K &= \frac{1}{2} \cdot m \cdot V^2 + \frac{1}{2} \cdot m_{RLV} \cdot V_{RLV}^2 - \frac{1}{2} \cdot (m + m_{RLV}) \cdot (V^*)^2 \\ &\approx \frac{1}{2} \cdot m \cdot (V - V_{RLV})^2 \end{aligned} \quad (6.5)$$

Given the ACCD's typical inertial and operational conditions (**KY-DCK.F-13/01**), the impact energy can be as high as 3125 J. To safely accommodate this, an industrial shock-absorber is needed, which is presented in subsection 6.5.1. Subsection 6.5.2 then discusses the mechanical integration of this system into the ACCD, which is in turn analysed in subsection 6.5.3.

6.5.1. Industrial Shock Absorber

In a previous SART study [10], an extensive comparison between energy-absorbing media was performed. Ultimately, the use of an industrial shock-absorber was recommended, because of its low reaction forces and deceleration times - which is further illustrated in Appendix M. More specifically, a COTS solution was proposed, developed by ACE Stoßdämpfer GmbH. Based on the peak docking velocity of 5 m/s (**KY-DCK.F-13/01**), and an expected maximum ACCD mass of 250 kg [38], ACE's in-house analysis tool recommends two potential solutions, listed in Table 6.1. The main mechanical difference between both is their stroke, with a 150 mm stroke having a larger energy absorption capacity, while being slightly heavier.

Property	MC64100	MC64150
Stroke [mm]	100	150
Mass [kg]	3.7	5.1
Energy Absorption Capacity [J]	3730	5650
Compressed Length [mm]	226	300
Diameter [mm]	64	64
Peak Impact Load [kN]	47	31

Table 6.1: Characteristics of the MC64100 and MC64150 Industrial Shock Absorbers [140]. The peak impact loads shown in this table correspond to the deceleration of an object with a mass of 250 kg, at a relative velocity of 5 m/s.

Because the MC64150's relative mass increase is minor (1.4 kg) compared to the overall ACCD mass, while the associated energy absorption capacity increases more significantly (+38%), the 150 mm stroke solution is proposed for this application. It offers more margin to account for uncertainty concerning the impact energy, while also being easily downgradable to the MC64100 system. Additionally, the longer stroke results in a lower impact force on the shock-absorbing assembly. However, to allow for a potential migration to the MC64100 solution, the more stringent 47 kN reaction force is used as a reference, and an impact design load of $F_{imp} = 50 \text{ kN}$ is defined (**CR-STR.NF-02/02**). With the MC64150 shock absorber, this load corresponds to an upper ACCD mass limit of 400 kg. Finally, the total duration of the positive (energy-absorbing) and negative strokes for these systems is 1 s [140], prompting the locking actuator deployment requirement of 0.5 s discussed in chapter 5.

6.5.2. Design

In order to integrate the selected MC64150 shock absorber into the ACCD, an overarching shock-absorbing assembly is needed. The main corresponding design freedom concerns the absorber's axial position inside the ACCD, which should be chosen with consideration for the vehicle's target CoG position (cf. chapter 3). Other subassemblies, such as the docking system, do not have the same amount of axial design freedom, and add significant mass to the ACCD's aft. To counteract their effect, the MC64150 is positioned as forwards as possible, using an Al2024-T6 absorber housing attached directly to the tether attachment with 6 M8x18mm Class 12.9 metric bolts - as shown in Figure 6.14. The M61450 then interfaces with this housing using its M64 metric thread, and is further secured with ACE's NM64 locking ring [140].

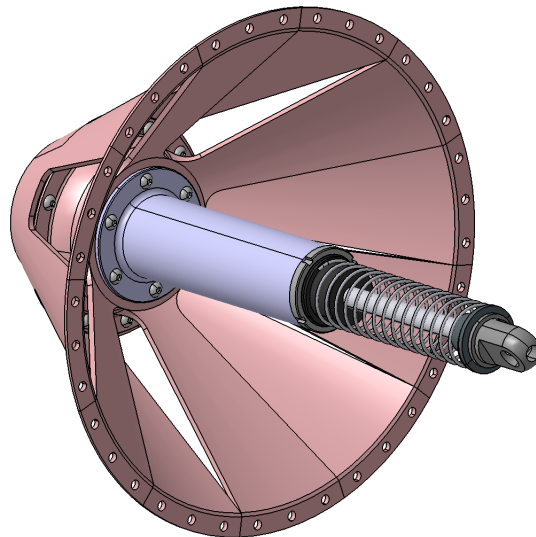


Figure 6.14: 3D View of the Shock Absorber Housing Design, and Interface with the Tether Attachment.

Because of the forwards position of this assembly, a structural gap exists between the shock absorber and the locking mechanism. This gap is bridged with an Al2024-T6 plunger, shown in Figure 6.15. The plunger's front end is attached to the absorber's C64 front clevis mount [140], using a cylindrical Al2024-T6 connector piece and two M16 Class 12 hexagonal metric nuts. Its aft end is equipped with a

diverging conical cup, designed to receive the tip of the RLV boom. Furthermore, two tapped M4 holes serve as the mounting points for the sensor triggers described in subsection 5.3.6 - which are made of Al6061-T3 given their non-structural nature.

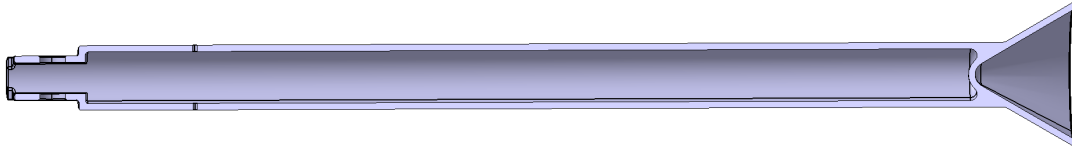


Figure 6.15: Cross-Section of the Shock-Absorbing Plunger Design.

Because of the plunger's slender design, and the significant compressive impact force (**CR-STR.NF-02/02**), buckling is considered its driving failure mode. For this, Euler's critical load is used as a preliminary design metric, shown in Equation 6.6 [137]. Here, E is the material's (constant) modulus of elasticity, while l is the unsupported beam length - which is not necessarily the same as the physical plunger length. With a cylindrical plunger design, the second moment of area I_c is given by Equation 6.7 [141], where R_p is the plunger's outer radius, while w_p is its thickness. Finally, a value of 2 is proposed for the effective length factor ξ , to conservatively model the plunger as a rigidly clamped beam. Although the shock-absorbing assembly could also be simplified with different boundary conditions, the proposed technique yields the most conservative Euler loads.

$$F_b = \frac{\pi^2 \cdot E \cdot I_c}{(\xi \cdot l)^2} \quad (6.6)$$

$$I_c = \pi/4 \cdot (R_p^4 - (R_p - w_p)^4) \quad (6.7)$$

Extending the structural 1.5 SF (**KY-STR.NF-02/05**) to this buckling case, and using the 50 kN impact design load (**CR-STR.NF-02/02**), the above equations can be used to determine the plunger's minimal cross-section for a given unsupported beam length. This is illustrated in Figure 6.16, which shows the plunger's resulting outer diameter and mass - calculated using the physical beam length of 750 mm shown in Figure 6.15. Solid and hollow geometries are compared, with the former characterized by $w_p = R_p$, and the latter having a fixed thickness $w_p = 5 \text{ mm}$. A 2700 kg/m^3 density and 72.4 GPa modulus of elasticity are assumed for the Al2024-T6 alloy [135].

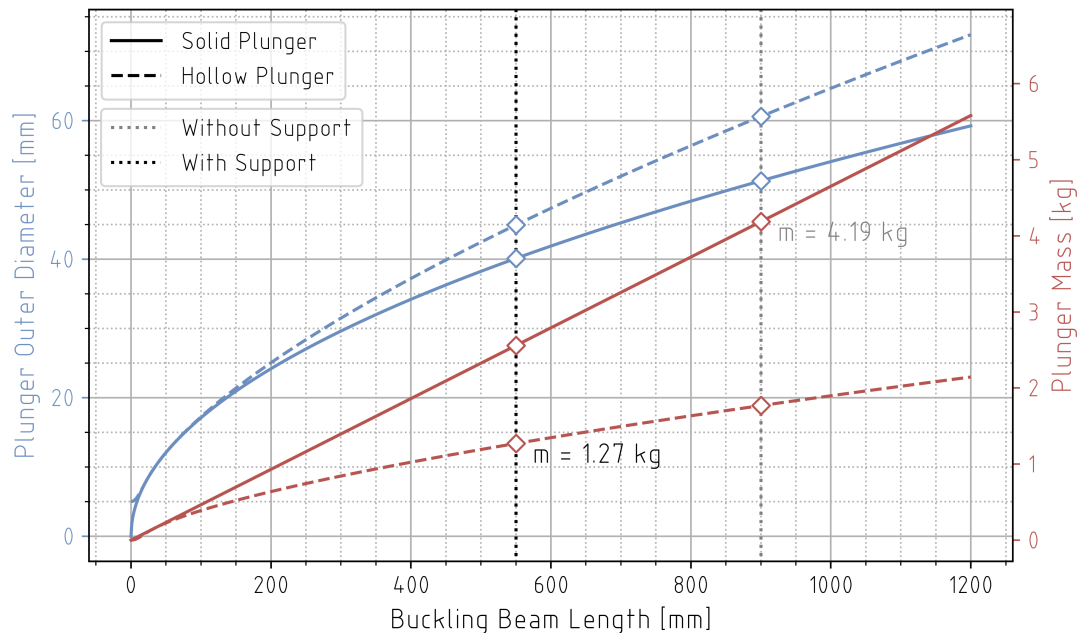


Figure 6.16: Minimal Diameter and Mass for Solid and Hollow Shock-Absorbing Plungers, with and without Added Support.

Additionally, the baseline, unsupported plunger design is compared to an alternative assembly, where an additional support is included - attached to the structural towing frame. This also supports the weight of the plunger itself, reducing bending stresses at its connection to the shock absorber. An unsupported plunger corresponds to $l \approx 900 \text{ mm}$ (i.e. 750 mm plunger + 150 mm shock absorber stroke), while the additional support reduces this length to around 550 mm. Comparing a *solid, unsupported* plunger with a *hollow, supported* design, a total mass decrease of 70% is achieved - as illustrated in the figure above. To add margin for the simplified buckling analysis, the final plunger design shown in Figure 6.15 has an increased outer diameter of 50 mm - compared to the calculated diameter of 45 mm.

The resulting design of the shock-absorbing assembly is shown in Figure 6.17, which includes the tether attachment, load-bearing frame, and plunger sensors. A linear bearing is proposed for the plunger support structure, to accommodate the axial translation of the plunger during its energy-absorbing stroke. As a representative component, the LBBR 50-2LS/HV6 is used [142], mounted inside the central hoop of the load-bearing structure. It includes two lip seals to ensure optimal functioning of its kinematics - with further details provided in Appendix M. The addition of a secondary support at the aft hoop is not possible, as it would hinder the assembly's kinematics. Technical drawings for the relevant components are included in Appendix O, while the mass breakdown analysis presented in Appendix C yields a structural subassembly mass of 8.463 kg.

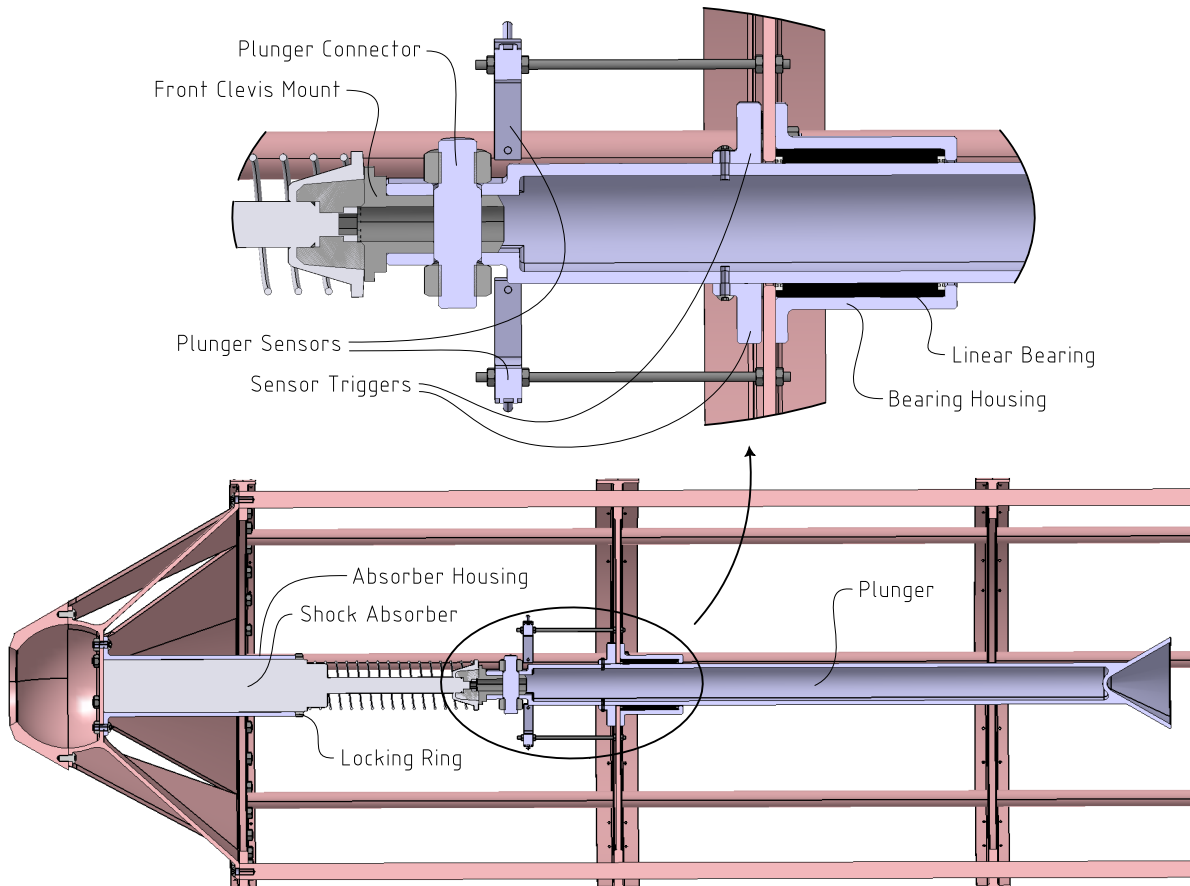


Figure 6.17: Cross-Section of the Shock-Absorbing Assembly Design and its Constituent Components. Note how the axial position of the plunger sensors can be adjusted using the threaded M4 mounting bars.

6.5.3. Analysis

The two main components analysed in terms of impact loads, are the plunger and absorber housing. Looking at the latter first, an FEM analysis is shown in Figure 6.18, using a similar setup as in subsection 6.3.3. The absorber housing is now included as well, bonded to the aft surface of the tether attachment, while the 50 kN design load (**CR-STR.NF-02/02**) is applied to its inner surface. The resulting peak von-Mises stress is 207 MPa, equivalent to a 1.67 SF. Deformations stay well below the

allowable limit of 1 mm (KY-STR.NF-02/06), with local extrema only reaching 0.490 mm.

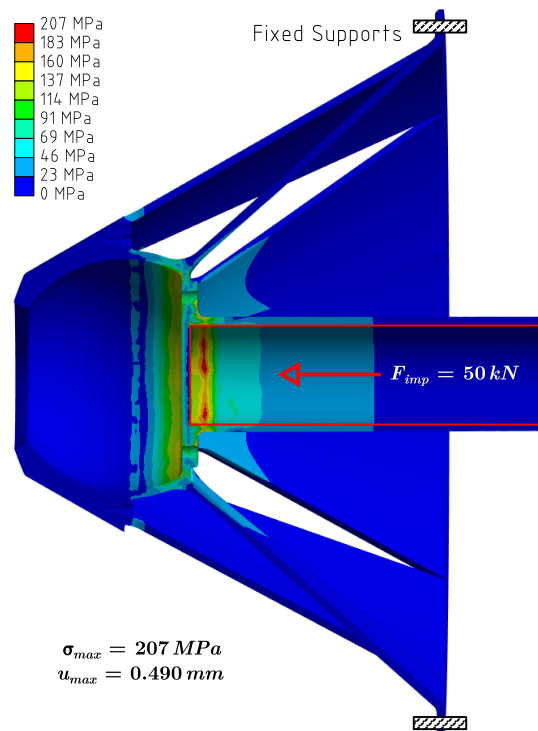


Figure 6.18: Equivalent von-Mises Stress in the Shock Absorber Housing under an Extreme Impact Load.

A similar FEM analysis for the plunger is visualized in Figure 6.19, with a fixed support added at the MC61450 connection. Since this analysis does not include buckling, the additional bearing support is not modelled. The 50 kN design load is applied to the inner surface of the plunger's receiving cone, which interfaces with the RLV boom. Resulting peak stresses of 221 MPa translate to a 1.56 SF, while the extreme deformation of 0.681 mm stays under the limit of 1 mm. For future studies, it is recommended to also analyse off-centred impact loads on this component, as well as more complex buckling and stability modes.

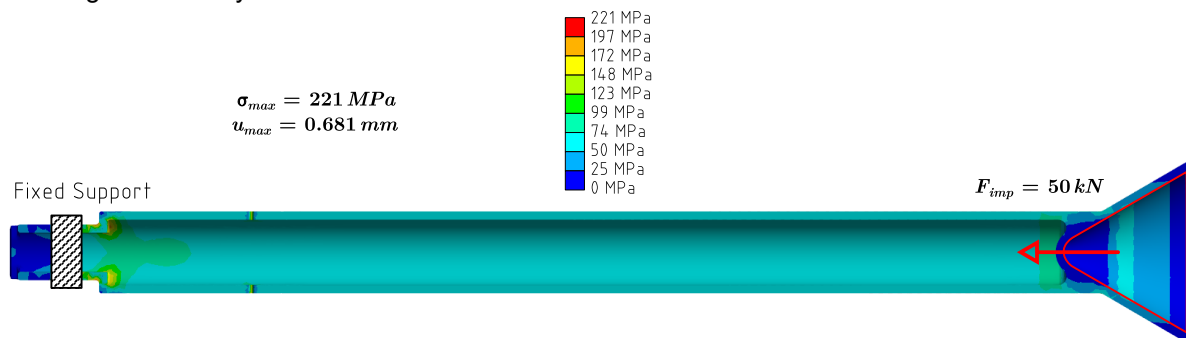


Figure 6.19: Equivalent von-Mises Stress in the Shock Absorber Plunger under an Extreme Impact Load.

6.6. Docking Mechanism

The ACCD's final, and core subassembly is its docking mechanism, which acts as the physical interface to the RLV (CR-SYS.F-13). As argued in section 6.2, a probe-drogue system is the most suitable solution for this task, using a boom attached to the RLV's nose [24]. Although the design of this boom has not been defined in previous studies, it has major implications for the structure of the docking mechanism. Hence, subsection 6.6.1 first analyses the RLV boom, proposing in an initial design concept. Subsection 6.6.2 then presents a mechanism used to lock the boom in place inside the ACCD. Finally,

a guiding cone is designed in subsection 6.6.3, covering the initial soft-docking phase of the mating procedure.

6.6.1. RLV Boom

For initial dimensioning of the boom’s geometry, the axial towing design load of 300 kN is used (**CR-STR.NF-02/03**). Using the same high-strength Al2024-T6 alloy as for the majority of the ACCD, a minimal boom diameter of 40.75 mm is required to provide a 1.5 SF (**KY-STR.NF-02/05**). Including a 23% margin to accommodate localized stress concentrations, a nominal diameter of 50 mm is proposed. Aspects such as the boom’s structural attachment to the RLV, deployability, or total length, are not studied, as they have less implications for the ACCD itself. On the contrary, the design of the boom’s tip is crucial, as it interfaces with the ACCD’s locking mechanism.

Figure 6.20 shows three possible designs for the RLV boom, with corresponding locking functionalities. The first solution purely relies on friction, by clamping the locking mechanism tightly around the boom. However, given the significant axial towing forces, this would require exuberantly high clamping forces, generating infeasible SWaP requirements for the locking actuators. The other two solutions create kinematic constraints on the boom, preventing it from being pulled out of the locking mechanism. This can either be achieved with an additive design (*Option 2a*), or a subtractive one (*Option 2b*).

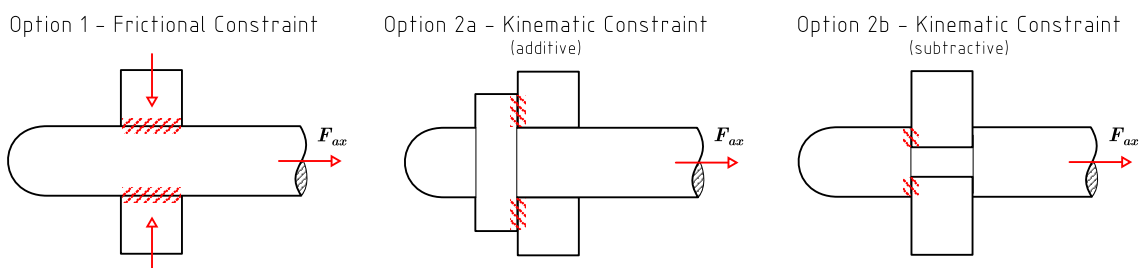


Figure 6.20: Schematic Comparison of Different Boom-Locking Solutions. The highlighted areas indicate the main interfaces where locking forces (either frictional or normal) arise.

While Heide used a subtractive design in her 2005 study [10], a corresponding stress analysis was not performed. Hence, a comparison between *Options 2a* and *2b* is provided in Figure 6.21, visualizing the resulting towing stresses. Although the peak stress is marginally lower (-0.75%) for the subtractive design, maintaining a minimal diameter of 50 mm also requires a significant mass increase (+54%) compared to the additive design. Hence, the latter is proposed as a more suitable solution, only increasing the boom’s diameter in critical areas (i.e. at the locking interface).

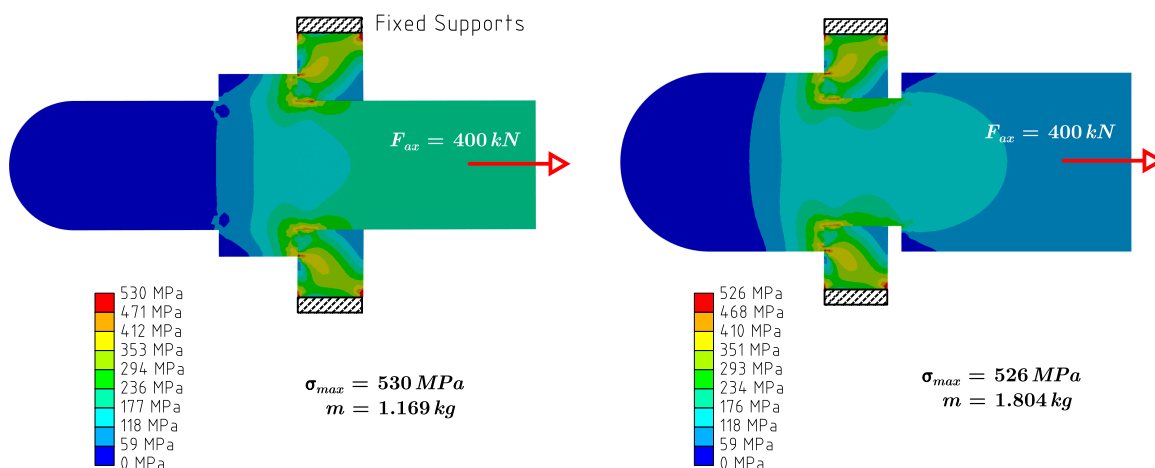


Figure 6.21: Comparative Analysis of Equivalent von-Mises Stress in RLV Booms with an Additive and Subtractive Design. The listed masses only concern the visualized portion of the boom. Contacts between the boom and locking mechanism are modelled as rough surfaces.

The above figure indicates very high localized stresses for both designs, related to their sharp and perpendicular boom geometry. To mitigate this issue, a modified, angled version of the additive design is proposed, shown in Figure 6.22. The conical tip of this design is beneficial during the soft-docking phase, as it reduces initial misalignments between both vehicles, in conjunction with the guiding cone described in subsection 6.6.3 [133]. The aft-facing tapered surface reduces localized stresses, while also providing a larger surface area for the locking mechanism to interface with. Further stress reduction is achieved by adding fillets to internal and external corners. For a preliminary boom length of 740 mm, the boom mass totals 5.31 kg - not yet including the attachment to the RLV itself. A technical drawing is included in Appendix O.

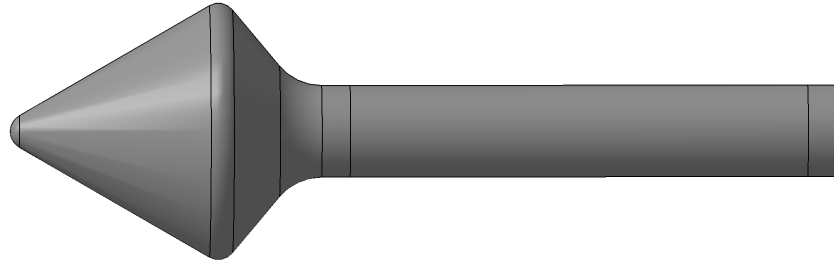


Figure 6.22: Side View of the Angled Boom Design.

Finally, an FEM analysis of the proposed boom design is shown in Figure 6.23, using the 300 kN axial towing design load (**CR-STR.NF-02/03**). With a peak von-Mises stress of 189 MPa, the design has an ample 1.83 SF. Although this analysis uses a lower load (-25%) than those in Figure 6.21, a comparison between both shows that the reduction in peak stresses is a lot more significant (-64%). This demonstrates the effectiveness of the angled boom design, and the mitigation of stress concentrations. Furthermore, deformations are almost exclusively in the axial direction, not interfering with any of the ACCD's mechanisms. Hence, the peak value of 1.825 mm is deemed acceptable (**KY-STR.NF-02/06**).

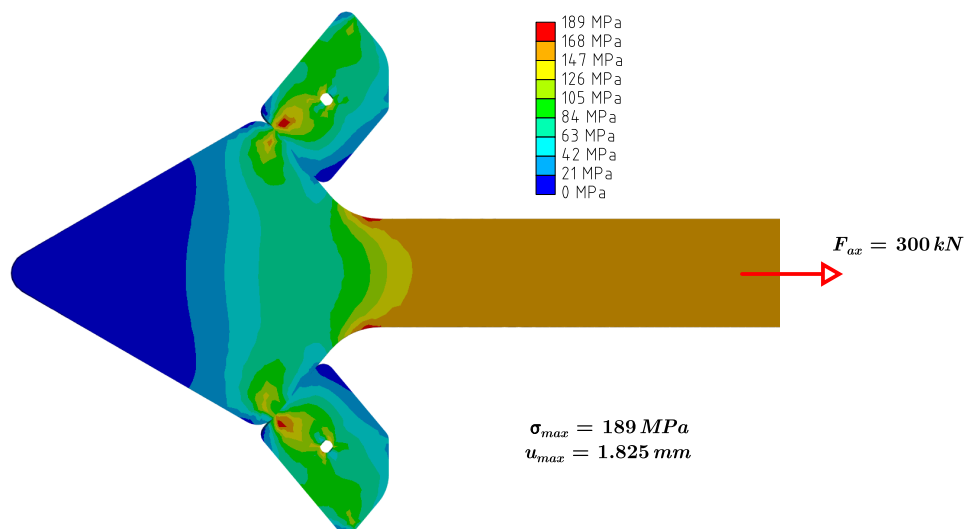


Figure 6.23: Equivalent von-Mises Stress in the RLV Boom under an Extreme Towing Load. Fixed supports and interfaces are the same as in Figure 6.26, while the peak stress and deformation do not include the depicted locking wedges.

6.6.2. Locking Mechanism

With a tentative boom geometry obtained, the ACCD's locking mechanism is designed to actuate the kinematic constraints that fix said boom in place. As argued in chapter 5, the mechanism's design should unload the locking actuators during towing, while respecting the ACCD volume limitations. Furthermore, the actuator's stroke should be minimized to reduce the required deployment time, and enable locking before the soft-docking phase is over. Finally, the overall complexity of the mechanism should be kept as low as possible, to increase the system's robustness, and mitigate the risk of jam-

ming (DCK-06) [66].

Based on the above requirements and constraints, the proposed design solution uses a structural ring and four locking wedges, enabling a locking functionality as illustrated in Figure 6.24. The locking wedges transfer towing loads to the structural ring, which in turn connects to the ACCD's load-bearing frame. Each wedge interfaces with the aft conical surface of the RLV boom, and is deployed into its engaged position using the linear actuators selected in chapter 5 - preventing the boom from exiting the ACCD. Furthermore, a compressive force is exerted on the tip of the RLV boom, due to the spring element inside the MC61450 shock absorber - clamping the entire assembly together. In practice, this is achieved by designing the shock-absorber assembly to be partially compressed when the boom is in a mated position. This is further illustrated in Appendix N, where an overview of the entire docking sequence is provided.

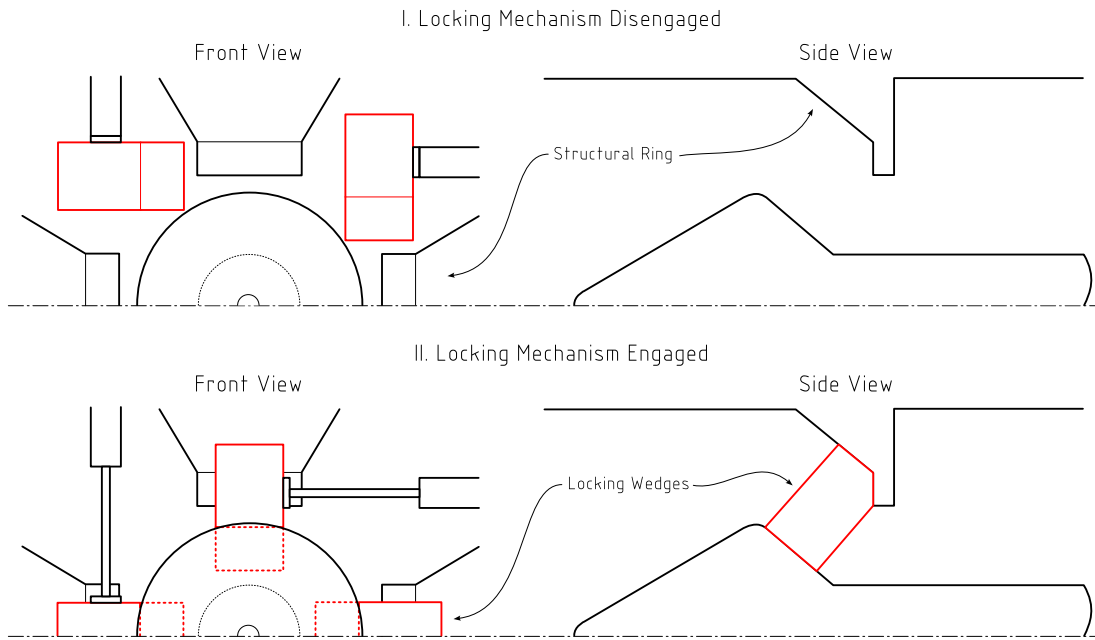


Figure 6.24: Schematic Depiction of the Locking Mechanism Design and Deployment.

Based on the above schematic sketch, a 3D design of the locking mechanism is shown in Figure 6.25 - which depicts the actuators in a deployed state. The locking ring contains 16 M1.6 clearance holes, serving as attachment points for the linear actuators. Each actuator is then connected to a locking wedge, by means of a flange and 6 M2x4mm Class 8.8 metric bolts. Additionally, the boom sensors discussed in chapter 5 are attached to the locking ring with Baumer's 300mm mounting plate series [143], and set of M3x16mm and M4x6mm metric bolts (per sensor). The locking ring itself is welded to the bars of the load-bearing frame, which run through eight holes around its outer perimeter. Appendix O provides technical drawings of all relevant components, while a total mass of 9.827 kg is obtained based on the BoM included in Appendix C - with the locking ring and wedges again made from Al2024-T6.

To verify the proposed design, a FEM analysis is performed using the axial design load of 300 kN (CR-STR.NF-02/03). As shown in Figure 6.26, von-Misses stresses in the entire assembly remain below 223 MPa, yielding a 1.55 SF (KY-STR.NF-02/05). Because of the kinematic criticality of the mechanism, deformations should be kept below 1 mm (KY-STR.NF-02/06) - which is the case given the maximum deformation of 0.611 mm.

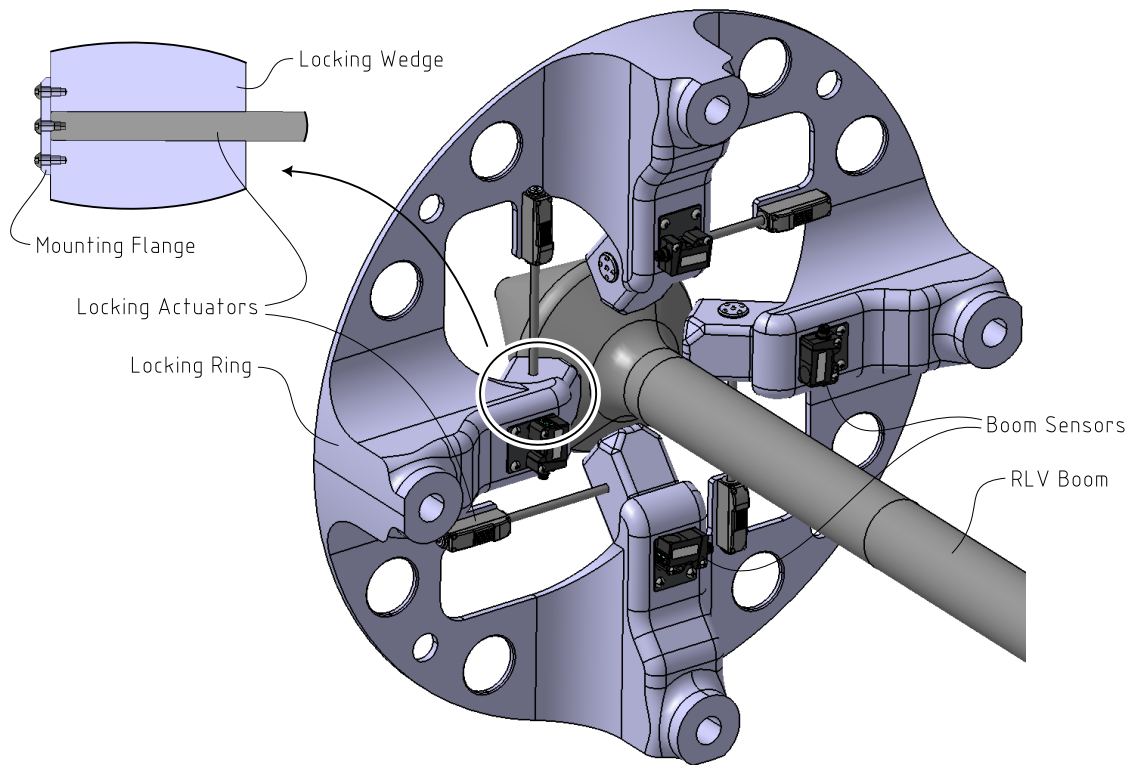


Figure 6.25: 3D View of the Locking Mechanism Design with Extended Actuators.

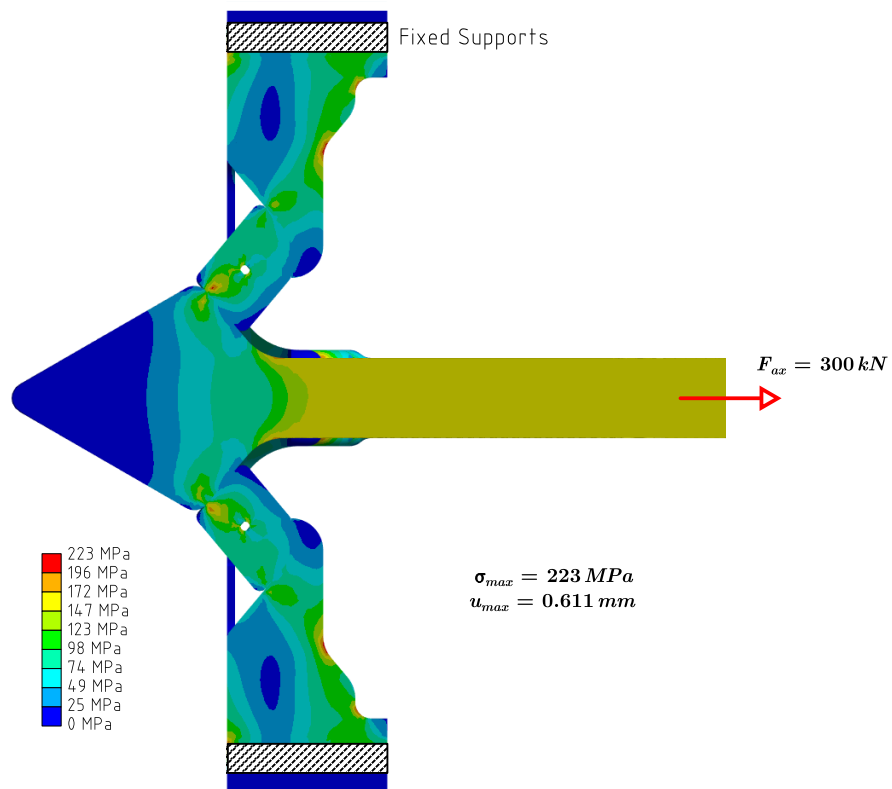


Figure 6.26: Equivalent von-Mises Stress in the Locking Mechanism under an Extreme Towing Load. The peak stress and deformation do not include the depicted RLV boom.

6.6.3. Guiding Cone

Finally, the guiding cone occupies the diverging aft section of the ACCD, and covers soft-docking with the RLV. By accommodating misalignments between both vehicles (**KY-DCK.F-13/02**), the likelihood of a successful capture is increased [133]. Following Heide's design [10], springs are used to absorb part of the initial impact energy, and accommodate associated shocks (**CR-STR.NF-02/01**). As a result, the proposed design consists of two major elements: a fixed base frame, attached to the rest of the ACCD's structure, and a guiding shell, connected to the base frame with springs. This allows the guiding shell to compress relative to the base frame, yielding the desired energy-absorbing and shock-damping properties. In order to enable such expanding and contracting movements of the guiding shell, it is made out of multiple individual components - which are designed to never interfere with each other. As shown in Figure 6.27, the proposed assembly uses two types of guiding elements: twelve conical ones for the expanding section of the cone, and twelve horizontal ones for its cylindrical part.

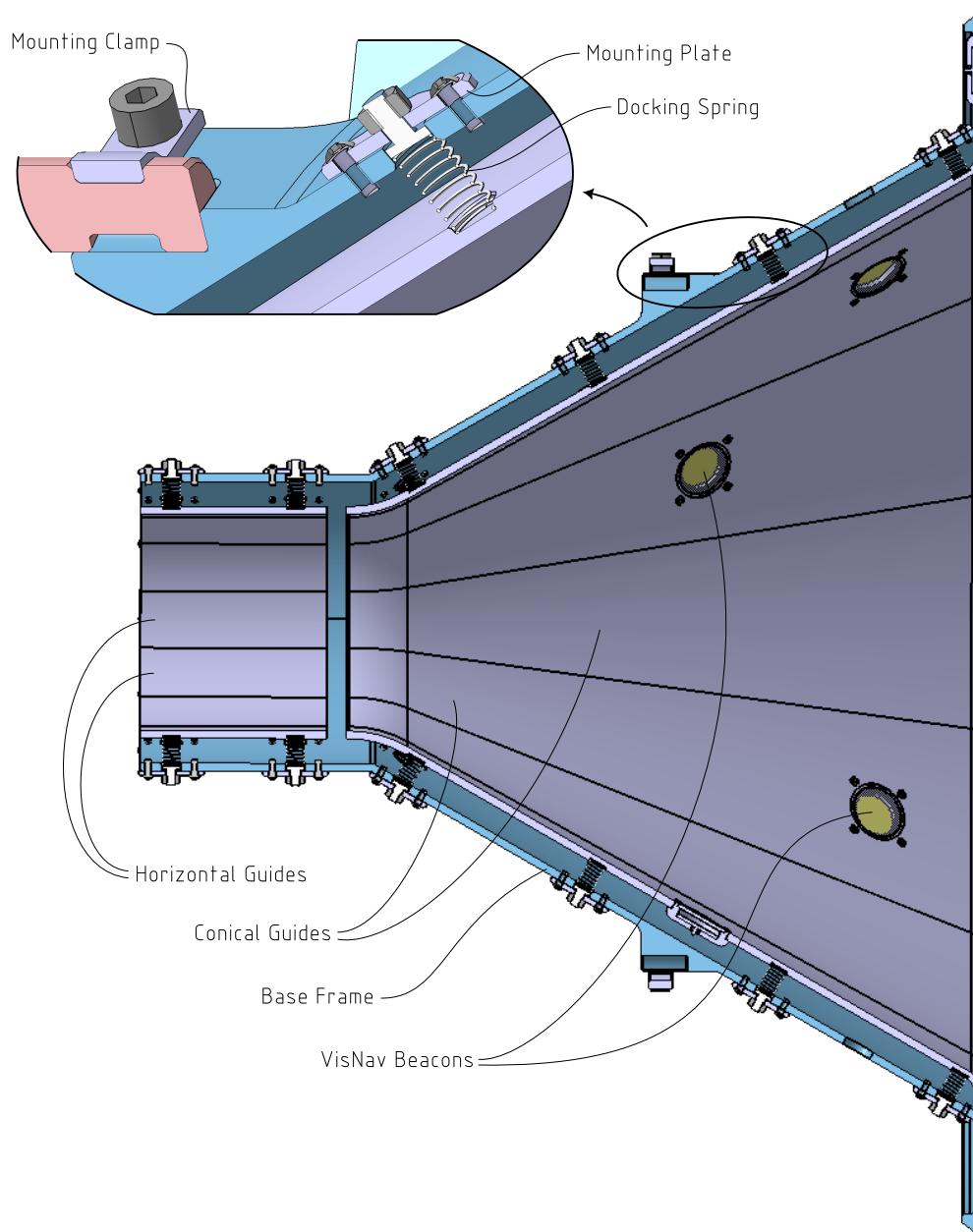


Figure 6.27: Cross-Section of the Guiding Cone Design. The depicted set of beacons corresponds to the final VisNav configuration determined in chapter 4.

Springs with a diameter of 10 mm and an uncompressed length of 20 mm are used as a reference, welded onto the guiding elements. Each spring is attached to the base frame using a mounting plate, an M6 Class 12 hexagonal metric nut, and two M4x10mm Class 12.9 metric bolts. Depending on typical contact scenarios and desired characteristics of the assembly, the number and type of springs can easily be changed. Furthermore, any of the conical guides can be swapped out for slightly modified versions, which include interfaces for the VisNav beacon designs presented in chapter 5. Consequently, rings of up to twelve beacons can be added inside the docking cone - with similar interfaces provided along the aft rim of the base frame. The base frame then attaches to the bars of the ACCD's load-bearing structure, using clamps and 16 M8x12mm Class 12.9 metric bolts. Finally, the outer rim of the base frame provides 36 tapped M4 attachment points for the conical sections of the ACCD's aerodynamic shell. Based on a detailed mass breakdown analysis in Appendix C, the total mass of the guiding cone is estimated at 21.789 kg - with technical drawings included in Appendix O. Because of their uncertainty and complexity, an FEM analysis of relevant loads on the guiding cone is not performed at this stage of the design. Nevertheless, future studies into such aspects are recommended.

6.7. Release System

As a final mechanical subassembly of the ACCD's, a tentative design for the release system is proposed. As argued in chapter 5, the addition of such a separate system is necessary to achieve a feasible locking mechanism in terms of SWaP footprint and complexity. For this to be a justifiable decision, it is vital that the release system itself has a limited impact on the vehicle's mass and power - which is demonstrated in this section.

In order to improve the simplicity of the release system, a disconnection between the ACCD and UHMWPE tether is proposed. This precludes the need for a complex system that disengages the locking mechanism's interface between the ACCD and RLV boom - or an equally complex solution disconnecting the boom from the RLV itself. Instead, the ACCD remains attached to the RLV during its autonomous landing, thanks to the compressive plunger force of the MC61450 shock absorber. Given the ACCD's relatively small footprint compared to the RLV, the latter's performance should not be significantly influenced by the presence of the former [24] - although further detailed studies are highly recommended. Once on the ground, the ACCD's locking mechanism can easily be disengaged, because the problematic friction is then virtually eliminated by the absence of towing loads.

Implementing the release system *inside* the ACCD's tether attachment is highly challenging, because of the already critical trade-off between its structural strength and kinematic freedom. Similarly, adding an additional mechanism *around* the attachment would entail a significant mass increase. Instead, the proposed solution - shown in Figure 6.28 - essentially 'cuts' the tether in two, at a point close to the ACCD's nose. This is achieved using two identical flanges, each bonded to a tether end, and bolted together with pyrotechnic fasteners. Triggering the activation of these fasteners then disconnects both tether ends, releasing the RLV from the TA.

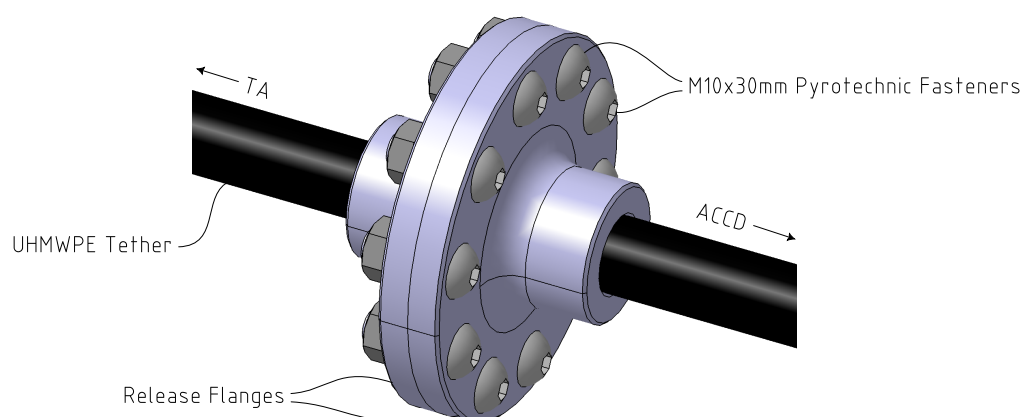


Figure 6.28: 3D View of the Release System Design.

Commercial suppliers of pyrotechnic fasteners include PacSci EMC [144], ArianeGroup's Pyroalliance [145], and Ensign-Bickford Aerospace & Defense Company [146]. They advertise maximum tensile bolt strengths from 50 to 4500 kN, and reaction times between 10 and 20 ms - with the latter providing ample margin for the required release times (**KY-RLS.F-15/02** and **KY-RLS.F-15/04**). Additionally, such fasteners only require a short activation signal [144], so that their influence on the ACCD's power system can be neglected. However, because of the limited available information concerning the strength of such COTS pyrotechnic fasteners, initial dimensioning is performed using standard metric bolts. To achieve a 1.5 SF (**KY-STR.NF-02/05**) under a 300 kN axial load (**CR-STR.NF-02/03**), at least seven M10 Class 12.9 metric bolts are required - each having a minimal tensile strength of 70.8 kN [135]. In order to compensate for the uncertainty concerning the strength of pyrotechnic fasteners, a ring of 10 M10x30mm Class 12.9 bolts is used. With both flanges made out of Al2024-T6 alloy, their combined mass amounts to 0.718 kg - excluding pyrotechnic fasteners. A detailed BoM is included in Appendix C, while technical drawings can be found in Appendix O.

6.8. Conclusion

Concluding the mechanical design of the ACCD, an assembly of the entire vehicle is shown in Figure 6.29 - including the avionics and power system presented in chapter 5. The design efforts uncovered a fundamental trade-off between the tether attachment's structural strength and kinematic freedom, while requiring the ACCD's structural mass to be spread around its outer perimeter. Additionally, an angled, additive boom design was found to be most suited for this application, with a separate pyrotechnic release system disconnecting the ACCD from the UHMWPE tether.

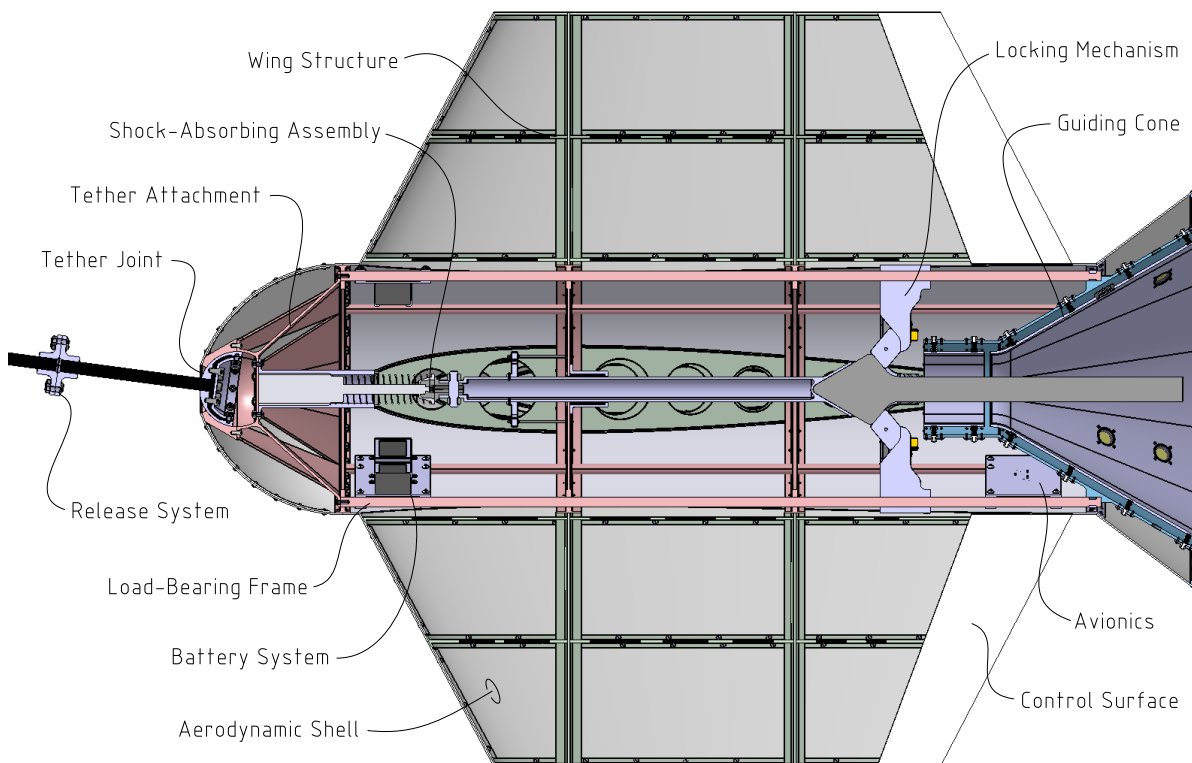


Figure 6.29: Cross-Section of the Final ACCD Design.

Because of the docking mechanism's aft-located structural mass, achieving a target CoG of 1 m behind the ACCD's nose was found to be non-trivial. It was partially compensated by locating as many components in the vehicle's nose as possible, including the tether attachment, shock-absorber, and battery systems. Furthermore, the cross-section above reveals that the ACCD has ample volume surplus in the axial direction, so that a shortening of the entire vehicle may be a possible solution to the CoG challenge.

Finally, three essential loads were identified and analysed, modelling towing, impact, and aerodynamic scenarios. Although all studied system were verified to meet the stress and deformation requirements, future studies should look into additional load scenarios - including structural stability, shocks, and localized loads. Additionally, validation of mass estimates and FEM analyses for the entire mechanical design are recommended, by developing (sub-scale) prototypes of the proposed design. In the subsequent, final chapter, an overview of the overall ACCD design is provided, summarizing the mass, stress, and deformation analyses described in this chapter.

7

Design Overview and Reflection

Combining the results from all previous chapters, a general overview of the ACCD's design can now be presented. First, in section 7.1, the ACCD's main inertial properties are estimated, and its resulting towing behaviour is analysed. Furthermore, three main design iterations are compared. Next, section 7.2 analyses the performance of the final VisNav configuration, corresponding to the guiding cone's design presented in chapter 6. Finally, section 7.3 assesses the compliance of all established design requirements, while section 7.4 briefly reiterates the chapter's main conclusions.

7.1. Vehicle Properties

As demonstrated in chapter 3, the ACCD's inertial properties have important implications for the behaviour of the towing system. Additionally, they enable a quantitative comparison between design iterations, and form relevant inputs for future IAC studies. Hence, a study of these properties is presented in this section, starting with a high-level breakdown analysis in subsection 7.1.1 - from which the ACCD's overall inertial properties are estimated. Then, the corresponding towing behaviour is studied in subsection 7.1.2. Finally, subsection 7.1.3 presents a comparative sensitivity study between three design iterations.

7.1.1. Breakdown Analysis

Based on chapters 5 and 6, detailed breakdown analyses are performed for three ACCD iterations: the initial design by Heide et al. (*Iteration 0*) [10]–[12], as well as two iterations performed within the context of this work (*Iterations 1* and *2*). While Appendix C contains in-depth BoMs for these three designs, Table 7.2 compares their high-level mass, stress, and deformation metrics. Mass estimates either use data from COTS components, or combine material density with CATIA's volume estimates. In order to enable a proper comparison between the different iterations, a trim mass is added to each, so that their CoG is at the target position of 1 m behind the ACCD's nose. Because the release system, tether, and RLV boom are not a physical part of the ACCD, they are not included in the mass breakdowns.

Load Type	Heide et al.	ICARUS	
	<i>Iteration 0</i>	<i>Iteration 1</i>	<i>Iteration 2</i>
Axial Towing Load [kN]	174.4	400	300
Axial Impact Load [kN]	27	50	50
90° AoA Aerodynamic Load [kN]	-	15	15

Table 7.1: Comparison of Design Loads used by Heide et al. [10], and by this Work (ICARUS).

In Table 7.2, m_k , SF_k , and u_k respectively refer to *Iteration k*'s mass, SF, and peak deformation. The listed percentual differences are always relative to the final design (*Iteration 2*). A vital caveat when comparing the three iterations, is that they are based on different design loads - as shown in Table 7.1. Furthermore, slightly different aluminium alloys are used as the main structural material for the three

designs: respectively Al2024-T3, Al6061-T6, and Al2024-T6. Finally, the categorization of all three designs into identical subassemblies is only approximative, with the full BoM's offering a more detailed and representative comparison.

Subassembly	Mass [kg]			Stress [-]			Deformation [mm]		
	m_2	m_1	m_0	SF_2	SF_1	SF_0	u_2	u_1	u_0
Tether Attachment	5.944	11.985	-	1.55	1.35	-	0.551	0.561	-
		-50.4%	-		+14.9%	-		-1.8%	-
Tether Joint	1.371	-	-	1.81	-	-	0.769	-	-
Load-Bearing Frame	15.696	12.106	21.195	1.51	1.42	8.18	1.904	3.404	0.271
		+29.1%	-25.9%		+6.3%	-81.5%		-44.1%	+602.6%
Wing Structures	68.396	67.560	29.400	1.57	1.57	-	3.810	3.413	-
		+1.2%	+132.6%		+0.0%	-		+11.6%	-
Shock-Absorbing Assembly	8.463	7.014	18.164	1.56	1.74	1.19	0.681	0.771	0.583
		+20.7%	-53.4%		-10.3%	+31.6%		-11.7%	+16.8%
Locking Mechanism	9.827	24.036	15.336	1.55	0.73	1.73	0.611	0.489	0.180
		-59.1%	-35.9%		+105.9%	-10.6%		+25.0%	+239.4%
Guiding Cone	21.789	16.495	-						
		+32.1%	-						
Body Shell	21.872	25.795	23.012						
		-15.2%	-5.0%						
Avionics	5.783	13.400	16.800						
		-56.8%	-65.6%						
Trim Mass	16.300	20.750	7.600						
		-21.5%	+114.5%						
Total	175.440	199.143	131.507	1.51	0.73	1.19	3.810	3.413	0.583
		-11.9%	+33.4%		+106.4%	+27.6%		+11.6%	+553.5%

Table 7.2: Comparative Mass, Stress, and Deformation Breakdown for Three ACCD Design Iterations.

Using the BoMs included in Appendix C, the position of the ACCD's overall CoG - denoted by e - can be estimated. This is done with Equation 7.1, which combines the mass m_i and axial CoG position e_i of all constituent components. Here, the axial CoG position is always denoted relative to the ACCD's nose. For the final design iteration, the total functional mass equals 159.14 kg, with an axial CoG position of 1071.9 mm. In order to attain the target CoG of 1 m behind the ACCD's nose, a trim mass of 16.3 kg is required, positioned at $e_i = 300$ mm.

$$e = \frac{\sum_i (m_i \cdot e_i)}{\sum_i m_i} \quad (7.1)$$

The analysed inertial properties can then be compared with estimates obtained directly from CATIA - which assumes a constant 2700 kg/m³ density for the entire structure. This yields a total functional mass of 183.22 kg, and an axial CoG located at $e = 1155.4$ mm - corresponding to a 15.13% and 7.8% overestimation compared to the values obtained with the detailed BoM approach. These differences are largely related to the modelling of the control surfaces as solid volumetric black boxes, resulting in an additional fictional mass towards the ACCD's aft.

Finally, CATIA also provides an estimate for the overall inertia tensor $[I]$ of the entire ACCD - shown in Equation 7.2. Given the estimate differences demonstrated above, this value should be treated with sufficient uncertainty margin. Nevertheless, the small products of inertia, as well as the 0.13% difference between the yaw and pitching moments of inertia, give an indication for the vehicle near-axisymmetric inertial properties (**TN-STR.NF-01/02**). Furthermore, the roll moment of inertia is considerably smaller than its yaw and pitch counterparts - which is consistent with the generally cylindrical design of the ACCD.

$$[I] = \begin{bmatrix} 9.402 & -0.047 & -0.009 \\ -0.047 & 23.213 & 0.015 \\ -0.009 & 0.015 & 23.183 \end{bmatrix} \text{ kg/m}^3 \quad (7.2)$$

7.1.2. Towing Behaviour

Having estimated the ACCD's inertial properties, its corresponding towing behaviour can be analysed with the 2D steady-state Towing Model established in chapter 3. Based on the system characteristics listed in Table 7.3, a pitch control trim of 7° is proposed during formation flight. As shown in Figure 7.1, this leaves a 3° control surplus in both directions, equivalent to a vertical displacement of -30.3 m (upwards) and $+32.3 \text{ m}$ (downwards). Because available CFD data only covers pitch deflection between $\pm 10^\circ$, these values are used as the operational limits for this analysis - rather than the full $\pm 15^\circ$ range. In case a larger control authority is indeed available, the neutral pitch trim could be further increased, enlarging the ACCD's control surplus and reachable area.

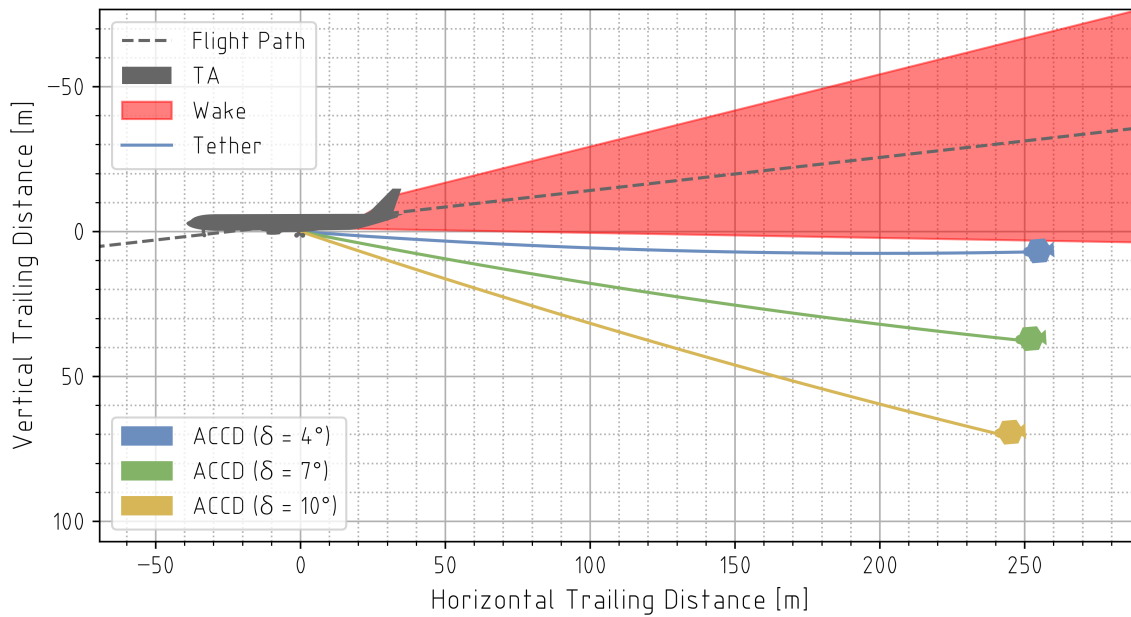


Figure 7.1: Operational Range of the Final ACCD Design During Formation Flight.

ACCD Properties		Tether Properties	
m	175.44 kg	l_T	250 m
e	1.0 m	d_T	24 mm
f	-0.4 m	ρ_T	755 kg/m ³
δ	4-10°	Environmental Parameters	
TA Properties		H	6000 m
m'	280 Mg	Ma	0.55
δ'	0°	γ	-6.5°

Table 7.3: Model Inputs for the Towing Analysis of the Final ACCD Design. For the TA, a *diving* configuration is used.

Additionally, the Towing Model can also be used to analyse the ACCD's attitudes during formation flight, as shown in Figure 7.2. Here, the ACCD's pitch angle ϕ is plotted together with its tether angle - which is an important metric to verify the available kinematic freedom in the tether attachment. For the analysed pitch deflections between -5° and 10° , the ACCD's pitch angle remains within the required $[-5^\circ, 5^\circ]$ range (KY-TOW.NF-01/11), while absolute tether angles stay below the 27.2° freedom angle (cf. section 6.3).

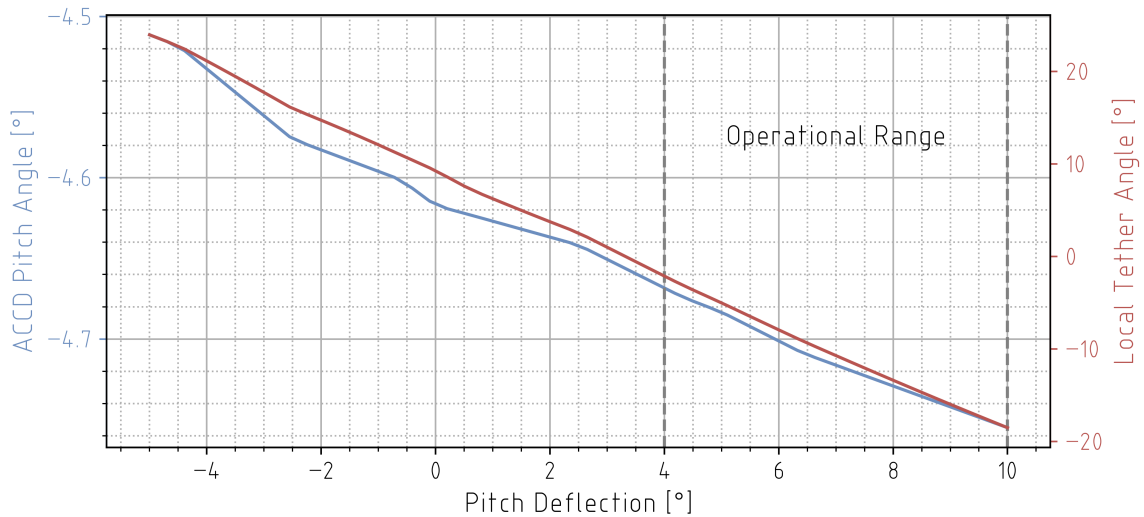


Figure 7.2: Steady-State Attitude and Local Tether Angle as a Function of the ACCD's Pitch Control Deflection.

Both analyses assume specific environmental conditions corresponding to a typical IAC formation flight - listed in Table 7.3. For different flight conditions - including altitude, velocity, and FPA - slightly adjusted control trims may be required. Nevertheless, corresponding effects are relatively limited, and can be compensated for by the available design margins.

7.1.3. Sensitivity Analysis

Finally, the breakdowns listed in Table 7.2 and Appendix C allow a comparative sensitivity study between the three ACCD iterations. Figure 7.3 compares subassembly masses, while Figure 7.4 visualizes their CoG contributions - corresponding to the terms in Equation 7.1's numerator. To give a clearer overview, Figure 7.3 only visualizes the mass of a *single* wing structure. Because the ACCD's power system was not analysed in previous studies, a comparison of power requirements is not included.

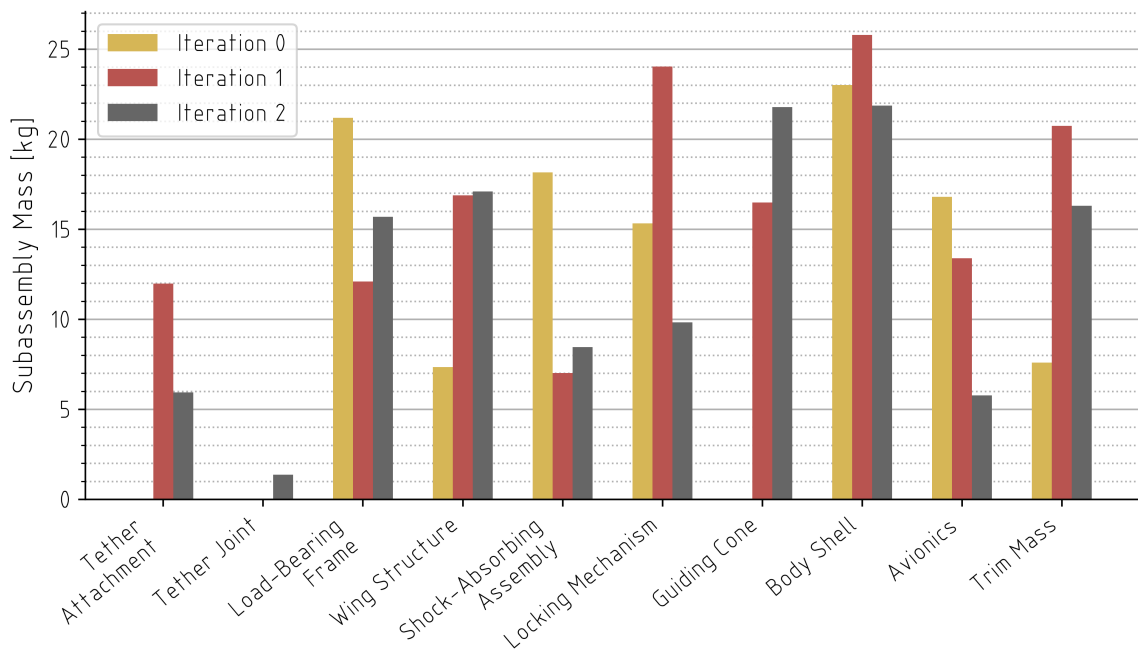


Figure 7.3: Comparison of Subassembly Masses for Three Design Iterations.

Comparing these designs, the lack of a tether attachment is very apparent for *Iteration 0*, as is its significantly lighter wing structure - which was not based on an actual structural design [12]. These two

aspects, in combination with the previously underestimated design loads, result in a significant mass increase of almost 45 kg from Heide's study to the currently proposed design (*Iteration 2*). Initially, this mass increase was even more pronounced for *Iteration 1*, but a structural reduction in the tether attachment and locking mechanism has brought the total mass down by roughly 25 kg. Additionally, a progressively more detailed design of the avionics and power system has reduced the corresponding subassembly mass - with the caveat that the control actuators have migrated to the wing structure subassembly for *Iteration 2's* BoM. Finally, the guiding cone's mass increase from *Iteration 1* to 2 was introduced to compensate for the uncertainty concerning this subassembly's load analysis.

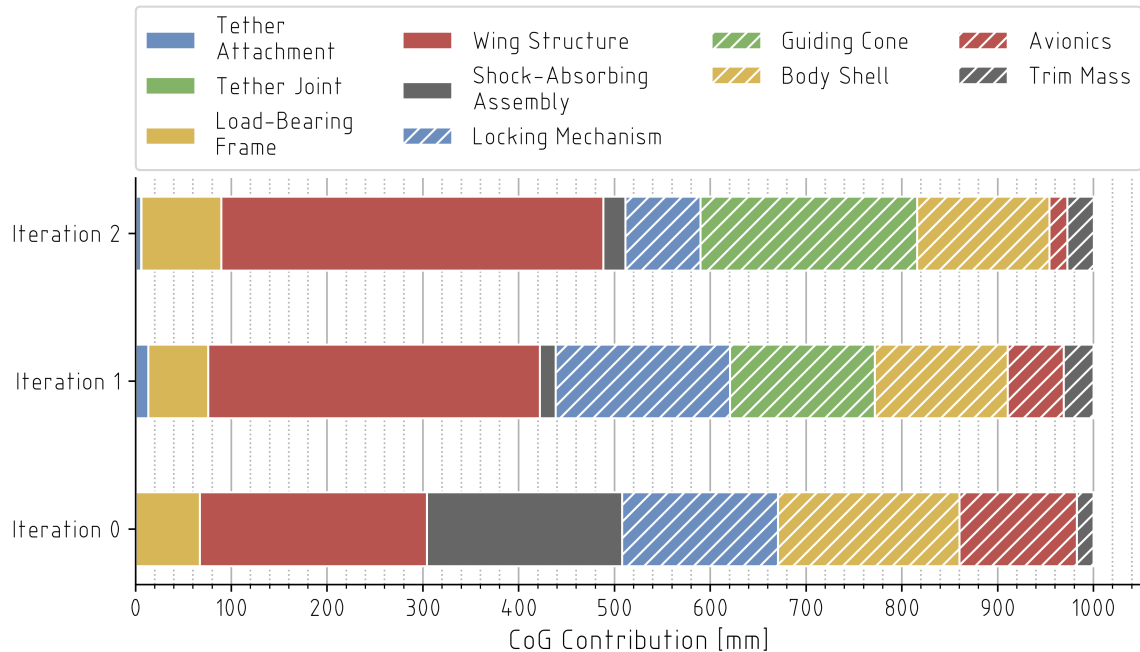


Figure 7.4: Comparison of CoG Contributions for Three Design Iterations.

Looking at the CoG contributions of the three designs, the reduction in trim mass from *Iteration 1* to 2 is a testimony of the improved inertial characteristics of the final design. Furthermore, the figure above shows that the ACCD's wings have the largest impact on its overall CoG, mainly because they constitute nearly 40% of the total system mass. Additionally, the locking mechanism and guiding cone also have a major influence on the vehicle's CoG: although their mass is lower, their aft position increases their influence. Hence, reducing the axial position e of the ACCD's CoG can be most easily achieved by focusing on a weight reduction of the wings, locking mechanism, and guiding cone.

Finally, Figures 7.5 and 7.6 show a comparison of the SFs and peak deformations of the three design iterations - demonstrating the compliance of corresponding requirements for the final iteration (**KY-STR.NF-02/05** and **KY-STR.NF-02/06**). Combining Figure 7.5 with Table 7.1 shows that, although the extreme towing load increased by 72% from *Iteration 0* to 2, the corresponding mass increase is only 33%. Meanwhile, the design's overall SF has increased by 28%, and the design has advanced towards a significantly more detailed state - as evinced by comparing Tables C.2 and C.4.

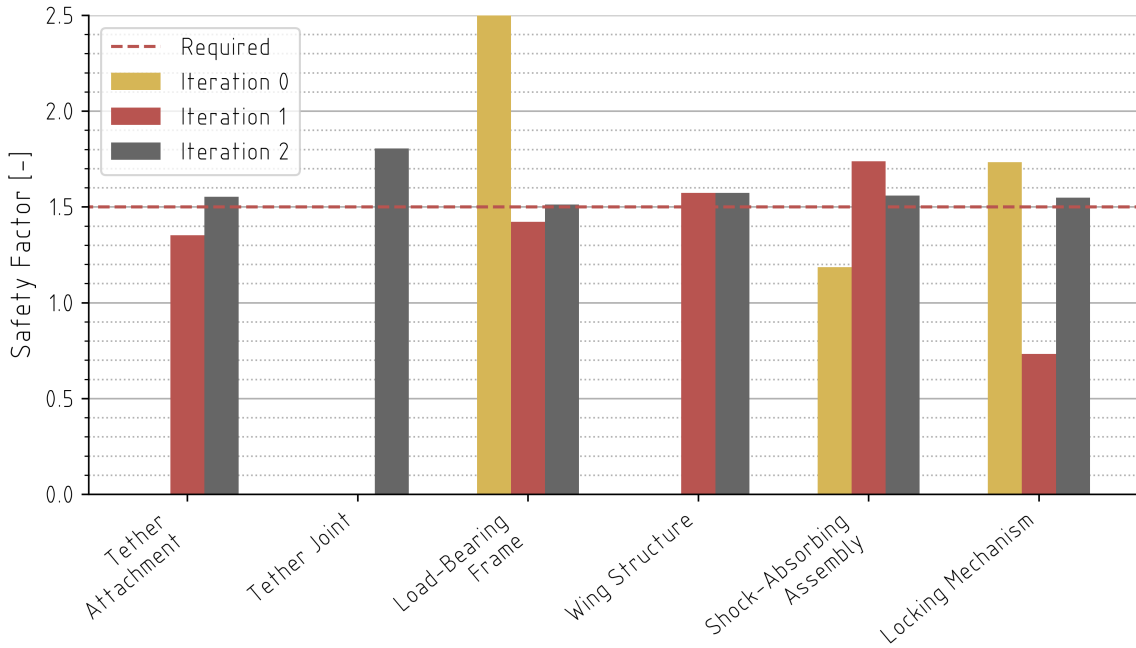


Figure 7.5: Comparison of Three Design Iterations' Safety Factors (SFs) Relative to the Stress Requirement (KY-STR.NF-02/05).

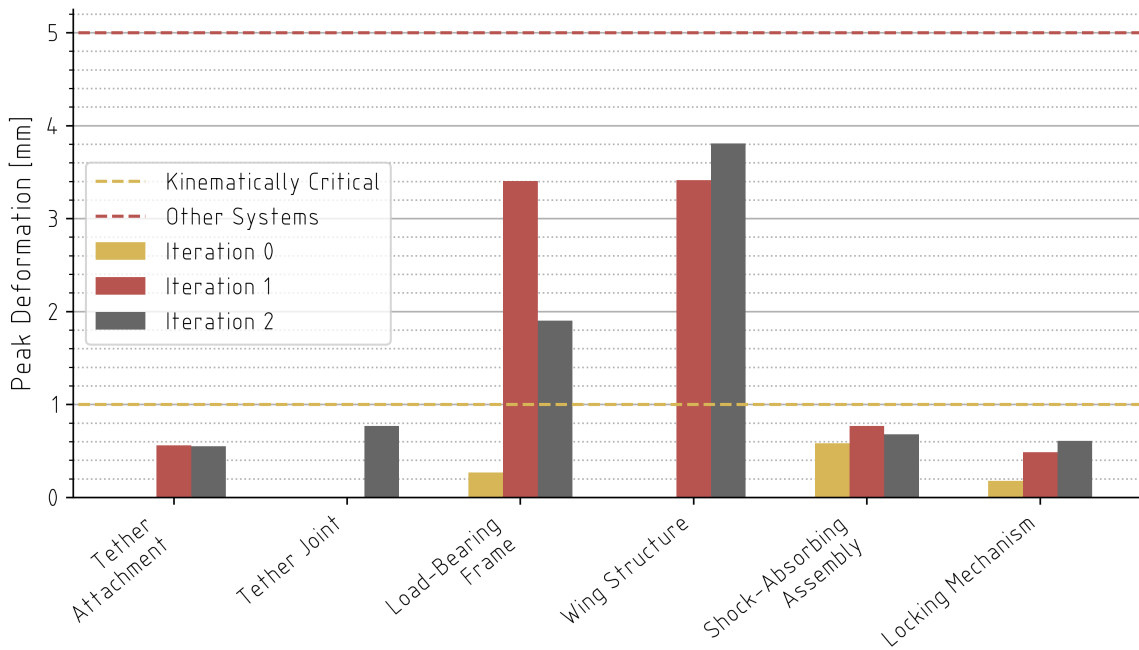


Figure 7.6: Comparison of Three Design Iterations' Peak Deformations Relative to the Deformation Requirement (KY-STR.NF-02/06).

7.2. VisNav Performance

With the mechanical design of the ACCD's guiding cone defined in chapter 6, the representative beacon configuration proposed in chapter 4 should be updated to reflect *Iteration 2*'s physical geometry. Corresponding characteristics are listed in Table 7.4, while Figures 7.7 and 7.8 visualize the approach corridor for this final design. Contrary to subsection 4.4.3, a 3600 m range is now used, based on the 1.5 W beacons described in chapter 5. Other differences are quite limited, indicating that the VisNav's performance is relatively insensitive to the exact geometry of the guiding cone. As can be seen in

Figure 7.7, the final approach corridor covers a roughly conical area behind the ACCD, spanning an angle significantly larger than the required 90° (KY-DTC.F-11/02).

Parameter	Value		
d_C	0.6 m		
d'_C	0.14 m		
λ	30°		
μ	150°		
FoV	60°		
Beacon Configuration	1	2	2
N	5	4	3
d_i	715 mm	510 mm	380 mm
r_0	3600 m	3600 m	3600 m

Table 7.4: Characteristics of the Final VisNav Configuration.

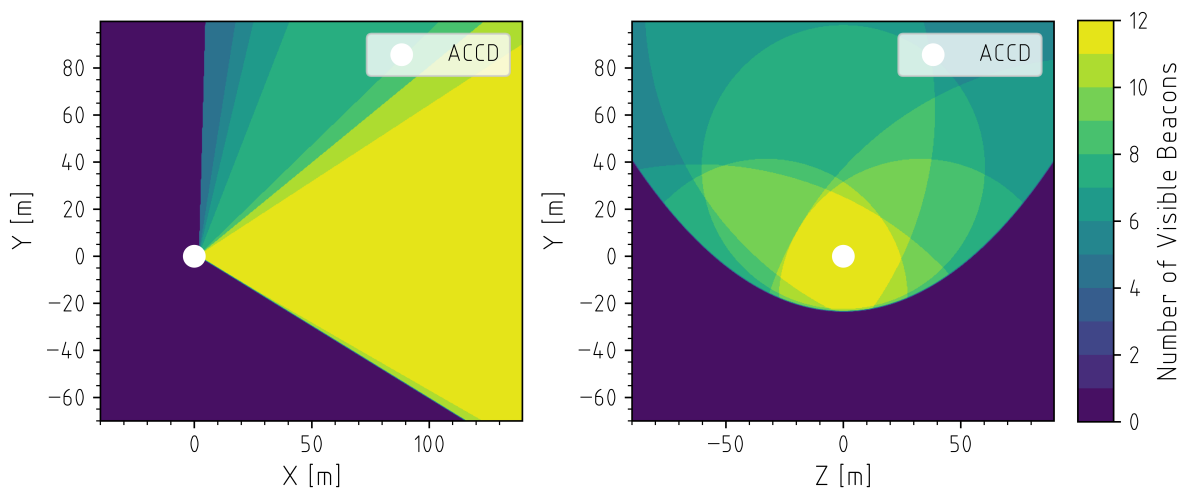


Figure 7.7: Approach Corridor of the Final VisNav Configuration. The left and right images respectively show a side ($Z = 0 m$) and front ($X = 40 m$) view.

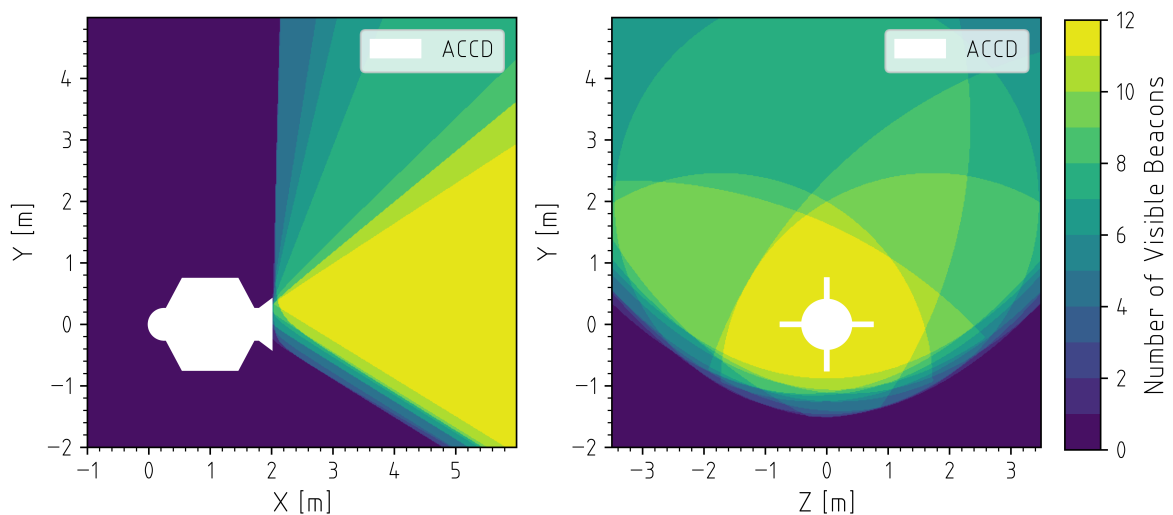


Figure 7.8: Close-Up of the Final VisNav Configuration's Approach Corridor. The left and right images respectively show a side ($Z = 0 m$) and front ($X = 4 m$) view.

7.3. Requirement Compliance

As a final part of the design overview, compliance is verified of the requirements formulated throughout this work. As the model requirements have already been verified in chapters 3 and 4, only the design requirements are shown in Table 7.5. For requirement **KY-DCK.F-13/01**, the final system mass of 175.44 kg is used in combination with the MC64150's energy-absorbing capacity of 5650 J, resulting in a maximum allowed relative velocity of 8.03 m/s. Although a number of requirements necessitate further analysis or verification efforts, this table shows that the proposed ACCD design is compliant with the vast majority of its design requirements. Hence, a limited number of future studies is needed to enable a fully compliant design.

7.4. Conclusion

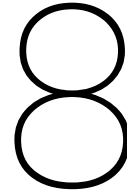
Throughout this chapter, a final overview of the ACCD design was presented, using BoMs as a starting point for determining vehicle characteristics. With inertial properties thus estimated, the towing behaviour of the ACCD was analysed, and sufficient controllability was demonstrated using a pitch trim of 7°. Three design iterations were compared, identifying the ACCD's wings, locking mechanism, and docking cone as the most impactful subsystems in terms of mass and CoG. Next, an analysis of the final VisNav configuration showed a relative insensitivity of this system to the geometry of the guiding cone. Finally, compliance of the proposed design with the vast majority of its requirements was demonstrated, and areas for future analyses were identified.

	Requirement	Compliance
Structural	TN-STR.NF-01/01	Fully compliant; the final design does not exceed the outer limits of the aerodynamic shell.
	TN-STR.NF-01/02	Fully compliant; as demonstrated in subsection 7.1.1, the ACCD has a quasi-axisymmetric inertia tensor.
	KY-STR.NF-01/03	Fully compliant; the tether attachment has a freedom angle of 27.2°.
	CR-STR.NF-02/01	Not investigated; shock-absorbing elements have been introduced into the ACCD's design, but an in-depth shock response analysis is required.
	CR-STR.NF-02/02	Fully compliant; stresses and deformations stay below the required limits for the impact design load.
	CR-STR.NF-02/03	Fully compliant; stresses and deformations stay below the required limits for the towing design load.
	KY-STR.NF-02/04	Fully compliant; stresses and deformations stay below the required limits for the aerodynamic design load.
	KY-STR.NF-02/05	Fully compliant; all SFs are above 1.5.
	KY-STR.NF-02/06	Fully compliant; all deformations stay below their respective limits.
Docking	KY-DCK.F-13/01	Fully compliant; the shock absorber can accommodate impact velocities up to 8 m/s.
	KY-DCK.F-13/02	Largely compliant; geometrically, the guiding cone can accommodate such misalignments. However, a more in-depth kinematic analysis is recommended.
	TN-DCK.F-13/03	Fully compliant; the axisymmetric design of the docking mechanism allows for any roll orientation between the RLV and the ACCD.
	CR-DCK.NF-13/04	Fully compliant; no elements of the docking mechanism are expendable.
	CR-DCK.F-13/05	Fully compliant; multiple docking sensors create a robust detection system.
	CR-DCK.F-13/06	Fully compliant; the shock absorber can absorb all impact energy.

Table 7.5: Compliance of the Subsystem Design Requirements.

	Requirement	Compliance
Release	CR-RLS.F-15/01	Fully compliant; the release system allows for a nominal release.
	KY-RLS.F-15/02	Fully compliant; the release system requires less than 0.5 s to activate.
	CR-RLS.F-15/03	Fully compliant; the release system allows for an emergency release.
	KY-RLS.F-15/04	Fully compliant; the release system requires less than 0.5 s to activate.
Towing	CR-TOW.NF-01/10	Largely compliant; the Towing Model indicates stable towing behaviour, but an in-depth, Six-Degrees-of-Freedom (6DoF) dynamic analysis is recommended.
	KY-TOW.NF-01/11	Fully compliant; as demonstrated in subsection 7.1.2, the ACCD's pitch angle stays within required bounds throughout its entire operational range.
	KY-TOW.NF-01/12	Fully compliant; as demonstrated in subsection 7.1.2, the ACCD stays outside the TA's wake zone.
	KY-TOW.F-12/01	Largely compliant; as demonstrated in subsection 7.1.2, the ACCD's operational range exceeds ± 30 m in the Y-direction. The Z-direction is not explicitly analysed, but should offer more freedom, as the full control deflections are available in this dimension.
	KY-TOW.F-12/02	Not investigated; however, initial analyses have shown a very high responsiveness to control deflections.
Power	KY-PWS.NF-03/01	Fully compliant; ample energy surplus is available.
	KY-PWS.NF-03/02	Fully compliant; ample energy surplus is available.
	KY-PWS.NF-03/03	Fully compliant; ample energy surplus is available.
Avionics	CR-AVN.F-01/20	Largely compliant; a potent communication module is included, but an in-depth bandwidth analysis is recommended.
	TN-AVN.F-01/21	Largely compliant; a potent communication module is included, but an in-depth bandwidth analysis is recommended.
	KY-AVN.F-01/22	Fully compliant; the chosen OBC solution includes a telemetry logging functionality.
Detection	KY-DTC.F-11/01	Largely compliant; as demonstrated in Appendix J, initial simulations of the relative navigation system meet the required accuracy. However, a more detailed analysis is recommended.
	KY-DTC.F-11/02	Fully compliant; the beacons' range exceeds the minimal requirement, while the final VisNav configuration has a visibility angle of 120° .
	KY-DTC.NF-11/03	Fully compliant; VisNav operates at frequencies up to 100 Hz.
	CR-DTC.F-11/04	Largely compliant; VisNav should function under all these conditions. However, verification of these claims is recommended.

Table 7.5: Compliance of the Subsystem Design Requirements (*continued*).



Conclusion

Throughout this work, the electromechanical design of an Aerodynamically Controlled Capturing Device (ACCD) was studied, with the aim of answering the following research question:

What is a suitable electromechanical design space for an Aerodynamically Controlled Capturing Device used for In-Air Capturing of Reusable Launch Vehicles?

As a concretization of this question, the following six design metrics were defined:

- METR-01:** Preliminary definition of essential subsystem requirements.
- METR-02:** Definition of an inertial design space for the ACCD, taking into account effects on the vehicle's towing behaviour.
- METR-03:** Definition of a representative sensor solution for relative position and attitude estimation.
- METR-04:** Selection of representative Commercial-off-the-Shelf (COTS) avionics, and preliminary definition of a corresponding power system.
- METR-05:** Computer-Aided Design (CAD) model of a preliminary ACCD design, in accordance with its requirements.
- METR-06:** Bill of Materials (BoM) for the proposed ACCD design, with a corresponding mass breakdown analysis and Centre of Gravity (CoG) estimate.

After providing relevant background concerning the overarching In-Air Capturing (IAC) procedure, a reference Towing Aircraft (TA) and Reusable Launch Vehicle (RLV) were defined. Additionally, a system definition for the ACCD was provided, introducing its fixed aerodynamic shell as a boundary condition for the design. Finally, an overview was given of a previous ACCD design iteration by Heide et al. [10]–[12], which mainly covered the mechanical definition of its docking system. Using this design as a starting point, a number of areas for improvement were identified, including the need for a more detailed analysis of design loads, as well as a definition of the vehicle's avionics and power system.

With the scope of the work investigated as such, a first analysis effort studied the behaviour of the entire towing system, consisting of the TA, tether, ACCD, and potentially the RLV. To accelerate such analyses, a two-dimensional (2D) steady-state model was developed, with a dual objective: on the one hand, enabling an exploration of the ACCD's design space (**METR-02**), while on the other hand allowing for an estimation of extreme towing loads on the ACCD. The latter is vital for a definition of subsystem requirements (**METR-01**), and the corresponding design of the ACCD's mechanical subsystems (**METR-05**). The design space exploration showed that [the towing system's behaviour is relatively insensitive to the ACCD's mass, while the position of its CoG has a significantly more pronounced influence](#). Based on the required operational range of the ACCD, [a maximum allowable axial CoG position of 1 m was established - as measured from the vehicle's nose](#). Additionally, extreme towing analyses

concluded with the definition of an axial towing design load of 300 kN.

Next, a study of the ACCD's relative navigation system was performed (**METR-03**). Using a set of subsystem requirements, state-of-the-art sensor solutions were compared, and the so-called *VisNav* system was proposed - using a sensor attached to the RLV in combination with an array of active beacons mounted to the ACCD's docking cone. To further explore the *VisNav* design space, a geometric visibility model was developed, analysing the performance of specific beacon and sensor configurations. Again, the aim of the model was two-fold: on the one hand, enabling a comparison between different *VisNav* configurations - in order to define a representative one - while on the other hand allowing model integration into an overarching relative navigation simulator. The latter was demonstrated in a paper presented at the 2024 High-Speed Vehicle Science and Technology Conference (HiSST), which is currently under peer review for publication in the CEAS Space Journal.

In light of previous studies' design gap regarding the ACCD's full-scale electronics, its power system and avionics were analysed (**METR-04**). After identifying a set of essential subsystems, representative COTS avionics were selected, including sensors, actuators, a communication module, and an On-Board Computer (OBC). In particular, an analysis of the locking actuators showed that [a combined docking/release mechanism generates unfeasible design requirements on the corresponding actuators. Hence, separate systems for each functionality are proposed. Additionally, the \(locking and control\) actuators were identified as the main electronic design drivers in terms of Size, Weight and Power \(SWaP\) footprint, with ample opportunities for sensor redundancy and diversity.](#) Combining the estimated SWaP footprints of electronic subsystems with a definition of three operational ACCD modes, the vehicle's total power and energy requirements were then analysed. As a conservative estimate, a peak power of 969 W was defined, with a total energy requirement of 625.1 Wh. Based on these values, [a solution with four 175 Wh lithium-ion batteries is proposed, with corresponding mass and volume estimates demonstrating the feasibility of such a battery-powered design.](#)

Subsequently, a detailed mechanical ACCD design was proposed (**METR-05**), covering all major subsystems: tether attachment, load-bearing and wing frames, shock-absorbing assembly, docking mechanism, and release system. The control surfaces' internal mechanism design was excluded from the scope of this work. Where relevant, structural strength of the subassemblies was analysed with Finite Element Methods (FEM), using a set of three design load scenarios: towing, (docking) impact, and aerodynamic. In particular, [a design for the ACCD's locking mechanism was proposed, using a ring of four actuated locking wedges that kinematically constrain a diverging-converging conical RLV\[blue\] boom. Additionally, the chosen energy-absorbing solution can accommodate vehicle masses up to 400 kg.](#) The entire mechanical design was generated with manufacturability and ease of (dis)assembly in mind, and includes an initial estimation of required fasteners. Looking at the final assembly, [ample volume surplus inside the ACCD was identified - especially in its axial dimension.](#)

Finally, a panoptic overview of the proposed electromechanical ACCD design was presented, based on BoMs for three distinct iterations (**METR-06**). Estimates for the ACCD's inertial properties were obtained, with [the total system mass of 175.44 kg increased by 33.4% compared to Heide's study.](#) Using these inertial properties, [a 7° pitch trim was found to leave sufficient control authority, allowing vertical translations of ±30 m relative to the TA - while staying clear of its wake.](#) Comparing the three design iterations, general trends were observed, and [the ACCD's wings, locking mechanism, and guiding cone were identified as the most influential to the vehicle mass and CoG - prompting the need for an additional trim mass.](#) Additionally, *VisNav*'s relative insensitivity to the exact geometry of its beacons was demonstrated. Finally, overall compliance of the formulated subsystem requirements was verified (**CRIT-01**).

The above summary shows that all formulated design metrics have been accounted for, and the overarching research question has thus been answered. In general, the study revealed no insurmountable design challenges, pointing towards the feasibility of the use of an ACCD for the In-Air Capturing of RLVs. Hence, the design effort can be wrapped up by presenting a list of recommendations for future work in the following chapter.

9

Recommendations

Based on the design conclusions formulated in the previous chapter, a number of recommendations for future work are proposed. They are grouped into three distinct categories, discussed in sections 9.1 through 9.3. They respectively cover future analyses complementing ICARUS's work, prototyping of the Aerodynamically Controlled Capturing Device (ACCD), and a potential aerodynamic redesign of said ACCD.

9.1. Complementary Analyses

In general, a large number of complementary analyses can be envisioned, increasing the accuracy and veracity of all models presented throughout this work, and maturing the overall theoretical design of the ACCD. Here, only the most vital and impactful studies will be briefly discussed.

First of all, studies concerning the fully dynamic, Six-Degrees-of-Freedom (6DoF) behaviour of the ACCD are recommended, based on the inertial and mechanical properties of the design proposed in this work. Using the Simulink model developed at the German Aerospace Centre's Department of Space Launcher System Analysis (SART), aspects such as aerodynamic stability, disturbance rejection, manoeuvrability, and tow-back flight regimes can be studied. Consequently, refined design loads, environmental parameters, and vehicle characteristics can be obtained.

Next, a more in-depth bandwidth analysis of the proposed avionics design is highly recommended, in order to determine whether the selected On-Board Computer (OBC) and communication solutions meet respective requirements. Furthermore, environmental compatibility of all Commercial-off-the-Shelf (COTS) systems should be investigated. Additionally, a detailed electronic design of the entire ACCD is also recommended, defining data and power interfaces, and ultimately obtaining a circuit diagram of the complete power system.

Similarly, different structural and kinematic studies are required to fully scrutinize the proposed mechanical design of the ACCD. These include Finite-Element-Method (FEM) analyses of radial towing loads and docking contact scenarios, as well as shock response analyses of relevant subassemblies. Additionally, future studies could investigate alternative methods of releasing the Reusable Launch Vehicle (RLV), including the use of explosive cartridge-activated devices, or quick-disconnect unreeling systems - both found in aerial refuelling applications [147]. Finally, an analysis of the (aero)dynamic behaviour of the coupled ACCD-RLV system is highly recommended, in order to investigate the feasibility of the RLV performing an autonomous landing will the ACCD is still attached.

Throughout all of the aforementioned studies, a further definition and refinement of (sub)system requirements is also recommended, introducing aspects such as reliability, safety, maintainability, and risk mitigation - which were not yet considered for ICARUS.

9.2. Prototyping

Apart from theoretical analyses, future studies should also take practical steps to mature the proposed ACCD design. These include prototyping different systems and subassemblies, in order to validate aspects such as estimated inertial properties, and verify the feasibility of manufacturing and (dis)assembly. Such (partial) prototypes can then also serve as test beds, assessing structural properties of primary load-bearing components. Additionally, results from the Towing and VisNav Models can be validated by performing flight tests, and designing adequate breadboard lab experiments. Such practical studies are especially vital given the unique nature of the ACCD, as it currently has no equivalent counterpart out there.

9.3. Aerodynamic Redesign

Finally, a potential redesign of the ACCD's aerodynamic shell should be investigated. In particular, a shortening of the total vehicle length, and associated reduction of its wing size seems promising, as it would remove unnecessary mass from the ACCD, while potentially bringing the Centre of Gravity (CoG) more towards the front of the vehicle.

Additionally, an even more fundamental redesign can be considered, taking inspiration from patents and concepts within the discipline of Automated Aerial Refuelling (AAR) - such as the one shown in Figure 9.1. In particular, these include the use of spoilers [58], grid fins [148], and cold-gas thrusters [85], [149], as well as deformable drogues [150]–[152], and annular lifting bodies [153]. Finally, some implementations achieve passive stabilization using a gyroscopic effect [154].

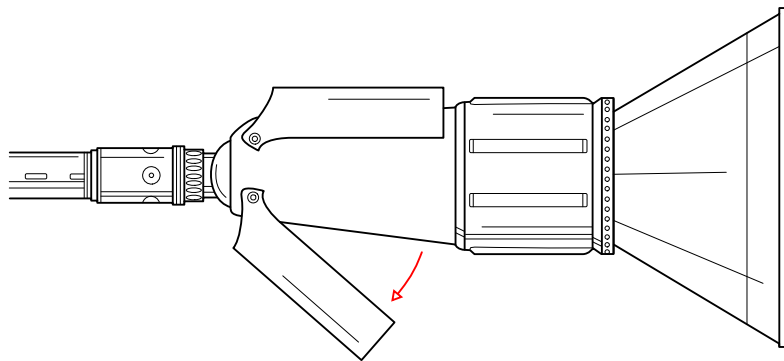


Figure 9.1: Example of an Alternative Control Method Used in Automated Aerial Refuelling (AAR) [58].

Combining any or all of the above recommendations, the electromechanical design of the ACCD can be progressed towards a more detailed state. By doing so, the overall Technology Readiness Level (TRL) of the In-Air Capturing (IAC) technique can be increased, ultimately paving the way for this innovative recovery method to be applied in the European launch market - and beyond.

References

- [1] H. W. Jones, "The Recent Large Reduction in Space Launch Cost," presented at the 48th International Conference on Environmental Systems, Albuquerque, United States of America, Jul. 8, 2018. [Online]. Available: <https://ntrs.nasa.gov/api/citations/20200001093/downloads/20200001093.pdf> (visited on 07/03/2024).
- [2] P. Bizony, A. Chaikin, and R. Launius, *The NASA Archives* (40th Edition Series), 1st ed. Köln, Germany: TASCHEN, 2022, 511 pp., ISBN: 978-3-8365-8808-9.
- [3] R. A. Pielke, "The Rise and Fall of the Space Shuttle," *American Scientist*, vol. 96, no. 5, pp. 432–434, Sep. 2008, ISSN: 0003-0996. DOI: 10.1511/2008.74.432. [Online]. Available: <https://www.americanscientist.org/article/the-rise-and-fall-of-the-space-shuttle> (visited on 11/30/2023).
- [4] D. R. Jenkins, *Space Shuttle: Developing an Icon - 1972-2013*. Specialty Press, Feb. 27, 2017, 1584 pp., ISBN: 978-1-58007-249-6. [Online]. Available: <https://www.abebooks.com/9781580072496/Space-Shuttle-Developing-Icon-1972-2013-1580072496/plp> (visited on 11/30/2023).
- [5] B. E. Chertok and A. A. Siddiqi, *Rockets and People* (The NASA History Series). Washington DC, United States of America, Jan. 2005, vol. 1, 402 pp. [Online]. Available: <https://ntrs.nasa.gov/api/citations/20050010181/downloads/20050010181.pdf> (visited on 12/29/2023).
- [6] J. Prisco. "Two Abandoned Soviet Space Shuttles Left in the Kazakh Steppe," CNN Style. (Dec. 21, 2017), [Online]. Available: <https://www.cnn.com/style/article/baikonur-buran-soviet-space-shuttle/index.html> (visited on 12/31/2023).
- [7] G. Soares dos Santos Vera-Cruz Pinto, "Reliability and Cost Modeling of Reusable Launch Vehicles: Predicting, Preventing and Mitigating the Cost of Failure," MSc Thesis, Delft University of Technology, Delft, The Netherlands, Jun. 28, 2022, 130 pp. [Online]. Available: <http://resolver.tudelft.nl/uuid:35d791b1-d613-4c2e-9faf-a0f67b435d2d> (visited on 11/27/2023).
- [8] J. Klevanski, A. Herbertz, M. Sippel, and J. Kauffmann, "Recovery method for ejected space rocket stage uses aircraft for attaching towing line to rocket stage in glider flight mode," German pat. 10147144C1, Feb. 13, 2003. [Online]. Available: <https://patents.google.com/patent/DE10147144C1/en> (visited on 11/28/2023).
- [9] S. Stappert, J. Wilken, L. Bussler, and M. Sippel, "A Systematic Assessment and Comparison of Reusable First Stage Return Options," in *Proceedings of the International Astronautical Congress*, Washington DC, United States of America, Oct. 2019. [Online]. Available: <https://elib.dlr.de/133400/> (visited on 11/29/2023).
- [10] J. Heide, "Auslegung eines Kopplungsmechanismus für das In-Air-Capturing Verfahren," Deutsches Zentrum für Luft- und Raumfahrt, Köln, Germany, SART TN-004/2005, 2005, p. 50. (visited on 12/12/2023).
- [11] U. Atanassov, "Finite-Elemente-Analyse des 'In-Air-Capturing'-Mechanismus mit dem Programmsystem I-DEAS," Deutsches Zentrum für Luft- und Raumfahrt, Köln, Germany, SART TN-005/2006, 2006, p. 46. (visited on 11/30/2023).
- [12] S. Stappert, "Aerodynamics of the ACCD for the In-Air-Capturing of the SpaceLiner Booster," Deutsches Zentrum für Luft- und Raumfahrt, Bremen, Germany, SART TN-016/2018, Jun. 17, 2021, p. 32. (visited on 11/30/2023).
- [13] B. Schlögl, "Systematische Analyse von Ankopplungsverfahren zum Bergen einer wiederverwendbaren Raumtransporterstufe in der Luft," Deutsches Zentrum für Luft- und Raumfahrt, Köln, Germany, SART TN-008/2003, 2003, p. 67. (visited on 12/21/2023).

- [14] S. Singh, M. Simioana, S. Stappert, *et al.*, “Control Design and Analysis of a Capturing Device Performing In-Air Capturing of a Reusable Launch Vehicle,” in *Proceedings of the 9th European Conference for Aeronautics and Space Sciences*, Lille, France, Jun. 2022. [Online]. Available: <https://elib.dlr.de/187073/> (visited on 11/29/2023).
- [15] S. Singh, B. Luyten, and M. Sagliano, “Relative Navigation Implementation for the In-Air-Capturing of a Winged Reusable Launch Vehicle,” presented at the 3rd International Conference on High-Speed Vehicle Science Technology (HiSST), Busan, South Korea, Apr. 14, 2024.
- [16] S. Krause, S. Cain, A. Funke, J. González, and M. Ferrándiz, “Overview of a Planned Flight Test Operation for a Scaled In-Air Capturing Demonstration,” in *Proceedings of the 9th European Conference for Aeronautics and Space Sciences*, Lille, France, Jun. 2022. [Online]. Available: <https://elib.dlr.de/188889/> (visited on 12/01/2023).
- [17] L. E. Briese and B. Gäßler, “Advanced Modeling and Trajectory Optimization of the In-Air-Capturing Maneuver for Winged RLVs,” *Acta Astronautica*, vol. 193, pp. 756–766, Apr. 1, 2022, ISSN: 0094-5765. doi: 10.1016/j.actaastro.2021.09.005. [Online]. Available: <https://www.sciencedirect.com/science/article/pii/S0094576521004914> (visited on 11/28/2023).
- [18] S. Singh, L. Bussler, K. Bergmann, and M. Sippel, “Mission Design and Sensitivity Analysis for In-Air Capturing of a Winged Reusable Launch Vehicle,” in *Proceedings of the International Astronautical Congress*, Baku, Azerbaijan, Oct. 4, 2023. [Online]. Available: <https://elib.dlr.de/198208/> (visited on 03/06/2024).
- [19] S. Singh, L. Bussler, S. Stappert, M. Sippel, Y. C. Kucukosman, and S. Buckingham, “Simulation and Analysis of Pull-Up Manoeuvre during In-Air Capturing of a Reusable Launch Vehicle,” in *Proceedings of the 9th European Conference for Aeronautics and Space Sciences*, Lille, France, Jun. 2022. [Online]. Available: <https://elib.dlr.de/187075/> (visited on 11/29/2023).
- [20] M. Sippel, S. Stappert, and M. Simioana, “Technical Report on Different RLV Return Modes’ Performances,” Deutsches Zentrum für Luft- und Raumfahrt, Bremen, Germany, FALCon D2.1, Oct. 19, 2020, p. 100. [Online]. Available: <https://elib.dlr.de/137735/> (visited on 11/30/2023).
- [21] G. J. D. Calabuig, “Conceptual Cost Estimation for Recovery and Refurbishment Operations of Reusable Launch Vehicles,” Deutsches Zentrum für Luft- und Raumfahrt, Bremen, Germany, SART TN-006/2019, Apr. 30, 2019, p. 62. (visited on 12/14/2023).
- [22] S. Singh, M. Sippel, and S. Stappert, “Full-Scale Simulations of ‘In-Air Capturing’ Return Mode for Winged Reusable Launch Vehicles,” in *Journal of Physics: Conference Series*, vol. 2526, Barcelona, Spain, Aug. 2023, ISBN: 1742-6588. doi: 10.1088/1742-6596/2526/1/012114. [Online]. Available: <https://iopscience.iop.org/article/10.1088/1742-6596/2526/1/012114/pdf> (visited on 12/01/2023).
- [23] J. Wilken, S. Stappert, L. Bussler, M. Sippel, and E. Dumont, “Future European Reusable Booster Stages: Evaluation of VTHL and VTVL Return Methods,” in *Proceedings of the International Astronautical Congress*, Bremen, Germany, Oct. 2018. [Online]. Available: <https://elib.dlr.de/122188/> (visited on 11/28/2023).
- [24] Y. C. Kucukosman, S. Buckingham, S. Lopes, *et al.*, “CFD Analysis of Interaction Effects Between Vehicles in Formation Flight for In-Air Capturing of Reusable Launchers,” in *Proceedings of the International Astronautical Congress*, Paris, France, Sep. 18, 2022. [Online]. Available: <https://elib.dlr.de/195199/> (visited on 11/28/2023).
- [25] “X-37B: Extended Space Flights,” Boeing. (2023), [Online]. Available: <https://www.boeing.com/defense/autonomous-systems/x37b/index.page> (visited on 12/29/2023).
- [26] S. Singh, S. Stappert, L. Bussler, M. Sippel, Y. Kucukosman, and S. Buckingham, “A Full-Scale Simulation and Analysis of Formation Flight during In-Air-Capturing,” in *Proceedings of the International Astronautical Congress*, Dubai, United Arab Emirates, Oct. 2021. [Online]. Available: https://www.researchgate.net/publication/355929785_A_Full-Scale_Simulation_and_Analysis_of_Formation_Flight_during_In-Air-Capturing (visited on 11/29/2023).
- [27] Airbus, “A340-500/-600: Aircraft Characteristics - Airport and Maintenance Planning,” Airbus SAS, Blagnac Cedex, France, Jan. 2021, p. 404.

- [28] S. Stappert, J. Wilken, L. Bussler, *et al.*, “European Next Reusable Ariane (ENTRAIN): A Multidisciplinary Study on a VTVL and a VTHL Booster Stage,” in *Proceedings of the International Astronautical Congress*, Washington DC, United States of America, Oct. 1, 2019. [Online]. Available: https://www.researchgate.net/publication/338536312_European_Next_Reusable_Ariane_ENTRAIN_A_Multidisciplinary_Study_on_a_VTVL_and_a_VTHL_Booster_Stage (visited on 11/29/2023).
- [29] S. Stappert, J. Wilken, L. Bussler, and M. Sippel, “A Systematic Comparison of Reusable First Stage Return Options,” in *Proceedings of the 8th European Conference for Aeronautics and Space Sciences*, Madrid, Spain, Jul. 2019. [Online]. Available: https://elib.dlr.de/128623/1/EUCASS2019_AKIRA_438_final.pdf (visited on 11/28/2023).
- [30] M. Sippel, S. Stappert, L. Bussler, S. Callsen, and M. Sippel, “High-Performance, Partially Reusable Launchers for Europe,” in *Proceedings of the International Astronautical Congress*, Oct. 2020. [Online]. Available: <https://elib.dlr.de/142199/1/IAC20-D2.4.1.pdf> (visited on 12/01/2023).
- [31] M. Sippel, S. Stappert, S. Callsen, *et al.*, “A Viable and Sustainable European Path into Space - for Cargo and Astronauts,” in *Proceedings of the International Astronautical Congress*, Dubai, United Arab Emirates, Oct. 2021. [Online]. Available: <https://elib.dlr.de/146954/1/IAC21-D2.4.4.pdf> (visited on 11/29/2023).
- [32] S. Stappert, M. Sippel, S. Callsen, and L. Bussler, “Concept 4: A Reusable Heavy-Lift Winged Launch Vehicle using the In-Air-Capturing Method,” presented at the 2nd International Conference on High-Speed Vehicle Science Technology (HiSST), Brugge, Belgium, Sep. 2022. [Online]. Available: <https://elib.dlr.de/188529/> (visited on 11/29/2023).
- [33] S. Callsen, S. Stappert, and M. Sippel, “Study on Future European Winged Reusable Launchers,” in *Proceedings of the 9th European Conference for Aeronautics and Space Sciences*, Lille, France, Jun. 2022. [Online]. Available: <https://elib.dlr.de/187063/> (visited on 11/29/2023).
- [34] S. Singh, “Towing Aircraft A340-600 Study for In-Air-Capturing of the RLVC4 Booster,” Deutsches Zentrum für Luft- und Raumfahrt, Bremen, Germany, SART TN-019/2019, Dec. 2019.
- [35] M. Sippel, L. Bussler, C. Messe, S. Stappert, and S. Schuster, “Preliminary Analyses of Winged Reusable First Stages in Two- and Three-Stage to Orbit Configurations (RLVC4),” Deutsches Zentrum für Luft- und Raumfahrt, Bremen, Germany, SART TN-015/2019, Jan. 2020, Num Pages: 106, p. 106. [Online]. Available: <https://elib.dlr.de/144128/> (visited on 07/10/2024).
- [36] Airbus, *A340 Flight Deck and Systems Briefing For Pilots*, Jan. 2000. [Online]. Available: https://www.smartcockpit.com/docs/A340_Flight_Deck_and_Systems_Briefing_For_Pilots.pdf (visited on 05/23/2024).
- [37] S. Singh and M. Mastrogiuseppe, “Multibody Modelling of Tether and Capture System for Dynamic Simulations of In-Air Capturing,” *Acta Astronautica*, vol. 218, pp. 59–69, May 1, 2024, ISSN: 0094-5765. doi: 10.1016/j.actaastro.2024.02.008. [Online]. Available: <https://www.sciencedirect.com/science/article/pii/S0094576524000663> (visited on 04/09/2024).
- [38] S. Stappert, S. Singh, A. Funke, and M. Sippel, “Developing an Innovative and High-performance Method for Recovering Reusable Launcher Stages: the In-Air Capturing Method,” *CEAS Space Journal*, Jul. 13, 2023, ISSN: 1868-2502, 1868-2510. doi: 10.1007/s12567-023-00512-0. [Online]. Available: <https://link.springer.com/10.1007/s12567-023-00512-0> (visited on 11/27/2023).
- [39] S. Cain, S. Krause, and J. Binger, “First Development Steps of an Actively Controlled Drogue,” presented at the 2018 International Conference on Unmanned Aircraft Systems (ICUAS), Dallas, United States of America: Institute of Electrical and Electronics Engineers (IEEE), Jun. 2018, pp. 660–669, ISBN: 978-1-5386-1354-2. doi: 10.1109/ICUAS.2018.8453453. [Online]. Available: <https://ieeexplore.ieee.org/document/8453453/> (visited on 12/12/2023).
- [40] S. Singh, S. Stappert, L. Bussler, M. Sippel, Y. C. Kucukosman, and S. Buckingham, “Full-Scale Simulation and Analysis of Formation Flight during In-Air-Capturing of a Winged Reusable Launch Vehicle,” *Journal of Space Safety Engineering*, vol. 9, no. 4, pp. 541–552, Dec. 2022, ISSN: 24688967. doi: 10.1016/j.jsse.2022.09.005. [Online]. Available: <https://linkinghub.elsevier.com/retrieve/pii/S2468896722001100> (visited on 11/27/2023).

- [41] S. Singh, S. Stappert, S. Buckingham, *et al.*, “Dynamic Modelling and Control of an Aerodynamically Controlled Capturing Device for ‘In-Air-Capturing’ of a Reusable Launch Vehicle,” presented at the 11th International ESA Conference on Guidance, Navigation & Control Systems (ESA GNC), Jun. 2021. [Online]. Available: https://www.researchgate.net/publication/353385379_Dynamic_Modelling_And_Control_Of_An_Aerodynamically_Controlled_Capturing_Device_For_'In-Air-Capturing'_Of_A_Reusable_Launch_Vehicle (visited on 11/27/2023).
- [42] M. Sippel, S. Stappert, L. Bussler, *et al.*, “Highly Efficient RLV-Return Mode In-Air-Capturing Progressing by Preparation of Subscale Flight Tests,” in *Proceedings of the 8th European Conference for Aeronautics and Space Sciences*, Madrid, Spain, Jul. 2019. DOI: 10.13009/EUCASS2019-750. [Online]. Available: <https://www.eucass.eu/doi/EUCASS2019-0750.pdf> (visited on 11/28/2023).
- [43] Y. C. Kucukosman, S. Lopes, S. Buckingham, *et al.*, “Aerodynamic Characterization of In-Air Capturing Vehicles Using CFD Simulations,” in *Proceedings of the 9th European Conference for Aeronautics and Space Sciences*, Lille, France, Jun. 2022. DOI: 10.13009/EUCASS2022-7473. [Online]. Available: <https://www.eucass.eu/doi/EUCASS2022-7473.pdf> (visited on 11/29/2023).
- [44] I. H. Abbott and A. E. Von Doenhoff, *Theory of Wing Sections*. New York, United States of America: Dover Publications, Inc., 1959, 705 pp., ISBN: 0-486-60586-8. [Online]. Available: https://www3.nd.edu/~ame40431/AME20211_2021/Other/AbbottDoenhoff_TheoryOfWingSectionsIncludingASummaryOfAirfoilData.pdf (visited on 08/09/2024).
- [45] S. Cain, “Tow Aircraft and Coupling Unit Design Description,” Deutsches Zentrum für Luft- und Raumfahrt, Bremen, Germany, FALCon D3.1, Mar. 26, 2020, p. 29. (visited on 11/30/2023).
- [46] T. Kuk, “Active Control of Aerial Refueling Drogue,” Ph.D. dissertation, Western Michigan University, Kalamazoo, United States of America, Apr. 2014, 157 pp. [Online]. Available: <https://scholarworks.wmich.edu/dissertations/256> (visited on 12/05/2023).
- [47] G. R. Flores, J. Escareno, R. Lozano, and S. Salazar, “Quad-Tilting Rotor Convertible MAV : Modeling and Real-time Hover Flight Control,” *Journal of Intelligent and Robotic Systems*, vol. 65, pp. 457–471, Jan. 1, 2012, ISSN: 978-94-007-3032-8. DOI: 10.1007/s10846-011-9589-x. [Online]. Available: https://www.researchgate.net/publication/220061685_Quad-Tilting_Rotor_Convertible_MAV_Modeling_and_Real-time_Hover_Flight_Control (visited on 08/09/2024).
- [48] Bureau International des Poids et Mesures, “Comptes Rendus des Séances de la Troisième Conférence Générale des Poids et Mesures,” Bureau International des Poids et Mesures, Paris, France, 1901, p. 104. [Online]. Available: <https://www.bipm.org/fr/committees/cg/cgpm/3-1901/resolution-2> (visited on 08/09/2024).
- [49] P. H. Zipfel, *Modeling and Simulation of Aerospace Vehicle Dynamics* (AIAA Education Series), 2nd ed. Reston, United States of America: American Institute of Aeronautics and Astronautics, Nov. 2006, vol. 54, 556 pp., ISBN: 978-1-56347-875-8. [Online]. Available: <https://asmedigitalcollection.asme.org/appliedmechanicsreviews/article/54/6/B101/458210/Modeling-and-Simulation-of-Aerospace-Vehicle> (visited on 07/09/2024).
- [50] S. Singh, L. Bussler, S. Callsen, S. Stappert, S. Lopes, and S. Buckingham, “A Superposition Approach to Aerodynamic Modelling of a Capturing Device used for In-Air Capturing of a Reusable Launch Vehicle,” in *Proceedings of the 9th European Conference for Aeronautics and Space Sciences*, Lille, France, Jun. 2022. [Online]. Available: <https://elib.dlr.de/187074/> (visited on 11/29/2023).
- [51] E. H. Lockwood, *A Book of Curves*. Cambridge, United Kingdom: Cambridge University Press, 1961, 210 pp., ISBN: 978-0-511-56934-0. [Online]. Available: <https://www.aproged.pt/biblioteca/ABookofCurvesLockwood.pdf> (visited on 08/09/2024).
- [52] E. J. Routh, *A Treatise on Analytical Statics*. Cambridge, United Kingdom: Cambridge University Press, 1891, vol. 1, 428 pp., ISBN: 978-1-139-23723-9.

- [53] Teufelberger Fiber Rope GmbH, *DuraTEN/DuraTEN+/HyperTEN/HyperTEN+ High Performance UHMWPE/Dyneema Fiber Ropes For Industrial Applications*, Jun. 2020. [Online]. Available: https://www.teufelberger.com/media/contentmanager/content/downloads/5000117_RZ_HyperTEN-DuraTEN_EN_Folder_A4_08_21_WEB.pdf (visited on 04/09/2024).
- [54] Météo France, "Fiche Climatologique: Statistiques 1991-2020 et Records," Direction de la Climatologie et des Services Climatiques, Toulouse, France, Aug. 6, 2024, p. 2. [Online]. Available: https://donneespubliques.meteofrance.fr/FichesClim/FICHECLIM_97304003.pdf (visited on 08/09/2024).
- [55] J. A. Curro II, "Automated Aerial Refueling Position Estimation Using a Scanning LiDAR," MSc Thesis, Air Force Institute of Technology, Dayton, United States of America, Mar. 22, 2012, 94 pp. [Online]. Available: <https://scholar.afit.edu/cgi/viewcontent.cgi?article=2102&context=etd> (visited on 12/05/2023).
- [56] T. G. Akshaya and S. Sreeja, "Multi-Sensor Data Fusion for Aerodynamically Controlled Vehicle Based on FGPM," *IFAC PapersOnLine*, vol. 53, no. 1, pp. 591–596, 2020, ISSN: 2405-8963. doi: 10.1016/j.ifacol.2020.06.099. [Online]. Available: <https://linkinghub.elsevier.com/retrieve/pii/S240589632030118X> (visited on 12/14/2023).
- [57] S. Krause, "Environment Perception Flight Test Description," Deutsches Zentrum für Luft- und Raumfahrt, Bremen, Germany, FALCon D8.1, Jan. 9, 2023, p. 27. (visited on 11/30/2023).
- [58] P. R. Thomas, U. Bhandari, S. Bullock, T. S. Richardson, and J. L. du Bois, "Advances in Air to Air Refuelling," *Progress in Aerospace Sciences*, vol. 71, pp. 14–35, Nov. 1, 2014, ISSN: 0376-0421. doi: 10.1016/j.paerosci.2014.07.001. [Online]. Available: <https://linkinghub.elsevier.com/retrieve/pii/S0376042114000657> (visited on 11/30/2023).
- [59] X. Xu, H. Duan, Y. Guo, and Y. Deng, "A Cascade Adaboost and CNN Algorithm for Drogue Detection in UAV Autonomous Aerial Refueling," *Neurocomputing*, vol. 408, pp. 121–134, Sep. 30, 2020, ISSN: 0925-2312. doi: 10.1016/j.neucom.2019.10.115. [Online]. Available: <https://linkinghub.elsevier.com/retrieve/pii/S0925231220303404> (visited on 12/07/2023).
- [60] S. Vendra, "Addressing Corner Detection Issues for Machine Vision Based UAV Aerial Refueling," MSc Thesis, West Virginia University, Morgantown, United States of America, 2006, 121 pp. [Online]. Available: <https://core.ac.uk/download/pdf/230486582.pdf> (visited on 12/07/2023).
- [61] S. Panzneri, F. Pascucci, and G. Ulivi, "An Outdoor Navigation System Using GPS and Inertial Platform," *IEEE/ASME Transactions on Mechatronics*, vol. 7, no. 2, pp. 134–142, Jun. 2002, ISSN: 1083-4435. doi: 10.1109/TMECH.2002.1011250. [Online]. Available: <https://doi.org/10.1109/TMECH.2002.1011250> (visited on 12/07/2023).
- [62] K. Gunnam, D. C. Hughes, J. Junkins, and N. Kehtornavaz, "A DSP Embedded Optical Navigation System," presented at the 6th International Conference on Signal Processing, vol. 2, Beijing, China, Aug. 2002, pp. 1735–1739, ISBN: 0-7803-7488-6. doi: 10.1109/ICOSP.2002.1180137. [Online]. Available: <https://ieeexplore.ieee.org/document/1180137> (visited on 12/07/2023).
- [63] M. Mammarella, G. Campa, M. R. Napolitano, B. Seanor, M. L. Fravolini, and L. Pollini, "GPS/MV Based Aerial Refueling for UAVs," presented at the 2008 AIAA Guidance, Navigation and Control Conference and Exhibit, Honolulu, United States of America, Aug. 18, 2008. doi: 10.2514/6.2008-7258. [Online]. Available: <https://arc.aiaa.org/doi/abs/10.2514/6.2008-7258> (visited on 12/06/2023).
- [64] J. Doebbler, J. Valasek, M. J. Monda, and H. Schaub, "Boom and Receptacle Autonomous Air Refueling Using Visual Snake Optical Sensor," presented at the 2006 AIAA Atmospheric Flight Mechanics Conference and Exhibit, Keystone, United States of America, Aug. 2006. doi: 10.2514/6.2006-6504. [Online]. Available: <https://arc.aiaa.org/doi/abs/10.2514/6.2006-6504> (visited on 12/07/2023).
- [65] J. Parry and S. Hubbard, "Review of Sensor Technology to Support Automated Air-to-Air Refueling of a Probe Configured Uncrewed Aircraft," *Sensors*, vol. 23, no. 2, p. 995, Jan. 15, 2023, ISSN: 1424-8220. doi: 10.3390/s23020995. [Online]. Available: <https://www.mdpi.com/1424-8220/23/2/995> (visited on 12/20/2023).

- [66] L. Lion, A. Caon, L. Olivieri, F. Branz, and A. Francesconi, "Kinematic Tests on a Docking Mechanism for Microsatellites," *CEAS Space Journal*, Jul. 21, 2023, ISSN: 1868-2510. doi: [10.1007/s12567-023-00516-w](https://doi.org/10.1007/s12567-023-00516-w). [Online]. Available: <https://doi.org/10.1007/s12567-023-00516-w> (visited on 12/07/2023).
- [67] J. H. Spencer, "Optical Tracking for Relative Positioning in Automated Aerial Refueling," MSc Thesis, Air Force Institute of Technology, Dayton, United States of America, Mar. 22, 2007, 93 pp. [Online]. Available: <https://core.ac.uk/reader/328161970> (visited on 12/05/2023).
- [68] C.-I. Chen and R. Stettner, "Drogue Tracking Using 3D Flash LIDAR for Autonomous Aerial Refueling," presented at the Laser Radar Technology and Applications XVI, vol. 8037, Orlando, United States of America: SPIE, Apr. 2011. doi: [10.1117/12.886572](https://doi.org/10.1117/12.886572). [Online]. Available: <https://doi.org/10.1117/12.886572> (visited on 12/08/2023).
- [69] J. M. Kelsey, J. Byrne, M. Cosgrove, S. Seereeram, and R. K. Mehra, "Vision-Based Relative Pose Estimation for Autonomous Rendezvous and Docking," presented at the 2006 IEEE Aerospace Conference, ISSN: 1095-323X, Big Sky, United States of America: Institute of Electrical and Electronics Engineers (IEEE), Mar. 2006, ISBN: 0-7803-9545-X. doi: [10.1109/AERO.2006.1655916](https://ieeexplore.ieee.org/document/1655916). [Online]. Available: <https://ieeexplore.ieee.org/document/1655916> (visited on 12/14/2023).
- [70] X. Wang, X. Kong, J. Zhi, Y. Chen, and X. Dong, "Real-Time Drogue Recognition and 3D Locating for UAV Autonomous Aerial Refueling Based on Monocular Machine Vision," *Chinese Journal of Aeronautics*, vol. 28, no. 6, pp. 1667–1675, Oct. 19, 2015, ISSN: 1000-9361. doi: [10.1016/j.cja.2015.10.006](https://linkinghub.elsevier.com/retrieve/pii/S1000936115001922). [Online]. Available: <https://linkinghub.elsevier.com/retrieve/pii/S1000936115001922> (visited on 12/07/2023).
- [71] H. Li and H. Duan, "Verification of Monocular and Binocular Pose Estimation Algorithms in Vision-Based UAVs Autonomous Aerial Refueling System," *Science China Technological Sciences*, vol. 59, no. 11, pp. 1730–1738, Nov. 2016, ISSN: 1869-1900. doi: [10.1007/s11431-016-6097-z](https://doi.org/10.1007/s11431-016-6097-z). [Online]. Available: <https://doi.org/10.1007/s11431-016-6097-z> (visited on 12/07/2023).
- [72] S. Krause and S. Cain, "UAV Pre-Study for In-Air-Capturing Maneuver," presented at the 2020 IEEE Aerospace Conference, ISSN: 1095-323X, Big Sky, United States of America, Mar. 2020. doi: [10.1109/AERO47225.2020.9172769](https://ieeexplore.ieee.org/document/9172769). [Online]. Available: <https://ieeexplore.ieee.org/document/9172769> (visited on 11/28/2023).
- [73] C. Harris and M. Stephens, "A Combined Corner and Edge Detector," in *Proceedings of the Alvey Vision Conference*, Manchester, United Kingdom: Alvey Vision Club, Sep. 1988, pp. 23.1–23.6. doi: [10.5244/C.2.23](http://www.bmva.org/bmvc/1988/avc-88-023.html). [Online]. Available: <http://www.bmva.org/bmvc/1988/avc-88-023.html> (visited on 12/30/2023).
- [74] S. M. Smith and J. M. Brady, "SUSAN - A New Approach to Low Level Image Processing," Defence Research Agency, Farnborough, United Kingdom, Technical Report TR95SMS1c, 1995, p. 58. [Online]. Available: <https://citeseerx.ist.psu.edu/document?repid=rep1&type=pdf&doi=35eb5c718b986952ba3c7c8d94cf4e34ac750661> (visited on 12/30/2023).
- [75] C.-P. Lu, G. D. Hager, and E. Mjolsness, "Fast and Globally Convergent Pose Estimation from Video Images," *IEEE Transactions on Pattern Analysis and Machine Intelligence*, vol. 22, no. 6, pp. 610–622, Jun. 2000, ISSN: 0162-8828. doi: [10.1109/34.862199](https://ieeexplore.ieee.org/document/862199/). [Online]. Available: <https://ieeexplore.ieee.org/document/862199/> (visited on 12/30/2023).
- [76] Y. Ma, R. Zhao, E. Liu, Z. Zhang, and K. Yan, "A Novel Autonomous Aerial Refueling Drogue Detection and Pose Estimation Method Based on Monocular Vision," *Measurement*, vol. 136, pp. 132–142, Mar. 2019, ISSN: 0263-2241. doi: [10.1016/j.measurement.2018.12.060](https://linkinghub.elsevier.com/retrieve/pii/S0263224118312053). [Online]. Available: <https://linkinghub.elsevier.com/retrieve/pii/S0263224118312053> (visited on 12/07/2023).
- [77] S. M. Khanafseh and B. Pervan, "Autonomous Airborne Refueling of Unmanned Air Vehicles Using the Global Positioning System," *Journal of Aircraft*, vol. 44, no. 5, pp. 1670–1682, Sep. 2007, ISSN: 0021-8669. doi: [10.2514/1.28195](https://arc.aiaa.org/doi/10.2514/1.28195). [Online]. Available: <https://arc.aiaa.org/doi/10.2514/1.28195> (visited on 12/12/2023).

- [78] X. Wang, X. Dong, X. Kong, J. Li, and B. Zhang, "Drogue Detection for Autonomous Aerial Refueling Based on Convolutional Neural Networks," *Chinese Journal of Aeronautics*, vol. 30, no. 1, pp. 380–390, Feb. 2017, issn: 1000-9361. doi: 10.1016/j.cja.2016.12.022. [Online]. Available: <https://linkinghub.elsevier.com/retrieve/pii/S1000936116302412> (visited on 12/07/2023).
- [79] J. L. Junkins, D. C. Hughes, K. P. Wazni, and V. Pariyapong, "Vision-Based Navigation for Rendezvous, Docking and Proximity Operations," in *Proceedings of the 4th International Conference on Dynamics and Control of Space Structures*, vol. 101, Cranfield, United Kingdom, May 1999. [Online]. Available: https://www.researchgate.net/publication/2497010_Vision-Based_Navigation_For_Rendezvous_Docking_And_Proximity_Operations (visited on 12/12/2023).
- [80] R. Mati, L. Pollini, A. Lunghi, M. Innocenti, and G. Campa, "Vision-Based Autonomous Probe and Drogue Aerial Refueling," presented at the 14th Mediterranean Conference on Control and Automation, Ancona, Italy: Institute of Electrical and Electronics Engineers (IEEE), Jun. 2006, ISBN: 978-0-9786720-1-0. doi: 10.1109/MED.2006.328794. [Online]. Available: <http://ieeexplore.ieee.org/document/4124967/> (visited on 12/12/2023).
- [81] C.-I. Chen, R. Koseluk, C. Buchanan, A. Duerner, B. Jeppesen, and H. Laux, "Autonomous Aerial Refueling Ground Test Demonstration - A Sensor-in-the-Loop, Non-Tracking Method," *Sensors*, vol. 15, no. 5, pp. 10 948–10 972, May 11, 2015, issn: 1424-8220. doi: 10.3390/s150510948. [Online]. Available: <https://www.mdpi.com/1424-8220/15/5/10948> (visited on 12/07/2023).
- [82] M. Mammarella, G. Campa, M. R. Napolitano, M. L. Fravolini, Y. Gu, and M. G. Perhinschi, "Machine Vision/GPS Integration Using EKF for the UAV Aerial Refueling Problem," *IEEE Transactions on Systems, Man, and Cybernetics - Part C: Applications and Reviews*, vol. 38, no. 6, pp. 791–801, Nov. 2008, issn: 1558-2442. doi: 10.1109/TSMCC.2008.2001693. [Online]. Available: <https://ieeexplore.ieee.org/document/4633664> (visited on 12/13/2023).
- [83] D. T. Johnson, S. L. Nykl, and J. F. Raquet, "Combining Stereo Vision and Inertial Navigation for Automated Aerial Refueling," *Journal of Guidance, Control, and Dynamics*, vol. 40, no. 9, pp. 2250–2259, Sep. 2017, issn: 0731-5090. doi: 10.2514/1.G002648. [Online]. Available: <https://arc.aiaa.org/doi/10.2514/1.G002648> (visited on 12/13/2023).
- [84] X. Wang, N. Cui, and J. Guo, "INS/VisNav/GPS Relative Navigation System for UAV," *Aerospace Science and Technology*, vol. 28, no. 1, pp. 242–248, Nov. 16, 2012, issn: 1270-9638. doi: 10.1016/j.ast.2012.11.004. [Online]. Available: <https://linkinghub.elsevier.com/retrieve/pii/S127096381200185X> (visited on 12/11/2023).
- [85] Y. Krispin and M. Velger, "Controllable Hose-and-Drogue In-Flight Refueling System," European pat. 1 094 001 A2, Apr. 25, 2001. [Online]. Available: <https://patents.google.com/patent/EP1094001A2/en> (visited on 12/05/2023).
- [86] A. Katake and H. Choi, "VisNav100: A Robust, Compact Imaging Sensor for Enabling Autonomous Air-to-Air Refueling of Aircraft and Unmanned Aerial Vehicles," in *Proceedings Volume 7538, Image Processing: Machine Vision Applications III*, San Jose, United States of America, Jan. 28, 2010, p. 753 809. doi: 10.1117/12.839120. [Online]. Available: <http://proceedings.spiedigitallibrary.org/proceeding.aspx?doi=10.1117/12.839120> (visited on 06/13/2024).
- [87] J. Valasek, K. Gunnam, J. Kimmet, M. D. Tandale, J. L. Junkins, and D. Hughes, "Vision-Based Sensor and Navigation System for Autonomous Air Refueling," *Journal of Guidance, Control, and Dynamics*, vol. 28, no. 5, pp. 979–989, Sep. 2005, issn: 0731-5090. doi: 10.2514/1.11934. [Online]. Available: <https://arc.aiaa.org/doi/10.2514/1.11934> (visited on 12/12/2023).
- [88] Y. M. Park, H. C. Bang, Y. H. Seo, and B. H. Kim, "Development of Surface-Mount-Type Crown-Shaped Lens for Reducing Glare Effect of Light-emitting Diode Light Source," *Journal of the Korean Society of Manufacturing Technology Engineers*, vol. 23, no. 1, pp. 64–68, Feb. 15, 2014, issn: 2233-6036. doi: 10.7735/ksmte.2014.23.1.064. [Online]. Available: https://www.researchgate.net/publication/264170955_Development_of_Surface-mount-type-Crown-shaped-Lens_for-Reducing-Glare-Effect-of-Light-emitting-Diode-Light-Source (visited on 08/09/2024).

- [89] F. L. Pedrotti and L. S. Pedrotti, *Introduction to Optics*, 2nd ed. Cambridge, United Kingdom: Cambridge University Press, Dec. 21, 2017, ISBN: 978-1-108-55249-3. [Online]. Available: <https://www.cambridge.org/highereducation/books/introduction-to-optics/8923BB7830091A58316177E029C5D420> (visited on 08/09/2024).
- [90] C. Perwass, *Geometric Algebra with Applications in Engineering* (Geometry and Computing 4). Berlin, Germany: Springer, Dec. 3, 2008, 389 pp., Google-Books-ID: 8IOypFqEkPMC, ISBN: 978-3-540-89067-6. [Online]. Available: https://books.google.be/books?id=8IOypFqEkPMC&pg=PA83&redir_esc=y#v=onepage&q&f=false (visited on 08/09/2024).
- [91] M. Sippel, L. Bussler, S. Krause, S. Cain, and S. Stappert, "Bringing Highly Efficient RLV-Return Mode "In-Air-Capturing" to Reality," presented at the 1st International Conference on High-Speed Vehicle Science Technology (HiSST), Moscow, Russia, Nov. 2018. [Online]. Available: <https://elib.dlr.de/125921/> (visited on 11/28/2023).
- [92] M. Sippel, S. Stappert, and S. Singh, "RLV-Return Mode "In-Air-Capturing" and Definition of its Development Roadmap," in *Proceedings of the 9th European Conference for Aeronautics and Space Sciences*, Lille, France, Jun. 2022. [Online]. Available: https://elib.dlr.de/187081/1/EUCASS2022-_RLV-Return_Mode_In-Air-Capturing_and_Definition_of_its_Development_Roadmap.pdf (visited on 12/04/2023).
- [93] GeoHack. "Guiana Space Centre." (), [Online]. Available: https://geohack.toolforge.org/geohack.php?pagename=Guiana_Space_Centre¶ms=5.169_N_52.6903_W_ (visited on 08/09/2024).
- [94] G. V. Brummelen, *Heavenly Mathematics: The Forgotten Art of Spherical Trigonometry*. Princeton, United States of America: Princeton University Press, 2013, 218 pp., Google-Books-ID: 0BCCz8Sx5wkC, ISBN: 978-0-691-14892-2.
- [95] H. Moritz, "Geodetic Reference System 1980," *Journal of Geodesy*, vol. 74, no. 1, pp. 128–133, Mar. 13, 2000, ISSN: 1432-1394. DOI: [10.1007/s001900050278](https://doi.org/10.1007/s001900050278). [Online]. Available: <https://doi.org/10.1007/s001900050278> (visited on 08/09/2024).
- [96] Holybro. "Pixhawk 6X," Holybro Docs. (Apr. 16, 2024), [Online]. Available: <https://docs.holybro.com/autopilot/pixhawk-6x> (visited on 08/09/2024).
- [97] Holybro. "H-RTK F9P Series," Holybro Docs. (Mar. 27, 2024), [Online]. Available: <https://docs.holybro.com/gps-and-rtk-system/f9p-h-rtk-series> (visited on 08/09/2024).
- [98] Microhard, *P840: Miniature 840 to 845 MHz Wireless Modem*, 2017. [Online]. Available: <https://www.microhardcorp.com/brochures/P840.Brochure.Rev.1.2.pdf> (visited on 08/09/2024).
- [99] Holybro. "Microhard Telemetry Radio," Holybro Store. (2024), [Online]. Available: <https://holybro.com/products/microhard-radio> (visited on 08/09/2024).
- [100] J. Roskam, H. Eijsink, and M. Rice, "A Study of Low-Cost Reliable Actuators for Light Aircraft," University of Kansas Center for Research, Kansas, United States of America, KU-FRL-351, Apr. 1, 1978, p. 162. [Online]. Available: <https://ntrs.nasa.gov/api/citations/19780012167/downloads/19780012167.pdf> (visited on 08/09/2024).
- [101] L. T. Nguyen, M. E. Ogburn, W. P. Gilbert, K. S. Kibler, P. W. Brown, and P. L. Deal, "Simulator Study of Stall/Post-Stall Characteristics of a Fighter Airplane with Relaxed Longitudinal Static Stability," NASA Langley Research Center, Hampton, United States of America, Technical Paper NASA-TP-1538, Dec. 1979, p. 233. [Online]. Available: <https://ntrs.nasa.gov/api/citations/19800005879/downloads/19800005879.pdf> (visited on 08/11/2024).
- [102] ebm-papst, *ECI-63.20-B00-K4*, 2024. [Online]. Available: <https://docs.rs-online.com/e432/0900766b816faf00.pdf> (visited on 08/09/2024).
- [103] *Handbook of Small Electric Motors*, in collab. with W. H. Yeadon and A. W. Yeadon. New York, United States of America: McGraw-Hill, 2001, 1146 pp., ISBN: 978-0-07-072332-0. [Online]. Available: <http://archive.org/details/handbookofsmalle0000unse> (visited on 08/09/2024).
- [104] S. Dereyne, P. Defreyne, E. Algoet, S. Derammelaere, and K. Stockman, "Efficiency Measurement Campaign on Gearboxes," in *Energy Efficiency in Motor Driven Systems, Proceedings*, Helsinki, Finland, Sep. 2015. [Online]. Available: <http://hdl.handle.net/1854/LU-7053979> (visited on 08/09/2024).

- [105] N. Sangeetha, V. M. Brathikan, D. Gideon, and B. Sangeethkumar, "Experimental Investigation of Frictional Force and Coefficient of Friction for Brass, Titanium and Steel Employed under Several Lubricants," *Journal of Ceramic Processing Research*, vol. 23, no. 5, pp. 1–8, 2022. doi: 10.36410/jcpr.2022.23.5.1. [Online]. Available: https://www.researchgate.net/publication/364359120_Experimental_investigation_of_frictional_force_and_coefficient_of_friction_for_brass_titanium_and_steel_employed_under_several_lubricants (visited on 08/09/2024).
- [106] Festo AG & Co. KG, *Electric Cylinder ESBF-BS-63-300-5P*, Jul. 16, 2020. [Online]. Available: <https://docs.rs-online.com/f6fd/A700000006958513.pdf> (visited on 04/29/2024).
- [107] Faulhaber, *Linear DC-Servomotors with Analog Hall Sensors*, Nov. 22, 2023. [Online]. Available: https://www.faulhaber.com/fileadmin/Import/Media/EN_LM1247_11_FMM.pdf (visited on 08/09/2024).
- [108] L. Dupré, *Elektromagnetische Energieomzetting*. Ghent, Belgium: Ghent University, Sep. 15, 2020, 283 pp.
- [109] Baumer, *U300.D50-DPMJ.72N Ultrasonic Distance Measuring Sensor*, Jan. 25, 2024. [Online]. Available: https://www.baumer.com/medias/__secure__/Baumer_U300.D50-DPMJ.72N_EN_20210813_DS.pdf?mediaPK=9027376250910 (visited on 08/09/2024).
- [110] Omron, *E3Z-G Grooved-Type Photoelectric Sensor with Built-In Amplifier*, 2023. [Online]. Available: https://www.ia.omron.com/data_pdf/cat/e3z-g_ds_e_9_4_csm434.pdf?id=1168 (visited on 08/09/2024).
- [111] C. C. Kwasi-Effah and T. Rabczuk, "Dimensional Analysis and Modelling of Energy Density of Lithium-Ion Battery," *Journal of Energy Storage*, vol. 18, pp. 308–315, Aug. 2018, issn: 2352-152X. doi: 10.1016/j.est.2018.05.002. [Online]. Available: <https://www.sciencedirect.com/science/article/pii/S2352152X18301282> (visited on 08/09/2024).
- [112] N. Muralidharan, E. C. Self, M. Dixit, *et al.*, "Next-Generation Cobalt-Free Cathodes – A Prospective Solution to the Battery Industry's Cobalt Problem," *Advanced Energy Materials*, vol. 12, no. 9, p. 2103050, Mar. 3, 2022, issn: 1614-6840. doi: 10.1002/aenm.202103050. [Online]. Available: <https://onlinelibrary.wiley.com/doi/abs/10.1002/aenm.202103050> (visited on 08/09/2024).
- [113] P. Stenzel, M. Baumann, J. Fleeer, B. Zimmermann, and M. Weil, "Database Development and Evaluation for Techno-Economic Assessments of Electrochemical Energy Storage Systems," presented at the 2014 IEEE International Energy Conference (ENERGYCON), Pages: 1342, Dubrovnik, Croatia, May 2014, isbn: 978-1-4799-2449-3. doi: 10.1109/ENERGYCON.2014.6850596. [Online]. Available: https://www.researchgate.net/publication/269297116_Database_development_and_evaluation_for techno-economic_assessments_of_electrochemical_energy_storage_systems (visited on 08/09/2024).
- [114] PX4. "Vibration Isolation," PX4 Guide. (2024), [Online]. Available: https://docs.px4.io/main/en/assembly/vibration_isolation.html (visited on 08/09/2024).
- [115] J. J. Zipay, C. T. Modlin, and C. E. Larsen, "The Ultimate Factor of Safety for Aircraft and Spacecraft - Its History, Applications and Misconceptions," in *Proceedings of the 57th AIAA/ASCE/AHS/ASC Structures, Structural Dynamics, and Materials Conference*, San Diego, United States of America: American Institute of Aeronautics and Astronautics, Jan. 4, 2016, isbn: 978-1-62410-392-6. doi: 10.2514/6.2016-1715. [Online]. Available: <https://arc.aiaa.org/doi/10.2514/6.2016-1715> (visited on 04/15/2024).
- [116] M. Sippel and J. Klevanski, "Simulation of Dynamic Control Environments of the In-Air-Capturing Mechanism," presented at the 6th International Symposium on Launcher Technology, München, Germany, Nov. 2005. [Online]. Available: <https://elib.dlr.de/119176/> (visited on 11/28/2023).
- [117] G. Zhan, S. Niu, W. Zhang, *et al.*, "A Docking Mechanism Based on a Stewart Platform and Its Tracking Control Based on Information Fusion Algorithm," *Sensors*, vol. 22, no. 3, p. 770, Jan. 20, 2022, issn: 1424-8220. doi: 10.3390/s22030770. [Online]. Available: <https://www.mdpi.com/1424-8220/22/3/770> (visited on 12/07/2023).

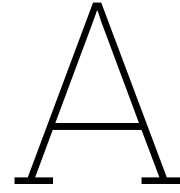
- [118] I. O'Hara, J. Paulos, J. Davey, *et al.*, "Self-Assembly of a Swarm of Autonomous Boats into Floating Structures," presented at the 2014 IEEE International Conference on Robotics and Automation (ICRA), Hong Kong, China: Institute of Electrical and Electronics Engineers (IEEE), Jun. 2014, pp. 1234–1240, ISBN: 978-1-4799-3685-4. DOI: [10.1109/ICRA.2014.6907011](https://doi.org/10.1109/ICRA.2014.6907011). [Online]. Available: <http://ieeexplore.ieee.org/document/6907011/> (visited on 12/12/2023).
- [119] J. Sugihara, T. Nishio, K. Nagato, M. Nakao, and M. Zhao, "Design, Control, and Motion Strategy of TRADY: Tilted-Rotor-Equipped Aerial Robot With Autonomous In-Flight Assembly and Disassembly Ability," *Advanced Intelligent Systems*, vol. 5, no. 10, p. 2300191, Jul. 20, 2023, ISSN: 2640-4567. DOI: [10.1002/aisy.202300191](https://doi.org/10.1002/aisy.202300191). [Online]. Available: <https://onlinelibrary.wiley.com/doi/abs/10.1002/aisy.202300191> (visited on 12/11/2023).
- [120] A. J. Choi, H.-H. Yang, and J.-H. Han, "Study on Robust Aerial Docking Mechanism with Deep Learning Based Drogue Detection and Docking," *Mechanical Systems and Signal Processing*, vol. 154, p. 107579, Jan. 7, 2021, ISSN: 0888-3270. DOI: [10.1016/j.ymssp.2020.107579](https://doi.org/10.1016/j.ymssp.2020.107579). [Online]. Available: <https://linkinghub.elsevier.com/retrieve/pii/S0888327020309651> (visited on 12/07/2023).
- [121] J. W. Nichols, L. Sun, R. W. Beard, and T. McLain, "Aerial Rendezvous of Small Unmanned Aircraft Using a Passive Towed Cable System," *Journal of Guidance, Control, and Dynamics*, vol. 37, no. 4, pp. 1131–1142, Mar. 21, 2014, ISSN: 0731-5090. DOI: [10.2514/1.62220](https://doi.org/10.2514/1.62220). [Online]. Available: <https://arc.aiaa.org/doi/10.2514/1.62220> (visited on 12/12/2023).
- [122] A. Boesso and A. Francesconi, "ARCADE Small-Scale Docking Mechanism for Micro-Satellites," *Acta Astronautica*, vol. 86, pp. 77–87, May 2013, ISSN: 0094-5765. DOI: [10.1016/j.actaastro.2013.01.006](https://doi.org/10.1016/j.actaastro.2013.01.006). [Online]. Available: <https://linkinghub.elsevier.com/retrieve/pii/S0094576513000180> (visited on 12/11/2023).
- [123] J. C. Pavlich, P. Tchoryk, A. B. Hays, and G. Wassick, "KC-135 Zero G Testing of a Micro Satellite Docking Mechanism," in *SPIE Proceedings Vol. 5088: Space Systems Technology and Operations*, vol. 5088, Orlando, United States of America: SPIE, Aug. 2003, pp. 31–42. DOI: [10.1117/12.497845](https://doi.org/10.1117/12.497845). [Online]. Available: <http://proceedings.spiedigitallibrary.org/proceeding.aspx?articleid=763710> (visited on 12/14/2023).
- [124] B. J. Theiss, "A Comparison of In-flight Refueling Methods for Fighter Aircraft: Boom-Receptacle vs. Probe-and-Drogue," *The Collegiate Aviation Review International*, vol. 25, no. 2, 2007, ISSN: 1523-5955. DOI: [10.22488/okstate.18.100498](https://doi.org/10.22488/okstate.18.100498). [Online]. Available: <https://ojs.library.okstate.edu/osu/index.php/CARI/article/view/7559> (visited on 12/11/2023).
- [125] A. Adomeit, M. Lakshmanan, P. Seefeldt, *et al.*, "Structures for Modular and Serviceable Spacecraft Systems," in *Proceedings of the 12th European Conference on Spacecraft Structures, Materials and Environmental Testing*, Noordwijk, The Netherlands, Mar. 2012, p. 177, ISBN: 978-92-9092-255-1. [Online]. Available: <https://articles.adsabs.harvard.edu/pdf/2012ESASP.691E.177A> (visited on 12/11/2023).
- [126] J. Cook, V. Aksamentov, T. Hoffman, and W. Bruner, "ISS Interface Mechanisms and their Heritage," presented at the AIAA SPACE 2011 Conference and Exposition, Long Beach, United States of America: American Institute of Aeronautics and Astronautics, Sep. 2011, ISBN: 978-1-60086-953-2. DOI: [10.2514/6.2011-7150](https://doi.org/10.2514/6.2011-7150). [Online]. Available: <https://arc.aiaa.org/doi/10.2514/6.2011-7150> (visited on 12/11/2023).
- [127] M. Cislighi and C. Santini, "The Russian Docking System and the Automated Transfer Vehicle: a Safe Integrated Concept," 3rd IAASS Conference, Rome, Italy, Oct. 2008. [Online]. Available: <https://www.pdfsearch.io/document/Videometer/1F86> (visited on 12/12/2023).
- [128] L. Olivieri and A. Francesconi, "Design and Test of a Semiandrogynous Docking Mechanism for Small Satellites," *Acta Astronautica*, vol. 122, pp. 219–230, Feb. 15, 2016, ISSN: 0094-5765. DOI: [10.1016/j.actaastro.2016.02.004](https://doi.org/10.1016/j.actaastro.2016.02.004). [Online]. Available: <https://linkinghub.elsevier.com/retrieve/pii/S0094576516000515> (visited on 12/11/2023).

- [129] L. Olivieri, F. Branz, L. Savioli, and A. Francesconi, "Conceptual Design of Small Spacecraft Docking Mechanism Actuated by Electroactive Polymers," presented at the 2nd IAA Conference on University Satellite Missions and Cubesat Workshop, Rome, Italy, Feb. 2013. [Online]. Available: https://www.researchgate.net/publication/264158328_Conceptual_Design_of_Small_Spacecraft_Docking_Mechanism_Actuated_by_Electroactive_Polymers (visited on 12/11/2023).
- [130] S. R. Donahoe, *International Docking System Standard (IDSS): Interface Definition Document (IDD)*, version Revision F, Jul. 2022. [Online]. Available: https://www.internationaldockingstandard.com/download/IDSS_IDD_Revision_F.pdf (visited on 12/11/2023).
- [131] M. Barbeta, A. Boesso, F. Branz, *et al.*, "ARCADE-R2 Experiment on Board BEXUS 17 Stratospheric Balloon," *CEAS Space Journal*, vol. 7, no. 3, pp. 347–358, Mar. 31, 2015, ISSN: 1868-2510. DOI: 10.1007/s12567-015-0083-3. [Online]. Available: <https://doi.org/10.1007/s12567-015-0083-3> (visited on 12/11/2023).
- [132] A. J. Choi, J. Park, and J.-H. Han, "Automated Aerial Docking System Using Onboard Vision-Based Deep Learning," *Journal of Aerospace Information Systems*, vol. 19, no. 6, pp. 421–436, Jun. 2022, ISSN: 2327-3097. DOI: 10.2514/1.I011053. [Online]. Available: <https://doi.org/10.2514/1.I011053> (visited on 12/11/2023).
- [133] L. Rodgers, N. Hoff, E. Jordan, M. Heiman, and D. W. Miller, "A Universal Interface for Modular Spacecraft," presented at the 19th Small Satellite Conference, Logan, United States of America, Aug. 2005. [Online]. Available: <https://digitalcommons.usu.edu/smallsat/2005/all2005/4> (visited on 12/11/2023).
- [134] F. Branz, L. Olivieri, F. Sansone, and A. Francesconi, "Miniature Docking Mechanism for CubeSats," *Acta Astronautica*, vol. 176, pp. 510–519, Nov. 2020, ISSN: 0094-5765. DOI: 10.1016/j.actaastro.2020.06.042. [Online]. Available: <https://linkinghub.elsevier.com/retrieve/pii/S0094576520304082> (visited on 12/11/2023).
- [135] H. Wittel, D. Jannasch, J. Vossiek, and C. Spura, *Roloff/Matek Machineonderdelen: Tabellenboek*, 6th ed. Amsterdam, the Netherlands: Boom, 2021, 264 pp., ISBN: 978-90-244-2868-7.
- [136] J. E. Hatch, *Aluminum: Properties and Physical Metallurgy*, 1st ed. American Society for Metals, May 1984, 424 pp., ISBN: 978-0-87170-176-3. [Online]. Available: <https://rayanmobadel.com/wp-content/uploads/2021/11/Aluminum-Properties-and-Physical-Metallurgy-by-John-E.-Hatch.pdf> (visited on 08/09/2024).
- [137] A. C. Ugural and S. K. Fenster, *Advanced Strength and Applied Elasticity*, 4th ed. Upper Saddle River, United States of America: Pearson Education, Jan. 30, 2003, 872 pp., ISBN: 978-0-13-244052-3.
- [138] J. G. Leishman, *Introduction to Aerospace Flight Vehicles*. Embry-Riddle Aeronautical University, Jan. 1, 2023, 2485 pp., Book Title: Introduction to Aerospace Flight Vehicles Publisher: Embry-Riddle Aeronautical University, ISBN: 979-8-9852614-0-0. [Online]. Available: <https://eaglepubs.erau.edu/introductiontoaerospaceflightvehicles/chapter/aerospace-structures/> (visited on 04/15/2024).
- [139] S. Kamle, R. Kitey, P. M. Mohite, C. S. Upadhyay, C. Venkatesan, and D. Yadav, "Design of Aircraft Structures: An Overview," in *Aerospace Materials and Material Technologies*, ser. Indian Institute of Metals Series (IIMS), N. E. Prasad and R. J. H. Wanhill, Eds., vol. 2, 2 vols., Singapore: Springer, 2017, pp. 231–250, ISBN: 978-981-10-2143-5. DOI: 10.1007/978-981-10-2143-5_12. [Online]. Available: https://doi.org/10.1007/978-981-10-2143-5_12 (visited on 04/15/2024).
- [140] ACE Stoßdämpfer GmbH, *ACE Damping Technology: Main Catalogue 2017*, Jul. 2017. [Online]. Available: https://www.ace-ace.de/media/acedownloads/ACE_Main-Catalogue-2017-EN_20210826.pdf (visited on 04/15/2024).
- [141] P. Verleysen, *Mechanica van Structuren*. Ghent, Belgium: Ghent University, 2021, 231 pp.
- [142] Ewellix, *Linear Bearings, Units and Shafts Catalogue*, Jan. 2023. [Online]. Available: https://www.dumotion.eu/pdf/ewellix_hardened_precision_shafts_catalog_ljm-ljmh-ljms-ljmr-ljt.pdf (visited on 08/09/2024).

- [143] Baumer, *Mounting Plate Series 300 and 12 mm*, Aug. 5, 2023. [Online]. Available: https://www.baumer.com/medias/__secure__/Baumer_Mounting-plate-series-300-and-%C3%B812-mm_EN_20230508_DS.pdf?mediaPK=9068135514142 (visited on 08/09/2024).
- [144] PacSci EMC, *Explosive Bolt Product Family*, 2024. [Online]. Available: <https://psemc.com/wp-content/uploads/2018/10/Explosive-Bolts-Datasheet.pdf> (visited on 08/09/2024).
- [145] Pyroalliance, *Explosive Bolts*, 2021. [Online]. Available: <https://pyroalliance.ariane.group/wp-content/uploads/sites/3/2021/09/Fiche-EXPLOSIVE-BOLTS.pdf> (visited on 08/09/2024).
- [146] Ensign-Bickford. "Separation Bolt Series," Ensign-Bickford Aerospace & Defense. (Feb. 14, 2020), [Online]. Available: <https://www.ebad.com/separation-bolt-series/> (visited on 08/09/2024).
- [147] D. Ferwerda, S. McLaughlin, J. Ingmire, *et al.*, "Aerial Refueling Probe/Drogue System," Aerial Refueling Systems Advisory Group (ARSAG), Xenia, United States of America, Technical Report ARSAG Document No. 04-06-18, Oct. 15, 2018, p. 22. [Online]. Available: <https://apps.dtic.mil/sti/pdfs/AD1064517.pdf> (visited on 12/14/2023).
- [148] K. Salehi Paniagua, P. García-Fogeda, and F. Arévalo, "Aeroelastic Stability of an Aerial Refueling Hose-Drogue System with Aerodynamic Grid Fins," *Aerospace*, vol. 10, no. 5, p. 481, May 18, 2023, ISSN: 2226-4310. doi: 10.3390/aerospace10050481. [Online]. Available: <https://www.mdpi.com/2226-4310/10/5/481> (visited on 12/07/2023).
- [149] E. N. Enig and J. W. Enig, "Hose-and-Drogue In-Flight Refueling System," U.S. Patent 2006/0065785 A1, Mar. 30, 2006. [Online]. Available: <https://patents.google.com/patent/US20060065785A1/en> (visited on 12/05/2023).
- [150] W. L. Kirkland and E. Reed, "Stabilized Controllable Drogue for Aerial Flight Refueling," U.S. Patent 2011/0226905 A1, Sep. 22, 2011. [Online]. Available: <https://patents.google.com/patent/US20110226905/en> (visited on 12/05/2023).
- [151] W. R. Williamson, E. Reed, G. J. Glenn, S. M. Stecko, J. Musgrave, and J. M. Takacs, "Controllable Drogue for Automated Aerial Refueling," *Journal of Aircraft*, vol. 47, no. 2, pp. 515–527, Mar. 2010, ISSN: 0021-8669. doi: 10.2514/1.44758. [Online]. Available: <https://arc.aiaa.org/doi/10.2514/1.44758> (visited on 11/28/2023).
- [152] J. F. Takacs, S. M. Stecko, G. R. Jefferson, G. A. Roberts, and J. D. Shoore, "Controllable Refueling Drogues and Associated Systems and Methods," European pat. 1 736 407 A1, Dec. 27, 2006. [Online]. Available: <https://patents.google.com/patent/EP1736407A1/en> (visited on 12/18/2023).
- [153] M. S. Feldmann, "Controllable Drogue," U.S. Patent 2010/0001124 A1, Jan. 7, 2010. [Online]. Available: <https://patents.google.com/patent/US20100001124A1/en> (visited on 12/05/2023).
- [154] F. Saggio III, W. B. Ribbens, and K. K. Ooi, "Stabilization of a Drogue Body," U.S. Patent 2005/0269456 A1, Dec. 8, 2005. [Online]. Available: <https://patents.google.com/patent/US20050269456A1/en> (visited on 12/05/2023).
- [155] M. T. Vernacchia and K. J. Mathesius, "Strategies for Reuse of Launch Vehicle First Stages," in *Proceedings of the International Astronautical Congress*, Bremen, Germany, Oct. 2018. [Online]. Available: https://github.com/mvernacc/lvreuse/blob/master/paper/IAC-18-D-2-4-3_strategies_for_reuse_of_launch_vehicle_first_stages.pdf (visited on 12/08/2023).
- [156] J. Amos, "Airbus Unveils 'Adeline' Reusable Rocket Concept," *BBC News*, Jun. 5, 2016. [Online]. Available: <https://www.bbc.com/news/science-environment-33006056> (visited on 12/29/2023).
- [157] M. M. Ragab, F. M. Cheatwood, S. J. Hughes, and A. Lowry, "Launch Vehicle Recovery and Reuse," presented at the AIAA SPACE 2015 Conference and Exposition, Pasadena, United States of America: American Institute of Aeronautics and Astronautics, Sep. 2015. doi: 10.2514/6.2015-4490. [Online]. Available: <https://arc.aiaa.org/doi/abs/10.2514/6.2015-4490> (visited on 11/30/2023).

- [158] “Europe’s Spaceport,” The European Space Agency. (2023), [Online]. Available: https://www.esa.int/Enabling_Support/Space_Transportation/Europe_s_Spaceport/Europe_s_Spaceport2 (visited on 12/29/2023).
- [159] J. Costa. “Launch Services Program Launch Sites,” NASA. Section: Launch Services Program. (Sep. 29, 2023), [Online]. Available: <https://www.nasa.gov/kennedy/launch-services-program/launch-services-program-launch-sites/> (visited on 12/29/2023).
- [160] S. Clark. “SpaceX Nails 200th Rocket Landing After Launch With 72 Small Satellites,” Spaceflight Now. (Jun. 12, 2023), [Online]. Available: <https://spaceflightnow.com/2023/06/12/spacex-nails-200th-rocket-landing-after-launch-with-72-small-satellites/> (visited on 12/29/2023).
- [161] S. Clark. “Blue Origin’s Suborbital Rocket Flies for First Time in 15 Months,” Ars Technica. (Dec. 19, 2023), [Online]. Available: <https://arstechnica.com/space/2023/12/blue-origins-suborbital-rocket-flies-for-first-time-in-15-months/> (visited on 12/29/2023).
- [162] “SpaceX - Mission,” SpaceX. (2023), [Online]. Available: <http://www.spacex.com> (visited on 12/29/2023).
- [163] “SpaceX - Starship,” SpaceX. (2023), [Online]. Available: <http://www.spacex.com> (visited on 12/29/2023).
- [164] M. Sippel, U. Atanassov, I. Klevanski, and V. Schmid, “First Stage Design Variations of Partially Reusable Launch Vehicles,” *Journal of Spacecraft and Rockets*, vol. 39, no. 4, pp. 571–579, Jul. 1, 2002. DOI: 10.2514/2.3846. [Online]. Available: <https://arc.aiaa.org/doi/10.2514/2.3846> (visited on 12/01/2023).
- [165] M. Sippel, S. Stappert, L. Bussler, and E. Dumont, “Systematic Assessment of Reusable First-Stage Return Options,” in *Proceedings of the International Astronautical Congress*, Issue: D2.4.4 Number: D2.4.4, Adelaide, Australia, Sep. 25, 2019. [Online]. Available: <https://iafastro.directory/iac/proceedings/IAC-17/> (visited on 11/28/2023).
- [166] “List of Falcon 9 and Falcon Heavy Launches,” Wikipedia. (Dec. 29, 2023), [Online]. Available: https://en.wikipedia.org/w/index.php?title=List_of_Falcon_9_and_Falcon_Heavy_launches&oldid=1192444377 (visited on 12/29/2023).
- [167] A. Prescott, *New Glenn Payload User’s Guide*, Oct. 2018. [Online]. Available: https://yellowdragonblogdotcom.files.wordpress.com/2019/01/new_glenn_payload_users_guide_rev_c.pdf (visited on 12/29/2023).
- [168] T. D. Wood, H. S. Kanner, D. M. Freeland, and D. T. Olson, “Solid Rocket Booster (SRB): Flight System Integration at its Best,” presented at the JANNAF 6th Liquid Propulsion Subcommittee Meeting, Huntsville, United States of America, Dec. 5, 2011. [Online]. Available: <https://ntrs.nasa.gov/api/citations/20120003006/downloads/20120003006.pdf> (visited on 12/29/2023).
- [169] D. S. Jorgensen, R. A. Haggard, and G. J. Brown, “The Past, Present, and Future of Mid-Air Retrieval,” presented at the 18th AIAA Aerodynamic Decelerator Systems Technology Conference and Seminar, ser. Aerodynamic Decelerator Systems Technology Conferences, München, Germany: American Institute of Aeronautics and Astronautics, May 2005. DOI: 10.2514/6.2005-1673. [Online]. Available: <https://arc.aiaa.org/doi/10.2514/6.2005-1673> (visited on 12/01/2023).
- [170] S. V. Antonenko and S. A. Belavskiy, “Mid-Air Retrieval Technology for Returning of Reusable Launch Vehicles’ Boosters,” in *Progress in Propulsion Physics*, vol. 1, Versailles, France: EDP Sciences, Jul. 2009, pp. 481–494, ISBN: 2493-3503. DOI: 10.1051/eucass/200901481. [Online]. Available: <https://www.eucass-proceedings.eu/articles/eucass/abs/2009/01/eucass1p481/eucass1p481.html> (visited on 11/28/2023).
- [171] G. M. Webb, A. Fadeev, and N. Pestmal, “The Inexpensive Injection of Small Satellites into GEO Using Russian/Ukrainian Solutions,” *Acta Astronautica*, vol. 59, no. 7, pp. 560–569, Jun. 27, 2006, ISSN: 0094-5765. DOI: 10.1016/j.actaastro.2006.04.005. [Online]. Available: <https://www.sciencedirect.com/science/article/pii/S0094576506001743> (visited on 01/05/2024).

- [172] NASA's Marshall Space Flight Center, *Space Shuttle Solid Rocket Boosters*, Apr. 28, 2009. [Online]. Available: <https://www.flickr.com/photos/nasamarshall/3482567165/> (visited on 01/05/2024).
- [173] S. Stappert, J. Wilken, G. J. D. Calabuig, and M. Sippel, "Evaluation of Parametric Cost Estimation in the Preliminary Design Phase of Reusable Launch Vehicles," presented at the 9th European Conference for Aeronautics and Space Sciences (EUCASS), Lille, France, Jul. 2022. [Online]. Available: <https://elib.dlr.de/187238/> (visited on 12/01/2023).
- [174] National Oceanic and Atmospheric Administration, National Aeronautics and Space Administration, and United States Air Force, "U.S. Standard Atmosphere, 1976," NOAA, Washington DC, United States of America, NOAA-S/T 76-1562, Oct. 1976, p. 243. [Online]. Available: https://www.ngdc.noaa.gov/stp/space-weather/online-publications/miscellaneous/us-standard-atmosphere-1976/us-standard-atmosphere_st76-1562_noaa.pdf (visited on 08/09/2024).
- [175] L. Bussler, "Project FALCon: Aerodynamic Database of In-Air-Capturing Candidate Towing Aircraft," Deutsches Zentrum für Luft- und Raumfahrt, Bremen, Germany, SART TN-012/2021, Dec. 2021, p. 30.
- [176] GasTurb GmbH, *GasTurb14 - Design and Off-Design Performance of Gas Turbines*, 2024. [Online]. Available: <https://gasturb.com/Downloads/Manuals/GasTurb14.pdf> (visited on 05/03/2024).
- [177] The MathWorks, Inc., *Symbolic Math Toolbox User's Guide*, Mar. 2024. [Online]. Available: https://nl.mathworks.com/help/pdf_doc/symbolic/symbolic_ug.pdf (visited on 05/10/2024).



Requirements and Risks

In this appendix, a brief overview is given of the systems engineering efforts performed throughout this work. To this end, generated design requirements for the ACCD are presented and briefly discussed in section A.1. Subsequently, section A.2 lists requirements for chapter 3's Towing Model and chapter 4's VisNav Model. Finally, a set of identified risks is presented in section A.3. The main focus in these sections is on the *technical* design of the ACCD, excluding general considerations regarding IAC, the TA, or the RLV. Similarly, no requirements are formulated concerning costs, reliability, reusability, safety, and maintainability, nor concerning mitigation of the identified risks. Furthermore, meta-systems engineering is also not considered, with no formulation of requirements or risks related to project management.

A.1. Design Requirements

To enable traceability and referability, each design requirement is given a unique identifier. These contain relevant information about the requirement itself, so that its importance and area of application are apparent at a glance. In general, such an identifier is given by **XX-YYY.ZZ-00/00**, where the first two letters (**XX**) indicate the criticality of the requirement - as defined in Table A.1.

Keyword	Criticality	Definition
CR	<i>Critical</i>	Non-negotiable; should be met verbatim.
KY	<i>Key</i>	Essential to the proper functioning of the ACCD, but contains some uncertainty in its exact formulation - especially concerning numerical values. Hence, some leeway and adaptations can be expected in future design iterations.
TN	<i>Tentative</i>	Used for the purposes of this work, but not necessarily vital to the functioning of the ACCD. Other implementations are imaginable, which may prompt the omission of this requirement in later design iterations.

Table A.1: Definition of the Criticality Keyword in Design Requirement Identifiers.

Next, the **YYY**-section of the identifier refers to the ACCD subsystem that the requirement is related to - with **SYS** indicating high-level system requirements. The latter capture the overall functions and constraints of the ACCD, and serve as the starting point for the subsystem requirements. Table A.2 defines seven main subsystems that have been identified, each related to an essential ACCD functionality.

The third keyword (**ZZ**) then indicates the nature of the requirement: functional (**F**) or non-functional (**NF**). Finally, the numerical part of the identifiers (**00/00**) serves different purposes for system and subsystem requirements. With the former, only a single number is included (**00**) for differentiation. With the latter, a first number (**00/**) enables traceability, referring to the parent high-level system requirement¹. A second number (**/00**) then distinguishes the different subsystem requirements, ensuring that each one has a unique identifier.

¹For example, docking requirement **CR-DCK.NF-13/04** is derived from system requirement **CR-SYS.F-13**.

Keyword	(Sub)system
SYS	High-level <i>system</i> requirements
STR	<i>Structural</i> requirements
DCK	Requirements related to the ACCD's <i>docking</i> functionality
RLS	Requirements related to the ACCD's <i>release</i> functionality
TOW	Requirements related to the ACCD's <i>towing</i> behaviour
PWS	Requirements related to the ACCD's <i>power</i> system
AVN	Requirements related to the ACCD's <i>avionics</i>
DTC	Requirements related to the ACCD's RLV- <i>detection</i> functionality

Table A.2: Definition of the (Sub)system Keyword in Design Requirement Identifiers.

All formulated design requirements are listed in the following subsections, with subsection A.1.1 covering system requirements, and subsections A.1.2 through A.1.8 listing subsystem requirements.

A.1.1. System

- KY-SYS.NF-01:** The ACCD shall be deployed from an Airbus A340-600 TA, connected by means of a tether [14].
- CR-SYS.NF-02:** During every stage of operations, the ACCD shall remain within safe structural limits [10].
- KY-SYS.NF-03:** The ACCD shall be able to remain operational during a period of at least 2h 35m.
- CR-SYS.F-11:** The ACCD shall enable relative position and attitude estimation between itself and a representative 80-ton RLV, in a robust and reliable manner [15].
- CR-SYS.F-12:** The ACCD shall be able to manoeuvre relative to the TA, in order to intercept the RLV [14].
- CR-SYS.F-13:** The ACCD shall be able to dock with the RLV, and ensure a solid interface between the two systems, in a reliable manner. The ACCD shall remain latched onto the RLV during the complete tow-back phase [10].
- CR-SYS.F-15:** It shall be possible to disengage the connection between the TA and the RLV at any point in the mission [16].

A.1.2. Structural

- TN-STR.NF-01/01:** The ACCD shall have an outer shell as defined in subsection 2.2.1, with a total length of 2 m, and a diameter of 1.5 m (including wings).
- TN-STR.NF-01/02:** The ACCD's design shall strive to maximize axisymmetry. As a quantifiable indication, the yaw and pitching moments of inertia shall not differ more than 1%.
- KY-STR.NF-01/03:** The connection between the ACCD and tether shall provide three Degrees of angular kinematic Freedom (3DoF), within a cone of 25° half angle.
- CR-STR.NF-02/01:** The ACCD shall be able to accommodate axial and radial shocks associated with the capture and release procedures between the ACCD and RLV.
- CR-STR.NF-02/02:** The ACCD shall be able to accommodate an axial compressive load of 50 kN, in order to withstand the docking impact with the RLV.
- CR-STR.NF-02/03:** The ACCD shall accommodate an axial tensile load of 300 kN, in order to withstand extreme tow-back regimes.
- KY-STR.NF-02/04:** The structural design of the ACCD's wings shall be able to withstand a load of 15 kN per wing, applied perpendicularly and uniformly to its upper surface.

KY-STR.NF-02/05: All Von Mises stresses shall remain below 66% of the yield strength of their respective materials.

KY-STR.NF-02/06: All deformations inside kinematically critical components shall remain below 1 mm, as to not hinder the functioning of internal mechanisms. Other parts of the ACCD shall not deform more than 5 mm.

A.1.3. Docking

KY-DCK.F-13/01: Successful docking shall be possible for relative axial velocities between the ACCD and RLV within a range of 2-5 m/s, and relative radial velocities below 1 m/s.

KY-DCK.F-13/02: Successful docking shall be possible in case of an angular yaw/pitch misalignment between the ACCD and RLV of up to 10°, and lateral misalignments of up to 25 cm.

TN-DCK.F-13/03: Successful docking shall be independent of the relative roll alignment between the ACCD and RLV.

CR-DCK.NF-13/04: The docking mechanism shall be reusable.

CR-DCK.F-13/05: The ACCD shall reliably detect when successful docking has been achieved.

CR-DCK.F-13/06: The docking mechanism shall ensure a fully inelastic collision between the ACCD and RLV, while safely absorbing the associated impact energy.

A.1.4. Release

CR-RLS.F-15/01: The ACCD shall have a nominal release mode, where the RLV is decoupled from the towing system when in close proximity to a landing site.

KY-RLS.F-15/02: The nominal release defined in **CR-RLS.F-15/01** shall take no longer than 5 s.

CR-RLS.F-15/03: The ACCD shall have an emergency release mode, allowing the disconnection of the RLV from the TA at any point during flight.

KY-RLS.F-15/04: The emergency release defined in **CR-RLS.F-15/03** shall take no longer than 1.5 s.

A.1.5. Towing

CR-TOW.NF-01/10: The ACCD shall be aerodynamically stable when in a passive towed configuration.

KY-TOW.NF-01/11: The ACCD's equilibrium state shall have a steady-state pitch angle within a range of $\pm 5^\circ$, independent of its pitch control deflection.

KY-TOW.NF-01/12: The ACCD shall stay outside a cone with a half angle of 7.5° , extending from the TA's tail, and aligned with the TA's flight path.

KY-TOW.F-12/01: The ACCD shall be capable of a ± 30 m lateral translation in the Y/Z-direction, relative to its trimmed equilibrium position.

KY-TOW.F-12/02: The ACCD shall be able to traverse a lateral distance of 30 m in the Y/Z direction within 20 s.

A.1.6. Power

KY-PWS.NF-03/01: The ACCD shall be able to remain in *Homing* mode for a period of at least 10 minutes. *Homing* mode entails a fully active vehicle state, with all electronic subsystems powered on.

KY-PWS.NF-03/02: The ACCD shall be able to remain in *Towing* mode for a period of at least 2 hours and 15 minutes. *Towing* mode concerns a semi-passive vehicle state, with only the subsystems required for communications (**CR-AVN.F-01/20**) and towing powered on.

KY-PWS.NF-03/03: The ACCD shall be able to remain in *Release* mode for a period of at least 10 minutes. *Release* mode includes the activation of all subsystems required to ensure a safe nominal release of the RLV (**CR-RLS.F-15/01**).

A.1.7. Avionics

CR-AVN.F-01/20: The ACCD shall be able to wirelessly communicate with the TA.

TN-AVN.F-01/21: The ACCD shall be able to wirelessly communicate with the RLV.

KY-AVN.F-01/22: The ACCD shall have a telemetry logging functionality.

A.1.8. Detection

KY-DTC.F-11/01: The detection system shall be able to measure the relative position between the RLV and ACCD with a minimal accuracy of 20 cm, while measuring its relative attitude with a minimal accuracy of 1°.

KY-DTC.F-11/02: The detection system shall be able to start its measurements defined in **KY-DTC.F-11/01** within a range of at least 400 m, and within an angle of view of at least 90°.

KY-DTC.NF-11/03: The detection system shall have a minimal measurement frequency of 50 Hz, in order to enable responsive vehicle control.

CR-DTC.F-11/04: The detection system shall be able to fulfil **KY-DTC.F-11/01** until **KY-DTC.NF-11/03** under any lighting or weather condition, including at night, or in fog/clouds.

A.1.9. Categorization of Subsystem Requirements

With the above (sub)system requirements generated, a large number of functionalities and constraints have been defined for the ACCD. In order to extract the most vital requirements from this extensive list, an additional categorization step is performed, evaluating the feasibility of each requirement. For this, a distinction is made between *trivial*, *feasible*, *challenging*, and *killer* requirements - corresponding to an increasing degree of difficulty. A categorization according to these criteria is shown in Figure A.1.

Trivial	
CR-RLS.F-15/03 KY-TOW.F-12/01 KY-PWS.NF-03/03	CR-AVN.F-01/20 KY-AVN.F-01/22
Feasible	
TN-STR.NF-01/01 TN-STR.NF-01/02 CR-STR.NF-02/01 CR-STR.NF-02/02 KY-DCK.F-13/01 TN-DCK.F-13/03 CR-DCK.NF-13/04 CR-RLS.F-15/01	KY-RLS.F-15/02 KY-RLS.F-15/04 KY-TOW.NF-01/11 KY-TOW.NF-01/12 KY-TOW.F-12/02 KY-PWS.NF-03/02 KY-DTC.F-11/01 KY-DTC.NF-11/03
Challenging	
KY-STR.NF-01/03 CR-STR.NF-02/03 KY-STR.NF-02/04 KY-STR.NF-02/05 CR-DCK.F-13/05	CR-DCK.F-13/06 CR-TOW.NF-01/10 KY-PWS.NF-03/01 TN-AVN.F-01/21 KY-DTC.F-11/02
Killer	
KY-DCK.F-13/02	CR-DTC.F-11/04

Figure A.1: Categorization of (Sub)system Requirements According to their Feasibility.

A.2. Model Requirements

For the model requirements, unique identifiers are again used - with a general format **YYY.ZZ-00**. Here, the first part indicates whether the requirement concerns chapter 3's Towing Model (**TWM**), or chapter 3's VisNav Model (**VNM**). As for the design requirements, the second part (**ZZ**) then indicates if the requirement is functional or non-functional in nature, while the numerical suffix serves for differentiation. All generated requirements for the Towing and VisNav Models are listed in subsections A.2.1 and A.2.2 respectively.

A.2.1. Towing Model

- TWM.NF-01:** The Towing Model shall analyse 2D steady-state conditions of the towing system. This 2D plane is defined as the TA's plane of symmetry, which is assumed to be coincident with the planes of symmetry of all other vehicles.
- TWM.F-02:** The Towing Model shall analyse the relative position and attitude of the ACCD/RLV with respect to the TA. The model shall furthermore be able to visualize this towing configuration graphically, including a representation of the TA's wake.
- TWM.F-03:** The Towing Model shall analyse the towing loads on the ACCD. In order to determine extreme scenarios, the model shall take into account potential excess thrust (i.e. more thrust than is required to maintain steady-state conditions) provided by the TA.
- TWM.F-04:** The Towing Model shall investigate the effect of the ACCD's mass, CoG, and pitch control deflection on the towing position (**TWM.F-02**), in order to characterize the design space and operational environment of the ACCD.
- TWM.NF-05:** The Towing Model shall use high-fidelity Computational Fluid Dynamics (CFD) data for estimating aerodynamic forces on all vehicles.
- TWM.NF-06:** As inputs, the Towing Model shall use the TA's altitude, air speed, and FPA, while differentiating between a *clean* and *diving* TA configuration.
- TWM.NF-07:** The Towing Model's steady-state solution shall not deviate more than $\pm 5\%$ from the equilibrium solution found with SART's Simulink model. The equilibrium solution of

said model is reached when the relative derivatives of the towing position are below 2%; i.e. $\partial y / \partial t < 0.02 \cdot y$.

TWM.F-08: For the purposes of model verification, the Towing Model shall be able to visualize the forces on the ACCD/RLV.

TWM.NF-09: The Towing Model shall be able to analyse towing conditions (**TWM.NF-01** through **TWM.F-03**) in less than 1% of the computation time needed by SART's Simulink model, using similar inputs, and the same workstation.

A.2.2. VisNav Model

VNM.F-01: The VisNav Model shall analyse the visibility of a three-dimensional (3D) VisNav beacon configuration, from the Point of View (PoV) of a VisNav sensor.

VNM.NF-02: The VisNav Model shall consider beacons mounted along the docking cone of the ACCD, either mounted inside the cone's surface, or along its aft rim. The sensor shall be mounted on the nose of the RLV.

VNM.NF-03: In order to allow for integration into an overarching relative navigation simulator, the VisNav Model shall include the following I/O-flow: given a certain beacon configuration and RLV position and attitude, the model shall output the visibility of each individual beacon. Relevant vectors shall be expressed in the ACCD body frame of reference.

VNM.F-04: The VisNav Model shall provide a means of comparing different beacon and sensor configurations, by determining corresponding approach corridors. These approach corridors are defined as the region in 3D space where the sensor detects enough beacons to perform relative position and attitude estimation.

VNM.F-05: Using the I/O-flow described in **VNM.NF-03**, the VisNav Model shall be able to analyse time-dependent beacon visibility, given a specific RLV trajectory.

VNM.F-06: To provide model insight and verification, the VisNav Model shall be able to produce sensor PoV imagery, where the visibility of individual beacons is visualized.

A.3. Risks

Another major cornerstone of this work's systems engineering framework, concerns the identification of relevant technical risks. These enable further insight into the ACCD design, identifying critical aspects that require special attention during different phases of the project. Additionally, the identified risks can also serve as a reference point for future studies. As for the generated requirements, each risk is given a unique identifier **XXX-00**. They are grouped according to the operational phase during which they are most likely to occur (**XXX**) - as defined in Table A.3. Subsections A.3.1 through A.3.5 present the identified risks in a roughly chronological order.

Keyword	Operational Phase
DTC	<i>Detection</i> of the RLV by the ACCD
APR	<i>Approach</i> between the RLV and ACCD
DCK	<i>Docking</i> between the RLV and ACCD
TOW	<i>Tow-back</i> of the RLV
RLS	<i>Release</i> of the RLV

Table A.3: Definition of the Operational Phase Keyword in Risk Identifiers.

A.3.1. Detection

DTC-01: The RLV and ACCD never get within range of the detection system, or do not stay there long enough to ensure relative navigation.

- DTC-02:** The RLV and ACCD never enter within the FoV of the detection system, or do not stay in it long enough to ensure relative navigation. This can be either due to the RLV's position, attitude, or sensor mounting configuration.
- DTC-03:** After successful initial detection, sensor connection is (temporarily) lost, due to range or FoV issues, or caused by an external obstruction (e.g. cloud) passing through the Line of Sight (LoS).
- DTC-04:** The detection system loses power.
- DTC-05:** Communication is lost between the ACCD and the TA/RLV.

A.3.2. Approach

- APR-01:** External disturbances (TA wake, wind, ...) are too high for the ACCD to be effectively controlled.
- APR-02:** The distance between the RLV and ACCD is too large to cross within the available time frame.
- APR-03:** One or more control surfaces malfunction, either mechanically or electronically.
- APR-04:** The relative navigation measurements are too coarse/noisy for proper alignment between the ACCD and RLV.

A.3.3. Docking

- DCK-01:** The relative velocity between the RLV and ACCD is too high, resulting in excessive impact energy, and structural damage/failure.
- DCK-02:** The relative velocity between the RLV and ACCD is too low to activate the docking mechanism.
- DCK-03:** The angular misalignment between the ACCD and RLV is too high for the docking mechanism to properly attach.
- DCK-04:** The RLV impacts the ACCD at an undesirable time and location, leading to structural damage to one or both vehicles - or, in a less severe case, creating an external disturbance to the ACCD.
- DCK-05:** The ACCD does not detect that it has docked with the RLV. This has an impact on the deployment of the locking mechanism, as well as on the control of the ACCD. Failure to detect docking can either be caused by faulty/unpowered sensors, or improper contact between the two vehicles.
- DCK-06:** The locking mechanism is jammed, resulting in an inability to properly secure the connection between the RLV and ACCD.
- DCK-07:** The locking mechanism has no power when engaging.
- DCK-08:** The RLV does not stay in place long enough for the locking mechanism to properly engage.

A.3.4. Towing

- TOW-01:** Dynamic towing loads exceed the modelled values for which the ACCD is designed. This can result in structural damage to the vehicle, and/or unwanted release of the docking mechanism.
- TOW-02:** Towing shocks, caused by slackening and tautening of the tether, exceed the ACCD's structural limits. This can lead to damage to the vehicle, and/or unwanted release of the docking mechanism.
- TOW-03:** The locking mechanism loses power while towing, potentially leading to a disconnect.

- TOW-04:** The RLV gets too close to the TA during towing manoeuvres, jeopardizing the safety of the TA and its (potential) crew.
- TOW-05:** A structural or control failure in the RLV leads to a loss of control, and/or a reduction in lift-generating capacity. This in turn would lead to a severe increase in towing loads - on the TA, tether, and ACCD.

A.3.5. Release

- RLS-01:** The release mechanism is jammed, resulting in an inability to properly disengage the connection between the RLV and ACCD.
- RLS-02:** The release mechanism loses power.
- RLS-03:** The release procedure results in an off-nominal load on the ACCD.
- RLS-04:** The release is not successfully detected.
- RLS-05:** Emergency release does not happen fast enough to prevent damage to, or loss of the TA.

A.3.6. Risk Map

In order to further characterize the risks formulated above, and assess their relative criticality, they are organized in a risk map. Here, each risk is assigned a degree of *likelihood* as well as *severity*. The corresponding degrees used in this work are defined in Table A.4 and Table A.5 respectively.

Degree of Likelihood	Definition
Rare	Should never actually happen, only on the rarest of occasions, given a very specific turn of events.
Unlikely	Only happens under specific circumstances, which do not arise for most missions.
Plausible	Will probably occur in some missions, so should be seen as a real possibility.
Likely	Significant probability to occur during a typical mission.
Almost Certain	Can be expected to occur in every mission. In fact, would be surprising if it did <i>not</i> happen.

Table A.4: Definition of Degrees of Likelihood for Risk Mapping.

Degree of Severity	Definition
Negligible	Inconvenient, but no real impact on mission success.
Marginal	The mission will still probably be successful, but is rendered noticeably more difficult.
Moderate	Does not directly jeopardize the mission, but could result in a loss of the RLV in combination with other factors.
Critical	Almost certainly leads to a loss of the RLV.
Catastrophic	Almost certainly leads to a loss of the ACCD (and as such of the RLV as well), and potentially even a loss of the TA.

Table A.5: Definition of Degrees of Severity for Risk Mapping.

With both of these characterization schemes defined, a *pre-mitigated* risk map is shown in Figure A.2 - indicating what would happen if the design were made without any concern for the identified risks. In this map, upper right positions represent the most critical risks, having a high degree of likelihood *and* severity. Note that the presented risk assessment was made assuming only a single RLV capture attempt.

Likelihood	Almost Certain			DTC-03		
	Likely				DTC-02 APR-01 DCK-08	
	Plausible			DTC-05 DCK-05 RLS-04	DTC-01 APR-02 APR-04	DCK-02 DCK-03
	Unlikely				DTC-04 DCK-06	DCK-07 TOW-03
	Rare					APR-03 TOW-04 RLS-01
		Negligible	Marginal	Moderate	Critical	Catastrophic
Severity						

Figure A.2: Pre-Mitigated Risk Map. The displayed colour code roughly corresponds to overall criticality of the risks.

The map above shows that most risks are critical because of their severity, rather than their likelihood. This is because a large number of risks lead to unsuccessful docking, which in turn automatically results in a loss of the RLV. Because these conditions are inherent to IAC, driving the risks' severity down past the *critical* point is often not possible. Instead, focus is mainly put on decreasing the risks' likelihood. In general, the following risks are identified as the most important ones - either being likely and critical, or plausible and catastrophic.

Detection: RLV not inside the detection system's FoV.

Approach: perturbing effect of external disturbances, such as the TA's wake.

Docking: impact between the RLV and ACCD is problematic in terms of velocity, location, or duration.

Towing: excessive and unexpected loads or shocks during towing.

Release: emergency release not fast enough.

B

Launch Vehicle Reusability

When systematically analysing and comparing different approaches to launch vehicle reusability, a large number of available options emerge. As observed by Vernacchia and Mathesius [155], they are characterized by a set of design questions, including the recovery propulsion method, recovery location, and landing method. Depending on the answers formulated to these design questions, unique reusability concepts arise.

In order to restrict the number of options relevant for the following analysis, a set of simplifying assumptions is made. For one, it is assumed that launcher's *entire* first stage is recovered and reused - as opposed to only retrieving critical parts, such as the engine bay¹. Furthermore, an archetypal, vertical launch scenario is considered, effectuating a trajectory above a large body of water². In other words, for a fully Expendable Launch Vehicle (ELV), the stage in question would splash down in water, rather than re-enter above land. Finally, a reference payload capability of 7.5 Mg to Geostationary Transfer Orbit (GTO) is used - corresponding to DLR studies for the European Next Reusable Ariane (ENTRAIN) Project [23].

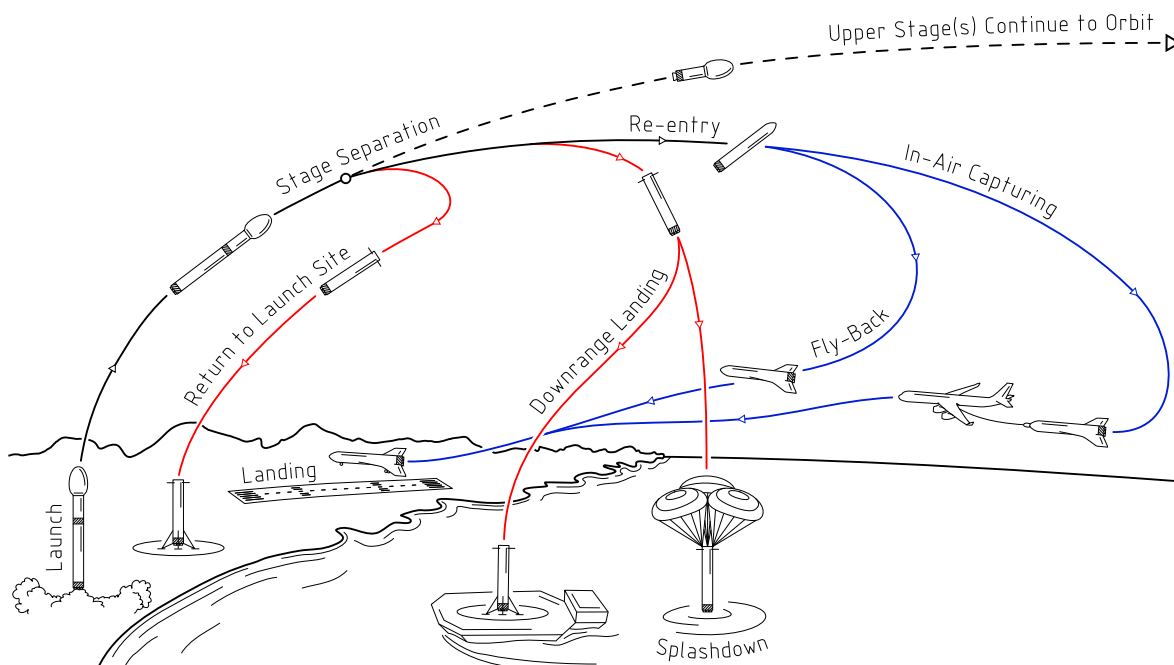


Figure B.1: Schematic Overview of Vertical-Takeoff/Vertical-Landing (VTVL; red) and Vertical-Takeoff/Horizontal-Landing (VTHL; blue) RLV Recovery Techniques

¹Although partial recovery has been proposed in the past [156], [157], its profitability is yet to be demonstrated [20], [155].

²This is generally the case when launching from sites such as Kourou or Cape Canaveral [158], [159].

Under these conditions, only a limited number of recovery options remain [9] - shown schematically in Figure B.1. Broadly speaking, they can be categorized based on two criteria: their landing method, and their return method. For the former, a distinction can be made between Vertical-Takeoff/Vertical-Landing (VTVL) - as successfully demonstrated by SpaceX [160] and Blue Origin [161] - and Vertical-Takeoff/Horizontal-Landing (VTHL). As the name suggests, the latter uses a landing strip to horizontally land the RLV, similar to a conventional aircraft.

Looking at the RLV's *return* method, two main options again emerge. On the one hand, the stage's onboard propulsive systems can be used to return autonomously to the launch site. This is the case for SpaceX's Return-to-Launch-Site (RTLS) missions - for both current Falcon vehicles [162] and future Super Heavy boosters [163]. Additionally, it is also the method used by the VTHL Fly-Back (FB) concept, which proposes the addition of dedicated air-breathing engines to the RLV. Examples of such FB vehicles include the Liquid Fly-Back Boosters (LFBB) investigated by DLR [164], and the Baikal boosters proposed for the Angara launcher [165] - as shown in Figure B.2a. On the other hand, the RLV can also rely on an external agent to handle the return journey to the launch site. For VTVL, this is typically achieved with a Downrange Landing (DRL) on a drone ship or barge, which then returns the stage back to port. DRL is used for the majority of Falcon 9 missions [166], and is also proposed for Blue Origin's New Glenn vehicle [167]. Alternatively, the IAC approach discussed in this work offers a VTHL alternative to DRL.

Finally, soft-surface deceleration and recovery systems should also be briefly considered. These were used for the recovery of the Space Shuttle's Solid Rocket Boosters (SRBs) [168] - shown in Figure B.2b - as well as for the so-called Mid-Air Recovery (MAR) concept. In the latter, the RLV is caught in mid-air by a helicopter (or aircraft), while suspended under parachutes [169]. However, MAR is not feasible for the heavy-lift RLV under consideration [165], partly because modern helicopters can only accommodate RLV masses up to 20 Mg [170]. Alternatively, having the stage splash down in the (salty and corrosive) ocean is highly undesirable in terms of refurbishment and recovery efforts and costs. Hence, four main promising return options remain: (VTVL) RTLS, (VTVL) DRL, (VTHL) FB, and (VTHL) FB.



(a) Full-Scale Engineering Model of the Baikal Fly-Back (FB) Booster at the Salon du Bourget (Paris Air Show) 2001 [171].



(b) Splashdown of a Space Shuttle Solid Rocket Booster (SRB) after STS-124 [172].

Figure B.2: Two Examples of Wildly Different RLV Recovery Techniques: VTHL FB (left) and VTVL Splashdown (right).

Based on multiple SART studies, a comparison of these four return options can be summarized as follows: from a pure performance perspective, both IAC and DRL offer the highest payload capacity [9] - or conversely, they require the lowest inert mass³ for a given target payload. Furthermore, both are estimated to result in similar recovery costs, in the order of 0.5-1 M\$ per launch - which is significantly lower in the case of RTLS and FB. However, because recovery costs are only a marginal fraction of total launch costs, this difference in launch costs does not justify the reduced performance of RTLS and FB - under these conditions [173]. This is further demonstrated in Figures B.3 and B.4, which respectively compare the mass properties and recovery costs for each of the four considered return options.

³i.e. dry mass + return propellant.

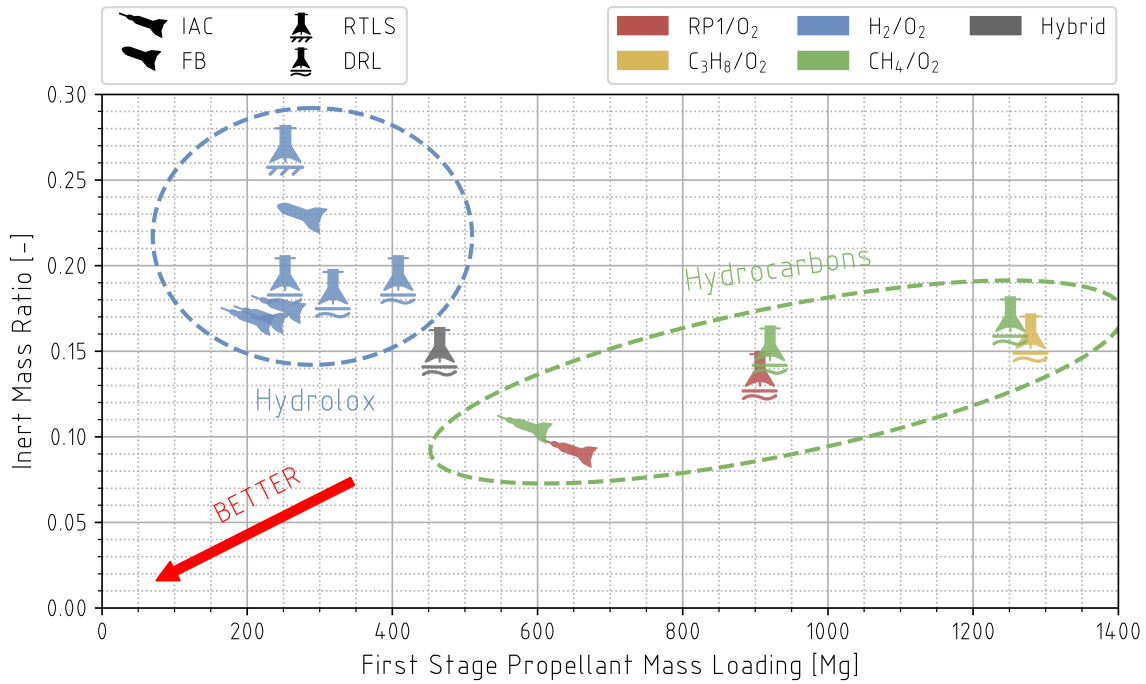


Figure B.3: Comparison of the Estimated Inert Mass Ratio and Total First Stage Propellant Mass for Different RLV Recovery Techniques. The *hybrid* system combines a methalox lower stage with a hydrolox upper stage [20].

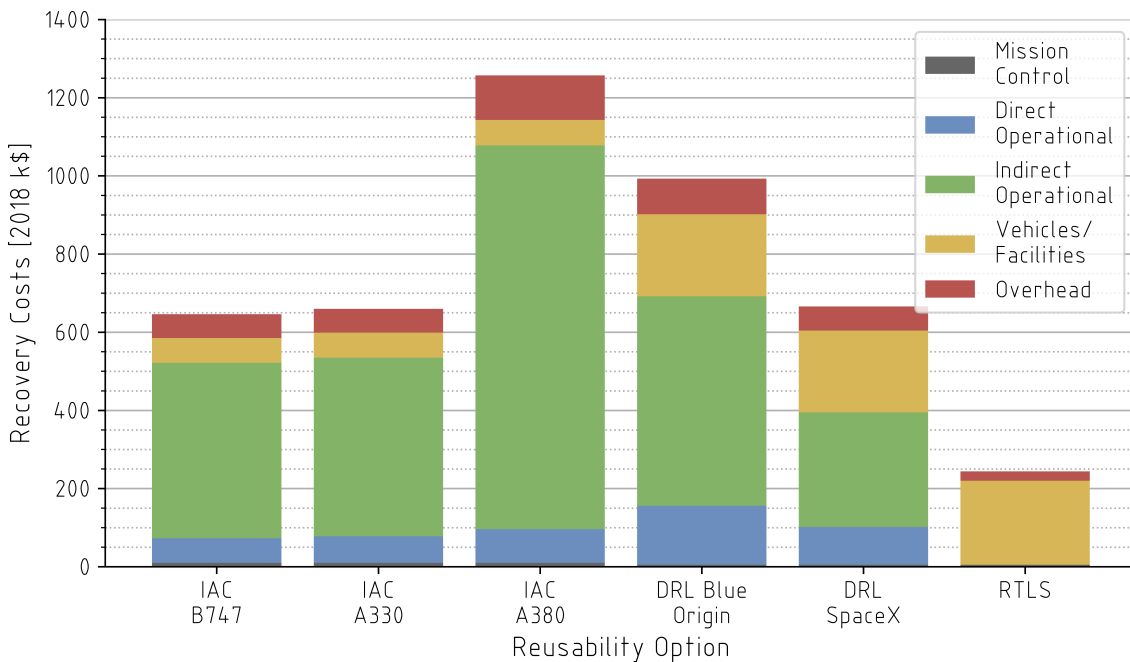
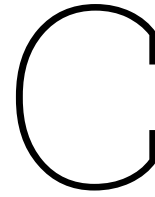


Figure B.4: Comparison of Estimated Recovery Costs for Different RLV Recovery Techniques. The difference between *DRL* (Downrange Landing) *SpaceX* and *DRL Blue Origin* concerns the type of recovery vessel that is used [20].

Finally, looking at IAC in the context of this broader picture of launch vehicle reusability, a number of its advantages can be identified. On the one hand, the use of an aerodynamic re-entry and TA tow-back precludes the need for an on-board propulsive return system - contrary to FB. On the other hand, no residual propellant is required for the return flight, as opposed to SpaceX's DRL approach [162]. Both aspects aid in decreasing the launcher's inert mass, by optimally dividing the recovery hardware between the launch vehicle and 'ground' equipment (which includes the TA) [170]. Additionally, IAC

is an intrinsically flexible procedure, which has no inherent lower limits in terms of mass or size of the RLV. In other words, similar systems could be used to recover smaller RLVs, or launcher subsystems - e.g. payload fairings [40].

Nevertheless, IAC also has a number of foreseeable challenges. For one, additional lift-generating surfaces are required on the RLV, with active aerodynamic control capabilities - adding to the launcher's inert mass and complexity. Furthermore, the novelty and unique nature of IAC means that its Technology Readiness Level (TRL) is not yet on par with VTVL DRL [38]. Hence, a number of technological hurdles need to be overcome, for example related to the high complexity and limited duration of the formation flight. Nonetheless, the evident analogy between IAC and AAR provides a source of reassurance, as different technologies and lessons from the latter discipline can be applied and adapted. Additionally, studies such ICARUS help in raising the overall TRL of IAC, aiding the potential realization of this promising recovery technique in the future.



Bills of Materials

The following pages include detailed BoMs for all three considered design iterations of the ACCD. Apart from listing the inertial properties of each design's constituent components, they also include a detailed breakdown of peak stresses and deformations, corresponding to the FEM analyses described in chapter 6. BoMs for *Iteration 0*, *1*, and *2* can be found in Tables C.2, C.3, and C.4 respectively. The inertial properties of *Iteration 0* are based on estimates published in Atanassov's 2006 study [11], while CoGs of all components listed in subsequent iterations are computed assuming a uniform material density - which is true for the majority of components. Different design loads corresponding to the FEM analyses can be distinguished by the subscripts defined in chapter 7. Since the tether, RLV boom, and tether release system are not integral parts of the ACCD itself, they are not included in any of the BoMs. A mass breakdown of the tether release system is shown in Table C.1 - which uses properties of standard metric bolts.

Assembly	Component	Quantity [-]	Material	Inertia		
				Density [kg/m^3]	Volume [m^3]	Mass [kg]
Release System		1				1.037
	Release Flange	2	Al2024-T6	2700	1.33E-04	0.359
	M10x30mm Class 12.9 Button	10	Steel	7800	2.63E-06	0.020
	M10 Class 12 Hexagonal Nut	10	Steel	7800	1.46E-06	0.011

Table C.1: Mass Breakdown of the ACCD's Release System.

Assembly	Component	Quantity [-]	Material	Inertia				Stress			Deformation		Load Scenario
				Density [kg/m^3]	Volume [m^3]	Mass [kg]	CoG [mm]	Peak [MPa]	Yield [MPa]	SF [-]	Peak [mm]	Allowed [mm]	
Load-Bearing Frame		1	Al2024-T3	2700	7.85E-03	21.195	415.0	42.2	345	8.175	0.271	N/A	Impact ₀
Wing Structure		4				7.350	1061.0						
Shock-Absorbing Assembly		1				18.164	1474.9	291		1.1856	0.583	N/A	
	Conical Spring	1	1020 Carbon Steel	7850	3.75E-05	2.944	1603.0	72	350	4.8611			Towing ₀
	Spherical Shell	1	Al2024-T3	2700	1.95E-03	5.265	1367.2	291	345	1.1856	0.583	N/A	Towing ₀
	Spherical Shell Ring	1	Al2024-T3	2700	2.10E-04	0.567	1400.0	250	345	1.3800	0.299	N/A	Impact ₀
	Struts	8	Al2024-T3	2700	1.26E-04	0.340	1403.4						
	Spring Mount	1	Al2024-T3	2700	6.19E-04	1.671	1569.0						
	Conical Support	1	Al2024-T3	2700	5.68E-03	4.995	1529.0						
Locking Mechanism		1	Al2024-T3	2700	5.68E-03	15.336	1395.4	199	345	1.7337	0.180		Towing ₀
								5.53	345	62.3870	0.004		Impact ₀
Body Shell		1				23.012	1082.9	238	345	1.4496			Towing ₀
	Shell	1	Al2024-T3	2700	7.71E-03	20.817	1024.0						
	Ring	1	Al2024-T3	2700	8.13E-04	2.195	1641.0						
Avionics		1				16.800	959.5						
	Actuators	1	Multiple			10.000	1347.0						
	Electronics	1	Multiple			4.300	500.0						
	Avionics	1	Multiple			2.500	200.0						
Trim Mass		1				7.600	300.0						
TOTAL						131.507	999.9	291		1.1856	0.583		

Table C.2: Bill of Materials (BoM) for ACCD Design *Iteration 0*. For individual components, *unit* mass and volume are listed.

Assembly	Component	Quantity [-]	Material	Inertia				Stress			Deformation		Load Scenario
				Density [kg/m^3]	Volume [m^3]	Mass [kg]	CoG [mm]	Peak [MPa]	Yield [MPa]	SF [-]	Peak [mm]	Allowed [mm]	
Tether Attachment		1	Al6061-T6	2700	4.44E-03	11.985	217.5	207.00	280	1.3527	0.561	1	Towing ₁
								190.00	280	1.4737	0.375	1	Impact ₁
Load-Bearing Frame		1				12.106	1031.8	196.72		1.4233	3.404		
	Frame Bars	8	Al6061-T6	2700	4.78E-04	1.289	1041.4	196.72	280	1.4233	3.404	5	Towing ₁
	Frame Hoops	2	Al6061-T6	2700	3.32E-04	0.986	976.5	144.23	280	1.9413	2.353	5	Towing ₁
Wing Structure		4				16.890	1020.7	177.83		1.5745	3.413		
	Leading Spar	1	Al6061-T6	2700	4.31E-04	1.164	750.0	177.83	280	1.5745	2.640	5	Aero ₁
	Trailing Spar	1	Al6061-T6	2700	3.04E-04	0.819	1200.0	125.58	280	2.2297	2.782	5	Aero ₁
	Root Rib	1	Al6061-T6	2700	7.56E-04	2.041	905.7	153.10	280	1.8289	0.448	5	Aero ₁
	Central Rib	1	Al6061-T6	2700	4.96E-04	1.339	932.1	48.89	280	5.7271	1.507	5	Aero ₁
	Tip Rib	1	Al6061-T6	2700	2.90E-04	0.783	958.8	71.10	280	3.9381	2.844	5	Aero ₁
	Wing Skin	2	Al6061-T6	2700	1.57E-03	4.234	949.6	75.65	280	3.7013	3.413	5	Aero ₁
	Control Surface	1	Multiple	1000	2.28E-03	2.277	1535.4						
Shock-Absorbing Assembly		1				7.014	463.6	161.00		1.7391	0.771		
	Plunger	1	Al6061-T6	2700	5.95E-04	1.607	969.9	161.00	280	1.7391	0.771	1	Impact ₁
	MC64150	1	Multiple		9.50E-04	5.100	286.8						
	LBBR 30-2LS	1	Multiple		2.75E-05	0.070	750.0						
	Bearing Cap	1	Al6061-T6	2700	7.04E-06	0.019	776.5						
	Bearing Structure	1	Al6061-T6	2700	8.06E-05	0.218	751.0						

Table C.3: BoM for ACCD Design *Iteration 1*. For individual components, *unit* mass and volume are listed.

Assembly	Component	Quantity [-]	Material	Inertia				Stress			Deformation		Load Scenario
				Density [kg/m ³]	Volume [m ³]	Mass [kg]	CoG [mm]	Peak [MPa]	Yield [MPa]	SF [-]	Peak [mm]	Allowed [mm]	
Locking Mechanism		1				24.036	1507.8	382.00		0.7330	0.489		
	Locking Ring	1	Al6061-T6	2700	8.45E-03	22.802	1511.3	382.00	280	0.7330	0.489	1	Towing ₁
	Locking Actuators	4	Multiple	2000	1.54E-04	0.309	1444.5						
Guiding Cone		1				16.495	1825.2						
	Base Frame	1	Al6061-T6	2700	2.88E-03	7.781	1830.5						
	Horizontal Guide	12				0.040	1532.5						
	- Guide	1	Al6061-T6	2700	1.34E-05	0.036	1532.5						
	- Spring	2	Steel	7800	2.72E-07	0.002	1532.5						
	Conical Guide	6				0.646	1837.5						
	- Guide	1	Al6061-T6	2700	2.36E-04	0.638	1837.5						
	- Spring	4	Steel	7800	2.72E-07	0.002	1835.8						
	Conical Guide w/ Beacon	6				0.725	1837.5						
	- Guide	1	Al6061-T6	2700	2.65E-04	0.717	1837.5						
	- Spring	4	Steel	7800	2.72E-07	0.002	1835.8						
Body Shell		1				25.795	1070.5						
	Nose Shell	4	Al6061-T6	2700	3.01E-04	0.814	155.7						
	Front Shell	4	Al6061-T6	2700	5.23E-04	1.411	513.6						
	Middle Shell	4	Al6061-T6	2700	5.00E-04	1.351	973.9						
	Aft Shell	4	Al6061-T6	2700	6.85E-04	1.850	1504.8						
	Cone Shell	4	Al6061-T6	2700	3.79E-04	1.024	1907.8						
Avionics		1				13.400	870.1						
	OBC	1	Multiple		1.00E-04	0.100	300.0						
	Communications Module	1	Multiple		3.38E-03	0.600	300.0						
	Control Actuators	4	Multiple			1.500	1500.0						
	VisNav Beacons	12	Multiple			0.042	1900.0						
	Docking Sensors	4	Multiple			0.050	1500.0						
	Battery	1	Multiple		3.38E-03	6.000	200.0						
Trim Mass		1				20.750	300.0						
TOTAL						199.143	1000.1	382.00		0.7330	3.413		

Table C.3: BoM for ACCD Design Iteration 1 (continued). For individual components, unit mass and volume are listed.

Assembly	Component	Quantity [-]	Material	Inertia				Stress			Deformation		Load Scenario
				Density [kg/m ³]	Volume [m ³]	Mass [kg]	CoG [mm]	Peak [MPa]	Yield [MPa]	SF [-]	Peak [mm]	Allowed [mm]	
Tether Attachment		1				5.944	169.5	221.96		1.5543	0.551	1	
	Frontal Segment	1	Al2024-T6	2700	1.21E-03	3.254	136.0	209.47	345	1.6470	0.551	1	Towing ₂
								36.99	345	9.3261	0.065	1	Impact ₂
	Aft Segment	1	Al2024-T6	2700	7.69E-04	2.077	194.0	221.96	345	1.5543	0.396	1	Towing ₂
								203.31	345	1.6969	0.490	1	Impact ₂
	M8x16mm Class 12.9 Button	12	Steel	7800	1.01E-06	0.008	85.6						
	M8x22mm Class 12.9 Button	36	Steel	7800	1.25E-06	0.010	293.7						
	M8 Class 12 Hexagonal Nut	32	Steel	7800	6.70E-07	0.005	304.1						
Tether Joint		1				1.371	50.6	191.08		1.8055	0.769		
	Frontal Segment	1	Al2024-T6	2700	2.40E-04	0.649	53.4	191.08	345	1.8055	0.767	1	Towing ₂
	Tether End	1	UHMWPE	755	2.37E-04	0.179	13.7						
	Aft Segment	1	Al2024-T6	2700	1.05E-04	0.284	60.8						
	M10x18mm Class 12.9 Cap Head	8	Steel	7800	2.79E-06	0.022	56.9						
	M8x12mm Class 12.9 Cap Head	8	Steel	7800	1.38E-06	0.011	59.8						

Table C.4: BoM for the Final ACCD Design Iteration. For individual components, unit mass and volume are listed.

Assembly	Component	Quantity [-]	Material	Inertia				Stress			Deformation		Load Scenario
				Density [kg/m^3]	Volume [m^3]	Mass [kg]	CoG [mm]	Peak [MPa]	Yield [MPa]	SF [-]	Peak [mm]	Allowed [mm]	
Load-Bearing Frame		1				15.696	931.0	228.06		1.5128	1.904		
	Standard Bar	4	Al2024-T6	2700	4.73E-04	1.277	1043.5	228.06	345	1.5128	1.904	5 Towing ₂	
	Threaded Bar	4	Al2024-T6	2700	4.72E-04	1.275	1044.5	201.96	345	1.7083	1.723	5 Towing ₂	
	Frontal Hoop	1	Al2024-T6	2700	7.07E-04	1.909	295.8	106.92	345	3.2267	1.896	5 Towing ₂	
	Central Hoop	1	Al2024-T6	2700	7.32E-04	1.976	745.8	121.90	345	2.8302	1.092	5 Towing ₂	
	Aft Hoop	1	Al2024-T6	2700	5.95E-04	1.606	1195.8	112.66	345	3.0623	0.306	5 Towing ₂	
Wing Structure		4				17.099	1022.6	219.13		1.5744	3.810		
	Leading Spar	1	Al2024-T6	2700	4.40E-04	1.188	745.5	219.13	345	1.5744	2.623	5 Aerodynamic ₂	
	Trailing Spar	1	Al2024-T6	2700	3.13E-04	0.845	1195.5	170.68	345	2.0213	2.877	5 Aerodynamic ₂	
	Root Rib	1	Al2024-T6	2700	5.89E-04	1.589	917.2	182.78	345	1.8875	0.453	5 Aerodynamic ₂	
	Central Rib	1	Al2024-T6	2700	4.47E-04	1.207	945.5	69.28	345	4.9800	1.606	5 Aerodynamic ₂	
	Tip Rib	1	Al2024-T6	2700	3.37E-04	0.910	956.9	109.7	345	3.1444	3.021	5 Aerodynamic ₂	
	Root Shell	2	Al6061-T3	2700	9.04E-04	2.441	934.3	92.79	280	3.0175	2.513	5 Aerodynamic ₂	
	Tip Shell	2	Al6061-T3	2700	6.67E-04	1.801	959.5	81.05	280	3.4547	3.810	5 Aerodynamic ₂	
	Root Connection Strip	1	Al6061-T3	2700	1.95E-05	0.053	405.3						
	Tip Connection Strip	1	Al6061-T3	2700	2.08E-05	0.056	537.6						
	4mm x 10mm Button Head Rivet	88	Steel	7800	1.76E-07	0.001	905.1						
	Control Surface	1				2.646	1489.6						
	- Shell	1	Al6061-T3	2700	4.80E-04	1.296	1530.9						
	- ECI-63.20-K4-B00	1	Multiple		3.71E-04	0.850	1450.0						
	- Gearbox	1	Multiple			0.500	1450.0						
Shock-Absorbing Assembly		1				8.463	480.9	221.12		1.5602	0.681		
	Absorber Housing	1	Al2024-T6	2700	2.83E-04	0.765	229.5	207.11	345	1.6658	0.432	1 Impact ₂	
	MC64150EUM-1 with C64 Front Clevis	1	Multiple		1.01E-0	5.100	307.2						
	NM64 Locking Ring	1	316L Steel	8000	1.15E-05	0.092	362.9						
	M8x18mm Class 12.9 Button	6	Steel	7800	1.09E-06	0.009	127.2						
	M8 Class 12 Hexagonal Nut	6	Steel	7800	6.70E-07	0.005	119.9						
	Plunger	1	Al2024-T6	2700	6.30E-04	1.701	1030.7	221.12	345	1.5602	0.681	1 Impact ₂	
	Plunger Connector	1	Al2024-T6	2700	1.74E-05	0.047	616.9						
	Sensor Trigger	2	Al6061-T3	2700	2.87E-06	0.008	736.0						
	M16 Class 12 Hexagonal Nut	2	Steel	7800	4.17E-06	0.033	616.9						
	M4x12mm Class 4.8 Button Head	2	Steel	7800	1.69E-07	0.001	727.4						
	Bearing Assembly	1				0.479	780.3						
	- LBBR 50-2LS/HV6	1	Multiple		7.29E-05	0.180	783.3						
	- Mounting Flange	1	Al6061-T3	2700	1.01E-04	0.274	781.0						
	- M6x16mm Class 8.8 Button	4	Steel	7800	5.07E-07	0.004	749.0						
	- M6 Class 8 Hexagonal Nut	4	Steel	7800	3.12E-07	0.002	755.8						
	Plunger Sensor	2				0.056	662.2						
	- E3Z-G62 0.5m	1	Multiple		1.19E-05	0.030	637.8						
	- M4 Class 4 Hexagonal Nut	8	Steel	7800	1.02E-07	0.001	691.8						
	- M4x130mm Class 4.9 Threaded Bar	2	Steel	7800	1.28E-06	0.0100	689.5						
Locking Mechanism		1				9.827	1397.1	222.69		1.5492	0.611		
	Locking Ring	1	Al2024-T6	2700	3.04E-03	8.219	1399.7	222.69	345	1.5492	0.490	1 Towing ₂	
	Locking Actuator	4				0.368	1379.4						
	- LM 1247-100-11	1	Multiple		1.42E-05	0.078	1378.8						
	- Locking Wedge	1	Al2024-T6	2700	1.06E-04	0.286	1379.6	199.50	345	1.7293	0.611	1 Towing ₂	
	- Mounting Flange	1	Al6061-T3	2700	5.53E-07	0.001	1377.1						
	- Stop Flange	1	Al6061-T3	2700	1.33E-07	0.001	1377.1						
	- M1.6x6mm Class 4.8 Cap Head	4	Steel	7800	1.84E-08	0.001	1367.1						
	- M2x4mm Class 8.8 Button	6	Steel	7800	1.62E-08	0.001	1377.1						

Table C.4: BoM for the Final ACCD Design Iteration (*continued*). For individual components, *unit* mass and volume are listed.

Assembly	Component	Quantity [-]	Material	Inertia			Stress			Deformation		Load Scenario
				Density [kg/m^3]	Volume [m^3]	Mass [kg]	CoG [mm]	Peak [MPa]	Yield [MPa]	SF [-]	Peak [mm]	
Boom Sensor		4				0.034	1430.9					
	- U300.D50-DPMJ.72N	1	Multiple		8.38E-06	0.021	1433.4					
	- Mounting Plate	1	Steel	7800	1.18E-06	0.009	1426.4					
	- M3x16mm Class 4.8 Button	2	Steel	7800	1.10E-07	0.001	1433.2					
	- M3 Class 4 Hexagonal Nut	2	Steel	7800	4.81E-08	0.001	1424.6					
	- M4x6mm Class 4.8 Button	2	Steel	7800	1.12E-07	0.001	1425.6					
Guiding Cone		1				21.789	1820.3					
Base Frame		1	Al2024-T6	2700	4.60E-03	12.409	1835.9					
Mounting Clamp		8	Al2024-T6	2700	4.18E-06	0.011	1788.3					
M8x12mm Class 12.9 Cap Head		16	Steel	7800	1.38E-06	0.011	1788.3					
Horizontal Guide		12				0.088	1512.7					
	- Guide	1	Al2024-T6	2700	2.24E-05	0.060	1512.7					
	- 10mm x 20mm Spring	2	Steel	7800	6.61E-07	0.005	1512.6					
	- Mounting Plate	2	Al2024-T6	2700	1.45E-06	0.004	1512.6					
	- M6 Class 12 Hexagonal Nut	2	Steel	7800	3.12E-07	0.002	1512.6					
	- M4x10mm Class 12.9 Button	4	Steel	7800	1.50E-07	0.001	1512.6					
Conical Guide w/o Beacons		6				0.663	1835.8					
	- Guide	1	Al2024-T6	2700	2.25E-04	0.607	1839.6					
	- 10mm x 20mm Spring	4	Steel	7800	6.61E-07	0.005	1796.0					
	- Mounting Plate	4	Al2024-T6	2700	1.45E-06	0.004	1794.2					
	- M6 Class 12 Hexagonal Nut	4	Steel	7800	3.12E-07	0.002	1792.2					
	- M4x10mm Class 12.9 Button	8	Steel	7800	1.50E-07	0.001	1795.1					
Conical Guide w/ Inner Beacon		2				0.664	1835.7					
	- Guide	1	Al2024-T6	2700	2.18E-04	0.589	1840.4					
	- 10mm x 20mm Spring	4	Steel	7800	6.61E-07	0.005	1796.0					
	- Mounting Plate	4	Al2024-T6	2700	1.45E-06	0.004	1794.2					
	- M6 Class 12 Hexagonal Nut	4	Steel	7800	3.12E-07	0.002	1792.2					
	- M4x10mm Class 12.9 Button	8	Steel	7800	1.50E-07	0.001	1795.1					
	- Beacon Case	1	ABS	1070	1.11E-05	0.012	1811.7					
	- Beacon Acrylic	1	PMMA	1180	1.92E-06	0.002	1814.8					
	- Beacon LED	1	Multiple		1.43E-06	0.003	1811.8					
	- M3x5mm Class 4.8 Cap Head	4	Steel	7800	8.80E-08	0.001	1813.8					
Conical Guide w/ Outer Beacon		3				0.664	1836.0					
	- Guide	1	Al2024-T6	2700	2.18E-04	0.589	1836.9					
	- 10mm x 20mm Spring	4	Steel	7800	6.61E-07	0.005	1796.0					
	- Mounting Plate	4	Al2024-T6	2700	1.45E-06	0.004	1794.2					
	- M6 Class 12 Hexagonal Nut	4	Steel	7800	3.12E-07	0.002	1792.2					
	- M4x10mm Class 12.9 Button	8	Steel	7800	1.50E-07	0.001	1795.1					
	- Beacon Case	1	ABS	1070	1.11E-05	0.012	1924.3					
	- Beacon Acrylic	1	PMMA	1180	1.92E-06	0.002	1927.4					
	- Beacon LED	1	Multiple		1.43E-06	0.003	1924.3					
	- M3x5mm Class 4.8 Cap Head	4	Steel	7800	8.80E-08	0.001	1926.3					
Conical Guide w/ Both Beacons		1				0.666	1835.9					
	- Guide	1	Al2024-T6	2700	2.12E-04	0.571	1837.6					
	- 10mm x 20mm Spring	4	Steel	7800	6.61E-07	0.005	1796.0					
	- Mounting Plate	4	Al2024-T6	2700	1.45E-06	0.004	1794.2					
	- M6 Class 12 Hexagonal Nut	4	Steel	7800	3.12E-07	0.002	1792.2					
	- M4x10mm Class 12.9 Button	8	Steel	7800	1.50E-07	0.001	1795.1					
	- Beacon Case	2	ABS	1070	1.11E-05	0.012	1868.0					
	- Beacon Acrylic	2	PMMA	1180	1.92E-06	0.002	1871.1					
	- Beacon LED	2	Multiple		1.43E-06	0.003	1868.1					
	- M3x5mm Class 4.8 Cap Head	8	Steel	7800	8.80E-08	0.001	1870.1					

Table C.4: BoM for the Final ACCD Design Iteration (*continued*). For individual components, *unit* mass and volume are listed.

Assembly	Component	Quantity [-]	Material	Inertia			Stress			Deformation		Load Scenario
				Density [kg/m^3]	Volume [m^3]	Mass [kg]	CoG [mm]	Peak [MPa]	Yield [MPa]	SF [-]	Peak [mm]	
Rim-mounted Beacon		5				0.020	1990.0					
- Beacon Case		1	ABS	1070	1.11E-05	0.012	1988.7					
- Beacon Acrylic		1	PMMA	1180	1.92E-06	0.002	1994.8					
- Beacon LED		1	Multiple		1.43E-06	0.003	1988.8					
- M3x5mm Class 4.8 Cap Head		4	Steel	7800	8.80E-08	0.001	1992.8					
Body Shell		1				21.872	1108.4					
Nose		1				3.694	158.9					
- Shell Section		4	Al6061-T3	2700	3.09E-04	0.833	160.8					
- Connection Strip		4	Al6061-T3	2700	2.31E-05	0.062	132.2					
- M4x6mm Class 8.8 Button		40	Steel	7800	1.12E-07	0.001	231.6					
- 4mm x 10mm Button Head Rivet		56	Steel	7800	1.76E-07	0.001	130.6					
Front Ring		1				3.800	497.0					
- Shell Section		4	Al6061-T3	2700	3.48E-04	0.940	497.5					
- M4x6mm Class 8.8 Button		48	Steel	7800	1.12E-07	0.001	450.5					
Central Ring		1				3.363	978.9					
- Shell Section		4	Al6061-T3	2700	3.08E-04	0.832	978.5					
- M4x6mm Class 8.8 Button		40	Steel	7800	1.12E-07	0.001	1013.8					
Aft Ring		1				6.315	1518.2					
- Shell Section		4	Al6061-T3	2700	5.79E-04	1.562	1517.3					
- M4x6mm Class 8.8 Button		24	Steel	7800	1.12E-07	0.001	1205.8					
- 4mm x 10mm Button Head Rivet		32	Steel	7800	1.76E-07	0.001	1785.8					
Cone		1				4.700	1891.4					
- Shell Section		4	Al6061-T3	2700	3.81E-04	1.028	1903.5					
- Connection Strip		4	Al6061-T3	2700	4.74E-05	0.128	1795.4					
- M4x6mm Class 8.8 Button		36	Steel	7800	1.12E-07	0.001	1986.9					
- 4mm x 10mm Button Head Rivet		32	Steel	7800	1.76E-07	0.001	1803.8					
Avionics		1				5.783	560.5					
Battery Module		2				2.141	395.8					
- 175Wh Battery		2	Multiple		2.79E-04	0.750	395.8					
- Battery Bracket		2	Al6061-T3	2700	1.71E-05	0.046	395.8					
- Mounting Platform		1	Al6061-T3	2700	1.35E-04	0.365	395.8					
- Mounting Clamp		4	Al6061-T3	2700	3.81E-06	0.010	395.8					
- M8x25mm Class 8.8 Button		8	Steel	7800	1.37E-06	0.011	395.8					
- M8 Class 8 Hexagonal Nut		8	Steel	7800	6.70E-07	0.005	395.8					
- M4x10mm Class 4.8 Button		8	Steel	7800	1.50E-07	0.001	395.8					
- M4 Class 4 Hexagonal Nut		8	Steel	7800	1.02E-07	0.001	395.8					
OBC Module		1				0.741	395.8					
- Pixhawk 6X Pro		1	Multiple		3.78E-05	0.123	395.9					
- Vibration Mount		1	ABS	1070	7.19E-05	0.077	395.8					
- Mounting Platform		1	Al6061-T3	2700	1.35E-04	0.366	395.8					
- Mounting Clamp		4	Al6061-T3	2700	3.81E-06	0.010	395.8					
- M8x25mm Class 8.8 Button		8	Steel	7800	1.37E-06	0.011	395.8					
- M8 Class 8 Hexagonal Nut		8	Steel	7800	6.70E-07	0.005	395.8					
- M4x10mm Class 4.8 Button		4	Steel	7800	1.50E-07	0.001	395.8					
- M4 Class 4 Hexagonal Nut		4	Steel	7800	1.02E-07	0.001	395.8					
Comms and GNSS Module		1				0.759	1651.0					
- P840		1	Multiple		1.40E-05	0.100	1652.3					
- H-RTK F9P Rover		1	Multiple		5.48E-05	0.123	1650.7					
- Mounting Platform		1	Al6061-T3	2700	1.36E-04	0.366	1650.8					
- Mounting Clamp		4	Al6061-T3	2700	3.81E-06	0.010	1650.8					
- M8x25mm Class 8.8 Button		8	Steel	7800	1.37E-06	0.011	1650.8					
- M8 Class 8 Hexagonal Nut		8	Steel	7800	6.70E-07	0.005	1650.8					
- M2.5x6mm Class 4.8 Cap Head		3	Steel	7800	5.81E-08	0.001	1650.8					
Trim Mass		1				16.300	300.0					
TOTAL						175.440	1000.2	228.06	1.5128	3.810		

Table C.4: BoM for the Final ACCD Design Iteration (continued). For individual components, unit mass and volume are listed.

D

Atmospheric Model

Throughout this work, the 1976 US Standard Atmosphere is used to model the height-dependence of local air temperature and pressure [174]. In particular, a piecewise interpolation is used between data points shown in Table D.1. In this table, H is the geopotential height above Mean Sea Level (MSL), T is the air temperature, p is the static pressure, and ζ is the temperature lapse rate - i.e. the derivative of the temperature with respect to altitude: $\partial T / \partial H$.

H [km]	T [K]	p [Pa]	ζ [K/m]
0	288.15	101,325	-0.0065
11	216.65	22,699.90	0
20	216.65	5529.29	0.001
32	228.65	889.06	0.0028
47	270.65	115.85	0
51	270.65	70.45	-0.0028
71	214.65	4.47	-0.00172
95	173.37	0.0729	0.00053
100	176.02	0.0283	0.00386
105	195.32	0.0116	0.00784
110	234.52	0.0054	0.01434
120	377.92	0.0018	0.01101
135	543.07	0.00062	0.00714
150	650.17	0.00027	0.00482
165	722.47	0.00013	0.00326
180	771.37	0.000068	0.00209

Table D.1: Data Points for the 1976 US Standard Atmosphere Model.

Using this table, a given altitude H is rounded down to the nearest altitude H_{ref} - with the corresponding reference point defined by T_{ref} , p_{ref} and ζ_{ref} . The temperature T at the considered altitude H is then computed with Equation D.1, while the local pressure p can be found with Equation D.2. In these equations, $g = 9.81 \text{ m/s}^2$ is the gravitational acceleration of the Earth at sea level, while $R_{air} = 287.052 \text{ J/kgK}$ and $\kappa_{air} = 1.4$ respectively are the specific gas constant, and isentropic expansion coefficient of air.

$$T = T_{ref} + \zeta_{ref} \cdot (H - H_{ref}) \quad (\text{D.1})$$

$$p = \begin{cases} p_{ref} \cdot \left(1 + \zeta_{ref} \cdot \left(\frac{H - H_{ref}}{T_{ref}} \right)^{-g / (\zeta_{ref} \cdot R_{air})} \right) & \text{if } \zeta_{ref} \neq 0 \\ p_{ref} \cdot \exp \left(\frac{-g}{R_{air} \cdot T} \cdot (H - H_{ref}) \right) & \text{if } \zeta_{ref} = 0 \end{cases} \quad (\text{D.2})$$

Figure D.1 shows the temperature and pressure curves computed with this model, corresponding to altitudes between 0 and 200 km - using a logarithmic scale for the pressure profile. For this work, only altitudes below 10 km are of interest, corresponding to data points 1 and 2 in Table D.1.

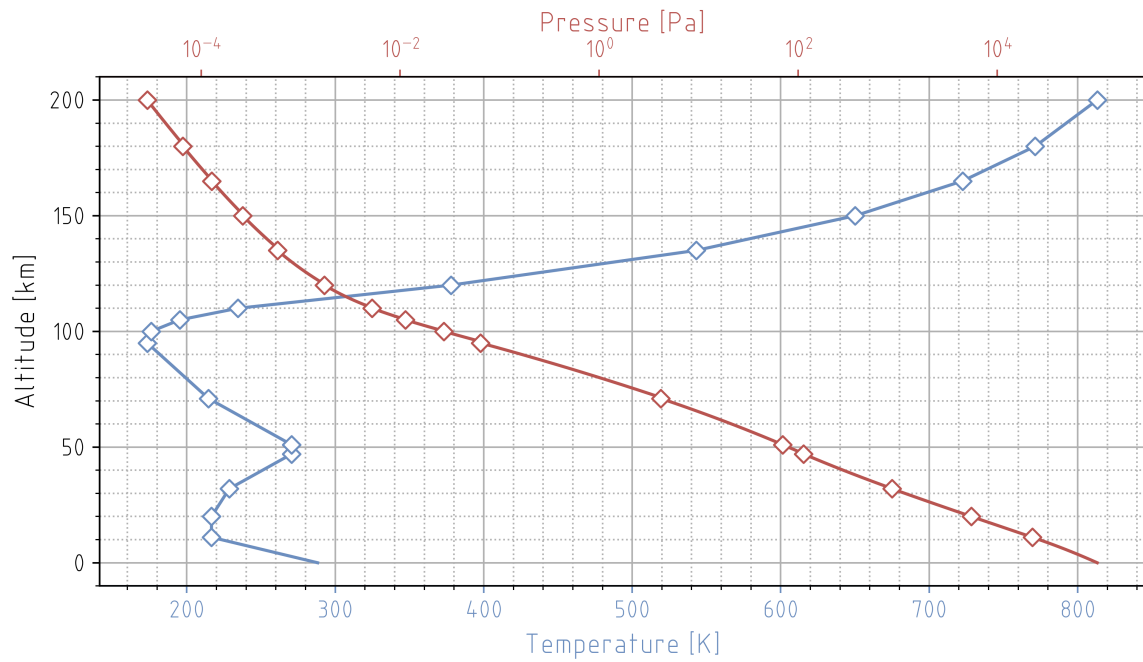


Figure D.1: Temperature and Pressure Profile as a Function of Mean Sea Level (MSL) Altitude, as Computed with the 1976 US Standard Atmosphere Model.

Once the local temperature and pressure at a given altitude have been found, the corresponding density ρ is computed with Equation D.3. Additionally, temperature can be combined with the Mach number Ma of local airflow to obtain an equivalent flow velocity V - expressed in m/s . This is done with Equation D.4, where the second factor represents the local speed of sound. An example of the resulting velocity relations at different altitudes is shown in Figure D.2.

$$\rho = \frac{p}{R_{air} \cdot T} \quad (D.3)$$

$$V = Ma \cdot \sqrt{\kappa_{air} \cdot R_{air} \cdot T} \quad (D.4)$$

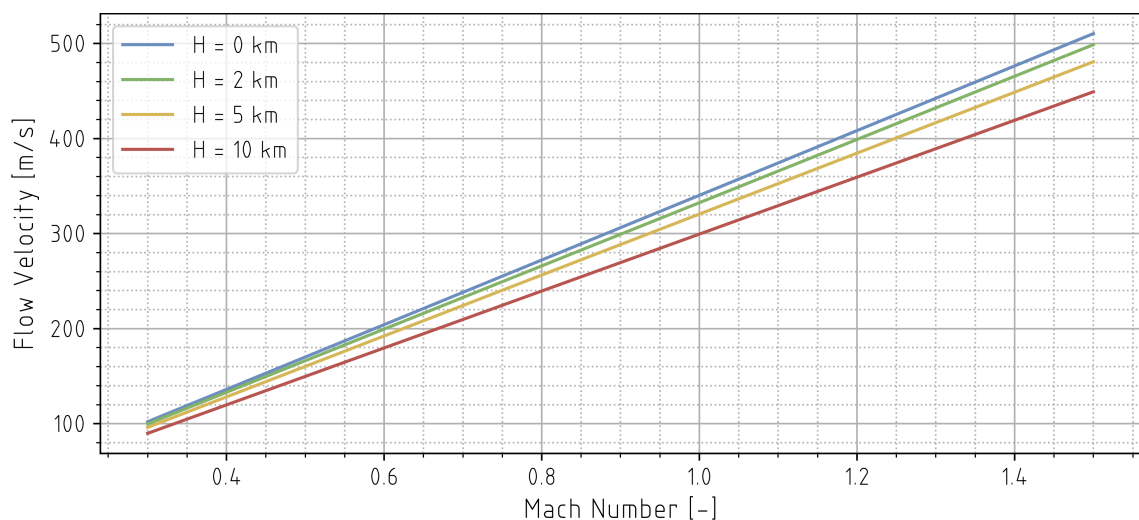


Figure D.2: Airflow Velocity as a Function of Mach Number and MSL Altitude, as Computed with the 1976 US Standard Atmosphere Model.

E

Aerodynamic Data

To model the aerodynamic behaviour of the IAC vehicles, interpolation of discretely modelled CFD data is used. This data has been generated during project FALCon, both at the von Karman Institute for Fluid Dynamics (VKI) in Sint-Genesius-Rode, Belgium [24], [43], and at SART [50], [175]. It is mainly used in chapter 3's Towing Model, and only covers pitch effects because of the 2D nature of this model. Figures E.1 through E.6 visualize the modelled aerodynamic coefficients for the ACCD, RLV, and TA - with a distinction between the latter's *clean* and *diving* configurations. Because of data confidentiality, the Y-axis scale is unspecified in all figures.

Vehicle	l_{ref} [m]	A_{ref} [m ²]	MRP [m]
ACCD	2	2	0.6
RLV	58	58	38
TA	47.77	437.3	39.013

Table E.1: Reference Geometry for the Aerodynamic Coefficients of IAC Vehicles.

All aerodynamic coefficients assume a free-flow velocity of Mach 0.45, with corresponding reference dimensions listed in Table E.1. This table also shows the location of the MRP, on which all aerodynamic forces and moments act - as measured from the nose of the vehicle. For the ACCD and the TA, available CFD data were expressed in the vehicle's body frame of reference - with corresponding aerodynamic coefficients C_A and C_N . Converting these to the aerodynamic frame - as defined in Appendix G -, drag and lift coefficients C_D and C_L are obtained using Equation E.1 - where α is the vehicle's AoA. The pitching moment coefficient C_M is unaffected by this frame transformation. The positive pitch deflection used in this work is defined in Figure 3.14.

$$\begin{bmatrix} C_L \\ C_D \end{bmatrix} = \begin{bmatrix} \cos \alpha & -\sin \alpha \\ \sin \alpha & \cos \alpha \end{bmatrix} \cdot \begin{bmatrix} C_N \\ C_A \end{bmatrix} \quad (\text{E.1})$$

The obtained aerodynamic coefficients are then used in Equation E.2 to compute aerodynamic forces and torques. Here, $1/2 \cdot \rho \cdot V^2$ represents the airflow's dynamic pressure, while l_{ref} and A_{ref} are the reference length and area defined in Table E.1.

$$\begin{cases} L = 1/2 \cdot \rho \cdot V^2 \cdot A_{ref} \cdot C_L \\ D = 1/2 \cdot \rho \cdot V^2 \cdot A_{ref} \cdot C_D \\ M = 1/2 \cdot \rho \cdot V^2 \cdot A_{ref} \cdot l_{ref} \cdot C_M \end{cases} \quad (\text{E.2})$$

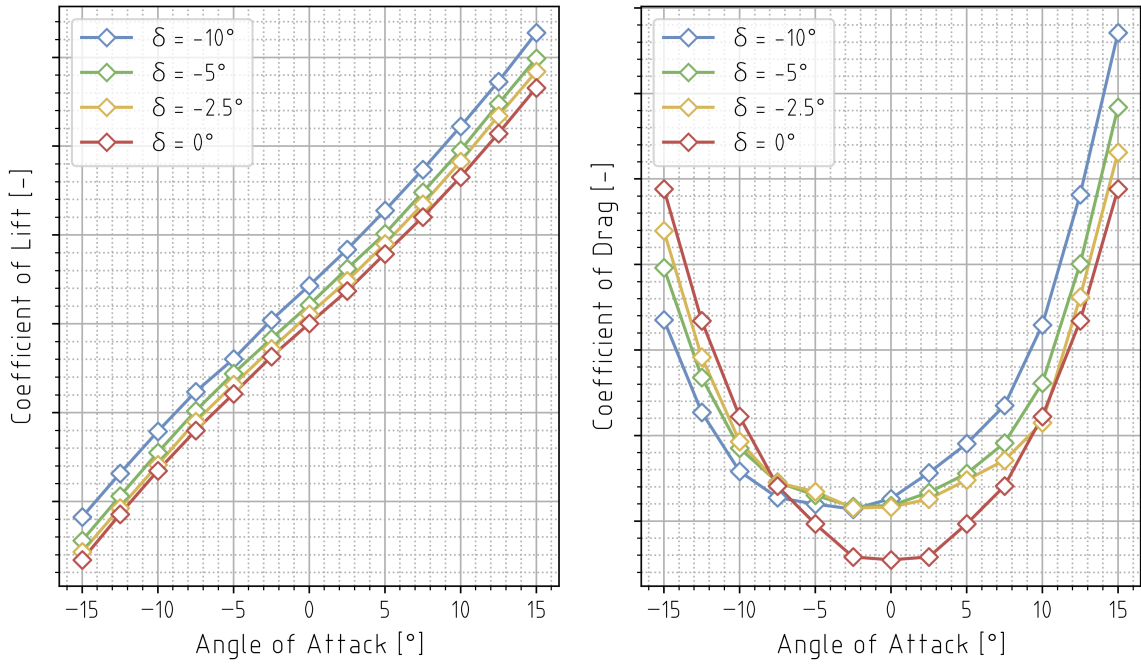


Figure E.1: ACCD Lift and Drag Coefficients as a Function of AoA and Control Deflection.

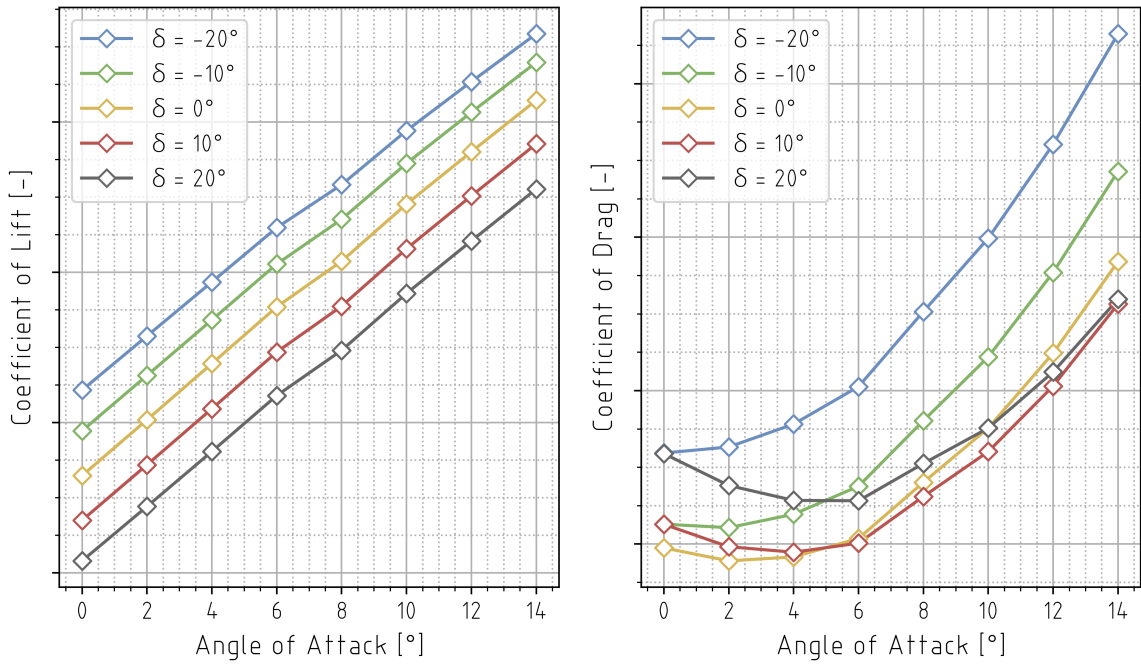


Figure E.2: RLV Lift and Drag Coefficients as a Function of AoA and Control Deflection.

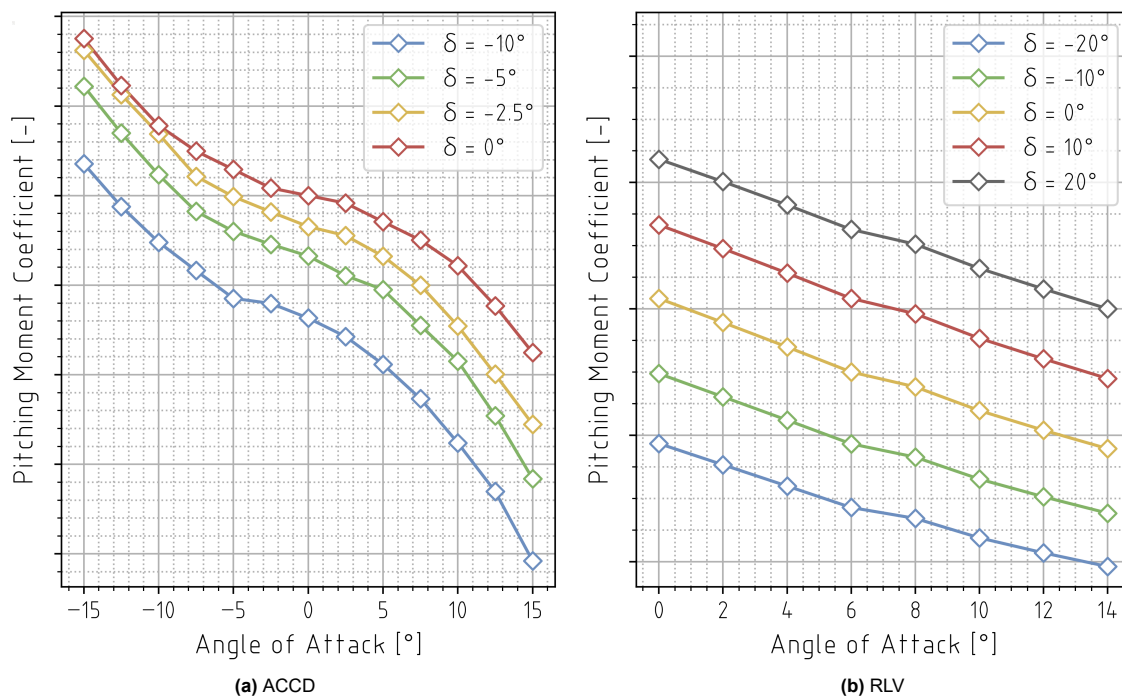


Figure E.3: ACCD and RLV Pitching Moment Coefficients as a Function of AoA and Control Deflection.

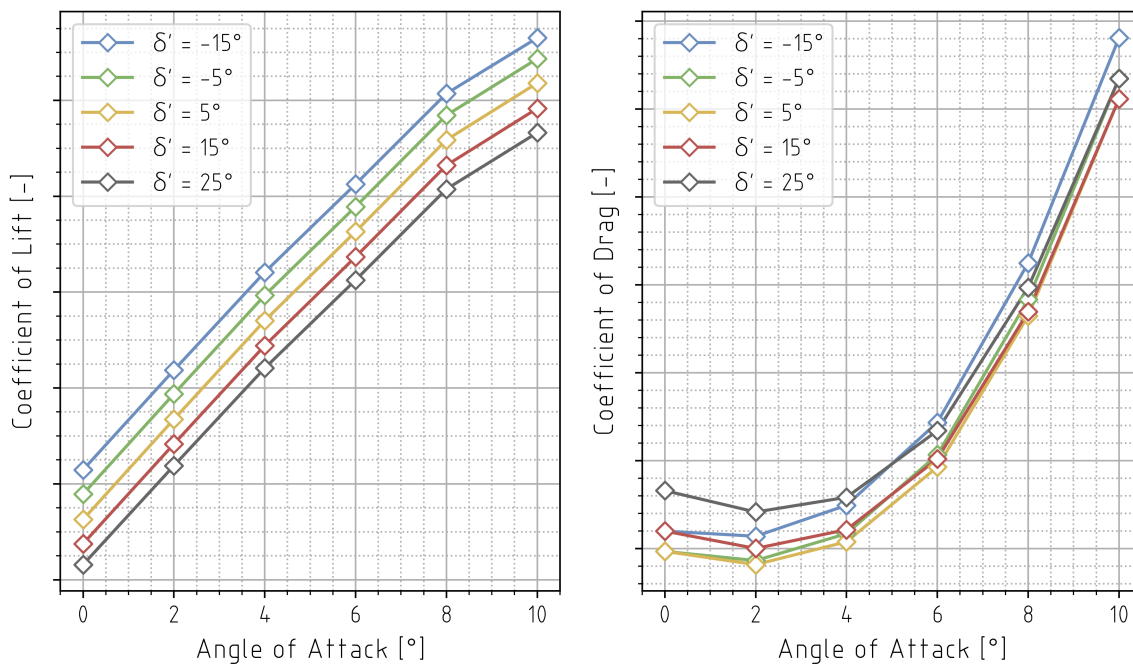


Figure E.4: TA Lift and Drag Coefficients as a Function of AoA and Control Deflection, for a Diving Configuration.

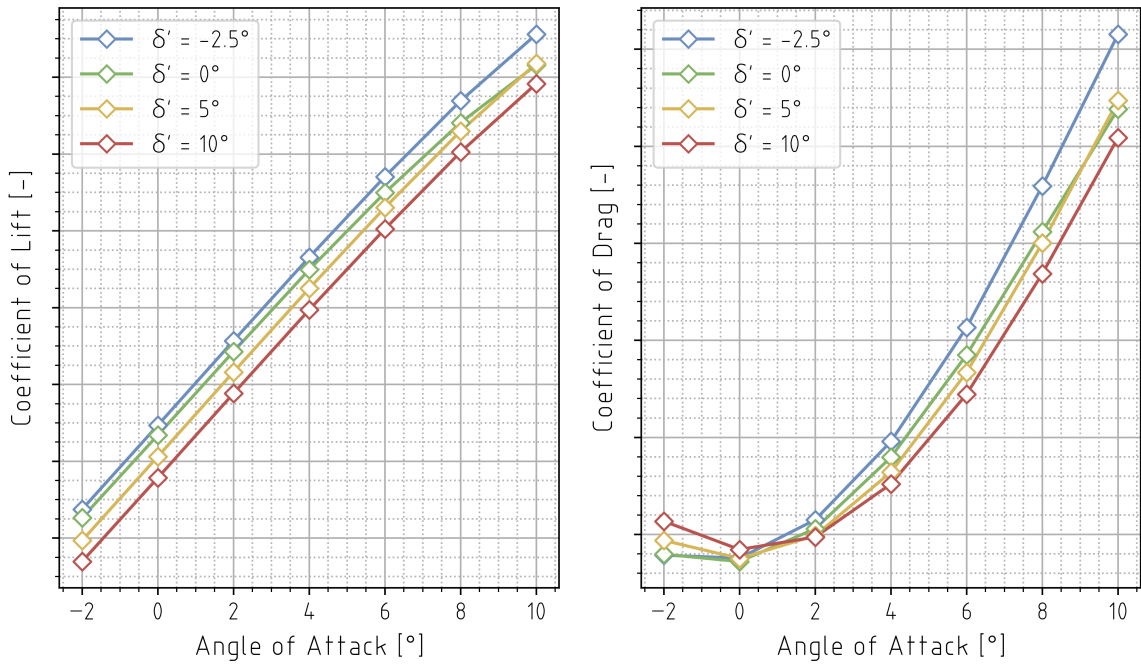


Figure E.5: TA Lift and Drag Coefficients as a Function of AoA and Control Deflection, for a *Clean* Configuration.

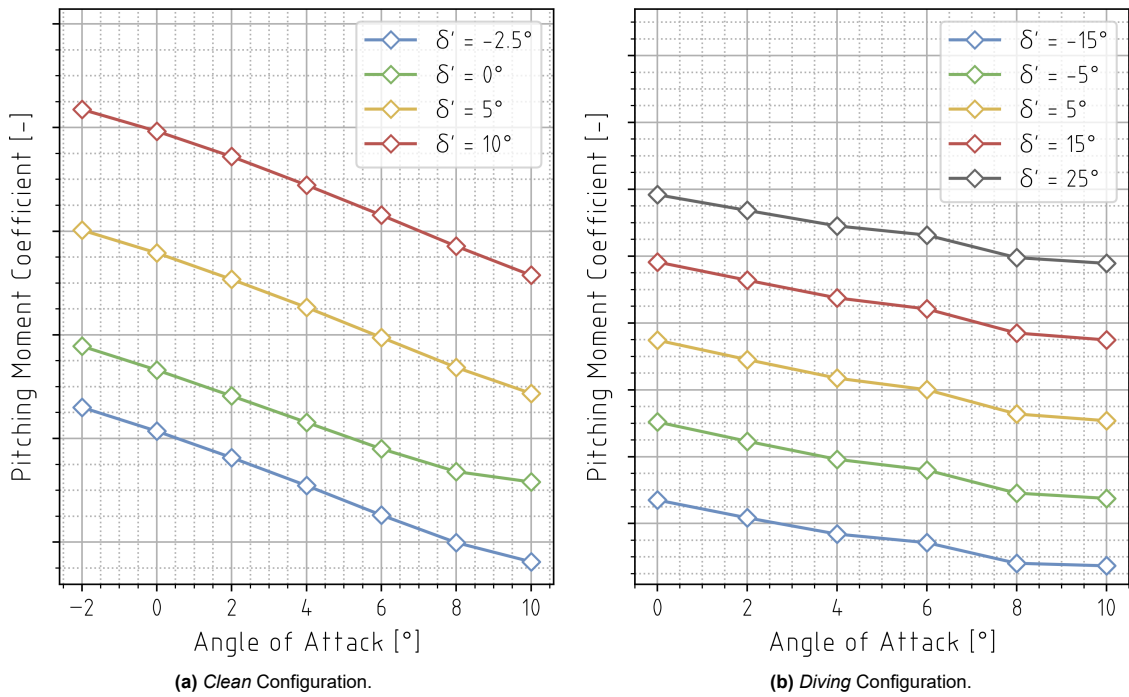
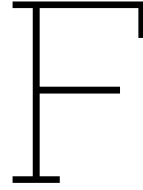


Figure E.6: TA Pitching Moment Coefficients as a Function of AoA and Control Deflection.



Rigid Tether Model

As an alternative to chapter 3's catenary tether model, a more simplified rigid link model can also be used to simulate the behaviour of the tether. In that case, its equilibrium state can be solved based on the free-body diagram shown in Figure F.1 - where the different symbols are the same as defined in chapter 3. Given the uniform cross-section and density of the tether, its CoG is located exactly at its midway point. As opposed to the catenary model, the angle θ is now constant throughout the entire tether, and fully dictates the relative position of the ACCD and TA. It can be found by solving the tether's moment equilibrium, yielding Equation F.1.

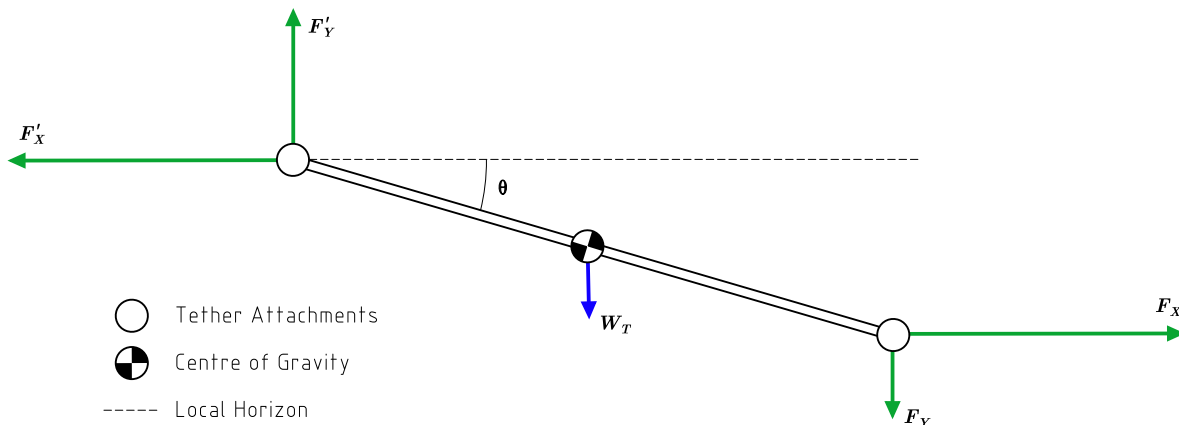


Figure F.1: Free-Body Diagram of a Rigid Link Tether Model. Note that the size of the displayed forces is not to scale.

$$\theta = \arctan \left(\frac{F_Y + W_T/2}{F_X} \right) \quad (\text{F.1})$$

Expressing the position of the ACCD's tether attachment in the global towing frame (introduced in chapter 3 and further defined in Appendix G) can then be done with Equation F.2. This combines the computed tether angle θ with the known value for its total length l_T .

$$\begin{cases} x_A = l_T \cdot \cos \theta \\ y_A = l_T \cdot \sin \theta \end{cases} \quad (\text{F.2})$$

Comparing the rigid link model with the catenary tether model discussed in chapter 3, Figure F.2 shows that the relative difference in computed towing positions remains very limited. Furthermore, steady-state towing forces are independent of the tether model, while differences in excess-thrust forces are also limited, given the minimal difference in computed towing positions. Nevertheless, the catenary model is used throughout this work, as it does not come with any noticeable increase in complexity. As an example, the average computation time for the rigid and catenary equilibrium states

shown in Figure F.2 are 326 ms and 318 ms, respectively. Model inputs for this comparison are listed in Table 3.1.

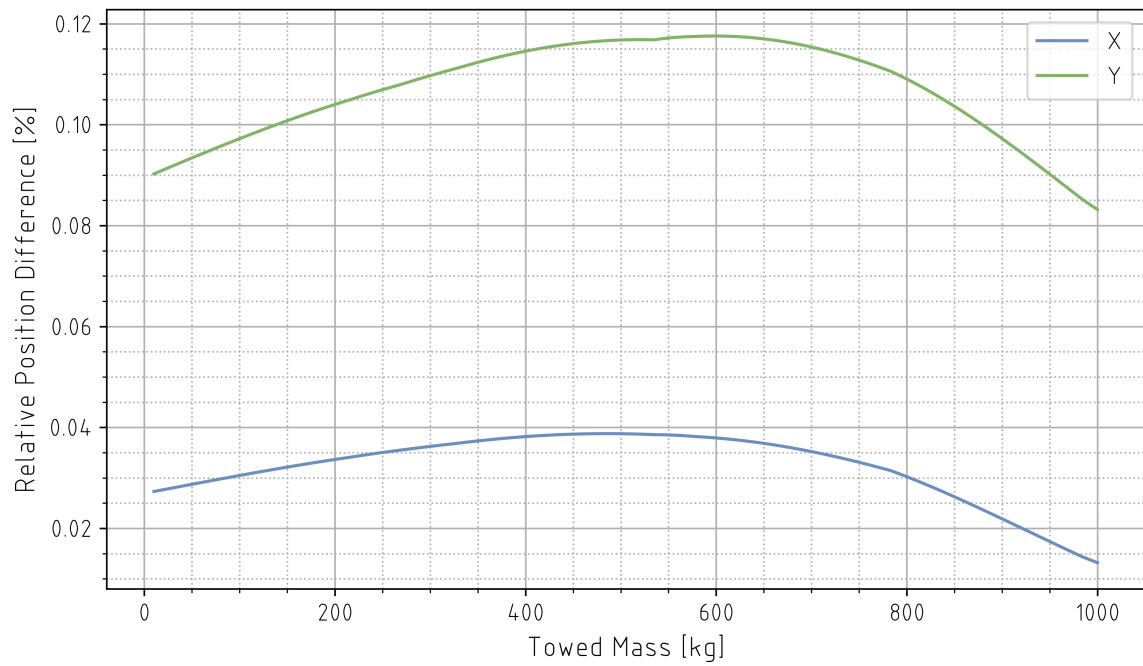


Figure F.2: Comparison of Towing Positions Computed with Rigid Link and Catenary Tether Models.

G

Reference Frames

Throughout this work, a number of reference frames have been used. These are listed below, and are defined in Figure G.1. This figure only shows a 2D representation of the frames, as their Z axes are aligned within the confines of this work.

1. **Global LVLH Frame:** used to express ACCD towing positions.
2. **Local LVLH Catenary Frame:** used to simulate the catenary tether model.
3. **ACCD Body Frame:** used to express towing loads and body-centred aerodynamic coefficients, as well to analyse visibility of VisNav beacons.
4. **Docking Cone Frame:** used to compute intersection points between the VisNav LoS and the ACCD's docking cone.
5. **Aerodynamic Frame:** used to express lift and drag coefficients.

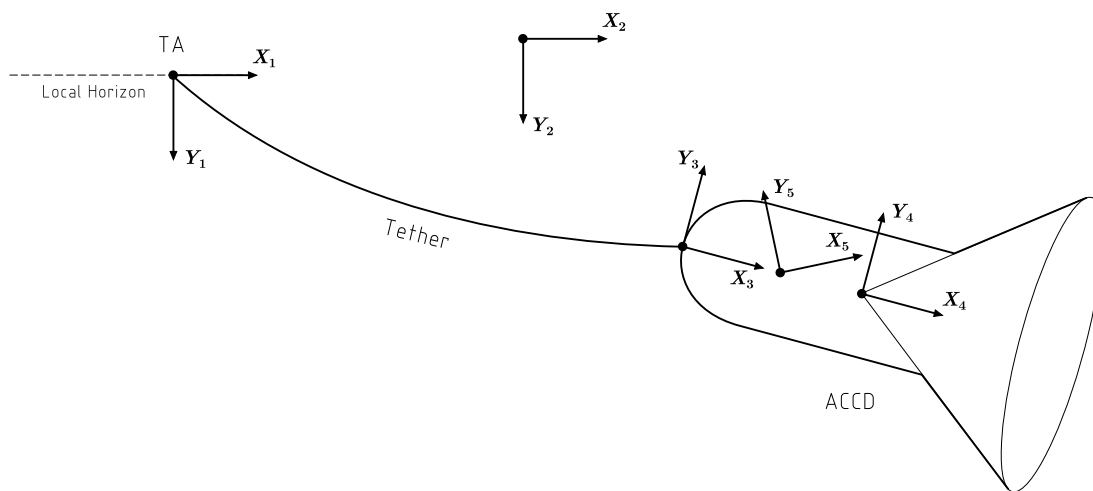
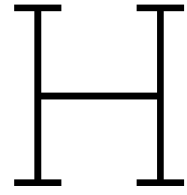


Figure G.1: Definition of Principal Reference Frames.



TA Thrust Model

To analyse excess-thrust scenarios, and to investigate the feasibility of towing configurations, a rudimentary thrust model for the TA has been implemented in chapter 3's Towing Model. In a previous study, the three-spool, high-bypass turbofan configuration [19] of the A340-600's four Rolls Royce Trent 500 engines [18] was modelled using the GasTurb tool [176]. The resulting data - visualized in Figure H.1 - allows an estimation of the TA's peak thrust as a function of its flight velocity and air speed. Additionally, fuel consumption data are also available, which can be used as a starting point for analysing desirable tow-back flight regimes. Details concerning the implementation of this thrust model into the overall Towing Model are provided in chapter 3.

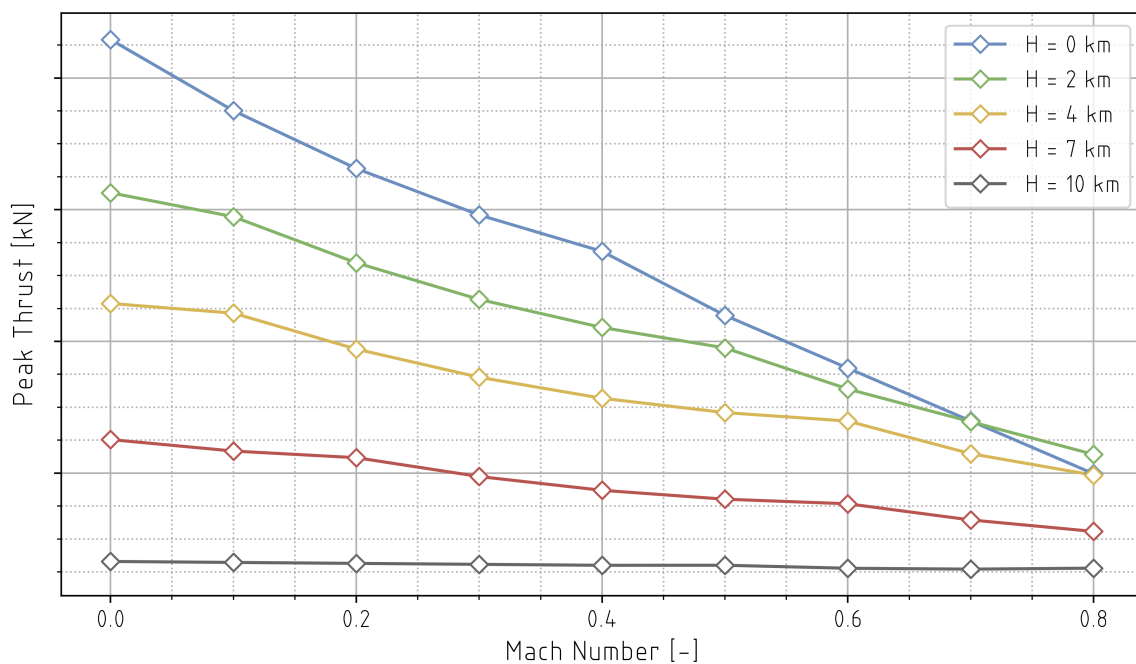


Figure H.1: Combined Peak Thrust of the A340-600 TA, as a Function of Flight Altitude and Airflow Velocity. Because of data confidentiality, the Y-axis scale is not specified.

Tether Design Space

Using chapter 3's Towing Model, the influence of the tether's length and diameter on the towing system can be studied. Although the tether is not a part of the ACCD design space considered for this work, such an analysis provides additional insight into the behaviour of the towing system, as well as additional verification for the implemented catenary tether model. In sections I.1 and I.2, the effect of the tether length and diameter are respectively studied, under a ceteris paribus assumption.

I.1. Tether Length

Figure I.1 shows that increasing the tether length can help the ACCD to stay clear of the TA's wake - as suggested in a 2023 SART paper [38]. Additionally, longer tethers also have an increased weight, slightly lowering the ACCD's towing position. However, because the tether length plays a significant role in the dynamic behaviour of the towing system - which was studied extensively in the past [37] - no explicit conclusions are drawn from the presented observations.

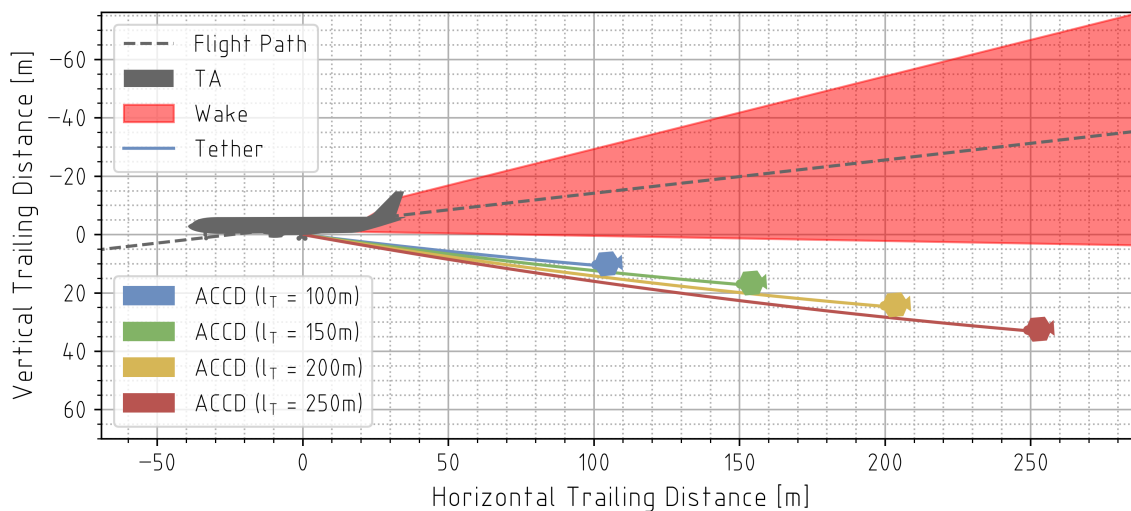


Figure I.1: Sensitivity of the ACCD's Towing Position to the Tether Length. Model inputs are listed in Table 3.1

I.2. Tether Diameter

Similarly, the tether diameter is mainly determined by the maximum towing loads that it needs to support, and does not provide practical design freedom within the context of this work. Nevertheless, the sensitivity study shown in Figure I.2 provides valuable verification insight into the modelling of the catenary tether. As can be expected from the theoretical background provided in chapter 3, thicker,

heavier tethers assume a catenary with an increased curvature, resulting in a lower ACCD towing position. Conversely, thin, light tethers effectively behave like a rigid link, with no noticeable curvature. This is consistent with the equations presented in chapter 3, as the tether's weight becomes negligible compared to the towing loads in such cases. This in turn results in a virtually constant tension throughout the length of the tether, which translates into a nearly unchanging tether angle throughout. A similar consideration concerns the tow-back phase of IAC: because of the significantly increased towing loads generated by the RLV, tether weight again becomes negligible, so that the tether essentially behaves as a rigid link - as can be observed in Figure 3.12.

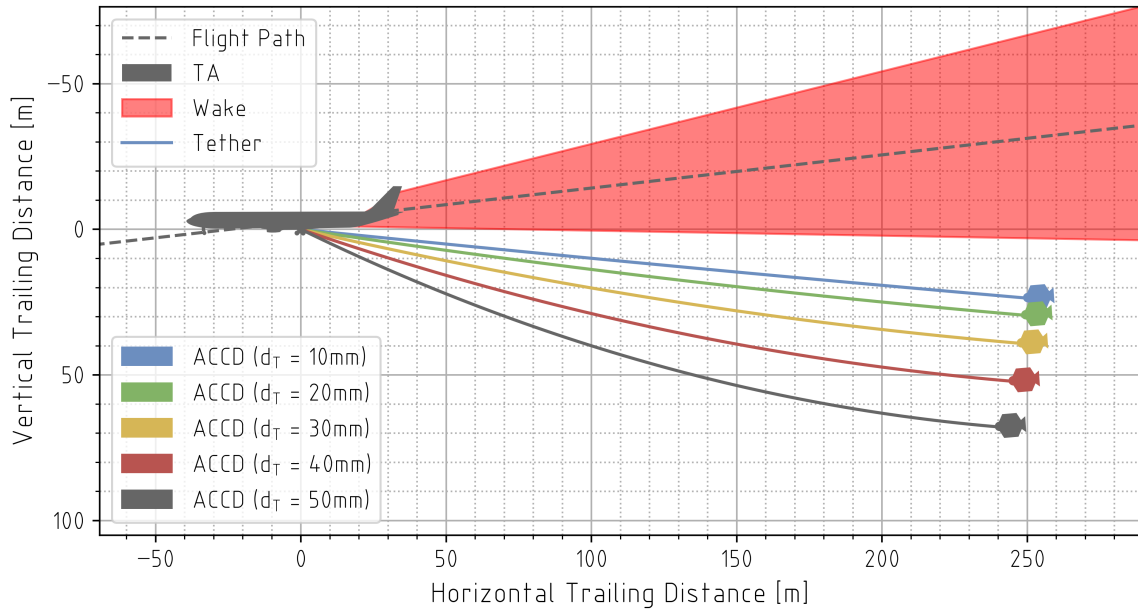


Figure I.2: Sensitivity of the ACCD's Towing Position to the Tether Diameter. Model inputs are listed in Table 3.1

J

Relative Navigation Paper

The following pages include a paper discussing the simulation of the ACCD's relative navigation system, using chapter 4's VisNav Model. The paper was presented at HiSST 2024 in Busan, South Korea [15]. Furthermore, an adapted version of this paper is currently under peer review for publication in the CEAS Space Journal.



Relative Navigation Implementation for the In-Air Capturing of a Winged Reusable Launch Vehicle

Sunayna Singh¹, Briek Luyten¹, Marco Sagliano¹

Abstract

In the 'In-Air Capturing' recovery mode, a winged rocket stage is captured mid-air by an aircraft and towed back to the launch site. A critical aspect of 'In-Air Capturing' involves a capturing device released from the towing aircraft, tasked with autonomously navigating to the launcher stage and connecting the vehicles with a tether. This operation demands high-precision close-range navigation sensors for the final docking maneuver. Hence, this paper proposes and studies different navigation solutions for the full-scale 'In-Air Capturing' application. A Vision-Based Navigation System (VisNav) is compared against the classical GPS/INS and a combined GPS/INS/VisNav navigation system. Simulations show that the GPS/INS/VisNav has a higher accuracy and provides a more robust navigation solution against model uncertainties and external disturbances.

Keywords: *In-Air Capturing, Reusable Launch Vehicles, Relative Navigation, VisNav, Capturing Device*

Nomenclature

Abbreviations

6DOF	Six degrees of freedom	B_i	Position vector of beacon i in object space
ACCD	Aerodynamically Controlled Capturing Device	c	Beacon Visibility Condition
AoA	Angle of attack	C	Transformation matrix between object space and image space
CCD	Charge-coupled device	d	Beacon Mounting Diameter
LOS	Line-of-sight	D	Docking Cone Outer Diameter
DSP	Digital Signal Processor	D'	Docking Cone Inner Diameter
EKF	Extended Kalman filter	$f(\theta, h)$	Docking Cone Surface
FoV	Field of view	FoE	Beacon Field of Emission Half Angle
GLSDC	Gaussian Least Squares Differential Correction	FoV	Sensor Field of View Half Angle
GPS	Global Positioning System	L	ACCD Length
LiDAR	Light Detection and Ranging	n	Number of Beacons
INS	Inertial Navigation System	\mathbf{n}	Pointing Vector
L/D	Lift-to-drag	\mathbf{o}	Position of the sensor in object space
MECO	Main engine cut-off	\mathbf{p}	Modified Rodrigues parameter indicating attitude of the sensor in object space
PSD	Position Sensing Diode	\mathbf{p}	Line of Sight Vector in ACCD Body Frame
RLV	Reusable launch vehicle	\mathbf{P}	Position in ACCD Body Frame
SWaP	Size, Weight and Power	R	Beacon Range
TA	Towing aircraft	V	Beacon Visibility
VisNav	Vision-Based Navigation System	y_i	Measured coordinates in horizontal direction in the image frame
		z_i	Measured coordinates in vertical direction in the image frame

Symbols

\mathbf{b}_i – Unit line of sight vector of beacon i in object space

¹ DLR Institute of Space Systems, Robert Hooke Straße, 1, 28359, Bremen, Germany

α – RLV Relative Pitch Angle
 γ – Docking Cone Half Angle
 μ – Sensor Mounting Angle

Φ – Principle rotation angle for modified rodrigues parameter

1. Introduction

The ‘In-Air Capturing’ return mode is an innovative launcher recovery method that has shown great potential for cost reduction compared to the currently operational Reusable Launch Vehicles (RLVs). This approach, first proposed by DLR [1], involves capture of a winged rocket stage mid-air using an aircraft, which tows it back to the launch site. This eliminates the need for a supplementary propulsion system for landing and brings down the inert mass [2]. This further reduces the overall cost of recovery when compared to vertical landing recovery methods, which require significant amount of fuel during descent. An assessment of the performance of various RLV approaches and the associated cost-benefit of ‘In-Air Capturing’ is presented in [3] and [4], respectively.

The complete (generic) mission cycle of ‘In-Air Capturing’ is shown in Fig. 1. The mission starts with a vertical launch from the launch pad. At main engine cut off (MECO), the winged first stage separates from the launch vehicle and the second stage moves on to the orbit. The first stage then begins a ballistic re-entry such that its velocity is reduced from supersonic to subsonic through atmospheric braking. In the meantime, a towing aircraft (TA) loiters at approximately 10 km altitude until the RLV is in the vicinity. Then, between an altitude of 2 km and 8 km, the TA approaches the RLV to form a gliding parallel formation. During this maneuver, a capturing device is released from the TA, which autonomously connects the two bodies via a tether. Finally, the RLV is towed back to an airstrip, where it is released to land horizontally.

Since an essential aspect of ‘In-Air Capturing’ involves close proximity formation flying and eventual docking/ mating with the capturing device, a reliable and accurate relative navigation system is necessary. The system should operate effectively even in turbulent weather conditions and poor visibility situations. Redundancy in sensor systems is crucial to ensure a safe and successful flight, mitigating the impact of sensor failures. Data from multiple sensors can be fused to achieve higher accuracy and improve robustness. Lightweight sensors with high update rates and low processing requirements add to the efficacy of the system. Thus, these factors must be considered for the selection of sensors. This study will analyze potential close-range relative navigation solutions for the full-scale ‘In-Air Capturing’ application. The main focus will be on the capture system, which requires interaction between the capturing device and the RLV for precise maneuvering and mating.

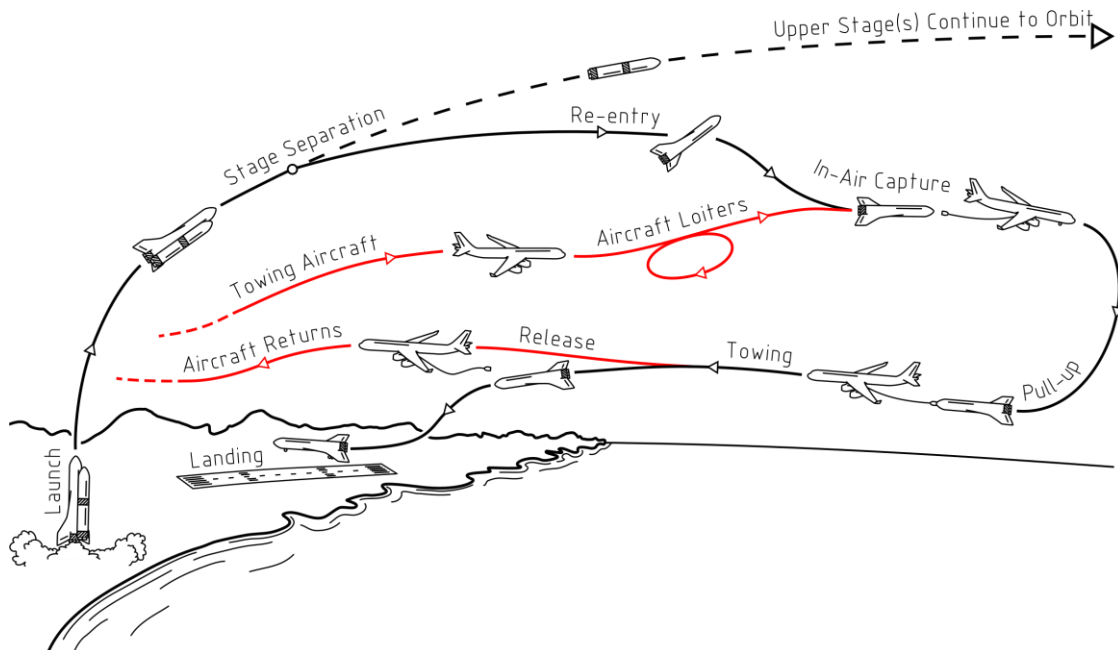


Fig. 1: Schematic of a typical In-Air Capturing mission cycle [1]

Similar scenarios to In-Air Capturing, which require precise close-range state estimation for rendezvous and docking can be found both in atmospheric flight and in space applications. In particular, the field of automated aerial refueling shows significant resemblance with the current application, and can offer a number of potential solutions to this relative navigation problem. A common approach is to use classical long-range sensors like the Global Positioning System (GPS) to calibrate the relative measurements from the relative Inertial Navigation Systems (INS) [6, 7]. This requires each aircraft or UAV to have the full GPS and INS sensor system. However, when precise measurements are required, GPS and INS based systems are often fused with other sensors (like electromagnetic detection systems), which can provide close-range, high-accuracy relative measurements [8, 9].

A prominent subset of these close-range sensors falls under the umbrella of computer vision. Computer vision systems typically use a generic, visible-wavelength camera, and rely on extensive image processing technologies to extract relevant data, such as relative position and attitude of a given target object. The cameras used can be grayscale [10] or color-sensitive [11], and can be mounted individually [12] or in pairs [13]. In some applications, the target body is left entirely unaltered and passive, purely relying on image processing algorithms, such as corner detection [14] and arc extraction [15]. Other systems depend on active markers that are applied to the target, and which increase the system's robustness to external lighting conditions [16]. One specific application, designed for boom-and-receptacle aerial refueling, employs a visual pressure snake sensor to detect a geometric pattern that has been applied to the target body [17].

Although computer vision techniques tend to achieve good performance with rates up to 55 Hz [18], and accuracies up to 10 cm [19], they come at the cost of significant computational power, which typically needs to be enabled using dedicated graphical processing units [20]. Additionally, the inherent reliance on visible-wavelength data creates a crucial sensitivity to environmental parameters, with most systems not being robust in low-light or low-visibility conditions [18]. One solution to this problem consists of shifting the relevant wavelength spectrum upwards, and using an infrared camera [21]. However, these solutions still require significant post-processing efforts.

Another major branch in this technological field can be found under electro-optical grid reference systems. A number of actively emitting beacons are mounted on the target, which a sensor on the main body detects. For the beacons, LEDs or laser diodes are typically used, while the sensor can be a Charge-Coupled Device (CCD detector), photodiode, or Position Sensing Diode (PSD) [22, 23]. Specific implementations of these systems include the VisNav technology developed at the Texas A&M University [24]. Contrary to computer vision techniques, these electro-optical grid reference systems are typically quite minimalistic in terms of Size, Weight and Power (SWaP) footprint, by relying on more elementary sensor elements which require less post-processing [23]. Additionally, when working with an IR-spectrum, the aforementioned robustness against environmental and lighting conditions can also be introduced [26].

Other solutions include ultrasonic or acoustic sensors [27], time-of-flight sensors [28], or radar technologies [22]. However, none of these are particularly suited to meet the In-Air Capturing requirements, respectively because of insufficient range and environmental robustness [29], and excessive power and size footprints [18]. Finally, LiDAR systems have also been used for these types of applications, either by using a scanning LiDAR [30], or a TriDAR system [31]. Although these systems are more robust to the effects of clouds, ambient light, and motion-blur [25], they suffer from attenuation due to atmospheric water vapour [22], while also having a significant SWaP footprint, with a relatively limited field of view (FoV) [33].

In conclusion, given the requirements of In-Air Capturing in terms of environmental robustness, accuracy, and SWaP, an electro-optical grid reference system for close-range navigation shows the greatest potential. In particular, VisNav technology is chosen as a potential solution for this application, and investigated in further detail. In Section 2, the theory and modelling of the VisNav system is reviewed. Additional models to simulate the VisNav system for In-Air Capturing applications are also presented in this section. This involves modelling of critical aspects like the line-of-sight (LOS) between RLV and ACCD, and placement of beacons on the ACCD to improve the likelihood of detection. Next, in Section 3, different sensor fusion configurations are proposed and analyzed. For performance analysis,

VisNav is compared against a classic GPS/INS system and also, an integrated GPS/INS/VisNav system. It is assumed that the ACCD sends GPS and INS data to the RLV, where the sensor fusion process takes place. Simulations are then performed for both ideal and non-ideal scenarios using a simplified representation of 'In-Air Capturing' trajectory in Section 4. Finally, the conclusion and future work are discussed in Section 5.

2. Vision Based Relative Navigation System

The VisNav navigation system provides a six degrees of freedom (6DOF) solution constituting the relative position and orientation between two vehicles or objects at close-range (up to 200 m at 100 Hz [35]). It operates by evaluating the LOS vectors between a sensor, mounted on one vehicle, and a series of structured light beacons rigidly fixed to the target vehicle. These beacons have predetermined positions in the target vehicle frame, enabling the determination of the sensor's relative position and orientation with respect to the target frame [34]. A widely studied application for VisNav navigation systems is the probe-drogue aerial refueling system [23-24, 34-36].

The probe-drogue aerial refueling system consists of drogue attached to a hose released from the tanker aircraft as shown in Fig. 2. The back of the drogue has a conical skirt-like structure within which the VisNav beacons are typically placed. The receiver aircraft then navigates its way to the drogue and connects itself using a boom. The working principle being similar to the 'In-Air Capturing' application, supports the selection of VisNav for the relative navigation solution. Fig. 3 illustrates the configuration of the chosen capturing device for 'In-Air Capturing,' referred to as the Aerodynamically Controlled Capturing Device (ACCD). It measures 2 meters in length with a cross-sectional diameter of 1.5 meters, including the fins. Equipped with four flaps capable of deflecting up to a maximum of $\pm 15^\circ$, it provides 6DOF for agility and control. The ACCD's nose is tethered to the TA via a rope, while the capturing mechanism located at the device's rear ensures a secure connection using a lock-in mechanism with a boom on the RLV. It also contains a guiding cone at the back, which could house the beacons for VisNav. The working principle and solution approach of Visnav is explained in Section 2.1.

Aerial refueling operations are typically performed at near constant altitude and velocity of the tanker aircraft. The receiver aircraft are usually highly maneuverable and can actively perform corrective maneuvers to reach the drogue. Conversely, the capture of the RLV during 'In-Air Capturing' is to be attempted in a descending formation flight as explained in [2]. The RLV, due to its lower aerodynamic performance, descends at a constant relative flight path angle of approximately -2° to the TA, even during the formation flight. Such a trajectory could lead to challenges in detection of the ACCD from the RLV and effective use of the VisNav technology. Thus, in Section 2.2, an analytical detection model is developed to analyze different configurations of beacons and placement of the VisNav sensor to improve the chances of successful detection. Finally, in Section 2.3, a sensitivity study is performed using this model, and the final configuration of VisNav for 'In-Air Capturing' application is selected.



Fig. 2: Aerial refuelling drogue with VisNav beacons and boom from the receiver aircraft [36]

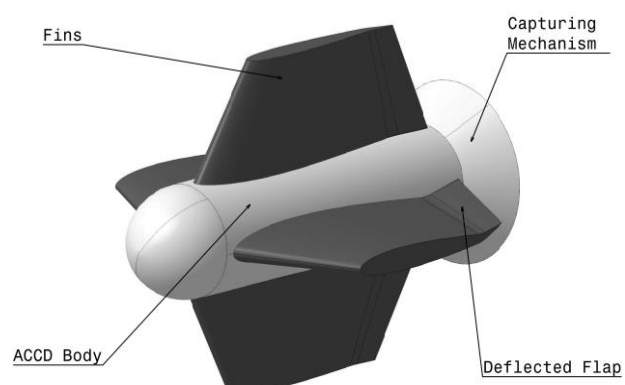


Fig. 3: Aerodynamically Controlled Capturing Device (ACCD) [37]

2.1. VisNav System

Fig. 4 shows a schematic of a VisNav sensor, when applied to the 'In-Air Capturing' application. The beacons, which can be actively controlled, are mounted on the cone located at the rear of ACCD (refer to Fig. 3). The sensor is mounted on the RLV body and comprises a Position Sensing Diode (PSD), wide-angle lens and a Digital Signal Processor (DSP). The beacons on the ACCD can be controlled to maintain different light intensities and activation sequences to ensure both preservation of the photo diode and optimal signal-to-noise ratio during operation [34]. During VisNav operation, as each beacon illuminates, light passes through the wide-angle lens, focusing onto the PSD. This focused light generates a centroid, or spot, on the photo diode, inducing a current imbalance across the four terminals on each side of the PSD. By measuring the voltage at each terminal, unit LOS vectors from the sensor to each beacon can be derived via a calibration function. Further details on the measurements and calibration with hardware can be found in [23].

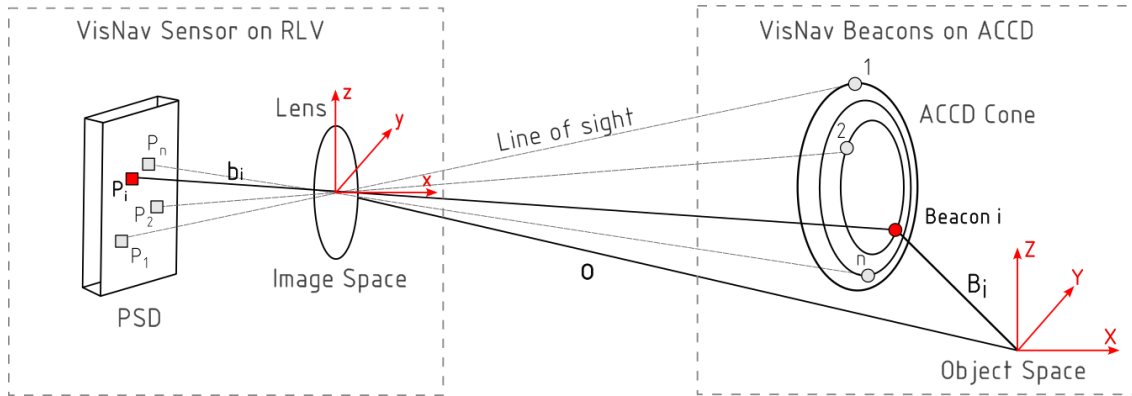


Fig. 4: VisNav sensor model applied to In-Air Capturing

Fig. 4 depicts two important coordinate frames. First, the object space frame is fixed to the ACCD body frame. The position of beacon i on the target vehicle is already known and its position vector in object space is denoted by \mathbf{B}_i . This can be written as:

$$\mathbf{B}_i = [X_i \quad Y_i \quad Z_i]^T \quad (1)$$

Second, the image space is a body-fixed frame located at the center of the lens on the sensor. The unit LOS vector of beacon i is measured from the image space to the PSD and is denoted by \mathbf{b}_i . Using this information, the position of the sensor in object space (\mathbf{o}), and the transformation matrix between image space and object space (\mathbf{C}) can be determined. They can be expressed using:

$$\mathbf{o} = [X_c \quad Y_c \quad Z_c]^T \quad (2)$$

And,

$$\mathbf{C} = \mathbf{I} + \frac{8[\mathbf{p} \times]^2 - 4(1 - \mathbf{p}^T \mathbf{p})[\mathbf{p} \times]}{(1 - \mathbf{p}^T \mathbf{p})^2} \quad (3)$$

Where,

$$[\mathbf{p} \times] = \begin{bmatrix} 0 & -p_3 & p_2 \\ p_3 & 0 & -p_1 \\ -p_2 & p_1 & 0 \end{bmatrix}$$

Here, the attitude parameterization is done using Modified Rodrigues Parameters (MRPs). They are a set of three attitude angles that can be linked to Euler parameters using principal rotation vector, \mathbf{e} , and principal rotation angle, Φ . Thus, the MRP (3x1) vector can be defined as $\mathbf{p} = \tan \frac{\Phi}{4} \mathbf{e}$. Further explanation on the attitude parameters can be found in [38]. Using collinearity equations (described in

detail in [36]), a nonlinear relationship between the measured image space coordinates (y_i, z_i) , and the six unknown states in object space $(X_c, Y_c, Z_c, p_1, p_2, p_3)$ can be established as follows:

$$y_i = -f \frac{C_{21}(X_i - X_c) + C_{22}(Y_i - Y_c) + C_{23}(Z_i - Z_c)}{C_{11}(X_i - X_c) + C_{12}(Y_i - Y_c) + C_{13}(Z_i - Z_c)} \quad (4)$$

$$z_i = -f \frac{C_{31}(X_i - X_c) + C_{32}(Y_i - Y_c) + C_{33}(Z_i - Z_c)}{C_{11}(X_i - X_c) + C_{12}(Y_i - Y_c) + C_{13}(Z_i - Z_c)} \quad (5)$$

Where f denotes the focal length of the wide-angle lens. Each beacon provides two equations through its measurements, necessitating a minimum of three beacons to derive a solution. However, to ensure a unique solution, a minimum of four measurements is required. A Gaussian Least Squares Differential Correction Algorithm (GLSDC) is used to solve for the position and orientation of the sensor with respect to the beacons. By integrating the measurement model and observation data, the algorithm generates an estimation of the unknown parameters that is optimal, considering a predetermined level of measurement noise [39]. A detailed explanation of the algorithm and the associated VisNav measurement model is given in [36].

2.2. Detection Model

In order to determine the visibility of each VisNav beacon, in conjunction with the relative states of both ACCD and RLV, a detection model is added to the simulation. The visibility of each beacon is calculated based on the geometry of the vehicles, the placement of each beacon on the ACCD and the placement of sensor on the RLV. The general configuration is shown in Fig. 5, which shows the relevant reference system and variables.

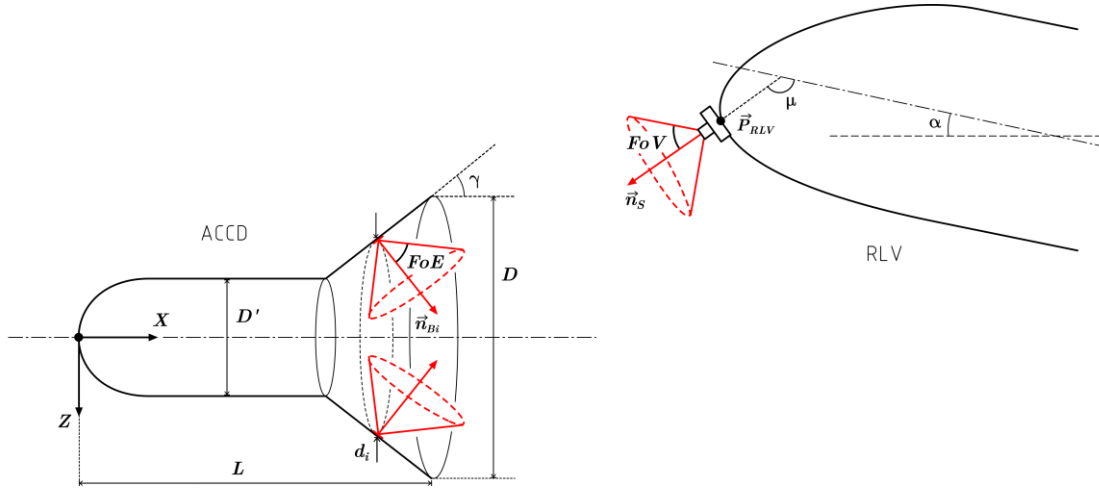


Fig. 5: Definition of reference system used in detection model

The detection model is based on a mathematical representation of the positions and normal vectors of all beacons and sensors. As a baseline configuration, a single sensor is mounted on the RLV. The RLV is modelled as a point mass with pitch angle α . The sensor position is assumed to be equal to the position of the RLV, P_{RLV} . This position is derived from the trajectory model and is updated at the given sensor frequency (100 Hz). Since both RLV and ACCD are expected to have a positive pitch angle during the approach and capture, the sensor is mounted at an angle μ relative to the RLV orientation to increase visibility (see Fig. 5). Assuming only pitch variations in RLV, the corresponding sensor pointing vector n_s is given by:

$$n_s = \begin{bmatrix} \cos(\alpha + \mu) \\ 0 \\ \sin(\alpha + \mu) \end{bmatrix} \quad (6)$$

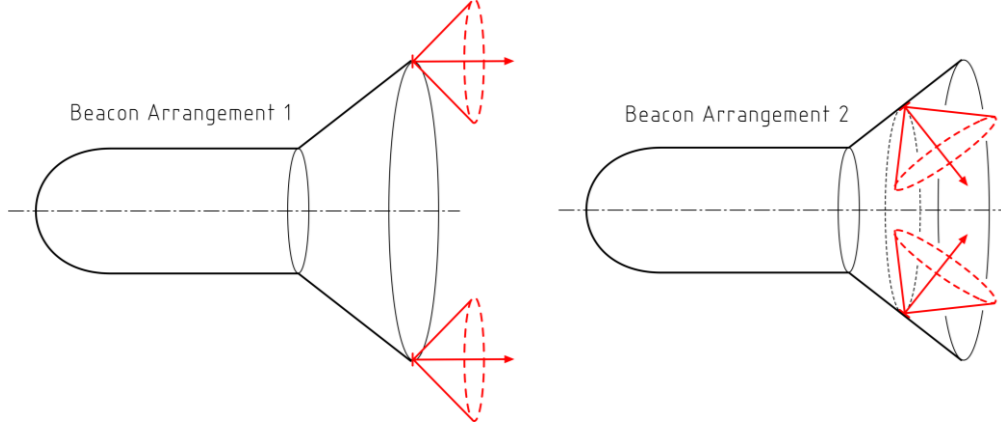


Fig. 6: Different types of beacon arrangements considered in the study

To improve the chances of detection, the beacons are mounted in two concentric arrangements on the ACCD cone. The first set of beacons are attached to the aft rim of the ACCD pointing along the positive X-axis of its body frame, seen in Fig. 6 as the outermost ring of beacons (Arrangement 1). This arrangement would facilitate detection from larger distances. Distributing n beacons equally over a circle with diameter d_i , results in the following position coordinates:

$$\mathbf{P}_{Bi} = \begin{bmatrix} L \\ d_i/2 \cdot \sin \phi_i \\ d_i/2 \cdot \cos \phi_i \end{bmatrix}, \quad \text{where } \phi_i = i \cdot \frac{2\pi}{n}, \quad i = 1 \dots n \quad (7)$$

The second set of beacons are mounted inside the ACCD's docking cone, pointing slightly inwards (Arrangement 2 in Fig. 6). Such a configuration would facilitate precision mating at shorter distances. This docking cone is characterized by an outer diameter D , inner diameter D' and cone half angle γ , which allows it to be parametrized mathematically as a function of h and θ ,

$$\mathbf{f}(h, \theta) = \begin{bmatrix} h \cdot \cos \gamma + L - D/(2 \cdot \tan \gamma) \\ h \cdot \sin \gamma \cdot \sin \theta \\ h \cdot \sin \gamma \cdot \cos \theta \end{bmatrix}, \quad \text{where } \begin{cases} h \in [D'/(2 \cdot \sin \gamma), D/(2 \cdot \sin \gamma)] \\ \theta \in [0, 2\pi] \end{cases} \quad (8)$$

For a mounting circle of diameter d_i and mounting angle ϕ_i , $h = d_i/(2 \cdot \sin \gamma)$ and $\theta = \phi_i$. The pointing vectors \mathbf{n}_{Bi} are equal to the unit normal vector to this surface, given by:

$$\mathbf{n}_{Bi}(h, \theta) = \left(\frac{\partial \mathbf{f}}{\partial h} \times \frac{\partial \mathbf{f}}{\partial \theta} \right) / \left\| \frac{\partial \mathbf{f}}{\partial h} \times \frac{\partial \mathbf{f}}{\partial \theta} \right\| \quad (9)$$

For a beacon to be successfully detected by the sensor, at least three conditions need to be fulfilled. The first one, c_{1i} , demands that the beacon be within the field of view of the sensor – defined as a half angle FoV . The sensor should also be within the beacon's field of emission (FoE_i), so that its emitted signal reaches the sensor. For this, an equivalent half angle FoE_i is defined for each beacon. In order to verify this condition, the LOS vector between each beacon and sensor is computed, and then compared to the pointing vectors of the corresponding beacon and sensor.

$$\mathbf{p}_{BiS} = (\mathbf{P}_S - \mathbf{P}_{Bi}) / \|\mathbf{P}_S - \mathbf{P}_{Bi}\| \quad (10)$$

As a second condition c_{2i} , the LOS vector should not be obstructed by any physical obstacle. In practice, the ACCD docking cone is the only potential source of obstruction in these configurations. The intersection point(s) between the LOS vector and cone surface are computed using Eq. (11) for unknown parameters h , θ , and t . Condition c_{2i} can then be checked by assuring that this intersection point lies outside of the physical ACCD cone – which can be done using the h -parameter of this point.

$$\mathbf{f}(h, \theta) = \mathbf{P}_{Bi} + \mathbf{p}_{BiS} \cdot t \quad \text{where } \begin{cases} h \geq 0 \\ \theta \in [0, 2\pi] \\ t \geq 0 \end{cases} \quad (11)$$

Finally, as a third condition c_{3i} , the sensor should be within the beacon's range of emissivity R , so that its signal is strong enough to be detected. For this, the distance $\|\mathbf{P}_S - \mathbf{P}_{Bi}\|$ between sensor and

beacon is used. Combining these three conditions, the overall visibility of each beacon can be assessed as follows:

$$V_i \Leftrightarrow (c_{1i} \wedge c_{2i} \wedge c_{3i}) \quad \text{where} \quad \begin{cases} c_{1i} = (\cos^{-1}(\mathbf{p}_{BiS} \cdot \mathbf{n}_{Bi}) \leq FoE_i) \wedge (\cos^{-1}(\mathbf{n}_S \cdot \mathbf{p}_{BiS}) \leq FoV) \\ c_{2i} = \|\mathbf{P}_S - \mathbf{P}_{Bi}\| \leq R \\ c_{3i} = h_{coll,i} > D/(2 \cdot \sin \gamma) \end{cases} \quad (12)$$

A schematic representation of the detection model and its variables can be seen in Fig. 7. This illustration also shows the connections with the VisNav model, described in section 2.1. At each time step, the RLV state is fed into the detection model, which updates the sensor position and pointing vector. Then, the visibility of each of the ACCD's beacons is determined, and returned to the VisNav model – together with the position of the beacons in the ACCD body frame. The fixed parameters associated with the ACCD docking cone are given in Table 1. The parameters associated with beacons and VisNav sensor are determined using a sensitivity study presented in the next sub-section.

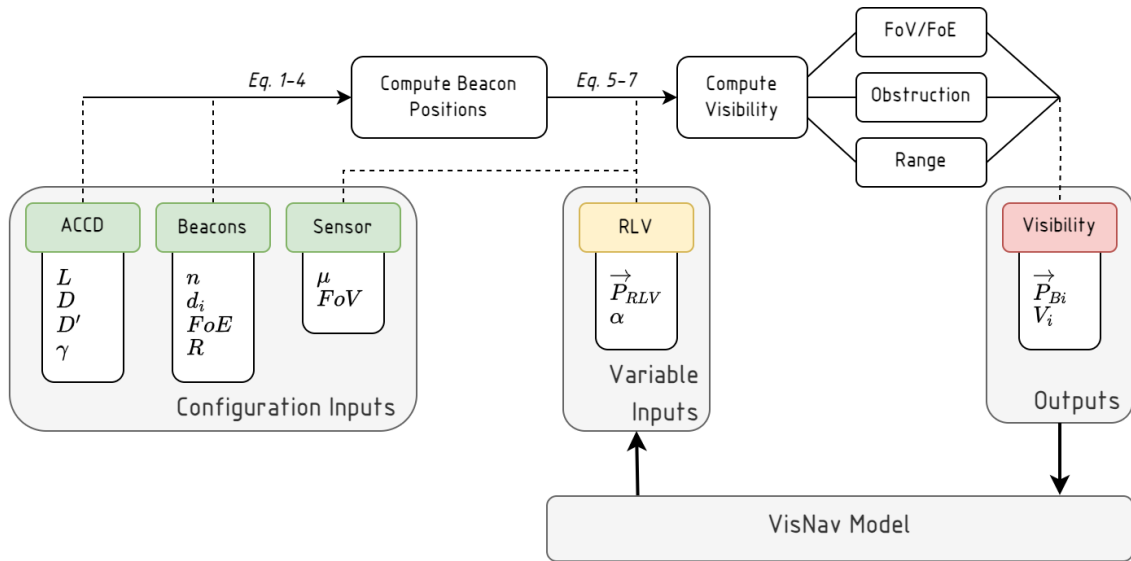


Fig. 7: Flow diagram of detection model

Table 1. Input parameters characterizing the ACCD docking cone

Parameter	Value(s)	Unit
L	2	[m]
D	0.7	[m]
D'	0.5	[m]
γ	30	[°]

2.3. Baseline Sensor and Beacon Configuration

Using the detection model, the expected performance of different beacon configurations is assessed, by varying the RLV position \mathbf{P}_{RLV} in a grid search, and determining the number of visible beacons at each of these positions. Examples of the resulting approach maps for the RLV are shown in Fig. 8. It can be observed from the figure that a lower sensor mounting angle is favourable for steep descents while a higher mounting angle enables detection of more beacons in a shallower descent trajectory of the RLV. For the current study, the FoV of sensor is assumed to be 60° [40] and the FoE of each beacon is assumed to be 45°. Based on these specifications and the reference trajectory for the study (shown in Fig. 14), the maximum visibility was achieved at a sensor mounting angle (μ) of 140°.

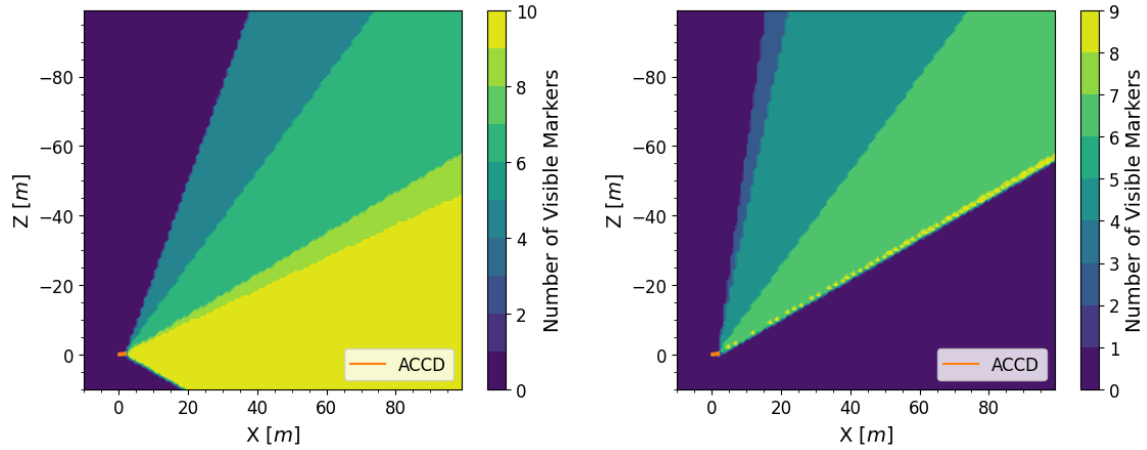


Fig. 8: Approach maps for two different VisNav configurations with different sensor mounting angles $\mu=160^\circ$ (left) and $\mu=100^\circ$ (right)

Table 2: Specifications of different beacon configurations on ACCD docking cone

	Beacons per Ring	Ring Diameter (d_i)
Configuration 1	[6, 6]	$1.05 * D$, $0.95 * D$
Configuration 2	[6, 6]	$1.05 * D$, $0.65 * D$
Configuration 3	[3, 4, 5]	$1.05 * D$, $0.95 * D$, $0.65 * D$

According to [34], the accuracy of VisNav depends on beacon geometry. Thus, the study is performed with different beacon configurations specified in Table 2 and visualized in Fig. 9. A total of 12 beacons are distributed over concentric rings on the ACCD docking cone. Each configuration has one ring of rim-mounted beacons, as indicated by Arrangement 1 in Fig. 6. The inner rings use the Arrangement 2 shown in Fig. 6. Then, using the reference trajectory shown in Fig. 14, each configuration is evaluated for visible beacons as well as accuracy of measurements. In Configuration 1, most of the beacons are placed on the outer edge of the ACCD cone. Although the placement facilitates the detection of higher number of beacons at long range at the beginning of the trajectory (shown in Fig. 10), inaccuracies arise in the final phases of docking. This can be observed in Fig. 11, which shows the relative attitude measurements from the VisNav sensor. Errors up to 1.5° can be observed in pitch and yaw configurations.

This issue is resolved by placing the inner ring slightly away from the outer ring (Configuration 2) or adding an additional ring of beacons (Configuration 3). It can be observed from Fig. 11, that the relative attitude errors decrease significantly compared to Configuration 1 and therefore, are more suitable for precision mating operations in In-Air Capturing. However, more beacons are detected in Configuration 3 compared to Configuration 2 at close-range towards the end of the trajectory (see Fig. 10). Hence, Configuration 3 is preferable to achieve higher beacon visibility during the final phases of docking. Additionally, the asymmetric arrangement of beacons in this configuration provides robustness for orientation measurements. Since the performance of both the configurations (2 and 3) are similar, Configuration 3 is selected as the baseline for the current study. The final positions of the beacons with respect to the ACCD body fixed frame are given in Table 3.

Table 3. Position of beacons in ACCD body frame, for the chosen baseline configuration – Configuration 3

Beacon	1	2	3	4	5	6	7	8	9	10	11	12
X [m]	1.79	1.79	1.79	1.97	1.97	1.97	1.97	2.00	2.00	2.00	2.00	2.00
Y [m]	0.23	-0.11	-0.11	0.33	0.00	-0.33	0.00	0.37	0.11	-0.30	-0.30	0.11
Z [m]	0.00	0.20	-0.20	0.00	0.33	0.00	-0.33	0.00	0.35	0.22	-0.22	-0.35

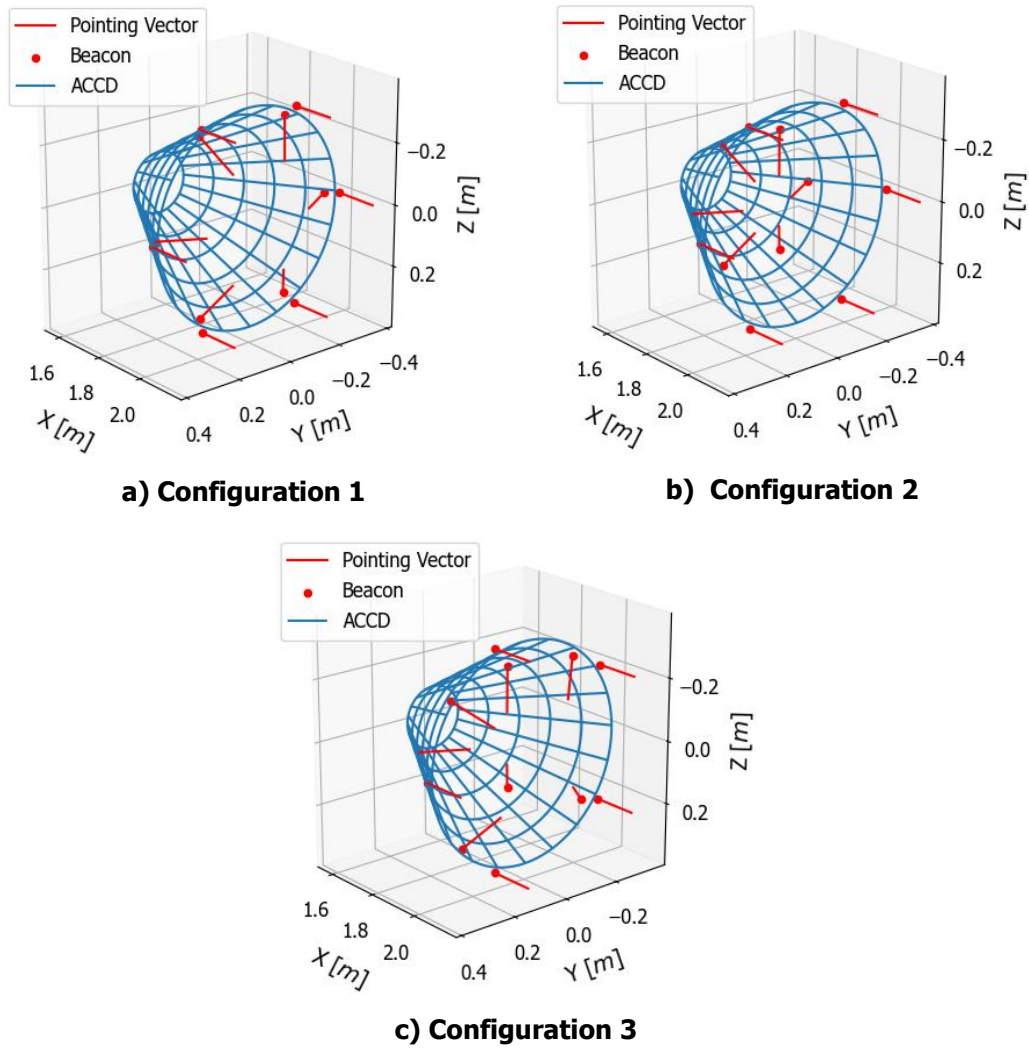


Fig. 9: 3D visualization of different beacon configurations mounted on the ACCD's docking cone

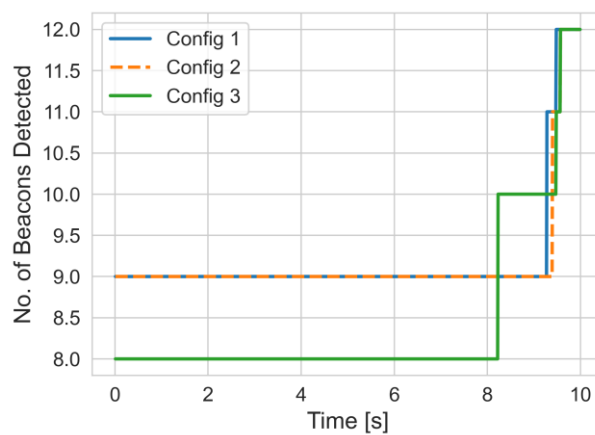


Fig. 10: Number of beacons visible throughout the trajectory of RLV given in section 4

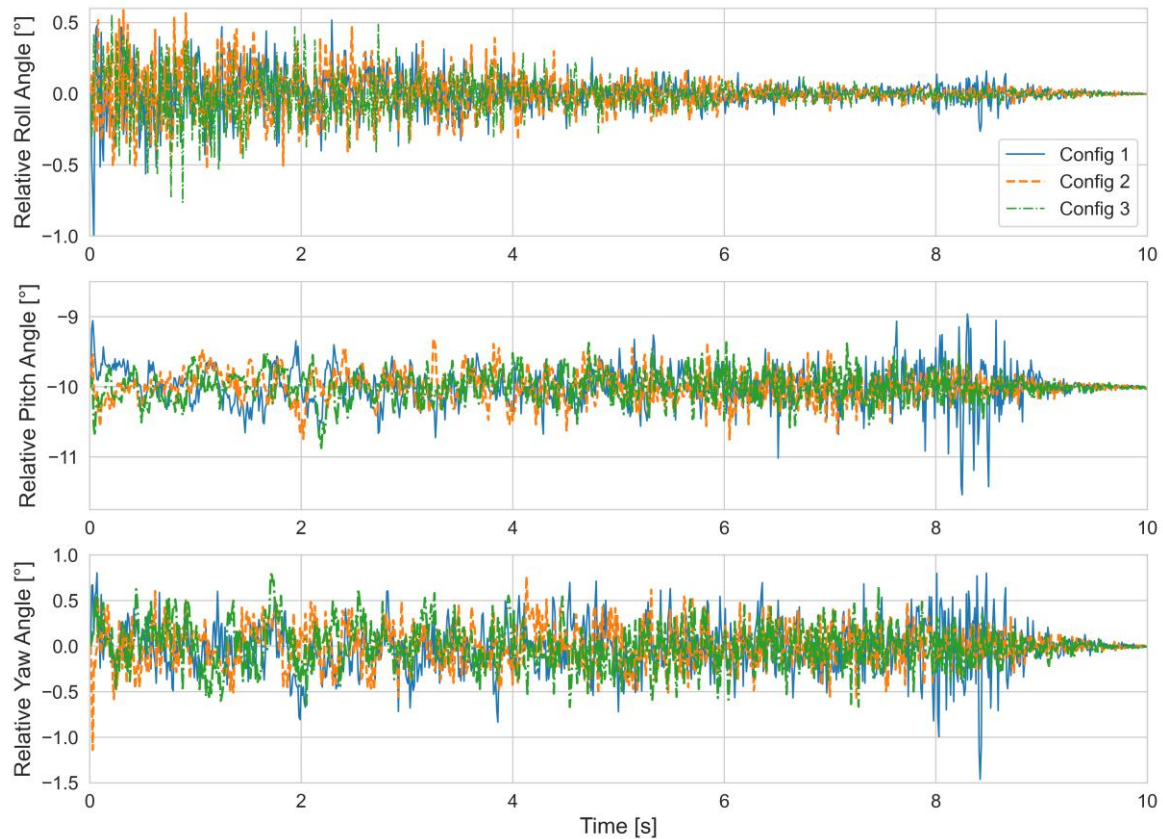


Fig. 11: Relative attitude between ACCD and RLV measured with VisNav, based on the reference trajectory given in section 4

3. Relative Navigation Model

For successful mating, the navigation system should measure the relative position with an accuracy of up to 0.35 m (slightly less than the outer radius of the ACCD guiding cone) and a relative orientation of 1° . This requirement can be met using the available sensors on the vehicles used for 'In-Air Capturing'. Fig. 12 shows the distribution of sensors available for relative navigation between ACCD and RLV. The active VisNav beacons are arranged on the ACCD docking cone while the VisNav camera is mounted on the RLV as discussed in the previous section. A set of GPS and INS sensor systems is included on both vehicles. It is assumed that a wireless communication system facilitates the sharing of GPS and IMU measurements between the two vehicles, ensuring that both sets of measurements are accessible for processing without delay. The data is fused together at their respective update rates using a simple master Extended Kalman Filter (EKF) assumed to be present on the RLV.

In the current study, three main architectures are studied for 6DOF close-range navigation (up to 200 m). The assessment involves comparing the standalone VisNav sensor, the traditional GPS/INS system, and a more comprehensive architecture combining all three systems, and evaluating their individual performances. In the coming section, specifications of the individual systems used in the simulations are explained.

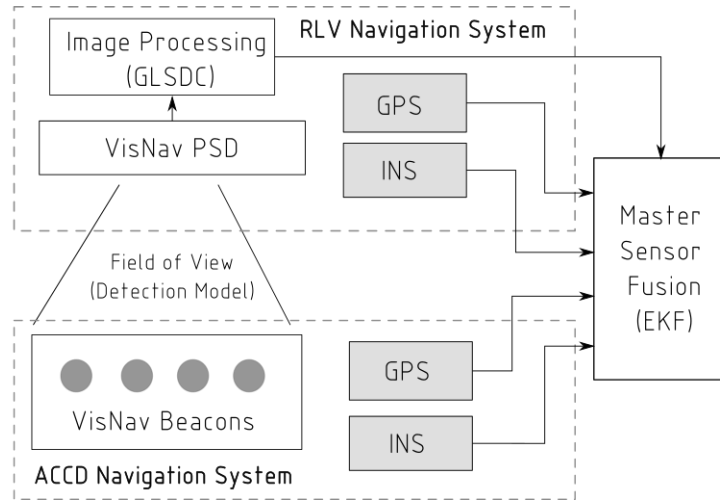


Fig. 12: Distribution of sensors and sensor fusion architecture for In-Air Capturing

3.1. VisNav Only

The VisNav system is capable of providing 6DOF measurements with an error of 1% in range and 0.1° in azimuth/elevation up to a range of 30 m and 1° error in direction for ranges up to 200m at 100Hz update rates [24],[40]. To model the measurement errors, a gaussian noise with zero mean and a standard deviation of $3500 \mu\text{rad}$ is considered [43]. The measurements obtained from VisNav (after data processing with GLSDC) could potentially be inputted into an EKF to enhance the navigation solution, giving supplementary estimations of relative velocity and acceleration. Further, it also provides the system with a prediction model using the simplified dynamics of the reference trajectory stated in Section 4. Details of EKF formulation can be found in [41]. The simplified linear dynamics used in the EKF is given by:

$$\dot{\mathbf{x}}(t) = \begin{bmatrix} \dot{\mathbf{z}}(t) \\ \ddot{\mathbf{z}}(t) \end{bmatrix} = \begin{bmatrix} 0 & I & 0 \\ 0 & 0 & I \\ 0 & 0 & 0 \end{bmatrix} \begin{bmatrix} \mathbf{z}(t) \\ \dot{\mathbf{z}}(t) \\ \ddot{\mathbf{z}}(t) \end{bmatrix} + \begin{bmatrix} 0 \\ 0 \\ I \end{bmatrix} \mathbf{w}(t) \quad (13)$$

Here,

$$\mathbf{z}(t) = \begin{bmatrix} \mathbf{o}(t) \\ \mathbf{p}(t) \end{bmatrix}$$

Where \mathbf{o} and \mathbf{p} indicate the position and orientation of the system. I is a (6×6) identity matrix and \mathbf{w} represents the process noise in the system. It is assumed that the relative translational and rotational accelerations are zero. This is valid assumption for the current reference trajectory (shown in Fig. 14) because the RLV is assumed to be descending with a constant velocity relative to the ACCD position. The current model also does not consider the effect of control input $\mathbf{u}(t)$. Future simulations will include a more intricate dynamics model for prediction of the state using EKF.

Using the reference trajectory given in Section 4, Fig. 13 shows the residual error in position of the RLV relative to ACCD using the VisNav (GLSDC) data alone and using GLSDC combined with EKF. It can be observed that lower errors and smoother response can be obtained by incorporating EKF with the GLSDC algorithm used to process VisNav data. Henceforth, all the simulations associated with VisNav in the study will include both GLSDC and EKF algorithms.

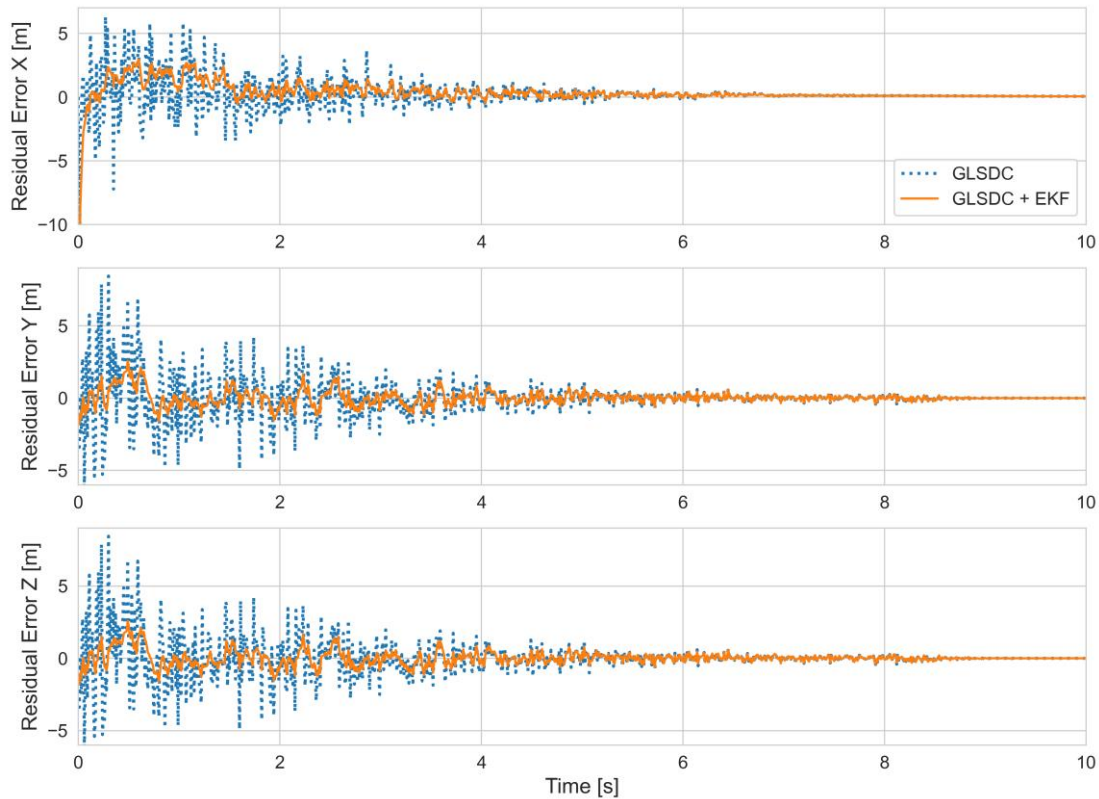


Fig. 13: Relative position error between ACCD and RLV with reference trajectory using GLSDC alone and GLSDC combined with EKF

3.2. GPS/INS

The prevalent method for relative navigation typically involves using relative GPS measurements to align with the relative INS [20]. This necessitates that each vehicle be equipped with a complete set of both GPS and INS sensors. Typically, GPS measurements can include satellite clock errors, atmospheric delays (ionospheric and tropospheric), multipath effects, and errors in the satellite's orbit data. These errors contribute to inaccuracies in the GPS position and velocity measurements. For this study, the GPS measurement error is simulated by introducing a nominal Gaussian noise with a standard deviation of 1.5 m to the position measurements [42]. A standard INS system includes accelerometers to measure linear acceleration and gyroscopes to measure angular velocity in the inertial frame. Initial position errors, integration drift (error accumulation over time due to inaccuracies in measured accelerations), and errors due to inaccuracies in the INS sensors (accelerometers and gyros) are typical errors observed in INS systems. Based on errors provided in [43], a gaussian noise with a standard deviation of 7500 $\mu\text{rad/s}$ is considered in the gyroscope measurements and a standard deviation of 0.05 m/s^2 is considered for the accelerometer measurements.

The integration of GPS and INS systems helps mitigate some of these errors. The GPS provides long-term stability and helps correct the INS drift errors, while the INS offers high-rate, real-time data that can fill the gaps when GPS signals are not available or are degraded. In this study, the INS system, with a higher update rate of 100 Hz is used to predict the system state while the less frequent GPS measurements are used as updates at 10 Hz. An EKF is again used to fuse the data at different frequencies.

3.3. GPS/INS/VisNav

Although, GPS/INS system can provide good accuracy up to a tenth of a meter for relative navigation, they are subjected to a number of conditions. GPS data may not be reliable in all regions of the world and the accuracy may vary from one location to another. Moreover, multiple vehicles in the vicinity can

cause GPS signals to be distorted by the aircraft. The lower update rates can also prove to be disadvantageous in case the ACCD needs to perform quick corrective maneuvers in the final phases of docking. Hence, the GPS/INS system alone may be insufficient for effective navigation during the capture.

On the other hand, VisNav systems can suffer from beacon dropout during which sufficient beacons are not available for navigation. Additionally, beacon visibility is subjected to environmental conditions. Some beacons may not appear bright enough to be detected by the VisNav sensor at longer range of operation. Thus, a combined GPS/INS/VisNav architecture can provide a robustness against beacon drop out and low visibility. Additionally, VisNav’s high update rates and high accuracy at less than 30 m, provides the precision required for mating of the ACCD and RLV. In this navigation system, the INS is used for prediction/ propagation of state, the GPS is used for low frequency updates of position, and the VisNav is used for high frequency updates.

4. Simulation Results

The navigation system proposed in the previous section is tested with a simplified capture trajectory shown in Fig. 14. It is assumed that RLV starts with an initial position which is 150 m behind (X-position) and 100 m above (Z-position) the ACCD. The ACCD position is assumed to be fixed to the origin and RLV is assumed to be descending with a constant velocity relative to the ACCD. This scenario is a reduced representation of the formation flight trajectory, during which the RLV descends at a constant rate relative to the TA [2]. With the aim of achieving an accuracy of up to 0.35 m in the relative position and 1° in relative orientation between ACCD and RLV, two scenarios are evaluated.

In the first case, the RLV descends with a constant pitch angle relative to the ACCD. No disturbances are considered and the trajectory is ideal. In the second case, small disturbances in RLV pitch angle are induced to imitate exposure to turbulence. This influences the pointing direction of the VisNav sensor mounted on the RLV and simulates a non-ideal scenario where sufficient beacons are not detected by the sensor. Fig. 15 shows the beacon visibility of the two simulated scenarios. It can be observed that in the ideal scenario, a minimum of 4 beacons required for VisNav data fusion, are visible throughout the trajectory. In the non-ideal scenario, multiple beacon drop-outs are observed between 5.5 s to 8 s. In the coming sub-sections, the performance of the three navigation systems – VisNav, GPS/INS and GPS/INS/VisNav will be evaluated.

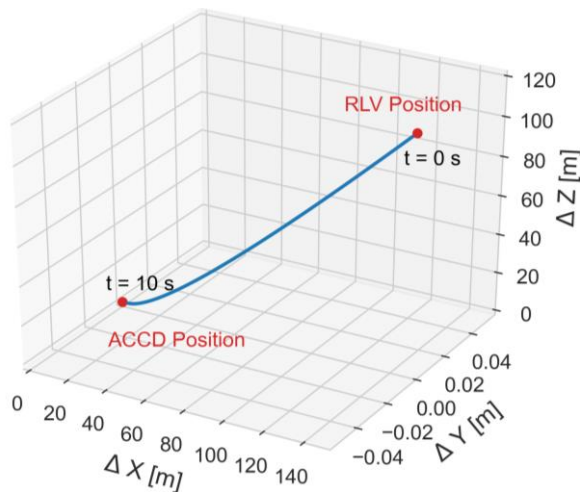


Fig. 14: Reference trajectory for approach of RLV towards ACCD during In-Air Capturing

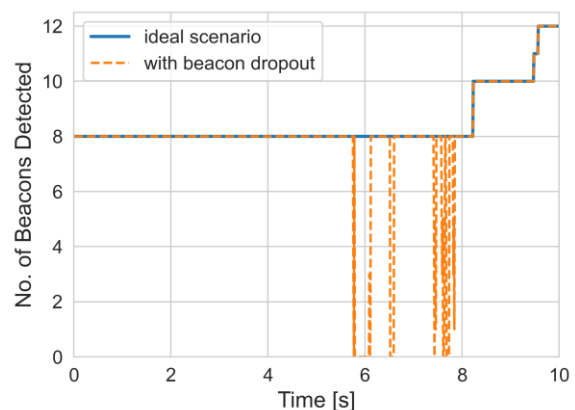


Fig. 15: Beacon visibility throughout the trajectory in ideal and non-ideal (with beacon drop out) scenarios

4.1. Ideal Scenario

Fig. 16 shows the error in relative position between RLV and ACCD using the three chosen relative navigation systems in the ideal scenario. It can be observed that the VisNav system provides higher accuracy measurements as the relative distance between the RLV and ACCD decreases. Although the error at the beginning of the trajectory is large (approximately 4 m), it quickly reduces to a small value towards the end of the trajectory, providing precise position for docking. Hence, in an ideal scenario when sufficient beacons are visible, VisNav alone can provide high accuracy navigation solution. The GPS/INS system on the other hand does not give very large errors at longer ranges but continues to have small errors throughout the trajectory. Closer to the mating point, the errors do not converge to a value below 0.35 m in all directions. Hence, the GPS/INS system may not be sufficient for the current application. Lastly, the combined GPS/INS/VisNav system appears to converge quickly without any large errors at the beginning of the trajectory. Close to the mating point, the errors are much smaller than the required 0.35 m. The navigation solution also appears smooth and remains within the covariance bounds shown in Fig. 16. Note that the covariance bounds shown in the results are associated with the GPS/INS/VisNav system.

Similar observations can also be made in Fig. 17, which shows the error in relative orientation between ACCD and RLV. The combined GPS/INS/VisNav appears to provide the most accurate solution and converges the fastest. The VisNav system also meets the required accuracy criteria as the error converges to a small value less than 1° , close to the mating point. Although the GPS/INS model also provides a solution in which the error remains within 1° , the other two systems exhibit superior close-range performance.

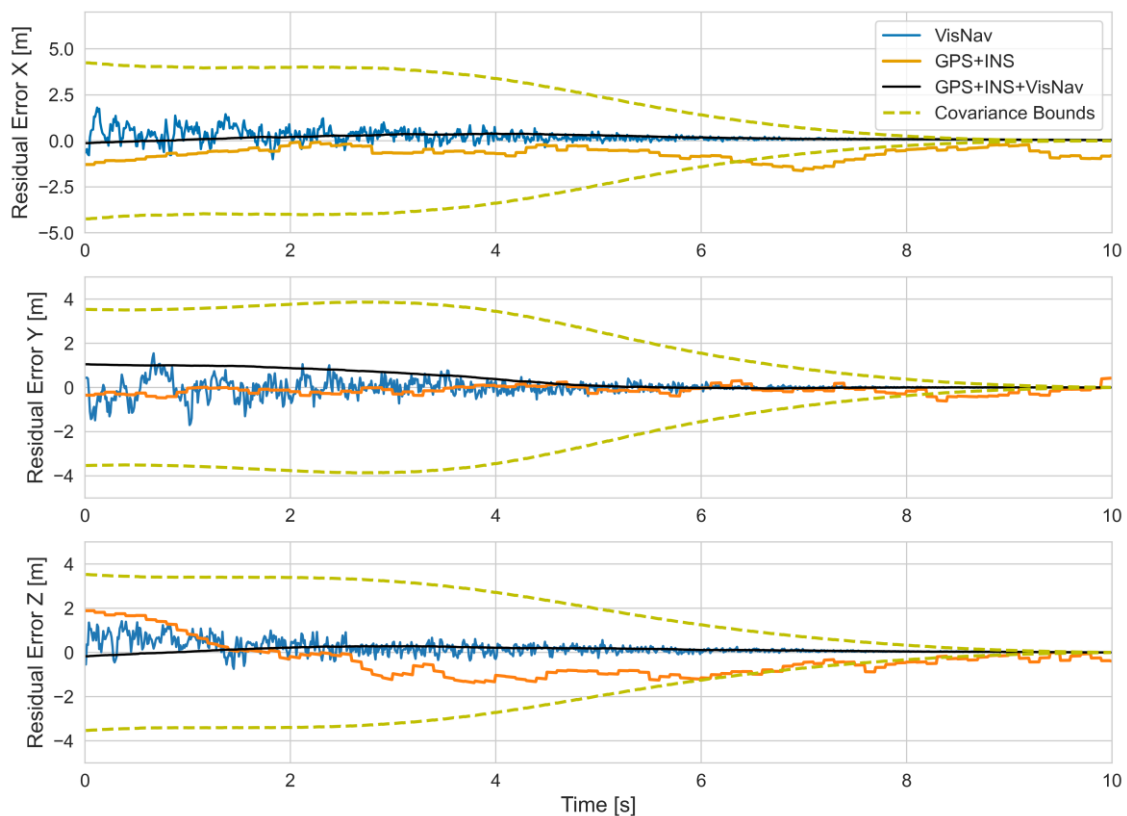


Fig. 16: Residual error in relative position between RLV and ACCD in ideal scenario

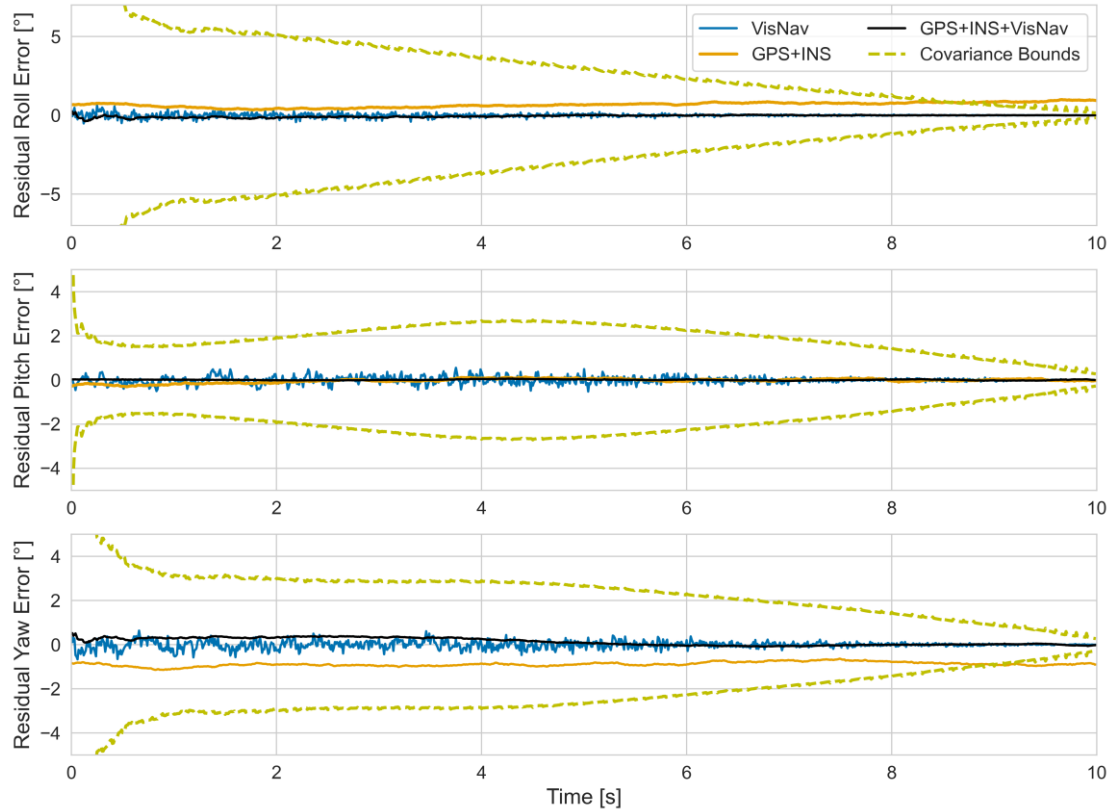


Fig. 17: Residual error in relative orientation between RLV and ACCD in ideal scenario

4.2. With Beacon Drop-Out

Since the docking maneuver of 'In-Air Capturing' happens behind the towing aircraft. It is likely that the ACCD and the RLV are exposed to the wake disturbances at some point in the capture trajectory. This could lead to significant disturbances in the angle of attack of both vehicles and lead to beacon drop out. Hence a non-ideal scenario is simulated to observe the effect of turbulence. In this simulation, the beacons drop out multiple times in the trajectory as shown in Fig. 15. During a beacon dropout, the last measured value by the VisNav system is held and propagated for the navigation with 'VisNav only'. The GPS/INS navigation system is not included in this simulation as the solution will remain unaffected by the visibility of beacons. In case of the GPS/INS/VisNav system, the low frequency GPS data are used for updates in case of beacon drop-out.

Fig. 18 and Fig. 19 show the errors in relative position and orientation using VisNav and GPS/INS/VisNav systems. It can be observed that the VisNav solution for relative position starts to diverge and contains major errors during periods of beacon dropouts. This could be attributed to the simplified propagation model, which holds the last valid measurement from VisNav and propagates the solution. Since the GPS in the GPS/INS/VisNav model continues to update the position despite loss of VisNav data, the navigation system provides a reliable high accuracy solution. Additionally, since the INS measurement data is used for propagation, the system remains robust despite uncertainties in the modelling of system dynamics.

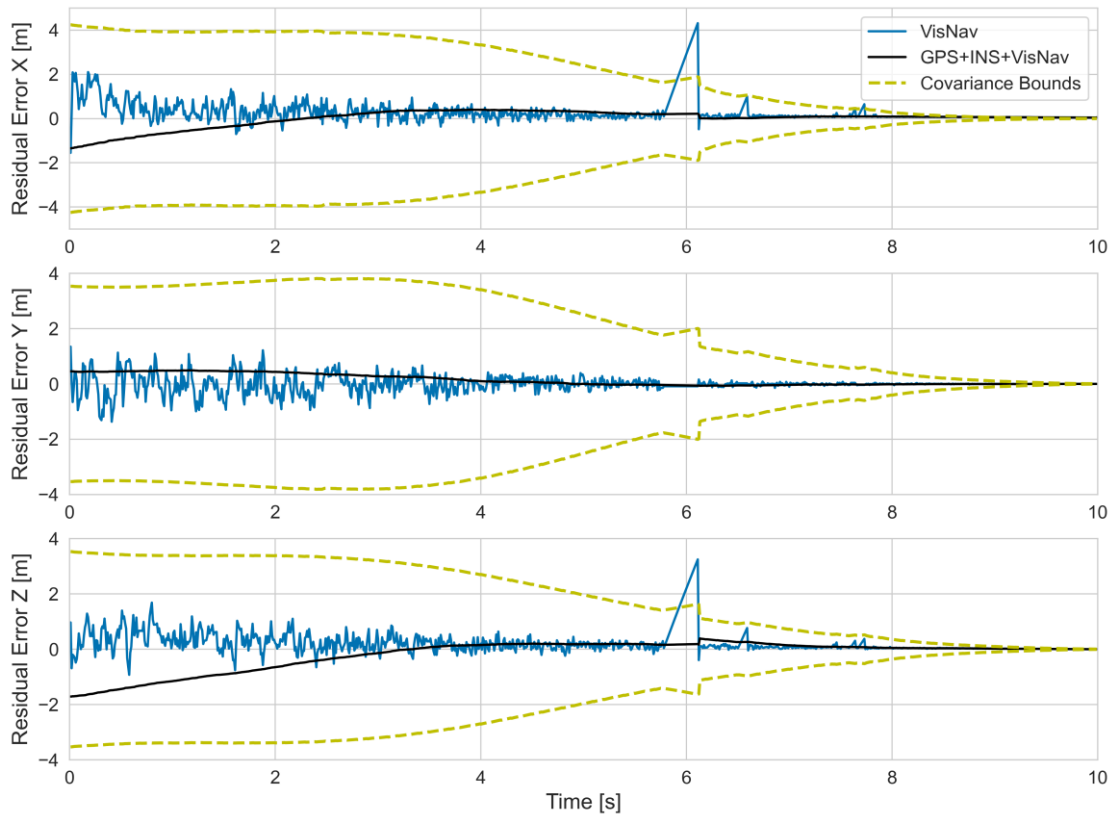


Fig. 18: Residual error in relative position between RLV and ACCD in non-ideal scenario

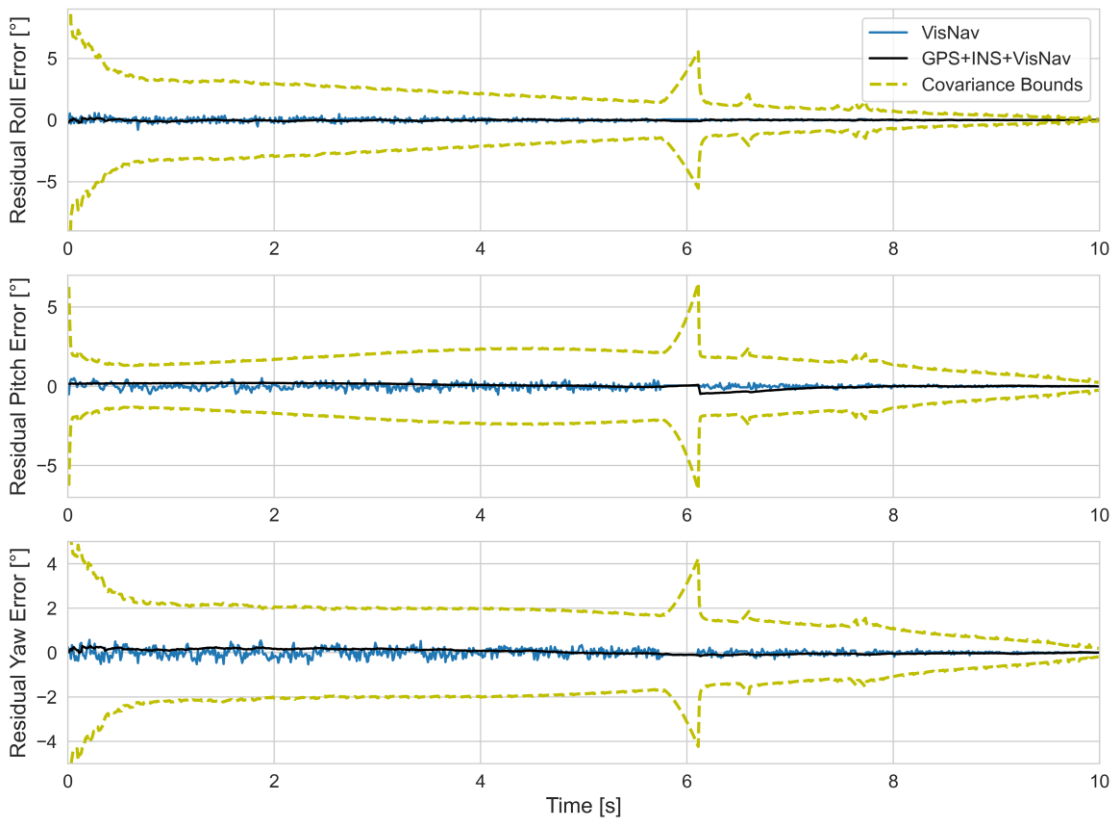


Fig. 19: Residual error in relative orientation between RLV and ACCD in non-ideal scenario

5. Conclusions and Future Work

This paper analyzes different architectures and configurations for the relative close-range navigation system for the full-scale 'In-Air Capturing' application. The 'In-Air Capturing' is a unique launcher recovery method during which, a winged Reusable Launch Vehicle (RLV) is captured mid-air by an aircraft and towed back to the launch site. An integral part of 'In-Air Capturing' is the autonomous navigation of a capturing device released from the towing aircraft to connect with the launcher stage, requiring precise close-range navigation sensors for the docking maneuver. The study examines a Vision-Based Navigation Sensor (VisNav), wherein active beacons are installed on the capturing device, and a position-sensing diode sensor is mounted on the RLV. This setup is explored as a prospective method for determining the relative position and orientation between the capturing device and RLV. Sensitivity studies are performed on placement of the beacons and orientation of sensor to improve detection and capture probability. VisNav is compared against the classical GPS/INS and a combined GPS/INS/VisNav navigation system to find the most reliable navigation system. Sensor fusion is achieved via Extended Kalman Filter (EKF) and a simplified capture trajectory is used to evaluate the performance of different configurations. Results demonstrate that GPS/INS/VisNav offers superior accuracy and a more resilient navigation solution, particularly in the face of model uncertainties and external disturbances.

Future extensions of this work will incorporate the complex dynamics from the capture trajectory, wherein the vibrations induced by the tether attached to the capturing device are included. Further, the model would integrate a high-fidelity model depicting the flowfield (wake) behind the towing aircraft, replacing the simplified model used in the current study. The measurement errors, biases and delays will also be added in more detail in the navigation model. Additionally, an improved model of system dynamics will be used in the EKF for more robust navigation. Finally, closed-loop simulations will be performed to analyze the feasibility and performance of 'In-Air Capturing'.

References

1. Patentschrift (patent specification) DE 101 47 144 C1, Verfahren zum Bergen einer Stufe eines mehr-stufigen Raumtransportsystems, released 2003.
2. Singh, S., Stappert, S., Bussler, L., Sippel, M., Kucukosman, Y. C., Buckingham, S.: Full-scale simulation and analysis of formation flight during in-air-capturing of a winged reusable launch vehicle. *Journal of Space Safety Engineering*, 9(4), 541-552 (2022). <https://doi.org/10.1016/j.jsse.2022.09.005>
3. Stappert, S., Wilken, J., Bussler, L., Sippel, M.: A Systematic Assessment and Comparison of Reusable First Stage Return Options, *Proceedings of the International Astronautical Congress* (2019).
4. Calabuig, G.J.D.: Conceptual cost estimation for recovery and refurbishment operations of reusable launch vehicles, SART TN-006/2019, DLR (2019), <https://elib.dlr.de/144125/> (accessed 3 April 2024).
5. Singh, S., Mastrogiuseppe, M.: Multibody modelling of tether and capture system for dynamic simulations of In-Air Capturing. *Acta Astronautica* 218, 59-69 (2024). <https://doi.org/10.1016/j.actaastro.2024.02.008>
6. Panzieri, S., Pascucci, F., Ulivi, G.: An Outdoor Navigation System Using GPS and Inertial Platform. *IEEE/ASME Transactions on Mechatronics* 7(2), 134-142 (2002). <https://doi.org/10.1109/TMECH.2002.1011250>
7. Ray, R., Cobleigh, B., Vachon, M., St. John, C.: Flight test techniques used to evaluate performance benefits during formation flight. *Proceedings of the AIAA Atmospheric Flight Mechanics Conference and Exhibit* (2002). <https://arc.aiaa.org/doi/pdf/10.2514/6.2002-4492>
8. Mammarella, M., Campa, G., Napolitano, M.R., Fravolini, M.L., Gu, Y., Perhinschi, M.G.: Machine Vision/GPS Integration Using EKF for the UAV Aerial Refueling Problem. *IEEE Transactions on Systems, Man, and Cybernetics – Part C: Applications and Reviews* 38(6), 197-801 (2008). <https://doi.org/10.1109/TSMCC.2008.2001693>

9. Johnson, D.T., Nykl, S.L., Raquet, J.F.: Combining Stereo Vision and Inertial Navigation for Automated Aerial Refueling. *Journal of Guidance, Control, and Dynamics* 40(9), 2250-2259 (2017). <https://doi.org/10.2514/1.G002648>
10. Krause, S., Cain, S.: UAV Pre-Study for In-Air-Capturing Maneuver. *Proceedings of the 2020 IEEE Aerospace Conference* (2020). <https://doi.org/10.1109/AERO47225.2020.9172769>
11. Xu, X., Duan, H., Guo, Y., Deng, Y.: A Cascade Adaboost and CNN Algorithm for Drogue Detection in UAV Autonomous Aerial Refueling. *Neurocomputing* 408, 121-134 (2020). <https://doi.org/10.1016/j.neucom.2019.10.115>
12. Wang, X., Kong, X., Zhi, J., Chen, Y., Dong, X.: Real-Time Drogue Recognition and 3D Locating for UAV Autonomous Aerial Refueling Based on Monocular Machine Vision. *Chinese Journal of Aeronautics* 28(6), 1667-1675 (2015). <https://doi.org/10.1016/j.cja.2015.10.006>
13. Li, H., Duan, H.: Verification of Monocular and Binocular Pose Estimation Algorithms in Vision-Based UAVs Autonomous Aerial Refueling System. *Science China Technological Sciences* 59(11), 1730-1738 (2016). <https://doi.org/10.1007/s11431-016-6097-z>
14. Vendra, S.: Addressing Corner Detection Issues for Machine Vision Based UAV Aerial Refueling. West Virginia University (2006).
15. Ma, Y., Zhao, R., Liu, E., Zhang, Z., Yan, K.: A Novel Autonomous Aerial Refueling Drogue Detection and Pose Estimation Method Based on Monocular Vision. *Measurement* 136, 132-142 (2019). <https://doi.org/10.1016/j.measurement.2018.12.060>
16. Khanafseh, S.M., Pervan, B.: Autonomous Airborne Refueling of Unmanned Air Vehicles Using the Global Positioning System. *Journal of Aircraft* 44(5), 1670-1682 (2007). <https://doi.org/10.2514/1.28195>
17. Doebbler, J., Valasek, J., Monda, M.J., Schaub, H.: Boom and Receptacle Autonomous Air Refueling Using Visual Snake Optical Sensor. *Proceedings of the 2006 AIAA Atmospheric Flight Mechanics Conference and Exhibit* (2006). <https://doi.org/10.2514/6.2006-6504>
18. Spencer, J.H.: Optical Tracking for Relative Positioning in Automated Aerial Refuelling. Air Force Institute of Technology (2007).
19. Chen, C.I., Koseluk, R., Buchanan, C., Duerner, A., Jeppesen, B., Laux, H.: Autonomous Aerial Refueling Ground Test Demonstration – a Sensor-in-the-Loop, Non-Tracking Method. *Sensors* 15(5), 10948-10972 (2015). <https://doi.org/10.3390/s150510948>
20. Wang, X., Dong, X., Kong, X., Li, J., Zhang, B.: Drogue Detection for Autonomous Aerial Refueling Based on Convolutional Neural Networks. *Chinese Journal of Aeronautics* 30(1), 380-390 (2017). <https://doi.org/10.1016/j.cja.2016.12.022>
21. Krause, S., Cain, S., Funke, A., González, J., Ferrándiz, M.: Overview of Planned Flight Test Operation for a Scaled In-Air Capturing Demonstration. *Proceedings of the 9th European Conference for Aeronautics and Space Sciences* (2022).
22. Thomas, P.R., Bhandari, U., Bullock, S., Richardson, T.S., du Bois, J.L: Advances in Air to Air Refuelling. *Progress in Aerospace Sciences* 71, 14-35 (2014). <https://doi.org/10.1016/j.paerosci.2014.07.001>
23. Gunnam, K., Hughes, D.C., Junkins, J., Kehtornavaz, N.: A DSP Embedded Optical Navigation System. *Proceedings of the 6th International Conference on Signal Processing*, 1735-1739 (2002). <https://doi.org/10.1109/ICOSP.2002.1180137>
24. Junkins, J.L., Hughes, D.C., Wazni, K.P., Pariyapong, V.: Vision-Based Navigation for Rendezvous, Docking and Proximity Operations. *Proceedings of the 4th International Conference on Dynamics and Control of Space Structures* (1999).
25. Krause, S.: FALCon D8.1 Technical Report – Environment Perception Flight Test Description. Deutsches Zentrum für Luft- und Raumfahrt (2023).
26. Curro II, J.A.: Automated Aerial Refueling Position Estimation Using a Scanning LiDAR. Air Force Institute of Technology (2012).

27. Parry, J., Hubbard, S.: Review of Sensor Technology to Support Automated Air-to-Air Refueling of a probe Configures Uncrewed Aircraft. *Sensors* 23(2), 995 (2023). <https://doi.org/10.3390/s23020995>
28. Lion, L., Caon, A., Olivieri, L., Branz, F., Francesconi, A.: Kinematic Tests on a Docking Mechanism for Microsatellites. *CEAS Space Journal* (2023). <https://doi.org/10.1007/s12567-023-00516-w>
29. Panzieri, S., Pascucci, F., Ulivi, G.: An Outdoor Navigation System Using GPS and Inertial Platform. *IEEE/ASME Transactions on Mechatronics* 7(2), 134-142 (2002). <https://doi.org/10.1109/TMECH.2002.1011250>
30. Krause, S.: FALCon D8.1 Technical Report – Environment Perception Flight Test Description. Deutsches Zentrum für Luft- und Raumfahrt (2023).
31. Curro II, J.A.: Automated Aerial Refueling Position Estimation Using a Scanning LiDAR. Air Force Institute of Technology (2012).
32. Chen, C.I., Stettner, R.: Drogue Tracking Using 3D Flash LiDAR for Autonomous Aerial Refueling. *Laser Radar Technology and Applications XVI* (2011). <https://doi.org/10.1117/12.886572>
33. Kelsey, J.M., Byrne, J., Cosgrove, M., Seereeram, S., Mehra, R.K.: Vision-Based Relative Pose Estimation for Autonomous Rendezvous and Docking. *Proceedings of the 2006 IEEE Aerospace Conference* (2006). <https://doi.org/10.1109/AERO.2006.1655916>
34. Tandale, M. D., Bowers, R., Valasek, J.: Trajectory tracking controller for vision-based probe and drogue autonomous aerial refueling. *Journal of guidance, control, and dynamics*, 29 (4), 846-857 (2006).
35. Katake, A., Choi, H.: VisNAV 100: a robust, compact imaging sensor for enabling autonomous air-to-air refueling of aircraft and unmanned aerial vehicles. *Image Processing: Machine Vision Applications III*, 7538, 66-76. SPIE (2010).
36. Valasek, J., Gunnam, K., Kimmet, J., Tandale, M. D., Junkins, J. L., Hughes, D.: Vision-based sensor and navigation system for autonomous air refueling. *Journal of guidance, control, and dynamics*, 28(5), 979-989 (2005).
37. Singh, S., Stappert, S., Buckingham, S., Lopes, S., Kucukosman, Y. C., Simioana, M., Planquart, P.: Dynamic Modelling and control of an aerodynamically controlled capturing device for 'in-air-capturing' of a reusable launch vehicle. *Proceedings of 11th International ESA Conference on Guidance, Navigation & Control Systems* (2021).
38. Wie, B.: *Space vehicle dynamics and control*. AIAA (1998).
39. Crassidis, J. L., Junkins, J. L.: *Optimal Estimation of Dynamic Systems*. Boca Raton, FL: Chapman and Hall/CRC (2004).
40. Katake, A., Choi, H.: VisNAV 100: a robust, compact imaging sensor for enabling autonomous air-to-air refueling of aircraft and unmanned aerial vehicles. *Image Processing: Machine Vision Applications III* (Vol. 7538, pp. 66-76). SPIE (2010).
41. Chui, C. K., Chen, G.: *Kalman filtering* (pp. 19-26). Berlin, Germany: Springer International Publishing (2017).
42. Fravolini, M. L., Ficola, A., Campa, G., Napolitano, M. R., Seanor, B.: Modeling and control issues for autonomous aerial refueling for UAVs using a probe-drogue refueling system. *Aerospace science and technology*, 8(7), 611-618 (2004).
43. Wang, X., Cui, N., & Guo, J.: INS/VisNav/GPS relative navigation system for UAV. *Aerospace science and Technology*, 28(1), 242-248 (2013).

K

Signal Blocking Solution

Within the context of chapter 4's VisNav Model, Equation K.1 needs to be solved in order to determine whether a given beacon-sensor LoS is blocked by the ACCD's docking cone (visibility condition c_{i2}). Further background and a definition of the various symbols are provided in chapter 4.

$$\vec{f}_C(h, \psi) = \begin{bmatrix} h \cdot \cos \lambda + l_{ACCD} - d_C / (2 \cdot \tan \lambda) \\ h \cdot \sin \lambda \cdot \sin \psi \\ h \cdot \sin \lambda \cdot \cos \psi \end{bmatrix} = \vec{P}_{Bi} + \vec{p}_{BiS} \cdot s \quad (\text{K.1})$$

In order to reduce the computational effort required to solve the above equation, a closed-form solution is used, based on a new reference frame. This frame is purely translated relative to the ACCD's body frame, so that its origin is located in the docking cone's origin (i.e. where $h = 0$). Denoting the sensor and beacon position vectors in the ACCD body frame as $\vec{P}_S = [x_S \ y_S \ z_S]$ and $\vec{P}_{Bi} = [x_{Bi} \ y_{Bi} \ z_{Bi}]$, the transformed coordinates $[x'_S \ y'_S \ z'_S]$ and $[x'_{Bi} \ y'_{Bi} \ z'_{Bi}]$ can be found with Equation K.2.

$$\begin{bmatrix} x'_S \\ y'_S \\ z'_S \end{bmatrix} = \begin{bmatrix} x_S - l_{ACCD} + d_C / (2 \cdot \tan \lambda) \\ y_S \\ z_S \end{bmatrix} \quad (\text{K.2})$$

$$\begin{bmatrix} x'_{Bi} \\ y'_{Bi} \\ z'_{Bi} \end{bmatrix} = \begin{bmatrix} x_{Bi} - l_{ACCD} + d_C / (2 \cdot \tan \lambda) \\ y_{Bi} \\ z_{Bi} \end{bmatrix}$$

The corresponding closed-form solution is then defined by Equations K.3 through K.5, obtained using MATLAB's *Symbolic Math Toolbox* [177]. They assume a double solution to Equation K.1, which further reduce to a single one in case both computed intersection points are identical. The mathematical edge case where the LoS coincides with the docking cone (yielding infinite solutions) is omitted, as it has no practical implications on the VisNav Model. The ψ and h parameters obtained with Equations K.3 through K.5 can then be used to verify visibility condition c_{i2} , while the exact coordinates of the intersection points can be computed with Equation K.6 - expressed in the ACCD body reference frame.

Finally, it should be noted that numerical errors arise when $z'_{Bi} \rightarrow 0$, caused by the fact that $\sigma_7 \rightarrow 0$. To remedy this, the cone reference frame is rotated 90° around the X'-axis when $z'_{Bi} \approx 0$ - essentially swapping the Y' and Z' axes. Reversing this additional transformation after the computation of the intersection points, the resulting solutions are free from such numerical errors.

$$\left\{ \begin{array}{l} h_{sol,1} = \sigma_3 - (\sigma_5 - \sigma_2 + \sigma_1) \cdot \sigma_6 / \sigma_4 \\ \psi_{sol,1} = \pi/2 - 2 \cdot \arctan((\sigma_5 - \sigma_2 + \sigma_1) / \sigma_{11}) \\ h_{sol,2} = \sigma_3 + (\sigma_5 + \sigma_2 - \sigma_1) \cdot \sigma_6 / \sigma_4 \\ \psi_{sol,2} = \pi/2 + 2 \cdot \arctan((\sigma_5 + \sigma_2 - \sigma_1) / \sigma_{11}) \end{array} \right. \quad \text{where} \quad \left\{ \begin{array}{l} \sigma_1 = 2 \cdot x'_S \cdot y'_{Bi} \cdot \tan(\lambda/2) \\ \sigma_2 = 2 \cdot x'_{Bi} \cdot y'_S \cdot \tan(\lambda/2) \\ \sigma_3 = \sum_{i=1}^{24} A_i / \sigma_7 \\ \sigma_4 = \sum_{i=1}^6 B_i \cdot \sigma_7 \\ \sigma_5 = \sqrt{\sum_{i=1}^{15} C_i} \\ \sigma_6 = \sum_{i=1}^{16} D_i \\ \sigma_7 = \sum_{i=1}^{21} E_i \\ \sigma_8 = \tan^3(\lambda/2) \\ \sigma_9 = \tan^4(\lambda/2) \\ \sigma_{10} = \tan^2(\lambda/2) \\ \sigma_{11} = \sum_{i=1}^6 F_i \end{array} \right. \quad (\text{K.3})$$

$$\left\{ \begin{array}{l} A_1 = -2 \cdot (x'_{Bi})^2 \cdot y'_S \cdot \sigma_8 \\ A_2 = -2 \cdot (x'_{Bi})^2 \cdot y'_S \cdot \tan(\lambda/2) \\ A_3 = 2 \cdot x'_{Bi} \cdot x'_S \cdot y'_{Bi} \cdot \sigma_8 \\ A_4 = 2 \cdot x'_{Bi} \cdot x'_S \cdot y'_{Bi} \cdot \tan(\lambda/2) \\ A_5 = 2 \cdot x'_{Bi} \cdot x'_S \cdot y'_S \cdot \sigma_8 \\ A_6 = 2 \cdot x'_{Bi} \cdot x'_S \cdot y'_S \cdot \tan(\lambda/2) \\ A_7 = x'_{Bi} \cdot y'_{Bi} \cdot y'_S \cdot \sigma_9 \\ A_8 = -x'_{Bi} \cdot y'_{Bi} \cdot y'_S \\ A_9 = -x'_{Bi} \cdot (y'_S)^2 \cdot \sigma_9 \\ A_{10} = x'_{Bi} \cdot (y'_S)^2 \\ A_{11} = x'_{Bi} \cdot z'_{Bi} \cdot z'_S \cdot \sigma_9 \\ A_{12} = -x'_{Bi} \cdot z'_{Bi} \cdot z'_S \\ A_{13} = -x'_{Bi} \cdot (z'_S)^2 \cdot \sigma_9 \\ A_{14} = x'_{Bi} \cdot (z'_S)^2 \\ A_{15} = -2 \cdot (x'_S)^2 \cdot y'_{Bi} \cdot \sigma_8 \\ A_{16} = -2 \cdot (x'_S)^2 \cdot y'_{Bi} \cdot \tan(\lambda/2) \\ A_{17} = -x'_S \cdot (y'_{Bi})^2 \cdot \sigma_9 \\ A_{18} = x'_S \cdot (y'_{Bi})^2 \\ A_{19} = x'_S \cdot y'_{Bi} \cdot y'_S \cdot \sigma_9 \\ A_{20} = -x'_S \cdot y'_{Bi} \cdot y'_S \\ A_{21} = -x'_S \cdot (z'_{Bi})^2 \cdot \sigma_9 \\ A_{22} = x'_S \cdot (z'_{Bi})^2 \\ A_{23} = x'_S \cdot z'_{Bi} \cdot z'_S \cdot \sigma_9 \\ A_{24} = -x'_S \cdot z'_{Bi} \cdot z'_S \end{array} \right. \quad \text{and} \quad \left\{ \begin{array}{l} B_1 = y'_{Bi} \cdot z'_S \\ B_2 = -y'_S \cdot z'_{Bi} \\ B_3 = 2 \cdot x'_{Bi} \cdot z'_S \cdot \tan(\lambda/2) \\ B_4 = -2 \cdot x'_S \cdot z'_{Bi} \cdot \tan(\lambda/2) \\ B_5 = -y'_{Bi} \cdot z'_S \cdot \sigma_{10} \\ B_6 = y'_S \cdot z'_{Bi} \cdot \sigma_{10} \\ C_1 = 4 \cdot (x'_{Bi} \cdot y'_S)^2 \cdot \sigma_{10} \\ C_2 = 4 \cdot (x'_{Bi} \cdot z'_S)^2 \cdot \sigma_{10} \\ C_3 = -8 \cdot x'_{Bi} \cdot x'_S \cdot y'_{Bi} \cdot y'_S \cdot \sigma_{10} \\ C_4 = -8 \cdot x'_{Bi} \cdot x'_S \cdot z'_{Bi} \cdot z'_S \cdot \sigma_{10} \\ C_5 = 4 \cdot (x'_S \cdot y'_{Bi})^2 \cdot \sigma_{10} \\ C_6 = 4 \cdot (x'_S \cdot z'_{Bi})^2 \cdot \sigma_{10} \\ C_7 = -(y'_{Bi} \cdot z'_S)^2 \cdot \sigma_9 \\ C_8 = 2 \cdot (y'_{Bi} \cdot z'_S)^2 \cdot \sigma_{10} \\ C_9 = -(y'_{Bi} \cdot z'_S)^2 \\ C_{10} = 2 \cdot y'_{Bi} \cdot y'_S \cdot z'_{Bi} \cdot z'_S \cdot \sigma_9 \\ C_{11} = -4 \cdot y'_{Bi} \cdot y'_S \cdot z'_{Bi} \cdot z'_S \cdot \sigma_{10} \\ C_{12} = 2 \cdot y'_{Bi} \cdot y'_S \cdot z'_{Bi} \cdot z'_S \\ C_{13} = -(y'_S \cdot z'_{Bi})^2 \cdot \sigma_9 \\ C_{14} = 2 \cdot (y'_S \cdot z'_{Bi})^2 \cdot \sigma_{10} \\ C_{15} = -(y'_S \cdot z'_{Bi})^2 \end{array} \right.$$

$$\begin{cases}
D_1 = 2 \cdot (x'_{Bi})^2 \cdot z'_S \cdot \sigma_8 \\
D_2 = 2 \cdot (x'_S)^2 \cdot z'_{Bi} \cdot \sigma_8 \\
D_3 = x'_{Bi} \cdot y'_{Bi} \cdot z'_S \\
D_4 = -x'_{Bi} \cdot y'_S \cdot z'_{Bi} \\
D_5 = -x'_S \cdot y'_{Bi} \cdot z'_S \\
D_6 = x'_S \cdot y'_S \cdot z'_{Bi} \\
D_7 = 2 \cdot (x'_{Bi})^2 \cdot z'_S \cdot \tan(\lambda/2) \\
D_8 = 2 \cdot (x'_S)^2 \cdot z'_{Bi} \cdot \tan(\lambda/2) \\
D_9 = -2 \cdot x'_{Bi} \cdot x'_S \cdot z'_{Bi} \cdot \tan(\lambda/2) \\
D_{10} = -2 \cdot x'_{Bi} \cdot x'_S \cdot z'_S \cdot \tan(\lambda/2) \\
D_{11} = -2 \cdot x'_{Bi} \cdot x'_S \cdot z'_{Bi} \cdot \sigma_8 \\
D_{12} = -2 \cdot x'_{Bi} \cdot x'_S \cdot z'_S \cdot \sigma_8 \\
D_{13} = -x'_{Bi} \cdot y'_{Bi} \cdot z'_S \cdot \sigma_9 \\
D_{14} = x'_{Bi} \cdot y'_S \cdot z'_{Bi} \cdot \sigma_9 \\
D_{15} = x'_S \cdot y'_{Bi} \cdot z'_S \cdot \sigma_9 \\
D_{16} = -x'_S \cdot y'_S \cdot z'_{Bi} \cdot \sigma_9 \\
F_1 = y'_{Bi} \cdot z'_S \\
F_2 = -y'_S \cdot z'_{Bi} \\
F_3 = 2 \cdot x'_{Bi} \cdot z'_S \cdot \tan(\lambda/2) \\
F_4 = -2 \cdot x'_S \cdot z'_{Bi} \cdot \tan(\lambda/2) \\
F_5 = -y'_{Bi} \cdot z'_S \cdot \sigma_{10} \\
F_6 = y'_S \cdot z'_{Bi} \cdot \sigma_{10}
\end{cases}
\quad \text{and} \quad
\begin{cases}
E_1 = -4 \cdot (x'_{Bi})^2 \cdot \sigma_{10} \\
E_2 = 8 \cdot x'_{Bi} \cdot x'_S \cdot \sigma_{10} \\
E_3 = -4 \cdot (x'_S)^2 \cdot \sigma_{10} \\
E_4 = (y'_{Bi})^2 \cdot \sigma_9 \\
E_5 = -2 \cdot (y'_{Bi})^2 \cdot \sigma_{10} \\
E_6 = (y'_{Bi})^2 \\
E_7 = -2 \cdot y'_{Bi} \cdot y'_S \cdot \sigma_9 \\
E_8 = 4 \cdot y'_{Bi} \cdot y'_S \cdot \sigma_{10} \\
E_9 = -2 \cdot y'_{Bi} \cdot y'_S \\
E_{10} = (y'_S)^2 \cdot \sigma_9 \\
E_{11} = -2 \cdot (y'_S)^2 \cdot \sigma_{10} \\
E_{12} = (y'_S)^2 \\
E_{13} = (z'_{Bi})^2 \cdot \sigma_9 \\
E_{14} = -2 \cdot (z'_{Bi})^2 \cdot \sigma_{10} \\
E_{15} = (z'_{Bi})^2 \\
E_{16} = -2 \cdot z'_{Bi} \cdot z'_S \cdot \sigma_9 \\
E_{17} = 4 \cdot z'_{Bi} \cdot z'_S \cdot \sigma_{10} \\
E_{18} = -2 \cdot z'_{Bi} \cdot z'_S \\
E_{19} = (z'_S)^2 \cdot \sigma_9 \\
E_{20} = -2 \cdot (z'_S)^2 \cdot \sigma_{10} \\
E_{21} = (z'_S)^2
\end{cases}
\quad (\text{K.5})$$

$$\begin{cases}
\begin{bmatrix} x_{sol,1} \\ y_{sol,1} \\ z_{sol,1} \end{bmatrix} = \begin{bmatrix} h_{sol,1} \cdot \cos \lambda + l_{ACCD} - d_C / (2 \cdot \tan \lambda) \\ h_{sol,1} \cdot \sin \lambda \cdot \sin \psi_{sol,1} \\ h_{sol,1} \cdot \sin \lambda \cdot \cos \psi_{sol,1} \end{bmatrix} \\
\begin{bmatrix} x_{sol,2} \\ y_{sol,2} \\ z_{sol,2} \end{bmatrix} = \begin{bmatrix} h_{sol,2} \cdot \cos \lambda + l_{ACCD} - d_C / (2 \cdot \tan \lambda) \\ h_{sol,2} \cdot \sin \lambda \cdot \sin \psi_{sol,2} \\ h_{sol,2} \cdot \sin \lambda \cdot \cos \psi_{sol,2} \end{bmatrix}
\end{cases}
\quad (\text{K.6})$$



Reference Approach Trajectory

When analysing the behaviour of the towing system, as well as the ACCD's relative navigation system, a reference approach trajectory between the RLV and the ACCD serves as a vital starting point. The trajectory used throughout this work is shown in Figures L.1 and L.2, and assumes the RLV plane of symmetry to coincide with that of the ACCD. Its position data - expressed in the ACCD's body reference frame - stems from a previous SART study [15], while the pitch attitude ϕ_R was generated with Equation L.1 - combining low-frequency oscillations with a higher frequency Gaussian random walk. Here, $\mathcal{N}(0^\circ, 0.1^\circ)$ represents Gaussian noise with an expected value of 0° , and a standard deviation of 0.1° . Additionally, a time step of 0.01 s was used for generating the random walk. Table L.1 lists numerical data for the reference trajectory, sampled at a frequency of 10 Hz.

$$\phi_R(t_j) = 5^\circ \cdot \left(1 + 3 \cdot \sin\left(\frac{t_j}{2}\right) + \frac{1}{8} \cdot \sin(5.9 \cdot t_j) - \frac{1}{4} \cdot \sin(4.3 \cdot t_j) + \frac{1}{9} \cdot \cos(2.7 \cdot t_j) \right) + \sum_{j=0}^i \mathcal{N}(0^\circ, 0.1^\circ) \quad (\text{L.1})$$

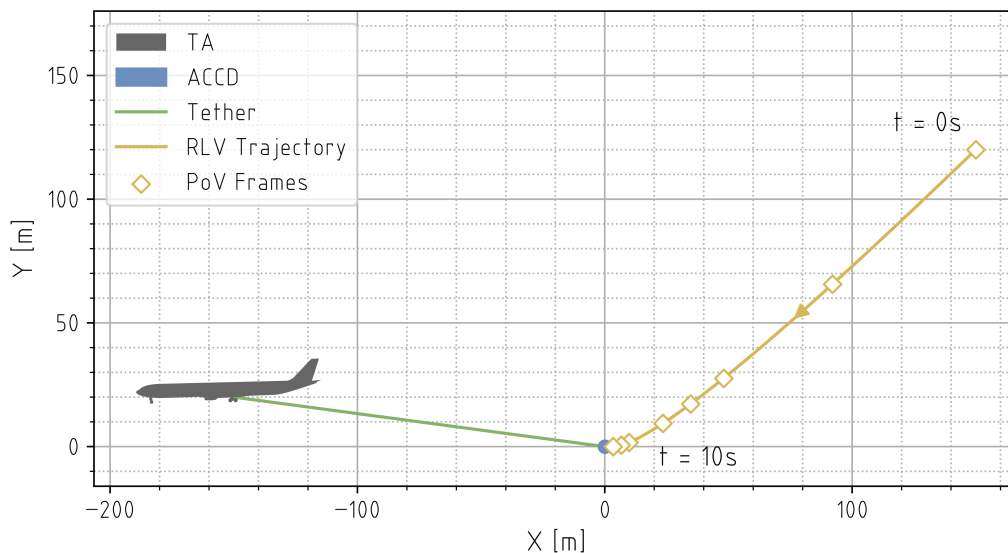


Figure L.1: Relative Position of IAC Vehicles During the Reference RLV Approach, in the ACCD Body Reference Frame.

t [s]	ϕ_R [°]	X [m]	Y [m]	t [s]	ϕ_R [°]	X [m]	Y [m]
0.0	5.507	150.00	120.00	5.0	13.260	50.93	29.94
0.1	6.047	147.52	117.61	5.1	13.139	49.47	28.75
0.2	6.560	145.06	115.24	5.2	12.956	48.03	27.59
0.3	6.711	142.61	112.90	5.3	12.983	46.61	26.45
0.4	7.111	140.19	110.58	5.4	12.860	45.21	25.33
0.5	7.221	137.79	108.29	5.5	12.168	43.83	24.24
0.6	7.643	135.412	106.02	5.6	11.938	42.47	23.17
0.7	8.769	133.05	103.77	5.7	10.037	41.13	22.13
0.8	9.902	130.71	101.55	5.8	8.615	39.82	21.11
0.9	11.112	128.40	99.35	5.9	6.561	38.52	20.11
1.0	12.170	126.10	97.18	6.0	4.383	37.24	19.14
1.1	13.353	123.82	95.03	6.1	3.401	35.99	18.19
1.2	14.411	121.56	92.90	6.2	2.287	34.75	17.27
1.3	15.469	119.32	90.80	6.3	2.234	33.54	16.37
1.4	16.091	117.11	88.72	6.4	2.480	32.34	15.50
1.5	16.526	114.91	86.67	6.5	2.790	31.17	14.65
1.6	15.867	112.74	84.64	6.6	3.115	30.02	13.82
1.7	15.067	110.58	82.63	6.7	3.496	28.88	13.01
1.8	15.059	108.45	80.65	6.8	3.281	27.77	12.24
1.9	15.622	106.33	78.70	6.9	2.855	26.68	11.48
2.0	16.238	104.24	76.76	7.0	1.534	25.61	10.75
2.1	17.706	102.16	74.85	7.1	0.405	24.55	10.04
2.2	18.884	100.11	72.97	7.2	-0.499	23.52	9.36
2.3	20.290	98.08	71.11	7.3	-1.644	22.51	8.70
2.4	21.195	96.07	69.27	7.4	-2.529	21.52	8.07
2.5	21.677	94.08	67.45	7.5	-3.280	20.55	7.46
2.6	21.643	92.10	65.67	7.6	-3.919	19.60	6.87
2.7	20.796	90.15	63.90	7.7	-4.268	18.68	6.31
2.8	19.684	88.22	62.16	7.8	-5.410	17.77	5.77
2.9	19.295	86.31	60.44	7.9	-5.980	16.88	5.25
3.0	18.908	84.42	58.75	8.0	-6.124	16.01	4.76
3.1	18.606	82.55	57.08	8.1	-6.021	15.16	4.30
3.2	18.726	80.71	55.44	8.2	-6.126	14.34	3.85
3.3	18.969	78.88	53.81	8.3	-6.431	13.53	3.43
3.4	19.663	77.07	52.22	8.4	-6.323	12.75	3.04
3.5	19.663	75.28	50.65	8.5	-6.180	11.98	2.67
3.6	19.637	73.52	49.10	8.6	-5.885	11.24	2.32
3.7	19.689	71.77	47.57	8.7	-6.772	10.51	2.00
3.8	19.601	70.04	46.07	8.8	-6.644	9.81	1.70
3.9	19.558	68.34	44.59	8.9	-6.983	9.12	1.43
4.0	19.265	66.65	43.14	9.0	-7.963	8.46	1.18
4.1	19.094	64.99	41.71	9.1	-8.344	7.82	0.95
4.2	18.366	63.34	40.31	9.2	-9.181	7.20	0.75
4.3	17.902	61.72	38.93	9.3	-9.666	6.59	0.57
4.4	17.841	60.12	37.57	9.4	-9.144	6.01	0.42
4.5	17.298	58.53	36.24	9.5	-8.280	5.45	0.29
4.6	17.022	56.97	34.93	9.6	-7.805	4.91	0.18
4.7	15.723	55.43	33.65	9.7	-7.316	4.39	0.10
4.8	14.102	53.91	32.39	9.8	-6.530	3.89	0.04
4.9	13.352	52.41	31.15	9.9	-7.057	3.41	0.019
				10.0	-7.287	3.00	0.00

Table L.1: Relative Position and Attitude Data for the Reference RLV Approach, in the ACCD Body Reference Frame.

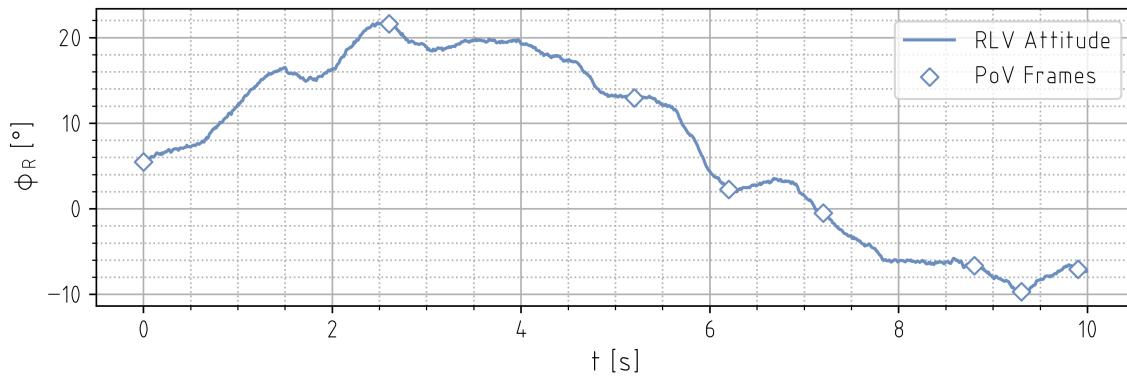


Figure L.2: Relative Pitch Attitude of the RLV During its Reference Approach, in the ACCD Body Reference Frame.

Using this reference trajectory as an input to chapter 4’s VisNav Model, the visibility of VisNav beacons throughout the final approach can be simulated - as shown in Figure L.3. Additionally, a sensor PoV animation can be generated, from which a number of frames are shown in Figure L.4. The timing of these frames is also indicated on Figures L.1 and L.2. For these simulations, a sensor with $FoV = 40^\circ$ and $\mu = 150^\circ$ was used in conjunction with the beacon configuration defined in Table 4.2.

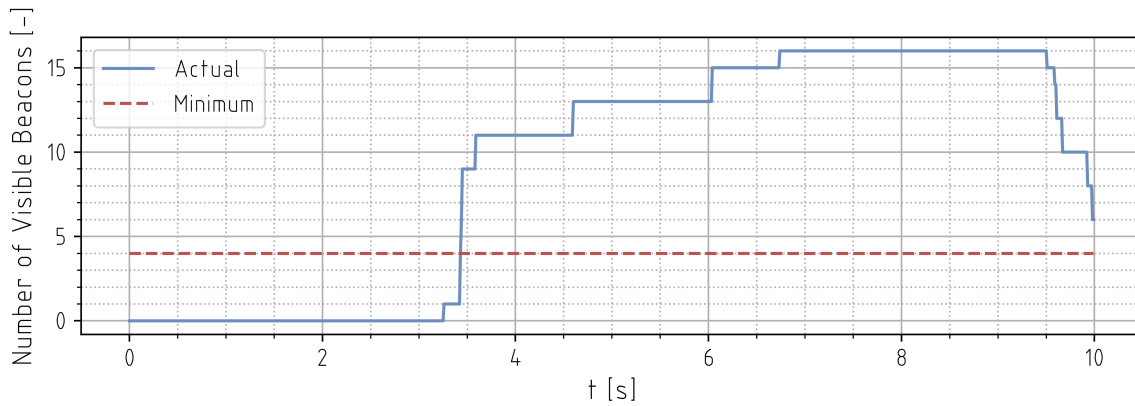


Figure L.3: Visibility of VisNav Beacons During the Reference RLV Approach.

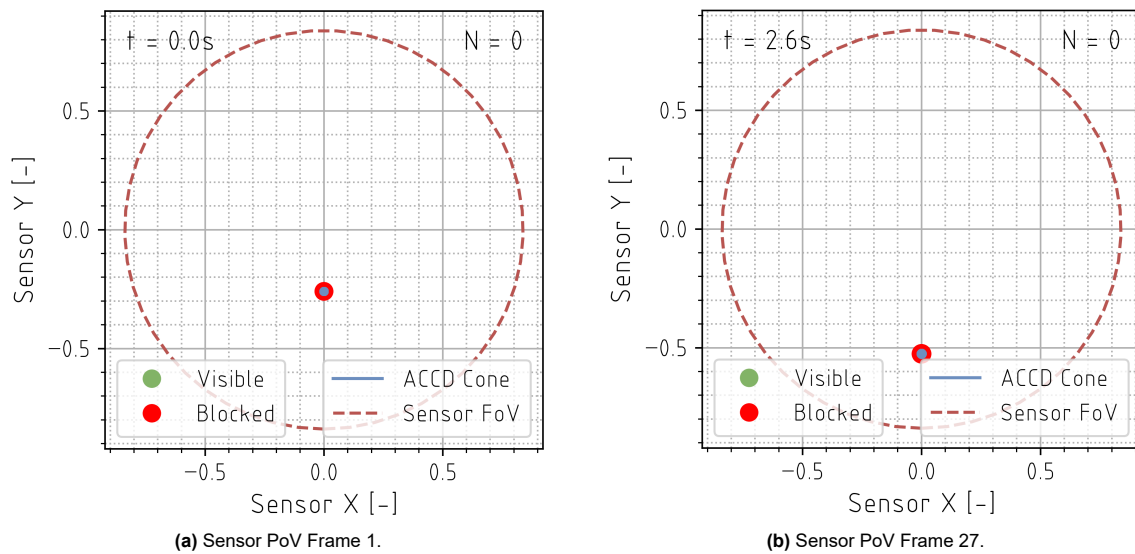


Figure L.4: Frames from a VisNav Sensor PoV Animation During the Reference RLV Approach.

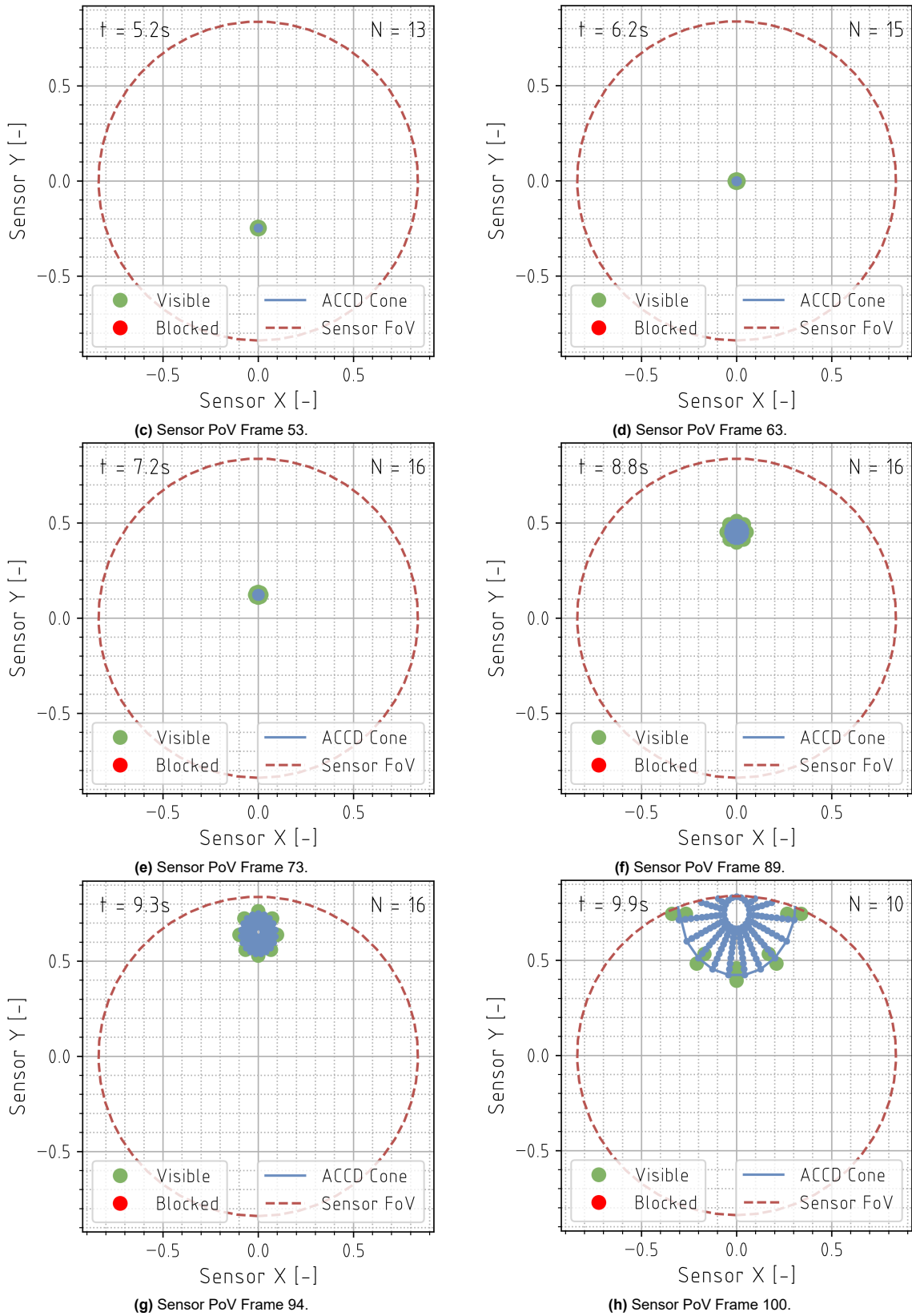


Figure L.4: Frames from a VisNav Sensor PoV Animation During the Reference RLV Approach (continued).

M

Commercial Components

The following sections present technical data for the various COTS components and systems discussed throughout this work. They serve as reference points for chapter 5's SWaP estimates, chapter 6's CAD design, and Appendix C's BoMs. Additionally, they can provide valuable starting points for future studies looking into the electromechanical design of the ACCD. Sections M.1 through M.3 present technical drawings and characteristics for the proposed OBC, GNSS, and communication modules, while sections M.4 and M.5 contain schematics for the ACCD's actuators and docking sensors respectively. Finally, details concerning the selected industrial shock absorber and linear bearing are included in sections M.6 and M.7.

M.1. On-Board Computer

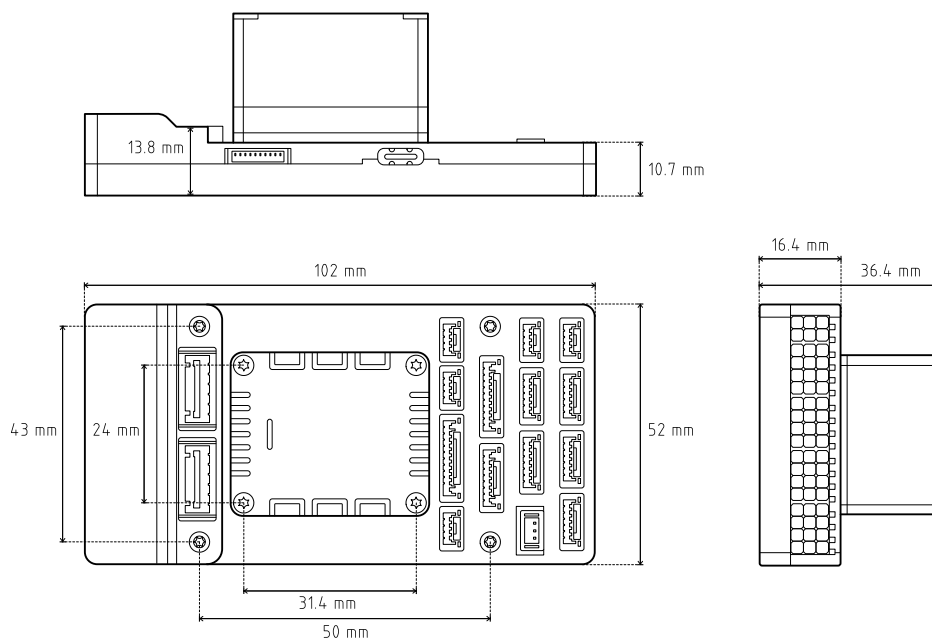


Figure M.1: Schematic of the Pixhawk 6X Pro OBC, Interfaced with a Standard Baseboard [96].

Processors	
Flight Management Unit	STM32H753 @ 480 MHz, 32-bit 2MB Flash 1MB RAM
Input/Output (I/O) Processor	STM32F103 @ 72 MHz, 32-bit 64kB SRAM
Sensors	
IMUs	ADIS16470, $\pm 40G$ IIM-42652, $\pm 16G$ ICM-45686, $\pm 32G$
Barometers	ICP20100 BMP388
Magnetometer	BMM150

Table M.1: Features of the Pixhawk 6X Pro OBC [96]. For the IMUs, the listed G-forces represent the acceleration saturation of each sensor.

M.2. GNSS Module

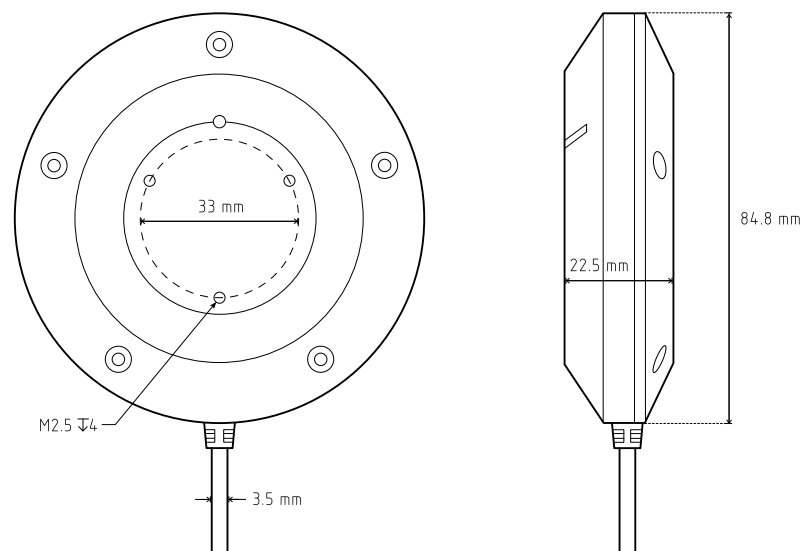


Figure M.2: Schematic of the DroneCAN H-RTK F9P Rover GNSS Module [97].

Architecture	
Processor	STM32G473 @ 170 MHz, 32-bit 512kB Flash 128kB SRAM
GNSS Module	U-blox ZED-F9P Receiver Ceramic Patch Antenna 20 dB Low-Noise Amplifier
Magnetometer	BMM150 or IST8310

Table M.2: Features of the DroneCAN H-RTK F9P Rover GNSS Module [97].

M.3. Communication Module

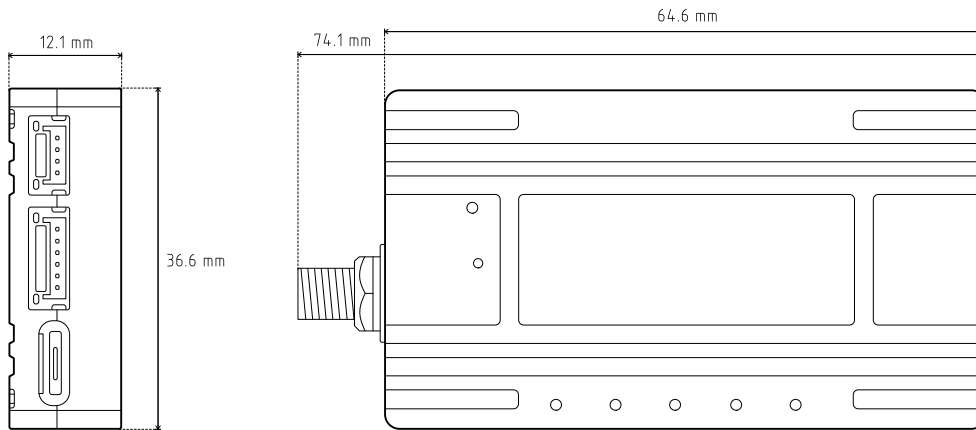


Figure M.3: Schematic of the Microhard P840 RF Communication Module [99].

Architecture

Frequency Band	840-845 MHz
Link Rate	345 kbps
Range	100 km

Table M.3: Characteristics of the Microhard P840 RF Communication Module [99].

M.4. Actuators

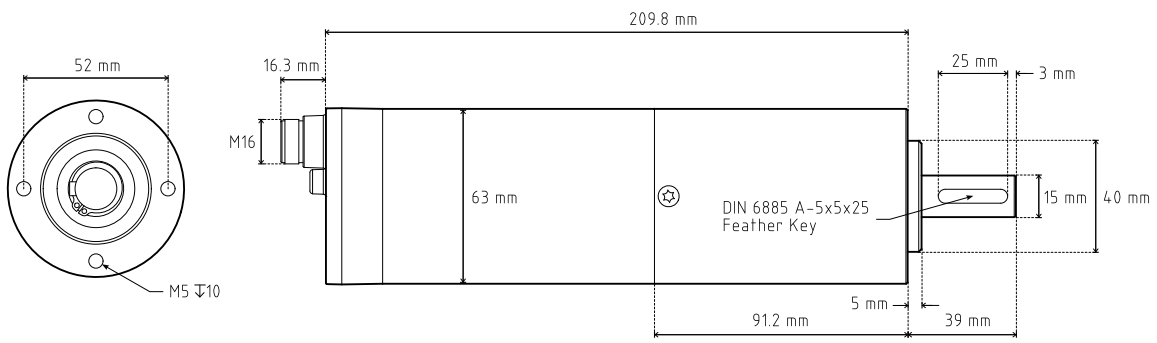


Figure M.4: Schematic of the ECI-63.20-K4-B00 Control Actuator [102].

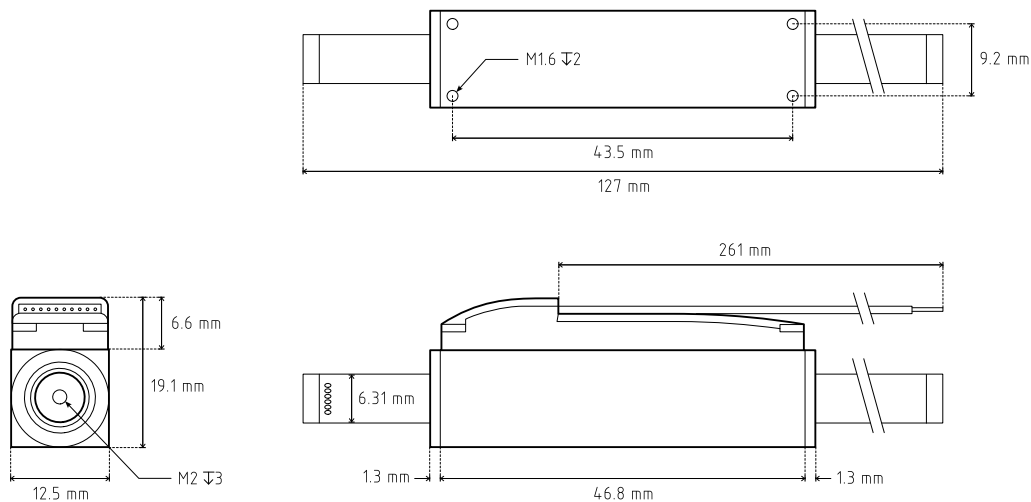


Figure M.5: Schematic of the LM1247-100-11 Linear Locking Actuator [107].

M.5. Docking Sensors

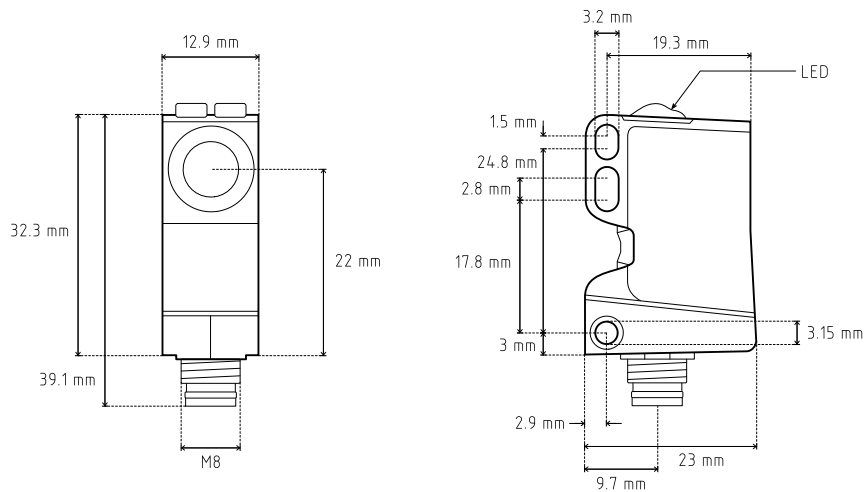


Figure M.6: Schematic of the U300.D50-DPMJ.72N Ultrasonic Distance Measuring Sensor [109].

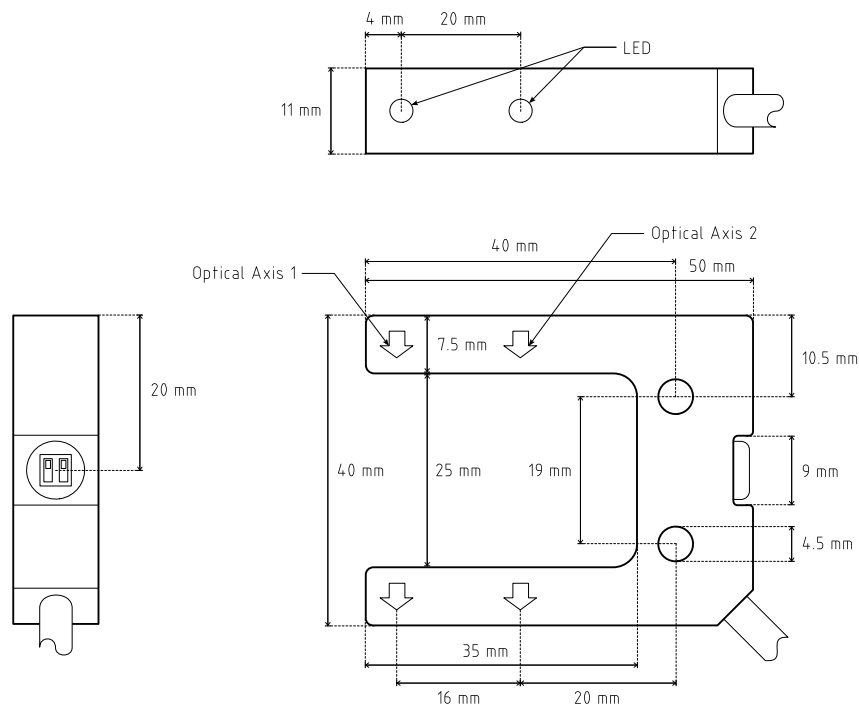


Figure M.7: Schematic of the Omron E3Z-G62 Grooved Photoelectric Sensor [110].

M.6. Industrial Shock Absorber

Figure M.8 shows a comparison of deceleration profiles for different potential energy-absorbing solutions. For the ACCD application, an industrial shock absorber such as the MC64150 is the most suitable option, given its lower deceleration force compared to alternative systems [10]. Figure M.9 defines the geometric characteristics of the MC641400 and MC641450 shock absorbers, as used in Table 6.1.

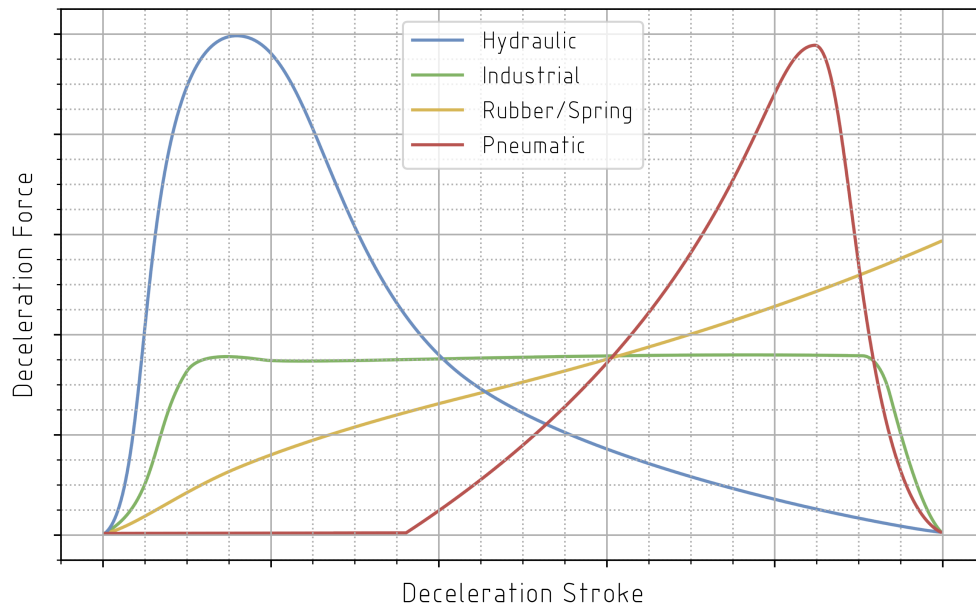


Figure M.8: Comparison of Deceleration Profiles of a Number of Typical Energy-Absorbing Solutions [140]. Since the area under each curve is constant, an equal amount of energy is absorbed in all four cases.

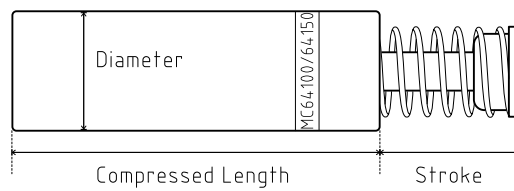


Figure M.9: Schematic of the ACE MC6140/MC64150 Industrial Shock Absorber, in an Uncompressed State [140].

M.7. Linear Bearing

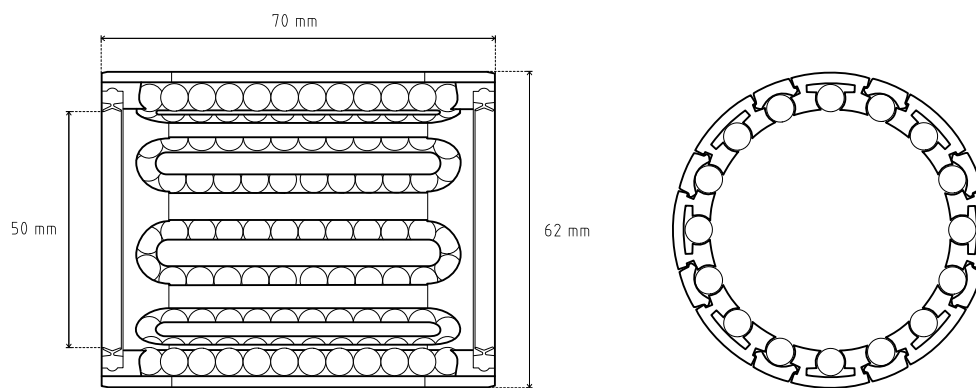


Figure M.10: Schematic of the Ewellix LBBR 50-2LS/HV6 Linear Ball Bearing [142].

N

Nominal Docking Sequence

In order to demonstrate the working principle of the proposed electromechanical design, a step-by-step overview of a nominal docking sequence between the RLV and ACCD is presented in this appendix. Already during formation flight - discussed in more detail in chapter 4 and Appendix L - the navigation sensors described in chapter 5 track the final approach of the RLV, priming the ACCD for an imminent docking attempt. The actual docking sequence then starts at the first physical contact between the RLV boom and the ACCD's guiding cone. Such a potential first contact scenario is shown in Figure N.1, including initial angular and lateral misalignments between both vehicles (**KY-DCK.F-13/02**).

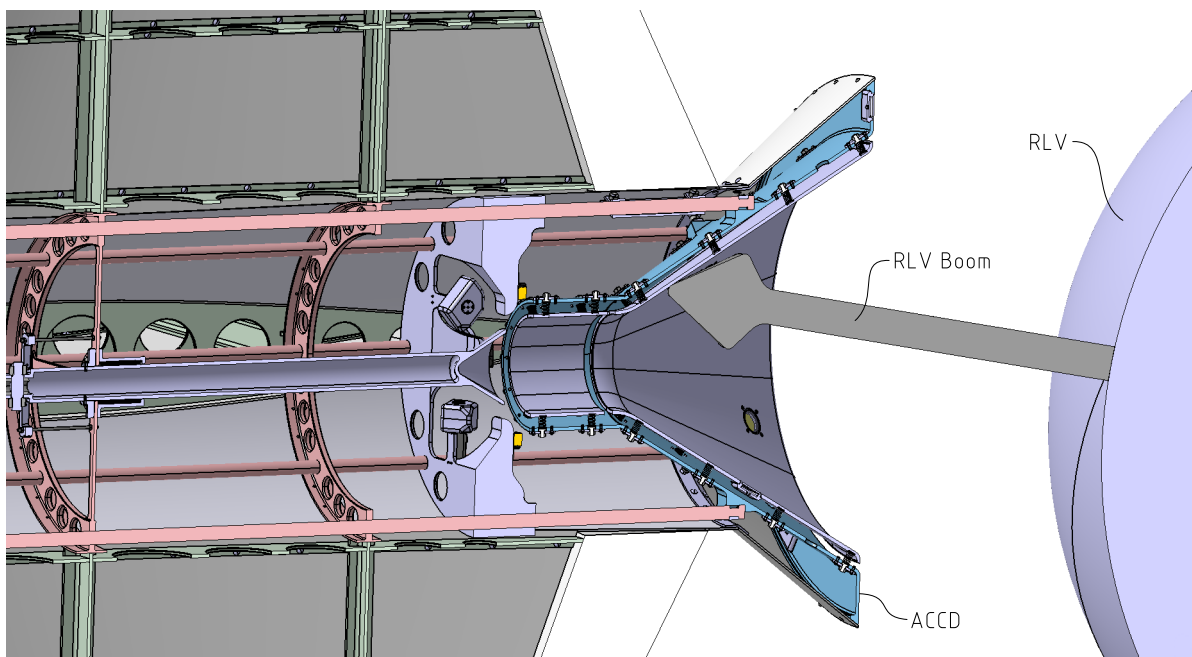


Figure N.1: Step 1 of a Nominal Docking Sequence: First Contact Between the RLV Boom and the ACCD's Guiding Cone.

Driven by the RLV's inertia, and aided by the mechanical design of the diverging guiding cone and conical boom tip, those misalignments are reduced during the soft docking phase. Considered in the ACCD's body reference frame, the RLV boom is guided towards the central opening at the throat of the guiding cone. Here, it is detected by the infrasonic distance-measuring sensors presented in chapter 5 - as illustrated in in Figure N.2. As described in chapter 5, each of the four sensors' measurements can be combined to obtain an estimate of the local boom thickness, which in turn yields information about its axial position relative to the ACCD - further priming the activation of the locking mechanism.

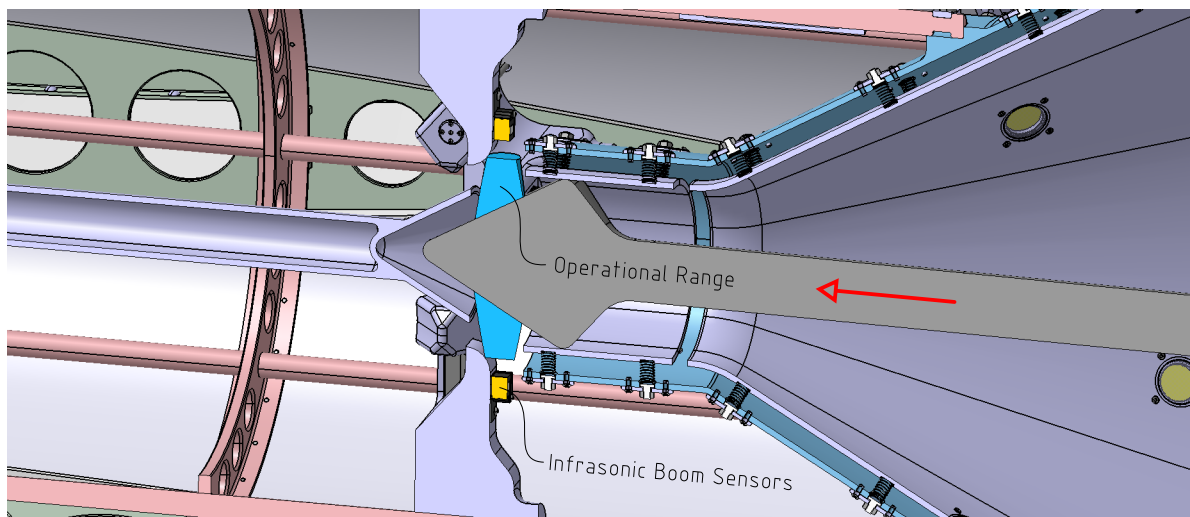


Figure N.2: Step 2 of a Nominal Docking Sequence: as the RLV Boom Enters the Cylindrical Section of the Guiding Cone, Four Boom Sensors Monitor its Position.

Continuing its path forwards, the RLV boom then interfaces with the shock-absorbing plunger, which translates axially, and starts compressing the MC61450 shock absorber. Because of this decompressive stroke, the relative velocity between the ACCD and the RLV decreases, as energy is absorbed by the shock-absorbing assembly. Figure N.3 shows the absorber in a slightly compressed state, with the RLV boom not yet in a position where it can be captured by the locking mechanism.

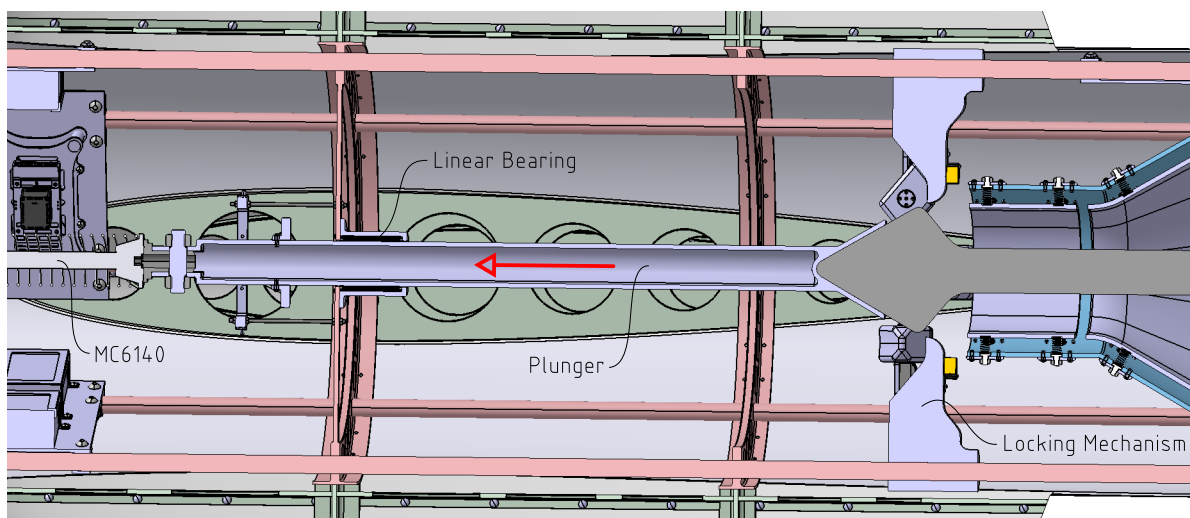


Figure N.3: Step 3 of a Nominal Docking Sequence: the RLV Boom Interfaces with the Plunger, and the Shock Absorber Starts Compressing and Absorbing Energy.

When the boom's diverging-converging conical section has just passed the locking mechanism, the two sensor triggers mounted onto the shock-absorbing plunger activate the photoelectric plunger sensors discussed in chapter 5 - as shown in Figure N.4. A signal is sent to the ACCD's OBC, where it is compared to data coming from the boom sensors - verifying whether they are still sensing the presence of the RLV boom. Only if both signals concur, the deployment of the locking actuators is triggered, moving the locking wedges into their engaged position. Their extension is monitored by the actuator's built-in Hall sensors, which can be used to detect a successful capture - in conjunction with data from the infrasonic boom sensors.

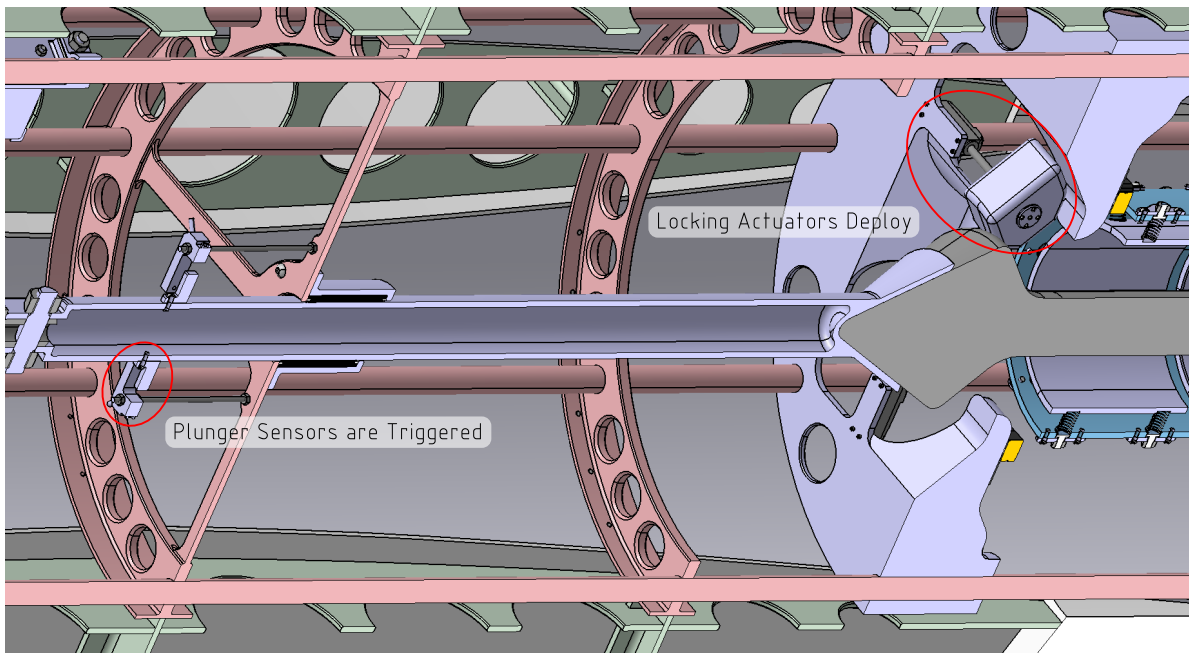


Figure N.4: Step 4 of a Nominal Docking Sequence: the Plunger Sensors are Triggered, and the Locking Actuators Engage.

Meanwhile, the shock-absorbing assembly continues its compressive stroke, and the relative velocity between both vehicles is reduced to zero. At the end of this stroke, the MC61450's internal spring initiates a decompressive stroke, pushing the ACCD and RLV apart again. However, the deployed locking wedges prevent the RLV boom from exiting the locking mechanism, and the system enters its stable docked state - shown in Figure N.5. The shock absorber applies a compressive force on the tip of the boom, clamping the complete locking mechanism rigidly together. Throughout the tow-back flight, this configuration is maintained, and the different docking sensors continue to monitor the interface between the ACCD and RLV. Finally, after the ACCD's release system has been triggered, the shock absorber's compressive force continues to support the interface between the ACCD and RLV during the latter's autonomous landing.

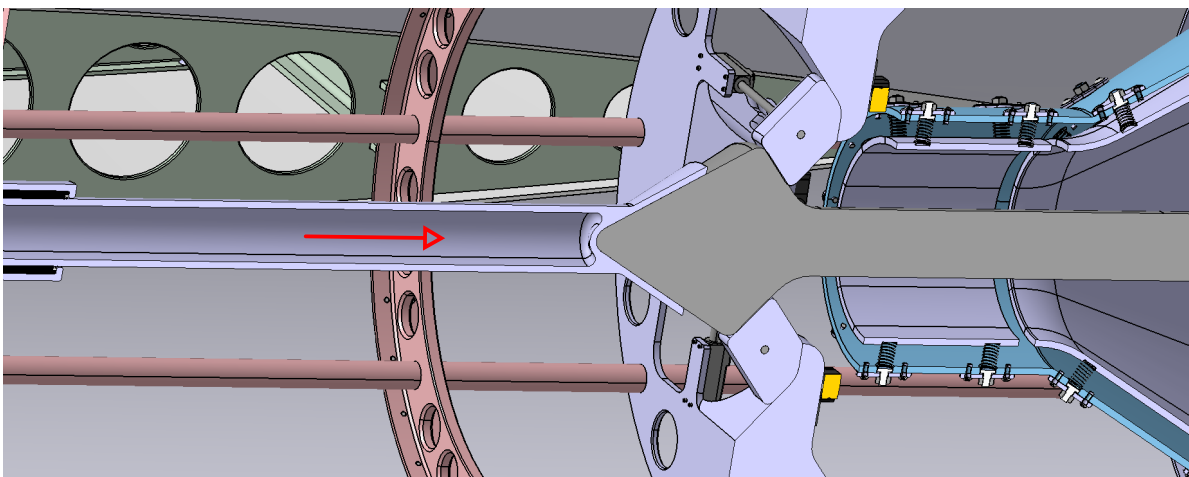
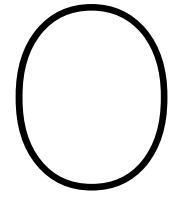


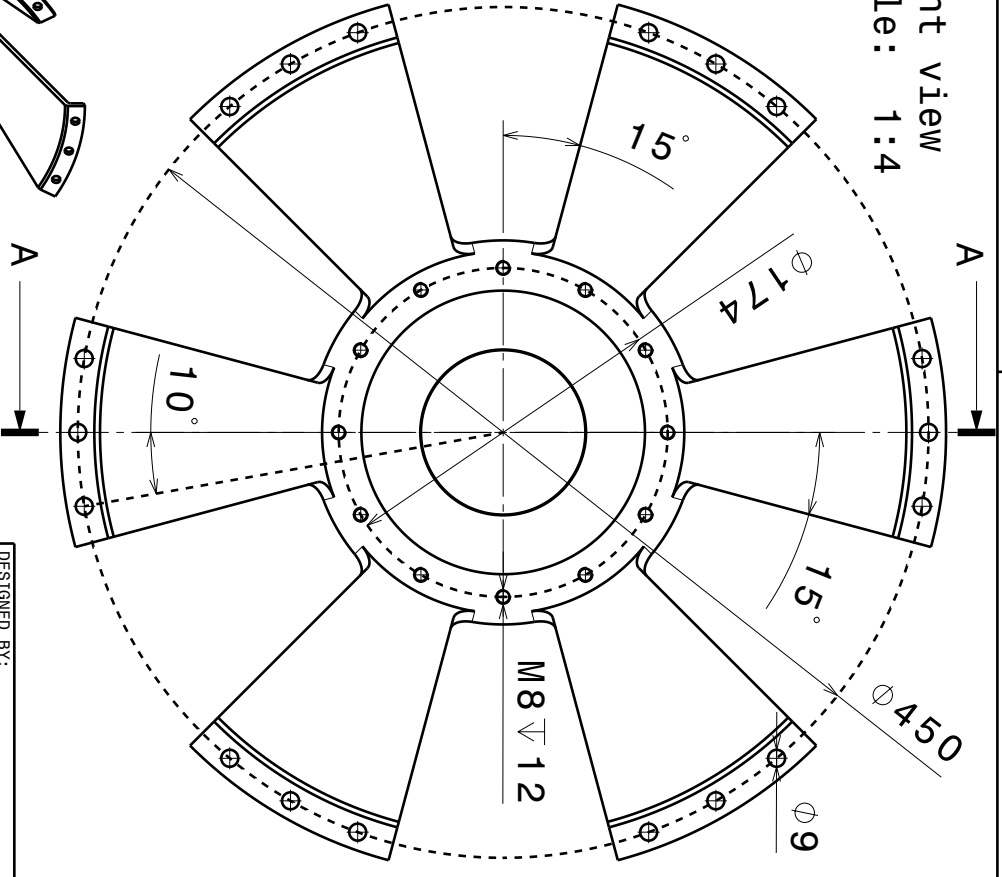
Figure N.5: Step 5 of a Nominal Docking Sequence: with the Locking Mechanism Engaged, and the Compressive Force of the Shock Absorber, the Entire Assembly is in a Stable, Docked State.



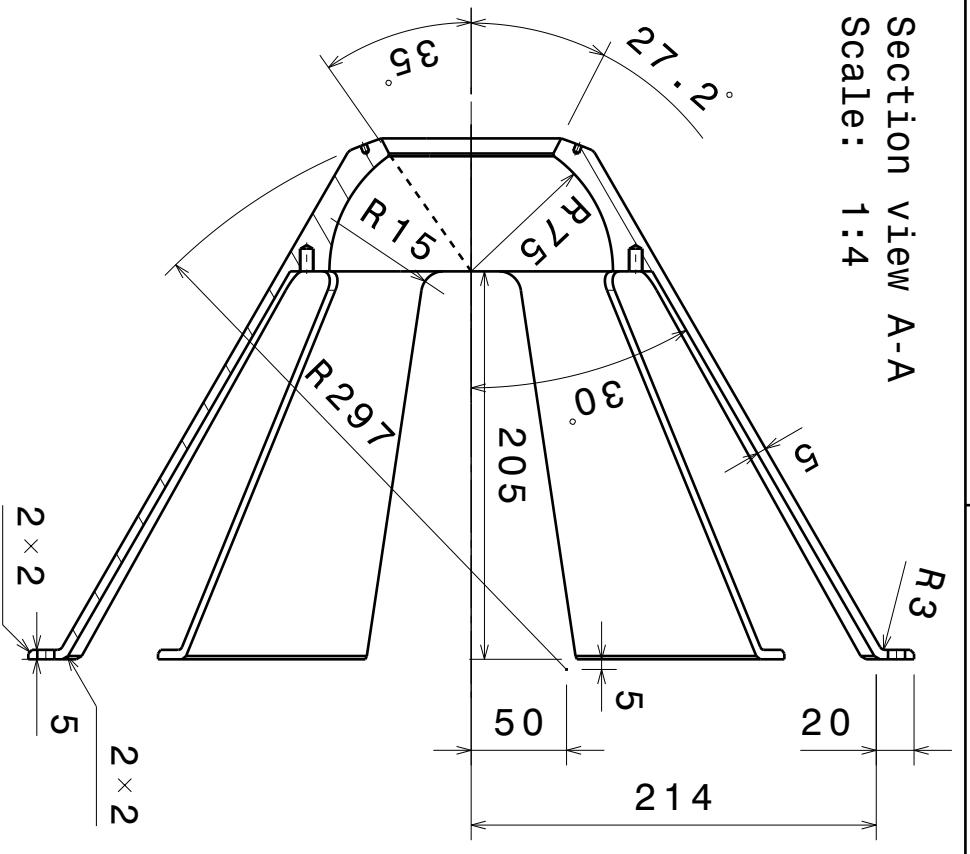
Technical Drawings

The following pages include technical drawings for all essential mechanical components designed throughout this work. Although only of a preliminary nature, they mainly serve as a reference guide for future iterations of the ACCD's mechanical design, while also giving a more detailed and comprehensive view of components that were only briefly discussed in chapter 6.

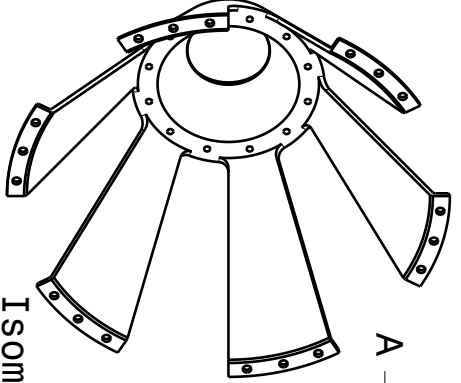
Front view
Scale: 1:4



Section view A-A
Scale: 1:4



Isometric view
Scale: 1:8



Front Rope Attachment Segment

ICARUS

DESIGNED BY:
B. Luyten

DATE:
01/07/2024

CHECKED BY:

XXX

DATE:

XXX

SIZE:

A4



SCALE:

1:4

3.25

DRAWING NUMBER

Rope Attachment Front

SHEET

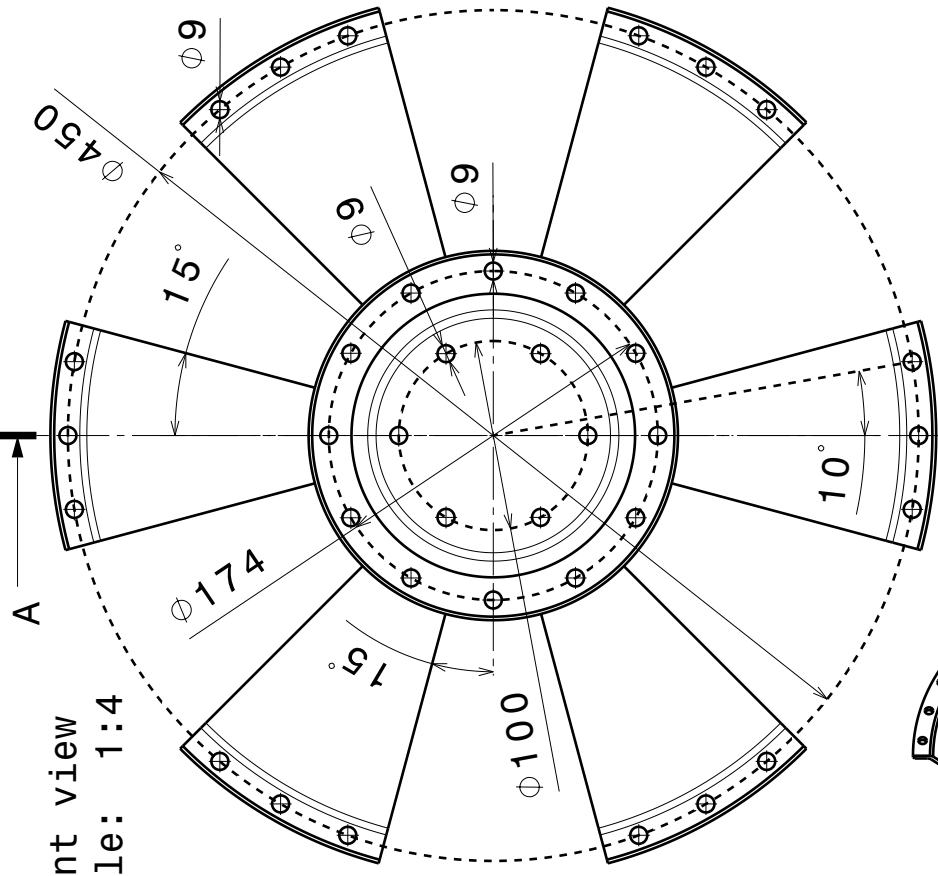
1 / 1

This drawing is our property; it can't be reproduced or communicated without our written agreement.

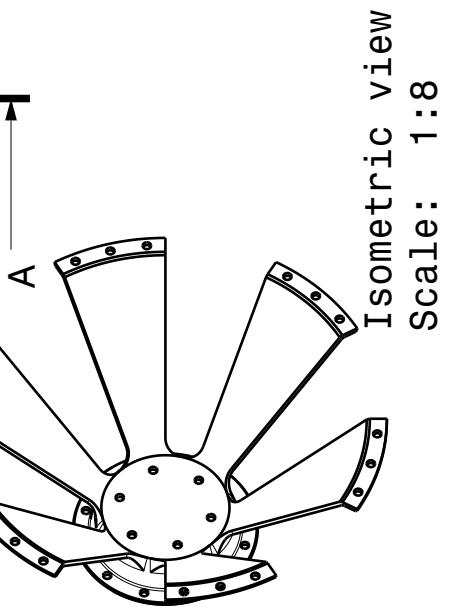
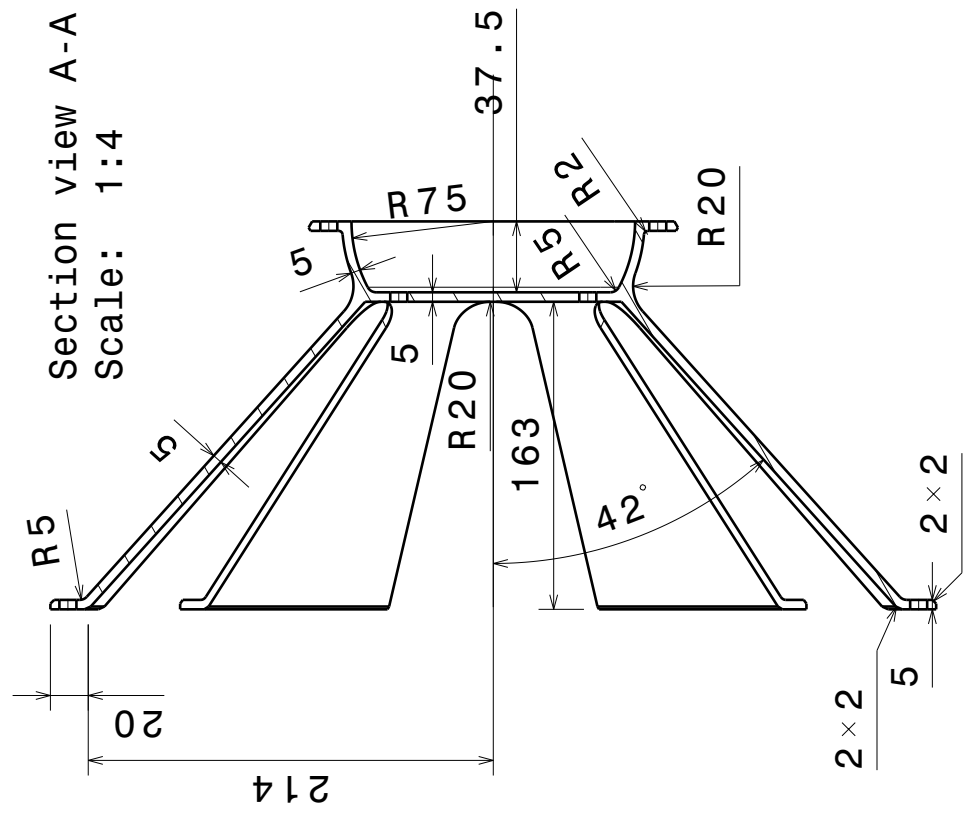
I	-
H	-
G	-
F	-
E	-
D	-
C	-
B	-
A	-

4 3 2 1

Front view
Scale: 1:4



Section view A-A
Scale: 1:4



Isometric view
Scale: 1:8

DESIGNED BY: B. Luyten	DATE: 01/07/2024
CHECKED BY: XXX	DATE: XXX
SIZE: A4	WEIGHT (kg): 2.08
SCALE: 1:4	DRAWING NUMBER: 1/1

Aft Rope Attachment Segment		I	-
		H	-
ICARUS		G	-
		F	-
ICARUS		E	-
		D	-
Rope Attachment Aft		C	-
		B	-
Rope Attachment Aft		A	-

This drawing is our property; it can't be reproduced or communicated without our written agreement.

m

C

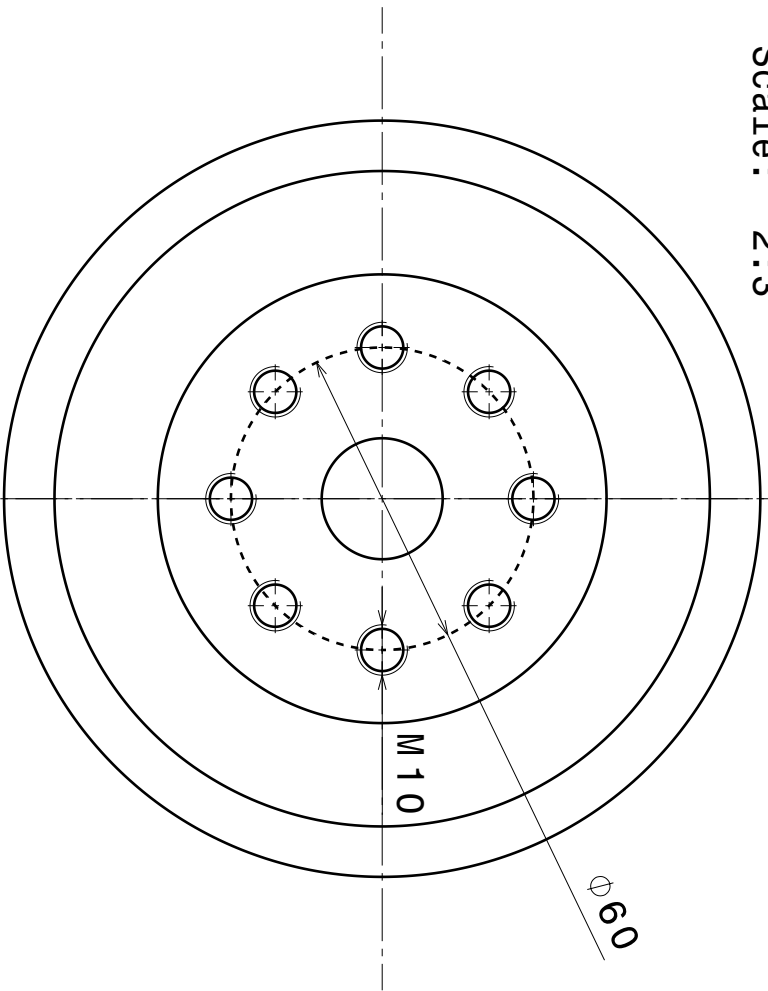
C

A

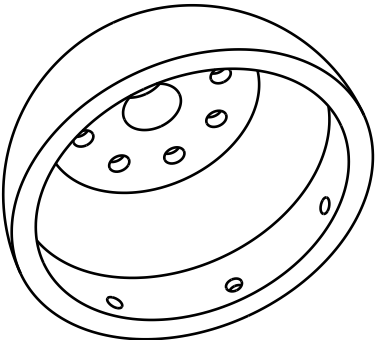
D

A

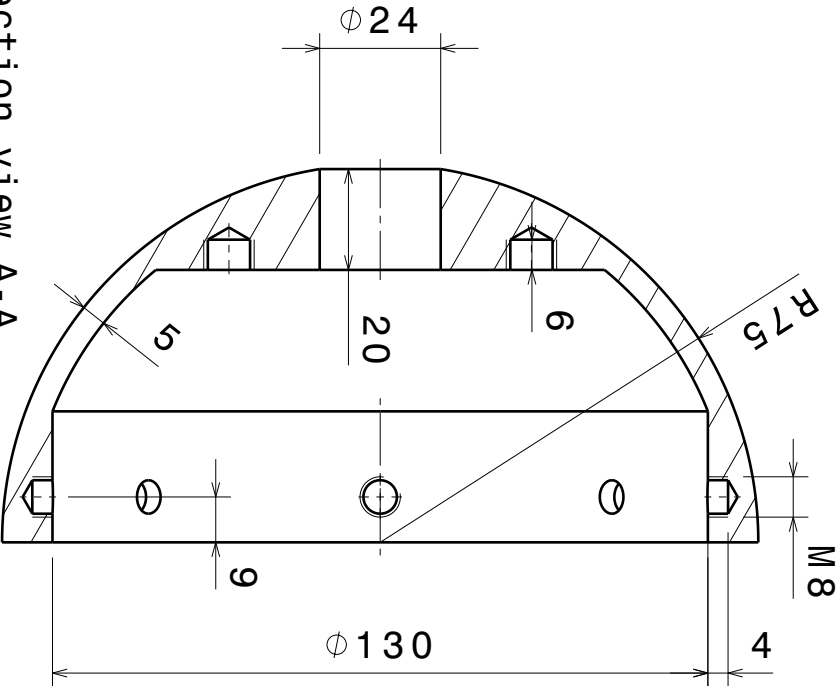
Front view
Scale: 2:3



Isometric view
Scale: 1:3



Section view A-A
Scale: 2:3



DESIGNED BY:
B. Luyten
DATE: 01/07/2024

CHECKED BY:
XXX
DATE: XXX

SIZE
A4



SCALE
2:3

WEIGHT (KG)
0.65

DRAWING NUMBER

RopeJoint Front

SHEET

1 / 1

Front Rope Joint Segment

ICARUS

This drawing is our property; it can't be reproduced or communicated without our written agreement.

I	-
H	-
G	-
F	-
E	-
D	-
C	-
B	-
A	-

4 3 2 1

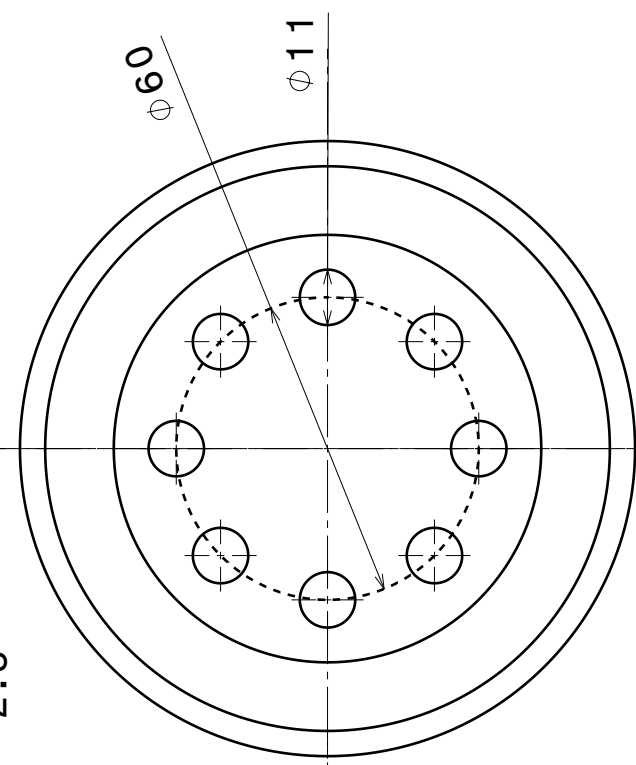
m

c

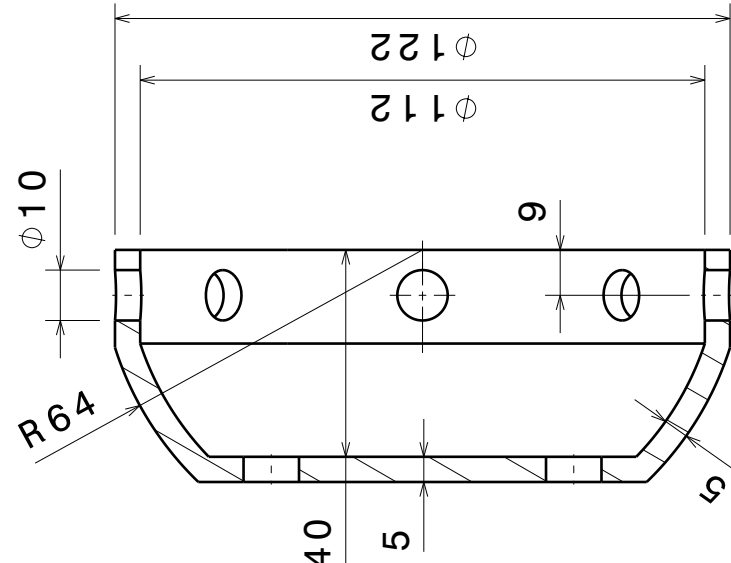
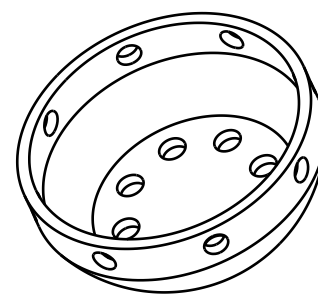
q

4

Front view
Scale: 2:3



Isometric view
Scale: 1:3



Section view A-A
Scale: 2:3

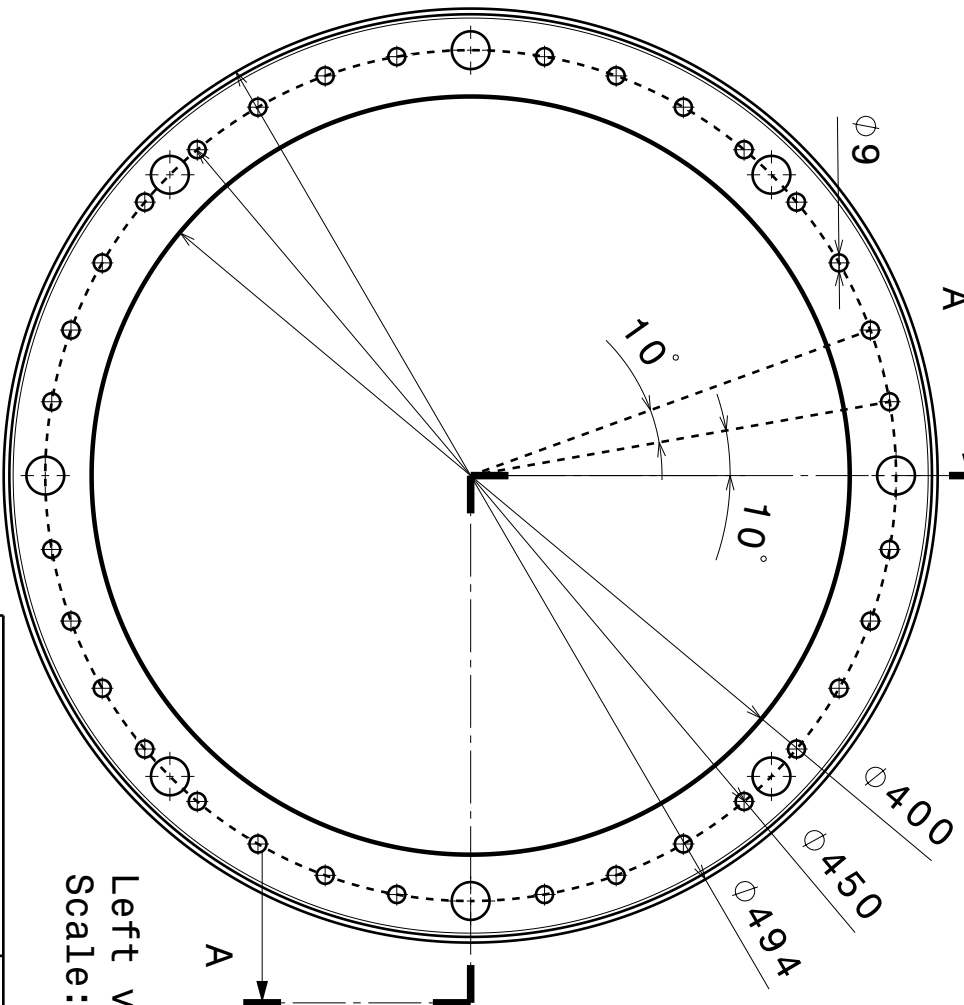
DESIGNED BY: B. Luyten	DATE: 01/07/2024	CHECKED BY: XXX	DATE: XXX	SIZE A4	WEIGHT (kg) 0.28	DRAWING NUMBER 1/1	SHEET 1/1	
Aft Rope Joint Segment				ICARUS				
				RopeJoint Aft				
I	H	G	F	E	D	C	B	A
-	-	-	-	-	-	-	-	-

This drawing is our property; it can't be reproduced or communicated without our written agreement.

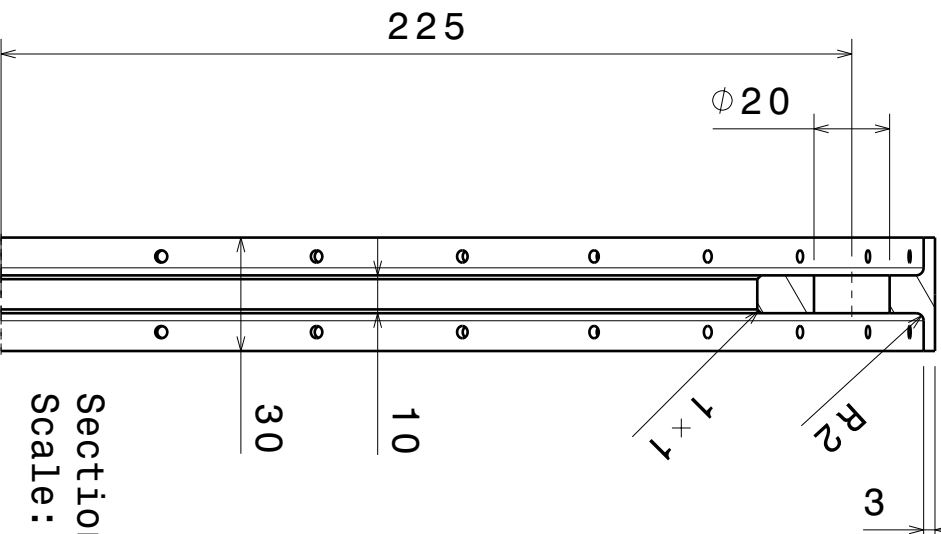
A

D

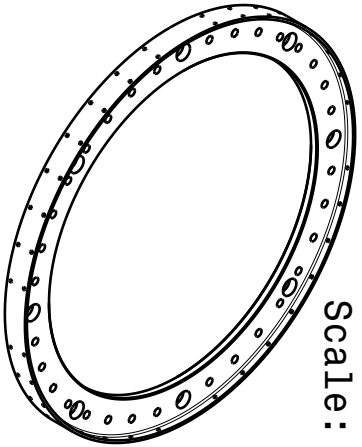
4 3 2 1



Front view
Scale: 1:4



Section view A-A
Scale: 1:2



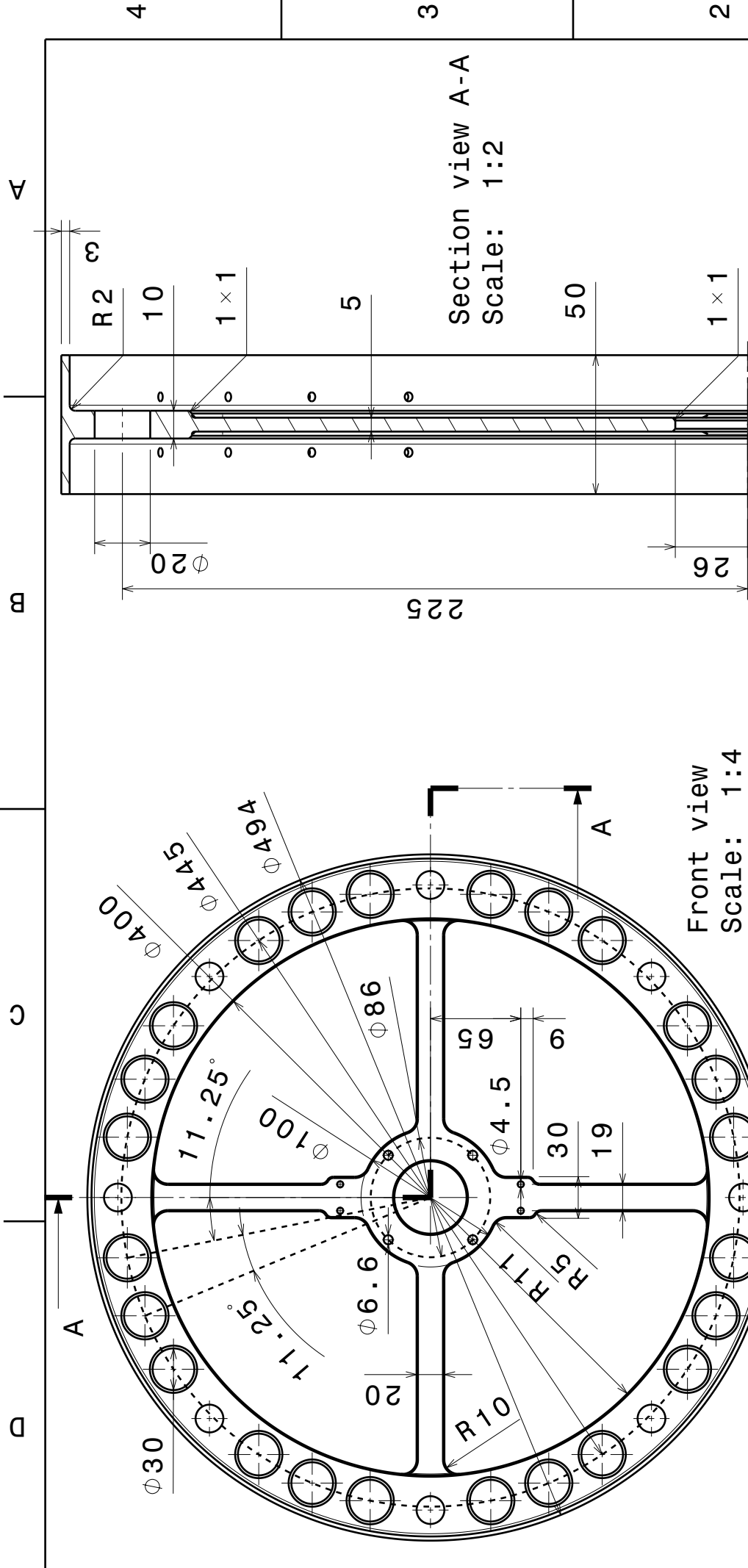
Isometric view
Scale: 1:8

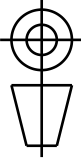
DESIGNED BY: B. Luyten	DATE: 28/06/2024
CHECKED BY: XXX	DATE: XXX
SIZE: A4	WEIGHT (kg): 1.98

Front Hoop	
ICARUS	
DRAWING NUMBER MainFrame RingFront	
SCALE: 1:4	SHEET 1 / 1

This drawing is our property; it can't be reproduced or communicated without our written agreement.

I	-
H	-
G	-
F	-
E	-
D	-
C	-
B	-
A	-



DESIGNED BY:	B. Luyten	
DATE:	01/07/2024	
CHECKED BY:	XXX	
DATE:	XXX	
SIZE		A4
SCALE	WEIGHT (kg)	1:4 1.98
DRAWING NUMBER		1/1
SHEET		1/1

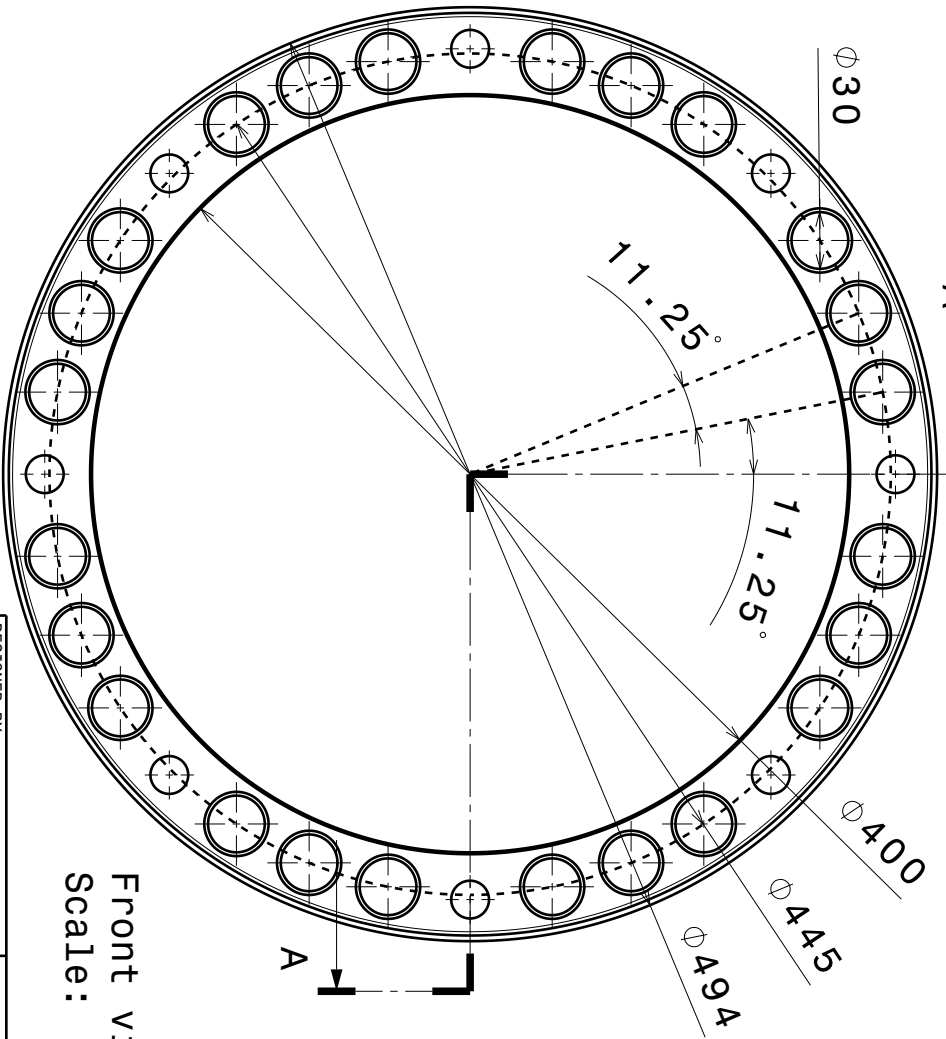
Central Hoop

ICARUS

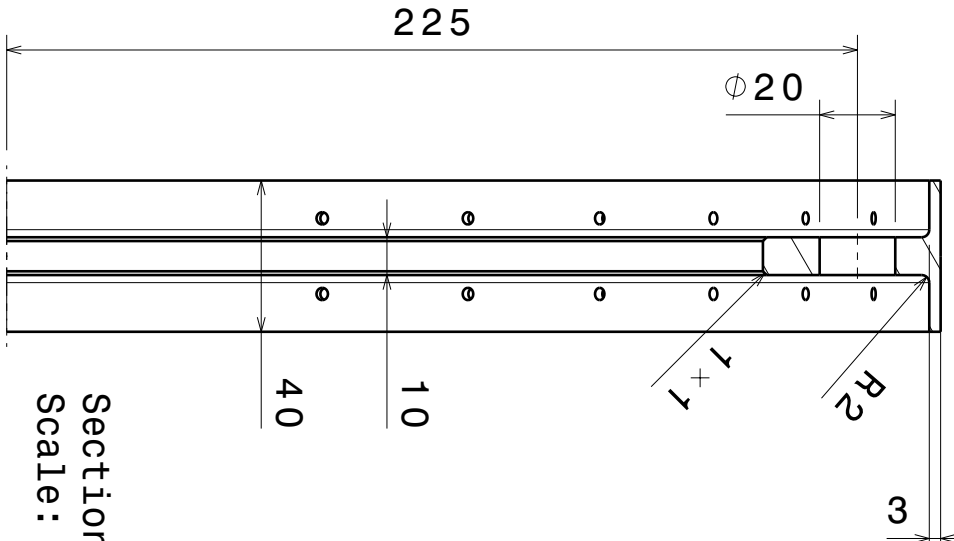
MainFrame RingMiddle

I	-
H	-
G	-
F	-
E	-
D	-
C	-
B	-
A	-

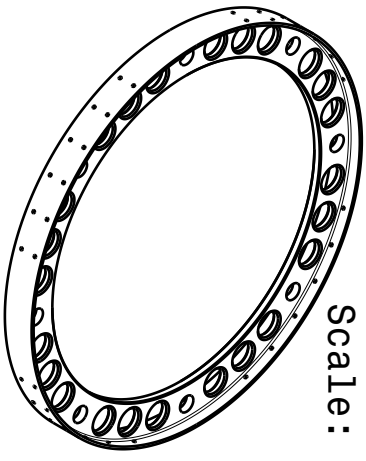
This drawing is our property; it can't be reproduced or communicated without our written agreement.



Front view
Scale: 1:4



Section view A-A
Scale: 1:2



Isometric view
Scale: 1:8

Aft Hoop

ICARUS

DESIGNED BY:
B. Luyten

DATE:
28/06/2024

CHECKED BY:
XXX

DATE:
XXX



SCALE
1:4

WEIGHT (kg)
1.61

DRAWING NUMBER
MainFrame Ringaft

SHEET
1 / 1

This drawing is our property; it can't be reproduced or communicated without our written agreement.

I	-
H	-
G	-
F	-
E	-
D	-
C	-
B	-
A	-

A

m

c

d

4

3

2

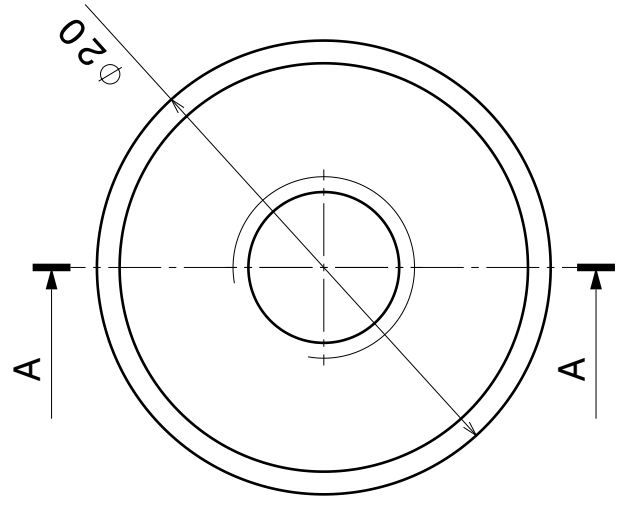
1

4

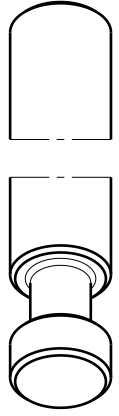
3

2

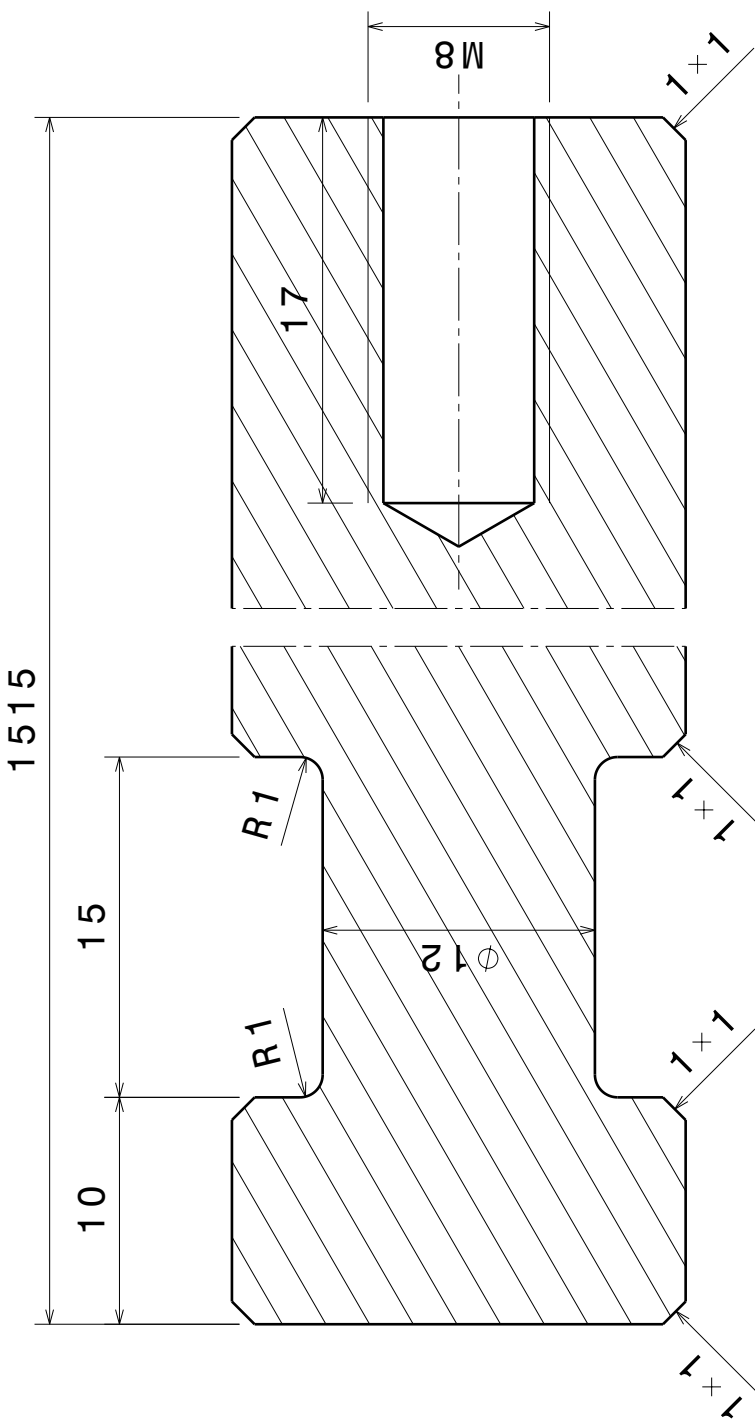
1



Front view
Scale: 3:1



Isometric view
Scale: 2:3



Section view A-A
Scale: 3:1

DESIGNED BY: B. Luyten	DATE: 01/07/2024
CHECKED BY: XXX	DATE: XXX
SIZE A4	WEIGHT (kg) 1.27
SCALE 3:1	DRAWING NUMBER 1.27

I	-
H	-
G	-
F	-
E	-
D	-
C	-
B	-
A	-

Structural Bar		SHEET 1/1
ICARUS		
MainFrame Strut Hole		

This drawing is our property; it can't be reproduced or communicated without our written agreement.

A

D

D

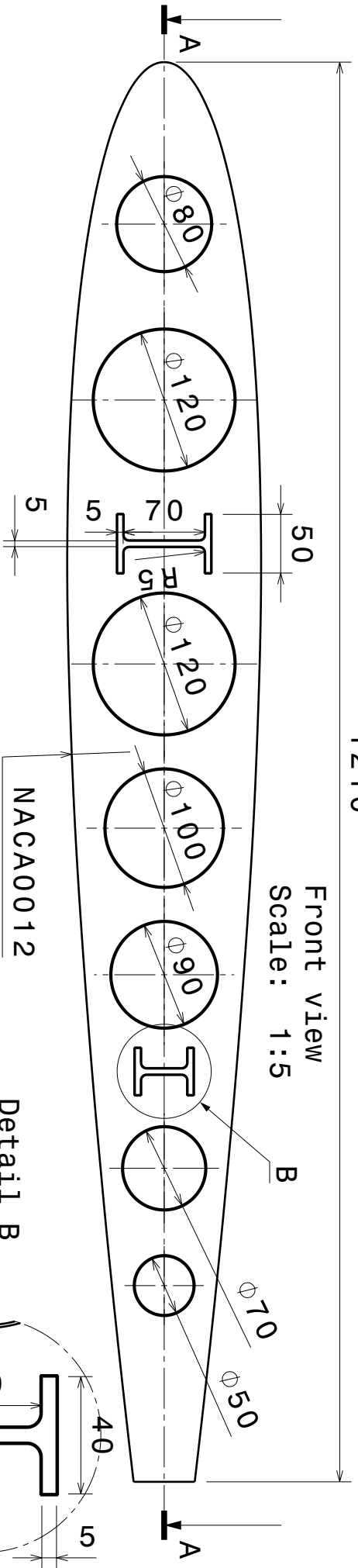
C

B

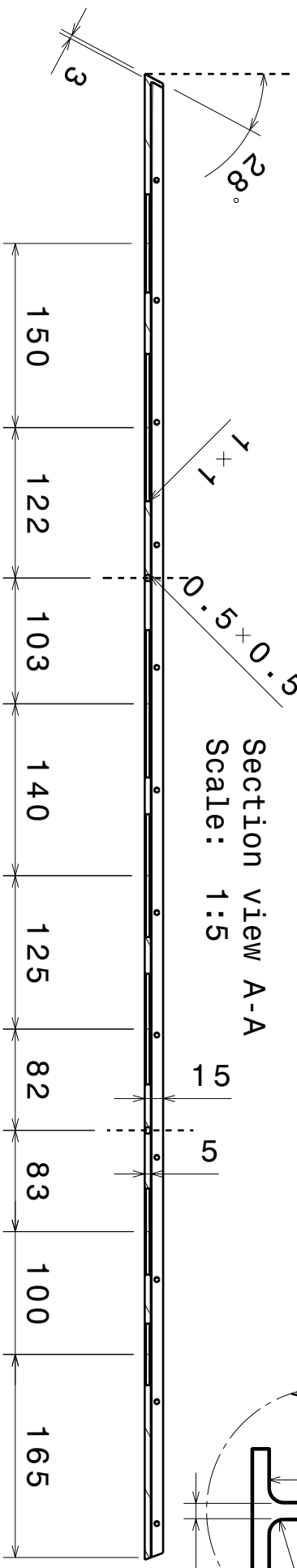
A

1210

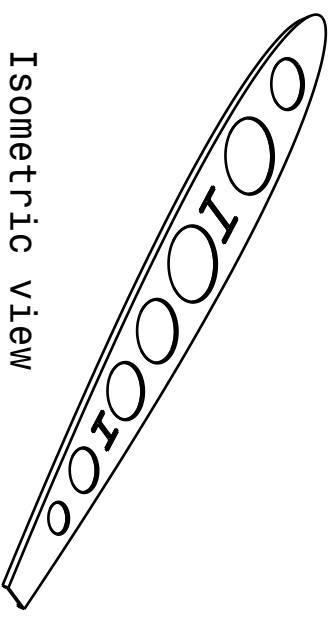
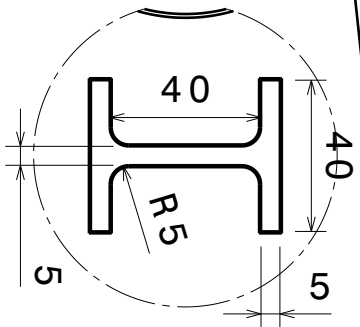
Front view
Scale: 1:5



Section view A-A
Scale: 1:5



Detail B
Scale: 1:2



Isometric view
Scale: 1:12

D

A

DESIGNED BY:

B. Luyten

DATE:

01/07/2024

CHECKED BY:

XXX

DATE:

XXX

SIZE:

A4



SCALE:

1:5 1.59

DRAWING NUMBER

Wing Rib Root

SHEET

1 / 1

This drawing is our property; it can't be reproduced or communicated without our written agreement.

2

3

4

1

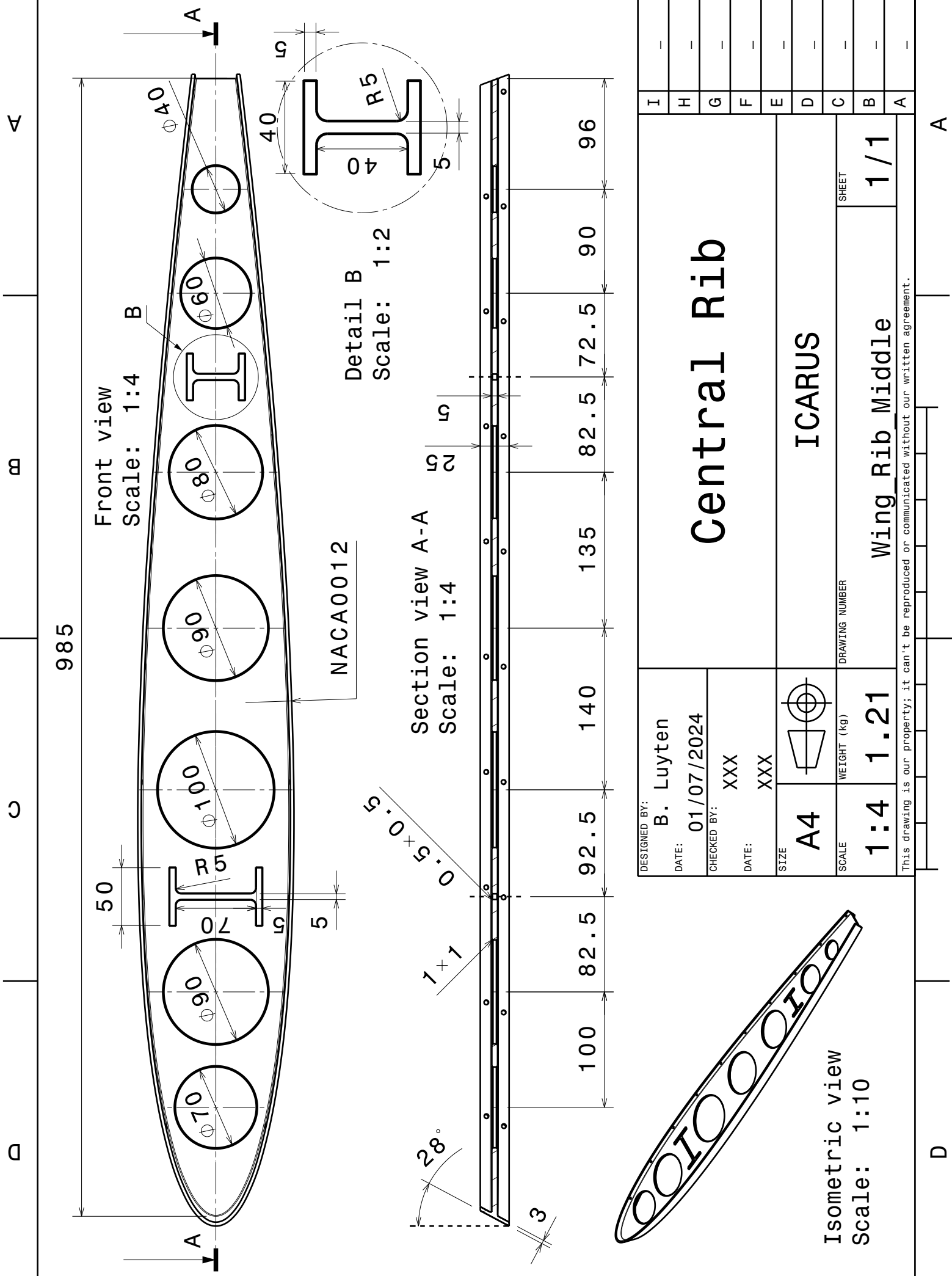
2

3

4

1

4 3 2 1



Front view
Scale: 1:4

Detail B
Scale: 1:2

Section view A-A
Scale: 1:4

Isometric view
Scale: 1:10

NACA0012

DESIGNED BY:	B. Luyten	
DATE:	01/07/2024	
CHECKED BY:	XXX	
DATE:	XXX	
SIZE		A4
SCALE	WEIGHT (kg)	1:4 1.21
DRAWING NUMBER		ICARUS
SHEET		1/1

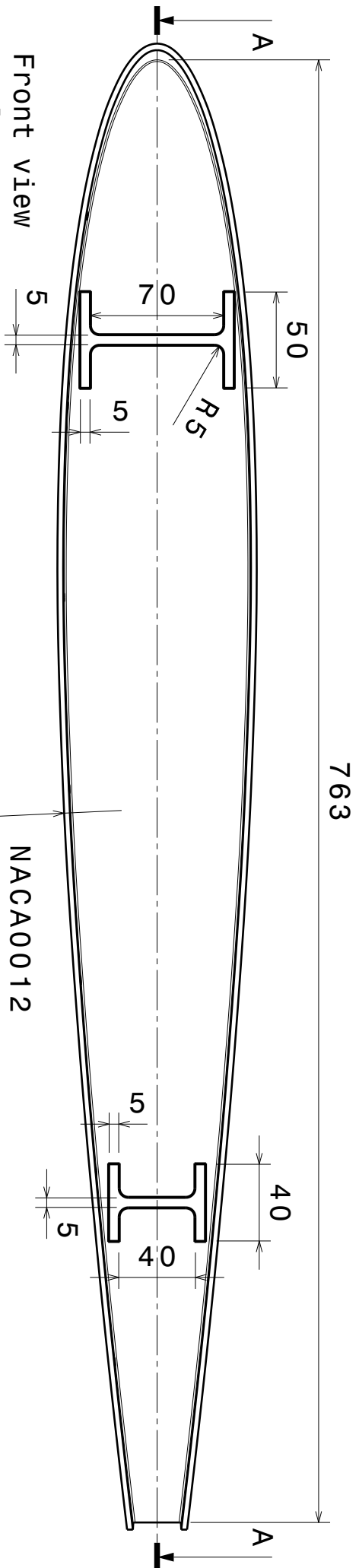
Central Rib

Wing Rib Middle

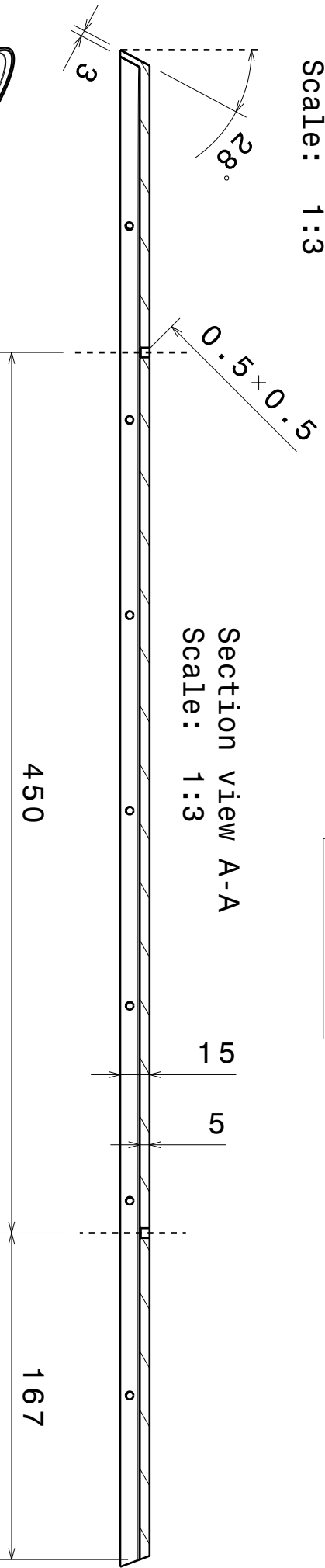
This drawing is our property; it can't be reproduced or communicated without our written agreement.

4 3 2 1

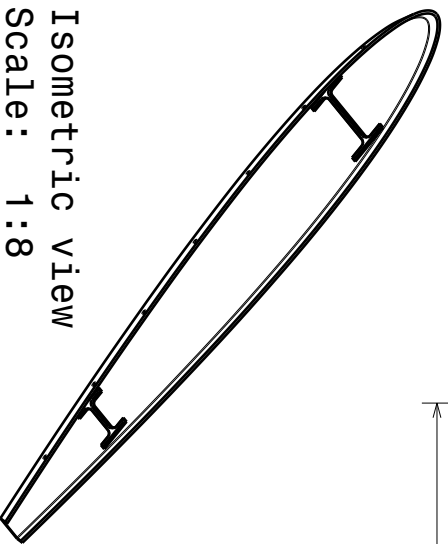
Front view
Scale: 1:3



Section view A-A
Scale: 1:3



Isometric view
Scale: 1:8



DESIGNED BY:
B. Luyten

DATE:
01/07/2024

CHECKED BY:
XXX

DATE:
XXX

SIZE
A4



SCALE

1:3

WEIGHT (KG)

0.91

DRAWING NUMBER

Wing Rib Tip

ICARUS

SHEET

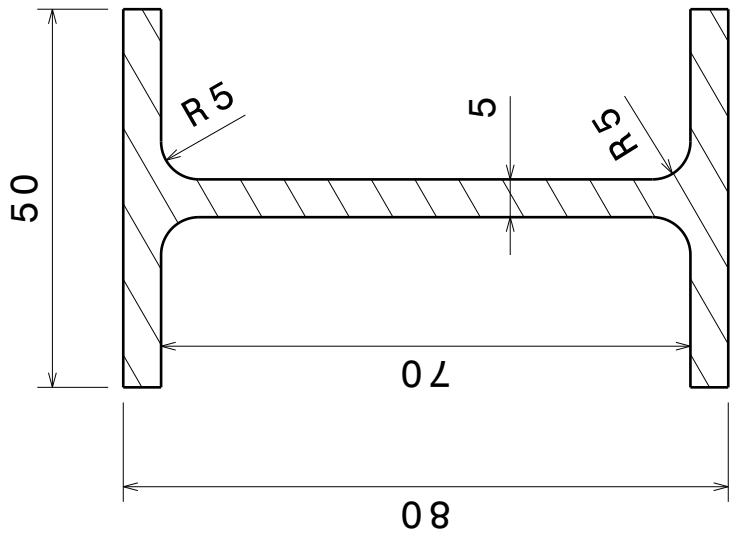
1 / 1

This drawing is our property; it can't be reproduced or communicated without our written agreement.

I	-
H	-
G	-
F	-
E	-
D	-
C	-
B	-
A	-

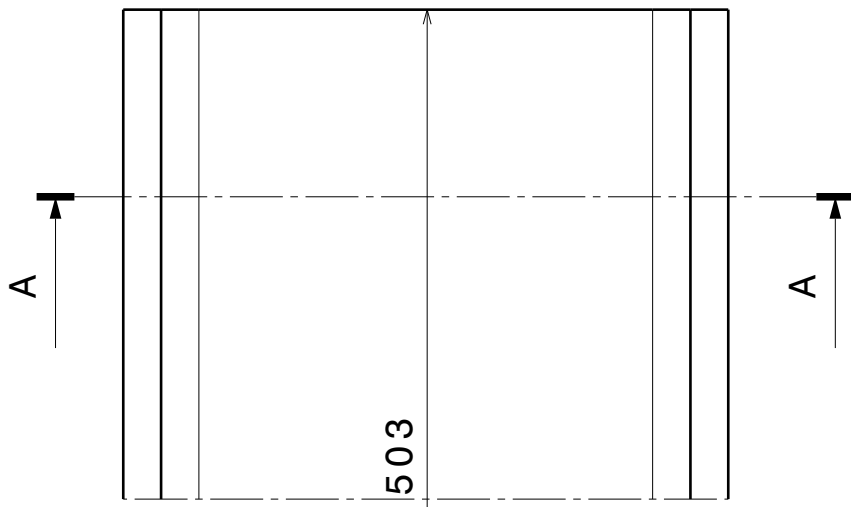
4 3 2 1

A



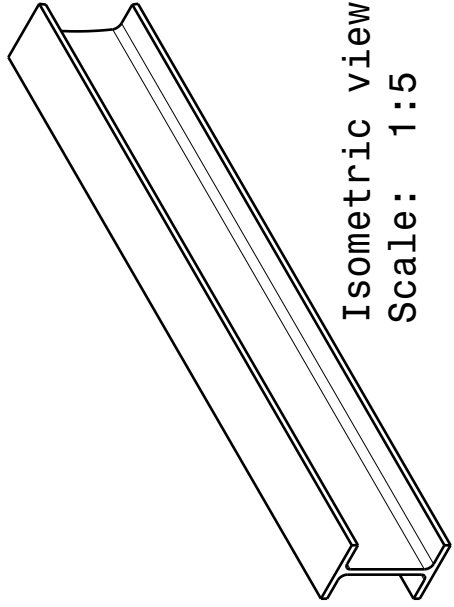
Section view A-A
Scale: 1:1

C

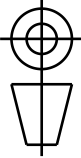
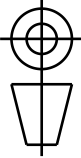
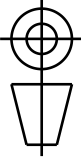


Top view
Scale: 1:1

4 3 2 1

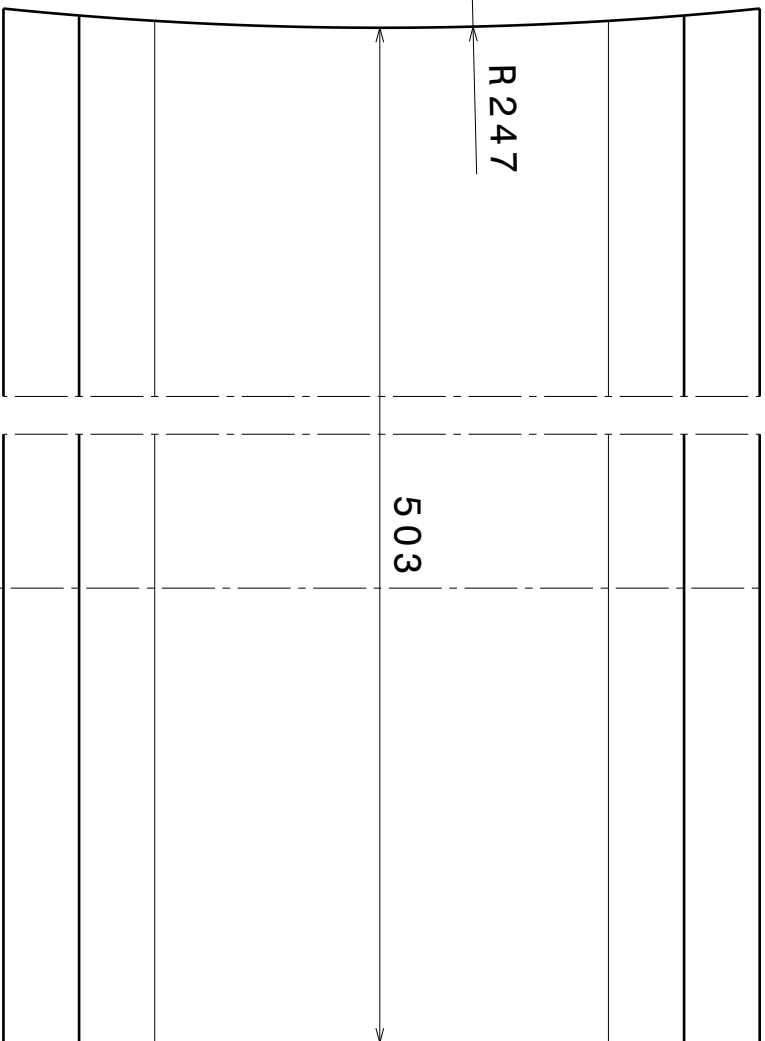


Isometric view
Scale: 1:5

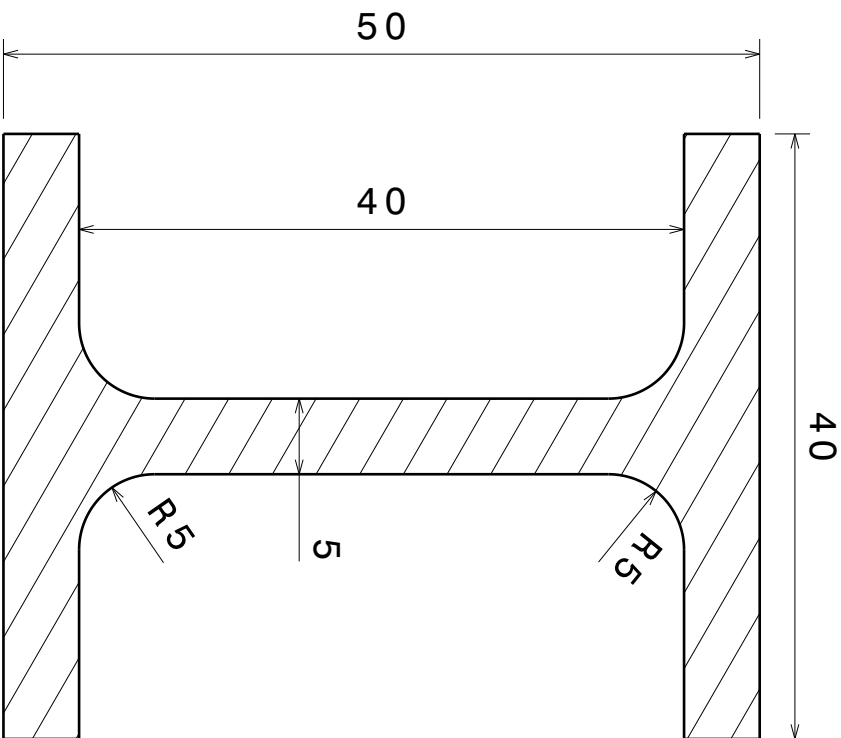
DESIGNED BY: B. Luyten	 A4	WEIGHT (kg) 1.19	DRAWING NUMBER Wing_SparFront	SHEET 1/1	I	-
DATE: 28/06/2024					H	-
CHECKED BY: XXX	 A4	WEIGHT (kg) 1.19	DRAWING NUMBER Wing_SparFront	SHEET 1/1	G	-
DATE: XXX					F	-
SIZE A4	 A4	WEIGHT (kg) 1.19	DRAWING NUMBER Wing_SparFront	SHEET 1/1	E	-
SCALE 1:1					D	-
Leading Spar					C	-
ICARUS					B	-
This drawing is our property; it can't be reproduced or communicated without our written agreement.					A	-

A

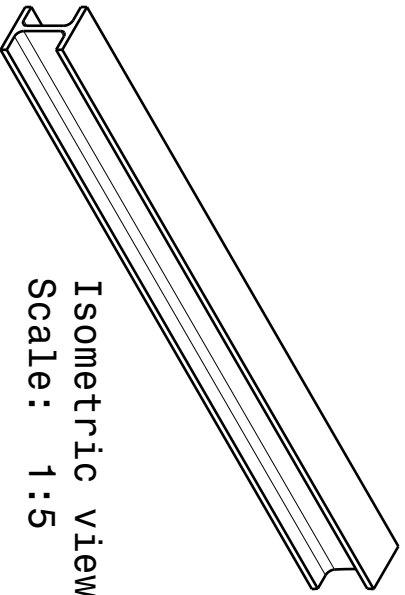
D



Front view
Scale: 2:1



Section view A-A
Scale: 2:1



Isometric view
Scale: 1:5

Trailing Spar

ICARUS

Wing Sparaft

DESIGNED BY:
B. Luyten

DATE:
28/06/2024

CHECKED BY:
XXX

DATE:
XXX

SIZE
A4



SCALE

2:1

WEIGHT (kg)

0.85

DRAWING NUMBER

Wing Sparaft

SHEET

1 / 1

This drawing is our property; it can't be reproduced or communicated without our written agreement.

I	-
H	-
G	-
F	-
E	-
D	-
C	-
B	-
A	-

4

3

2

1

C

D

4

B

A

4

C

D

B

A

4

C

D

B

A

4

C

D

B

A

4

C

D

B

A

4

C

D

B

A

4

C

D

B

A

4

C

D

B

A

4

C

D

B

A

4

C

D

B

A

4

C

D

B

A

4

C

D

B

A

4

C

D

B

A

4

C

D

B

A

4

C

D

B

A

4

C

D

B

A

4

C

D

B

A

4

C

D

B

A

4

C

D

B

A

4

C

D

B

A

4

C

D

B

A

4

C

D

B

A

4

C

D

B

A

4

C

D

B

A

4

C

D

B

A

4

C

D

B

A

4

C

D

B

A

4

C

D

B

A

4

C

D

B

A

4

C

D

B

A

4

C

D

B

A

4

C

D

B

A

4

C

D

B

A

4

C

D

B

A

4

C

D

B

A

4

C

D

B

A

4

C

D

B

A

4

C

D

B

A

4

C

D

B

A

4

C

D

B

A

4

C

D

B

A

4

C

D

B

A

4

C

D

B

A

4

C

D

B

A

4

C

D

B

A

4

C

D

B

A

4

C

D

B

A

4

C

D

B

A

4

C

D

B

A

4

C

D

B

A

4

C

D

B

A

4

C

D

B

A

4

C

D

B

A

4

C

D

B

A

4

C

D

B

A

4

C

D

B

A

4

C

D

B

A

4

C

D

B

A

4

C

D

B

A

4

C

D

B

A

4

C

D

B

A

4

C

D

B

A

4

C

D

B

A

4

C

D

B

A

4

C

D

B

A

4

C

D

B

A

4

C

D

B

A

4

C

D

B

A

4

C

D

B

A

4

C

D

B

A

4

C

D

B

A

4

C

D

B

A

4

C

D

B

A

4

C

D

B

A

4

C

D

B

A

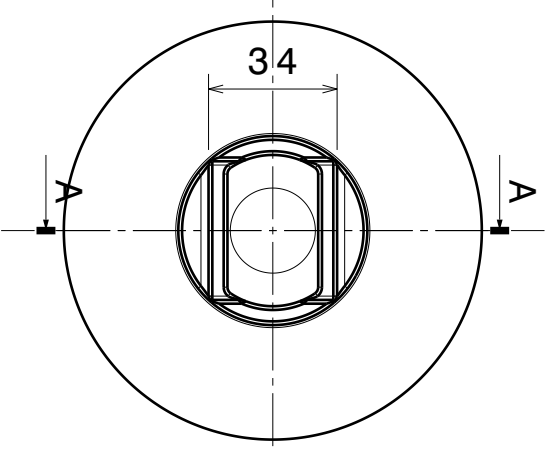
4

C

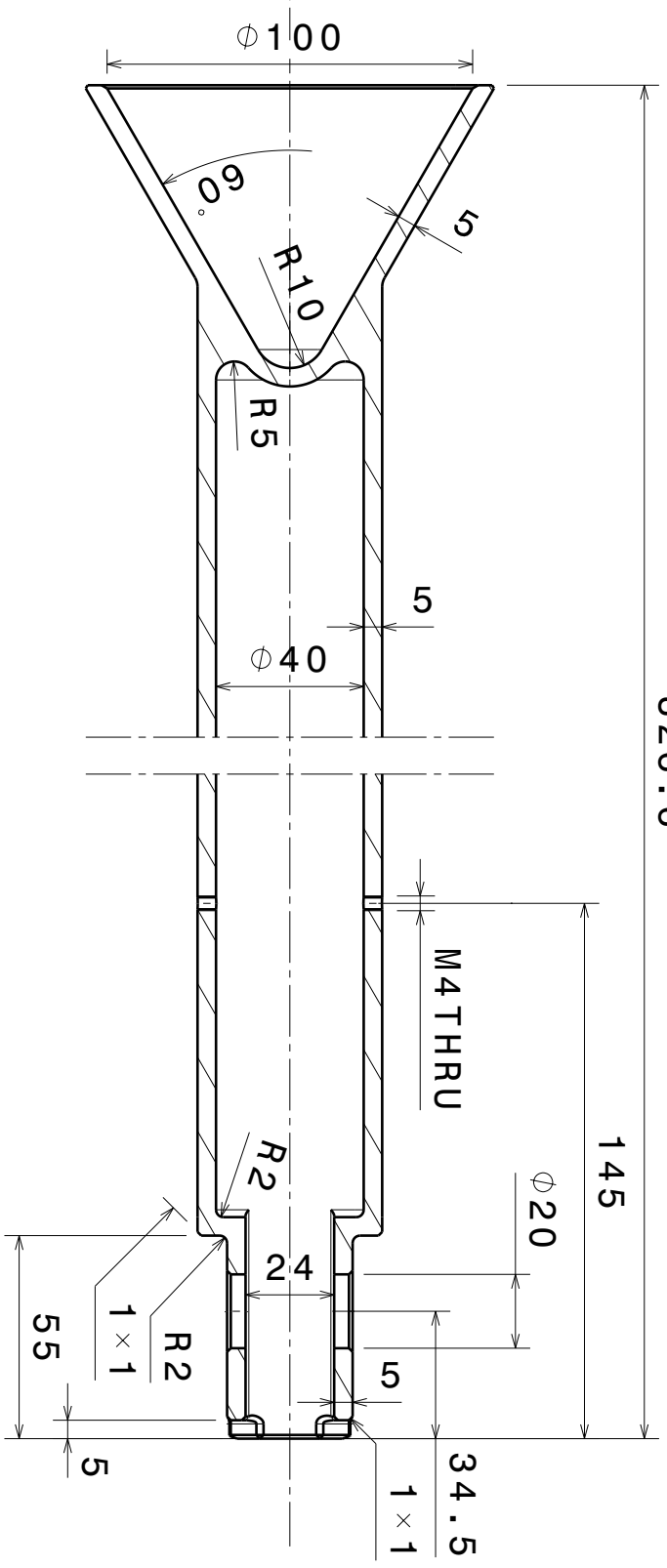
D

B

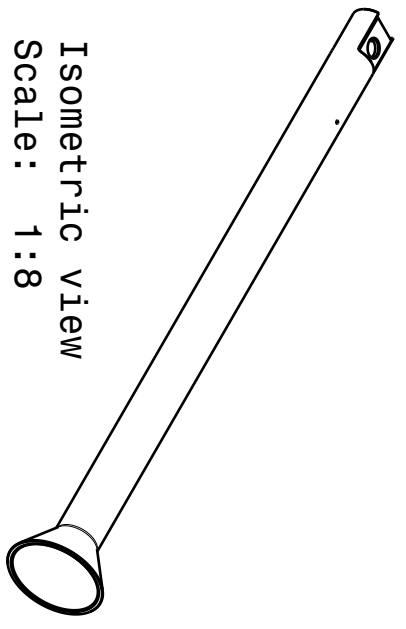
A



Front view
Scale: 1:2



Section view A-A
Scale: 1:2



Isometric view
Scale: 1:8

DESIGNED BY: B. Luyten			
DATE: 27/06/2024			
CHECKED BY: XXX			
DATE: XXX			
SIZE A4			
SCALE 1:2	WEIGHT (KG) 1.70		
DRAWING NUMBER PLunger		SHEET 1/1	
ICARUS			
PLunger			
This drawing is our property; it can't be reproduced or communicated without our written agreement.			

4

3

2

1

70

30

∅ 20

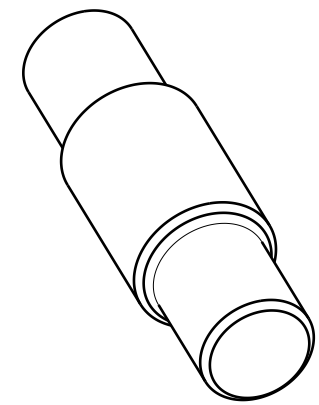
M 9

R 1

1 + 1

1 + 45°

Front view
Scale: 3:1



Isometric view
Scale: 1:1

DESIGNED BY:

B. Luyten

DATE:

27/06/2024

CHECKED BY:

XXX

DATE:

XXX

SIZE

A4



WEIGHT (kg)

3:1 0.05

DRAWING NUMBER

PlungerConnector

SHEET

1/1

Plunger Connector

ICARUS

I -

H -

G -

F -

E -

D -

C -

B -

A -

This drawing is our property; it can't be reproduced or communicated without our written agreement.

A

m

c

d

A

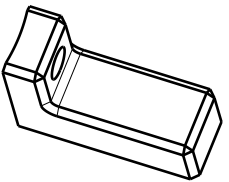
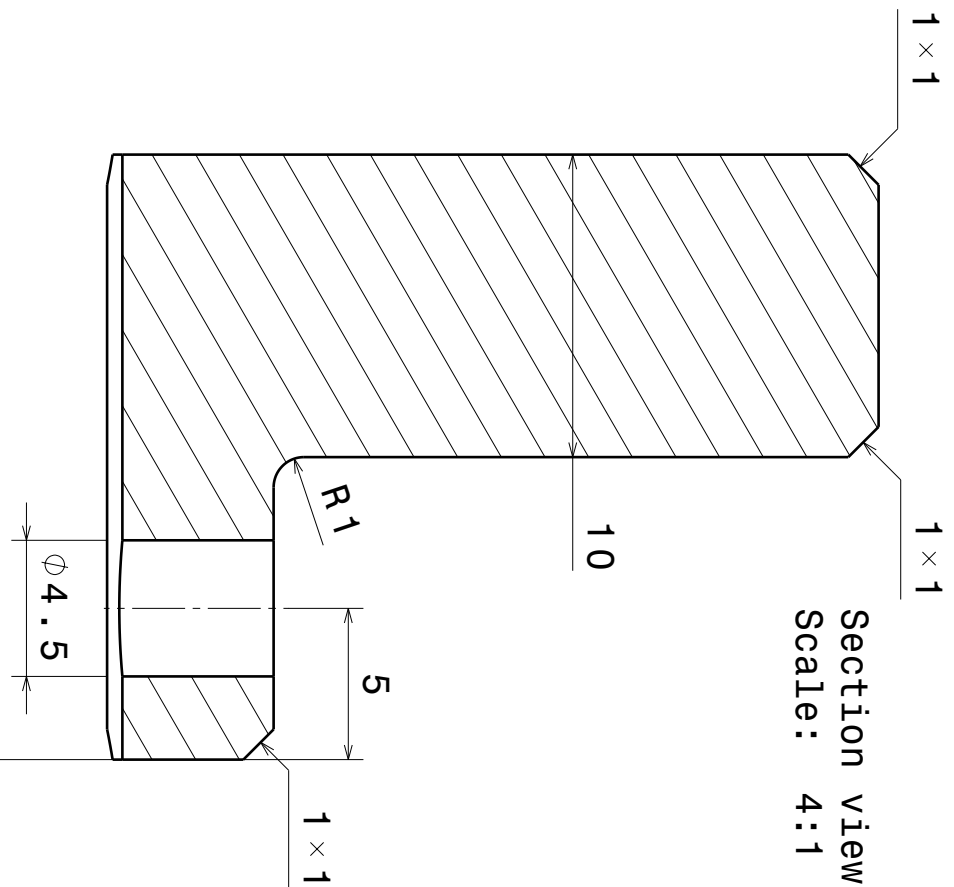
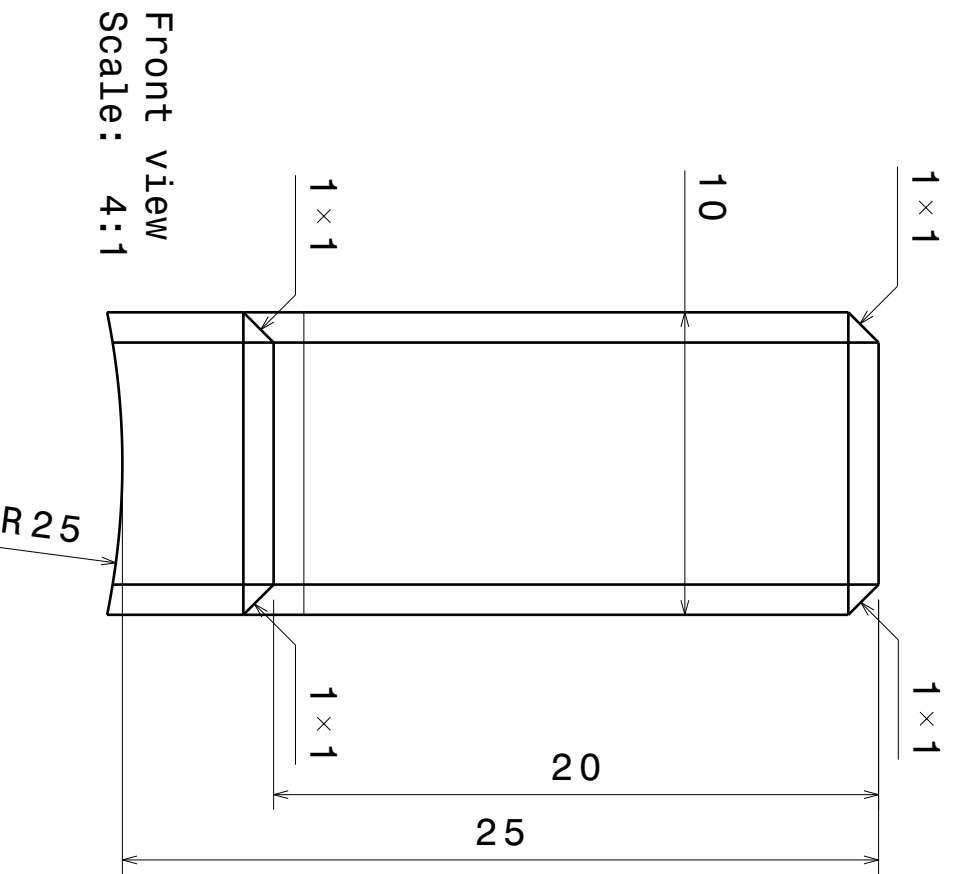
D

4


3


2

1



Isometric view
Scale: 1:1

DESIGNED BY:	B. Luyten	
DATE:	27/06/2024	
CHECKED BY:	XXX	
DATE:	XXX	
SIZE	A4	
SCALE	4:1	0.01
WEIGHT (kg)	0.01	

DESIGNED BY:	B. Luyten	
DATE:	27/06/2024	
CHECKED BY:	XXX	
DATE:	XXX	
SIZE	A4	
SCALE	4:1	0.01
WEIGHT (kg)	0.01	
DRAWING NUMBER	PlungerExtrusion	
SHEET	1 / 1	

Plunger Sensor Trigger

ICARUS

I	-
H	-
G	-
F	-
E	-
D	-
C	-
B	-
A	-

This drawing is our property; it can't be reproduced or communicated without our written agreement.

4 3 2 1

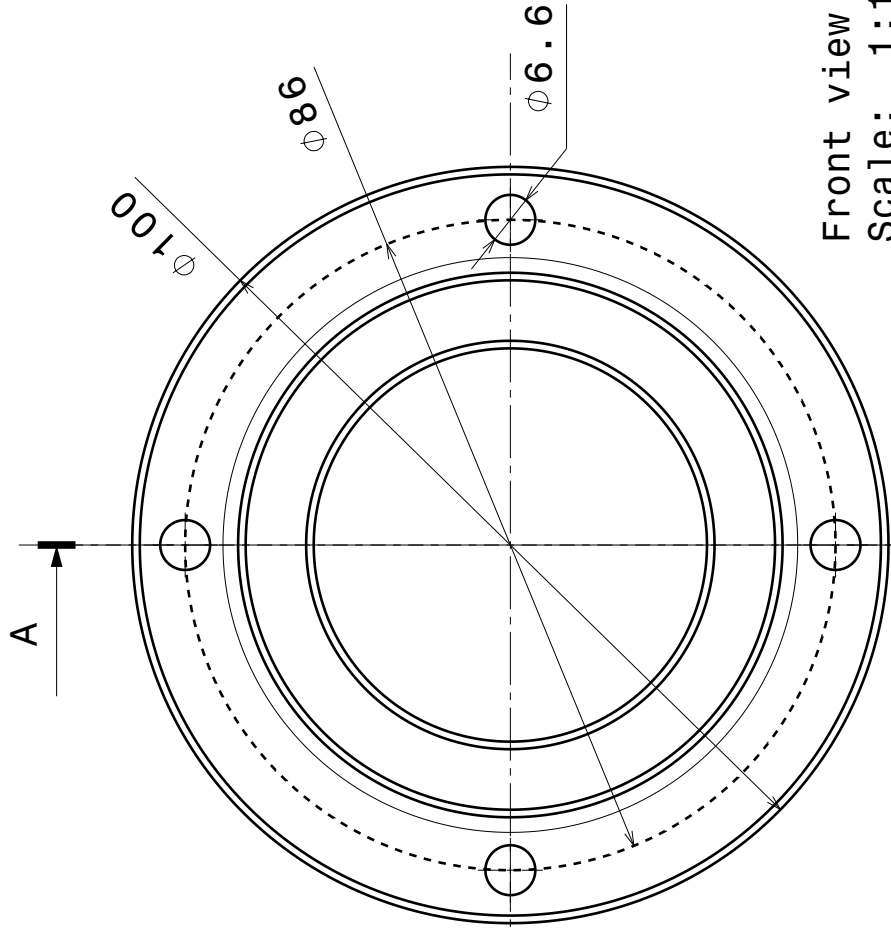
A

m

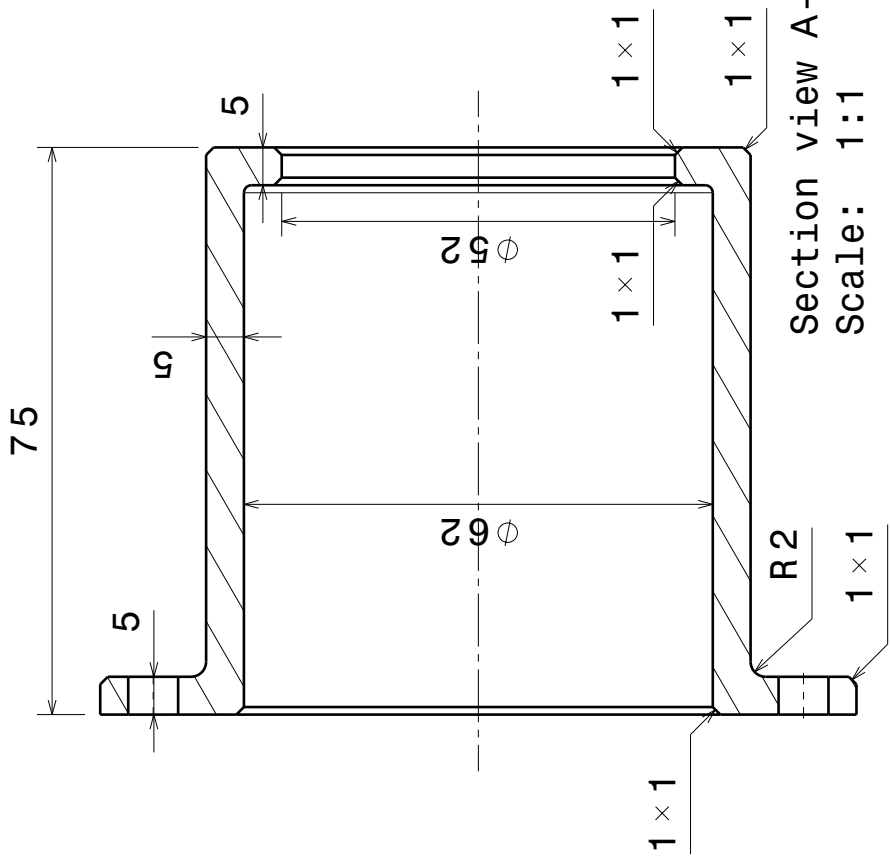
C

D

4 3 2 1



Isometric view
Scale: 1:3



Front view
Scale: 1:1

Section view A-A
Scale: 1:1

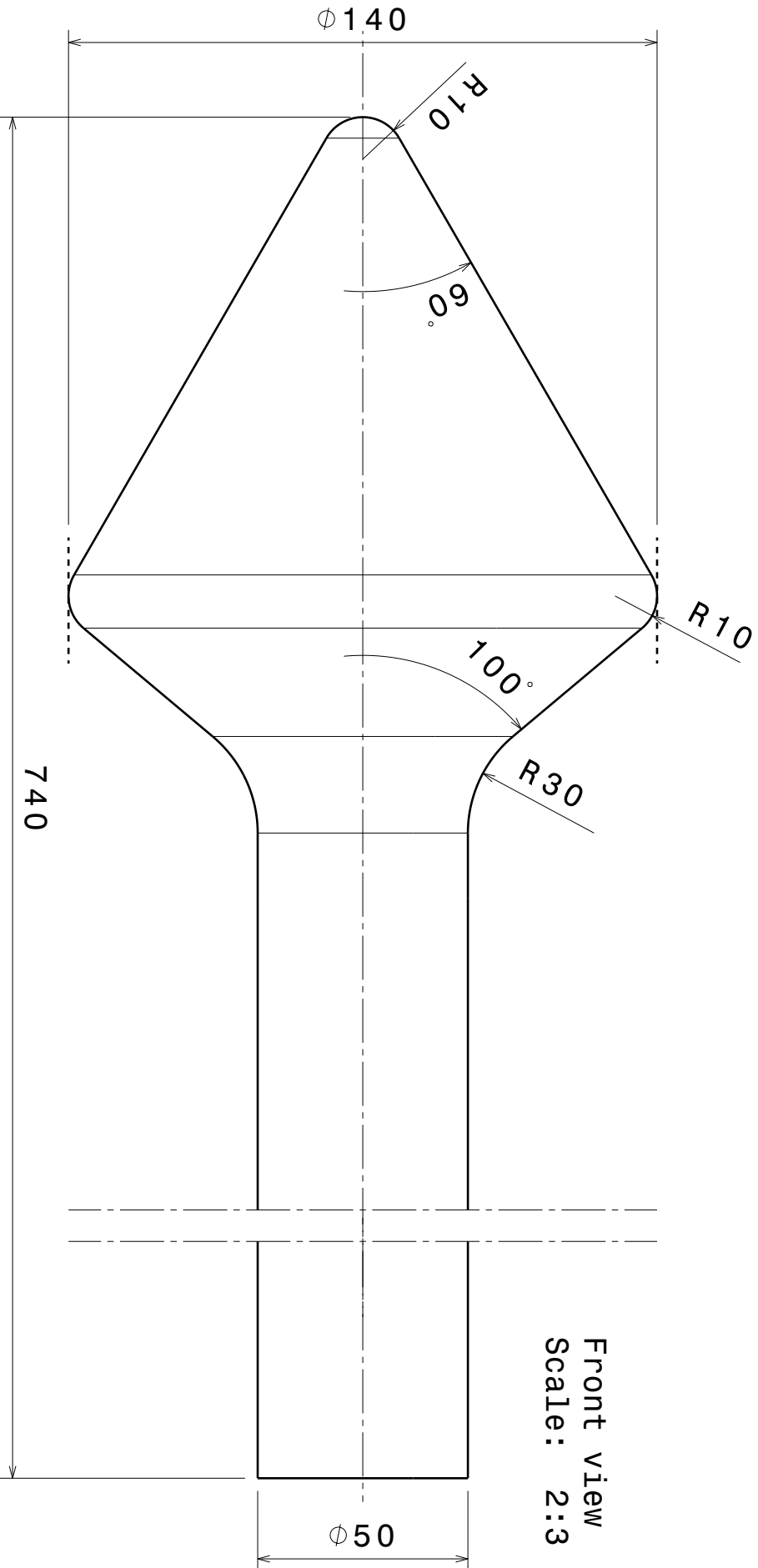
DESIGNED BY: B. Luyten	DATE: 27/06/2024	CHECKED BY: XXX	DATE: XXX	SIZE A4	SCALE 1:1	WEIGHT (kg) 0.27	DRAWING NUMBER LinearBearing_Cap	SHEET 1/1
Bearing Mounting Flange				ICARUS				
I	H	G	F	E	D	C	B	A
-	-	-	-	-	-	-	-	-

This drawing is our property; it can't be reproduced or communicated without our written agreement.

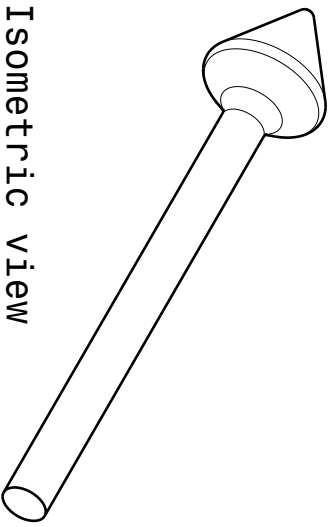
A

D

4 3 2 1



Front view
Scale: 2:3



Isometric view
Scale: 1:8

DESIGNED BY: B. Luyten		DRAWING NUMBER ICARUS		SHEET 1 / 1	
DATE: 27/06/2024		RLV Boom		SHEET	
CHECKED BY: XXX				A	
DATE: XXX		ICARUS		B	
SIZE A4				C	
SCALE 2:3		Boom		D	
WEIGHT (kg) 5.31				E	
DRAWING NUMBER ICARUS		ICARUS		F	
SHEET 1 / 1				G	
This drawing is our property; it can't be reproduced or communicated without our written agreement.		ICARUS		H	
				I	

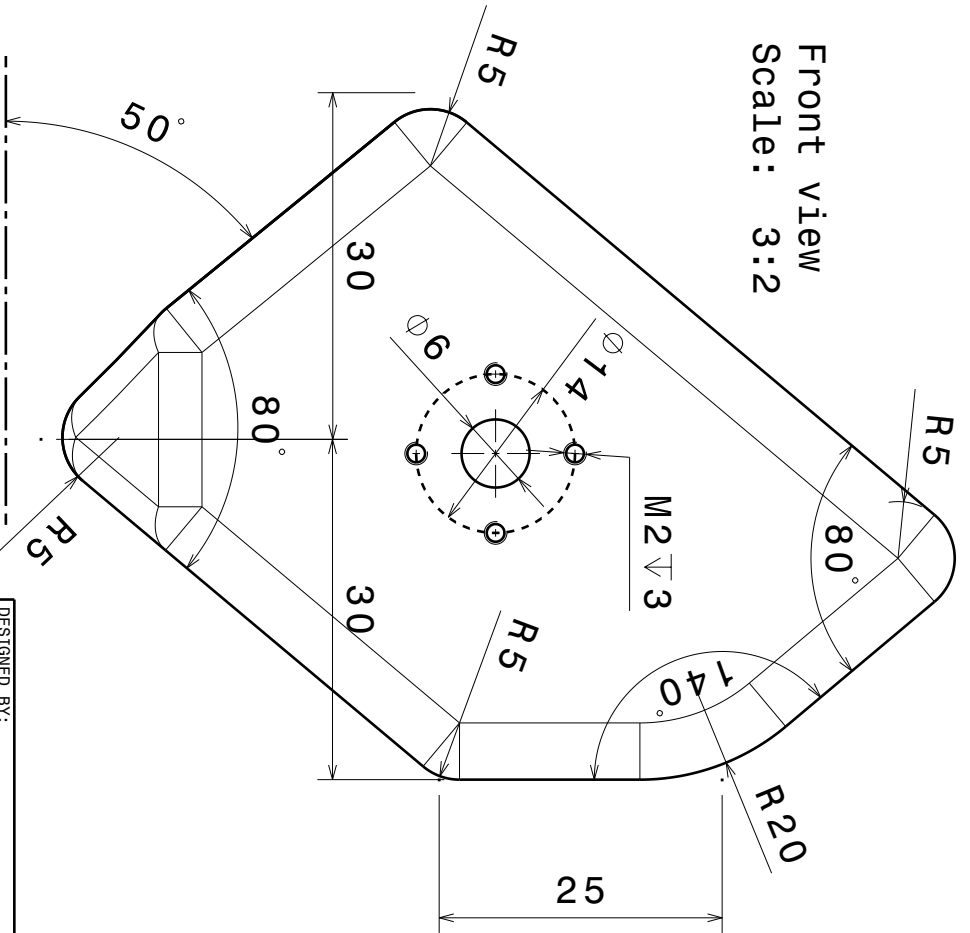
D

C

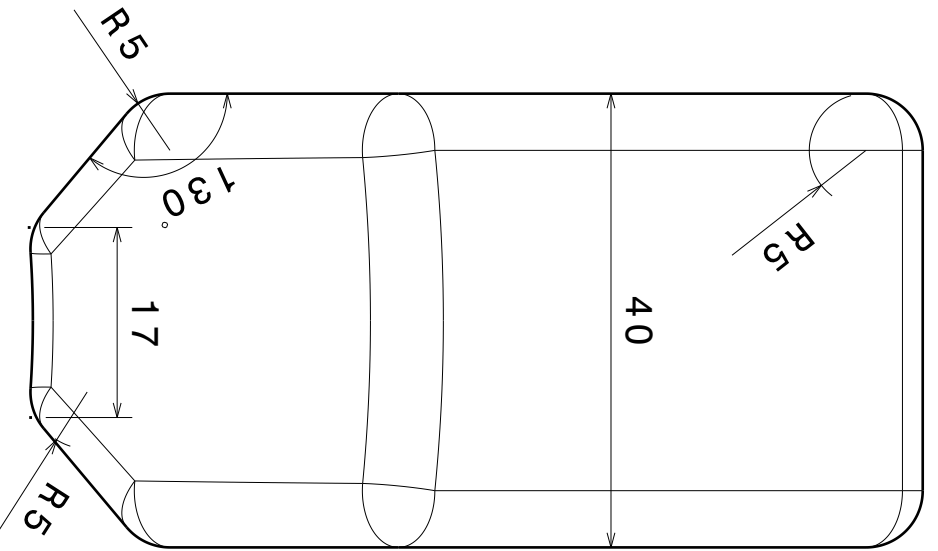
B

A

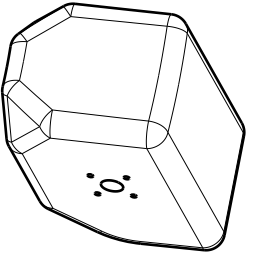
Front view
Scale: 3:2



Left view
Scale: 3:2



Isometric view
Scale: 1:2



Locking Wedge

ICARUS

DESIGNED BY:
B. Luyten

DATE:
27/06/2024

CHECKED BY:
XXX

DATE:
XXX

SIZE:
XXX

SCALE:
3:2



WEIGHT (KG)
0.29

DRAWING NUMBER

LockingWedge

SHEET

1 / 1

This drawing is our property; it can't be reproduced or communicated without our written agreement.

D

A

1

2

3

4

1

2

3

4

4 3 2 1

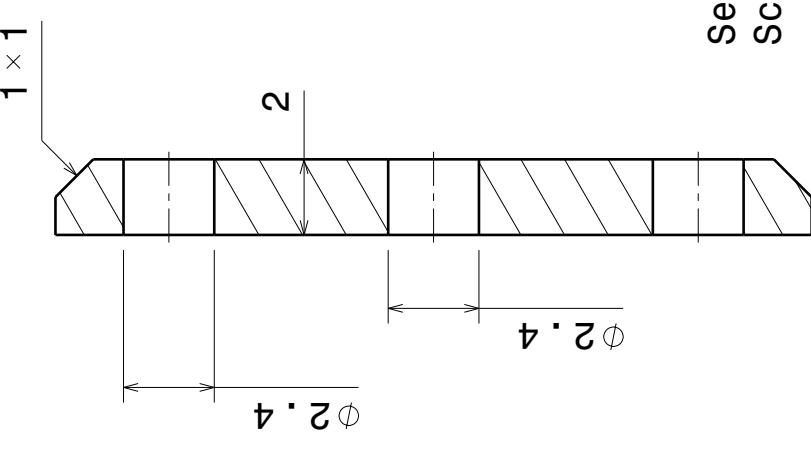
A

B

C

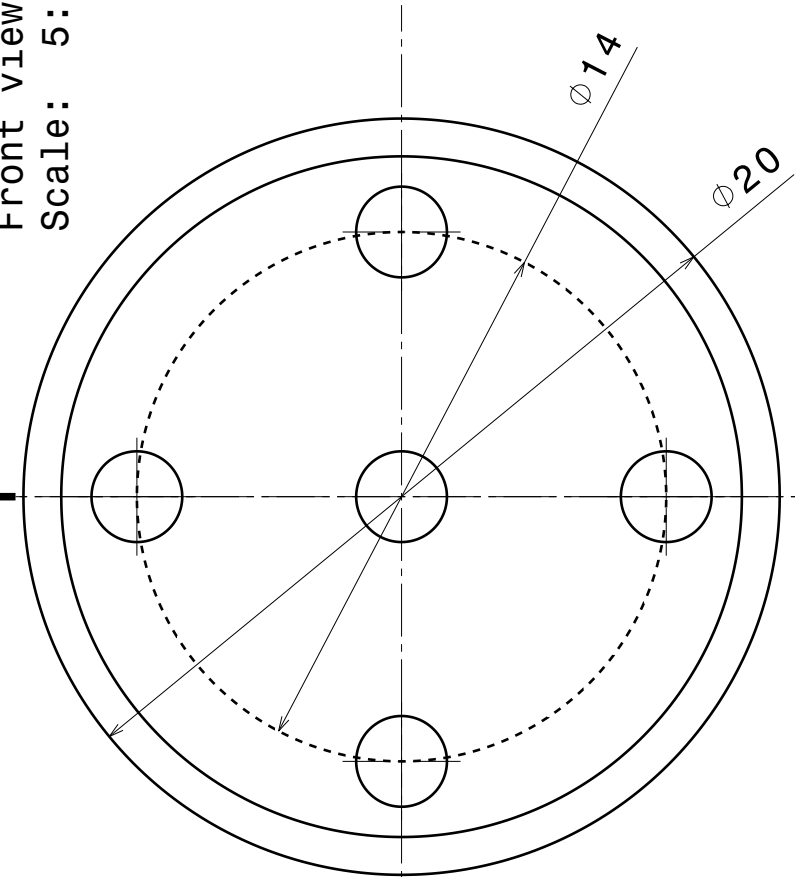
D

4 3 2 1

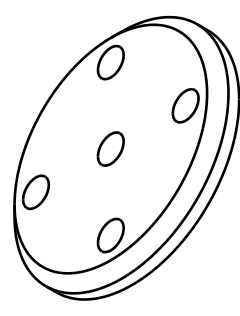


Section view A-A
Scale: 5:1

Front view
Scale: 5:1



Isometric view
Scale: 2:1



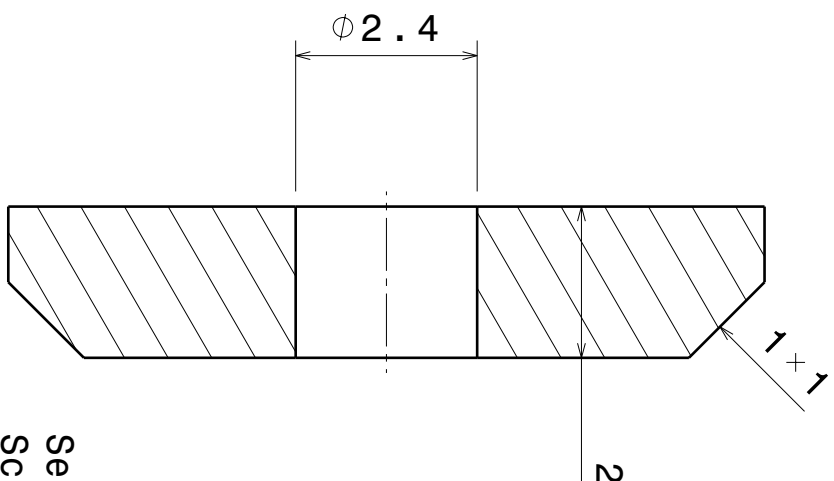
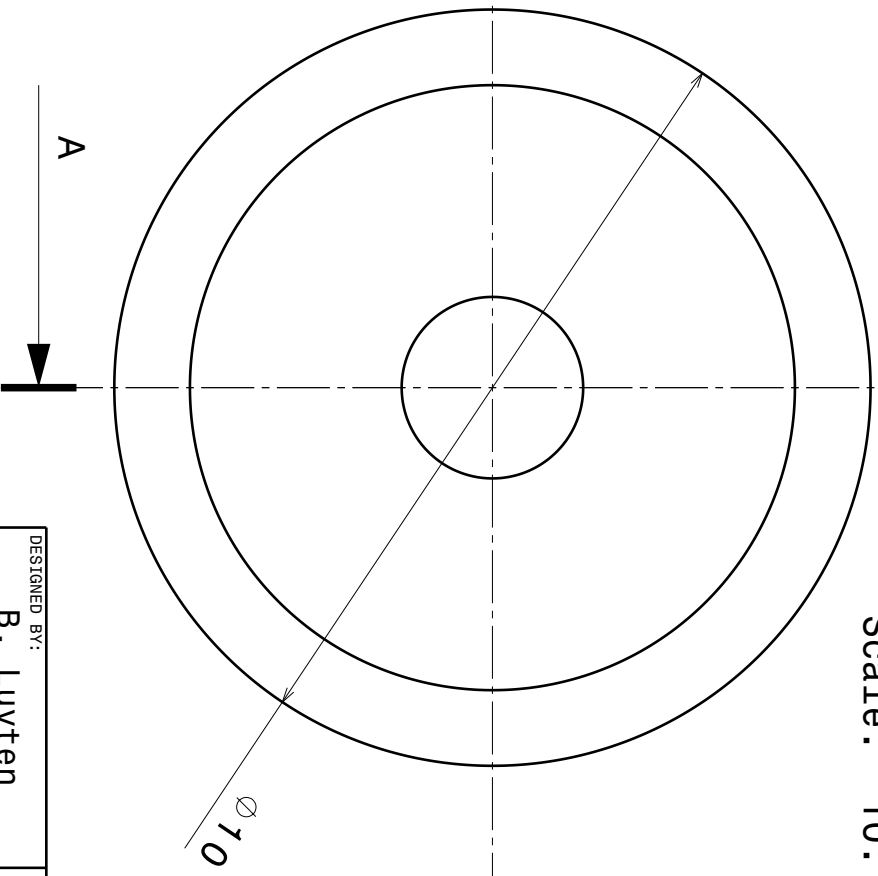
DESIGNED BY: B. Luyten	DATE: 27/06/2024	CHECKED BY: XXX	DATE: XXX	SIZE A4	WEIGHT (kg) 0.01	DRAWING NUMBER ActuatorWasher	SHEET 1/1																		
Locking Actuator Mounting Flange				ICARUS																					
<table border="1"> <tr> <td>I</td> <td>-</td> </tr> <tr> <td>H</td> <td>-</td> </tr> <tr> <td>G</td> <td>-</td> </tr> <tr> <td>F</td> <td>-</td> </tr> <tr> <td>E</td> <td>-</td> </tr> <tr> <td>D</td> <td>-</td> </tr> <tr> <td>C</td> <td>-</td> </tr> <tr> <td>B</td> <td>-</td> </tr> <tr> <td>A</td> <td>-</td> </tr> </table>								I	-	H	-	G	-	F	-	E	-	D	-	C	-	B	-	A	-
I	-																								
H	-																								
G	-																								
F	-																								
E	-																								
D	-																								
C	-																								
B	-																								
A	-																								

This drawing is our property; it can't be reproduced or communicated without our written agreement.

A

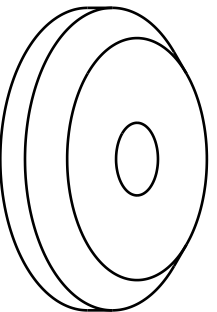
D

Front view
Scale: 10:1



Section view A-A
Scale: 10:1

Isometric view
Scale: 4:1



Locking Actuator Stop Flange

ICARUS

DESIGNED BY: B. Luyten	DATE: 27/06/2024	CHECKED BY: XXX	DATE: XXX	SIZE A4	WEIGHT (kg) 0.01	SCALE 10:1
---------------------------	---------------------	--------------------	--------------	------------	---------------------	---------------

DRAWING NUMBER ActuatorStopper		SHEET 1 / 1
-----------------------------------	--	----------------

This drawing is our property; it can't be reproduced or communicated without our written agreement.

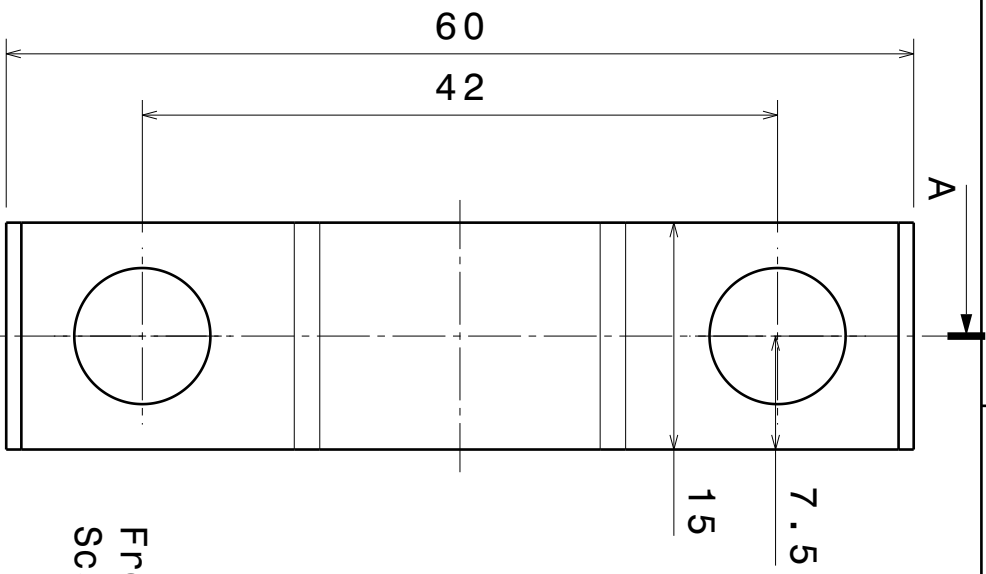
I	-
H	-
G	-
F	-
E	-
D	-
C	-
B	-
A	-

D

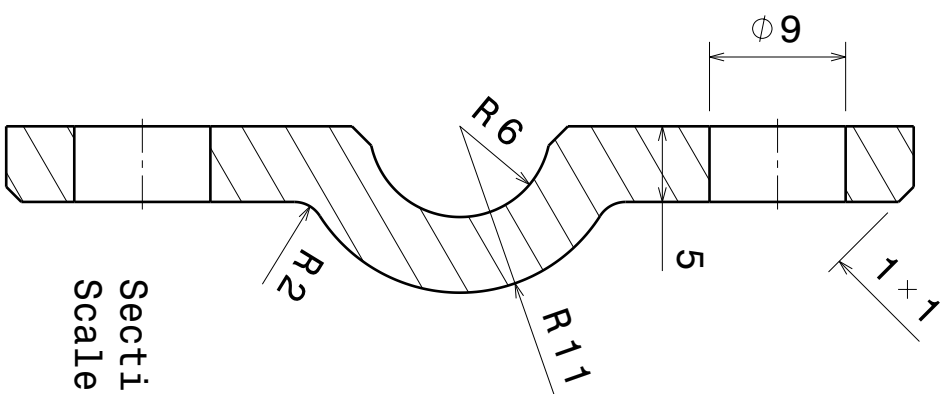
C

B

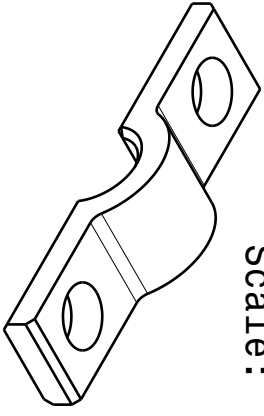
A



Front View
Scale: 2:1



Section view A-A
Scale: 2:1



Isometric view
Scale: 1:1

1

2

3

4

1

2

3

4

D

A

DESIGNED BY:

B. Luyten

DATE:

28/06/2024

CHECKED BY:

XXX

DATE:

XXX

SIZE

A4



SCALE

2:1

WEIGHT (kg)

0.01

DRAWING NUMBER

DockingCone Clamp

SHEET

1 / 1

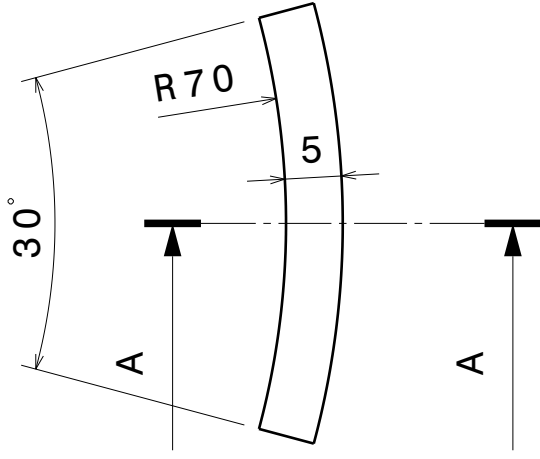
Guiding Cone Mounting Clamp

ICARUS

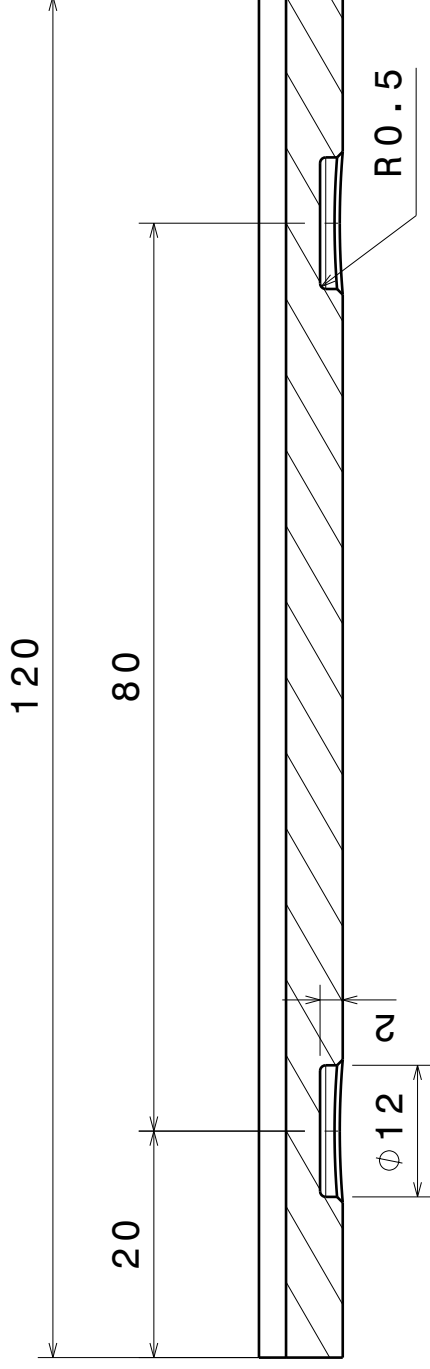
This drawing is our property; it can't be reproduced or communicated without our written agreement.

I	-
H	-
G	-
F	-
E	-
D	-
C	-
B	-
A	-

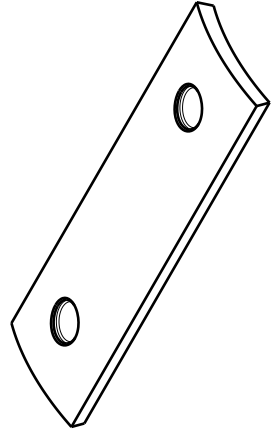
Front view
Scale: 3:2



Section view A-A
Scale: 3:2



Isometric view
Scale: 1:2



DESIGNED BY:

B. Luyten

DATE:

27/06/2024

CHECKED BY:

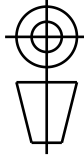
XXX

DATE:

XXX

SIZE

A4



WEIGHT (kg)

3:2 0.06

DRAWING NUMBER

HorizontalGuide

SHEET

1/1

DESIGNED BY:		B. Luyten	
DATE:		27/06/2024	
CHECKED BY:		XXX	
DATE:		XXX	
SIZE		A4	
WEIGHT (kg)		0.06	
DRAWING NUMBER		HorizontalGuide	
SHEET		1/1	
I	-		
H	-		
G	-		
F	-		
E	-		
D	-		
C	-		
B	-		
A	-		

This drawing is our property; it can't be reproduced or communicated without our written agreement.

4

3

2

1

4

3

2

1

A

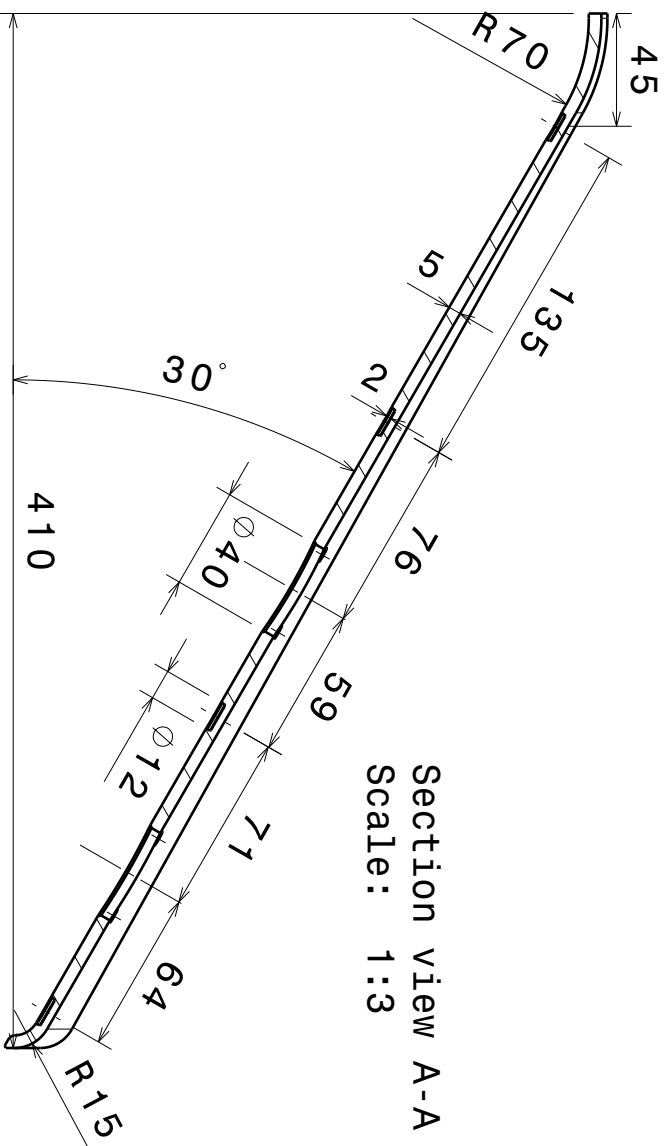
B

C

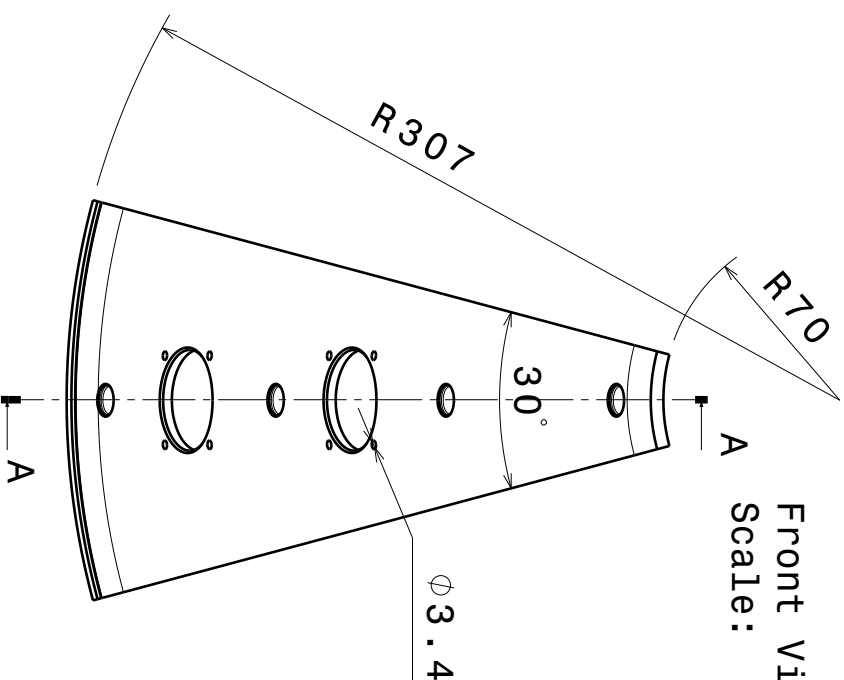
D

A

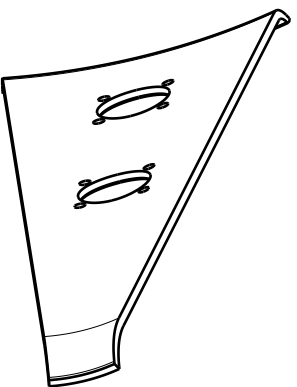
D



Section view A-A
Scale: 1:3



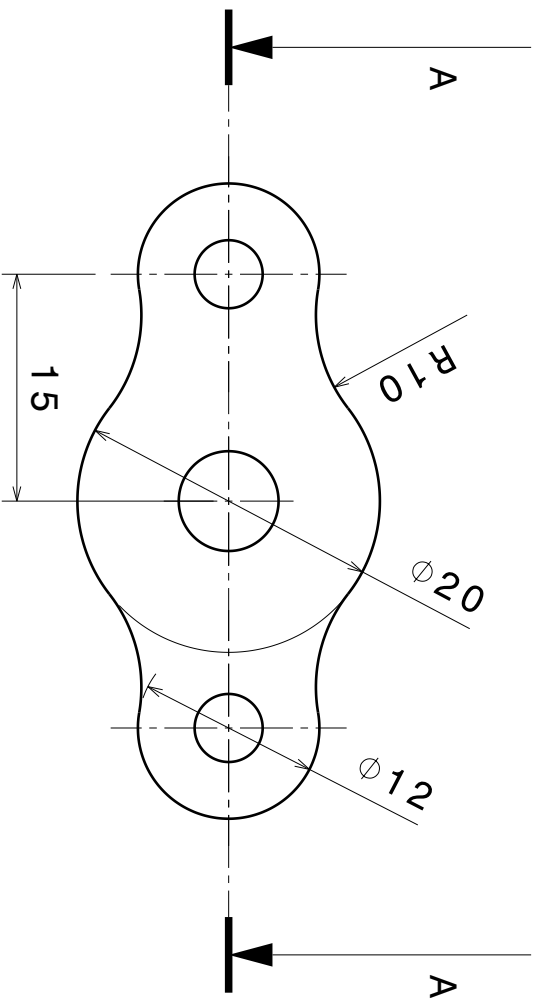
Front View
Scale: 1:3



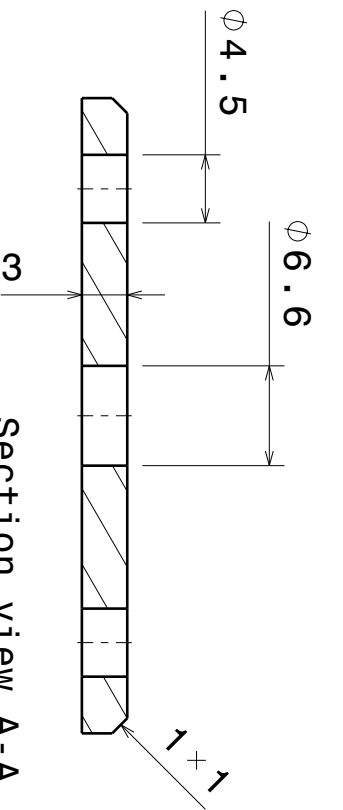
Isometric view
Scale: 1:4

DESIGNED BY: B. Luyten	Conical Guide w/ Beacons	
DATE: 27/06/2024		
CHECKED BY: XXX	ICARUS	
DATE: XXX		
SIZE: A4	ConicalGuide BothBeacons	
SCALE: 1:3		
WEIGHT (kg): 0.57	1 / 1	
DRAWING NUMBER: ConicalGuide BothBeacons		
This drawing is our property; it can't be reproduced or communicated without our written agreement.		

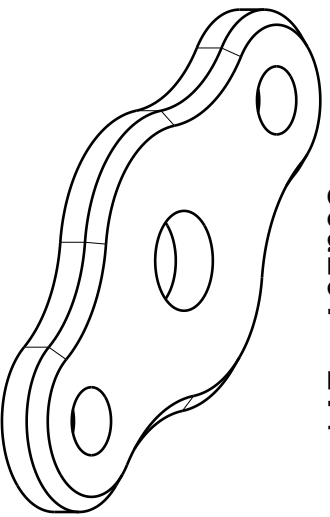
I	-
H	-
G	-
F	-
E	-
D	-
C	-
B	-
A	-



Front view
Scale: 2:1



Section view A-A
Scale: 2:1

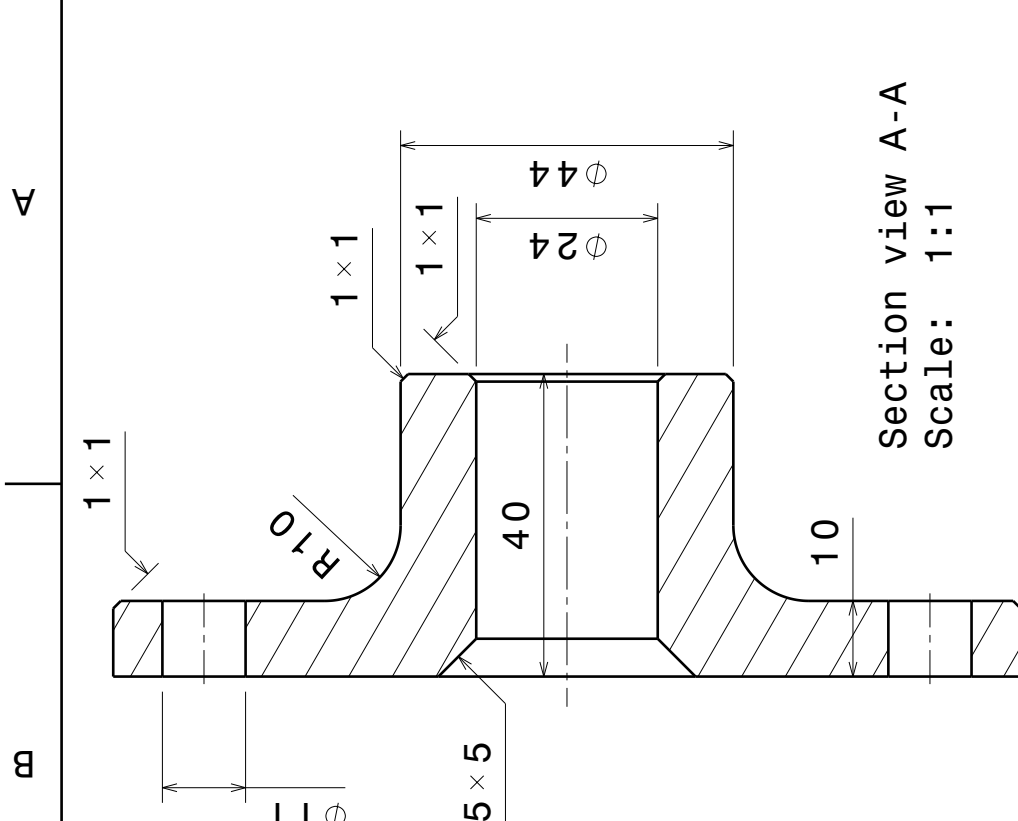


Isometric view
Scale: 2:1

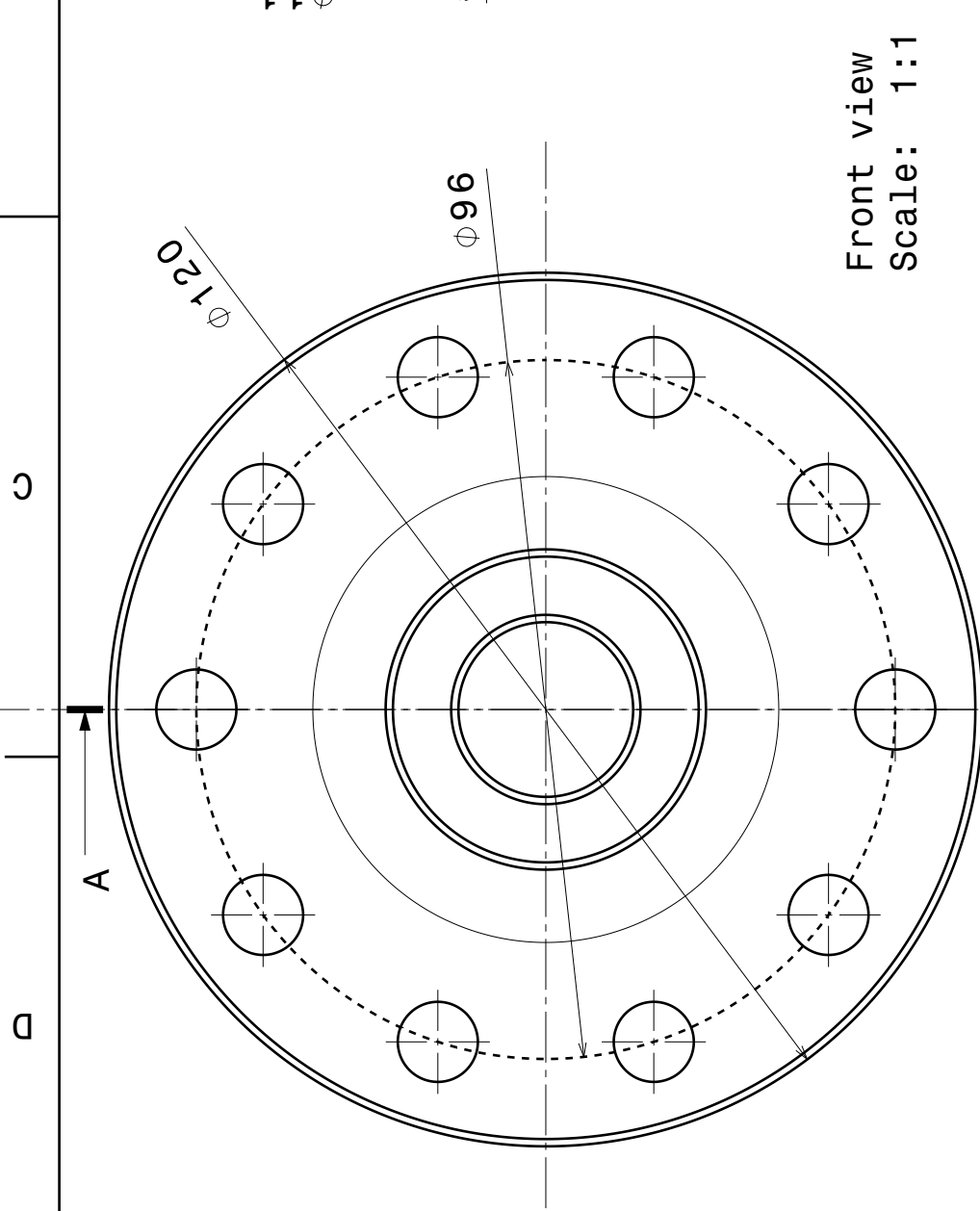
DESIGNED BY: B. Luyten		<h1>Spring Mounting Plate</h1>	
DATE: 27/06/2024			
CHECKED BY: XXX		<h2>ICARUS</h2>	
DATE: XXX			
SIZE: A4		Dockingspring Washer	
SCALE: 2:1	WEIGHT (kg): 0.01		
DRAWING NUMBER		SHEET	
		1 / 1	
This drawing is our property; it can't be reproduced or communicated without our written agreement.			

I	-
H	-
G	-
F	-
E	-
D	-
C	-
B	-
A	-

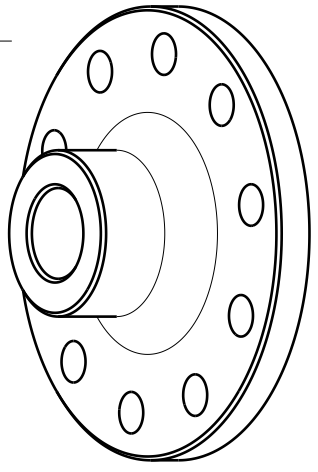
4 3 2 1



Front view
Scale: 1:1



Isometric view
Scale: 1:2



I	-
H	-
G	-
F	-
E	-
D	-
C	-
B	-
A	-

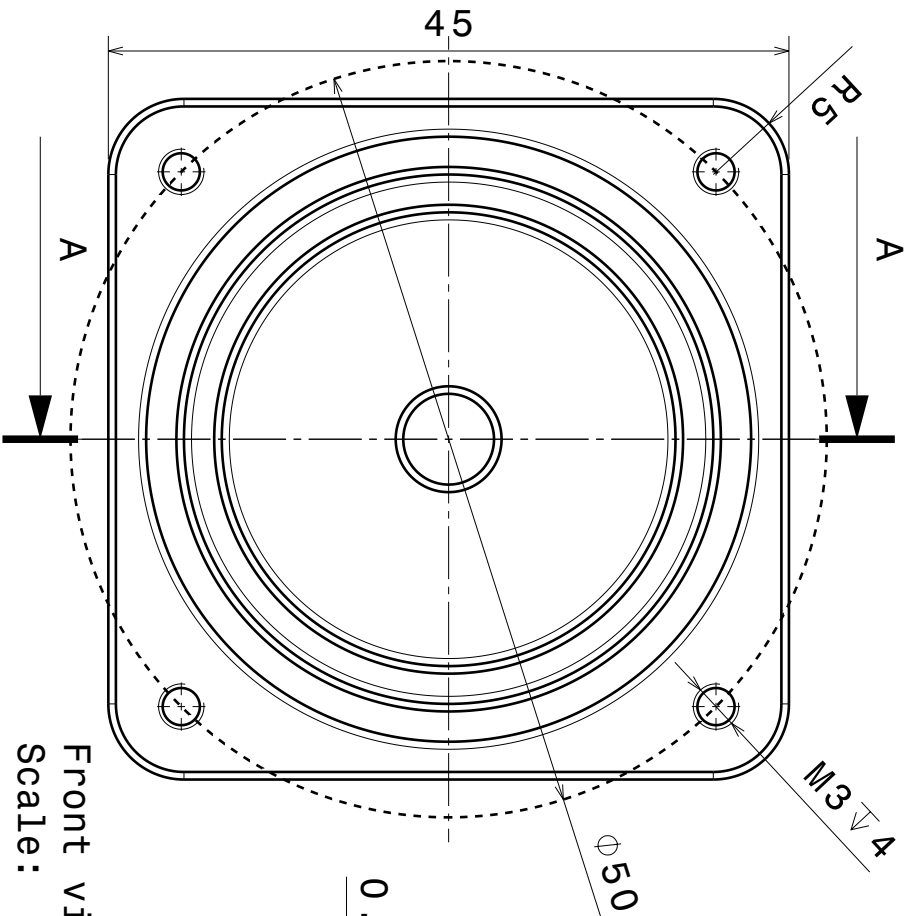
DESIGNED BY: B. Luyten		DATE: 27/06/2024	
CHECKED BY: XXX		DATE: XXX	
SIZE A4		DRAWING NUMBER ReleaseFlange	
SCALE 1:1	WEIGHT (kg) 0.36	SHEET 1/1	

Release Flange

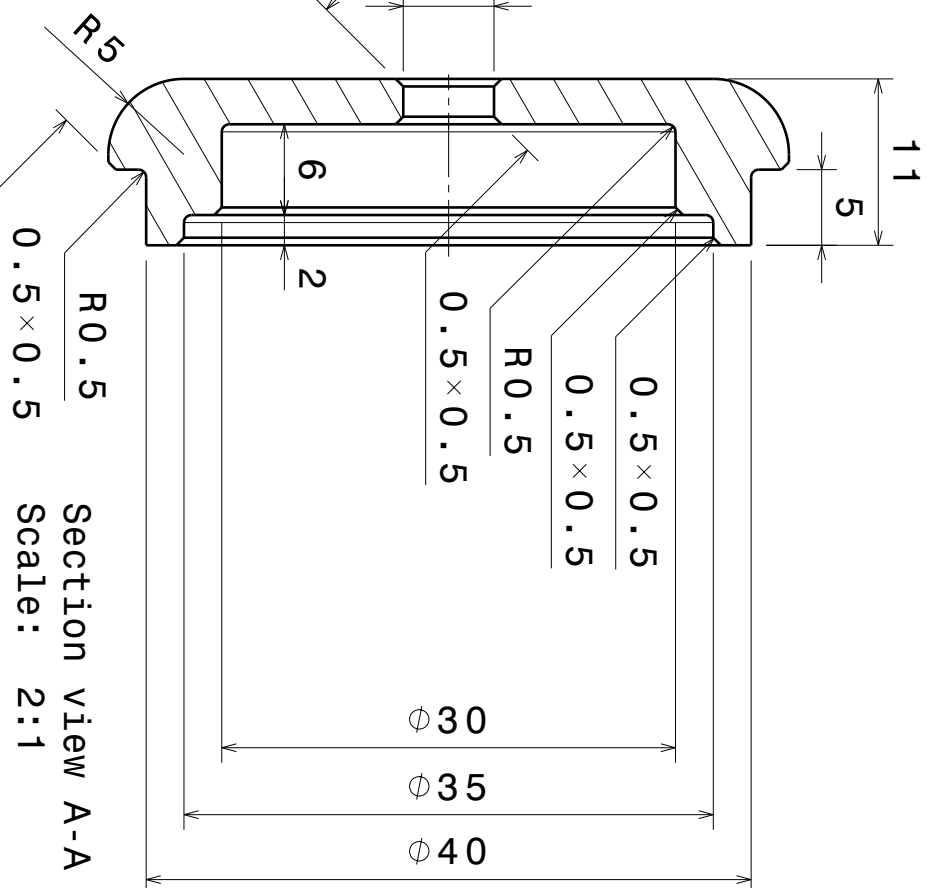
ICARUS

This drawing is our property; it can't be reproduced or communicated without our written agreement.

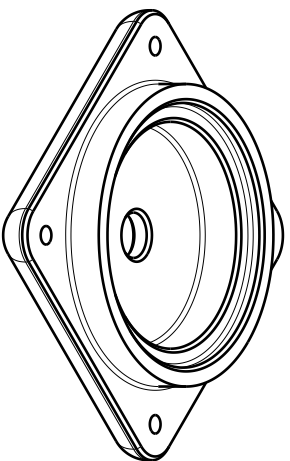
4 3 2 1



Front view
Scale: 2:1



Section view A-A
Scale: 2:1



Isometric view
Scale: 1:1

DESIGNED BY:

B. Luyten

DATE:

27/06/2024

CHECKED BY:

XXX

DATE:

XXX

SIZE:

A4



SCALE:

2:1

WEIGHT (kg):

0.01

DRAWING NUMBER:

Beacon Case

SHEET:

1/1

Beacon Case

ICARUS

This drawing is our property; it can't be reproduced or communicated without our written agreement.

I	-
H	-
G	-
F	-
E	-
D	-
C	-
B	-
A	-

D

C

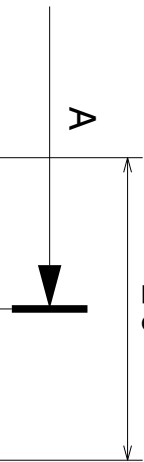
B

A

4

A

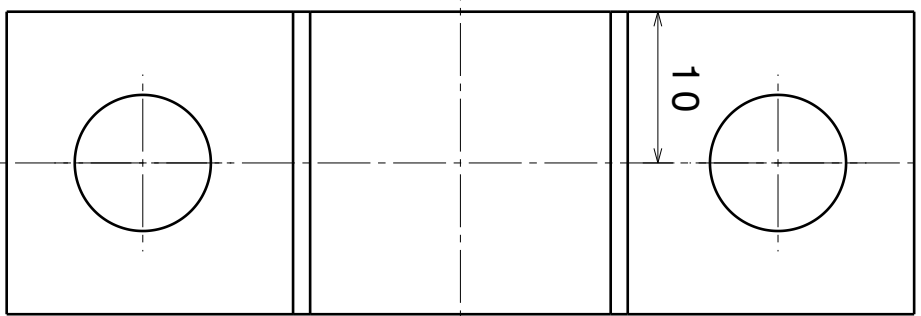
20



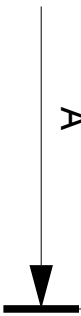
3

10

60

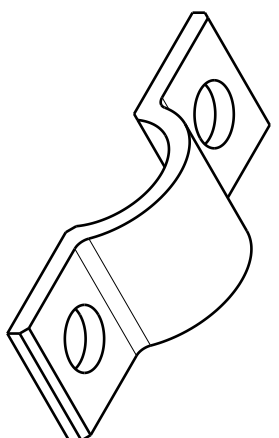


A



Front view
Scale: 2:1

D

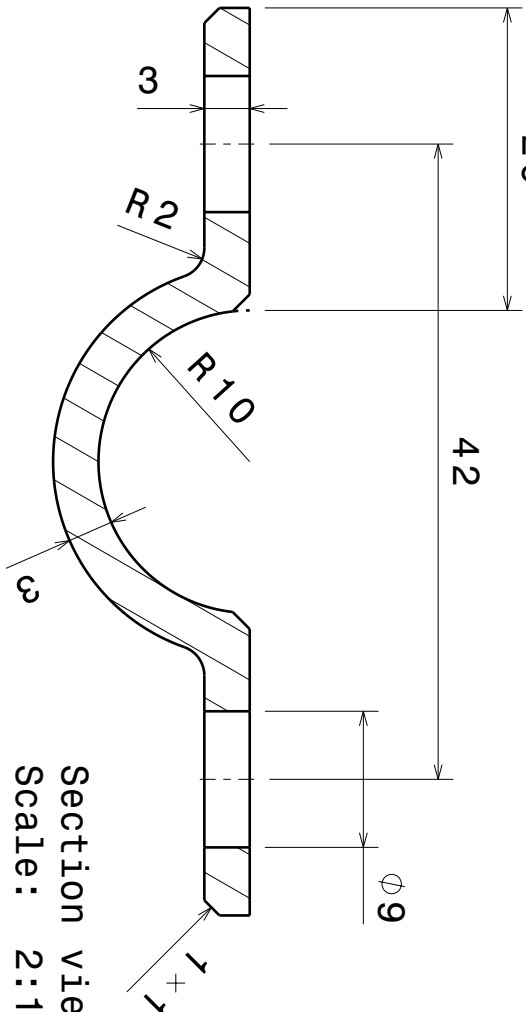


Isometric view
Scale: 1:1

20

42

$\phi 9$



Section view A-A
Scale: 2:1

2

DESIGNED BY:

B. Luyten

DATE:

27/06/2024

CHECKED BY:

XXX

DATE:

XXX

SIZE

A4



SCALE

2:1

WEIGHT (kg)

0.01

DRAWING NUMBER

AvionicsMount clamp

SHEET

1 / 1

Avionics Mounting Clamp

ICARUS

This drawing is our property; it can't be reproduced or communicated without our written agreement.

I	-
H	-
G	-
F	-
E	-
D	-
C	-
B	-
A	-

1

2

3

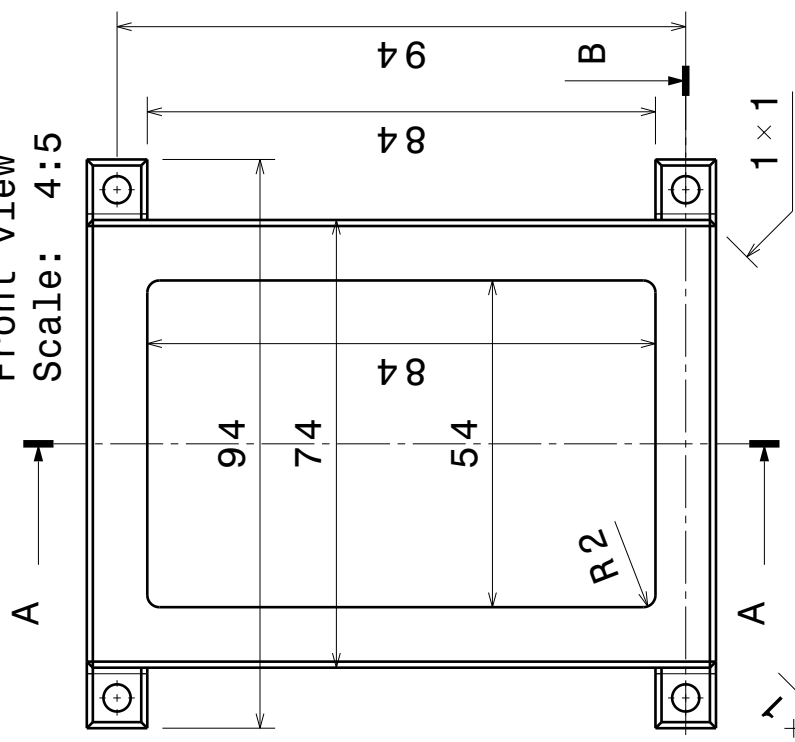
4

A

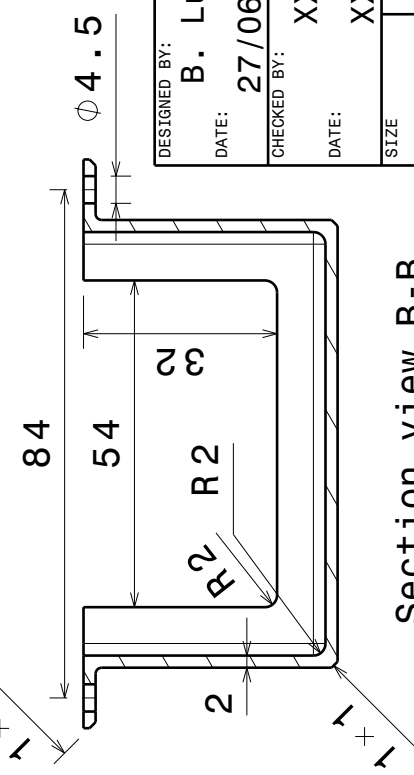
4 3 2 1

A B C D

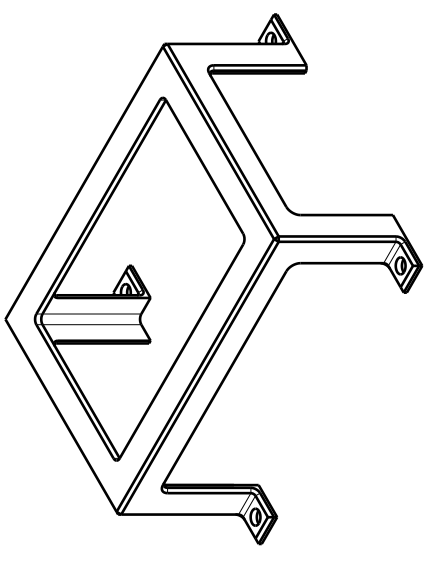
Front view
Scale: 4:5



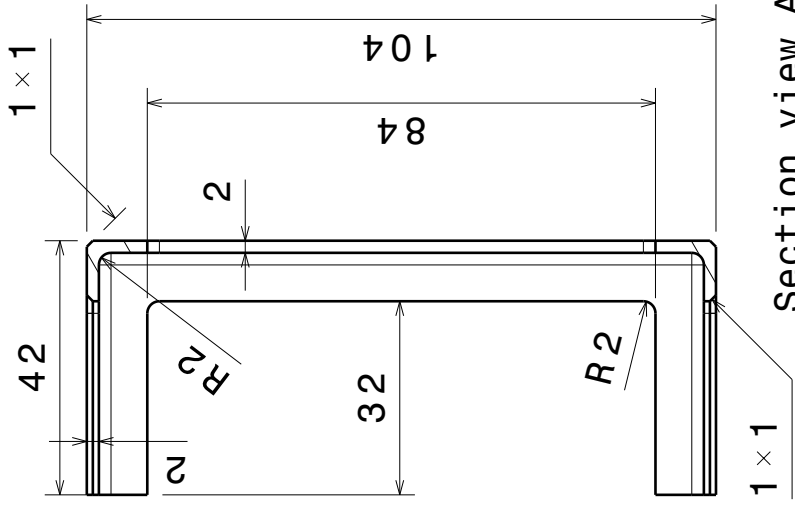
Section view B-B
Scale: 4:5



Isometric view
Scale: 1:2



Section view A-A
Scale: 4:5



DESIGNED BY: B. Luyten
DATE: 27/06/2024
CHECKED BY: XXX
DATE: XXX

SIZE: A4
SCALE: 4:5
WEIGHT (kg): 0.05



DRAWING NUMBER

Battery Bracket

SHEET

1/1

I	-
H	-
G	-
F	-
E	-
D	-
C	-
B	-
A	-

This drawing is our property; it can't be reproduced or communicated without our written agreement.

4 3 2 1

A B C D